

Springer Proceedings in Physics 395

Hexu Sun · Wei Pei · Yan Dong ·
Hongmei Yu · Shi You *Editors*

Proceedings of the 10th Hydrogen Technology Convention, Volume 3

WHTC 2023, 22–26 May, Foshan, China

 Springer

Indexed by Scopus

The series Springer Proceedings in Physics, founded in 1984, is devoted to timely reports of state-of-the-art developments in physics and related sciences. Typically based on material presented at conferences, workshops and similar scientific meetings, volumes published in this series will constitute a comprehensive up to date source of reference on a field or subfield of relevance in contemporary physics. Proposals must include the following:

- Name, place and date of the scientific meeting
- A link to the committees (local organization, international advisors etc.)
- Scientific description of the meeting
- List of invited/plenary speakers
- An estimate of the planned proceedings book parameters (number of pages/articles, requested number of bulk copies, submission deadline).

Please contact:

For Americas and Europe: Dr. Zachary Evenson; zachary.evenson@springer.com

For Asia, Australia and New Zealand: Dr. Loyola DSilva; loyola.dsilva@springer.com

Hexu Sun · Wei Pei · Yan Dong · Hongmei Yu ·
Shi You
Editors

Proceedings of the 10th Hydrogen Technology Convention, Volume 3

WHTC 2023
22–26 May, Foshan, China

 Springer

Editors

Hexu Sun
Hebei University of Science and Technology
Shijiazhuang, China

Yan Dong
Department of New Energy Science
and Engineering
Hebei University of Technology
Tianjin, China

Shi You
Department of Wind and Energy Systems
Technical University of Denmark
Kongens Lyngby, Denmark

Wei Pei
Power Grid Sciences and Technology Lab
Institute of Electrical Engineering
Beijing, China

Hongmei Yu
Department of Fuel Cells
Dalian Institute of Chemical Physics
Chinese Academy of Sciences
Dalian, China

ISSN 0930-8989

ISSN 1867-4941 (electronic)

Springer Proceedings in Physics

ISBN 978-981-99-8580-7

ISBN 978-981-99-8581-4 (eBook)

<https://doi.org/10.1007/978-981-99-8581-4>

© The Editor(s) (if applicable) and The Author(s), under exclusive license to Springer Nature Singapore Pte Ltd. 2024

This work is subject to copyright. All rights are solely and exclusively licensed by the Publisher, whether the whole or part of the material is concerned, specifically the rights of translation, reprinting, reuse of illustrations, recitation, broadcasting, reproduction on microfilms or in any other physical way, and transmission or information storage and retrieval, electronic adaptation, computer software, or by similar or dissimilar methodology now known or hereafter developed.

The use of general descriptive names, registered names, trademarks, service marks, etc. in this publication does not imply, even in the absence of a specific statement, that such names are exempt from the relevant protective laws and regulations and therefore free for general use.

The publisher, the authors, and the editors are safe to assume that the advice and information in this book are believed to be true and accurate at the date of publication. Neither the publisher nor the authors or the editors give a warranty, expressed or implied, with respect to the material contained herein or for any errors or omissions that may have been made. The publisher remains neutral with regard to jurisdictional claims in published maps and institutional affiliations.

This Springer imprint is published by the registered company Springer Nature Singapore Pte Ltd. The registered company address is: 152 Beach Road, #21-01/04 Gateway East, Singapore 189721, Singapore

Paper in this product is recyclable.

Preface

The 10th World Hydrogen Technology Convention (WHTC2023), organized by the International Association for Hydrogen Energy, China Association for Science and Technology and China Machinery Industry Federation was held in Foshan, Guangdong Province, China, during 23–26 May 2023.

These proceedings highlight the latest advances in fundamental research, technologies and applications of hydrogen energy and fuel cells. In recent years, energy conversion between electricity and hydrogen energy has attracted increasing attention as a way to adjust the load of the grid. These conference records discuss and exchange cutting-edge findings and technological developments in fields such as new proton exchange membrane electrolyzers, new electrode materials and catalysts, renewable energy, off-grid/grid-connected water electrolysis for hydrogen production, key materials and components of fuel cells, high-temperature solid oxide water electrolysis, energy storage technologies and research, CO₂ hydrogenation to methanol, nitrogen to ammonia and other applications with industrial potential.

The main topics of the proceedings include but are not limited to:

- (1) Policies and strategies for hydrogen energy and fuel cells;
- (2) Advanced proton exchange membranes, electrodes and catalyst materials for water electrolysis;
- (3) Advanced hydrogen compression, storage, transportation and distribution technologies;
- (4) Safety and related standards; and
- (5) Manufacture and R&D of key materials and components of fuel cells and stack systems.

Shijiazhuang, China
Beijing, China
Tianjin, China
Dalian, China
Kongens Lyngby, Denmark

Hexu Sun
Wei Pei
Yan Dong
Hongmei Yu
Shi You

Contents

| | |
|---|----|
| Numerical Research on the Impact of Sloshing Frequencies of a Liquid Hydrogen Tank Under Massive Heat Leakage Conditions | 1 |
| <i>Shihao Li, Ye Liu, Wei Wei, Yan Yan, and Zhonghua Ni</i> | |
| Review of Liquid Hydrogen Leakage: Factors and Safety Measures | 7 |
| <i>Bowen Liang, Yuan Gao, Huanxia Wei, Tong Zhang, and Yongping Hou</i> | |
| Study on the Poisoning and Fine-Powdering Resistance Mechanism of SiO ₂ -Coating on La-Ni Hydrogen Storage Alloy | 20 |
| <i>Xiumei Guo, Hongqiang Shi, Zhinian Li, Baolong Yuan, Wu Yuanfang, Shumao Wang, and Lijun Jiang</i> | |
| Study on Energy Management Strategy for Reducing Equivalent Hydrogen Consumption in a Combined Heat and Power System Based on PEMFC | 28 |
| <i>Ruitao Li, Haolin Wang, Naiyuan Yao, Zishun Xu, and Tiancai Ma</i> | |
| A New Perspective on the Influence of the Electrolytic Bubbles on the Pressure Drop in the Vertical Pipe Flow | 44 |
| <i>Liandong Sha, Ruomei Qi, and Jin Lin</i> | |
| Capacity Optimization Method for Off-Grid Photovoltaic Hydrogen Production System Based on Improved Honeybadger Algorithm | 52 |
| <i>Hongcan Ma, Yan Dong, and Bin Liu</i> | |
| Design of PEMFC Stack Intelligent Diagnosis System Based on Improved Neural Network | 59 |
| <i>Huipeng Chen, Wenhua Luo, Dongting Pan, Shaopeng Zhu, Ping Chen, and Congxin Li</i> | |
| An Optimal Dispatch Method for the Hydrogen-Electric Coupled Energy Microgrid | 69 |
| <i>Yanda Huo, Zhen Wu, Jianfeng Dai, Wei Duan, Hao Zhao, Jintao Jiang, and Riwu Yao</i> | |
| Marine Scheme and Experimental Study of Liquid Organic Hydrogen Carrier Technology | 76 |
| <i>Zhen Wang, Zengshi Xu, Rui Chen, and Yuanting Peng</i> | |

| | |
|---|-----|
| Research on Sampling and Analysis Methods for Trace Particulate in Hydrogen Fuel | 91 |
| <i>Xiaolu Chen, Xiaomin Liu, Yanmei Yang, Miaomiao Huo, Juan Wang, Wei Bao, and Ling Lin</i> | |
| IrNi Nanoparticles as Highly Efficient Electrocatalysts Towards the Oxygen Evolution Reaction in an Acidic Medium | 99 |
| <i>Yongwen Sun, Hong Lv, Dingyun Gao, and Cunman Zhang</i> | |
| Estimation of the Volume Flow Rate at the Anode Side of Hydrogen Fuel Cells | 108 |
| <i>Xing Huang, Ke Song, Zhen Cai, and Feiqiang Li</i> | |
| The Energy Consumption Method Based on Synthetic Optimization of Speed and Power Allocation for Fuel Cell-Battery Hybrid Tramway | 117 |
| <i>Guorui Zhang</i> | |
| Research on Safety Management Mode of Hydrogen Fuel Cell Vehicle Demonstration Operation Based on Intrinsic Safety Control | 126 |
| <i>Guozhu Liu, Yao Lu, Liming Wang, Yuzhe Gao, and Yupeng Yang</i> | |
| Study on the Effect of Hydrogen Doping Ratio on the Operating Characteristics of Hydrogen-Rich Gas Turbine | 136 |
| <i>Yongyi Li, Yingqi Liang, and Yi Cai</i> | |
| Modeling of a Stand-Alone Microgrid Based on Solar-Hydrogen Energy Systems for the Design of Energy Management Systems | 150 |
| <i>Zipeng Hou, Fengxiang Chen, Yafeng Guo, Tiande Mo, Yu Li, and Fenglai Pei</i> | |
| Coordinated Control Technology for Multi-stack Fuel Cell System | 159 |
| <i>Duankai Li and Guorui Zhang</i> | |
| Global Hydrogen Refueling Infrastructures Development Evaluation in 2022 | 166 |
| <i>Wei Liu, Yanming Wan, Yan Zhang, and Hanchen Lin</i> | |
| Grid-Connected PV-Hydrogen Systems Providing Secondary Frequency Regulation: Modeling, Controller Design and Verification | 174 |
| <i>Mingjun Zhang, Xiang Cheng, Liandong Sha, Jin Lin, Weijie Qian, and Weiliang Liu</i> | |
| Ortho- to Para-Hydrogen Spin Conversion Performance of Ho-Fe ₂ O ₃ Catalytic at 77 K | 186 |
| <i>Hong Xu, Jiawei Wang, Yisong Han, Mingzhe Xue, and Cunman Zhang</i> | |

| | |
|---|-----|
| Optimal Scheduling for Integrated Hydrogen Production System Based on Exergy Analysis | 195 |
| <i>Mengshu Zhu, Zhiyao Zhong, Jiakun Fang, and Xiaomeng Ai</i> | |
| Fault Diagnosis of PEMFC Stack Based on PSO-DBN | 206 |
| <i>Shaopeng Zhu, Bo Zhang, Liming Wang, Ping Chen, Huipeng Chen, and Yekai Xu</i> | |
| Impact of Operational Parameters on Shutdown Characteristic of Industrial AWE Cell | 217 |
| <i>Danji Huang, Ang Lu, Xiaomeng Ai, Zhiyao Zhong, Kewei Hu, and Jiakun Fang</i> | |
| Performance Analysis Based on Energetic and Exergetic Ecological Index of a High-Temperature Proton Exchange Membrane Fuel Cell | 226 |
| <i>Zhaoda Zhong, Samuel Simon Araya, and Vincenzo Liso</i> | |
| Dynamically Fed Anion-Conducting Matrix-Based Water Electrolyzer | 234 |
| <i>Dmitry G. Kondratyev, Konstantin G. Bolshakov, Alexander S. Stikhin, Vladimir I. Matrenin, and Mikhail A. Aboimov</i> | |
| Thermal Insulation Simulation of Small Proton Exchange Membrane Fuel Cell | 243 |
| <i>Zhifei Fang, Jiaxu Zhou, and Huichao Deng</i> | |
| Investigation of the Effect of Operating Conditions on the Polarization Process of Proton Exchange Membrane Fuel Cells Based on the Distribution of Relaxation Times Using Orthogonal Test Method | 250 |
| <i>Tiancai Ma, Ziheng Gu, Chang Du, Jinxuan Qi, and Juexiao Chen</i> | |
| Development of 130 kW Self-Humidifying Proton Exchange Membrane Fuel Cell System | 262 |
| <i>Tiancai Ma, Jixuan Qi, Ziheng Gu, Chang Du, and Weikang Lin</i> | |
| A Neural Network Based PEMFC Dynamic Model for Hardware-in-the-Loop Application | 275 |
| <i>Naiyuan Yao, Tiancai Ma, Ruitao Li, Kun Yuan, Weikang Lin, and Yonghao Liang</i> | |
| Hydrogen Energy Application in Rail Transit Under the “Double Carbon” Strategy: The State of the Art and Prospects | 288 |
| <i>Liang Jianying</i> | |

Optimization of the Hollow Shaft in an Air Compressor Rotor
for Hydrogen Fuel Cell 304
Shang Sang, Wei Ni, Ming Cheng, and Zhixue He

Numerical Simulation of a Two-Stage Centrifugal Air Compressor
Cooling Structure for Hydrogen Fuel Cells 315
Cheng Yang, Wei Ni, Cong Pang, and Zhixue He

PEMFC Seal Design and Optimization by Taking into Account of Gasket
Shape Profile and Stack-Up Assembly Tolerance 325
Zhicheng Cao, Wenfeng Zhu, Zhiguo Cheng, Zhen Yang, and Yue Fang

Research on the Scale Coefficient in the Interface Leakage Rate
Multi-scale Model and the Performance Study of the Gasket-BPP Sealing
Interface in PEMFCs 335
Zhen Yang, Wenfeng Zhu, Zhiguo Cheng, and Zhicheng Cao

Author Index 345

Contributors

Mikhail A. Aboimov TVEL JSC, Novouralsk, Russia

Xiaomeng Ai State Key Laboratory of Advanced Electromagnetic Engineering and Technology, School of Electrical and Electronic Engineering, Huazhong University of Science and Technology, Wuhan, China

Samuel Simon Araya AAU Energy, Aalborg University, Aalborg, Denmark

Wei Bao China National Institute of Standardization, Beijing, China;
Foshan Green Development Innovation Research Institute, Foshan, China

Konstantin G. Bolshakov RME Centrotech LLC, Novouralsk, Russia

Yi Cai Department of Power Engineering, North China Electric Power University, Baoding, Hebei, China

Zhen Cai School of Automotive Studies, Tongji University, Shanghai, China

Zhen Cai National Fuel Cell Vehicle and Powertrain System Engineering Research Center, Tongji University, Shanghai, China

Zhicheng Cao School of Mechanical Engineering, Tongji University, Shanghai, People's Republic of China

Fengxiang Chen School of Automotive Studies, Tongji University, Shanghai, China

Huipeng Chen School of Mechanical Engineering, HangZhou DianZi University, Zhejiang, China;
Jiaxing Research Institute, Zhejiang University, Zhejiang, China;
Power Machinery and Vehicular Engineering Institute, College of Energy Engineering, Zhejiang University, Zhejiang, China

Juexiao Chen School of Automotive Studies, Tongji University, Shanghai, China

Ping Chen State Power Investment Group, Hydrogen Technology Development Co. Ltd., Zhejiang, China

Rui Chen Wuhan Institute of Marine Electric Propulsion, Wuhan, China

Xiaolu Chen China National Institute of Standardization, Beijing, China;
Foshan Green Development Innovation Research Institute, Foshan, China

Ming Cheng CRRC Yongji Electric Co. LTD, Xi'an, China

Xiang Cheng Tsinghua University, Beijing, China

Zhiguo Cheng Legend New Energy Technology (Shanghai) Co., Ltd, Shanghai, People's Republic of China

Jianfeng Dai China Electric Power Planning and Engineering Institute, Beijing, China

Huichao Deng Beihang University, Beijing, China

Yan Dong Hebei University of Technology, Tianjin, China

Chang Du School of Automotive Studies, Tongji University, Shanghai, China

Wei Duan China Electric Power Planning and Engineering Institute, Beijing, China

Jiakun Fang State Key Laboratory of Advanced Electromagnetic Engineering and Technology, School of Electrical and Electronic Engineering, Huazhong University of Science and Technology, Wuhan, China

Yue Fang School of Mechanical Engineering, Tongji University, Shanghai, People's Republic of China

Zhifei Fang Beihang University, Beijing, China

Dingyun Gao Shanghai SUNWISE New Energy System Co. Ltd, Shanghai, China

Yuan Gao The New Energy Vehicle Engineering Center, Tongji University, Shanghai, China;
School of Automotive Studies, Tongji University, Shanghai, China

Yuzhe Gao State Key Laboratory of Electromechanical Integrated Manufacturing of High-Performance Electronic Equipment, Xidian University, Xi'an, China

Ziheng Gu School of Automotive Studies, Tongji University, Shanghai, China

Xiumei Guo GRINM Group Co., Ltd., National Engineering Research Center of Non-ferrous Metals Materials and Products for New Energy, Beijing, China;
GRIMAT Engineering Institute Co., Ltd., Beijing, China

Yafeng Guo Department of Control Science and Engineering, Tongji University, Shanghai, China

Yisong Han Hangzhou Oxygen Plant Group Co., Ltd, Hangzhou, Zhejiang, People's Republic of China

Zhixue He CRRC Yongji Electric Co. LTD, Xi'an, China

Yongping Hou The New Energy Vehicle Engineering Center, Tongji University, Shanghai, China;
School of Automotive Studies, Tongji University, Shanghai, China

Zhipeng Hou Department of Control Science and Engineering, Tongji University, Shanghai, China

Kewei Hu State Key Laboratory of Advanced Electromagnetic Engineering and Technology, School of Electrical and Electronic Engineering, Huazhong University of Science and Technology, Wuhan, China

Danji Huang State Key Laboratory of Advanced Electromagnetic Engineering and Technology, School of Electrical and Electronic Engineering, Huazhong University of Science and Technology, Wuhan, China

Xing Huang School of Automotive Studies, Tongji University, Shanghai, China; National Fuel Cell Vehicle and Powertrain System Engineering Research Center, Tongji University, Shanghai, China

Miaomiao Huo Foshan Green Development Innovation Research Institute, Foshan, China

Yanda Huo China Electric Power Planning and Engineering Institute, Beijing, China; Tianjin University, Tianjin, China

Jintao Jiang State Grid Changchun Power Supply Company, Changchun, China

Lijun Jiang GRINM Group Co., Ltd., National Engineering Research Center of Non-ferrous Metals Materials and Products for New Energy, Beijing, China; GRIMAT Engineering Institute Co., Ltd., Beijing, China; GRINM (Guangdong) Institute for Advanced Materials and Technology, Foshan, China

Liang Jianying National Innovation Center of High Speed Train, Qingdao, China

Dmitry G. Kondratyev The Scientific and Production Association “Centrotech”—RME Centrotech, Novouralsk, Russia

Bowen Liang The New Energy Vehicle Engineering Center, Tongji University, Shanghai, China; School of Automotive Studies, Tongji University, Shanghai, China; Innovation Center PACE, Tongji University, Shanghai, China

Yingqi Liang Department of Power Engineering, North China Electric Power University, Baoding, Hebei, China

Yonghao Liang Tongji University, Shanghai, China

Congxin Li SPIC Hydrogen Energy Tech Ningbo Research Institute, Zhejiang, China

Duankai Li CRRC Qingdao Sifang Company Ltd., Qingdao, China

Feiqiang Li Beijing SinoHytec Co., Ltd., Beijing, People’s Republic of China

Ruitao Li School of Automotive Studies, Tongji University, Shanghai, People’s Republic of China

Shihao Li School of Mechanical Engineering, Southeast University, Nanjing, China

Yongyi Li Department of Power Engineering, North China Electric Power University, Baoding, Hebei, China

Yu Li Smart City Division, Hong Kong Productivity Council, Hong Kong, China

Zhinian Li GRINM Group Co., Ltd., National Engineering Research Center of Non-ferrous Metals Materials and Products for New Energy, Beijing, China; GRIMAT Engineering Institute Co., Ltd., Beijing, China

Hanchen Lin China Hydrogen Alliance Research Institute, Beijing, China

Jin Lin Department of Electrical Engineering, Tsinghua University, Beijing, China

Ling Lin China National Institute of Standardization, Beijing, China

Weikang Lin Shanghai Champspower Technology Co., Ltd., Shanghai, China

Vincenzo Liso AAU Energy, Aalborg University, Aalborg, Denmark

Bin Liu Hebei University of Technology, Tianjin, China

Guozhu Liu Hydrogen Power (Beijing) Technology Service Co., Ltd, Beijing, China

Wei Liu CHN Energy Guohua Energy Investment Co., LTD., Beijing, China; China Hydrogen Alliance Research Institute, Beijing, China

Weiliang Liu State Grid Zhejiang Electric Power Co., Ltd. Jiaxing Power Supply Company, Jiaxing, China

Xiaomin Liu Foshan Green Development Innovation Research Institute, Foshan, China

Ye Liu School of Mechanical Engineering, Southeast University, Nanjing, China

Ang Lu State Key Laboratory of Advanced Electromagnetic Engineering and Technology, School of Electrical and Electronic Engineering, Huazhong University of Science and Technology, Wuhan, China

Yao Lu Hydrogen Power (Beijing) Technology Service Co., Ltd, Beijing, China

Wenhua Luo School of Mechanical Engineering, HangZhou DianZi University, Zhejiang, China

Hong Lv School of Automotive Studies, Tongji University, Shanghai, China

Hongcan Ma Hebei University of Technology, Tianjin, China

Tiancai Ma School of Automotive Studies, Tongji University, Shanghai, People's Republic of China; Institute of Carbon Neutrality, Tongji University, Shanghai, People's Republic of China

Vladimir I. Matrenin RME Centrotech LLC, Novouralsk, Russia

Tiande Mo Smart City Division, Hong Kong Productivity Council, Hong Kong, China

Wei Ni CRRC Yongji Electric Co. LTD, Xi'an, China

Zhonghua Ni School of Mechanical Engineering, Southeast University, Nanjing, China

Dongting Pan State Power Investment Group, Hydrogen Technology Development Co. Ltd., Zhejiang, China

Cong Pang CRRC Yongji Electric Co. LTD, Xi'an, China

Fenglai Pei Shanghai Motor Vehicle Inspection Certification & Tech Innovation Center Co. Ltd., Shanghai, China

Yuanting Peng Wuhan Institute of Marine Electric Propulsion, Wuhan, China

Jinxuan Qi School of Automotive Studies, Tongji University, Shanghai, China

Jixuan Qi School of Automotive Studies, Tongji University, Shanghai, China

Ruomei Qi Department of Electrical Engineering, Tsinghua University, Beijing, China

Weijie Qian State Grid Zhejiang Electric Power Co., Ltd. Jiaxing Power Supply Company, Jiaxing, China

Shang Sang CRRC Yongji Electric Co. LTD, Xi'an, China

Liandong Sha Department of Electrical Engineering, Tsinghua University, Beijing, China

Hongqiang Shi GRINM Group Co., Ltd., National Engineering Research Center of Nonferrous Metals Materials and Products for New Energy, Beijing, China;
GRIMAT Engineering Institute Co., Ltd., Beijing, China;
General Research Institute for Nonferrous Metals, Beijing, China

Ke Song School of Automotive Studies, Tongji University, Shanghai, China;
National Fuel Cell Vehicle and Powertrain System Engineering Research Center, Tongji University, Shanghai, China

Alexander S. Stikhin RME Centrotech, Novouralsk, Russia

Yongwen Sun School of Automotive Studies, Tongji University, Shanghai, China

Yanming Wan CHN Energy Guohua Energy Investment Co., LTD., Beijing, China;
China Hydrogen Alliance Research Institute, Beijing, China

Haolin Wang School of Automotive Studies, Tongji University, Shanghai, People's Republic of China

Jiawei Wang Hangzhou Oxygen Plant Group Co., Ltd, Hangzhou, Zhejiang, People's Republic of China

Juan Wang Foshan Green Development Innovation Research Institute, Foshan, China

Liming Wang State Power Investment Group Hydrogen Energy Technology Development Co., Ltd, Beijing, China;
SPIC Hydrogen Energy Tech Ningbo Research Institute, Zhejiang, China

Shumao Wang GRINM Group Co., Ltd., National Engineering Research Center of Nonferrous Metals Materials and Products for New Energy, Beijing, China;
GRIMAT Engineering Institute Co., Ltd., Beijing, China

Zhen Wang School of Mechanical Engineering, Shanghai Jiao Tong University, Shanghai, China;

Wuhan Institute of Marine Electric Propulsion, Wuhan, China;
Wuhan Hydrogen and Fuel Cell Industry Technology Research Institute Co. Ltd, Wuhan, China

Huanxia Wei School of Automotive Studies, Tongji University, Shanghai, China;
Innovation Center PACE, Tongji University, Shanghai, China

Wei Wei Zhangjiagang Research Institute of Hydrogen Energy, Zhangjiagang, China

Zhen Wu China Electric Power Planning and Engineering Institute, Beijing, China

Hong Xu Clean Energy Automotive Engineering Center, School of Automotive Studies, Tongji University, Shanghai, People's Republic of China

Yekai Xu Power Machinery and Vehicular Engineering Institute, College of Energy Engineering, Zhejiang University, Zhejiang, China

Zengshi Xu Wuhan Institute of Marine Electric Propulsion, Wuhan, China;
Wuhan Hydrogen and Fuel Cell Industry Technology Research Institute Co. Ltd, Wuhan, China

Zishun Xu School of Automotive Studies, Tongji University, Shanghai, People's Republic of China

Mingzhe Xue Clean Energy Automotive Engineering Center, School of Automotive Studies, Tongji University, Shanghai, People's Republic of China

Yan Yan School of Mechanical Engineering, Southeast University, Nanjing, China

Cheng Yang CRRC Yongji Electric Co. LTD, Xi'an, China

Yanmei Yang China National Institute of Standardization, Beijing, China

Yupeng Yang State Key Laboratory of Electromechanical Integrated Manufacturing of High-Performance Electronic Equipment, Xidian University, Xi'an, China

Zhen Yang School of Mechanical Engineering, Tongji University, Shanghai, People's Republic of China

Naiyuan Yao School of Automotive Studies, Tongji University, Shanghai, People's Republic of China

Riwu Yao Zhejiang University, Hangzhou, China

Baolong Yuan GRINM Group Co., Ltd., National Engineering Research Center of Nonferrous Metals Materials and Products for New Energy, Beijing, China;
GRIMAT Engineering Institute Co., Ltd., Beijing, China

Kun Yuan Shanghai Champspower Technology Limited Company, Shanghai, China

Wu Yuanfang GRINM Group Co., Ltd., National Engineering Research Center of Nonferrous Metals Materials and Products for New Energy, Beijing, China;
GRIMAT Engineering Institute Co., Ltd., Beijing, China

Bo Zhang School of Mechanical Engineering, HangZhou DianZi University, Zhejiang, China

Cunman Zhang School of Automotive Studies, Tongji University, Shanghai, China;
Clean Energy Automotive Engineering Center, School of Automotive Studies, Tongji University, Shanghai, People's Republic of China

Guorui Zhang CRRC Qingdao Sifang Company Ltd., Qingdao, China

Mingjun Zhang Tsinghua University, Beijing, China

Tong Zhang The New Energy Vehicle Engineering Center, Tongji University, Shanghai, China;
School of Automotive Studies, Tongji University, Shanghai, China

Yan Zhang China Hydrogen Alliance Research Institute, Beijing, China

Hao Zhao China Energy Engineering Group Tianjin Electric Power Design Institute Co., Ltd, Tianjin, China

Zhaoda Zhong AAU Energy, Aalborg University, Aalborg, Denmark

Zhiyao Zhong State Key Laboratory of Advanced Electromagnetic Engineering and Technology, School of Electrical and Electronic Engineering, Huazhong University of Science and Technology, Wuhan, China

Jiaxu Zhou Beihang University, Beijing, China

Mengshu Zhu Huazhong University of Science and Technology, Wuhan, China

Shaopeng Zhu College of Energy Engineering, Power Machinery and Vehicular Engineering Institute, Zhejiang University, Zhejiang, China;
Zhejiang Key Laboratory of Clean Energy and Carbon Neutrality, Zhejiang, China

Wenfeng Zhu School of Mechanical Engineering, Tongji University, Shanghai, People's Republic of China



Numerical Research on the Impact of Sloshing Frequencies of a Liquid Hydrogen Tank Under Massive Heat Leakage Conditions

Shihao Li¹, Ye Liu¹, Wei Wei², Yan Yan¹, and Zhonghua Ni¹ (✉)

¹ School of Mechanical Engineering, Southeast University, Nanjing 211189, China
{shihaoli, nzh2003}@seu.edu.cn

² Zhangjiagang Research Institute of Hydrogen Energy, Zhangjiagang 215600, China

Abstract. Hydrogen energy has great potential for wide utilization due to its considerable mass and energy density. However, liquid hydrogen (LH₂) tanks are subject to sloshing due to repetitive acceleration and vibration, which can be abstractly described by a sinusoidal oscillation. In this study, we investigate the dual influence of sloshing and massive heat leakage on tank performance under such dangerous situations.

Applying the multiple-layer isolation (MLI) method, the 40 ft ISO LH₂ tank we chose is assumed to be exposed in the atmosphere of 293K at 1 atm. The content of the liner is liquid hydrogen of 20.3K with a 50% filling level. The whole tank endures 115.431W heat leakage, and all physical features of hydrogen are obtained from NIST.

Based on the $k - \varepsilon$ model and an optimized Hertz-Knudsen equation, a well-validated numerical model is developed to investigate the hydrodynamics and thermodynamics performance of the tank. Five different types of longitudinal sinusoidal oscillation are set and imposed on the Cartesian meshes successfully. The heat leakage for all cases is set to 100 times the normal condition.

The results show that the pressure-increasing rate drops and then slightly climbs up with the increase in frequency. In the stationary condition, the pressure-rising rate is approximately 80.999 Pa/s, which in the case of 40% of natural frequency are reduced to 14.89% respectively. In terms of temperature, the maximum increments in the gas phase are influenced by sloshing, as the case of 40% of natural frequency reduces the increment of temperature in gas region. Besides, in a vacuum loss emergency at 50% filling level, drivers have over 5000 s before pressure hits the safety valve's release threshold.

This investigation predicts LH₂ evaporation in sloshing and insulation failure tanks. It also provides advice for emergency assistance and road-driving strategies as well as a reference for designing cryogenic fluid containers and release equipment.

Keywords: Liquid Hydrogen · Sloshing · Heat Leakage · Evaporation

1 Introduction

As a clean, efficient and renewable energy, liquid hydrogen (LH₂) has a broad application prospect in aerospace, transportation and other fields [1, 2]. However, its cryogenic characteristics bring great challenges to its storage and transportation. How to ensure the stability and safety of liquid hydrogen in the tank is an urgent problem to be solved. The liquid hydrogen storage tank will be subject to sloshing excitation of different frequencies and amplitudes during transportation, resulting in severe fluctuations and mixing of liquid hydrogen in the tank, which will affect its temperature, pressure, evaporation, and other thermodynamic parameters. Besides, vacuum lost caused by accidents is one of the common failure forms of cryogenic liquids tank. And massive heat leakage is the significant phenomenon of the aftermath.

Therefore, the numerical simulation of the thermodynamic phenomena of a liquid hydrogen tank under different sloshing frequencies and massive heat ingress is of great significance for improving storage efficiency, and reducing evaporation loss as well as potential secondary disasters.

2 Numerical Models

In this section, the majority models are the same with our previous work [3]. Due to space limitations, the following only contents a brief introduction.

2.1 Calculation Models

The general governing equations are given as follows.

Continuity Equation

$$\frac{\partial \rho}{\partial t} + \nabla \cdot (\rho \mathbf{v}) = S_m \quad (1)$$

Momentum Equation

$$\frac{\partial}{\partial t}(\rho \mathbf{v}) + \nabla \cdot (\rho \mathbf{v} \mathbf{v}) = -\nabla P + \nabla \cdot \left\{ (\mu + \mu_t) \left[\nabla \mathbf{v} + (\nabla \mathbf{v})^T \right] \right\} + \rho \mathbf{g} \quad (2)$$

Energy Equation

$$\frac{\partial}{\partial t}(\rho E) + \nabla \cdot [\mathbf{v}(\rho E + p)] = \nabla \cdot (K \nabla T) + S_h \quad (3)$$

where, ρ is the density, \mathbf{v} is the mean velocity vector, S_m is the mass source term, P is the pressure, μ is the dynamic molecular viscosity, μ_t is the eddy viscosity, \mathbf{g} is the gravity acceleration, E is the energy term, K is the thermal conductivity, and S_h is the energy source term.

The $k - \varepsilon$ model is selected as the turbulence model, as it has the characteristics of good computational stability and high efficiency. The volume of fluid method (VOF) is the common technique to capture the interface of liquid-gas two-phase flow, and it is

used here. For phase change model, Clapeyron Equation and a modified Hertz-Knudsen model are adopted and the latter is given by Eq. (4).

$$S_m = r \frac{(P_{\text{sat}} - P)}{V_{\text{cell}} \sqrt{2\pi R_v T_{\text{int}}}} \quad (4)$$

in which, R_v is the mean gas constant of the vapor, T_{int} is the liquid temperature at the free surface, V_{cell} is the volume of the cell in the mesh, and r is the tuning coefficient of phase change model. Recommended by M. Barkhudarov [4], $r = 0.5$ is selected in the study.

2.2 Tank Model

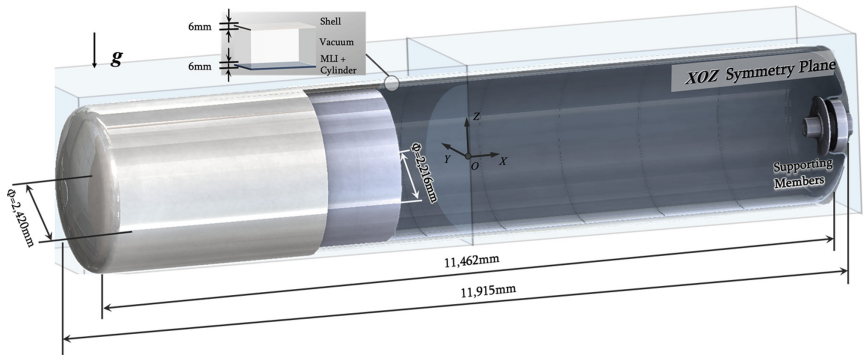


Fig. 1. Structure and computational region of the tank

The LH₂ container we selected is a 40-foot ISO tank. For simplification, the auxiliary parts including pipes and valves are ignored. Besides, the half of the inner cylinder is chosen as the computation domain as its symmetrical shape. Thus, its basic structures and size are shown in Fig. 1.

Under the standard circumstance of 20 °C ambient temperature and a vacuum layer of 1e-3 Pa, our prior calculations indicate the heat leakage of 57.716 W in the computational domain. The initial liquid temperature is 20.36 K. The gas temperature varies between 20.369 K and 20.371 K, incrementing counter to gravity's direction. The ullage's initial absolute pressure is set at 1 atm.

Certain physical property parameters, including mass, saturation temperature, and saturation pressure, are derived from the REFPROP physical property query software. The density of GH₂ is determined by the ideal gas equation, given that it's treated as compressible flow.

2.3 Mesh and Model Validation

Uniformed Cartesian grids are applied as the mesh construction method. According to our previous study, the mesh size of 30 mm performed best among five, as it well balanced accuracy and time-efficiency.

A self-pressurization experiment conducted by NASA [5] is chosen to validate the model. The temperature simulation results align well with experimental data, as demonstrated by three sensors recording temperature from various regions. Regarding pressure, the calculation demonstrates over 90% accuracy, affirming the reliability of the model.

3 Results and Discussion

In the study, five massive heat-ingress cases with various frequencies are simulated. Key parameters of those cases are listed in Table 1.

Table 1. Simulation cases and key parameters list.

| Case | Frequency (ω_{EX}) | Common conditions | |
|------|-----------------------------|----------------------------|--------------------------------------|
| 1 | 0 | Sinusoidal Excitation | $a_x = 0.3\sin(\omega_{EX} \cdot t)$ |
| 2 | 0.3ω | Natural Frequency ω | 3.541 rad/s |
| 3 | 0.4ω | Filling Rate | 50% |
| 4 | 0.45ω | Heat Leakage | 100 \times standard condition |
| 5 | 0.5ω | Duration | 5000 s |

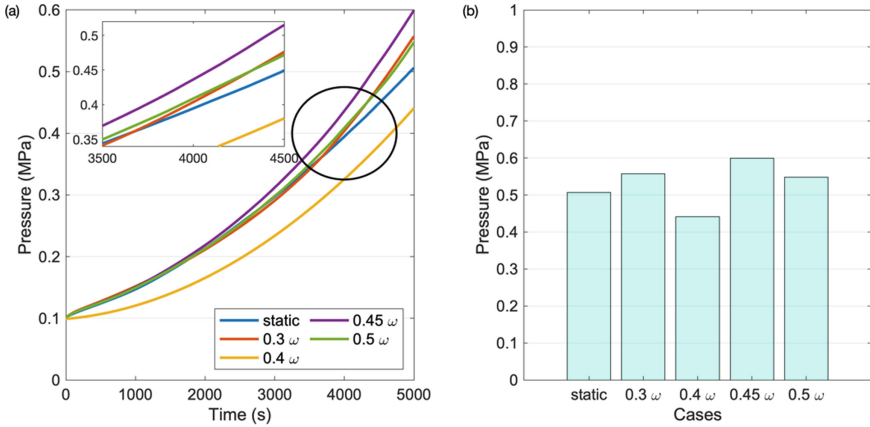


Fig. 2. Pressure variance. (a) variance with time; (b) variance at the final moment

Figure 2 (a) shows the ullage pressure variance with time. Starting from 1 atm, the inconstant increase rates of the five cases contribute to the curvature shape of the pressure variance lines. For most of the duration, the pressure of Case 2 is high than that of Case 4 within a rather close slot. But the latter takes the advantage at nearly the 4300th second. Besides, all of the cases exceed 0.4 MPa at the final moment. And specifically, shown in Fig. 2 (b), Case 1 reaches 0.506 MPa at the 5000th second, 14.89% higher than Case 3 whose pressure increases the least among them. The pressure of Case 4 is the highest of 0.600 MPa, while the ones of Case 2 and Case 5 are around 0.5 MPa, sharing relatively limited pressure gap of 0.01 MPa.

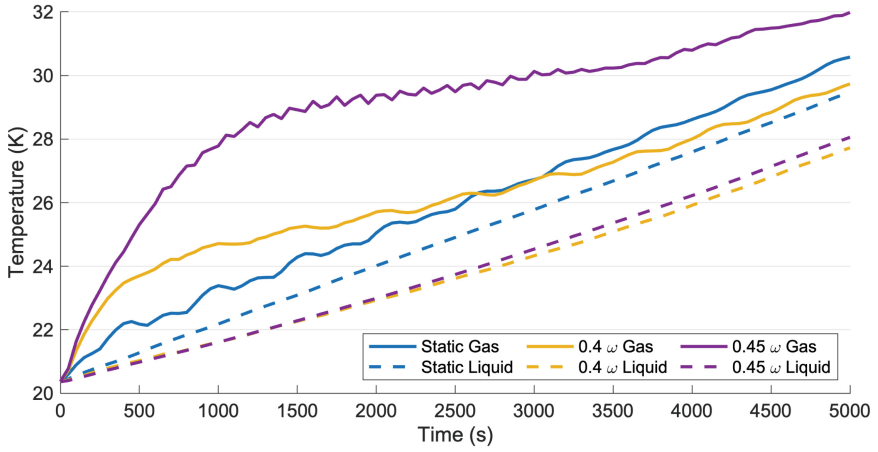


Fig. 3. Temperature variance.

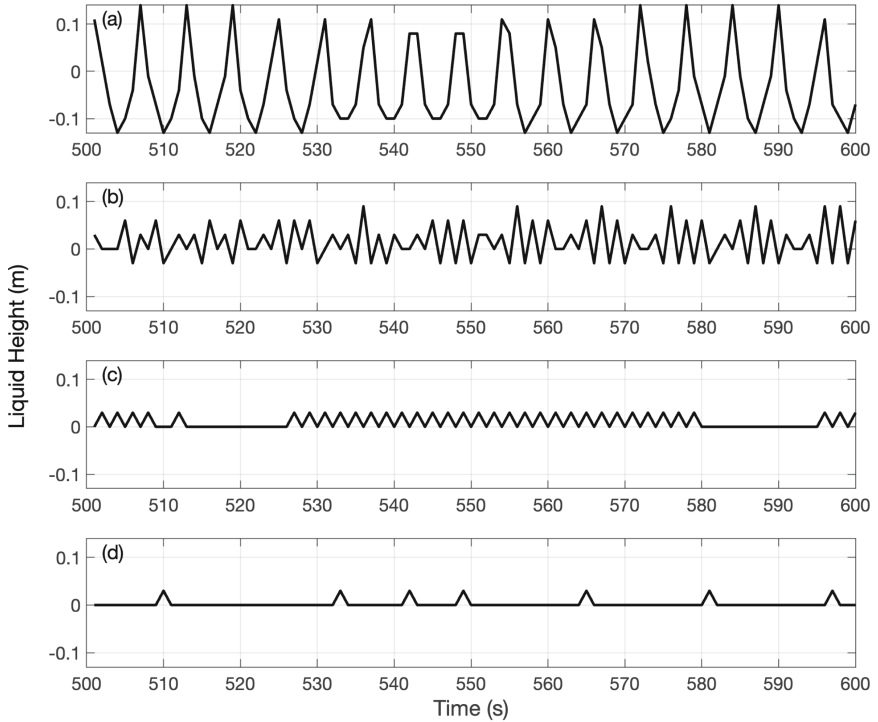


Fig. 4. Liquid height variance. (a) 0.3ω ; (b) 0.4ω ; (c) 0.45ω ; (d) 0.5ω .

Two probes, coordinated at $(0, 0.6, 0.3)$ and $(0, 0.6, -0.3)$, are set to record the temperature in both gas and liquid region. The temperature variance can be illustrated in Fig. 3. It can be seen that the temperature of liquid region increases linearly, while

that of gas region can be divided into three parts. In the initial stage, increasing rates are obviously greater than those in liquid bulk. Since then, they climb slowly, and finally grow in the same rate of the liquid.

Figure 4 depicts the variance in liquid height between 500th and 600th second, as recorded by a vertical probe line at coordinates $(0, 0.6, z)$. The static case is not included.

It can be seen that the liquid sloshing period becomes longer, but amplitude becomes intense as the frequency decreases. In Case 2, the amplitude of the liquid height is within ± 0.12 m, and the figure of Case 3 declines to ± 0.10 m. However, for Case 4 and Case 5, they drop significantly. Besides, the fluctuations of the liquid in those two cases are too slight to be captured, as the amplitude of them are less than 0.06 m or even 0.03 m, which is the size of the mesh.

4 Conclusion

In the current study, five cases of various longitudinal sloshing frequencies under 100 times of standard heat ingress in a liquid hydrogen tank are analyzed by numerical simulation. Based on previous analysis, some conclusions can be drawn:


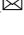

1. Compared to static case, a 40% of natural frequency sloshing can reduce no less than 14% in pressure rise rate.
2. Among five cases, Case 3 of 0.4ω is the trade-off between eliminating the thermal stratification phenomena of the tank, and conversion of the kinetic energy to heat.
3. Under 50% filling level conditions, in the event of a vacuum loss emergency, drivers would have over 5000 s to operate before the pressure reaches the safety valve's release threshold.

References

1. Andersson, J., Grönkvist, S.: Large-scale storage of hydrogen. *Int. J. Hydrogen Energy* **44**, 11901–11919 (2019)
2. Ratnakar, R.R., et al.: Hydrogen supply chain and challenges in large-scale LH2 storage and transportation. *Int. J. Hydrogen Energy* **46**, 24149–24168 (2021)
3. Li, S., Yan, Y., Wei, W., Wang, Z., Ni, Z.: Numerical simulation on the thermal dynamic behavior of liquid hydrogen in a storage tank for trailers. *Case Stud. Therm. Eng.* **40**, 102520 (2022)
4. Barkhudarov, M.: Two-field temperature model for two-fluid flows. Technical Report, Flow Science (2019)
5. Aydelott, J.C.: Normal gravity self-pressurization of 9-inch-/23cm/diameter spherical liquid hydrogen tankage. Technical Report, NASA (1967)



Review of Liquid Hydrogen Leakage: Factors and Safety Measures

Bowen Liang^{1,2,3} , Yuan Gao^{1,2} , Huanxia Wei^{2,3} , Tong Zhang^{1,2},
and Yongping Hou^{1,2}

¹ The New Energy Vehicle Engineering Center, Tongji University, Shanghai 201804, China
yuangao@tongji.edu.cn

² School of Automotive Studies, Tongji University, Shanghai 201804, China

³ Innovation Center PACE, Tongji University, Shanghai 201804, China

Abstract. Liquid hydrogen, as a kind of energy carrier with high energy density, has shown significant advantages in fields such as aerospace, shipping, and large-scale hydrogen refueling stations. However, safety issues remain a key factor restricting its widespread application, especially research on liquid hydrogen leakage. This review summarizes important experiments in the field of liquid hydrogen leakage, then summarizes the main factors affecting liquid hydrogen leakage in open environments, including leakage sources, ground conditions, wind conditions, and atmospheric conditions, with the degree of influence decreasing in that order. In addition, this article also summarizes the influencing factors of liquid hydrogen leakage in restricted environments such as buildings, refueling stations. The current research limitation is the limited diversity of liquid hydrogen leakage scenarios and a lack of standardized research for application scenarios, which restricts in-depth and comprehensive quantitative analysis. The review concludes with a summary of research on the prevention and safety measures of liquid hydrogen leakage and prospects for the application of more advanced technologies such as AI and unmanned technology in the field of liquid hydrogen leakage prevention.

Keywords: Liquid Hydrogen · Hydrogen Safety · Hydrogen Leakage

1 Introduction

1.1 Development of Hydrogen Energy

Hydrogen energy, due to its wide availability, environmental friendliness, and high efficiency, is considered the most promising energy source of the 21st century and a viable alternative to fossil fuels [1]. Consequently, countries such as China, US, and EU nations established goals and plans to develop hydrogen energy industries in order to reduce carbon emissions and increase renewable energy shares [2].

As hydrogen energy research and application progresses worldwide, hydrogen storage and transportation are becoming increasingly prominent issues. Currently, there are three main methods of hydrogen storage and transportation: gaseous, liquid, and solid.

Selecting the appropriate hydrogen storage method depends on factors such as application scenarios, transportation mode, and storage lifespan [3]. Although liquid hydrogen storage incurs energy losses, it offers economic advantages in large-scale supply and medium-to-long distance transportation due to its high volumetric density, hydrogen purity, and transport efficiency [4, 5]. A report by the California Air Resources Board predicts that by 2025, hydrogen fuel stations will primarily be supplied with liquid hydrogen [6]. According to Qin et al.'s model predictions, considering factors such as construction and transportation costs, the unit investment for a liquid hydrogen station is lower than that of a high-pressure gaseous hydrogen refueling station, and the unit investment advantage becomes more apparent as the scale of construction increases [7]. In recent years, the application scenarios for liquid hydrogen have continued to expand. Initially, it was only used on a small scale in the aerospace industry, but it has gradually expanded to include refueling stations, large aircraft, liquid hydrogen drones, shipping, and other fields [8–11]. With the increasing demand for clean energy, liquid hydrogen is expected to play a more important role in the future.

1.2 Liquid Hydrogen Safety

The Fig. 1 shows the basic industrial supply chain of liquid hydrogen, which involves production, liquefaction, transportation, storage, and utilization [12]. Hydrogen can be obtained from fossil fuels and green renewable energy sources, and after liquefaction, it is transported by trucks, ships, or trains, then re-gasified at storage sites and distributed to small-scale refueling stations or consumers.

However, due to the highly flammable and explosive nature of hydrogen molecules [13], liquid hydrogen leakage can lead to explosions. Furthermore, hydrogen can penetrate metal materials, causing material embrittlement and leading to storage equipment rupture [14]. As the application of liquid hydrogen in various sectors, such as automotive, energy, and industrial, becomes increasingly widespread, investigating the influencing factors and protective measures of liquid hydrogen leakage is essential to improve its safety and minimize the risk of accidents. A systematic understanding of the factors involved in liquid hydrogen leakage in various scenarios can help identify potential hazards and develop effective safety measures.

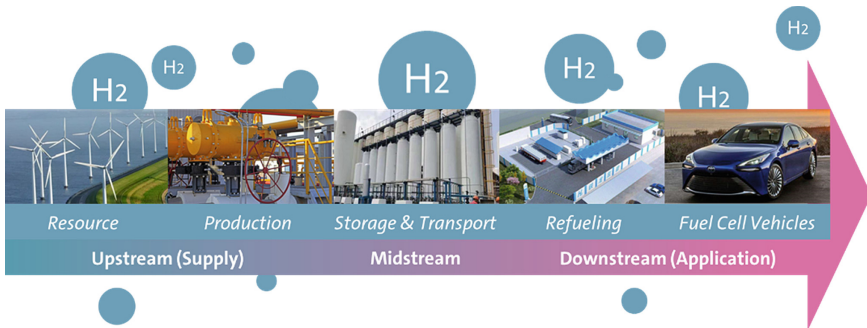


Fig. 1. Industrial chain of hydrogen industry.

2 Influence Factors

2.1 Key Experiments

Due to the high cost of liquid hydrogen leakage testing, there are limited number of groups did on-site liquid hydrogen leakage tests and experiments. In this paper, the authors have compiled important liquid hydrogen leakage experiments.

Firstly, in 1983, the National Aeronautics and Space Administration (NASA) conducted a large-scale liquid hydrogen leakage experiment in an open environment, simulating the scenario of a large-scale liquid hydrogen storage device rupture [15]. The experimental results preliminarily indicated that a combustible gas cloud is generated after liquid hydrogen leakage, and turbulent flow caused by heat and momentum is an important factor influencing liquid hydrogen leakage. In 1994, the Federal Institute for Materials Research and Testing (BAM) conducted an accidental low-temperature liquid hydrogen leakage experiment in a residential area, studying the behavior of liquid hydrogen leakage in residential areas [16]. In 2011, the UK Health and Safety Laboratory (HSL) simulated an experiment in which typical hose failure resulted in liquid hydrogen leakage [17]. The experimental results showed that the release of liquid hydrogen in contact with concrete surfaces could lead to liquid accumulation, and a flammable mixture would be produced at least 9 m downwind of the release point. In 2014, HSL conducted an experiment on passive ventilation of liquid hydrogen, in which passive ventilation was applied to the hydrogen-rich space above the free surface area of approximately 40 m² of liquid hydrogen using a chimney, proving that passive exhaust can maintain the hydrogen concentration below the explosive limit [18]. The specific timeline is shown in Fig. 2.

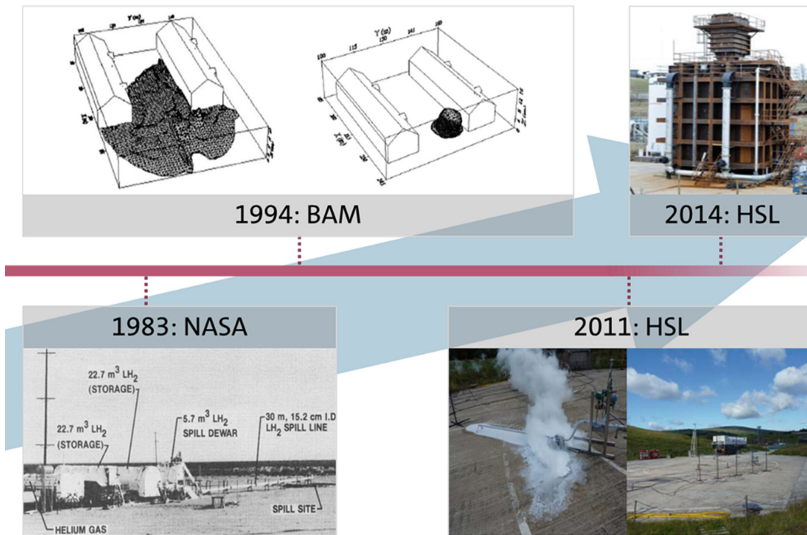


Fig. 2. Representative four on-site liquid hydrogen leakage experiments.

Table 1. Relevant influence factors of liquid hydrogen leakage.

| Influence factors | | Related works |
|------------------------|-------------------------|---|
| Leakage source | Liquid mass fraction | Liu [19] |
| | Leakage mass | Liu [19], Holborn [20] |
| | Leakage speed | Liu [19, 21], Holborn [20], Tang [22], Schmidt [23] |
| | Leakage height | Tang [22], Wu [24], Chen [25] |
| Ground conditions | Ground temperature | NASA [15], Liu [21], Jin [26], Statharas [27] |
| | Ground materials | Holborn [20] |
| Wind conditions | Wind speed | Holborn [20], Liu [21], Schmidt [23], Jin [26], Shao [28] |
| | Wind temperature | Jin [26] |
| Atmospheric conditions | Atmospheric pressure | Shao [28] |
| | Atmospheric temperature | Shao [28] |
| | Atmospheric humidity | Giannissi [29], Liu [30] |
| | Atmospheric composition | Ichard [31] |

2.2 Open Environment

In general, large-scale liquid hydrogen leaks in open environments can form a pool, while small-scale leaks may immediately spray and evaporate [32]. Therefore, the study of factors influencing liquid hydrogen leakage mainly focuses on the diffusion and evaporation behavior of the liquid hydrogen pool [33, 34], as well as the diffusion behavior of the resulting vapor cloud [35]. Based on literature review, the main external influencing factors can be divided into four categories: leak source conditions, ground conditions, external wind fields, and atmospheric conditions. Leak source conditions include liquid mass fraction, spill rate, leak height, and release velocity. Ground conditions include ground temperature and material, while external wind fields primarily include the effects of wind speed and wind temperature. Atmospheric conditions mainly include three factors: atmospheric pressure, environmental temperature, humidity, and atmospheric composition. The relevant influencing factors are shown in Table 1.

In terms of leak source research, Liu et al. used Fluent to conduct simulation on systematically compare the effects of liquid mass fraction, release velocity, and spill rate on leaks, and found that the time variation of the maximum hydrogen concentration in the flow field is most sensitive to liquid mass fraction, followed by spill rate, and lastly spill volume [19, 21]. As the liquid mass fraction at the outlet increases, the cloud is diluted to below the danger range more quickly. An increase in spill rate leads to an increase in hydrogen concentration near the source, making it difficult to dilute, and the maximum length of the flammable cloud is longer. An increase in spill volume leads to an increase in the size of the danger zone and the length of the total danger time. Furthermore, P.G. Holborn et al. used pool models of Gexcon FLACS, which is a commercial explosion

consequence simulation software platform empowered by reactive flow models, to study and confirm that increases in leakage rate and leakage volume both lead to an increase in the size of the danger zone, and found that the leakage rate and duration (rather than wind speed) are the main factors determining the size of the flammable cloud [20, 33]. Tang et al. [22] developed a mixed flow model of pipeline leakage based on HSL experiments to study the effects of explosions and low-temperature damage ranges at different flow rates on the surrounding environment in open environments, finding that the higher the flow rate, the farther the flammable and cold-effect clouds move downwind, the larger the cloud surface area, and the greater the danger. They also studied the heat transfer and diffusion behavior of the cloud under different leakage heights, finding that the closer to the ground, the greater the range of liquid hydrogen diffusion, and the larger the danger zone, a conclusion also confirmed in the studies of Wu et al. and Chen et al. [24, 25].

Then we come to the previous researches on ground conditions. NASA liquid hydrogen leakage experiments [15] and Statharas [27] based on BAM leakage experiments have both confirmed that ground thermal is one of the important factors affecting liquid hydrogen leakage, with higher than 97% of the heat for evaporation coming from the ground. Tao et al. further explored the effects of different ground temperatures on liquid hydrogen diffusion, finding that as ground temperature increases, the diffusion range and duration of liquid and gaseous hydrogen decrease [26]. However, in Liu's research, the conclusion is significantly different. It was found that ground temperature has little effect on the stable size of the flammable gas cloud, and this may need further confirmation of its impact [21]. Holborn, P. G. et al. compared the effects of different pool model ground types (wet coarse sand, concrete, and insulation) on liquid hydrogen leakage and found that materials with higher thermal conductivity (such as wet sand) accelerate the gasification of the liquid pool, making the leakage near the source denser (higher mass fraction of hydrogen), resulting in a larger gas cloud. Nevertheless, the existing time of gas cloud is shorter [20].

In terms of external wind conditions, the main focus has been on wind speed [20, 21, 23, 26, 28], and research results have shown that the wind field mainly affects the behavior of the gas cloud after liquid hydrogen leakage. An increase in wind speed reduces the height of the downwind flammable cloud layer and to some extent accelerates cloud dilution, but the downwind distance also increases. Therefore, how to use wind speed as a factor to improve the safety of liquid hydrogen applications requires specific analysis of individual scenarios. Furthermore, Tao et al. used Computational Fluid Dynamics (CFD) models to study the effects of wind temperature on liquid hydrogen leakage and found that an increase in wind temperature impedes the diffusion of hydrogen in the air, which may be related to an increase in atmospheric pressure and air viscosity [26]. In addition, the authors of this review believe that, turbulence conditions (turbulence intensity, integral length, etc.) may also have an effect on hydrogen diffusion. Flame propagating characteristics in turbulent airflow may change.

In atmospheric condition research, Shao et al. conducted a comprehensive study, finding that an increase in atmospheric temperature hinders the dispersion of flammable clouds, while an increase in atmospheric pressure inhibits the diffusion of gas clouds [28]. Giannissi et al. and Liu et al. used CFD simulations, respectively, to focus on the effects of humidity on liquid hydrogen leakage [29, 30], coming to the conclusion that

due to the heat released by water phase changes, the buoyancy of the gas cloud rises, making it easier for the hydrogen cloud to spread. Ichard used CFD models to simulate the evaporation and diffusion of liquid hydrogen on the ground, mainly studying the effects of oxygen and nitrogen in the air, and found that the condensation of air components releases heat, increasing gas cloud buoyancy [31].

In summary, the four main influencing factors on liquid hydrogen leakage, in order of decreasing impact, are listed as: leak source, ground conditions, wind conditions, and atmospheric conditions. Among them, the three most important factors that affect the danger level of liquid hydrogen leakage are the leak source itself, followed by geothermal, and then wind speed. The specific influence factors and the danger level of liquid hydrogen leakage show a positive or negative correlation, as shown in Fig. 3, for a more intuitive display.

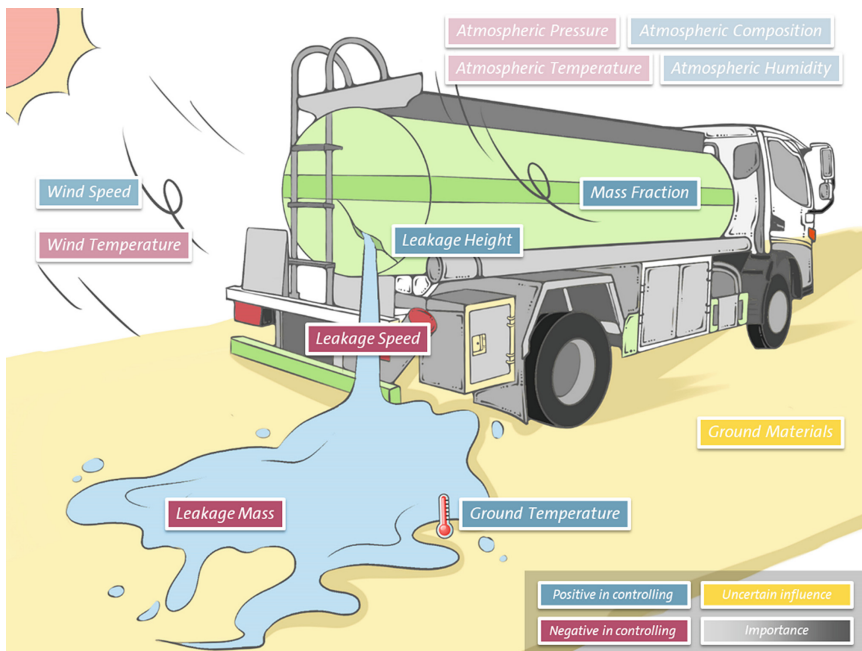


Fig. 3. The influence of various factors on the hazards of leakage in an open environment. Blue labels indicate that an increase in the value of this factor is beneficial for mitigating the harm (positive for hazards controlling), red ones are the opposite, and yellow ones indicate that this factor is not quantifiable. The brightness of labels represents the degree of influence (i.e. importance of specific factor).

2.3 Specific Scenarios

In addition to studying the factors affecting liquid hydrogen leakage in open environments, further works are needed to investigate the main factors affecting liquid hydrogen leakage in specific confined spaces based on actual application scenarios.

Schmidt et al. simulated large-scale liquid hydrogen leakage with Fluent in the presence of buildings and found that the concentration field was affected when the hydrogen cloud approached the wall, hindering the dispersion of the cloud and leading to the expansion of explosive mixtures [23]. Statharas et al. also confirmed that the presence of buildings makes the diffusion of liquid hydrogen leakage more complex due to the shielding effect of the buildings and the formation of complex wind conditions [27]. Tang et al. used Fluent simulation to study the leakage of liquid hydrogen in garages and tunnels [36]. In garages, the released gas cloud moved upward due to the blockage of the preceding car during the release period, and then spread in all directions along the top wall. Meanwhile, the obstruction of cars and limited exhaust ports hindered the dispersion of the hydrogen cloud, extending the danger time. In tunnels, the structure of the tunnel led to the longest horizontal ignition and explosion distance. Then it can be concluded that the presence of obstacles such as buildings, garages, and tunnels affects the behavior of liquid hydrogen leakage, mainly because the obstacles prevent or restrict the dispersion of the gas cloud, and the formation of more complex wind fields.

Wu and Chen et al. have studied the leakage of liquid hydrogen stored in high-pressure containers [24, 25]. In addition to the container structure having a significant impact, an increase in leakage pressure and a shorter distance from the leakage point to the ground lead to an increase in the range of low-temperature hazard zones and combustible zones of hydrogen gas. Meanwhile, blowing upward will be very beneficial to reducing the level of hydrogen danger. Kim et al. [37] conducted a more comprehensive study on tank leakage and found that the larger the leakage, the larger the risk range.

Feng et al. studied the leakage of high-pressure gaseous hydrogen on ships [38], while Hansen et al. studied the use of liquid hydrogen on large ships, finding that the design of the storage location and ship speed can affect liquid hydrogen leakage [39].

Based on the relevant researches, the obstacles in different scenarios are summarized in Table 2.

Table 2. The impact of specific factors on liquid hydrogen leakage in different scenarios.

| Scenarios | Specific influence factors |
|--|---|
| Building scenarios like hydrogen refueling stations, garages, tunnels, warehouses, etc | Obstruction of gas cloud flow (spatially) |
| | Complex wind conditions caused by the presence of buildings |
| Liquid hydrogen tanks | Storage pressure of liquid hydrogen |
| | Leakage location (especially leakage height) |
| Transportation facilities like transport vessels and trains | The special structural design required by transportation facilities and environment |

Nevertheless, the present research displays several inadequacies, particularly in terms of the relatively limited research on liquid hydrogen in different scenarios and the lack of diversity in research scenarios. Additionally, there is a dearth of standardized scenarios for conducting in-depth and comprehensive research on application scenarios, and the

impact of liquid hydrogen leakage in scenarios has yet to be quantified. Moreover, the majority of research focuses on individual factors, rather than exploring the correlation between them. Thus, further investigation is required to explore the relationships between scenarios and factors in-depth.

Concurrently, research on gaseous hydrogen leakage has already achieved significant depth, and insights from this research can partially inform the study of liquid hydrogen leakage. The two fields of research should be better integrated to reduce duplication of effort and maximize research efficiency. This will contribute to the provision of more robust technical support for the safe application of liquid hydrogen.

3 Safety Measures

3.1 Simulation on Measures

Research on the prevention and control of liquid hydrogen leakage can be mainly divided into two categories: safety measures based on liquid hydrogen leakage modeling and safety measures based on risk analysis. Furthermore, prevention and control measures can be mainly divided into identification and prevention before the occurrence of hazards and reduction and handling after their occurrence. The previous section provided ideas for safety measures by summarizing the influencing factors of liquid hydrogen leakage in open and confined environments.

Regarding identification and prevention before the occurrence of hazards, designing a hydrogen detection system for refueling stations is one of the commonly used methods [40, 41]. Determining the safety distance between facilities is another major protective measure [42–44]. To determine the safety distance in specific scenarios, Liu et al. used CFD to study the correlation between safety distance, wind speed, and leakage in open environments [45]. In addition, reasonable heating of the ground or the selection of different ground materials can improve the diffusion and evaporation of liquid hydrogen after a hazard occurs [27]. Setting up obstacles (guardrails and embankments) can help reduce the diffusion of liquid hydrogen leakage [46, 47]. Regarding handling after the occurrence of hazards, Proper utilization of wind conditions can dilute the hydrogen gas, and blowing wind upwards can decrease its concentration [24]. In enclosed scenarios such as garages, passive ventilation can maintain the hydrogen concentration below the explosion limit [18]. Additionally, Matsuura et al. discussed the influence of various roof ventilation positions, leak positions, leak volume flow rate, and exhaust volume flow rate on forced ventilation for hydrogen leakage and determined appropriate roof ventilation positions [48].

The above researches provide theoretical basis and application analysis for the prevention of liquid hydrogen accidents in various scenarios. With potential industrialization in the future, more prediction and protection methods would be proposed and validated from production.

3.2 Risk Assessment on Measures

In addition to using model simulation to verify and evaluate related safety measures, risk analysis can also be used to obtain prevention and control measures for liquid

Table 3. The main safety measures for liquid hydrogen refueling stations.

| Location | Safety measures |
|-----------------------|---|
| General | Policies concerning materials used (corrosion, hydrogen embrittlement, low temperature embrittlement) |
| | Installation of a fire protection wall along station boundaries |
| | Laying pipes in trenches |
| | Liquid hydrogen equipment to be installed on a common foundation |
| Liquid hydrogen tanks | Design of quakeproof storage tanks |
| | Monitoring pressure of the thermally insulated vacuum layer in storage tanks |
| Dispensers | Installation of a collision guard |
| | Installation of a break-away device under development |
| Vent lines | Installation of a heater and orifice in the secondary covers of the valves and manual line valves |
| | Connection of the purge valve to the vent line |

hydrogen leakage [49, 50]. Kikukawa et al. conducted a systematic risk assessment of liquid hydrogen refueling stations [51], proposing a series of safety measures and clarifying the need for safety distances, safe handling of low-temperature liquids, design requirements for liquid hydrogen tanks, and so on, to ensure the high safety of liquid hydrogen refueling stations. Sixty-seven safety measures are required to ensure the high safety of liquid hydrogen refueling stations, with the main safety measures of four locations listed in Table 3.

3.3 New Technologies

The development of artificial intelligence and unmanned technology has provided more options for preventing liquid hydrogen leakage. Xiao et al. established a model using an artificial neural network to predict the distance of flammable clouds released by liquid hydrogen, enabling quick identification of risk areas [52]. The combination of unmanned vehicles and drones equipped with hydrogen sensors can safely and efficiently conduct regular inspections and detect the dangers of liquid hydrogen leakage. Additionally, the combination of unmanned vehicle monitoring technology and robotic arms offers a more reliable and secure approach for reducing and managing accidents [53]. Additionally, the authors think that some industrial technologies like predictive maintenance (PdM) and digital twin (DT) may be applied to empower the monitoring.

4 Summary and Outlook

As an efficient and clean energy source, liquid hydrogen faces safety challenges that hinder its widespread application. This article introduces and explores the development prospects of liquid hydrogen, factors that influence its leakage in open and closed environments, safety measures and standards against liquid hydrogen leakage. Future research needs to strengthen the study of diverse scenarios and the relationships between various influencing factors. Moreover, it is necessary to establish comprehensive and systematic models to quantify the hazards and further investigate protective measures with more model data.

New technologies, such as artificial intelligence (AI) tools, can assist in real-time monitoring of liquid hydrogen leakage. Intelligent systems can predict the likelihood and severity of leaks and develop corresponding response strategies. Unmanned vehicles and drones provide safer and more efficient solutions for hydrogen storage and transportation companies. Future research should continue to explore and enhance the safety of liquid hydrogen, which will contribute to the wider adoption and application of this clean energy source.

Acknowledgments. This research is supported by the National Key Research and Development Program of China (No. 2021YFB4001005).

References

1. Dunn, S.: Hydrogen futures: toward a sustainable energy system. *Int. J. Hydrogen Energy* **27**(3), 235–264 (2002)
2. Li, Y., Lan, S., Ryberg, M., Perez-Ramirez, J., Wang, X.: A quantitative roadmap for China towards carbon neutrality in 2060 using methanol and ammonia as energy carriers. *iScience* **24**(6), 102513 (2021)
3. Kovač, A., Paranos, M., Marcuš, D.: Hydrogen in energy transition: a review. *Int. J. Hydrogen Energy* **46**(16), 10016–10035 (2021)
4. Cardella, U., Decker, L., Klein, H.: Roadmap to economically viable hydrogen liquefaction. *Int. J. Hydrogen Energy* **42**(19), 13329–13338 (2017)
5. Li, M., Bai, Y., Zhang, C., Song, Y., Jiang, S., Grouset, D., et al.: Review on the research of hydrogen storage system fast refueling in fuel cell vehicle. *Int. J. Hydrogen Energy* **44**(21), 10677–10693 (2019)
6. TRU. Staff report: initial statement of reasons for proposed rulemaking (2010)
7. Qin, N., Brooker, P., Srinivasan, S.: Hydrogen fueling stations infrastructure (2014)
8. Stroman, R., Schuette, M., Swider-Lyons, K., Rodgers, J., Edwards, D.: Liquid hydrogen fuel system design and demonstration in a small long endurance air vehicle. *Int. J. Hydrogen Energy* **39**(21), 11279–11290 (2014)
9. Mills, G.L., Buchholtz, B., Olsen, A. (eds.): Design, fabrication and testing of a liquid hydrogen fuel tank for a long duration aircraft. In: Joint Conference on Transactions of the Cryogenic Engineering Conference (CEC), June 13–17. Spokane, WA2012 (2011)
10. Benson, C.M., Ingram, J.M., Battersby, P.N., Mba, D., Sethi, V., Rolt, A.M., et al. (eds.): An analysis of civil aviation industry safety needs for the introduction of liquid hydrogen propulsion technology. In: ASME Turbo Expo: turbomachinery Technical Conference and Exposition, June 17–21. Phoenix, AZ2019 (2019)

11. Atilhan, S., Park, S., El-Halwagi, M.M., Atilhan, M., Moore, M., Nielsen, R.B.: Green hydrogen as an alternative fuel for the shipping industry. *Curr. Opin. Chem. Eng.* **31** (2021)
12. Aziz, M.: Liquid hydrogen: a review on liquefaction, storage, transportation, and safety. *Energies* **14**(18) (2021)
13. Verhelst, S., Wallner, T.: Hydrogen-fueled internal combustion engines. *Prog. Energy Combust. Sci.* **35**(6), 490–527 (2009)
14. Moradi, R., Groth, K.M.: Hydrogen storage and delivery: review of the state of the art technologies and risk and reliability analysis. *Int. J. Hydrogen Energy* **44**(23), 12254–12269 (2019)
15. Witcofski, R.D., Chirivella, J.E.: Experimental and analytical analyses of the mechanisms governing the dispersion of flammable clouds formed by liquid-hydrogen spills. *Int. J. Hydrogen Energy* **9**(5), 425–435 (1984)
16. Schmidtchen, U., Marinescupasoi, L., Verfondern, K., Nickel, V., Sturm, B., Dienhart, B.: Simulation of accidental spills of cryogenic hydrogen in a residential area. *Cryogenics* **34**, 401–404 (1994)
17. Hooker, P., Willoughby, D., Royle, M.: Experimental releases of liquid hydrogen (2011)
18. Hedley, D., Hawksworth, S.J., Rattigan, W., Brentnall, R., Allen, J.: Large scale passive ventilation trials of hydrogen. *Int. J. Hydrogen Energy* **39**(35), 20325–20330 (2014)
19. Liu, Y., Wei, J., Lei, G., Lan, Y., Chen, H., Jin, T.: Dilution of hazardous vapor cloud in liquid hydrogen spill process under different source conditions. *Int. J. Hydrogen Energy* **43**(15), 7643–7651 (2018)
20. Holborn, P.G., Benson, C.M., Ingram, J.M.: Modelling hazardous distances for large-scale liquid hydrogen pool releases. *Int. J. Hydrogen Energy* **45**(43), 23851–23871 (2020)
21. Liu, Y., Wei, J., Lei, G., Chen, H., Lan, Y., Gao, X., et al.: Spread of hydrogen vapor cloud during continuous liquid hydrogen spills. *Cryogenics* **103** (2019)
22. Tang, X., Shao, X., Lei, G., Chen, Q., Pu, L.: Influence of liquid hydrogen release state on safety of continuous leakage and diffusion. *Cryogenics* **4**, 14 (2019)
23. Schmidt, D., Krause, U., Schmidtchen, U.: Numerical simulation of hydrogen gas releases between buildings. *Int. J. Hydrogen Energy* **24**(5), 479–488 (1999)
24. Wu, N., Duan, C., Jiang, Y., Lian, J.: Simulation and safety analysis of the leakage of liquefied hydrogen from high-pressure container. *Therm. Sci.* **23**, S829–S836 (2019)
25. Chen, H., Chen, W., Shen, S.: Simulation and analysis of leakage and diffusion of liquefied hydrogen using CFD modeling. *Cryogenics* **2**, 24–29 (2018)
26. Jin, T., Wu, M., Liu, Y., Lei, G., Chen, H., Lan, Y.: CFD modeling and analysis of the influence factors of liquid hydrogen spills in open environment. *Int. J. Hydrogen Energy* **42**(1), 732–739 (2017)
27. Statharas, J.C., Venetsanos, A.G., Bartzis, J.G., Wurtz, J., Schmidtchen, U.: Analysis of data from spilling experiments performed with liquid hydrogen. *J. Hazard. Mater.* **77**(1–3), 57–75 (2000)
28. Shao, X., Pu, L., Li, Q., Li, Y.: Numerical investigation of flammable cloud on liquid hydrogen spill under various weather conditions. *Int. J. Hydrogen Energy* **43**(10), 5249–5260 (2018)
29. Giannissi, S.G., Venetsanos, A.G., Markatos, N., Bartzis, J.G.: CFD modeling of hydrogen dispersion under cryogenic release conditions. *Int. J. Hydrogen Energy* **39**(28), 15851–15863 (2014)
30. Liu, Y., Wei, J., Lei, G., Wang, T., Lan, Y., Chen, H., et al.: Modeling the development of hydrogen vapor cloud considering the presence of air humidity. *Int. J. Hydrogen Energy* **44**(3), 2059–2068 (2019)
31. Ichard, M., Hansen, O.R., Middha, P., Willoughby, D.: CFD computations of liquid hydrogen releases. *Int. J. Hydrogen Energy* **37**(22), 17380–17389 (2012)
32. Winters, W.S., Houf, W.G.: Simulation of small-scale releases from liquid hydrogen storage systems. *Int. J. Hydrogen Energy* **36**(6), 3913–3921 (2011)

33. Middha, P., Ichard, M., Arntzen, B.J.: Validation of CFD modelling of LH2 spread and evaporation against large-scale spill experiments. *Int. J. Hydrogen Energy* **36**(3), 2620–2627 (2011)
34. Verfondern, K., Dienhart, B.: Pool spreading and vaporization of liquid hydrogen. *Int. J. Hydrogen Energy* **32**(2), 256–267 (2007)
35. Chitose, K., Okamoto, M., Takeno, K., Hayashi, K., Hishida, M.J.J.E.R.T.: Analysis of a large scale liquid hydrogen dispersion using the multi-phase hydrodynamics analysis code (CHAMPAGNE) **124**(4), 283–9 (2002)
36. Tang, X., Pu, L., Shao, X., Lei, G., Li, Y., Wang, X.: Dispersion behavior and safety study of liquid hydrogen leakage under different application situations. *Int. J. Hydrogen Energy* **45**(55), 31278–31288 (2020)
37. Kim, S., Lee, M.K.Y., Kim, J., Lee, J.H.: Diffusion range and pool formation in the leakage of liquid hydrogen storage tank using CFD tools. *Appl. Chem. Eng.* **33**(6), 653–660 (2022)
38. Li, F., Yuan, Y., Yan, X., Malekian, R., Li, Z.: A study on a numerical simulation of the leakage and diffusion of hydrogen in a fuel cell ship. *Renew. Sustain. Energy Rev.* **97**, 177–185 (2018)
39. Hansen, O.R.: Liquid hydrogen releases show dense gas behavior. *Int. J. Hydrogen Energy* **45**(2), 1343–1358 (2020)
40. Zhu, S., Xu, H., Guan, J., Wang, F., Sun, L., Xue, X., et al.: Hydrogen leakage monitoring system for liquid hydrogen refueling station, has integrated hydrogen leak monitoring device includes infrared thermal imager, camera, image recognition module, leak alarm module and leak location module. CN112762361-A
41. Nakano, A., Shimazaki, T., Sekiya, M., Shiozawa, H., Ohtsuka, K., Aoyagi, A., et al.: Research and development of liquid hydrogen (LH2) temperature monitoring system for marine applications. *Int. J. Hydrogen Energy* **46**(29), 15649–15659 (2021)
42. Kim, E., Park, J., Cho, J.H., Moon, I.: Simulation of hydrogen leak and explosion for the safety design of hydrogen fueling station in Korea. *Int. J. Hydrogen Energy* **38**(3), 1737–1743 (2013)
43. Hall, J.E., Hooker, P., Willoughby, D.: Ignited releases of liquid hydrogen: safety considerations of thermal and overpressure effects. *Int. J. Hydrogen Energy* **39**(35), 20547–20553 (2014)
44. Houf, W.G., Winters, W.S.: Simulation of high-pressure liquid hydrogen releases. *Int. J. Hydrogen Energy* **38**(19), 8092–8099 (2013)
45. Liu, Y., Liu, Z., Wei, J., Lan, Y., Yang, S., Jin, T.: Evaluation and prediction of the safe distance in liquid hydrogen spill accident. *Process. Saf. Environ. Prot.* **146**, 1–8 (2021)
46. Liu, Y., Wei, J., Lei, G., Lan, Y., Chen, H., Gao, X., et al.: Numerical investigation on the effects of dike around liquid hydrogen source on vapor cloud dispersion. *Int. J. Hydrogen Energy* **44**(10), 5063–5071 (2019)
47. Wang, Y., Chen, Y., Zhao, H., Xiong, Y.: Study on the influence of barriers in the diffusion process of liquid hydrogen leakage. *IOP Conf. Ser. Earth Environ. Sci.* **546**(4) (2020)
48. Matsuura, K., Nakano, M., Ishimoto, J.: Forced ventilation for sensing-based risk mitigation of leaking hydrogen in a partially open space. *Int. J. Hydrogen Energy* **35**(10), 4776–4786 (2010)
49. Correa-Jullian, C., Groth, K.M.: Data requirements for improving the quantitative risk assessment of liquid hydrogen storage systems. *Int. J. Hydrogen Energy* **47**(6), 4222–4235 (2022)
50. Yoo, B.H., Wilailak, S., Bae, S.H., Gye, H.R., Lee, C.J.: Comparative risk assessment of liquefied and gaseous hydrogen refueling stations. *Int. J. Hydrogen Energy* **46**(71), 35511–35524 (2021)
51. Kikukawa, S., Mitsuhashi, H., Miyake, A.: Risk assessment for liquid hydrogen fueling stations. *Int. J. Hydrogen Energy* **34**(2), 1135–1141 (2009)

52. Xiao, J., He, P., Li, X., Benard, P., Yang, T., Chahine, R.: Computational fluid dynamics model based artificial neural network prediction of flammable vapor clouds formed by liquid hydrogen releases. *Int. J. Energy Res.*
53. Liang, B., Li, H., Gao, Y., Wei, H., Zhao, Z., Li, J., et al.: An intelligent hydrogen safety inspection vehicle. CN217689809U (2022)



Study on the Poisoning and Fine-Powdering Resistance Mechanism of SiO₂-Coating on La-Ni Hydrogen Storage Alloy

Xiumei Guo^{1,2(✉)}, Hongqiang Shi^{1,2,3}, Zhinian Li^{1,2}, Baolong Yuan^{1,2},
Wu Yuanfang^{1,2}, Shumao Wang^{1,2}, and Lijun Jiang^{1,2,4}

¹ GRINM Group Co., Ltd., National Engineering Research Center of Nonferrous Metals Materials and Products for New Energy, Beijing 100088, China
guoxiumei@grinm.com

² GRIMAT Engineering Institute Co., Ltd., Beijing 101407, China

³ General Research Institute for Nonferrous Metals, Beijing 100088, China

⁴ GRINM (Guangdong) Institute for Advanced Materials and Technology, Foshan 528000, China

Abstract. Hydrogen storage alloys can be poisoned by impurity gases such as H₂O, O₂, N₂, CO, etc., and be fine-powdered by hydride formation. In order to improve the durability of hydrogen storage alloys against surface poisoning by impurity gases and fine-powdering during hydriding process, effectiveness of SiO₂-coating layer prepared by fumed silica method was examined for La-Ni based alloy particles as a model system. It was found that, the La-Ni alloy particles were embedded in a porous SiO₂ matrix. SiO₂-coating effectively improved the durability of La-Ni alloy surface to impurity gases containing oxygen and nitrogen atoms. The anti-poisoning mechanism of the SiO₂-coating was investigated. It was found that, the cubic structured phase regions with short-range order arrangement of atoms were formed in the amorphous SiO₂-coating layer during the heat treatment process, which were the hydrogen permeation regions with, effectively restricting the passage of larger molecules of oxygen and other harmful impurities. Therefore, the SiO₂-coating provided protection to the metal hydride particles from these impurities. Furthermore, the porous SiO₂ matrix embedded La-Ni alloy particles were fracture resistant and could withstand more than 1000 hydrogen absorption/desorption cycles without generating fines.

Keywords: SiO₂-coating · La-Ni alloy · Mechanism · Poisoning resistance · Fine-powdering resistance

1 Introduction

La-Ni based hydrogen storage alloys have the advantages of easy activation, fast hydrogen absorption and release speed, stable cycle performance, strong helium fixation ability, certain anti-poisoning and antioxidation abilities, and hydrogen storage and release at room temperature. It can be used for hydrogen storage, transport, nickel-metal hydride

battery anode materials, high-purity hydrogen preparation, storage of hydrogen isotopes, etc. [1]. However, some impurity gases in hydrogen (O_2 , H_2O , N_2 , CO , etc.) will passivate the surface of the alloy, affect the hydrogen absorption rate and hydrogen absorption capacity of the alloy, and cause the deterioration of the hydrogen storage performance of the alloy [2, 3]. The residual thermal stress during the heat treatment of the alloy itself and the volume expansion strain during the hydrogen absorption process together lead to the pulverization of the alloy during the hydrogen absorption and desorption process [4], and the more severe the volume change during the hydrogen absorption and desorption process, the alloy pulverization faster.

In recent years, domestic and foreign researchers have improved the hydrogen absorption kinetics of materials by surface modification without changing the basic hydrogen storage properties of materials (such as phase structure, hydrogen absorption, plateau pressure, etc.). Cycle stability, anti-poisoning and antichalking properties [5] have attracted much attention in industry. Wang et al. [6, 7] proposed a method of alloy surface fluorination and used a fluoride ion solution to impregnate $LaNi_{4.7}Al_{0.3}$ on the surface to improve the alloy's anti-poisoning performance. Guo et al. [8] studied the plating of Pb film on the surface of ZrCo alloy, which significantly improved the anti-toxicity performance of the alloy. Ren [9] studied Cu plating on the surface of AB_5 alloy, which significantly improved the alloy's anti-poisoning performance. Heung et al. [10] used the sol-gel method to coat $LaNi_{4.25}Al_{0.75}$ alloy with SiO_2 , which greatly enhanced the powdering resistance of hydrogen storage alloys. Cheng et al. [11] used the fumed silica method to coat $LaNi_{4.25}Al_{0.75}$ alloy with SiO_2 and systematically studied the activation process, P-C-T curve, hydrogen absorption kinetics and anti-pulverization of $LaNi_{4.25}Al_{0.75}/SiO_2$ composite materials. Compared with the alloy before coating, the anti-poisoning and anti-pulverization performance of the composite materials is significantly improved.

In this work, a $LaNi_{3.7}Al_{0.75}Mn_{0.55}$ alloy was modified by the SiO_2 surface coating method, and the P-C-T curves of La-Ni/ SiO_2 composite materials in high-purity hydrogen was studied systematically with different heat treatment temperatures and times. Hydrogen absorption kinetics and anti-poisoning and antipulverization properties in standard hydrogen containing N_2 , O_2 , etc.

2 Experiment

2.1 Sample Preparation

The $LaNi_{3.7}Al_{0.75}Mn_{0.55}$ alloy was studied as the base alloy. The hydrogen absorption capacity of this alloy is 1.08 wt% at 20 °C, and the hydrogen absorption equilibrium pressure is 39 Pa [12]. The alloy was crushed mechanically into 500 mesh powder s to be the base sample coated by SiO_2 in this experiment.

The La-Ni/ SiO_2 composite was prepared by the fumed silica method. Under high-speed stirring, fumed silic was slowly added to the water. When the fumed silic was fully dispersed in the water to form SiO_2 sol, the 500 mesh alloy powders were slowly added into the sol. The mass ratio of $H_2O:SiO_2:alloy$ was 10:2:3. The gel was extruded into a rod-shaped sample with a diameter of approximately 2 mm by extrusion molding. And

then the rod-shaped sample was dried in atomosphere. The rod-shaped sample was heat treated at 200 °C for 2 h to form the La-Ni/SiO₂ composite.

Figure 1(a) is a photograph of a sample of La-Ni/SiO₂ composite materials. Figure 1(b) shows a cross-sectional scanning electron micrograph (SEM) of the composite materials.

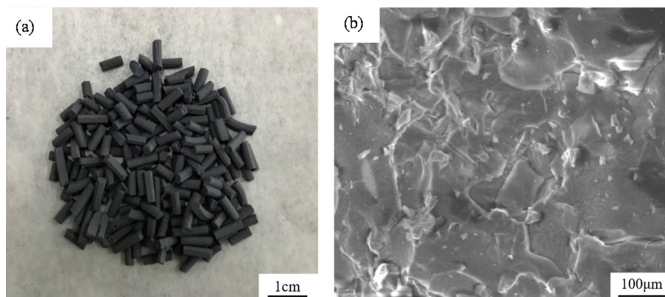


Fig. 1. La-Ni-Al-Mn/SiO₂ composite materials picture (a) Macro photo and (b) sectional scanning electron microscope picture

2.2 Structure Characterization

The surface morphology and grain size of the La-Ni/SiO₂ composite materials were characterized and analysed by a JEOL JEOL thermal field emission scanning electron microscope JSM-7900F. An FEI-Tecnai-G2-F20 high-resolution field emission transmission electron microscope produced by FEI Company of the United States was used to characterize and analyse the surface morphology and grain size of the FIB cut samples of the composite materials.

2.3 Sample Test Conditions

The kinetic curves of hydrogen absorption and the anti-poisoning performance for the La-Ni/SiO₂ composite were measured using a Sieverts-type hydrogenator. About 2 g of composite was loaded into the sample holder of the apparatus. The sample holder was vacuumized for 1 h at 200 °C, and then cooled down to room temperature. Then, the absorption kinetics were measured under the condition of room temperature and 0.1MPa. The experimental gases included high-purity hydrogen (H₂ ≥ 99.999%) and standard gas containing different component impurity gases, such as O₂, N₂, etc.

3 Results and Discussion

3.1 Poisoning Resistance Performance of La-Ni/SiO₂ Composite

The anti-poisoning performance of La-Ni/SiO₂ composite was investigated in different standard gases. Figure 2 showed the hydrogen absorption kinetic curves of LaNi alloy and La-Ni/SiO₂ composite in standard gas (0.2 vol.%O₂ + 0.8 vol.%N₂ + 99 vol.%H₂).

As shown in Fig. 2, La-Ni alloy didn't absorb hydrogen entirely, meaning that the alloy was poisoned by the impurity gases seriously. The La-Ni/SiO₂ composite sample could absorb hydrogen fastly after an incubation period for about 120 min. Although the maximum hydrogen capacity of the composite in standard gas was reduced to 1.03wt% from 1.16wt% in purity hydrogen, it still exhibited excellent anti poisoning ability compared with the non-modified alloy.

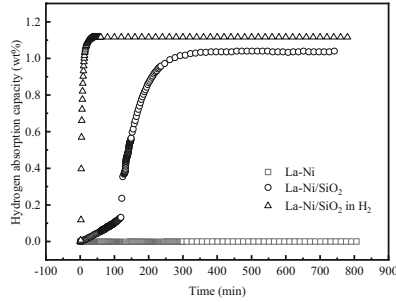


Fig. 2. Hydrogen absorption kinetic curves of LaNi alloy and La-Ni/SiO₂ composite.

Figure 3 exhibits the hydrogen absorption curves of La-Ni/SiO₂ composite in hydrogen with different nitrogen contents of 5%, 10%, 15% and 20%. It is shown in Fig. 3, La-Ni/SiO₂ composites could absorb hydrogen in standard gases contained nitrogen. Furthermore, there was no decrease in the hydrogen absorption capacity and kinetics with the hydrogen absorption cycles after first activation cycle indicating that the La-Ni/SiO₂ composite showed a good cycling performance even in standard gas with high nitrogen content as shown in Fig. 5. However, from Figs. 4 and 5, it can be seen that the durability of La-Ni/SiO₂ composite against nitrogen appeared a decreasing tendency with the increasing of nitrogen contents in hydrogen significantly.

To investigate the poisoning resistance mechanism of the La-Ni/SiO₂ composite, the micro morphology of the sample was analysed by transmission electron microscopy. As shown in Fig. 6, the SiO₂ cubic structured phase regions with short-range order arrangement of atoms were formed in the amorphous SiO₂-coating layer during the heat treatment process, which were the hydrogen permeation regions with, effectively restricting the passage of larger molecules of oxygen and other harmful impurities. It is noteworthy that the phenomenon of short range ordered arrangement of SiO₂ atoms didn't occur in the sample without heat treatment (Fig. 7).

In order to evaluate the performance stability of La-Ni/SiO₂ composite in application conditions. The composite was tested for 1000 hydrogen absorption and desorption cycles in hydrogen gas with 15% nitrogen. From Fig. 8, it can be found that there was no marked difference in the hydrogen absorption curves after first activation cycle. The hydrogen absorption capacity was basically maintained at around 0.76wt%. Based on the above phenomena, it can be concluded that La-Ni/SiO₂ composite exhibited excellent resistance to poisoning and cycle life.

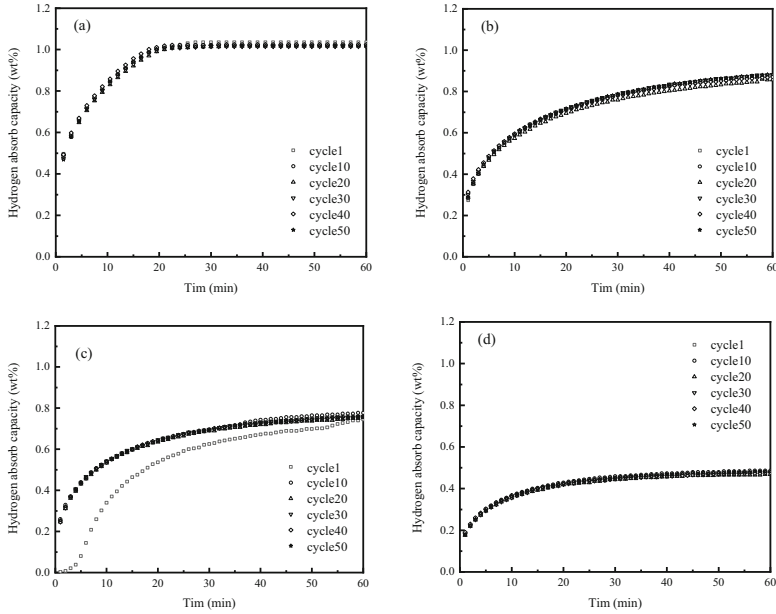


Fig. 3. Hydrogen absorption curves of La-Ni/SiO₂ composite in different standard gases. (a) 5%N₂ + 95%H₂, (b) 10%N₂ + 90%H₂, (c) 15%N₂ + 85%H₂ and (d) 20%N₂ + 80%H₂.

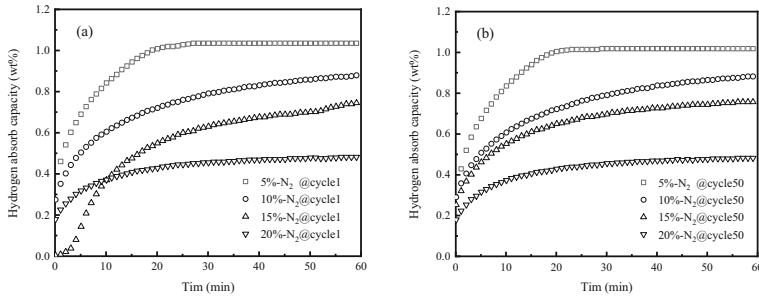


Fig. 4. Hydrogen absorption curves of La-Ni/SiO₂ composites in different standard gases. (a) cycle 1 and (b) cycle 50.

3.2 Fine-Powdering Resistance Performance of La-Ni/SiO₂ Composite

La-Ni/SiO₂ composite was prepared into rod-shaped sample and its anti-pulverization performance was evaluated by the morphology changes of the sample after multiple cycles. The morphologies of the composite after certain number of cycles are displayed in Fig. 9. There was no sign of any powder detachment from the matrix after 1000 cycles of hydrogen absorption and desorption, indicating that the material has good resistance to pulverization. There is a strong interaction force between SiO₂ in the composite matrix. In addition, some interspaces were left in the composite due to the evaporation of water during the drying process before heat treatment. Although the La-Ni alloy would

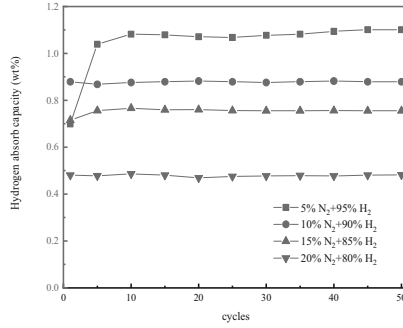


Fig. 5. Hydrogen absorb capacities of La-Ni/SiO₂ composites with hydrogen absorption cycles in different standard gases.

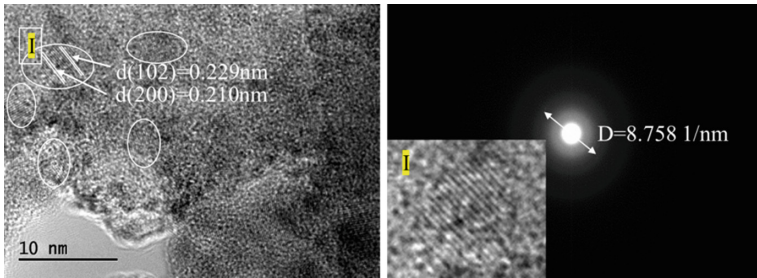


Fig. 6. TEM image of La-Ni/SiO₂ composite.

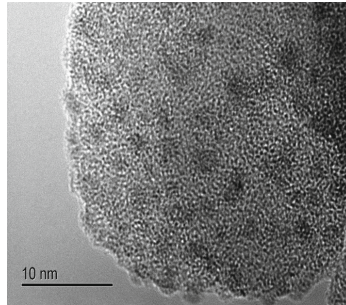


Fig.7. TEM image of La-Ni/SiO₂ sample without heat treatment.

expand after hydrogen absorption, the vacancies in the composite could also withstand the expansion of the alloy. In addition, the high-strength SiO₂ coated on the surface of the alloy powder can also control the alloy within its formed spatial structure.

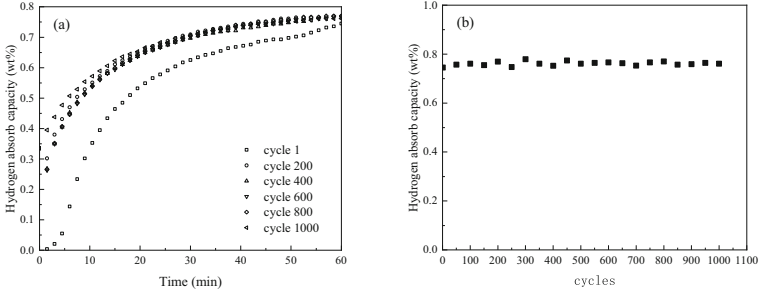


Fig. 8. Hydrogen absorption properties of La-Ni/SiO₂ composites with hydrogen absorption cycles in standard gas. (a) hydrogen absorption curves and (b) hydrogen capacities.

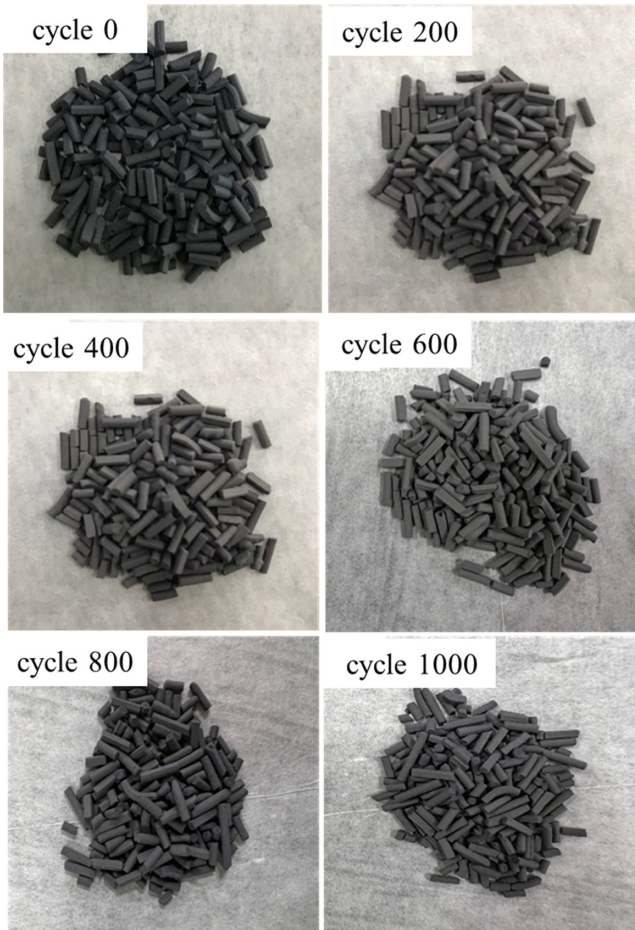


Fig. 9. Morphologies of La-Ni/SiO₂ composite after certain number of cycles

4 Conclusions

La-Ni alloy powders could be embedded in a matrix of porous silica via a fumed silica method. After heat treatment at 200 °C for 2 h, a short range ordered cubic structural distribution appeared in the amorphous SiO₂ coating layer, which permeated hydrogen molecules to penetrate and restrict the passage of larger molecules of oxygen and other harmful impurities. Furthermore, the granules of this silica embedded metal hydride were fracture resistant and could withstand many absorption/desorption cycles without generating fines. As a result, the La-Ni/SiO₂ composite demonstrated good poisoning, fine-powdering resistance and cyclic stability. After 1000 cycles of hydrogen absorption and desorption, the composite still maintained its original hydrogen storage performance and the matrix had no pulverization phenomenon.

References

1. Cheng, H.H., Yang, H.G., Li, S.L.: Effect of hydrogen absorption/desorption cycling on hydrogen storage performance of LaNi_{4.25}Al_{0.75}. *J. Alloy. Compd.* **453**(4), 448–452 (2006)
2. Jeu, R.A.M.D., Wagner, W., Holmes, T.R.H., et al.: Global soil moisture patterns observed by space borne microwave radiometers and scatterometers. *Surv. Geophys.* **29**(4), 399–420 (2008)
3. Han, J.I., Lee, J.Y.: The effect of CO impurity on the hydrogenation properties of LaNi₅, LaNi_{4.7}Al_{0.3} and MmNi_{4.5}Al_{0.5} during hydriding-dehydriding cycling. *J. Less-Common Metals* **152**, 319–327 (1989)
4. Okumura, M., Ikado, A., Saito, Y., et al.: Pulverization mechanism of hydrogen storage alloys on microscale packing structure[J]. *Int. J. Hydrogen Energy* **37**(14), 10715–10723 (2012)
5. Rusman, N.A.A., Dahari, M.: A review on the current progress of metal hydrides materials for solid-state hydrogen storage applications. *Int. J. Hydrogen Energy* **41**(28), 12108–12126 (2016)
6. Wang, X.L., Iwata, K., Suda, S.: Hydrogen purification using fluorinated LaNi_{4.7}Al_{0.3} alloy. *J. Alloy. Compd.* **231**(1–2), 860–864 (1995)
7. Wang, X.L., Iwata, K., Suda, S.: Effects of carbon monoxide on the hydriding reactions of the untreated and fluorinated LaNi_{4.7}Al_{0.3} alloys. *J. Alloy. Compd.* **231**(1–2), 829–834 (1995)
8. Xiang, F.L., Guo, X.M., et al.: Kinetic mechanism of electroless palladium coating on surface of ZrNi based hydrogen storage alloy. *Chin. J. Rare Met.* **43**(7), 713–718 (2019)
9. Guo, X., Wang, S., Li, Z., et al.: Study on the poisoning resistance of Pd-coated ZrCo alloy prepared by electroless plating method. *Fusion Eng. Des.* S0920379616305774 (2016)
10. Ren, J., Williams, M., Lototsky, M., et al.: Improved tolerance of Pd/Cu-treated metal hydride alloys towards air impurities. *Int. J. Hydrogen Energy* **35**(16), 8626–8630 (2010)
11. Heung, L.K., Wicks, G.G.: Silica embedded metal hydrides. *J. Alloy. Compd.* **s293–295**(none), 446–451 (1999)
12. Cheng, H.H., Yang, H.G., Li, S.L., et al.: Hydrogen storage performance of LaNi_{4.25}Al_{0.75}/SiO₂ composite. *Rare Metal Metals Eng.* **37**(8), 1427–1430 (2008)



Study on Energy Management Strategy for Reducing Equivalent Hydrogen Consumption in a Combined Heat and Power System Based on PEMFC

Ruitao Li¹, Haolin Wang¹, Naiyuan Yao¹, Zishun Xu¹, and Tiancai Ma^{1,2}(✉)

¹ School of Automotive Studies, Tongji University, Shanghai 201804, People's Republic of China

matiancai@tongji.edu.cn

² Institute of Carbon Neutrality, Tongji University, Shanghai 200092, People's Republic of China

Abstract. Combined heat and power (CHP) system based on proton exchange membrane fuel cells (PEMFC) can improve the overall efficiency by recycling the heat generated within the electrochemical reaction process of H₂, which is a potential, environmentally friendly and efficient co-production mode. Due to the soft output characteristics of fuel cells, it is always equipped with auxiliary power equipment as a hybrid energy system. A number of studies have been carried out on the energy and efficiency analysis of CHP. However, few people pay attention to the energy distribution strategy and its effect on hydrogen consumption in real application scenarios. In this work, a 10kW PEMFC CHP system and the corresponding simulation model were built based on the energy demands of a family, and the model was verified by the measured data. Under the electric-following operation mode in the off-grid scenario, the minimum equivalent H₂ consumption were optimized by the follow strategy, compound fuzzy logic control strategy (Compound-FLC), genetic algorithm optimized FLC (GA-FLC) and energy strategy based on Pontriagin's minimum principle (PMP). The results show that the equivalent H₂ consumption of CHP has been significantly improved by GA-FLC, and the state of charge (SOC) of the battery are relatively stable. PMP strategy can further reduce the equivalent H₂ consumption and the operating cost by 4.22% and 4.17%, respectively, compared with the follow strategy. The strategy proposed in this paper can effectively improve the economy of PEMFC-CHP system.

Keywords: PEMFC · Combined Heat and Power System · Energy Distribution Strategy · Equivalent H₂ Consumption

1 Introduction

The PEMFC combined heat and power system (PEMFC-CHP) has emerged as a promising, environmentally friendly, and highly efficient co-generation method with significant research significance and economic value due to its energy efficiency exceeding 80%.

In recent years, PEMFC-CHP systems have been widely demonstrated in both civil and commercial fields [1, 2]. Literature [3–5] has studied the application of CHP systems with power grades ranging from 1 to 10 kW in residential settings. Herrmann et al. [6] conducted a theoretical analysis on the electrical efficiency and total efficiency of residential co-generation systems based on low-temperature PEMFCs, which were found to be approximately 50% and 95%, respectively. Literature [7, 8] investigated the economy and evaluation methods of large-scale PEMFC-CHP systems in industrial and commercial buildings, such as data centers. Depending on energy load demand, CHP operation can be categorized into electric-leading strategy, thermal-leading strategy, or combined strategy that focuses on comprehensive efficiency or economy [9]. However, relevant studies show that when a single strategy dominated by electrical or thermal is adopted, another kind of energy will be wasted [10]. In light of this limitation, scholars have progressively integrated FC-CHP systems with other equipment to create hybrid energy systems. Driven by the pursuit of low-carbon development, CHP systems are increasingly incorporating renewable energy sources and energy conversion technologies such as photovoltaic power generation (PV) [11], wind power generation (WP), heat pumps (HP) [12], thermoelectric conversion devices (TEG) [13] and so on. This approach significantly enhances energy efficiency and effectively mitigates carbon emissions.

Due to the soft output characteristics of fuel cells and slow dynamic response process, fuel cells are unable to meet the power demands during start/stop and rapid load changes [14]. Additionally, frequent load change can impact the service life of fuel cells directly [15]. Therefore, a PEMFC-CHP system must be equipped with corresponding auxiliary power equipment such as lithium-ion batteries (LIB) or supercapacitors. To fully leverage the benefits of fuel cells and energy storage devices in a hybrid energy system, it is essential to implement effective energy management strategies (EMS) that ensure each device operates within its designated range and optimally distribute energy instructions among various sources to achieve maximum efficiency and other objectives [16], while also considering the impact of EMS on the lifecycle of the hybrid power system [17].

The EMS of mixed energy system can be categorized into rule-based and optimization-based EMS. Rule-based strategies, such as frequency separation method (FSM) [18], switching [19, 20], fuzzy logic control (FLC) [11, 21, 22], rely primarily on simple rules derived from optimization methods or engineering experience and are easily implemented in practical applications. The FSM effectively eliminates high frequency variable conditions that result in frequent load fluctuations of the fuel cell, thereby restricting operating conditions to prolong its lifespan [18]. Sheng et al. [19] have developed a rule-based EMS for a hybrid power system comprising PEMFC and lithium-ion battery, with inputs including water content, SOC and power demand of the PEMFC. Water content is used as an indicator of fuel cell health while catalyst aggregation serves as an indicator of fuel cell decay. FLC is distinguished by its ease of use, insensitivity to system models, strong robustness, adaptability to dynamic processes, and ability to solve complex nonlinear time-varying problems [22]. However, rule-based control strategies have two significant limitations: they require expertise in designing rules and are insufficient for addressing critical business objectives such as fuel economy, health degradation, and storage constraints [23]. Therefore, rule-based

control strategies embedded with optimization methods have been extensively studied. Yuan et al. [21] employed genetic algorithm (GA) to optimize and adjust control variables in rule-based EMS, with battery charging time as a single objective. In terms of fuel economy, battery charging time, fuel cell efficiency, and system durability, the proposed strategy performs more closely to ideal performance than conventional rule-based EMS, FLC, and Dynamic programming algorithm (DP). Fu et al. [22] proposed a frequency decoupling optimization strategy for FLC for FC/LIB/supercapacitor hybrid system with the goal of minimizing the H₂ consumption and power fluctuations of fuel cells. They also adopted GA to optimize the fuzzy controller, effectively lowering the H₂ consumption and power fluctuations.

Dynamic programming (DP) is considered to be the most ideal optimization algorithm for steady-state process of mixed energy systems. The state variable is divided into N nodes by DP according to a specific step size within the range of maximum and minimum values. To choose the node with the smallest optimization goal function, each node recursively reaches the cycle's end after saving the optimal trajectory to itself. The trajectory data that nodes save can be used to determine the overall best strategy. Because it ensures optimality, it has been widely employed in EMS design in both academia and industry. The enhancement of DP and various optimization techniques in fuel cell hybrid energy systems was compared in the literature [24, 25]. However, because DP uses an off-line global optimization approach, it necessitates knowledge of the driving conditions in advance, and the cost of calculation rises exponentially as the number of variables or dimensions increases [16]. In order to find approximate global optimal solutions, a number of instantaneous optimization techniques have been presented. These techniques include equivalent consumption minimization (ECMS), Pontryagin minimum principle (PMP), and model predictive control (MPC). These algorithms have the benefits of a straightforward optimization framework, minimal computational cost, and online implementation [18]. Ettahir et al. [26] investigated an EMS based on adaptive PMP that took into account the change in maximum power and efficiency with FC attenuation and integrated it with the adaptive recursive least squares algorithm to obtain the best operating parameters for PEMFC in real-time operation. By comparing the EMS simulation of the PI control strategy based on PMP and FLC under 6 operating circumstances, Odeim et al. [27] found that the PI based on PMP had lower equivalent H₂ consumption and less loss to lithium batteries.

In conclusion, rule-based compound FLC with optimization algorithm and minimal principle is more likely to achieve online optimization of CHP systems. This paper takes the 10 kW CHP system in the residential scene as the object, and studies its power follow strategy in off-grid operation. Firstly, a 10 kW PEMFC-CHP system and the simulation model were constructed. The measured data was then used to confirm the model. Finally, under the simulated household energy demand in Shanghai, China, the follow strategy, the compound FLC, the fuzzy control strategy optimized by GA (GA-FLC) and PMP strategy were compared with a focus on the minimum H₂ consumption.

2 System Model

2.1 System Description

The architecture of a typical CHP system typically consists of the following modules: external high pressure H_2 supply module, H_2 supply module, air supply module, fuel cell stack module, cooling module, auxiliary power supply module, power conversion system, and heat recovery module. The schematic diagram is depicted in Fig. 1(a), and the system design approach is referenced in the literature [28].

Figure 1(b) displays the experimentally determined CHP system performance. With the increase of current density, the net output power P_{stack} is rising from 1.67 kW to 12.2 kW, and the electric efficiency η_{elec} steadily falls from 51.7% to 37.8%, thermal efficiency $\eta_{thermal}$ increases from 12.7% to 50.1%. When P_{stack} exceeds 4.7 kW, the overall efficiency η_{total} exceeds 80%, and it reaches a maximum of 91.2% when P_{elec_net} is greater than 10 kW.

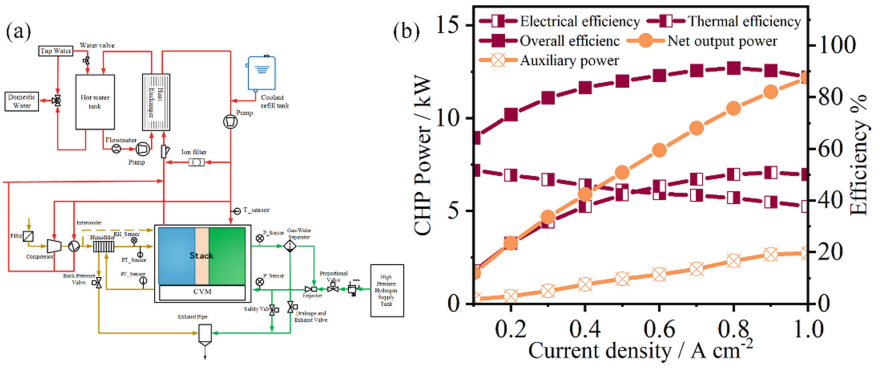


Fig. 1. PEMFC-CHP system: (a) schematic diagram, (b) experimental data

2.2 Mathematical Model

In this part, mathematical representations of PEMFC voltage, stack temperature, LIB, plate heat exchanger, and insulated water tank are introduced. For more detailed introduction, please refer to our previous study [29].

The output voltage of the stack is expressed as:

$$P_{stack} = N_{cell} V_{cell} I_{cell} \quad (1)$$

where, N_{cell} is the number of cells in the stack, I_{cell} is the working current, and V_{cell} is the output voltage of single cell. The output voltage of single cell can be expressed as:

$$V_{cell} = E_{nernst} - \eta_{act} - \eta_{ohm} - \eta_{con} \quad (2)$$

where, E_{nernst} is the open-circuit voltage of the fuel cell. η_{act} is the activation overvoltage; η_{ohm} is ohm overvoltage; η_{con} is the concentration overvoltage.

The thermal generation of the stack is:

$$P_{thermal} = N_{cell} I_{cell} (E_{equ} - V_{cell}) \quad (3)$$

where, E_{equ} refers to the thermal balance potential (low calorific value).

The heat produced by the stack is exchanged by the coolant. Through a heat exchanger, tap water absorbs heat from the coolant to be reused. In this process, the coolant loss thermal power \dot{Q}_{cool} and tap water absorption of thermal power \dot{Q}_{water} :

$$\begin{cases} \dot{Q}_{cool} = \dot{m}_{cool} C_{cool} (T_1 - T_2) \\ \dot{Q}_{water} = \dot{m}_{water} C_{water} (t_1 - t_2) \end{cases} \quad (4)$$

where, the \dot{m}_{cool} , \dot{m}_{water} refers to the mass flow of coolant and tap water, kg/s . C_{cool} , C_{water} represents the specific heat capacity of coolant and tap water, $J/(kg \cdot ^\circ C)$; T_1, t_1 respectively indicate the inlet temperature of coolant and tap water, $^\circ C$; T_2, t_2 indicate the outlet temperature of coolant and tap water, $^\circ C$.

The function of the insulation water tank is to store the tap water heated by the heat exchanger. According to the law of energy conservation, the temperature change of stored water can be expressed as:

$$m_{ht} c_{p,h} \frac{dT_{ht}}{dt} = \dot{Q}_{recovery} - \dot{Q}_{demand} \quad (5)$$

where, m_{ht} is the mass of hot water, kg ; $C_{p,h}$ is the specific heat capacity of hot water, $J/(kg \cdot ^\circ C)$; T_{ht} is the hot water temperature within the tank, K .

The commonly used LIB models include equivalent circuit model, data-based model, mechanism model, electrochemical model, etc. The equivalent circuit model is the most widely used, and Rint equivalent circuit model is used in this paper. According to Kirchhoff's voltage law:

$$U_b = U_{oc} - I_b R \quad (6)$$

$$P_b = U_{oc} \cdot I_b - R \cdot I_b^2 \quad (7)$$

$$I_b = \frac{U_{oc} - \sqrt{U_{oc}^2 - 4R \cdot P_b}}{2R} \quad (8)$$

where, U_b, P_b, I_b, R are discharge voltage, discharge power, discharge current and internal resistance of LIB, respectively. The ampere-hour integral method is used to calculate the remaining battery power:

$$SOC_t = SOC_0 - \frac{\int_0^t I_b \cdot dt}{3600 \cdot Q_{bat}} \quad (9)$$

where, SOC_t is the current lithium-ion battery capacity; SOC_0 is the remaining charge of lithium-ion battery at the initial time; Q_{bat} indicates the capacity of the LIB, Ah .

The polarization curves of the model and experimental data are displayed in Fig. 2(a). The simulated results have an average relative error of roughly 0.23%, the maximum relative error is 1.2%. Except for the first three points, as shown in Fig. 2 (b), the average relative error of recovery power is 1.5%, and the single maximum error is 5.2% at 170 A. Small discrepancies exist between simulation and experimental test results, which can satisfy simulation test standards.

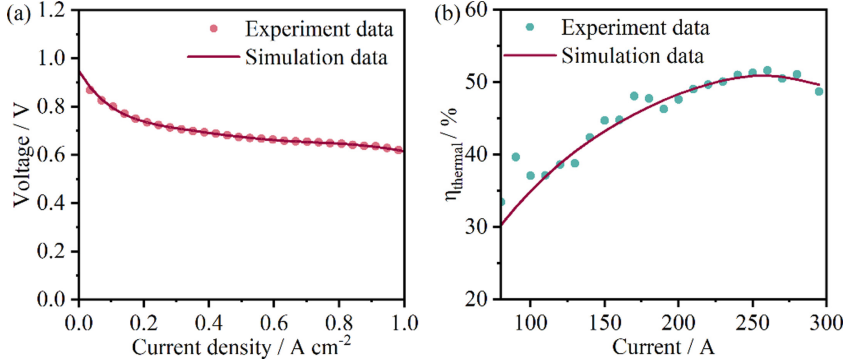


Fig. 2. Comparison of experimental data and simulation results of (a) polarization curves, and (b) heat recovery power of CHP system

2.3 Electric and Thermal Load

In this study, the energy use of a 90 m² Shanghai, China, home with three bedrooms and one living room is examined. This location is a typical “hot summer and cold winter” environment, according to Chinese National Standard GB 50178-93, and as such, needs air conditioning in the summer and heat supply in the winter. The combined energy use of heating and cooling should therefore be taken into account. Based on the findings [29] and the analysis above, we calculated the typical summer household’s electrical and thermal loads, which are depicted in Fig. 3(a).

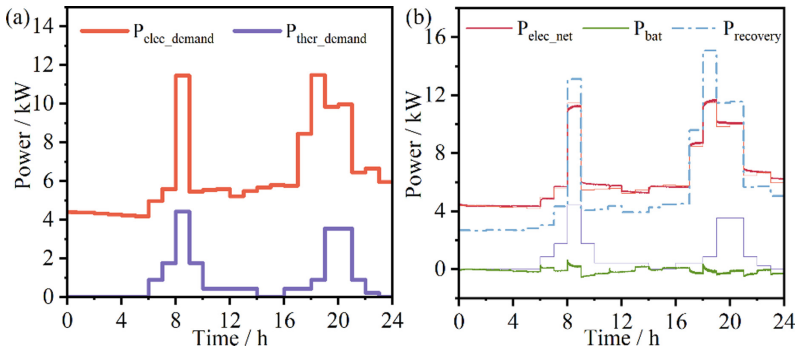


Fig. 3. (a) Typical household energy load demand curves in summer, (b) energy supply of CHP under fuel cell electric-leading strategy

The power and thermal supply conditions obtained by experiments are shown in Fig. 3(b) in accordance with the aforementioned energy needs. The PEMFC output power P_{stack} and battery power P_{bat} work together to meet the electric load $P_{\text{elec_demand}}$. Figure 3(b) shows that P_{stack} can follow $P_{\text{elec_demand}}$. When $P_{\text{stack}} > P_{\text{elec_demand}}$, the LIB is in the charging state, $P_{\text{bat}} < 0$; When $P_{\text{stack}} < P_{\text{elec_demand}}$, it is in discharge state, $P_{\text{bat}} > 0$. Therefore, as an auxiliary power source of PEMFC, the battery plays

a good role of power compensation. In addition, the CHP system is able to meet the house’s hot water needs in the summer. The waste heat recovery system can recover 134 kWh of heat energy within 24 h.

3 Energy Management Strategy

The energy management strategies studied in this section comprehensively considers the following rules: (1) CHP system works in high efficiency zone as much as possible; (2) Reduce the frequent load variation conditions; (3) SOC should be kept within a reasonable range to improve its reliability.

3.1 Compound FLC Strategy

In our previous study [29], the discharge conditions of fuel cells and lithium batteries under the switch strategy and FLC strategy had been analyzed respectively. The switch control strategy led to the frequently starts/stops condition of PEMFC. FLC can reduce the fluctuation of the PEMFC output power, while the battery tended to be overcharged in the low-energy demand period. Therefore, on the basis of the above studies, this paper combines the switch strategy and FLC, and a sliding filter module is added to reduce the high-frequency variation of fuel cell power, as shown in Fig. 4.

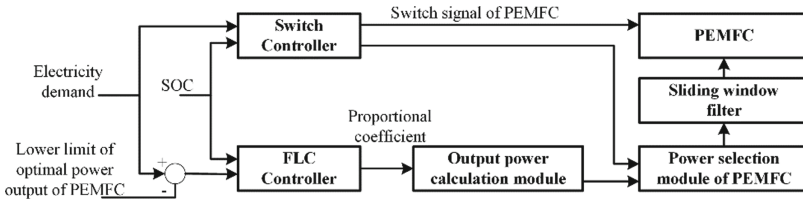


Fig. 4. Flowchart of compound FLC strategy

The expression of the new sequence of sliding filtering is:

$$P_{FC} = \frac{1}{N} \times \sum_{k=0}^{N-1} P[T - k] \tag{10}$$

where, N is the number of sampling points in the sliding window; T is the current sampling time; k is the scale of the sequence in the sliding window; $P[T - k]$ is the fuel cell power at the $N - K + 1$ sampling point in the sliding window.

3.2 Genetic Algorithm Optimized FLC Strategy

The membership function and fuzzy rules are optimized in this part using a genetic algorithm. The flow chart and more detailed content of genetic algorithm optimization can be referred to our previous research [30]. The objective is to optimize the economy of the CHP system. Factors such as PEMFC H_2 consumption, LIB equivalent H_2 consumption

and thermal recovery should be considered. Therefore, the design of the cost function is:

$$cost = \frac{((m_{H_{fc}} + m_{H_{bat}}) \times C_{H_2} - Q_{recovery} \times C_{hot_water})}{x} \quad (11)$$

where, $m_{H_{fc}}$, $m_{H_{bat}}$ are equivalent H_2 consumption of fuel cell and battery, kg ; C_{H_2} is the price of H_2 , $\text{¥}/kg$; $Q_{recovery}$ is the heat recovery, kJ . C_{hot_water} is the price of hot water, $\text{¥}/kJ$; x is the running time, h .

H_2 consumption rate of PEMFC and LIB are shown as Eqs. (12), (13):

$$\dot{m}_{H_{fc}} = \frac{N_{cell} N M_H}{t \eta_H} = \frac{N_{cell} I_{st}}{F \eta_H} \approx 9.818 \times 10^{-4} I_{st} \quad (12)$$

$$m_{H_{bat}} = \begin{cases} -\frac{V_{bat_{avg}} \cdot \Delta Q_{bat} \cdot \eta_{bat_{dis_{avg}}}}{\eta_{DC} \cdot \eta_{fc_avg} \cdot LHV_H}, & Q_{bat} > 0, \text{ charging} \\ -\frac{V_{bat_{avg}} \cdot \Delta Q_{bat}}{\eta_{DC} \cdot \eta_{bat_{chg_{avg}}} \cdot \eta_{fc_avg} \cdot LHV_H}, & Q_{bat} \leq 0, \text{ discharging} \end{cases} \quad (13)$$

where, $\dot{m}_{H_{fc}}$ is H_2 consumption rate, g/s . M_H is the molar mass of H_2 , g/mol ; η_H is the H_2 utilization efficiency, and N is mole number of H^+ participating in the reaction. $V_{bat_{avg}}$ is the average working voltage of the battery, V ; η_{DC} is the efficiency of the DC/DC converter; $\eta_{bat_{dis_{avg}}}$, $\eta_{bat_{chg_{avg}}}$ are the average charging and discharging efficiency of batteries.

The reciprocal of the cost function was selected as the fitness value. In order to take the reliability and computing speed of the genetic algorithm into account, the population size is set as 20 and the algebra is set as 10. The crossover probability is 0.7 and the mutation probability is 0.1.

3.3 Pontriagin Minimum Principle Optimization Strategy

The optimization objective of this section is to minimize the fuel consumption of the CHP system from the initial time t_0 to the last time t_f in 24 h operating condition. Select $SOC(t)$ as the state variable and P_{elec_net} as the system control variable. Therefore, the performance function of the control system can be expressed as:

$$J = \int_{t_0}^{t_f} \dot{m}_{H_{fc}} dt \quad (14)$$

H_2 consumption rate of fuel cell:

$$\dot{m}_{H_{fc}} = \frac{P_{elec_net}}{\eta_{fc} \cdot LHV_H} = f(P_{elec_net}) \quad (15)$$

where, η_{fc} is the system efficiency of the CHP, including the power consumed by the DC/DC converter and auxiliary system.

Fit $\dot{m}_{H_{fc}}$, P_{elec_net} and get Eq. (16):

$$\begin{aligned} \dot{m}_{H_{fc}} = & -7.331e-07 \times P_{elec_net}^4 - 6.624e-06 \times P_{elec_net}^3 \\ & + 0.0006362 \times P_{elec_net}^2 + 0.01233 \times P_{elec_net} + 0.000297 \end{aligned} \quad (16)$$

The change rate of SOC can be obtained by combining Eqs. (8), (9), that is, the equation of state of the control system is:

$$\begin{aligned} \dot{SOC}(t) = & -\frac{I_{bat}(t)}{3600Q_{bat}} = \\ & -\frac{1}{3600Q_{bat}} \frac{U_{oc}(t) - \sqrt{U_{oc}(t)^2 - 4R(t) \cdot (P_{elec_demand}(t) - P_{elec_net}(t))}}{2R_{bat}(t)} \end{aligned} \quad (17)$$

The boundary conditions of state variables are:

$$SOC(0) = SOC(t_f) = SOC_{ref} \quad (18)$$

where, SOC_{ref} is the reference value of battery SOC, 60%.

The constraint conditions for output power of LIB are:

$$\begin{cases} P_{bat}(t) = P_{elec_demand}(t) - P_{elec_net}(t) \\ P_{bat_min} < P_{bat}(t) < P_{bat_max} \end{cases} \quad (19)$$

where, P_{bat_min} , P_{bat_max} are the minimum and maximum output power of the battery kW.

In order to avoid the idle condition and frequent load change condition, P_{elec_net} should also be constrained:

$$\begin{cases} P_{elec_net_min} < P_{elec_net}(t) < P_{elec_net_max} \\ \Delta P_{elec_net_min} < \Delta P_{elec_net}(t) < \Delta P_{elec_net_max} \end{cases} \quad (20)$$

where, $P_{elec_net_min}$, $P_{elec_net_max}$ are the upper and lower limits of the fuel cell working efficiency zone, kW; $\Delta P_{elec_net_min}$, $\Delta P_{elec_net_max}$ is the maximum reduction rate and lift rate of the fuel cell, kW/s.

When the minimum principle is used to solve the optimal control problem of the system, the Hamiltonian function needs to be established according to Eqs. (14) and (17), as shown below:

$$H = \dot{m}_{H_{fc}} + \lambda(t)\dot{SOC}(t) \quad (21)$$

Pontryagin minimum principle is a necessary condition for optimal control, so the optimal $P_{elec_net}^*$ must minimize Hamiltonian function of the system, that is:

$$P_{elec_net}^* = \operatorname{argmin} H[t, SOC(t), P_{elec_net}(t), \lambda(t)] \quad (22)$$

According to the minimum principle, the optimal state variable $SOC^*(t)$, $\lambda^*(t)$ need to satisfy the regular equation:

$$\dot{SOC}^*(t) = \frac{\partial H[t, SOC^*(t), P_{elec_net}^*(t), \lambda^*(t)]}{\partial \lambda(t)} \quad (23)$$

$$\dot{\lambda}^*(t) = - \frac{\partial H[t, SOC^*(t), P_{elec_net}^*(t), \lambda^*(t)]}{\partial SOC(t)} \quad (24)$$

$$\dot{\lambda}^*(t) = \frac{\lambda^*(t)}{3600Q_{bat}} \cdot \left(\frac{\partial I_{bat}^*}{\partial U_{oc}} \frac{\partial U_{oc}}{\partial SOC} + \frac{\partial I_{bat}^*}{\partial R_{bat}} \frac{\partial R_{bat}}{\partial SOC} \right) \quad (25)$$

According to the characteristic curve of the battery, the open-circuit voltage and the internal resistance vary little with the SOC during charging and discharging and can be ignored. By Eq. (25), the change rate of $\lambda(t)$ is 0, it can be set as a fixed value [31]. Accordingly, the most appropriate value of λ ($\lambda^*(t)$) can be tested off-line after find the $\lambda(0)$ by dichotomy method.

4 Result and Discussions

The simulation results of the matching between the output power of the CHP system and the power load demand of the user under the control of the four strategies discussed above are shown in Fig. 5. The power supply curves of all strategies basically coincides with the power demand curve, which indicates that the CHP system can fully cover the power demand of the user with any strategy.

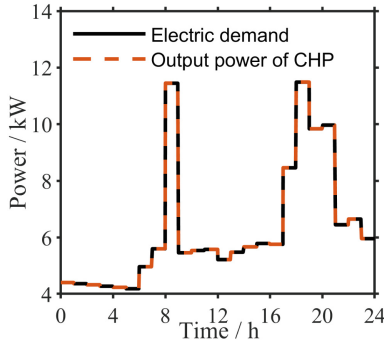


Fig. 5. Power load matching under different control strategy

Figure 6 (a) presents the P_{elec_net} curves of fuel cells under different strategies. For the follow strategy, the P_{stack} tracks the load demand closely, with dramatic operating condition changes occurring at the beginning and end of high load demand periods. For Compound-FLC strategy, the LIB initially provides power at 6:00, gradually increasing output power to a maximum at around 7:00 due to the intervention of PEMFC. The P_{stack} sharply drops to around 9 kW at 9:00, and then drops again to around 7 kW between 10:00 and 11:00. The most significant difference, however, is in 18:00–21:00, the P_{stack} remains stable and no longer fluctuates with load. It can be seen that the power change is significantly slowed down due to the addition of FLC and sliding filter. In the GA-FLC strategy, the power output of PEMFC is similar to that of Compound FLC strategy, but the change rate is slower. Noticeable changes appear in the PMP strategy. The P_{stack} is solely maintained within the range of 7.3 ~ 7.7 kW. The variable load and start-stop

conditions that are easy to cause degradation of core components such as catalysts and membranes are eliminated, and the service life of the fuel cell is going to be greatly extended.

According to Fig. 6 (b), the P_{bat} curves are opposite of the P_{stack} curves. In the follow strategy, the power fluctuates of P_{bat} within ± 0.5 kW, which is only work for loading and unloading, and SOC is nearly unchanged, as Fig. 6 (c). Both Compound FLC and GA-FLC strategies have more intense power output, especially in the latter strategy, which is attributed to the more moderate change of P_{stack} under this strategy. The output power and changing frequency of lithium batteries both rise significantly when using the PMP strategy. It requires more P_{bat} to meet power output in order to maintain the relatively stable P_{stack} . Besides, under the FLC strategies, LIB takes longer to charge, so the SOC decreases from the initial level with a relatively smooth fluctuation. However, under the PMP strategy, due to the maintained P_{stack} , SOC increases significantly from 21:00–7:00 and 9:00–17:00 with a low demand period, kept in 60–80%.

According to Eq. (3), the Compound FLC and GA-FLC have similar P_{stack} , so the recovery heat is close to each other, showing the same trend as the generation power curves, as shown in Fig. 6 (d). CHP produces much more heat than the heat load needs. Since there is less heat demand in the summer, the excess heat will be stored or diverted, resulting in some waste. In contrast, PMP strategy had less surplus heat recovery, the follow strategy generates the most excess heat.

Table 1. Comparison of the 4 strategies under electric load conditions

| | H ₂ consumption kg/24h | Thermal recovery kJ/24h | Cost (¥/h) |
|--------------------|-----------------------------------|-------------------------|------------|
| 1. Follow strategy | 10.66 | 138.227 | 17.76 |
| 2. Compound-FLC | 10.57 | 133.206 | 17.61 |
| 3. GA-FLC | 10.27 | 128.679 | 17.12 |
| 4. PMP | 10.21 | 127.22 | 17.02 |
| 4 versus 1 | – 4.22% | – 7.96% | – 4.17% |
| 4 versus 2 | – 3.41% | – 4.49% | – 3.35% |
| 4 versus 3 | – 0.58% | – 1.13% | – 0.58% |

For a more realistic strategy, PEMFC-CHP needs to meet the energy requirements while keeping the P_{stack} as flat as possible and reducing the combined equivalent H₂ consumption. According to the above discussion, all the strategies discussed are qualified for energy demands. The results of equivalent H₂ consumption are shown in Fig. 6 (e), and the specific values are shown in Table 1. It can be seen that the superiority of the four strategies is PMP > GA-FLC > Compound-FLC > follow strategy. Compared with the simplest follow strategy, PMP can reduce the equivalent H₂ consumption, heat recovery and running cost by 4.22%, 7.96% and 4.17%, respectively.

Figure 7 shows the occurrence frequency of P_{stack} under different working conditions and different strategies. According to Fig. 7 (a), the follow strategy's power variation

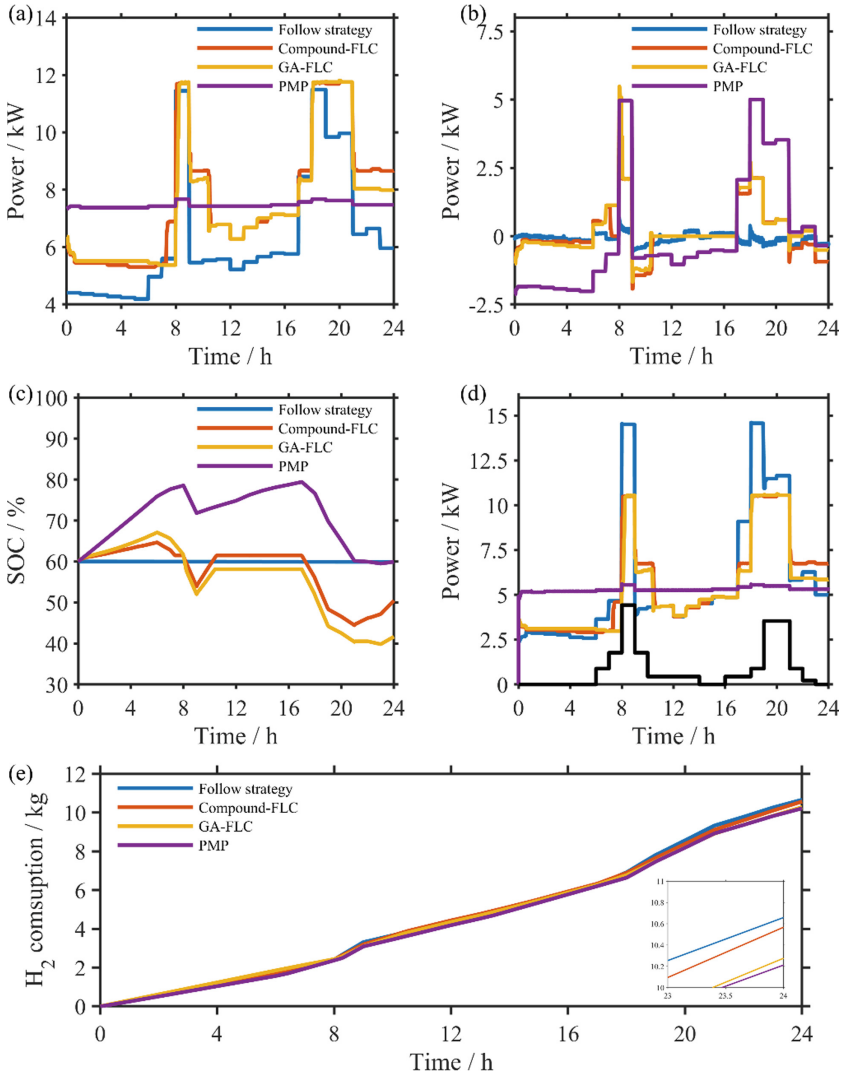


Fig. 6. Results of four strategies: (a) fuel cell output power; (b) battery output power; (c) SOC of LIB; (d) heat recovery power of CHP system; (e) total H₂ consumption

range is the widest, spanning 5–12 kW. Compound-FLC strategy is comparable to GA-FLC strategy. Under the PMP strategy, as shown in Fig. 7 (d), the P_{stack} is distributed centrally at 7–8 kW with an average single cell voltage of about 0.67 V. As we all know, the cycling voltage and high potential maintenance during fuel cell operation are important reasons for fuel cell attenuation [15]. Under cycling voltage conditions, catalyst particles are more likely to agglomerate and dissolve, leading to a decrease in the effective catalytic surface area (ECSA) and an increase in polarization loss. The catalyst is more prone to be oxidized in the presence of high potential maintenance, which lowers

ECSA and worsens the hydrophilic and hydrophobic properties. Additionally, under high potential conditions, the current density is smaller while the gas flow rate is larger. The dry environment within MEA will not only increase ohm resistance but also accelerate the chemical decomposition and physical attenuation of the membrane and ionomer, increasing the difficulty of water management. Therefore, the voltage of a single fuel cell should be kept as close to 0.65V and 0.7V under typical working conditions.

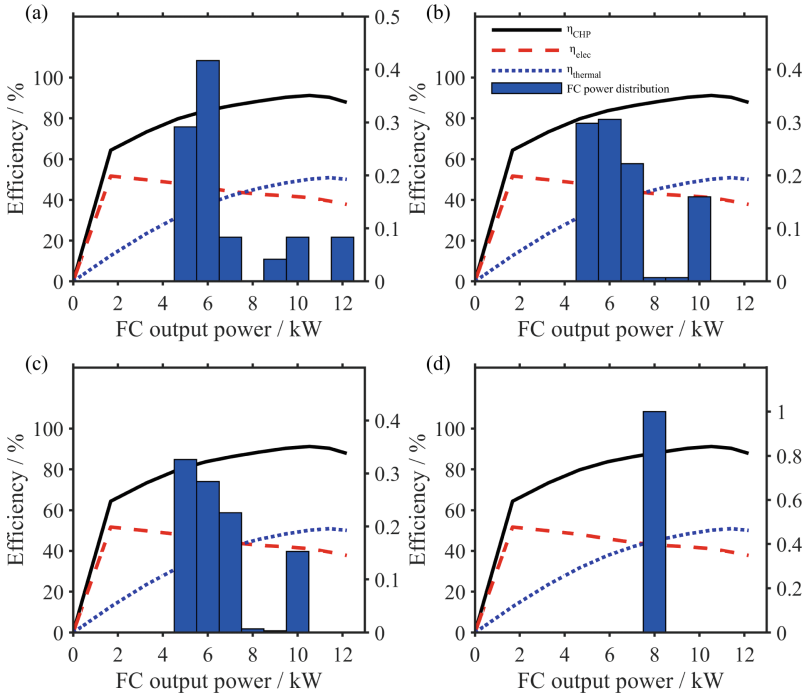


Fig. 7. Fuel cell power distribution under four strategies, (a) follow strategy, (b) Compound-FLC, (c) GA-FLC, (d) PMP

5 Conclusions

This article examined the EMS in off-grid operation using the PEMFC-CHP system in the home setting as the object. The simulation model as well as a 10 kW PEMFC CHP system were constructed. The measured data was used to confirm the model after that. This paper compared and assessed the follow strategy, Compound FLC, GA-FLC, and PMP control strategy in light of the energy needs of the Shanghai area. It was found that H₂ consumption of CHP system was improved after genetic algorithm optimization, and the SOC of battery was kept in expected range. Under the PMP strategy, the P_{bat} and SOC of LIB fluctuated greatly, but PMP could further reduce the H₂ consumption of the CHP system, and restrict the stack works in the high efficiency condition, and

effectively increase the working life of fuel cell. Compared with the follow strategy, the PMP strategy reduced the equivalent H_2 consumption, heat recovery and running cost by 4.22%, 7.96% and 4.17%, respectively, which can effectively improve the economy of the CHP system. The research results of this paper can provide important reference value for the EMS of CHP system.

However, this paper only studied the electric load of a household located in Shanghai in summer. The household power consumption varies greatly in different seasons and different climate regions. More comprehensive data need to be expanded. Additionally, the hybrid energy system studied in this paper did not consider the attenuation of the battery, which is also the direction of our further research.

References




1. Ramadhani, F., Hussain, M.A., Mokhlis, H.: A comprehensive review and technical guideline for optimal design and operations of fuel cell-based cogeneration systems. *Processes* **7**(12), 950 (2019). <https://doi.org/10.3390/pr7120950>
2. Tomal, M.U., Gabbar, H.A.: Key performance assessment of fuel cell based distributed energy generation system in resilient micro energy grid. In: 2015 IEEE International Conference on Smart Energy Grid Engineering (SEGE), pp. 1–6. IEEE (2015)
3. Ozawa, A., Kudoh, Y.: Performance of residential fuel-cell-combined heat and power systems for various household types in Japan. *Int. J. Hydrogen Energy* **43**(32), 15412–15422 (2018)
4. Chen, X., Gong, G., Wan, Z., et al.: Performance analysis of 5 kW PEMFC-based residential micro-CCHP with absorption chiller. *Int. J. Hydrogen Energy* **40**(33), 10647–10657 (2015)
5. Di Marcoberardino, G., Chiarabaglio, L., Manzolini, G., et al.: A Techno-economic comparison of micro-cogeneration systems based on polymer electrolyte membrane fuel cell for residential applications. *Appl. Energy* **239**, 692–705 (2019)
6. Herrmann, A., Mädlow, A., Krause, H.: Key performance indicators evaluation of a domestic hydrogen fuel cell CHP. *Int. J. Hydrogen Energy* **44**(35), 19061–19066 (2019)
7. Zhao, J., Cai, S., Luo, X., et al.: Multi-stack coupled energy management strategy of a PEMFC based-CCHP system applied to data centers. *Int. J. Hydrogen Energy* **47**(37), 16597–16609 (2022)
8. Zhao, J., Cai, S., Luo, X., et al.: Dynamic characteristics and economic analysis of PEMFC-based CCHP systems with different dehumidification solutions. *Int. J. Hydrogen Energy* **47**(22), 11644–11657 (2022)
9. Arsalis, A.: A comprehensive review of fuel cell-based micro-combined-heat-and-power systems. *Renew. Sustain. Energy Rev.* **105**, 391–414 (2019). <https://doi.org/10.1016/j.rser.2019.02.013>
10. Fan, L., Tu, Z., Luo, X., Chan, S.H.: MW cogenerated proton exchange membrane fuel cell combined heat and power system design for eco-neighborhoods in North China
11. Abadlia, I., Bahi, T., Bouzeria, H.: Energy management strategy based on fuzzy logic for compound RES/ESS used in stand-alone application. *Int. J. Hydrogen Energy* **41**(38), 16705–16717 (2016)
12. Sorace, M., Gandiglio, M., Santarelli, M.: Modeling and techno-economic analysis of the integration of a FC-based micro-CHP system for residential application with a heat pump. *Energy* **120**, 262–275 (2017)
13. Kwan, T.H., Shen, Y., Yao, Q.: An energy management strategy for supplying combined heat and power by the fuel cell thermoelectric hybrid system. *Appl. Energy* **251**, 113318 (2019)

14. Das, V., Padmanaban, S., Venkitesamy, K., Selvamuthukumar, R., Blaabjerg, F., Siano, P.: Recent advances and challenges of fuel cell based power system architectures and control a review. *Renew. Sustain. Energy Rev.* **73**, 10–8 (2017). <https://doi.org/10.1016/j.rser.2017.01.148>
15. Ren, P., Pei, P., Li, Y., et al.: Degradation mechanisms of proton exchange membrane fuel cell under typical automotive operating conditions. *Prog. Energy Combust. Sci.* **80**, 100859 (2020)
16. Liu, Z., Zhao, J., Qin, Y., et al.: Real time power management strategy for fuel cell hybrid electric bus based on Lyapunov stability theorem. *Int. J. Hydrogen Energy* **47**(85), 36216–36231 (2022)
17. Hou, S., Gao, J., Zhang, Y., et al.: A comparison study of battery size optimization and an energy management strategy for FCHEVs based on dynamic programming and convex programming. *Int. J. Hydrogen Energy* **45**(41), 21858–21872 (2020)
18. Iqbal, M., Ramadan, H.S., Becherif, M.: Health-aware frequency separation method for online energy management of fuel cell hybrid vehicle considering efficient urban utilization. *Int. J. Hydrogen Energy* **46**(29), 16030–16047 (2021)
19. Sheng, C., Fu, J., Li, D., et al.: Energy management strategy based on health state for a PEMFC/Lithium-ion batteries hybrid power system. *Energy Convers. Manage.* **271**, 116330 (2022)
20. Hong, Z., Li, Q., Han, Y., et al.: An energy management strategy based on dynamic power factor for fuel cell/battery hybrid locomotive. *Int. J. Hydrogen Energy* **43**(6), 3261–3272 (2018)
21. Yuan, H., Zou, W., Jung, S., et al.: Optimized rule-based energy management for a polymer electrolyte membrane fuel cell/battery hybrid power system using a genetic algorithm. *Int. J. Hydrogen Energy* **47**(12), 7932–7948 (2022)
22. Fu, Z., Zhu, L., Tao, F., et al.: Optimization based energy management strategy for fuel cell/battery/supercapacitor hybrid vehicle considering fuel economy and fuel cell lifespan. *Int. J. Hydrogen Energy* **45**(15), 8875–8886 (2020). Gao, D., Jin, Z., Lu, Q.: Energy management strategy based on fuzzy logic for a fuel cell hybrid bus. *J. Power Sources* **185**(1), 311–317 (2008)
23. Hu, X., Zou, C., Tang, X., Liu, T., Hu, L.: Cost-optimal energymangement of hybrid electric vehicles using fuel cell/battery health-aware predictive control. *IEEE Trans. Power Electron.* **35**, 382–392 (2019)
24. Ferahtia, S., Rezk, H., Djerioui, A., et al.: Optimal heuristic economic management strategy for microgrids based PEM fuel cells. *Int. J. Hydrogen Energy* (2022)
25. Rezk, H., Nassef, A.M., Abdelkareem, M.A., et al.: Comparison among various energy management strategies for reducing hydrogen consumption in a hybrid fuel cell/supercapacitor/battery system. *Int. J. Hydrogen Energy* **46**(8), 6110–6126 (2021)
26. Ettahir, K., Boulon, L., Agbossou, K.: Optimization-based energy management strategy for a fuel cell/battery hybrid power system. *Appl. Energy* **163**, 142–153 (2016)
27. Odeim, F., Roes, J., Wülbeck, L., et al.: Power management optimization of fuel cell/battery hybrid vehicles with experimental validation. *J. Power. Sources* **252**, 333–343 (2014)
28. Ma, T., Li, R., Gao, T., et al.: Development of 10kW proton exchange membrane fuel cell combined heat and power system for domestic building services. *SAE Technical Paper* (2022)
29. Ma, T., Wang, H., Li, R., et al.: Research on control strategy of combined heat and power system based on PEMFC[R]. *SAE Technical Paper* (2022)

30. Liang, J., Li, Y., Jia, W., et al.: Comparison of two energy management strategies considering power system durability for PEMFC-LIB hybrid logistics vehicle. *Energies* **14**(11), 3262 (2021)
31. Du, G., Xie, H., Lu, Z., et al.: Analysis for the energy management problem of extended-range electric city buses based on Pontryagin's minimum principle. *J. Chongqing Univ. Technol. (Natural Science)* **3**, 10–17 (2018)



A New Perspective on the Influence of the Electrolytic Bubbles on the Pressure Drop in the Vertical Pipe Flow

Liandong Sha^(✉) , Ruomei Qi , and Jin Lin 

Department of Electrical Engineering, Tsinghua University, Beijing, China
sld21@mails.tsinghua.edu.cn

Abstract. The utilization of stack clusters incorporating shared balance-of-plant (BoP) systems presents a promising approach for scaling up the water electrolysis for hydrogen. However, shared BoP design causes the coupling between different electrolysis stacks, necessitating the optimization of the piping system to ensure safe cluster operation. The fluid flow within the piping system exhibits characteristics of two-phase flow, which is more intricate compared to single-phase flow. In this study, an engineering model is proposed to elucidate the influence of electrolytic bubbles on fluid flow pressure in a vertical pipe. Experiments are conducted to investigate various influential factors, such as pipe diameter, water flow rate, and the oxygen content regulated by the electrolytic current. The proposed model combines the benefits of both the homogeneous model and the separated model, leading to improved predictions. Furthermore, the analysis of pressure vibration is included, offering a novel perspective for comprehending the standard errors of the pressure drop.

Keywords: Pressure drop · Two-phase flow · Empirical model · Pressure vibration

1 Introduction

Green hydrogen is a promising clean energy for mitigating carbon dioxide emissions. Among various technical methods to produce green hydrogen, water electrolysis is the most mature approach. However, achieving large-scale production of green hydrogen through electrolysis is an urgent challenge. One approach to scaling up is the implementation of a shared balance of plant (BoP), which involves increasing the number of stacks instead of enlarging a single stack [1]. However, the shared BoP design causes stack coupling through interconnected pipes. Therefore, optimizing the piping system becomes crucial to ensure the safe operation of the electrolysis system.

The fluid flow in the piping system possesses the properties of the two-phase flow, which is more complex than the single-phase flow. Simulating two-phase flow in the piping system requires computationally intensive CFD models. To facilitate the engineering application, previous studies have focused on flow pattern, gas content, and

pressure drop [2]. Given the consistent positioning of the stack below the gas-liquid separator, this study investigates vertical pipe flow.

Extensive research on flow patterns in vertical pipe flow has established a consensus that five patterns exist, namely bubbly flow, slug flow, churn flow, wispy-annular flow, and annular flow [3]. The flow pattern significantly influences flow characteristics, and previous investigations on gas content and pressure drop have primarily focused on specific flow patterns.

Two types of models describing the frictional drop in two-phase pipe flow are proposed in previous research, named homogeneous model and separated model [2]. Numerous studies have investigated the homogeneous model, which is proved to be better than the separated model when describing the frictional term [4–7]. The separated model was first proposed by Lockhart et al. [8] and further developed by Chisholm et al. [9] The void fraction α , a crucial parameter in the separated model, is typically estimated using the drift flux model [10].

Many studies solely focus on discussing frictional pressure drop and comparing different models [4, 7, 11]. These studies attribute any deviations between theory and experiment to model inaccuracies. However, it should be noted that the measured pressure drop includes not only the frictional drop but also static pressure drop and accelerative pressure drop [12], particularly in vertical flow. Separating these three components is challenging, thus leading to great errors when dealing with frictional pressure drop in isolation. Therefore, it is important to investigate all three factors simultaneously in vertical pipe flow when the operating conditions changes.

This study measures the total pressure drop of two-phase water-oxygen flow in a vertical circular tube and discusses its three components. A comparison is made between the homogeneous model and the separated model, and a hybrid model that incorporates the strengths of both is introduced.

This paper is organized as follows: Sect. 2 presents the experimental setup and error reduction methods. Section 3 introduces the models discussed in this article, namely the homogeneous model, the separated model, and the proposed model. Section 4 presents and analyzes the experimental results. Lastly, Sect. 5 presents three conclusions drawn from the study.

2 Experimental Setup

This study involves modifying and repurposing a $1\text{Nm}^3/\text{h}$ PEM electrolysis stack as a bubble generator, as depicted in Fig. 1. The PEM electrolysis stack consists of 40 cells, each with an area of 90 cm^2 . The Faraday's efficiency of this stack is approximately measured to be 95%. A rotameter and a needle valve are installed at the inlet of the stack. The needle valve is manually operated to control the liquid flow rate, with a maximum volumetric rate of 100 L/h . At the stack outlet, a one-meter-long PMMA tube is positioned, and a differential pressure gauge is connected in parallel to the tube. The connecting pipes between the gauge and the PMMA tube are filled with water to minimize the vibration of measurement.

The experiment reveals the presence of two flow patterns, namely, bubbly flow and slug flow, as shown in Fig. 1. In slug flow, the length of the gas segment varies from

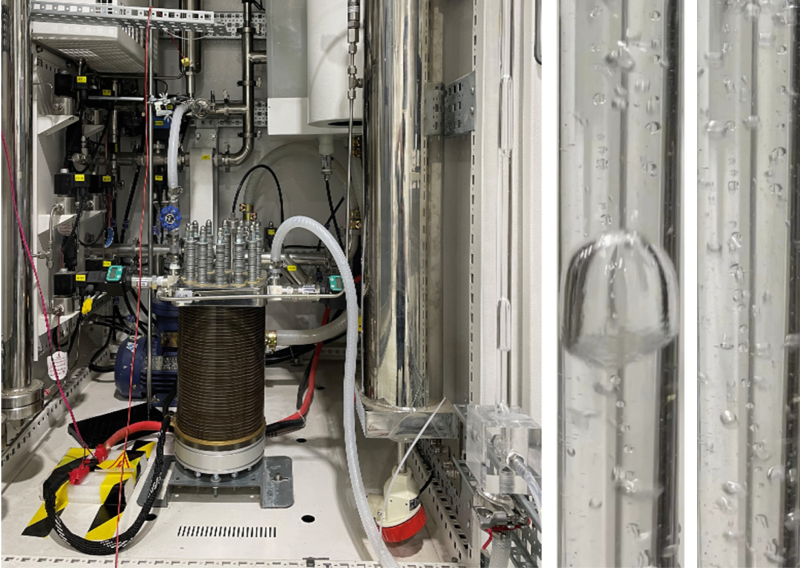


Fig. 1. The experimental setup and the flow pattern in this study

3 cm to 50 cm according to the gas-liquid volumetric flow rate ratio β . This phenomenon is attributed to the downward flexing of the flexible tube connecting the stack and the PMMA tube. A local gas-liquid separator is formed at the bend, which affects the flow conditions in the subsequent tube. Still and all, this phenomenon does not impact the pressure drop of the PMMA tube, although it does reduce the diversity of the flow patterns.

The experiments investigate the pressure drop across 3 tubes of varying diameters, 6 liquid flow rates, and 11 gas flow rates. The pressure drop of the PMMA tube is measured for 2 min at each point, with a sampling interval of 1 s.

3 Model

The vertical pipe flow is commonly simplified as one-dimensional flow, resulting in a pressure drop composed of three parts. These three components are calculated differently in various models.

$$\frac{\partial p}{\partial z} = \left(\frac{\partial p}{\partial z} \right)_{\text{friction}} + \left(\frac{\partial p}{\partial z} \right)_{\text{gravity}} + \left(\frac{\partial p}{\partial z} \right)_{\text{acceleration}} \quad (1)$$

The homogeneous model assumes no slip between gas and liquid, and the total pressure drop is formulated as follows [2]:

$$\frac{\partial p}{\partial z} = \Phi_{Lo}^2 \left(\frac{dp_f}{dz} \right)_{Lo} + [\beta \rho_G + (1 - \beta) \rho_L] g + G^2 \frac{\partial}{\partial z} \left[\frac{(1 - x)^2}{\rho_L (1 - \beta)} + \frac{x^2}{\rho_G \beta} \right] \quad (2)$$

In the equation, ϕ_{Lo}^2 represents the liquid-only two-phase friction multiplier, x denotes the mass fraction of the gas, β indicates the gas-liquid volumetric flow rate ratio, and G represents the mass flux. Various correction methods exist for ϕ_{Lo}^2 , but this paper employs one of the simplest approaches:

$$\Phi_{Lo}^2 = \left[1 + x \left(\frac{\rho_L}{\rho_G} - 1 \right) \right] \left[1 + x \left(\frac{\mu_L}{\mu_G} - 1 \right) \right]^{-\frac{1}{4}} \quad (3)$$

The widely recognized separated model is referred to as the L-M model, and its formulation is as follows:

$$\frac{\partial p}{\partial z} = \Phi_L^2 \left(\frac{dp_f}{dz} \right)_L + [\alpha \rho_G + (1 - \alpha) \rho_L] g + G^2 \frac{\partial}{\partial z} \left[\frac{(1-x)^2}{\rho_L(1-\alpha)} + \frac{x^2}{\rho_G \alpha} \right] \quad (4)$$

In this equation, ϕ_L^2 represents the two-phase friction multiplier and is calculated based on the approach proposed by Chisholm et al. [9]:

$$\Phi_L^2 = 1 + \frac{C}{X} + \frac{1}{X^2}, \quad X = \sqrt{\left(\frac{dp_f}{dz} \right)_L / \left(\frac{dp_f}{dz} \right)_G} \quad (5)$$

It should be noted that the void friction α is used in Eq. (4). The drift flux model is widely employed for calculating α :

$$\alpha = \frac{\beta}{C_0 + \langle j_m \rangle / j} \quad (6)$$

C_0 is an empirical parameter that is typically assigned a value of $C_0 = 1$. $\langle j_m \rangle$ represents the average drift velocity, and for slug flow, it can be calculated as follows [10]:

$$\langle j_m \rangle = 0.35 \left[\frac{gD(\rho_L - \rho_G)}{\rho_L} \right]^{0.5} \quad (7)$$

To enhance accuracy, this paper proposes a model that integrates both the homogeneous model and the separated model:

$$\frac{\partial p}{\partial z} = \Phi_{Lo}^2 \left(\frac{dp_f}{dz} \right)_{Lo} + [\alpha \rho_G + (1 - \alpha) \rho_L] g + G^2 \frac{\partial}{\partial z} \left[\frac{(1-x)^2}{\rho_L(1-\alpha)} + \frac{x^2}{\rho_G \alpha} \right] \quad (8)$$

In this study, the accelerative pressure drop is considered a disturbance in the pressure drop, which is only relevant to the conditions at the inlet and outlet of the tube. Due to the inconsistency between x and α in slug flow, vibration occurs when x changes at both ends of the tube. The accelerative pressure drop calculated using the average x can serve as a reference for the disturbance. To evaluate the vibration of the pressure drop, an empirical equation is proposed:

$$\sigma_{dp} = C_1 Fr_L^{C_2} Re_L^{C_3} G^2 \left[\frac{(1-x)^2}{\rho_L(1-\alpha)} + \frac{x^2}{\rho_G \alpha} - \frac{1}{\rho_L} \right] \quad (9)$$

In Eq. (9), C_1 , C_2 , and C_3 represent undetermined coefficients that will be adjusted in Sect. 4. Fr_L corresponds the Froude number of the liquid flow, while Re_L represents the Reynolds number of the liquid flow.

4 Results

The data obtained from the experiments are presented in Fig. 2. The data of pressure drop under various gas flow rates is depicted, along with standard error bars. The curves of the predicted pressure drop from the supposed model are represented as dotted lines.

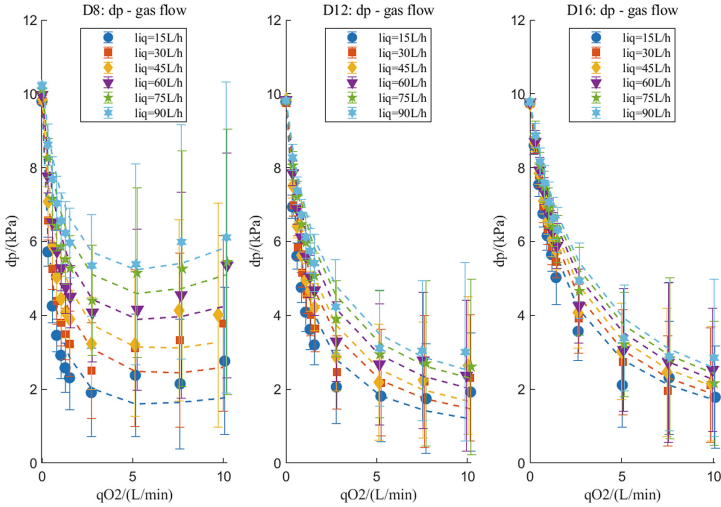


Fig. 2. Pressure drops in different operating conditions with error bar plot, and the predicted results of the proposed model.

It is observed that the pressure drop of the tube initially decreases with an increase in gas flow rate and then increases. A tube with a smaller diameter leads to a higher superficial velocity, making the pressure drop more sensitive to the flow rates of both liquid and gas.

The pressure drop can be divided into two components: the frictional term and the static term. The decomposition is illustrated in Fig. 3 using the proposed model.

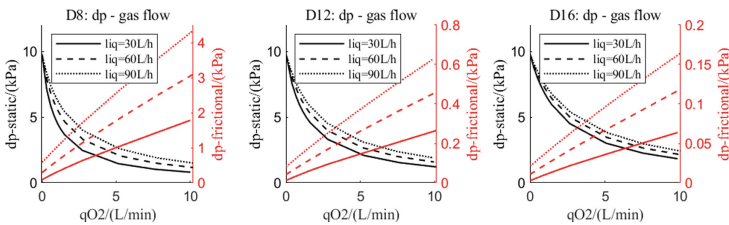


Fig. 3. Decomposition of the pressure drop

With an increase in liquid flow rate, the static term increases due to an increase in α , while the frictional term also increases with the rise in velocity. Conversely, when

the gas flow rate increases, the static term decreases while the frictional term increases. Thus, for a given tube, there exists a minimum pressure drop point for every liquid flow rate.

The proposed model accurately predicts the pressure drop and demonstrates greater precision compared to the homogeneous model and the separated model, as shown in Fig. 4. The dashed lines denote the relative error of $\pm 30\%$.

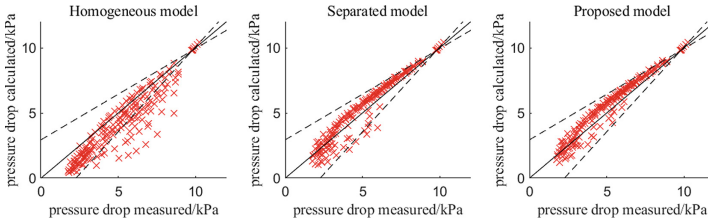


Fig. 4. The comparison of the models

This improvement in precision confirms that the homogeneous model is more appropriate for describing the frictional pressure drop. Meanwhile, upon comparing Figs. 2 and 3, it becomes evident that the static term introduces significant errors. Therefore, it is crucial to carefully adjust the static term when analyzing the frictional pressure drop.

Figure 5 presents the analysis of the standard error of the measured pressure drop using Eq. (9). The first two graphs illustrate the relationship between the standard error and the predicted accelerative pressure drop for a specific diameter of 12 mm and a liquid flow rate of 60 L/h, respectively.

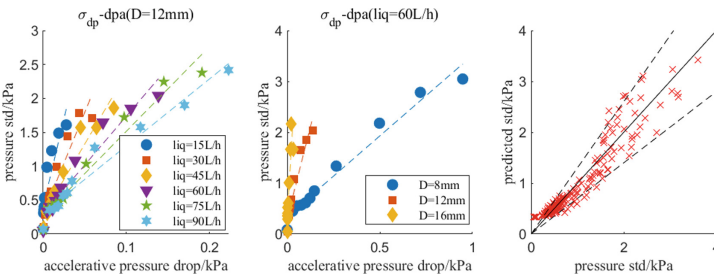


Fig. 5. Prediction of the measured standard error of the pressure drop

The predicted standard errors are compared with the measured standard errors in the third graph of Fig. 5, where the 30% boundary is represented by dashed lines. The parameters $C_1 = 0.208$, $C_2 = -1.12$, and $C_3 = 1.34$ are obtained, assuming a linear relationship between the standard error and the accelerative term. The results demonstrate a slight nonlinearity, possibly due to the inaccuracy of α . Moreover, the deviation in flow pattern at higher gas flow rates may also attribute to this nonlinearity.

According to Eq. (9), the accelerative pressure loss leads to the vibration of the pressure drop of the two-phase flow at the pipe ends. The void fraction α is the primary

factor influencing the vibration, and increasing the diameter or reducing the liquid flow rate can partially mitigate the vibration.

5 Conclusion

This paper proposes a model, which combines the strengths of the homogeneous model and the separated model to describe the pressure drop of the two-phase flow in vertical circular pipes. The frictional term, static term, and accelerative term are examined and discussed from a fresh perspective. Experiments are conducted on one-meter-long tubes with diameters of 8 mm, 12 mm, and 16 mm, respectively. The experimental results show that all data points locate within the relative error range of $\pm 30\%$, indicating superior performance compared to the homogeneous model and the separated model. In addition, the standard errors of the measured pressure drop are discussed, and an empirical relationship between the standard error and the accelerative pressure drop is established.

This paper presents three key conclusions:

- Inaccurate handling of the static pressure drop results in additional errors when analyzing the frictional pressure drop. Therefore, it is preferable to analyze the static term and the frictional term together.
- Employing the homogeneous model to estimate frictional pressure drop and the separated model to calculate the static term yields improved predictions.
- The accelerative pressure drop can partially characterize the pressure fluctuations, and the vibration is responsive to the void friction.

Acknowledgment. This work was sponsored by Tsinghua-Toyota Joint Research Institute Interdisciplinary Program.

References

1. Rizwan, M., Alstad, V., Jäschke, J.: Design considerations for industrial water electrolyzer plants. *Int. J. Hydrog. Energy*, S0360319921034984 (2021). <https://doi.org/10.1016/j.ijhydene.2021.09.018>
2. Holland, F., Bragg, R.: *Fluid flow for chemical engineers*. Elsevier (1995)
3. Hewitt, G.F., Roberts, D.N.: *Studies of two-phase flow patterns by simultaneous x-ray and fast photography*. Atomic Energy Research Establishment, Harwell, England (United Kingdom), AERE-M-2159, Feb. 1969. Accessed 24 Apr 2023. [Online]. Available: <https://www.osti.gov/biblio/4798091>
4. Xu, Y., Fang, X., Su, X., Zhou, Z., Chen, W.: Evaluation of frictional pressure drop correlations for two-phase flow in pipes. *Nucl. Eng. Des.* **253**, 86–97 (2012). <https://doi.org/10.1016/j.nucengdes.2012.08.007>
5. Friedel, L.: Improved friction pressure drop correlations for horizontal and vertical two-phase pipe flow. In: *European Two-Phase Flow Group Meeting*. Ispra, Italy (1979)
6. Sun, L., Mishima, K.: Evaluation analysis of prediction methods for two-phase flow pressure drop in mini-channels. In: *International Conference on Nuclear Engineering*, pp. 649–658 (2008)

7. Filip, A., Băltărețu, F., Damian, R.-M.: Comparison of two-phase pressure drop models for condensing flows in horizontal tubes. *Math. Model. Civ. Eng.* **10**(4), 19–27 (2014). <https://doi.org/10.2478/mmce-2014-0019>
8. Lockhart, W.R.: Proposed correlation of data for isothermal two-phase, two-component flow in pipes. *Chem. Eng. Prog.* **45**(1), 39–48 (1949)
9. Chisholm, D.: A theoretical basis for the Lockhart-Martinelli correlation for two-phase flow. *Int. J. Heat Mass Transf.* **10**(12), 1767–1778 (1967). [https://doi.org/10.1016/0017-9310\(67\)90047-6](https://doi.org/10.1016/0017-9310(67)90047-6)
10. Zuber, N., Findlay, J.A.: Average volumetric concentration in two-phase flow systems (1965)
11. Sun, S., Shao, Z., Yu, H., Li, G., Yi, B.: Investigations on degradation of the long-term proton exchange membrane water electrolysis stack. *J. Power. Sources* **267**, 515–520 (2014). <https://doi.org/10.1016/j.jpowsour.2014.05.117>
12. Wallis, G.B.: One-dimensional two-phase flow. Courier Dover Publications (2020)



Capacity Optimization Method for Off-Grid Photovoltaic Hydrogen Production System Based on Improved Honeybadger Algorithm

Hongcan Ma, Yan Dong^(✉), and Bin Liu

Hebei University of Technology, Tianjin, China
dongyan73@hebut.edu.cn

Abstract. This paper proposed a method for optimizing the capacity of an off-grid photovoltaic hydrogen production system. By analyzing several different operating states (production, standby, and shutdown) of the electrolyzer, and the process of changing several operating states, the energy management strategy for system operation is formulated based on the process of changing several different operating states of the electrolyzer. The amount of photovoltaic power generation determines when the energy storage battery is charged and discharged and the operating state of the electrolyzer. Finally, the capacity of the system is optimized by improving the honeybadger optimization algorithm, and the model and optimization algorithm has been validated through actual case studies. The validation results show that the capacity optimization method that takes into account the process of electrolyzer state changes can effectively reduce the leveling cost of hydrogen, and the improved honeybadger algorithm can quickly and effectively solve the capacity optimization problem involved in this article.

Keywords: Capacity optimization · Solar photovoltaic · Off-grid hydrogen production

1 Foreword

With the use of a large number of fossil fuels, CO₂ emissions are increasing. Therefore, there is an urgent need for clean energy to replace traditional energy to reduce carbon emissions [1]. As a clean energy source, hydrogen energy can be coupled with renewable energy sources to provide long-term solutions for climate neutrality. Compared to grid-connected hydrogen production, off-grid hydrogen production is not dependent on the power grid and is not subject to geographical constraints. It can achieve on-site hydrogen production in hydrogen consumption areas, reducing the transportation cost of hydrogen energy. At the same time, in the past few decades, the installed capacity of photovoltaic power generation has increased significantly, and the manufacturing cost of photovoltaic modules has decreased rapidly, which provides a cost advantage for off-grid photovoltaic hydrogen production [2].

To overcome the intermittency of renewable energy, many scholars have studied capacity optimization methods for off-grid renewable energy storage systems. In literature [3], a capacity optimization method combining mixed integer nonlinear programming optimization models is proposed to minimize the overall cost of the system. In literature [4], a capacity optimization method based on a dynamic control strategy for wind power storage hybrid power plants to improve the life of energy storage systems is proposed. For off-grid renewable energy hydrogen production systems, Christopher Varela et al. [5] proposed an optimal scheduling method for using renewable energy to produce hydrogen, which optimizes system tuning by considering the operational state change process of the electrolyzer and using one-hour resolution wind speed to simulate wind power generation. F. Gutiérrez-Martín et al. [6] proposed a method for optimizing the number of solar photovoltaic modules, electrolyzers, and battery capacity, achieving the goal of reducing the production cost of hydrogen as much as possible while ensuring stable system operation.

Currently, the capacity optimization of off-grid hydrogen production primarily does not adequately describe the operating state of the electrolyzer. To better simulate the actual operation of electrolyzer in the photovoltaic hydrogen production process and reduce the cost of hydrogen production, this paper proposes a capacity optimization method that considers the operational state changes of electrolyzer by analyzing several operational state changes. The system capacity is optimized by improving the honeybadger optimization algorithm. The verification results show that the improved honeybadger algorithm can quickly and effectively solve the capacity optimization problem in this paper, and the capacity optimization method considering the process of electrolyzer state changes, effectively reduces the production cost of hydrogen.

2 System Mathematical Model

The structural diagram of the photovoltaic hydrogen production system studied in this paper is shown in Fig. 1, including a photovoltaic power generation system, energy management system, energy storage battery, and electrolyzer.

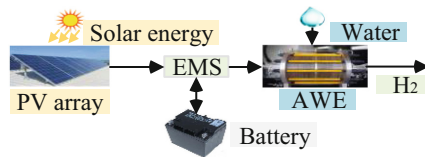


Fig. 1. Structure diagram of the photovoltaic hydrogen production system.

2.1 Photovoltaic Power Generation Model

The calculation formula for photovoltaic power generation is shown in Eq. (1).

$$P_{pv}(t) = N_{pv} \times Y_{pv} \times f_{pv} \times (G(t)/G_{stc}(t)) [1 + \alpha \times (T_c(t) - T_{c,stc})] \quad (1)$$

where N_{pv} and Y_{pv} represent the number of PV plates and the rated capacity of the individual photovoltaic plate. f_{pv} and α represent the integrated photovoltaic loss coefficient and the temperature coefficient. $G(t)$ and $G_{stc}(t)$ represent the solar radiation intensities under actual and standard conditions. $T_c(t)$ and $T_{c,stc}$ represent the actual temperature of the solar panel and the temperature under the standard test.

2.2 Energy Storage Battery Model

The primary role of the energy storage battery is to suppress frequent fluctuations in photovoltaic power. The state of charge of the energy storage battery is:

$$SOC(t) = \begin{cases} SOC(t-1) + P_b(t) \times \eta_b \times (\Delta t / N_{bs} \times C \times V), & P_b(t) \geq 0 \\ SOC(t-1) + P_b(t) / \eta_b \times (\Delta t / N_{bs} \times C \times V), & P_b(t) < 0 \end{cases} \quad (2)$$

where η_b , C and V represent the battery efficiency, capacity, and voltage.

2.3 Alkaline Electrolyzer Model

According to the load operating range of the electrolyzer, the power during the shutdown is zero, and the standby power is $P_{e,wt}$, the power during operation is $P_e(t) = \min\{P_{e,input}(t), P_{e,norm}\}$, $P_{e,norm}$ is the electrolyzer's nominal power and minimum operating power. In this paper, at the same time, a first-order polynomial was used to describe the hydrogen production rate in kg/h .

$$F(t) = (0.1857 \times P_e(t) + 14.28) \times \Delta t \times 0.089, P_e(t) \geq P_{e,min} \quad (3)$$

3 Capacity Optimization Method

3.1 Energy Management Strategies

In this paper, three states of the electrolyzer (shutdown, standby, and operation) are reserved, and the operating state of the electrolyzer is shown as follows:

$$Y(t) = \begin{cases} I, & P_e(t) < P_{e,wt} \\ S, & P_e(t) = P_{e,wt} \\ L, & P_e(t) \geq P_{e,min} \end{cases}, M = \begin{cases} 1, & Y(t) = L, Y(t-1) = I \\ 1/3, & Y(t) = L, Y(t-1) = S \\ 0, & else \end{cases} \quad (4)$$

To minimize the number of start-up and close of the electrolytes as much as possible, an energy management strategy for the system was developed based on photovoltaic generation, the size of the charge inside the energy storage batter, and the state model of the electrolyzer. The entire state change flow chart is shown in Fig. 2.

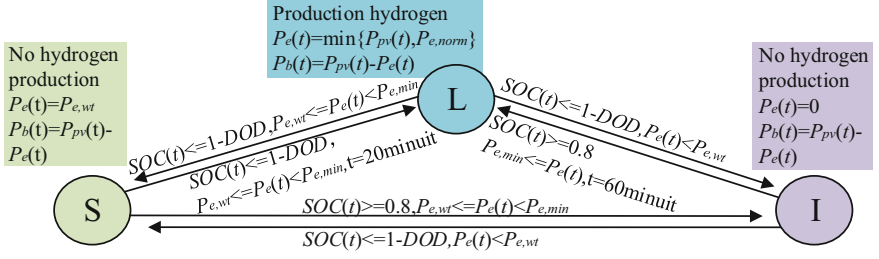


Fig. 2. Diagram of the changing state of the electrolyzer.

3.2 Objective Function

Levelized hydrogen cost (LOCH) is an important economic indicator for evaluating hydrogen production systems, choosing the LOCH as the objective function to solve.

$$\min[f(x)] = C / (F \times (1 - Q(t))), Q(t) = (1 / e^{1000/P_e(t)} + 1) \times M \quad (5)$$

$$C = (C_{cap_pv} + C_{cap_bat} + C_{cap_ele}) \times (r(1+r))^K / ((1+r)^K - 1) + C_{om_pv} + C_{om_bat} + C_{om_ele} \quad (6)$$

where F refers to the total annual hydrogen production, and C refers to the total annual cost. To express the impact of the start-up process of electrolyzer on hydrogen production, a penalty function $Q(t)$ is added to the total annual hydrogen production. Convert the initial investment cost of the system to annual cost using a capital recovery factor. r is the discount rate and K is the service life.

3.3 Constraint Condition

The number of PV arrays and the number of the energy storage batteries can only be an integer: $N_{pv}, N_{bs} \in N$. When the system operates stably, the power of system components is always balanced: $P_{pv}(t) = P_e(t) + P_b(t)$. To avoid overcharging or discharging of energy storage battery, battery SOC and power are constrained. DOD is the maximum discharge depth of the energy storage battery.

$$(1 - DOD) \leq SOC \leq 1, P_{bc} \leq P_{bc \max}, P_{bdc} \geq P_{bdc \max} \quad (7)$$

3.4 Honeybadger Algorithm with Reverse Learning and Cauchy Mutation

In order to expand the diversity of the initialization population, an elite reverse learning strategy is added to the initialization.

$$x_{ij} = lb_j + r_1 \times (ub_j - lb_j), x_{oij} = lb_j + ub_j - x_{ij} \quad (8)$$

where x_{ij} and x_{oij} denote the population individuals, lb_j and ub_j denote the upper and lower bounds of the variable search domain in dimension, respectively.

To trap the algorithm into local optimization, a Cauchy operator is introduced into the honeybadger algorithm to improve the global search ability of the algorithm.

$$x_{inew} = x_{prey} + F \times \beta \times I_i \times x_{prey} + F \times r_3 \times \alpha \times d_i \times |\cos(2\pi r_4) \times (1 - \cos(2\pi r_5))| \quad (9)$$

$$x_{inew} = x_{prey} + F \times r_7 \times \alpha \times d_i, x_{inewx} = x_{inew} + x_{inew} \times Cauchy(0, 1) \quad (10)$$

where I is the odor intensity, d_i is the distance of the prey from the i_{th} honeybadger. x_{inew} and x_{prey} are the positions of the updated population and the optimal individuals in the previous generation of population, and α is a random factor that changes over time. β is a constant greater than one, F is a change in search direction flag. x_{inewx} is the position of the individual after the Cauchy mutation.

4 Computational Analysis

This paper selects 600 s temporal resolution solar irradiance data from Chongli, Hebei, China, for capacity optimization. System parameters are shown in Table 1.

Table 1. Technical parameters and price of system equipment.

| Variable | Value | Unit | Variable | Value | Unit | Variable | Value | Unit |
|---------------|-------|-------------------|----------------|--------|----------|----------------|-------|----------|
| Y_{pv} | 0.55 | Kw | N_{pv} | 10981 | / | N_{bs} | 674 | / |
| f_{pv} | 21.3% | / | $P_{e,norm}$ | 1000 | Kw | $C \times V$ | 296 | W·h |
| $G_{t,sc}$ | 1 | Kw/m ² | α | -0.34% | °C | K | 20 | Year |
| $T_{c,sc}$ | 25 | °C | $P_{bdc,max}$ | 0.502 | Kw | $P_{bc,max}$ | 0.1 | Kw |
| C_{cap_pv} | 1870 | RMB/Kw | C_{cap_ele} | 1500 | RMB/Kw | C_{cap_bat} | 1350 | RMB/unit |
| C_{om_pv} | 34 | RMB/year | C_{om_bat} | 13 | RMB/year | C_{om_ele} | 160 | RMB/year |
| r | 5.88% | / | DOD | 0.45 | / | η_b | 95% | / |

where Fig. 3(a), an iterative diagram of the capacity optimization process is shown. It can be seen that the improved honeybadger algorithm has a faster convergence speed and strong global convergence ability. Where Fig. 3(b), is given the system operation curve calculated using the solar irradiance on 11 July in the chongli area of China. The system can absorb fluctuating power for continuous hydrogen production.

In Fig. 4(a), the number of start-up for simple models and the state change models are given, as can be seen from the figure, and the state change model can effectively reduce the number of cold starts, thereby improving hydrogen production.

In Fig. 4(b), the monthly hydrogen production and photovoltaic power are given. As can be seen from the figure, the hydrogen production in summer is high and the monthly hydrogen production is saturated at this time. The electrolytic cell can continuously produce hydrogen at rated power.

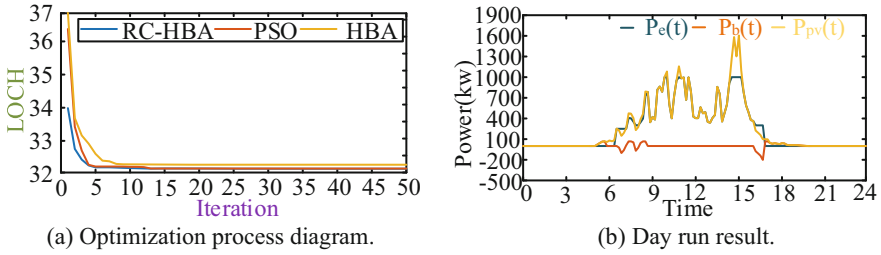


Fig. 3. Optimization process diagram and day run result.

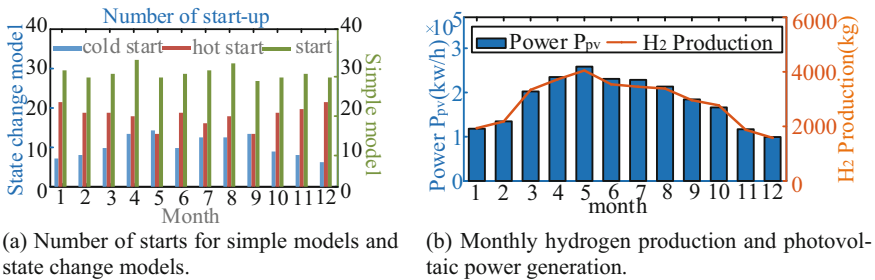


Fig. 4. Number of starts and monthly hydrogen production and photovoltaic power generation.

5 Conclusion

This paper proposed a capacity optimization method for off-grid photovoltaic hydrogen production based on an improved honeybadger algorithm. Compared to the simple model of an electrolyzer, the capacity optimization method considering the dynamic model of the electrolyzer effectively reduces the production cost of hydrogen. However, due to the significant relationship between the dynamic operation and the temperature of the electrolyzer, failure to consider the temperature of the electrolyzer may lead to inaccurate optimization results. Therefore, future work will focus on combining the dynamic operation and temperature of the electrolyzer, to more accurately describe the operation of the electrolyzer.

References

1. Li, Y., Phoumin, H.: Hydrogen sourced from renewables and clean energy: feasibility of large-scale demonstration projects. *Int. J. Hydrogen Energy* **47**(58), 24464 (2022)
2. David, S.: Réné: progress, opportunities and challenges of achieving net-zero emissions and 100% renewables. *Solar Compass* **1**, 100007 (2022)
3. Wang, J., Deng, H., Qi, X.: Cost-based site and capacity optimization of multi-energy storage system in the regional integrated energy networks. *Energy* **261**(A), 125240 (2022)
4. Yi, T., Ye, H., Li, Q., Zhang, C., Ren, W., Tao, W.: Energy storage capacity optimization of wind-energy storage hybrid power plant based on dynamic control strategy. *J. Energy Storage* **55**(A), 105372 (2022)

5. Varela, C., Mostafa, M., Zondervan, E.: Modeling alkaline water electrolysis for power-to-x applications: a scheduling approach. *Int. J. Hydrogen Energy* **46**(14), 9303–9313 (2021)
6. Gutiérrez-Martín, F., Lidia, A., Pagano, M.: Hydrogen production by water electrolysis and off-grid solar PV. *Int. J. Hydrogen Energy* **46**(57), 29038–29048 (2021)



Design of PEMFC Stack Intelligent Diagnosis System Based on Improved Neural Network

Huipeng Chen^{1,4}, Wenhua Luo¹, Dongting Pan², Shaopeng Zhu^{3,5(✉)}, Ping Chen², and Congxin Li⁶

¹ School of Mechanical Engineering, HangZhou DianZi University, Zhejiang, China

² State Power Investment Group, Hydrogen Technology Development Co. Ltd., Zhejiang, China

³ College of Energy Engineering, Power Machinery and Vehicular Engineering Institute, Zhejiang University, Zhejiang, China

spzhu@zju.edu.cn

⁴ Jiaxing Research Institute, Zhejiang University, Zhejiang, China

⁵ Zhejiang Key Laboratory of Clean Energy and Carbon Neutrality, Zhejiang, China

⁶ SPIC Hydrogen Energy Tech Ningbo Research Institute, Zhejiang, China

Abstract. To address the difficulty in obtaining fault data and improve the accuracy of fault diagnosis in the operation of proton exchange membrane fuel cells (PEMFC), this paper proposes a mechanism modeling method based on operational data. This method corrects the mechanism model of the proton exchange membrane fuel cell stack and auxiliary systems by actual operational data and uses it to simulate faults under given working conditions to obtain sample data. In addition, an improved GA-BP neural network algorithm is designed for the fault diagnosis system, which serially trains and tests the simulated fault data. Simulation results show that compared with the traditional BP neural network algorithm, the improved GA-BP neural network algorithm designed in this paper increases the minimum diagnostic accuracy of a single fault to above 93.5% and improves the average diagnostic accuracy by about 4.5%. This research method has important engineering application value.

Keywords: PEMFC model · Data-driven · GA · Neural network · Fault diagnosis

1 Introduction

Fuel cells can convert hydrogen and oxygen into electrical energy, with advantages such as high efficiency and environmental friendliness. In particular, proton exchange membrane fuel cell has the advantages of low working temperature, quick start, long life, making them a potential power generation device with enormous potential [1].

As fuel cells are widely used, their reliability issues have received significant attention. The complex operating conditions require us to pay close attention to every small issue, as any neglected problem may have a destructive impact on the fuel cell system. Therefore, research and development of fuel cell fault diagnosis technology is a critical technology that must be taken seriously [2].

PEMFC fault diagnosis methods are mainly based on models, data and experiments [3]. For example, in reference [4], a PEMFC system analytical model was established, and a residual analysis method was used to effectively diagnose nine faults such as valve blockage, cathode gas leakage and membrane drying. Reference [5] proposed a fault diagnosis method based on an unknown input observer on the existing PEMFC model, which can accurately diagnose faults such as abnormal outlet flow rate of the air compressor and abnormal actuator of the manifold outlet, and determine the time when the faults occur. Reference [6] proposed a PEMFC system fault recognition method based on extreme learning machine, which has the advantages of fast training speed and strong generalization ability. Reference [7] conducted fault diagnosis research on a high-power PEMFC system using a decision tree-based ensemble learning algorithm, and the diagnostic results showed good identification effects for membrane drying and hydrogen leakage faults. Reference [8] used an external magnetic field measurement method to identify changes in stack current density in two-dimensional and three-dimensional space, thereby diagnosing fuel cell water flooding, membrane drying faults, and changes in stack component material properties due to aging.

Model-based fault diagnosis technology has a lower cost but requires a profound understanding of the operating mechanism of the fuel cell, making it very difficult to establish a complete fuel cell system model. Data-based fault diagnosis technology can analyze fault characteristics well, especially neural networks have good performance in diagnosing nonlinear systems. However, this technology requires a large amount of sample data support, and experimental data acquisition is difficult [9]. Experiment-based fault diagnosis technology is limited by the types of fault diagnosis, and considering safety and cost factors, it is difficult to promote this technology for practical engineering applications.

This paper focuses on the PEMFC system, using a model-based method to simulate partial faults and obtain a large amount of fault data, thereby solving the problem of difficult fault data acquisition and insufficient sample quantities. At the same time, an improved GA-BP neural network diagnostic algorithm is designed to diagnose faults in the cathode air supply system, anode air supply system, and cooling liquid circulation system of proton exchange membrane fuel cells.

2 Model and Fault

2.1 Proton Exchange Membrane Fuel Cell System Model

The fuel cell system consists of a voltage output system, cathode air supply system, anode air supply system, thermal management system, and control system that coordinates various subsystems [10]. The model presented in this paper aims to simulate partial faults to obtain fault data, thus simplifying the system model. It is assumed that all individual fuel cells are identical and that the gases studied are ideal gases to facilitate subsequent modeling. Figure 1 shows the schematic diagram of the proton exchange membrane fuel cell system.

In the actual operation of fuel cells, various internal resistances need to be overcome, resulting in three types of energy losses: activation loss, ohmic loss, and concentration

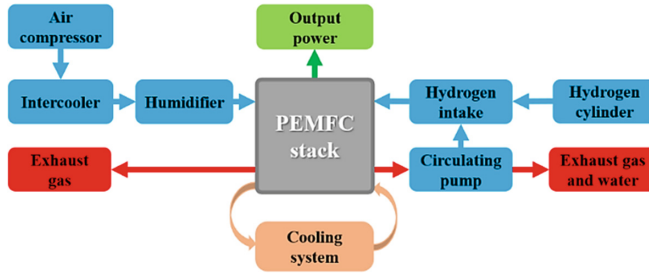


Fig. 1. Principle block diagram of PEMFC system.

loss [11]. Therefore, the actual output voltage of a single cell cannot reach the theoretical value.

This paper assumes that the air flowing through the cathode air supply system contains only oxygen, nitrogen, and water, and other gases are neglected. And the main function of the anode air supply system is to mix and humidify the hydrogen gas from the hydrogen cylinder and hydrogen circulating pump, and then input it into the fuel cell stack to react with oxygen through some valves and devices.

Fuel cells have an optimal operating temperature range, and if the stack is maintained at a high temperature for a long time, the proton exchange membrane will lose water or even rupture, thereby affecting the service life of the cell [12]. Therefore, the function of the cooling system is to regulate heat dissipation to ensure that the temperature of the gas and coolant entering the stack and the temperature of the entire fuel cell stack are within the optimal range.

2.2 Feasibility Verification of the Model

This paper is based on data collected from a 115 kW rated PEMFC of a certain company, and its specific parameters are shown in Table 1. After using Simulink to establish the model, the polarization curve experimental data of the fuel cell and the output voltage experimental data under a certain working condition were compared with the model output data to verify the feasibility of the model.

Table 1. The specific parameters of PEMFC and some parameters of the model.

| Parameter | Value | Unit |
|----------------------------------|-------|-------------------|
| Nominal power | 115 | kW |
| Maximum limiting current density | 2.2 | A/cm ² |
| Proton exchange membrane area | 282 | cm ² |
| Number of single cell | 330 | / |

As shown in Fig. 2, the comparison between the experimental output voltage and the model output voltage under the polarization curves and a given working condition are

presented. There are certain differences between the obtained polarization curve and the experimental one due to the influence of experimental conditions and assumptions made before model establishment. It can also be found that when the voltage changes rapidly in a short period of time, errors caused by controller parameter settings and other issues may cause the model to not follow the experimental curve.

However, considering that the purpose of this paper is to simulate fault data through the model, this influence can be ignored. Therefore, within the allowable range of error, the curve obtained by the model can follow the changing trend of the experimental curve very well. Thus, the model established in this paper can simulate the operation of the experimental equipment well and prove that partial faults can be simulated through the model.

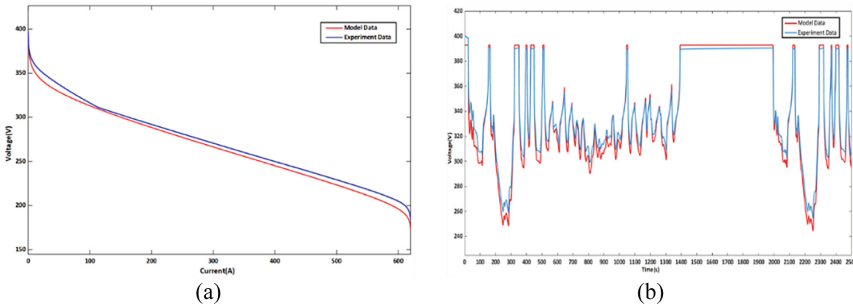


Fig. 2. Model comparison verification (a) Polarization curve comparison (b) Comparison of fuel cell output voltage under given conditions.

2.3 Fault Simulation

This paper divides the faults that need to be simulated into three categories: cathode air supply system faults, anode air supply system faults, and cooling liquid circulation system faults.

Adding a gain module greater and connecting it to the exhaust pressure signal of the air compressor to simulate the fault of excessive or insufficient air intake pressure; reducing the area parameter of the cooler radiator in Simulink to simulate the failure of the cooler radiator or high air intake temperature. Adding a gain module and connecting it to the hydrogen cylinder gas flow rate and pipeline outlet pressure signals to simulate the faults of poor hydrogen intake or hydrogen supply pipeline leakage. Adding a gain module and connecting it to the cooling liquid pressure signal to simulate the fault of cooling liquid pipeline leakage; reducing some pipeline volume parameters or reducing the volume parameter to nearly 0 to simulate the blockage or complete blockage of the cooling liquid pipeline.

3 Diagnostic Algorithm Design

3.1 Diagnostic Algorithm Flow

The widely used BP neural network algorithm is affected by the randomness of initial weights and thresholds, and may have different performances when processing the same problem. Moreover, the global convergence rate of this algorithm is slow and it is prone to local extremes [13]. To improve this situation, this paper proposes an improved GA-BP neural network algorithm, which optimizes the BP neural network by adding a momentum term and genetic algorithm, so that it can update weights more quickly and improve fault diagnosis accuracy. The diagnostic algorithm flowchart is shown in Fig. 3.

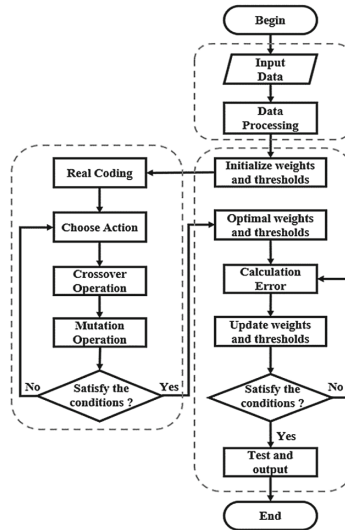


Fig. 3. Diagnostic algorithm flow chart.

3.2 Neural Network Structure

The neural network used in this paper has a four-layer feedforward network structure, as shown in Fig. 4. The input layer contains ten input variables representing current, voltage, hydrogen inlet pressure, oxygen inlet pressure, hydrogen inlet temperature, oxygen inlet temperature, oxygen inlet humidity, hydrogen inlet humidity, cooling water inlet temperature and stack temperature. The nine outputs of the output layer represent the fault states.

The collected data needs to be normalized before being inputted into the neural network. To solve the problem of slow convergence speed and easy local optimum trapping of gradient learning algorithm, momentum term is introduced to speed up the weight update [14], which improves the prediction accuracy of neural network. The

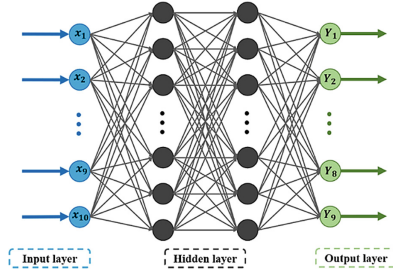


Fig. 4. Neural network topology diagram.

weight update formula (1) is:

$$\omega_{mi}^{(k)} = \omega_{mi}^{(k)} - \eta_1 \frac{\partial E}{\partial \omega_{mi}^{(k)}} + \eta_2 * \Delta \omega_{mi}^{(k)} \quad (1)$$

where $\omega_{mi}^{(k)}$ represents the connection weight between the m -th node in the input layer and the i -th node in the first hidden layer optimized k times, and η_1 and η_2 are the learning rates, E is the target for neural weight correction of each sample group.

If the Sigmoid function is used as the activation function, then the input and output of the hidden layer is represented by formula (2):

$$U_j = F(u_j) = \frac{1}{1 + e^{-\alpha u_j}} \quad (2)$$

where u_j is the input of the j -th node in the second hidden layer, U_j is the output of the j -th node in the second hidden layer, α is the slope adjustment value. The output can be calculated using formula (3):

$$Y_n = \sum_{n=1}^J \varphi_{jn}^{(p)} U_j - \theta_n \quad (3)$$

where $\varphi_{jn}^{(p)}$ represents the connection weight between the j -th node in the second hidden layer and the n -th node in the output layer optimized p times, J is the number of nodes in the second hidden layer, and θ_n is the threshold of the n -th node in the output layer.

3.3 Genetic Algorithm

Genetic algorithm is a computational model that simulates natural evolution of organisms, which can be used to solve optimization problems, including individual encoding, fitness function and genetic operators [15].

Real coding has stronger search ability and provides more genetic operators to choose from [16]. Therefore, this paper uses real coding method to encode the weights and thresholds, and the encoding form is shown in Fig. 5:

| | | | | | | | | | | | | | | |
|---------------|---------------|---------|---------------|---------|------------|---------|--------------------|---------|------------|---------|----------------|---------|------------|---------|
| ω_{11} | ω_{12} | \dots | ω_{21} | \dots | γ_1 | \dots | ε_{11} | \dots | σ_1 | \dots | φ_{11} | \dots | θ_1 | \dots |
|---------------|---------------|---------|---------------|---------|------------|---------|--------------------|---------|------------|---------|----------------|---------|------------|---------|

Fig. 5. Real number coding of weights and thresholds.

The algorithm proposed in this paper detects and classifies faults by reducing calculation errors, so the fitness function can be expressed by formula (4):

$$f(s) = \frac{1}{2} \sum_{n=1}^9 (T_n - Y_n)^2 \quad (4)$$

When assigned to the current chromosome through the fitness function, the three genetic operators of selection, crossover, and mutation need to be inherited to the next generation. In this paper, roulette wheel selection is used as the selection function, as shown in formula (5):

$$P_R(s) = \frac{f(s)}{\sum_{s=1}^G f(s)} \quad (5)$$

where $P_R(s)$ represents the probability of being selected.

To ensure diversity of the population, the probability of the crossover operator in traditional genetic algorithm is adjusted to an adaptive probability. In the mutation process, non-uniform mutation is used to adjust the operator, as shown in formula (6):

$$q'_k = \begin{cases} q_k + \Delta(t, U - q_k), \text{rand}(0, 1) < 0.5 \\ q_k - \Delta(t, q_k - L), \text{rand}(0, 1) \geq 0.5 \\ \Delta(t, y) = y \left(1 - \text{rand}(0, 1) * \left(1 - \frac{t}{T_i} \right)^\lambda \right) \end{cases} \quad (6)$$

where q'_k is the k-th gene after mutation, q_k is the k-th gene before mutation, U and L are the maximum and minimum values of the gene, t is the current iteration number, T_i is the total iteration number of the algorithm.

4 Analysis of Simulation Results

Under the same simulation conditions, this paper compared the diagnostic performance of the improved GA-BP neural network algorithm with that of the traditional BP neural network algorithm to verify the feasibility of the improved algorithm in improving the accuracy of fault diagnosis. The experiment used 90,000 sets of sample data from the previous simulation experiment, with 80% used as the training set and the remaining 20% used as the test set. Figure 6 shows the diagnostic results of the traditional BP neural network and the improved GA-BP neural network algorithms on the test data, respectively. Table 2 lists the comparison results of state numbers and the diagnostic accuracy of the test data.

As shown in Figs. 6 and Table 2, for the five states of normal operation, high air intake pressure, high air intake temperature, hydrogen pipeline leakage, and complete

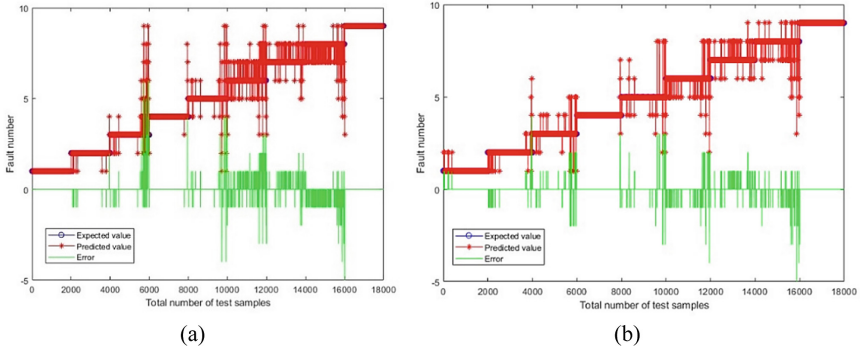


Fig. 6. Diagnosis results (a) Diagnosis error based on traditional BP neural network algorithm (b) Diagnosis error based on improved GA-BP neural network algorithm.

Table 2. Comparison of fault diagnosis accuracy between traditional BP neural network and improved GA-BP neural network algorithm.

| No. | Fault | Train | Test | Test accuracy | |
|-----|--|--------|--------|---------------|--------------------|
| | | | | BP (%) | Improved GA-BP (%) |
| 1 | Normal operation | 8000 | 2000 | 100.00 | 99.50 |
| 2 | Air intake pressure is too high | 8000 | 2000 | 99.20 | 98.50 |
| 3 | Air intake pressure is too low | 8000 | 2000 | 86.00 | 96.80 |
| 4 | The air inlet temperature is too high | 8000 | 2000 | 99.55 | 98.65 |
| 5 | Poor hydrogen intake | 8000 | 2000 | 91.40 | 94.90 |
| 6 | Hydrogen supply pipeline leakage | 8000 | 2000 | 94.00 | 94.75 |
| 7 | Coolant leakage | 8000 | 2000 | 87.00 | 93.55 |
| 8 | Partial blockage of coolant pipe | 8000 | 2000 | 73.90 | 95.00 |
| 9 | The coolant pipe is completely blocked | 8000 | 2000 | 100.00 | 100.00 |
| / | / | 72,000 | 18,000 | 92.34 | 96.85 |

blockage of coolant pipeline, both the traditional BP neural network and the improved GA-BP neural network algorithms have small fluctuations in diagnostic errors and can achieve an accuracy of over 94%. In this case, both diagnostic algorithms perform well.

However, for the traditional BP neural network diagnostic algorithm, there is large fluctuation in diagnostic errors for the four fault states of low air intake pressure, poor

hydrogen intake, coolant leakage, and partial blockage of the coolant pipeline. Especially for the fault state of partial blockage of the coolant pipeline, the diagnostic accuracy is as low as 73.90%. In contrast, the improved GA-BP neural network not only improves the diagnostic accuracy of all fault states to above 93.5%, but also increases the average diagnostic accuracy from 92.34 to 96.85%, an increase of about 4.5%. This indicates that the improved GA-BP neural network diagnostic algorithm designed in this paper can effectively improve the accuracy of fault diagnosis, and also verifies the feasibility of using model simulation of fault data.

5 Conclusion

Based on the model of a proton exchange membrane fuel cell system, this paper simulated some faults and obtained a large number of fault sample data. To address the shortcomings of the traditional BP neural network algorithm, such as slow global convergence, this paper designed momentum learning and GA algorithms to improve it. Simulation results show that compared with the traditional BP neural network algorithm, the improved GA-BP neural network diagnostic algorithm in this paper improves the accuracy of fault diagnosis and can diagnose every fault well.

However, it should be noted that the faults mentioned in this paper are only a part of the actual fuel cell system faults in operation. Therefore, in the future, more complete and accurate models and better fault diagnosis algorithms could be studied and established to achieve the fault diagnosis of the entire fuel cell system, which can then be applied in engineering.

Acknowledgments. This work is supported by the National key research and development program, Fuel cell stack with High performance membrane electrode and ultra-thin titanium electrode plate under Grant 2022YFB2502401.

References

1. Lü, X., Qu, Y., Wang, Y.: A comprehensive review on hybrid power system for PEMFC-HEV: issues and strategies. *Energy Convers. Manage.* **171**, 1273–1291 (2018)
2. Sinha, V., Mondal, S.: Recent development on performance modelling and fault diagnosis of fuel cell systems. *Int. J. Dyn. Control* **6**, 511–528 (2018)
3. Wang, J., Yang, B., Zeng, C.: Recent advances and summarization of fault diagnosis techniques for proton exchange membrane fuel cell systems: a critical overview. *J. Power. Sources* **500**, 229932 (2021)
4. Polvernio, P., Frisk, E., Jung, D.: Model-based diagnosis through structural analysis and causal computation for automotive polymer electrolyte membrane fuel cell systems. *J. Power. Sources* **357**, 26–40 (2017)
5. Bougatif, Z., Abdelkrim, N., Aitouche, A.: Fault detection of a PEMFC system based on delayed LPV observer. *Int. J. Hydrogen Energy* **45**(19), 11233–11241 (2020)
6. Liu, J., Li, Q.: A fast fault diagnosis method of the PEMFC system based on extreme learning machine and dempster-shafer evidence theory. *IEEE Trans. Transp. Electrification* **5**(1), 271–284 (2018)

7. Dang, H., Ma, R., Zhao, D.: A novel diagnosis method of proton exchange membrane fuel cells based on the PCA and XGBoost algorithm. In: IECON 2020 The 46th Annual Conference of the IEEE Industrial Electronics Society, pp. 3951–3956. IEEE, Singapore (2020)
8. Ifrek, L., Rosini, S., Cauffet, G.: Fault detection for polymer electrolyte membrane fuel cell stack by external magnetic field. *Electrochim. Acta* **313**, 141–150 (2019)
9. Yuan, Z., Huang, L.: Fault classification of proton exchange membrane fuel cell based on convolutional neural network coupled with support vector machine. In: 2022 China Automation Congress, pp. 6879–6884. IEEE, Xiamen, China (2022)
10. Xi, C., Qian, W., Peipei, P.: Output characteristics simulation analysis of PEMFC. In: 2020 IEEE 3rd International Conference on Automation, Electronics and Electrical Engineering, pp. 253–258. IEEE, Shenyang, China (2020)
11. Khan, S.S., Shareef, H., Kandidayeni, M.: Dynamic semiempirical PEMFC model for prognostics and fault diagnosis. *IEEE Access* **9**, 10217–10227 (2021)
12. Yan, C., Chen, J., Liu, H.: Model-based fault tolerant control for the thermal management of PEMFC systems. *IEEE Trans. Ind. Electron.* **67**(4), 2875–2884 (2019)
13. Yang, J., Hu, Y., Zhang, K.: An improved evolution algorithm using population competition genetic algorithm and self-correction BP neural network based on fitness landscape. *Soft. Comput.* **25**, 1751–1776 (2021)
14. Chen, J., Dong, C., He, G.: A method for indoor Wi-Fi location based on improved back propagation neural network. *Turk. J. Electr. Eng. Comput. Sci. Comput. Sci.* **27**(4), 2511–2525 (2019)
15. Zhao, Y., Li, J., Wang, P.: Research on optimization of GA-BP algorithm based on LM. In: 2021 IEEE 4th International Conference on Computer and Communication Engineering Technology (CCET), pp. 115–119. IEEE, Beijing, China (2021)
16. Li, H., Sun, C., Lu, L.: Research on fault diagnosis of ship generator based on GA-BP neural network. In: 2022 7th International Conference on Automation, Control and Robotics Engineering (CACRE), pp. 234–238. IEEE, Xi'an, China (2022)



An Optimal Dispatch Method for the Hydrogen-Electric Coupled Energy Microgrid

Yanda Huo^{1,2(✉)}, Zhen Wu¹, Jianfeng Dai¹, Wei Duan¹, Hao Zhao³, Jintao Jiang⁴,
and Riwu Yao⁵

¹ China Electric Power Planning and Engineering Institute, Beijing 100120, China
ydhuo@eppei.com

² Tianjin University, Tianjin 300072, China

³ China Energy Engineering Group Tianjin Electric Power Design Institute Co., Ltd,
Tianjin 300400, China

⁴ State Grid Changchun Power Supply Company, Changchun 130000, China

⁵ Zhejiang University, Hangzhou 310027, China

Abstract. The hydrogen-electric coupled energy microgrid (HEMG) is a novel hydrogen-centered energy system that is promising to facilitate the decarbonization of the energy system. The HEMG can realize the deep integration of various renewable energy resources (RES), including photovoltaics (PV), wind turbines (WT), and other clean energy equipment such as polymer electrolyte membrane (PEM), hydrogen storage tanks (HST), solid oxide fuel cells (SOFC), and electric energy storages (EES). However, fluctuating RES outputs and diversified energy demands will greatly challenge the operational performance of HEMG. To achieve efficient coordination, an optimal dispatch method is proposed for the HEMG to minimize the total operating cost and carbon emissions. A mixed-integer linear programming (MILP) model is established to formulate the coordination of multiple energy devices with different operational characteristics in the HEMG. The proposed dispatch method is validated using a HEMG test case under construction in Foshan, China. The results demonstrate its effectiveness in reducing the operating cost and carbon emissions of the HEMG. This study provides a practical approach for the optimal dispatch of HEMGs, which can contribute to the development of sustainable multi-energy systems.

Keywords: Hydrogen-electric coupled energy microgrid (HEMG) · Optimal dispatch · Coordination

1 Introduction

As a clear and renewable energy, hydrogen energy has aroused worldwide attention. Generated by renewable energy sources (RES), green hydrogen is seen as a promising way for decarbonization and environmental protection [1]. In the short timescale, the hydrogen generation equipment can rapidly respond to the fluctuation of RES outputs,

that is improve the usage efficiency of RES. In the long timescale, hydrogen can be used as seasonal energy storage to reduce the monthly energy unbalance. Besides, as an important form of industrial chemicals and fuel, the demand for hydrogen is increasing in the past decades [2]. The replacement of grey hydrogen with green hydrogen has become a trend in energy sectors.

The hydrogen-electric coupled energy microgrid (HEMG) is a novel hydrogen-centered energy system that provides good application prospects in industrial parks or cities with hydrogen energy fueling stations [3]. The HEMG consists of various energy equipment, including photovoltaics (PV), wind turbines (WT) polymer electrolyte membrane (PEM), hydrogen storage tanks (HST), solid oxide fuel cells (SOFC), and electric energy storages systems (EESS). A typical HEMG is shown in Fig. 1.

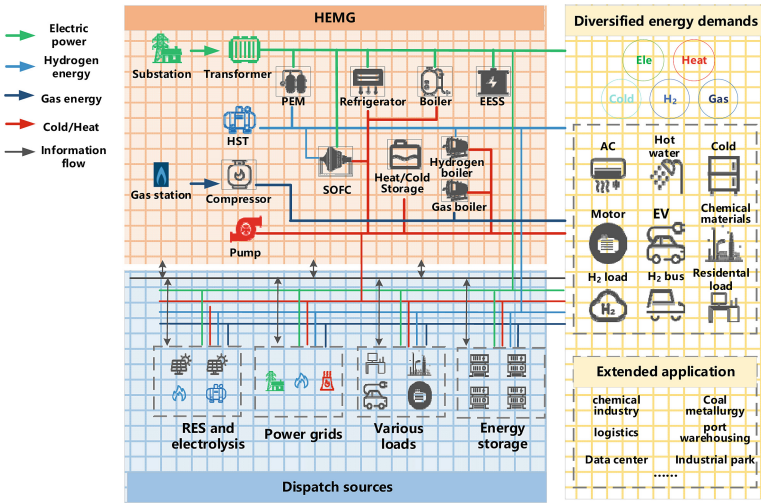


Fig. 1. A typical structure of HEMG

It is significant to coordinate the equipment in HEMG to satisfy the diversified energy demands including the electrical, heat, and hydrogen load. To achieve efficient coordination, an optimal dispatch method is proposed for the HEMG to minimize the total operating cost and carbon emissions. A mixed-integer linear programming (MILP) model is established in this paper to formulate the coordination of multiple energy devices with different operational characteristics in the HEMG.

2 Optimal Dispatch Method of HEMG

A day-ahead optimal dispatch method is proposed in this section. There are three operational objectives of the studied HEMG: (1) Satisfying the various energy demands. (2) Minimizing carbon emissions. (3) Minimizing the cost of energy purchase. To achieve these goals, the information on loads, PV curves, and electrical power prices is necessary to be predicted a day ahead.

Objective Function

Since there is no carbon emission inside HEMG, the only way of minimizing the carbon emission is to reduce the amount of energy purchased from the upper power grid. Besides, considering the operational cost, the objective function can be formulated as follows.

$$f = \min(C_{\text{Grid}}[t] * P_{\text{Grid}}[t]) \quad (1)$$

where t is the time indices. $C_{\text{Grid}}[t]$ is the power purchase cost during time t . $P_{\text{Grid}}[t]$ denotes the power purchase amount during time t .

Constraints

(1) *Operational constraints of the hydrogen energy system*

$$0 \leq P_{\text{PEM}}[t] \leq B_{\text{PEM}}[t] * S_{\text{PEM}} \quad (2)$$

$$0 \leq P_{\text{SOFC}}[t] \leq B_{\text{SOFC}}[t] * S_{\text{SOFC}} \quad (3)$$

$$SOH[t + 1] * S_{\text{H}_2} = SOH[t] * S_{\text{H}_2} + \eta_{\text{PEM}} P_{\text{PEM}}[t] - \eta_{\text{SOFC}} P_{\text{SOFC}}[t] \quad (4)$$

$$L_{\text{SOH}} \leq SOH[t] \leq U_{\text{SOH}} \quad (5)$$

where $P_{\text{PEM}}[t]$ and $P_{\text{SOFC}}[t]$ are the power consumption of PEM and SOFC during time t . $B_{\text{PEM}}[t]$ and $B_{\text{SOFC}}[t]$ are the binary indicators of operational states. S_{PEM} and S_{SOFC} respectively denote the capacity of PEM and SOFC. $SOH[t]$ is the state of the hydrogen storage system. η_{PEM} and η_{SOFC} are the efficiency parameters. L_{SOH} and U_{SOH} are the upper and lower limits of SOH.

(2) *Operational constraints of the electric energy storage system (EESS)*

$$0 \leq P_c[t] \leq B_c[t] * S_{\text{EESS}} \quad (6)$$

$$0 \leq P_d[t] \leq B_d[t] * S_{\text{EESS}} \quad (7)$$

$$SOC[t + 1] * S_{\text{EESS}} = SOC[t] * S_{\text{EESS}} + \eta_{\text{EESS}} P_c[t] - \eta_{\text{EESS}} P_d[t] \quad (8)$$

$$L_{\text{SOC}} \leq SOC[t] \leq U_{\text{SOC}} \quad (9)$$

$$L_{\text{SOC}} \leq SOC[t] \leq U_{\text{SOC}} \quad (10)$$

where $P_c[t]$ and $P_d[t]$ are the charging and discharging power of EESS during time t . $B_c[t]$ and $B_d[t]$ are the binary indicators of charging/discharging states of EESS. S_{EESS} denotes the capacity of EESS. $SOC[t]$ is the state of charge. η_{EESS} is the efficiency parameter of EESS. L_{SOC} and U_{SOC} are the upper and lower limits of SOC. T is the end of the dispatch duration.

(3) *Coordination constraints*

$$0 \leq B_c[t] + B_d[t] \leq 1 \quad (11)$$

$$0 \leq B_{PEM}[t] + B_{SOFC}[t] \leq 1 \quad (12)$$

$$0 \leq B_c[t] + B_{SOFC}[t] \leq 1 \quad (13)$$

Equations (11)–(13) show coordination relationships between EESS, PEM, and SOFC.

(4) *Constraints of energy balance*

$$P_{L_e}[t] + P_c[t] + P_{SOFC}[t] = P_{PEM}[t] + P_d[t] + P_{Grid}[t] + P_{RES}[t] \quad (14)$$

$$P_{L_{H2}}[T] \leq (SOH[T] - SOH[0]) * S_{H2} \quad (15)$$

$$0 \leq P_{Grid}[t] \quad (16)$$

where $P_{L_e}[t]$ denotes the load of electrical power during time t . $P_{RES}[t]$ is the power outputs of RES during time t . $P_{L_{H2}}[T]$ represents the demand of hydrogen energy in the dispatch duration.

In the normal HEMG, it is necessary to absorb the energy of PV locally. Then the optimal dispatch model is formulated. The flowchart of the proposed optimal dispatch method is shown in Fig. 2.

3 Case Study

In this section, the proposed optimal dispatch method is tested on an application case in Foshan. The proposed model is implemented in MATLAB R2022a. The numerical experiments were carried out on a computer with an Intel(R) Core(TM) i7–10700 processor running at 2.90 GHz and 16 GB of RAM.

The application case consists of a HEMG, of which the maximum electric power demands are 1 MW. The hydrogen demand is 1000kg/day, which works out to 66MWh/day. A 6.5 MW PV, a 6 MW PEM, a 0.6 MW SOFC, a 300MWh HST, and a 2.5MW/10MWh EESS are integrated into the test HEMG. The structure of the test case is shown in Fig. 3. The operation curves of PV and loads are shown in Fig. 4 (Fig. 5).

Based on the proposed dispatch method, the daily optimal dispatch results are shown in Figs. 6, 7 and 8. Figure 6 demonstrates the optimal dispatch strategies of HEMG. It can be seen that the PEM is in work condition from 7:00–17:00 when the PV has power output. In addition, it also works during the night when the electricity price is low. The EESS also works in the charging mode to buy cheap electricity, and discharges to satisfy the electricity demands when the price is high. By utilizing the proposed optimal dispatch method, the EESS, and the hydrogen energy system are coordinated to satisfy the diversified energy demands. The dispatch strategies of the hydrogen energy system and EESS are shown in Figs. 7 and 8. By cooperating with the multiple energy equipment in HEMG, the operation efficiency can be improved.

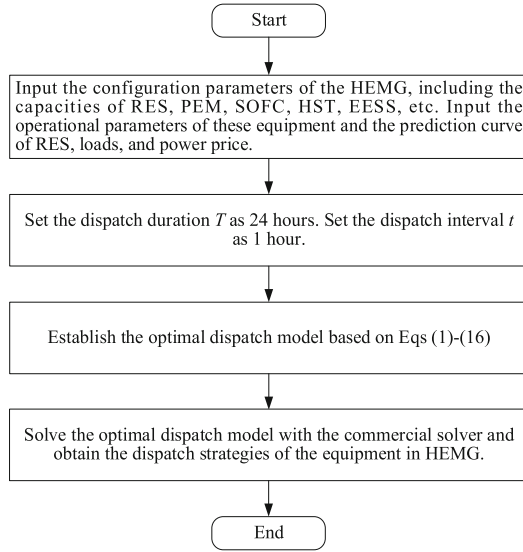


Fig. 2. The flowchart of the proposed optimal dispatch method.

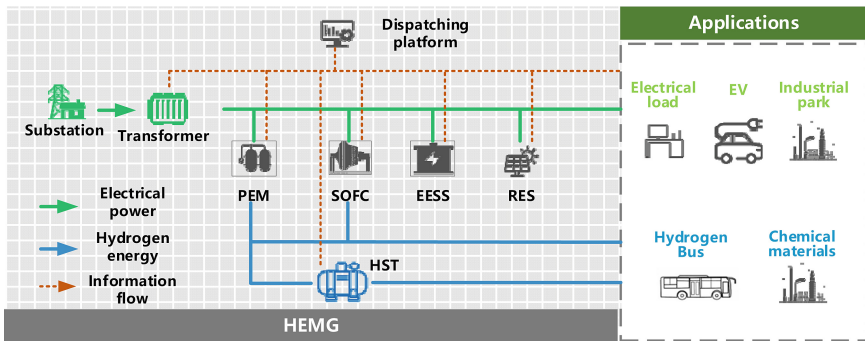


Fig. 3. The application case in Foshan.

4 Conclusion

In this paper, we have explored the application of a hydrogen-electric coupling system. The optimal dispatch method presented in this paper has shown promising results in terms of improving the system's efficiency and reducing its operating costs for the HEMG. By incorporating the hydrogen energy system and EESS with the PV and electricity price, the HEMG can achieve a balanced and stable operation condition, taking into account the electricity and hydrogen demands of its users. The findings of this study contribute to the operation of the hydrogen-electric coupling microgrids and hold significant potential for the sustainable and efficient use of hydrogen energy in the future.

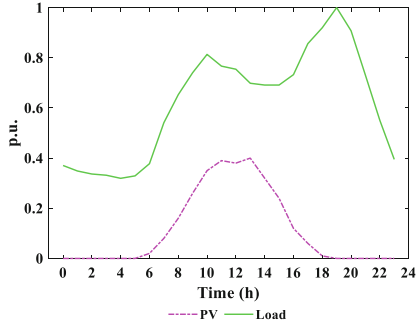


Fig. 4. The operation curves of PV and loads.

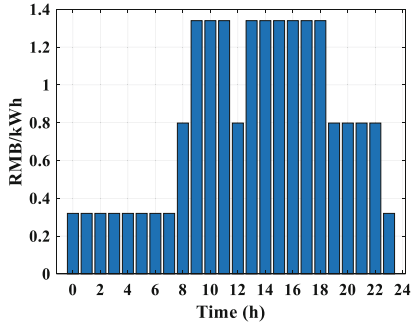


Fig. 5. The operation curves of electrical price.

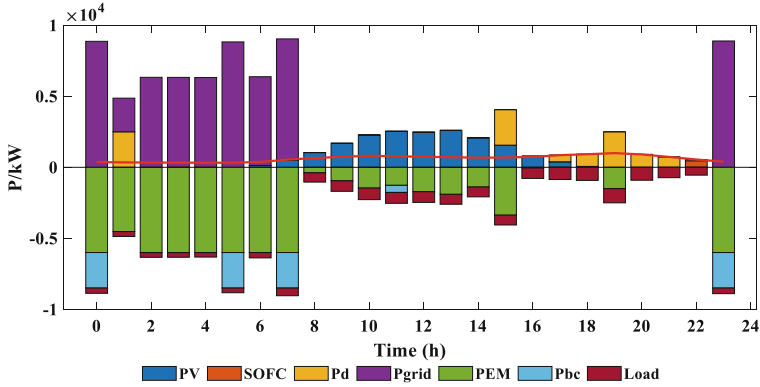


Fig. 6. The dispatch strategies of HEMG.

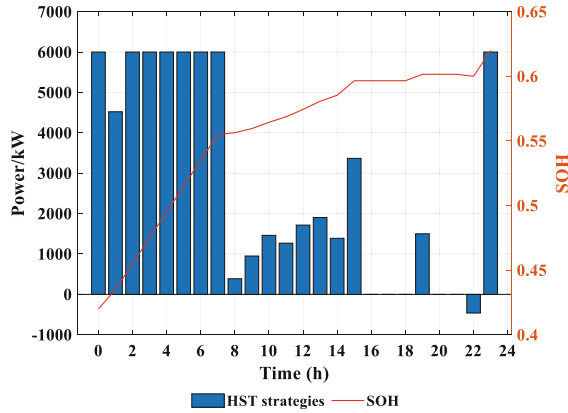


Fig. 7. The dispatch strategies of the hydrogen energy system.

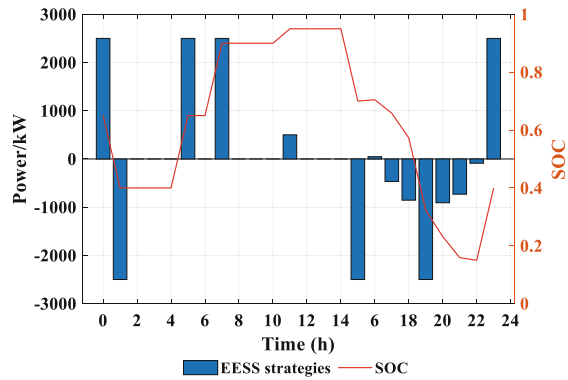


Fig. 8. The dispatch strategies of EESS.

References

1. Brey, J.: Use of hydrogen as a seasonal energy storage system to manage renewable power deployment in Spain by 2030. *Int. J. Hydrogen Energy* **4**, 89 (2020)
2. Endo, N., Shimoda, E., Goshome, K., et al.: Simulation of design and operation of hydrogen energy utilization system for a zero emission building. *Int. J. Hydrogen Energy* **44**(14), 7118–7124 (2019)
3. Li, Q., Zou, X., Pu, Y., et al.: A real-time energy management method for electric-hydrogen hybrid energy storage microgrid based on DP-MPC. *CSEE J. Power Energy Syst.* (2021)



Marine Scheme and Experimental Study of Liquid Organic Hydrogen Carrier Technology

Zhen Wang^{1,2,3}✉, Zengshi Xu^{2,3}, Rui Chen², and Yuanting Peng²

¹ School of Mechanical Engineering, Shanghai Jiao Tong University, Shanghai 200240, China
kingowang@163.com

² Wuhan Institute of Marine Electric Propulsion, Wuhan 430064, China

³ Wuhan Hydrogen and Fuel Cell Industry Technology Research Institute Co. Ltd,
Wuhan 430070, China

Abstract. Liquid organic hydrogen carrier technology, with its characteristics of high mass and volume hydrogen storage density, normal temperature and pressure storage and replenishment, and repeated cycles and long life, is a potential solution for large-scale hydrogen storage and transportation, as well as an ideal hydrogen storage technology in the marine field. This paper proposes a marine fuel cell system solution based on liquid organic hydrogen carrier technology for specific ship types. Then, hydrogen storage and release experiments were carried out on a 40 kW level liquid organic hydrogen carrier device to verify its hydrogen storage efficiency, release efficiency, and reaction internal friction. Through experiments and theoretical calculations, it was also proved that the hydrogen catalytic combustion heating scheme can improve the effective utilization rate of hydrogen by 25% compared to the electric heating scheme. Finally, an operational compatibility test was conducted between the liquid organic hydrogen carrier device and the proton exchange membrane fuel cell. The research results indicate that the liquid organic hydrogen carrier technology has no significant differences from traditional high-pressure hydrogen storage technology in terms of hydrogen supply flow stability and impact on the electrical performance of the fuel cell stack, and it was verified that its release rate, pressure, and purity of hydrogen can meet the needs of stable power generation by fuel cells.

Keywords: Liquid organic hydrogen carrier · Marine · Experimental study

1 Introduction

The emissions-reduction strategy of IMO [1] and the national double-carbon strategy have required China's shipping industry to accelerate the action of energy conservation and emission reduction. Thus, developing green ship manufacturing and green shipping, building a green ocean has become an important direction of green and sustainable development in the future [2].

Compared with the traditional ship power system such as diesel engine and steam turbine, the hydrogen fuel cell system has been seen as an ideal power source for green

ships, because of its characteristics of high-energy conversion efficiency, low vibration noise and zero emission [3]. However, the hydrogen storage density, supply characteristics, system complexity, cost and other characteristics of the hydrogen fuel unit determine the endurance, safety and economy of hydrogen fuel cell ships. High efficient and high safety of hydrogen storage and transportation has become the most important issues for the application of hydrogen energy in the field of ship.

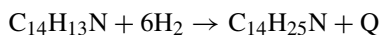
At present, most Marine hydrogen sources at home and abroad adopt high-pressure hydrogen storage technology, and other hydrogen storage technologies with development potential include: Liquid Organic Hydrogen Carrier (LOHC) [4], low temperature liquid hydrogen, methanol reforming hydrogen production, metal hydrolysis hydrogen production, ammonia hydrogen production and solid hydrogen storage. All these hydrogen storage technologies have different advantages and disadvantages in physical characteristics, hydrogen storage density, safety, supply guarantee, availability, economy and other aspects [5, 6]. The LOHC technology has the characteristics of high hydrogen storage density, relatively mild dehydrogenation temperature and no emissions. More importantly, it has stable performance and high safety at normal temperature and pressure [7], existing diesel transportation mode and gas station structure for transportation, storage and replenishment [8], These above characteristics also make it quite economical [9, 10]. By further solving the engineering problem, the LOHC technology will be an ideal way of Marine hydrogen storage.

Recently, the theoretical and experimental research on fuel cell system based on LOHC and supply technology has been carried out at home and abroad, especially in Germany and Japan [11]. Lee et al. [12] preliminarily proved the feasibility of the scheme through low-power organic liquid dehydrogenation and fuel cell coupling test. Viitakangas et al. [13] studied the impact of organic liquids themselves on fuel cells. Wang et al. [14] studied the energy flow distribution of organic liquids from hydrogenation to dehydrogenation; Makaryan et al. [15] believed that the main reason why the LOHC technology had not been commercialized on a large scale was its large heat absorption and insufficient stability of the dehydrogenation catalyst. Eypaschdeng et al. [16] demonstrated the feasibility of an energy supply system based on the production of hydrogen and LOHC and supply technology.

2 LOHC Technology Marine Scheme

2.1 Basic Principle of LOHC Technology

The basic principle of LOHC technology is to use the liquid organic molecular material containing unsaturated C=C double bonds as the hydrogen storage carrier. The reversible chemical reaction with hydrogen is formed to realize the cyclic hydrogenation-dehydrogenation process. There are so many kinds of organic liquids [17, 18], take N-ethyl carbazole as an example, the reactions are the flowing:



2.2 Characteristics of LOHC Technology

The main features of LOHC technology are as follows:

(1) High Hydrogen Storage Density

The hydrogen storage volume density of organic molecular materials (such as N-ethyl carbazole) as hydrogen storage carrier is about 56 g/L. Its hydrogen storage mass amount is 5.58 wt%, which is comparable to the 70MPa high pressure hydrogen storage. The theoretical hydrogen storage mass density of LOHC reaches over 6.5 wt%.

(2) Hydrogen Storage, Transportation and Supply is Safe and Convenient

The hydrogen storage organic liquid is a liquid high flash point compound, which does not burn in open fire, and the storage is very safe. Ordinary pipelines, tank trucks and other equipment can be used to quickly complete the material supply at the wharf, there will not be any hydrogen or energy loss in the whole transportation and replenishment process.

(3) High Hydrogen Purity, No Tail Gas Emissions

The hydrogen obtained by LOHC has a high purity (99.99%). In addition, the CO and sulfide content fully meet the hydrogen demand of fuel cell device, there is no exhaust emission problem in the process of dehydrogenation.

(4) Liquid Hydrogen Storage Carrier Material Can be Reused

The addition and dehydrogenation reaction of hydrogen storage organic liquid is complete, the reaction process is highly reversible, and the liquid hydrogen storage carrier material can be used repeatedly.

2.3 Typical LOHC and Marine Use Scheme

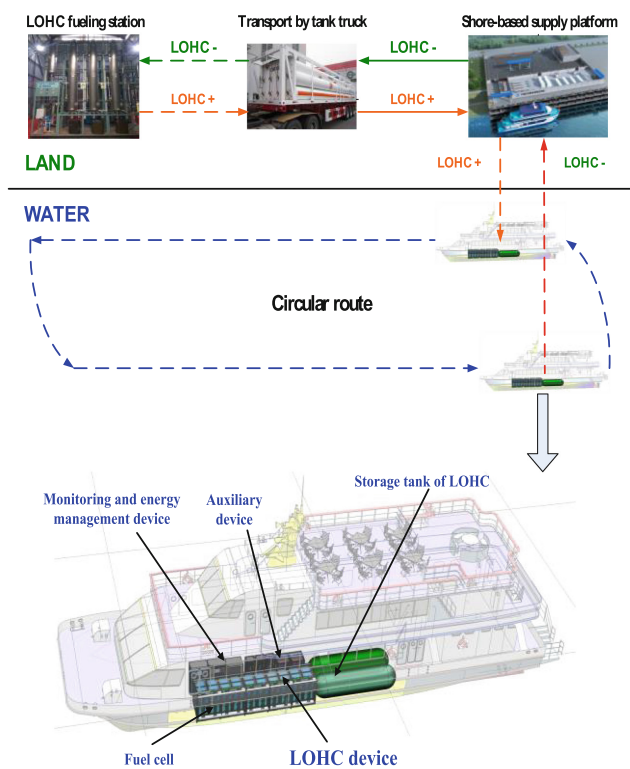
With a certain type of 300 passengers position pure electric ferry as the target image, the specific parameters of the ship are shown in Table 1. The composition and layout and ship operation mode of the fuel cell system based on LOHC technology are shown in Fig. 1.

The rated power of the Marine fuel cell system is 500kW, the total energy storage of hydrogen is about 10 MWh. It mainly includes fuel cell, organic liquid storage and dehydrogenation device, organic liquid storage tank, monitoring and energy management device, auxiliary device, etc. The total weight of the system is about 26 tons, of which the organic liquid weighs about 16 tons. The existing power scheme of the pure electric ship is lithium iron phosphate battery pack, the system weight is also 26 tons, and the total energy storage is about 2.5 MWh. It can be seen that the fuel cell system based on LOHC technology is about four times that of the lithium battery system under the same weight.

The operation process of hydrogen fuel cell powered ship based on organic liquid storage and supply technology are as follows: Hydrogen-rich organic liquid is stored in the ship bottom storage tank, transfer to the dehydrogenation unit through the metering pump; After the preheating of the hydrogen-rich organic liquid, Dehydrogenation

Table 1. Main parameters of the target ship

| | |
|----------------------------|--|
| Total length | 52.5 m |
| Total width | 13.4 m |
| Molded breadth | 10.8 m |
| Molded depth | About 2.7 m |
| Navigation area and type | Inland river class B, Five types of passenger ships |
| Maximum passenger capacity | 300 People |
| Max speed (6 m depth) | 10 ± 0.3 kn |
| Propeller power | 2×200 kW |
| Total length | 52.5 m |

**Fig. 1.** Composition, layout and ship operation mode of the fuel cell system

reaction under certain temperature and catalyst conditions, produce hydrogen and dehydrogenation of organic liquids; After the gas-liquid mixture product is cooling and gas-liquid separation, hydrogen is delivered directly to the fuel cell, liquid dehydrogenation organic liquid returns to the bottom storage tank of the empty vessel; The production of hydrogen-rich organic liquid is completed in the land hydrogenation station, by tanker truck transport to the supply terminal; After the ferry reaches the supply terminal, in the form of the pumping, out of the dehydrogenation organic liquid, fill with a hydrogen-rich organic liquid, complete the replacement and replenishment of hydrogen fuel.

3 Experimental Study on a Typical Organic Liquid Dehydrogenation Device

3.1 Hydrogen Storage Efficiency Test of Organic Liquid

The LOHC efficiency was tested by gas chromatography mass spectrometry combined tester, and the test related data are shown in Table 2.

Table 2. LOHC efficiency test data

| Components content (wt%) | 1 # Sample | 2 # Sample | 3 # Sample |
|--|------------|------------|------------|
| H-0 | 0 | 0 | 0 |
| H-4 | 0.81 | 0.57 | 0.94 |
| H-6 | 1.27 | 1.15 | 1.31 |
| H-8 | 2.33 | 2.07 | 2.17 |
| H-12 | 95.59 | 96.21 | 95.58 |
| Hydrogen storage efficiency (%) | 98.05 | 98.36 | 98.0 |
| Average hydrogen storage efficiency (Xm) | 98.14% | | |

From the above data, it can be concluded that:

The hydrogen storage efficiency of the 1 # sample is: $(40.81\% + 61.27\% + 82.33\% + 1295.59\%)/12 \times 100\% = 98.05\%$;

The hydrogen storage efficiency of the 2 # sample is: $(40.57\% + 61.15\% + 82.07\% + 1296.21\%)/12 \times 100\% = 98.36\%$;

The hydrogen storage efficiency of the 3 # sample is: $(40.94\% + 61.31\% + 82.17\% + 1295.58\%)/12 \times 100\% = 98.0\%$.

The average hydrogen storage efficiency of the hydrogen storage organic liquid is:

$$X_m = (98.05\% + 98.36\% + 98.0\%)/3 = 98.14\%$$

According to the analysis of the above data, the hydrogen storage efficiency of the organic liquid reaches 98.14%. The theoretical value of the material hydrogen storage mass density of the organic liquid is 5.58%, while the actual value is $5.58\% \times 98.14\% = 5.5\%$.

3.2 Hydrogen Discharge Test of Organic Liquid Dehydrogenation Unit

The hydrogen discharge test was carried out with the 40kW organic liquid dehydrogenation device as the test object, mainly completing four tests, including the dehydrogenation reaction efficiency, the average internal friction of the dehydrogenation device, the thermal efficiency of the dehydrogenation reaction and the purity of the dehydrogenation hydrogen (Fig. 2).



Fig. 2. 40 kW LOHC device and fuel cell module

3.2.1 Dehydrogenation Reaction Efficiency

The cumulative value of hydrogen discharge is recorded through the hydrogen mass flow meter, and then recorded the weight before and after the test of hydrogen storage organic liquid. The specific values and results are as shown in Table 3.

Table 3. Dehydrogenation reaction efficiency test

| Parameter (wt%) | Unit | Numeric value |
|--|------|---------------|
| Ambient temperature | °C | 27 |
| Weight of hydrogen storage organic liquid and container (M1) | kg | 166.5 |
| Weight of hydrogen storage organic liquid and container (M2) | kg | 121.5kg |
| Mass flowmeter starting value (MA) | SL | 0 |
| Mass flowmeter starting value (MB) | SL | 25672 |

The dehydrogenation reaction efficiency is:

$$\frac{\frac{(25672-0)SL}{22.4 \text{ L/mol}} \times 2 \text{ g/mol}}{(166.5 - 121.5) \text{ kg} \times 5.5\%} = \frac{2292.14 \text{ g}}{2475 \text{ g}} = 92.6\%$$

3.2.2 Average Internal Consumption of the Dehydrogenation Unit

The organic liquid dehydrogenation unit adopts an electric heating method to provide the heat required for dehydrogenation (Table 4). If the unit operates for about 1.1 h, the

Table 4. Average internal friction test of the dehydrogenation unit

| Parameter (wt%) | Unit | Numeric value |
|--|------|---------------|
| Ambient temperature | °C | 27 |
| Starting time of the hydrogen supply system (t1) | \ | 12:08 |
| Downtime of hydrogen supply system (t2) | \ | 13:15 |
| Start Memeter starting reading (W1) | kWh | 699 |
| Electricity meter termination reading (W2) | kWh | 719 |

average internal consumption is:

$$(719 \text{ kWh} - 699 \text{ kWh}) / 1.1 \text{ h} = 18.2 \text{ kW}$$

3.2.3 Thermal Efficiency of the Dehydrogenation Reaction

Electric Heating Scheme Test The 40kW organic liquid dehydrogenation device contains two sets of electric heating preheater, the power of about 1.0kW resistance wire electric heater. In addition, it is also equipped with metering pump, solenoid valve and other small power components, auxiliary power is about 2kW.

In this test, the energy consumption of the dehydrogenation reaction is:

$$719 \text{ kWh} - 699 \text{ kWh} - 2 \times 1.0 \text{ kW} \times 1.1 \text{ h} \approx 18 \text{ kWh} = 64080 \text{ kJ}.$$

According to the enthalpy value of the dehydrogenation reaction, the heat absorption of the dehydrogenation reaction is:

$$25672 \text{ SL} / 22.4 \text{ L/mol} \times 50.18 \text{ kJ/mol} = 57510 \text{ kJ}$$

The thermal efficiency of the electric heating is:

$$57510 \text{ kJ} / 64080 \text{ kJ} \approx 90\%$$

This value is consistent with the calibration efficiency of the electric heater.

The electricity used for electric heating accounts for about 41% ($18.2 \text{ kWh} / (40 \text{ kW} \times 1.1 \text{ h})$) of the total electricity generation, namely about 59% of the total hydrogen amount is used for effective power generation by fuel cell modules. Therefore, its effective hydrogen storage density is about (Fig. 3):

$$5.58 \text{ wt\%} \times 98.14\% \times 92.6\% \times 59\% \approx 3 \text{ wt\%}$$

$$56 \text{ g/L} \times 98.14\% \times 92.6\% \times 59\% \approx 30 \text{ g/L}$$

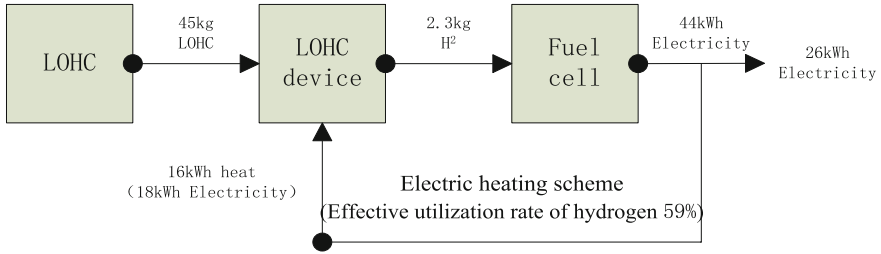


Fig. 3. Energy flow diagram of the electric heating scheme system

Estimation of Hydrogen Catalytic Combustion Scheme

(1) Estimation of the Thermal Efficiency of Hydrogen Catalytic Combustion

In order to improve the effective hydrogen utilization rate of the organic liquid dehydrogenation device, the catalytic combustion device is used for heating. First, the hydrogen catalytic combustion device produces high temperature gas produced by the exothermic reaction of hydrogen and air. Then the high temperature gas gradually heats the thermal oil and accurately controls the temperature from 220°C to 240°C to maintain the stability of the dehydrogenation reaction. Finally, the low temperature gas after heating the thermal conductive oil preheat the air entering the catalytic combustion device to improve its thermal efficiency.

The heat loss method was used [19] to estimate the thermal efficiency of the catalytic combustion unit:

$$\eta = 100 - (Q_2 + Q_3 + Q_4) \times 100/Q_r = 100 - (q_2 + q_3 + q_4)$$

where η (%) is the thermal efficiency of the catalytic combustion device, Q_2 (kJ/kg) is the exhaust heat loss, Q_3 is the combustible gas incompletely combustion heat loss, Q_4 (kJ/kg) is the fuel heat loss, Q_r (kJ/kg) is the fuel input heat, q_2 (%) is the percentage of smoke exhaust heat loss, q_3 (%) is the percentage of incomplete combustion heat loss of combustible gas and q_4 (%) is the percentage of heat dissipation loss.

The mixed high temperature gas produced by catalytic combustion of hydrogen and air has a temperature range of 700°C ~ 800°C. By heating the thermal conductive oil and air, the exhaust temperature is 120°C ~ 150°C. The main component of the mixed high temperature gas is N_2 , its specific heat capacity is close to the air. The air specific heat capacity is about 4 kJ/kg at 0.1 MPa and 800 °C, and about 1.5 kJ/kg.°C at 0.1 MPa and 150 °C. According to the empirical formula, the smoke exhausts heat loss q_2 does not exceed 15%. Empirically, q_3 and q_4 generally do not exceed 1%. The thermal efficiency of the catalytic combustion device η is not less than 83%, and 80% is taken in the energy flow calculation.

(2) Energy Flow Calculation

According to the electric heating scheme, the heat needs 57510 kJ to release 25672SL (2308g) hydrogen. Therefore, the hydrogen consumption through the catalytic combustion heating device is:

$$Q_{\text{burn}} = 57510 \text{ KJ}/80\%/120\text{KJ/g} \approx 599 \text{ g.}$$

The hydrogen used for catalytic combustion heating accounts for about 599g/2308g≈26% of the total hydrogen production, that is, about 74% of the total hydrogen production is used for effective power generation by fuel cell modules. Compared with electric heating and hydrogen catalytic combustion schemes, it is obvious that the effective utilization rate of hydrogen is higher, which can be increased by about 26%. The corresponding effective hydrogen storage density is approximately (Fig. 4):

$$5.58 \text{ wt}\% \times 98.14\% \times 92.6\% \times 74\% \approx 3.8 \text{ wt}\%$$

$$56 \text{ g/L} \times 98.14\% \times 92.6\% \times 74\% \approx 38 \text{ g/L}$$

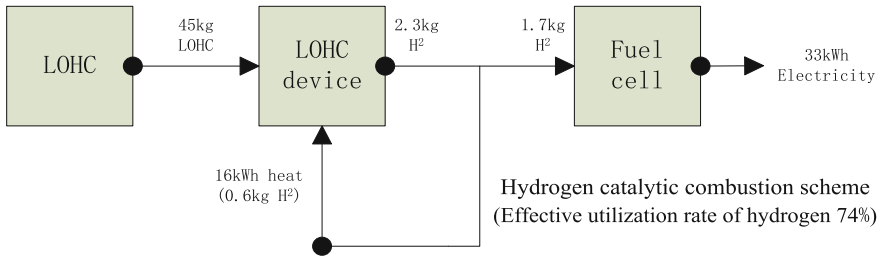


Fig. 4. Energy flow diagram of hydrogen catalytic combustion scheme system

3.2.4 Dehydrohydrogen Gas Purity

During the test, sampling from the sampling port and conduct purity test by gas chromatograph for hydrogen purity test, the results are shown in Table 5.

The purity of hydrogen produced by the dehydrogenation unit is 99.99795%, with the CO content is 0.57ppm, which meets the requirement of ≤ 1ppm for CO content in high-purity hydrogen in the national standard [20]. It is also consistent with the similar purity test results [21].

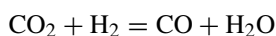
The main causes of CO generation in organic liquid devices are:

- (1) The organic liquid material of hydrogen storage is a thick heterocyclic compound containing N, whose N atoms are in the SP 3 hybrid orbit. It is an organic alkali structure that can adsorb traces of carbon dioxide in the air. In the storage process, the hydrogen storage organic liquid is in an open state, being in direct contact with the air and absorbing trace amounts of carbon dioxide in the air.

Table 5. Test results of dehydrohydrogen purity

| Order number | Surveillance project | Detection result |
|--------------|----------------------|---------------------------------------|
| 1 | H ₂ | $99.99795 \times 10^{-2}(\text{v/v})$ |
| 2 | O ₂ | $5.2 \times 10^{-6}(\text{v/v})$ |
| 3 | CO | $0.573625 \times 10^{-6}(\text{v/v})$ |
| 4 | CH ₄ | $0.293641 \times 10^{-6}(\text{v/v})$ |
| 5 | CO ₂ | $1.738044 \times 10^{-6}(\text{v/v})$ |
| 6 | NH ₃ | Not detected |
| 7 | NO ₂ | Not detected |
| 8 | SO ₂ | Not detected |

In the dehydrogenation reactor, under the catalyst and a certain temperature condition, carbon dioxide reacts with hydrogen to produce carbon monoxide and water.



- (2) The liquid hydrogen storage carrier material is an industrial-grade raw material, which is not further purified during its use. The trace molecular compounds contained in the raw materials are decomposed under the action of the catalyst, producing carbon monoxide, methane and carbon dioxide.
- (3) Dehydrogenation device currently uses resistance wire direct heating. During the long heating process, traces of hydrogen storage organic liquid molecules adhesion on heating resistance wire casing wall, because of the casing local temperature is too high, adhesion of organic liquid molecules may occur carbonization decomposition, produce small molecules such as carbon monoxide and carbon dioxide.

Although organic liquid dehydrogenation devices produce trace CO because of the three aforementioned reasons, they can be purified by setting up purification devices. The dehydrogenation device in this test adopts the grade 1 molecular sieve adsorption method, which can realize the CO concentration of about 0.57 ppm. In the design of the marine dehydrogenation device, the multistage molecular sieve adsorption method will be adopted to reduce the CO content to less than 0.1 ppm.

3.3 Operation Matching Test Between Dehydrogenation Unit and Fuel Cell

The joint test of 40kW fuel cell power generation module and organic liquid dehydrogenation unit has been completed. The details are as follows.

Figure 5 shows the changes in hydrogen supply flow rate and power generation after continuous operation for 12h, it can be observed that the hydrogen supply flow of the organic liquid dehydrogenation device is stable and controllable for 12h, with an average flow rate of about 378 SL/min, which can meet the operation requirements of the fuel cell module of 40 kW.

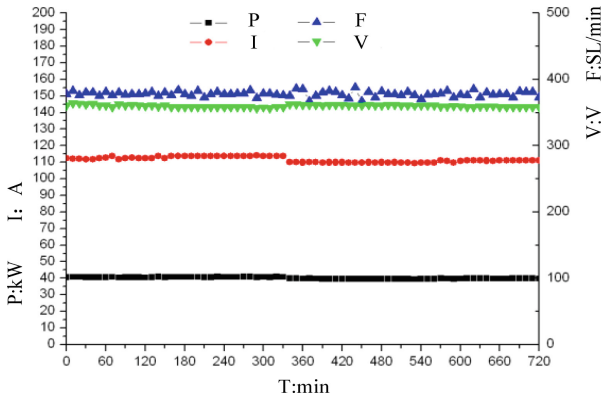


Fig. 5. Match of hydrogen supply flow and power generation in 12h continuous operation

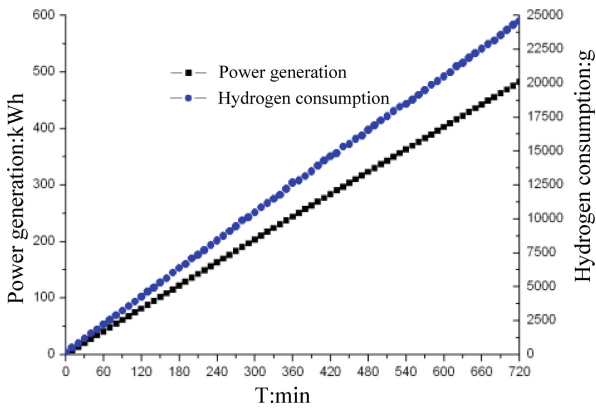


Fig. 6. Hydrogen supply and power generation for 12h

Figure 6 shows the cumulative hydrogen supply of the organic liquid dehydrogenation unit is 273,392 SL (24,578 g) in 12h, the cumulative generating capacity is 482 kWh, and the average hydrogen consumption is about 51g per kWh.

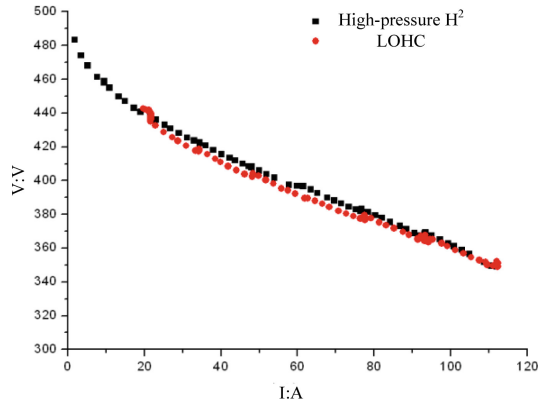


Fig. 7. Comparison of hydrogen supply from organic liquid and high-pressure gas cylinder on the performance of fuel cell module

It can be observed from Fig. 7 that there was no obvious difference in the electrical performance indexes of fuel cell polarization curve test was conducted using LOHC and high-pressure gas cylinder hydrogen supply.

Figure 8 shows the organic liquid dehydrogenation and high-pressure gas cylinder hydrogen supply is adopted, and there is no significant difference in the voltage level of a single cell under the condition of 40kW of the fuel cell module.

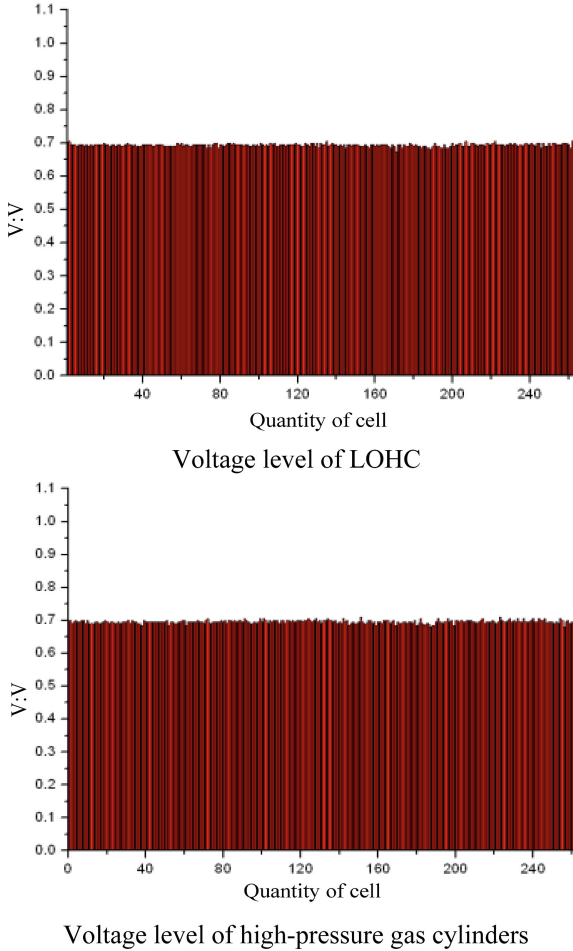


Fig. 8. Fuel cell voltage levels under different hydrogen storage technologies

4 Conclusion

Through the hydrogen discharge test of organic liquid dehydrogenation device, compared the actual hydrogen storage density of organic liquid under two heating methods, the effective hydrogen storage density of organic liquid dehydrogenation unit fuel by electric heating is 3 wt% and 30g/L, and the effective hydrogen storage density of organic liquid dehydrogenation unit by hydrogen catalytic combustion heating is 3.8 wt% and 38g/L. In addition, the operation matching test of dehydrogenation device and fuel cell was carried out. Compared with the two schemes of organic liquid dehydrogenation and high-pressure gas cylinder hydrogen supply, there was no obvious difference in the stability of hydrogen supply flow and the impact on the electric performance of fuel cell stack.

In summary, although the effective hydrogen storage density of organic liquid dehydrogenation unit has certain reduction, its mass density and volume density of hydrogen storage are equivalent to 35MPa and 70MPa high-pressure gas cylinder, respectively. However, its convenient storage, transportation characteristics, as well as physical characteristics such as high flash point and incombustible when exposed to open flames, make it certain advantages in the field of large capacity energy storage, and with the technological progress and engineering degree, the hydrogen storage density is expected to further improve.

References

1. Elkafas, A.G., Rivarolo, M., Gadducci, E.: Fuel cell systems for maritime: a review of research development, commercial products, applications, and perspectives. *Processes* **11**, 97 (2023)
2. Xing, H., Stuart, C., Spence, S.: Fuel cell power systems for maritime applications: progress and perspectives. *Sustainability* **13**, 1213 (2021)
3. Baolian, Y.: *Fuel Cell Principle, Technology and Application*. Chemical Industry Press, Beijing (2003)
4. Meille, V., Pitault, I.: Liquid organic hydrogen carriers or organic liquid hydrides: 40 years of history. *Reactions* **2**, 94–101 (2021)
5. Singh, R., Singh, M., Gautam, S.: Hydrogen economy, energy, and liquid organic carriers for its mobility. *Mater. Today Proc* **46**, 5420–5427 (2021)
6. Akhtar, M.S., Dickson, R., Jay Liu, J.: Life cycle assessment of inland green hydrogen supply chain networks with current challenges and future prospects. *ACS Sustain. Chem. Eng.* **9**, 17152–17163 (2021)
7. Leea, S., Kima, T., Han, G.: Comparative energetic studies on liquid organic hydrogen carrier: a net energy analysis. *Renew. Sustain. Energy Rev.* **150**, 111447 (2021)
8. Brigljevic, B., Lee, B., Dickson, R.: Concept for temperature-cascade hydrogen release from organic liquid carriers coupled with SOFC power generation. *Cell Rep. Phys. Sci.* **1**, 100032 (2020)
9. Wulf, C., Zapp, P.: Assessment of system variations for hydrogen transport by liquid organic hydrogen carriers. *Int. J. Hydrogen Energy* **43**, 11884–11895 (2018)
10. Peschel, A.: Industrial perspective on hydrogen purification, compression, storage, and distribution. *Fuel Cells* **20**(4), 385–393 (2020)
11. Wu, Z.: The comparative study on hydrogen energy strategies of Germany, Australia, Canada, and Japan. *Int. Petrol. Econ.* **29**(4), 60–66 (2021)
12. Lee, S., Han, G., Kim, T.: Connected evaluation of polymer electrolyte membrane fuel cell with dehydrogenation reactor of liquid organic hydrogen carrier. *Int. J. Hydrogen Energy* **45**, 13398–13405 (2020)
13. Viitakangas, J., Auvinen, S., Costantino, M.: Effect of toluene on PEMFC performance. *Fuel Cells* **20**(3), 245–252 (2020)
14. Wang, H., Zhou, X., Ouyang, M.: Efficiency analysis of novel liquid organic hydrogen carrier technology and comparison with high pressure storage pathway. *Int. J. Hydrogen Energy* **41**, 18062–18071 (2016)
15. Makaryan, I.A., Sedov, I.V., Maksimov, A.L.: Hydrogen storage using liquid organic carriers. *Russ. J. Appl. Chem.* **93**(12), 1815–1830 (2020)
16. Eypasch, M., Schimpe, M., Aastha Kanwar. Model-based techno-economic evaluation of an electricity storage system based on Liquid Organic Hydrogen Carriers [J] *Applied Energy* **185** (2017) 320–330

17. Niermann, M., Beckendorff, A., Kaltschmitt, M.: Liquid organic hydrogen carrier- assessment based on chemical and economic properties. *Int. J. Hydrogen Energy* **44**, 6631–6654 (2019)
18. Rao, P.C., Yoon, M.: Potential liquid-organic hydrogen carrier (LOHC) systems: a review on recent progress. *Energies* **13**, 6040 (2020)
19. Zhao, Q.: *Boiler Principle*. China Electric Power Press, Beijing (2009)
20. GB/T3634.2-2011 Hydrogen Part 2: Pure Hydrogen, High-Purity Hydrogen, and Ultrapure Hydrogen
21. Jang, M., Jo, Y.S., Lee, W.J.: A high-capacity, reversible liquid organic hydrogen carrier: H₂-release properties and an application to a fuel cell. *ACS Sustain. Chem. Eng.* **7**, 1185–1194 (2019)



Research on Sampling and Analysis Methods for Trace Particulate in Hydrogen Fuel

Xiaolu Chen^{1,2}, Xiaomin Liu², Yanmei Yang¹, Miaomiao Huo², Juan Wang², Wei Bao^{1,2}, and Ling Lin¹✉

¹ China National Institute of Standardization, Beijing, China
13485485485336@163.com

² Foshan Green Development Innovation Research Institute, Foshan, China

Abstract. The quality control of hydrogen for fuel cells has an important impact on the scale application of hydrogen energy. The international and China national standards have strict regulations on the content of gas and particulate impurities in hydrogen fuel. Particulate impurity is one of the important causes for the failure of hydrogen fuel cell systems. However, few studies were done on the sampling and analysis of trace particulates in hydrogen fuel, especially in China. It shows that the lack of basic data on particulate impurity is not conducive to the control of trace particulate impurity in hydrogen fuel. The hydrogen refueling station is an important part of the particulate impurity control. It is recommended that various sampling and analysis methods are required for different locations of the hydrogen refueling station system. Future research directions are also proposed, including the establishment of a particulate source analysis database and the development of standards for on-line measurement of particulate in hydrogen fuel, which can provide effective support for the control of trace particulate impurity in hydrogen fuel.

Keywords: Hydrogen fuel · Particulate · Sampling · Analysis

In the context of global energy crisis and climate change, hydrogen energy is an important component of the global energy structure adjustment and has a promising future. In the development of the hydrogen energy industry, the quality control of hydrogen fuel plays a significant role in its large-scale application, but there are still obvious technical shortcomings in the research on the measurement technology and the development of measurement instruments for trace impurity components in hydrogen fuel. At present, hydrogen used in fuel cells is mainly sourced from coal-based hydrogen production, industrial by-product hydrogen production, natural gas hydrogen production, and water electrolysis hydrogen production, and each hydrogen production method requires different purification processes to ensure that the quality of the hydrogen delivered from the factories conforms to the requirements of hydrogen fuel cells. However, due to the difficulty of detecting trace impurities in hydrogen, and the high precision required in some component measurement, there are some big problems in the quality control of hydrogen purification process. In addition, some trace impurities will be introduced in the transportation, compression and filling of the purified hydrogen, which will affect

the quality of hydrogen. Particulate impurity is one of the important factors causing the failure of hydrogen fuel cell system. As shown in Table 1, ISO 14687, SAE J2719 and GB/T 37244 all put forward higher limit requirements for hydrogen quality standards for fuel cell vehicles. It shows that all standards have the same limit requirements for particulate impurity in hydrogen fuel, which is all lower than 1 mg/kg [1–5].

Table 1. Standards of hydrogen fuel quality for fuel cell vehicles

| Constituents | Limits/ $\mu\text{mol}\cdot\text{mol}^{-1}$ | | |
|--|---|----------------|-----------------|
| | ISO 14687:2019 | SAE J2719:2015 | GB/T 37244–2018 |
| Water (H ₂ O) | 5 | 5 | 5 |
| Total hydrocarbons | 2 | 2 | 2 |
| Oxygen (O ₂) | 5 | 5 | 5 |
| Helium (He) | 300 | 300 | 300 |
| Nitrogen (N ₂) | 300 | 100 | 100 |
| Argon (Ar) | 300 | 100 | 100 |
| Carbon dioxide (CO ₂) | 2 | 2 | 2 |
| Carbon monoxide (CO) | 0.2 | 0.2 | 0.2 |
| Total sulfur compounds | 0.004 | 0.004 | 0.004 |
| Formaldehyde (HCHO) | 0.2 | 0.01 | 0.01 |
| Formic acid (HCOOH) | 0.2 | 0.2 | 0.2 |
| Ammonia (NH ₃) | 0.1 | 0.1 | 0.1 |
| Halogenated compounds (Halogen ion equivalent) | 0.05 | 0.05 | 0.05 |
| Particulate concentration | 1 mg/kg | 1 mg/kg | 1 mg/kg |

The sources and components of particulate impurity in hydrogen fuel is relatively complex. At present, there are no on-line measurement methods recommended in international or national standards, so the measurement of particulate impurity in hydrogen fuel needs to be analyzed in the laboratory after on-site sampling. However, due to the extremely low content of trace particulate in hydrogen fuel, the analysis results generally indicate a high uncertainty. Few studies have been done on particulate impurity in China, which leads to the lack of effective data support for the particulate control, and also limits the development of measurement technology of trace particulate impurity in hydrogen fuel.

1 Research Status

Some studies on the measurement of impurities in hydrogen fuel have been carried out, but most focus on the gaseous impurities [6–11]. Smart Chemistry in the United States, SINTEF Industry in Norway and National Physics Laboratory in Britain have advanced

research on the particulate sampling and analysis in the HRS. They jointly carried out the HyCoRA project in Europe, 28 hydrogen gas samples and 13 particulate samples were collected from 2014 to 2017. The online sampling location of particulate samples was between the nozzle and FCEV receptacle. The particulate samples were weighed to calculate the content of particulate in hydrogen, and the test results were shown in Fig. 1 [12]. It showed that the content of particulate in hydrogen fuel is lower than the standard limit, while analysis results indicated a high uncertainty that could potentially affect fuel quality control results.

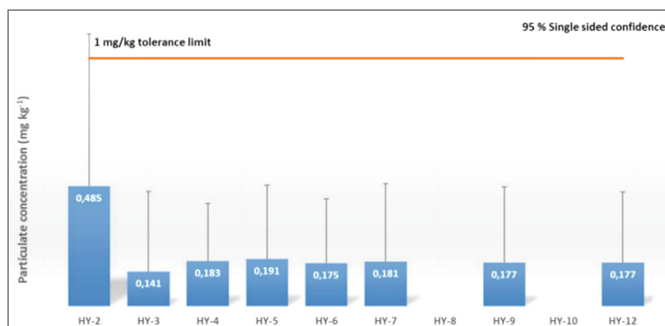


Fig. 1. The test results of online sampling particulate in hydrogen fuel [12]

Smart Chemistry collected 100 particulate samples in hydrogen fuel obtained from 16 HRSs in different regions of the United States. It was found that particulate impurity have been found in 94% of the hydrogen fuel at the HRSs. The particulate impurity mainly came from stainless steel pipes and inline filters (as shown in Fig. 2). In addition, organic coating is also one of the sources of particulate impurity in hydrogen fuel. In China, only a few research institutions have carried out relevant research on hydrogen quality control for fuel cells [1, 14–16]. Relevant research and analysis results show that the national standard GB/T 37244–2018 requires that the content of particulate should not exceed 1 mg/kg, but no explanation was given regarding its analysis method. However, the current measurement methods for particulate in other gases in China are not suitable for detecting particulate in hydrogen [14]. It is found that there is no published research on particulate sampling and analysis of in hydrogen fuel in China, which is mainly due to the strict management regulations for the HRS, and the technology and equipment are still immature.

With the development of the hydrogen energy, more research institutions and scholars pay attention to the equality control of hydrogen fuel. It is necessary to accelerate the research on sampling and analysis methods for particulate in hydrogen fuel, and develop related standards, to promote the equality control of hydrogen fuel.

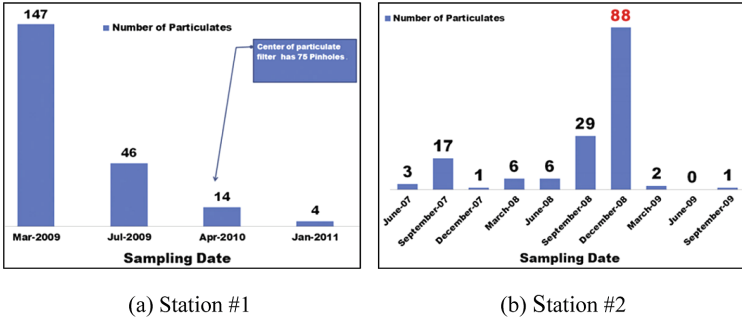


Fig. 2. The number of particulate sampled from different HRSs [13]

2 Standards for Particulate Measurement in Hydrogen Fuel

In China national standards, the recommended method for the determination of particulate in gas is gravimetric method (or weighing method), including GB/T 15432-1995: “Ambient air - Determination of total suspended particulates- Gravimetric method”, GB/T 16157-1996: “Determination of particulates and sampling methods of gaseous pollutants emitted from exhaust gas of stationary source” and GB/T 27893-2011: “Natural gas - Determination of particles content - Gravimetric method”. The measurement method standard of particulate in natural gas has a certain reference for the measurement of particulate in hydrogen, but the standard stipulates that the measurement pressure range from 0.1 to 6.0 MPa and the measurement range from 0.1 to 100.0 mg/m³, so it is not suitable for the measurement of particulate in high-pressure hydrogen flow. In addition, the particle counter method based on light scattering is recommended in the national standard for the determination of airborne particles. But its measurement of particulate size range from 0.1 to 10.0 μm, and the measurement results are not measured based on the mass concentration of particulate, which does not meet the standard requirements. So the light scattering method is not fully applicable to the particulate measurement in hydrogen fuel.

At present, particulate sampling is mainly based in ASTM standards. The ASTM D7650-10 (Standard Test Method for Sampling of Particulate Matter in High Pressure Hydrogen used as a Gaseous Fuel with an In-Stream Filter) proposes a sampling method for particulate in high-pressure hydrogen. High-pressure filter and PTFE filter membrane with a maximum operating pressure of 42 MPa are used to collect particulate with a diameter greater than or equal to 0.2 μm. After sampling of the filter membrane, weighing method is used to confirm the content of particulate in hydrogen [17]. During the particulate sampling, hydrogen flows through the HRS nozzle—high pressure sampling device—hose and nozzle—hydrogen fuel cell vehicle, and the particulate impurity is captured by the filter membrane in the gas stream. The ASTM D7651-10 (Standard Test Method for Gravimetric Measurement of Particulate Concentration of Hydrogen Fuel) provides a method of gravimetric determination of particulate in hydrogen fuel.

3 Scheme for Particulate Sampling and Analysis in Hydrogen Fuel

Sampling and analysis of trace particulate in HRS system is critical for quality control of hydrogen fuel. Based on the research status, sources of particulate impurity in hydrogen fuel are relatively complex. Therefore, in addition to the hydrogen equality at the inlet of hydrogen vehicles, it is also necessary to sample and analyze the particulate impurity that may be introduced into the HRS system.

Figure 3 shows sampling points in a HRS system. In general HRS system, in order to ensure the quality of the refueled hydrogen, particulate filtration devices are installed before and after the compressor and dispenser. The filters require regular cleaning or replacement, in this case, off-line sampling of particulate from the filters can be carried out, while other sampling points in the system need online sampling device. Therefore, the sampling points of a HRS system can be divided into online (1, 4, 6) and offline (2, 3, 5) sampling points, the particulate samples obtained from different sampling points should be characterized by different analysis methods according to the actual sampling situation.

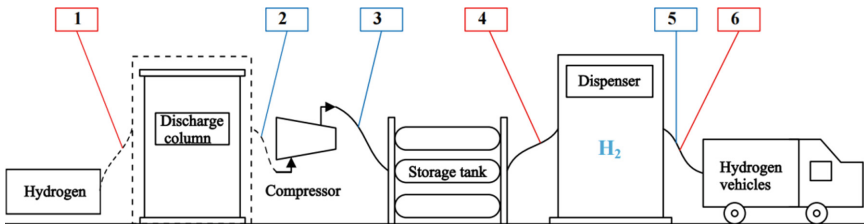


Fig. 3. Sampling points in HRS system

3.1 On-line Sampling Point

Particulate sampling at on-line sampling points need high-pressure sampling device. The online sampling points are located at: sampling point 1 - inlet of the discharge column; sampling point 4 - outlet of the hydrogen storage tank; sampling point 6 - between the nozzle and FCEV receptacle.

The high-pressure sampling device used at sampling points 1 and 4 are connected by bypass to collect particulate online in the hydrogen stream, which is composed of a filter holder and connecting fittings. The sampling devices can be self-made according to the recommended device in ASTM standards. For instance, Hsu [18] used a self-made sampling device to collect particulate in a HRS system. In contrast, the online sampling system involved in particulate sampling at sampling point 6 is relatively complex, due to the high pressure. Meanwhile, pressure compensation is required after the hydrogen flows through the filter.

In the online particulate sampling system, the high-pressure gas filter is the core device. Especially at the sampling point 6, the highest pressure capacity of the high-pressure gas filter should be higher than 70 MPa. Before sampling, the particulate filter

membrane installed inside the filter should be weighed under certain temperature and humidity conditions (W_1 , mg). During the sampling process, after the sampling device is connected to the hydrogen filling station, follow the normal operation process of hydrogen refueling for vehicles. After the hydrogen filling is completed, remove the filter membrane and weigh it again (under the same temperature and humidity conditions, W_2 , mg). At the same time, the hydrogen amount W_3 (kg) is copied down from the display screen of the hydrogen dispenser. The concentration of particulate can be calculated according to the following formula: $C = (W_2 - W_1)/W_3$ (mg/kg). The weighed filter membrane can be used for particulate characterization.

3.2 Off-line Sampling Point

Off-line sampling points for particulate: off-line sampling of the installed high-pressure filters in the HRS system is conducted, and the main sampling points are 2, 3, and 5 (as shown in Fig. 3). Due to the restrictions of HRS operation management, off-line sampling can only be conducted during routine maintenance or stop inspection of the HRS.

Sampling point 2 - Inlet of the compressor, particulate sampling and analysis in the hydrogen source and pipeline along the front of the compressor.

Sampling point 3 - Outlet of the hydrogen storage tank, sampling and analysis of particulate introduced by the compressor.

Sampling point 5- Between the nozzle and FCEV receptacle, particulate sampling and analysis in hydrogen before filling.



Fig. 4. In-line filters at compressor outlet

Figure 4 shows the inline filters taken from two different stations in Foshan, China. Materials of the filters can be glass fiber or Stainless steel. After sampling, the filtering material with particulate needs to be prepared before analysis. Since particulates are trapped in the micropores of the filtering material, the filtering material can be disassembled and the particulates can be removed from the pores of the filtering material by microwave cleaning or dissolved in a cleaning solvent. The particulates can then be separated for analysis, or the filtering material with particulates can be directly dissolved to obtain a sample for analysis to determine the composition of the particulates.

3.3 Source Analysis of Trace Particulate in Hydrogen Fuel

After particulate sampling, the samples should be analyzed to determine the content and composition of the particulate, conducting the source analysis of the particulate. Only by

deeply studying the source and cause of particulate impurity in the HRS system can we effectively control the particulate impurity that may be introduced in different positions of the HRS system. Samples that need to be characterized include solid powder samples and dissolved liquid samples after preparation. Laboratory characterization methods for these two types of samples are relatively mature.

The characterization of particulate samples is mainly analysing the components of particulate, including elemental composition and compound composition. The characterization of solid powder samples can be analyzed by scanning electron microscope with energy dispersive spectrometer (SEM-EDS) and transmission electron microscope (TEM), which can be used to analyze the micro-structure and element distribution. If the amount of particulate sample meets the analysis conditions, X-ray fluorescence spectrometer (XRF) and X-ray diffractometer (XRD) can also be used to analyze the elemental and compound composition of the sample. For liquid samples of dissolved particulate, there are also a variety of analysis methods, can be used inductively coupled plasma-mass spectrometer (ICP-MS) for metal element content analysis and ion chromatograph (IC) for inorganic negative and cation analysis.

4 Conclusion

At present, there are no mature online measurement method or instrument for trace particulate in hydrogen fuel. This paper proposes the sampling scheme and analysis method of particulate in HRS system. Further research from the following two aspects will effectively promote the development of the measurement and control technology of trace particulate in hydrogen fuel:

- (1) Quality control of hydrogen is beneficial for the healthy development of hydrogen industry. Analysis data of hydrogen impurities is an important basis for achieving hydrogen quality control. Under the current measurement level, collecting and analyzing samples of particulate impurity from different hydrogen sources and establishing a source analysis database of trace particulate in hydrogen fuel can effectively support the hydrogen quality control for hydrogen application.
- (2) Currently, there is no recognized online measurement method for trace particulate impurity in hydrogen fuel. Sampling by gravimetric method is complicated and takes a long time, which is not conducive to the control of particulate impurity in hydrogen. Further research should be done on the online measurement method for trace particulate in hydrogen fuel and develop related standards.

Funding. The research has been supported by Dean's Fund of China Institute of Standardization (542023Y-10360), Guangdong Basic and Applied Basic Research Foundation (2021A1515110441, 2022A1515140163) and Dean's Fund of China Institute of Standardization (542022Y-9371).

References

1. Xu, C., Xu, G., Zong, B., et al.: Analytical progress of trace impurities in hydrogen for fuel cell vehicles. *Chem. Ind. Eng. Progress* **40**(2), 688–702 (2021)

2. Iu, X., Zhang, B., Ai, B., et al.: Development and current status of hydrogen quality standards for proton exchange membrane fuel cell. *Chem. Ind. Eng. Progress* **40**(2), 703–708 (2021)
3. International Standardization Organization: Hydrogen fuel quality—Product specification, ISO 14687:2019. ISO, Switzerland (2019)
4. Society of Automotive Engineers: Hydrogen Fuel Quality for Fuel Cell Vehicles: SAE J2719. SAE (2015)
5. State Administration for Market Regulation, Standardization Administration of the People's Republic of China: Fuel Specification for Proton Exchange Membrane Fuel Cell Vehicles Hydrogen: GB/T 37244-2018. Standards Press of China, Beijing (2018)
6. Mukundan, R., Brosha, E.L., Romero, C.J., et al.: Development of an electrochemical hydrogen contaminant detector. *J. Electrochem. Soc.* **167**(14), 147507 (2020)
7. Bacquart, T., Moore, N., Mattelaer, V., et al.: First hydrogen fuel sampling from a fuel cell hydrogen electrical vehicle-validation of hydrogen fuel sampling system to investigate FCEV performance. *Processes* **10**(9) (2022)
8. Kim, D., Lim, J.S., Lee, J.: Current status of standardization for quality control of hydrogen fuel in hydrogen refueling stations for fuel cell electric vehicles. *Trans. Korean Hydrogen New Energy Soc.* **33**(4), 284–292 (2022)
9. Murugan, A., Brown, A.S.: Review of purity analysis methods for performing quality assurance of fuel cell hydrogen. *Int. J. Hydrogen Energy* **40**(11), 4219–4233 (2015)
10. Papadias, D.D., Ahmed, S., Kumar, R., et al.: Hydrogen quality for fuel cell vehicles—a modeling study of the sensitivity of impurity content in hydrogen to the process variables in the SMR–PSA pathway. *Int. J. Hydrogen Energy* **34**(15), 6021–6035 (2009)
11. Morris, A.S.O., Bacquart, T., Allen, N.D.C., et al.: Challenges in hydrogen fuel sampling due to contaminant behaviour in different gas cylinders. *Int. J. Hydrogen Energy* **46**(35), 18167–18178 (2021)
12. Aarhaug, T.A., Kjos, O.: D3.3 results from the 2nd HRS measurement campaign. HyCoRA—Hydrogen Contaminant Risk Assessment Grant Agreement No. 621223 (2017)
13. Aarhaug, T.A., Kjos, O.S., Ferber, A., et al.: Mapping of hydrogen fuel quality in Europe. *Front. Energy Res.* **8**, 585334 (2020)
14. Pan, Y., Deng, F., Wang, W., et al.: Status quo and discussion on the standardization of analysis methods for the impurity components in hydrogen of vehicle fuel: a case study on the proton exchange membrane fuel cell vehicle. *Nat. Gas Ind.* **41**(4), 115–123 (2021)
15. General Administration of Quality Supervision, Inspection and Quarantine of the PRC & Standardization Administration of China: Determination of Particle in Gases Light-Scattering Method—Part 1: Determination of Particle in Pipeline Gases: GB/T 26570.1-2011. Standards Press of China, Beijing (2011)
16. General Administration of Quality Supervision, Inspection and Quarantine of the PRC & Standardization Administration of China: Natural Gas. Determination of Particles Content Gravimetric Method: GB/T 27893-2011. Standards Press of China, Beijing (2011)
17. ASTM International: D7650 Standard Test Method for Sampling of Particulate Matter in High Pressure Hydrogen Used as a Gaseous Fuel with an In-Stream Filter. ASTM International, West Conshohocken, PA (2013)
18. Hsu, J.P.: Recommended pre-operation cleanup procedures for hydrogen fueling station. *Int. J. Hydrogen Energy* **37**(2), 1770–1780 (2012)



IrNi Nanoparticles as Highly Efficient Electrocatalysts Towards the Oxygen Evolution Reaction in an Acidic Medium

Yongwen Sun¹, Hong Lv¹(✉), Dingyun Gao², and Cunman Zhang¹

¹ School of Automotive Studies, Tongji University, Shanghai, China
lvhong@tongji.edu.cn

² Shanghai SUNWISE New Energy System Co. Ltd, Shanghai, China

Abstract. The development of efficient and durable bifunctional electrocatalysts for oxygen evolution reaction (OER), still poses huge challenges. Herein, we utilize a facile hydrothermal method to synthesize a novel IrNi nanocrystals. In particular, the electronic structure is altered when a portion of the iridium atom is replaced by a Ni atom, which causes the center of the d band to shift downward, favoring the catalytic reaction. The overpotentials for OER of 273 mV at a current density of 10 mA cm⁻², exceed the capabilities of commercial Ir catalysts. The alloying of Ir with Ni reduces the adsorption energy of oxygen intermediates to achieve a fast oxygen evolution reaction. This work highlights a potentially powerful strategy toward the general synthesis of novel, Ir-based alloy as highly active and durable bifunctional electrocatalysts for high-performance electrochemical overall-water-splitting devices.

Keywords: Catalyst · Iridium based · Water electrolysis · Oxygen evolution reaction

1 Introduction

The development of highly efficient water-splitting catalysts is of great importance for the production of green hydrogen for sustainable energy. In addition to various renewable energy sources such as solar, wind, or hydroelectric power, the high specific energy density value of hydrogen paves the way for the sustainable production of hydrogen [1–4]. Among various hydrogen production methods, the same electrocatalytic water splitting has attracted much attention due to its zero-carbon emission behavior [5]. The electrocatalytic water splitting reaction consists of two half-cell reactions: the oxygen evolution reaction (OER) and the hydrogen evolution reaction at the anode and cathode [6, 7]. When comparing the two half-cell reactions, OER is the bottleneck of the whole water splitting reaction due to its complicated four-electron transfer and multi-step behavior. Currently, ruthenium and iridium oxides (RuO₂ and IrO₂) are considered as the most advanced catalysts for industrial applications of OER [8–10]. Because of their great activity and durability, Ir-based nanomaterials are regarded as the most promising

catalysts for acidic OER. However, their implementation in H_2 production is significantly limited by their high cost and relatively high overpotential [11]. To this end, iridium-based alloy catalysts exhibiting improved noble metal utilization efficiency and controllable structure have been designed to reduce the amount of expensive noble metal required [12, 13]. More importantly, considering the ligand effect brought about by the alloying of IrM with Ni, the d-band center of IrNi is far away from the Fermi level; thus, IrNi is less active in forming chemical bonds with other active species, leading to oxygen [14–20]. The adsorption energy of the intermediate on Ir decreases. According to the research of Ying Wang [20] et al., the alloy of Ir and transition metal has good OER catalytic activity, and the catalytic activity follows the trend of IrNi > IrCo > IrFe > IrO₂, and according to the theory According to the calculation, the binding energy of oxygen intermediates in the reaction process follows the order of IrO₂ > IrFe > IrCo > IrNi that is, when IrNi is used as the catalytic material, the activation energy required for the oxygen evolution reaction is the smallest, and the overpotential is the smallest. Therefore, the research object selected in this experiment is the IrNi alloy catalyst material.

The discovery that acidic water splitting produces purer H_2 and improves OER kinetics has triggered considerable efforts to develop efficient catalysts for acidic OER [21]. Many catalysts are known to dissolve in acidic media; thus, although promising, the development of efficient OER catalysts in acidic environments remains a major challenge [22]. In addition, changing the catalyst structure has been shown to have a significant enhancement effect on catalyst performance [21, 23]. Designing catalysts with an open structure and increased specific surface area is crucial to expose a large number of active reaction sites with unsaturated coordination by exposing corner and edge atoms [24]. Nanosizing has shown improved electrochemical surface area (ESCA), increased number of reactive sites, and overall enhanced catalytic performance. Although considerable efforts have been made to design optimized Ir-based materials, including IrM (M = Co, Ni, Fe) nanocrystals [19, 25]. Their electrocatalytic behavior for overall water splitting, especially OER in acidic media, is still below expectations. Therefore, designing iridium-based hollow nanocatalysts with large specific surface areas as efficient bifunctional catalysts for total water splitting remains a formidable challenge [26–28].

We adopt a one-pot synthesis method to synthesize the IrNi alloy catalyst material. In this work, IrNi nanoparticles with nanostructured nanostructures and excellent catalytic performance were synthesized via a one-pot method. The as-prepared IrNi has a unique structure with optimized active site exposure, increased catalytically active surface area, and reduced noble metal usage. This nano size structure allows the reactants to easily access the active sites of IrNi, thereby enhancing the catalytic performance for OER in acidic media. It is worth noting that in an acidic medium, the overpotential at 10 mA cm^{-2} is 273 mV.

2 Experimental

2.1 Synthesis of IrNi Alloy Catalytic Materials

0.192 mmol of Ir(acac)₃ and 0.288 mmol Ni(acac)₂ dissolve it in 30 mL of oleylamine and heat to 60 °C to completely dissolve 28.6 mg (0.096 mmol) of 1,2-hexadecane-diol, placed in a 100 mL three-necked flask, and then 16 mL of oleylamine was added to the three-necked flask, and nitrogen was continuously fed into the solution to prevent the IrNi alloy from being oxidized by oxygen during the reaction. The oil bath was heated to 160 °C under a nitrogen atmosphere and then kept for 30 min. After the solution was clear and turned yellow-green, it was heated to 250 °C. When the solution reached 250 °C, the color of the solution in the three-necked flask changed from yellow-green to black. It was then incubated at 250 °C for 60 min and then cooled to room temperature. The right side of the three-necked flask was continuously fed with nitrogen, and heated in an oil bath with magnetic stirring.

2.2 Characterization of the Catalysts

The physical morphology of the catalyst material was tested by a transmission electron microscope (TEM), and its model is JEM-2010. The scanning electron microscope energy spectrum of the IrNi alloy catalyst material was also tested, which was tested on a scanning electron microscope energy spectrum analyzer (SEM-EDS), and its model was ULTRA 55. The morphology of the IrNi alloy catalyst material was photographed and observed by high-resolution transmission electron microscopy (HRTEM). The X-ray diffraction pattern of the IrNi alloy catalyst material is tested by an X-ray diffractometer, the model is D2 PHASER, the scan rate is 5°/min, and the test range is 10° to 80°.

2.3 Performance Test of IrNi Material Under a Three-Electrode System

The electrochemical performance of the IrNi material was tested using a traditional three-electrode system. Take 4.94 mg of IrNi in a 5 mL glass bottle, add 2 mL of cyclohexane, 20 μL of 5wt% Nafion solution, and ultrasonically disperse for 30 min. Take another 4.94 mg iridium in a 5 mL glass bottle, add 2 mL cyclohexane, 20 μL 5wt% Nafion solution, and ultrasonically disperse in an ultrasonic cleaner for 30 min. The three-electrode system used in testing CV and LSV is Pt as the counter electrode, Ag/AgCl as the reference electrode, rotating disk electrode as the working electrode, and 0.5 mol/L dilute sulfuric acid solution saturated with nitrogen as the electrolyte.

During the test, use a pipette gun to take 5 μL of the prepared Ir solution or IrNi solution, drop it on the rotating disk electrode, drop it twice, and then dry it naturally at room temperature to ensure that the glassy carbon electrode A uniform catalyst layer is formed on the glassy carbon electrode, and the amount of catalyst loaded on the glassy carbon electrode is 0.196 cm⁻². Open the electrochemical workstation during the test, set appropriate parameters, and test the cyclic voltammetry (CV) curves of Ir and IrNi respectively. When the LSV curve was tested by linear sweep voltammetry, the rotational speed of the rotating disc electrode was 1600 r/min. The potential (E) mentioned in this article is relative to the reversible hydrogen potential (RHE), and the resistance of the

solution is corrected. The conversion relationship between $E(\text{Ag}/\text{AgCl})$ and $E(\text{RHE})$ is shown in formula 1:

$$E(\text{RHE}) = E(\text{Ag}/\text{AgCl}) + 0.059 \text{ PH} + 0.197\text{V} \quad (1)$$

3 Results and Discussion

The morphology of the IrNi alloy catalyst material was photographed and observed by a transmission electron microscope. The material morphology is shown in Fig. 1. It can be seen from the figure that the prepared IrNi nanoparticles are polyhedral particles with irregular shapes, the diameter is about 10 nm, the particle size is relatively uniform, and there is an agglomeration phenomenon, but the agglomeration is not serious. Figure 1c shows the interplanar spacing of IrNi nanoparticles. The interplanar spacing in Fig. 1c is 0.222 nm, which is equal to the interplanar spacing of 0.222 nm for the (111) crystal plane of Ir [29]. The elemental composition of IrNi nanoparticles was analyzed by EDS, and the analysis results are shown in Fig. 1d. In the image, red dots represent Ni elements, green dots represent Ir elements and yellow dots represent O elements. It can be seen that Ni and Ir are uniformly combined, preliminarily indicating that the material is an IrNi alloy. But at the same time, O elements are also uniformly distributed in the image, indicating that the IrNi material may be partially oxidized. Through the energy spectrum, it can be seen that the material contains Ir, Ni, and other elements. According to elemental analysis, the atomic number ratio of Ir to Ni is about 2/3.

As shown in Fig. 2a, the bimetallic catalysts have the same face-centered cubic (fcc) structure as Ir, but the diffraction peaks are slightly shifted to higher angles. The 2θ peaks at 40.7° correspond to Ir (111) and Ni (111), respectively. This observation, together with the absence of peaks from the impure crystalline phase, evidences the distribution of alloying elements in IrNi, suggesting that transition metal atoms in the 3d Ir lattice reduce the Ir-Ir bond length in solid solution [30]. Asymmetric reflection peaks with tails of 2θ values towards the Ir plane indicate an Ir-rich surface alloy structure due to Ir segregation to the alloy surface. The surface chemistry of IrNi nanoparticles and Ir nanoparticles was analyzed by XPS. In Fig. 2b, the Ir 4f spectrum is deconvoluted into two pairs of peaks located at 61.0 eV and 63.7 eV, and 62.30 eV and 65.5 eV, corresponding to $4f_{7/2}$ and $4f_{5/2}$ of metallic Ir (Ir) and Oxidized Ir (Ir 4+). It should be noted that the binding energy of Ir $4f_{7/2}$ is 0.5 eV for IrNi nanoparticles compared to Ir nanoparticles. A negative shift indicates that electrons can transfer from Ni to Ir. Therefore, electron transfer changes the electronic structure of Ir after alloying. At the same time, IrNi nanoparticles has the highest negative shift, indicating that the alloy structure enhances the electronic effect.

The electrochemically active area can reflect the size of the active sites exposed by the catalyst. It is expressed by ECSA. The larger the value of the electrochemically active area of the catalytic material, the better the electrochemical performance of the material. To evaluate the electrochemically active area of the catalytic material, cyclic voltammetry (CV) was used in this experiment at 2 mV/s, 3 mV/s, 5 mV/s, 7 The voltage scan rates of mV/s and 10 mV/s were used to scan the catalyst material respectively. The calculation formula of ECSA is shown in formula 2:

$$\text{ECSA} = \frac{C_{dl}}{C_s} \quad (2)$$

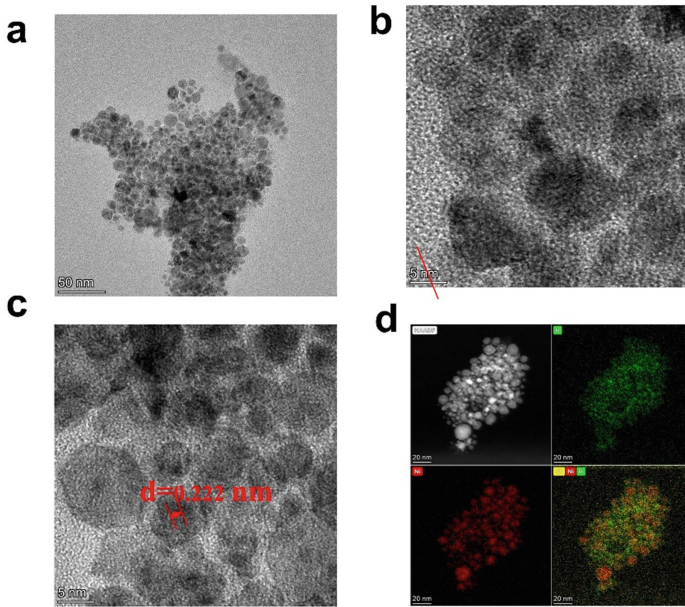


Fig. 1. Morphology and composition analysis IrNi. (a,b) TEM image, (c) HRTEM (d) distribution of Ni (red) and Ir (green) across the EDX composition maps.

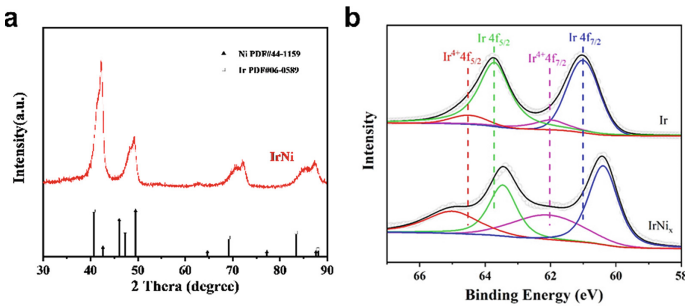


Fig. 2. (a) XRD patterns of IrNi. (b) X-ray photoelectron spectra of NiIr and Ir in the Ir.

In the formula, C_{dl} represents the electric double-layer capacitance, and the value of C_{dl} is determined by the slope of the line graph of different voltage scan rates and corresponding current densities. C_s is the capacitance of an ideal metal oxide with a smooth surface, C_s is a constant value, take $0.3 \text{ mF}\cdot\text{cm}^{-2}$.

After the IrNi material was tested by cyclic voltammetry at different scan rates, the current density corresponding to each scan rate was taken when the voltage was 0.92 V, and 5 sets of data were obtained. Take these data as the abscissa with the voltage scanning rate, make a scatter diagram with the current density as the ordinate, then do a linear regression, and determine the value of C_{dl} by the slope k of the regression line obtained,

k and C_{dl} the relationship is shown in Formula 3:

$$k = 2C_{dl} \quad (3)$$

It can be seen from the image that as the voltage scan rate increases, the current density also increases. Among them, the C_{dl} of Ir is $3.681 \text{ mF}\cdot\text{cm}^{-2}$, and the C_{dl} of IrNi is $\text{mF}\cdot\text{cm}^{-2}$. According to formula 2, take $C_s = 0.3 \text{ mF}\cdot\text{cm}^{-2}$, so the electrochemically active area of Ir is $\text{mF}\cdot\text{cm}^{-2}$ IrNi has an electrochemically active area of $13.34 \text{ mF}\cdot\text{cm}^{-2}$. Therefore, the electrochemically active area of IrNi is larger, and the reason may be that the unique structure of IrNi alloy exposes more active sites of Ir (Fig. 3).

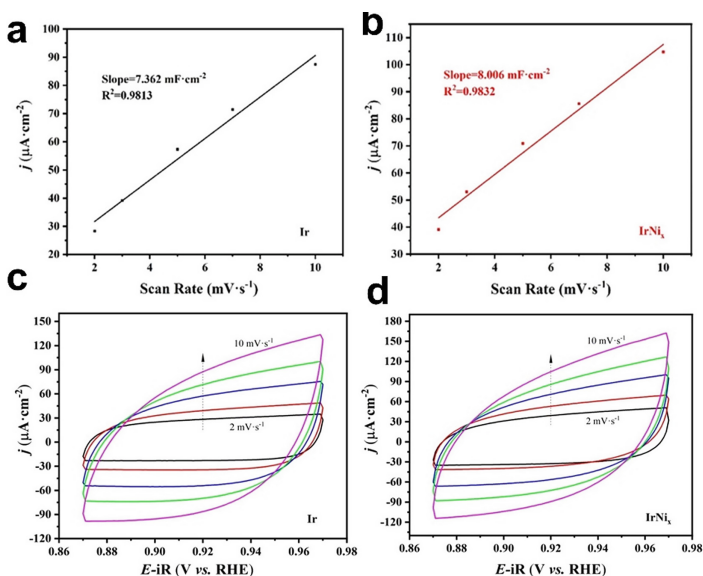


Fig. 3. (a) (b) Corresponding plots of the current densities at 0.919 V versus RHE with the different scan rates (2, 3, 5, 7, 10 mVs⁻¹) (c) (d) CV curves

The polarization curves of Ir and IrNi measured in 0.5M H₂SO₄ saturated with nitrogen gas are shown in Fig. 4. The polarization curve shows that when the applied voltage increases, the current density of IrNi grows quicker and the curve is steeper than that of Ir, indicating that IrNi has stronger OER catalytic activity. Because the Tafel slope is also a commonly used criterion for judging the activity of catalysts, the data of the polarization curves were further processed to obtain the Tafel slopes of the two catalytic materials, as shown in Fig. 4b. It can be seen from the figure that the Tafel slope of Ir is $91 \text{ mV}\cdot\text{dec}^{-1}$, while the Tafel slope of IrNi is $77 \text{ mV}\cdot\text{dec}^{-1}$. The smaller the Tafel slope, it proves that when the same current is increased, the voltage rises smaller, the energy consumption is smaller, and the electrolysis efficiency is higher. The Tafel slope of IrNi is smaller than that of Ir, so the OER catalytic activity of IrNi is better. Figure 4c shows the overpotential of Ir and IrNi at $10 \text{ mA}\cdot\text{cm}^{-2}$. It can be seen from the figure that the overpotential of Ir at $10 \text{ mA}\cdot\text{cm}^{-2}$ is 324 mV, while IrNi is at $10 \text{ mA}\cdot\text{cm}^{-2}$,

the overpotential is 273 mV, and the overpotential of IrNi is lower than that of Ir, so the actual voltage of electrolyzed water in IrNi is lower than Smaller, better catalytic performance. At 1.51 V, the estimated average–mass activity was 711 A·mgIr⁻¹ for the IrNi, 103 A·gIr⁻¹ for Ir. The IrNi showed a 7-fold improved mass activity than the Ir. The IrNi nanoparticles has a higher current density than Ir, hence when the same voltage is given to the two materials, the higher the current created.

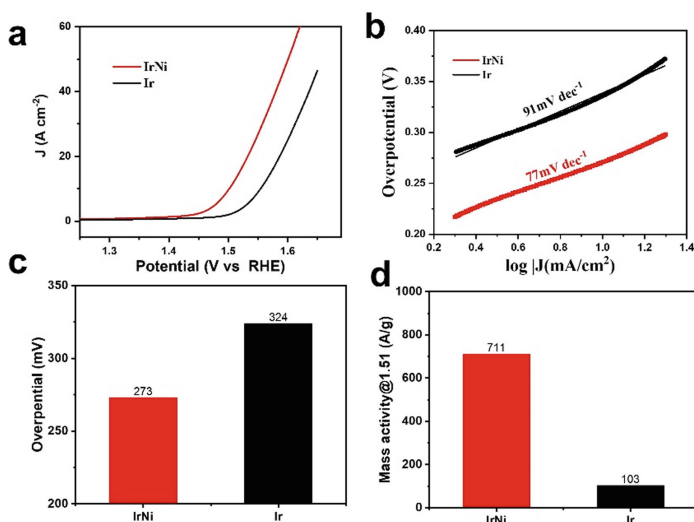


Fig. 4. Electrocatalytic activity of the NiIr by comparison with Ir (a) LSV curves of the NiIr and Ir 0.5 M H₂SO₄ (b) the corresponding Tafel plots (c) bar graph displaying the overpotentials to drive 10 mA·cm⁻²; (d) Ir mass activities at 1.51 V (vs RHE)

4 Conclusions

In this paper, the synthesis of IrNi alloy and its OER catalytic performance are investigated. The particle diameter of the IrNi material was found to be approximately 10 nm through TEM, and Ir and Ni were evenly distributed throughout the material. Ir and Ni have an atomic ratio of roughly 2/3, according to EDS analysis. The XRD pattern shows that the material corresponds to the characteristic peaks of Ir and Ni, and shows that IrNi alloy is partially formed. In the electrochemical characterization, compared with the OER performance of iridium, IrNi shows better OER catalytic performance, and the Tafel slope is only 77 mVdec⁻¹, which is lower than 91 mVdec⁻¹ of Ir. The NiIr nanoparticles were tested as electrocatalysts for the oxygen evolution reaction in an acidic electrolyte and showed enhanced electrocatalytic activity (273 mV at 10 mA·cm⁻²) and mass activity (711 A·gIr⁻¹) compared to commercial Ir.

References

1. She, Z.W., Kibsgaard, J., Dickens, C.F., Chorkendorff, I., Nørskov, J.K., Jaramillo, T.F.: Combining theory and experiment in electrocatalysis: insights into materials design. *Science* **355**, eaad4998 (2017)
2. Schuler, T., Kimura, T., Schmidt, T.J., Büchi, F.N.: Towards a generic understanding of oxygen evolution reaction kinetics in polymer electrolyte water electrolysis. *Energy Environ. Sci.* **13**, 2153–2166 (2020)
3. Wang, S., Lv, H., Tang, F., Sun, Y., Ji, W., Zhou, W., et al.: Defect engineering assisted support effect: IrO₂/N defective g-C₃N₄ composite as highly efficient anode catalyst in PEM water electrolysis. *Chem. Eng. J.* **419**, 129455 (2021)
4. Dang, N.K., Tiwari, J.N., Sultan, S., Meena, A., Kim, K.S.: Multi-site catalyst derived from Cr atoms-substituted CoFe nanoparticles for high-performance oxygen evolution activity. *Chem. Eng. J.* **404**, 126513 (2021)
5. Liu, S., Liu, B., Gong, C., Li, Z.: Finely prepared and optimized Co/Fe double hydroxide nanofilms at an ionic layer level on rough Cu substrates for efficient oxygen evolution reaction. *Appl. Surf. Sci.* **478**, 615–622 (2019)
6. Shi, Z., Li, J., Jiang, J., Wang, Y., Wang, X., Li, Y., et al.: Enhanced acidic water oxidation by dynamic migration of oxygen species at the Ir/Nb₂O₅-x catalyst/support interfaces. *Angew. Chem. Int. Ed.* **61**, e202212341 (2022)
7. Mazúr, P., Polonský, J., Paidar, M., Bouzek, K.: Non-conductive TiO₂ as the anode catalyst support for PEM water electrolysis. *Int. J. Hydrogen Energy* **37**, 12081–12088 (2012)
8. Wang, X., Habte, B.T., Zhang, S., Yang, H., Zhao, J., Jiang, F., et al.: Localized electrochemical impedance measurements on Nafion membranes: observation and analysis of spatially diverse proton transport using atomic force microscopy. *Anal. Chem.* **91**, 11678–11686 (2019)
9. Wang, Y., Chu, F., Zeng, J., Wang, Q., Naren, T., Li, Y., et al.: Single atom catalysts for fuel cells and rechargeable batteries: principles, advances, and opportunities. *ACS Nano* **15**, 210–239 (2021)
10. Ruiz Esquiús, J., Morgan, D.J., Algara Siller, G., Gianolio, D., Aramini, M., Lahn, L., et al.: Lithium-directed transformation of amorphous iridium (Oxy)hydroxides to produce active water oxidation catalysts. *J. Am. Chem. Soc.* **145**, 6398–6409 (2023)
11. Zhu, J., Wei, M., Meng, Q., Chen, Z., Fan, Y., Hasan, S.W., et al.: Ultrathin-shell IrCo hollow nanospheres as highly efficient electrocatalysts towards the oxygen evolution reaction in acidic media. *Nanoscale* **12**, 24070–24078 (2020)
12. Daiane Ferreira da Silva, C., Claudel, F., Martin, V., Chattot, R., Abbou, S., Kumar, K., et al.: Oxygen evolution reaction activity and stability benchmarks for supported and unsupported IrOx electrocatalysts. *ACS Catal.* **11**, 4107–4116 (2021)
13. Mom, R.V., Falling, L.J., Kasian, O., Algara-Siller, G., Teschner, D., Crabtree, R.H., et al.: Operando structure–activity–stability relationship of iridium oxides during the oxygen evolution reaction. *ACS Catal.* **12**, 5174–5184 (2022)
14. Kwon, T., Hwang, H., Sa, Y.J., Park, J., Baik, H., Joo, S.H., et al.: Cobalt assisted synthesis of IrCu hollow octahedral nanocages as highly active electrocatalysts toward oxygen evolution reaction. *Adv. Func. Mater.* **27**, 1604688 (2017)
15. González, D., Sodupe, M., Rodríguez-Santiago, L., Solans-Monfort, X.: Metal coordination determines the catalytic activity of IrO₂ nanoparticles for the oxygen evolution reaction. *J. Catal.* **412**, 78–86 (2022)
16. Xue, Y., Fang, J., Wang, X., Xu, Z., Zhang, Y., Lv, Q., et al.: Sulfate-functionalized RuFeOx as highly efficient oxygen evolution reaction electrocatalyst in acid. *Adv. Func. Mater.* **31**, 2101405 (2021)

17. Duan, Z., Zhang, M., Mao, Q., Deng, K., Yu, H., Wang, Z., et al.: Synergistic coupling of IrNi/Ni(OH)₂ nanosheets with polypyrrole and iron oxyhydroxide layers for efficient electrochemical overall water splitting. *Nanotechnology* **34**, 275401 (2023)
18. Liu, S., Hu, Z., Wu, Y., Zhang, J., Zhang, Y., Cui, B., et al.: Dislocation-strained IrNi alloy nanoparticles driven by thermal shock for the hydrogen evolution reaction. *Adv. Mater.* **32**, 2006034 (2020)
19. Pi, Y., Shao, Q., Wang, P., Guo, J., Huang, X.: General formation of monodisperse IrM (M = Ni, Co, Fe) bimetallic nanoclusters as bifunctional electrocatalysts for acidic overall water splitting. *Adv. Func. Mater.* **27**, 1700886 (2017)
20. Wang, Y., Zhang, L., Yin, K., Zhang, J., Gao, H., Liu, N., et al.: Nanoporous iridium-based alloy nanowires as highly efficient electrocatalysts toward acidic oxygen evolution reaction. *ACS Appl. Mater. Interfaces* **11**, 39728–39736 (2019)
21. Lv, F., Zhang, W., Yang, W., Feng, J., Wang, K., Zhou, J., et al.: Ir-based alloy nanoflowers with optimized hydrogen binding energy as bifunctional electrocatalysts for overall water splitting. *Small Methods* **4**, 1900129 (2020)
22. Jin, H., Hong, Y., Yoon, J., Oh, A., Chaudhari, N.K., Baik, H., et al.: Lanthanide metal-assisted synthesis of rhombic dodecahedral MNi (M = Ir and Pt) nanoframes toward efficient oxygen evolution catalysis. *Nano Energy* **42**, 17–25 (2017)
23. Harzandi, A.M., Shadman, S., Nissimagoudar, A.S., Kim, D.Y., Lim, H.-D., Lee, J.H., et al.: Ruthenium core-shell engineering with nickel single atoms for selective oxygen evolution via nondestructive mechanism. *Adv. Energy Mater.* **11**, 2003448 (2021)
24. Su, R., Hsain, A.L., Wu, M., Zhang, D.W., Hu, X.H., Wang, Z.P., et al.: Nano-ferroelectric for high efficiency overall water splitting under ultrasonic vibration. *Angew. Chem. Int. Ed.* **58**, 15076–15081 (2019)
25. Liao, J., Ding, W., Tao, S., Nie, Y., Li, W., Wu, G., et al.: Carbon supported IrM (M = Fe, Ni, Co) alloy nanoparticles for the catalysis of hydrogen oxidation in acidic and alkaline medium. *Chin. J. Catal.* **37**, 1142–1148 (2016)
26. Moriau, L., Smiljanić, M., Lončar, A., Hodnik, N.: Supported iridium-based oxygen evolution reaction electrocatalysts—recent developments. *ChemCatChem* **14**, e202200586 (2022)
27. Islam, J., Kim, S.-K., Thien, P.T., Kim, M.-J., Cho, H.-S., Cho, W.-C., et al.: Enhancing the activity and durability of iridium electrocatalyst supported on boron carbide by tuning the chemical state of iridium for oxygen evolution reaction. *J. Power. Sources* **512**, 230506 (2021)
28. Park, S., Shviro, M., Hartmann, H., Besmehn, A., Mayer, J., Stolten, D., et al.: Nickel structures as a template strategy to create shaped iridium electrocatalysts for electrochemical water splitting. *ACS Appl. Mater. Interfaces* **13**, 13576–13585 (2021)
29. Feng, J., Lv, F., Zhang, W., Li, P., Wang, K., Yang, C., et al.: Iridium-based multimetallic porous hollow nanocrystals for efficient overall-water-splitting catalysis. *Adv. Mater.* **29**, 1703798 (2017)
30. Kuttiyiel, K.A., Choi, Y., Sasaki, K., Su, D., Hwang, S.-M., Yim, S.-D., et al.: Tuning electrocatalytic activity of Pt monolayer shell by bimetallic Ir-M (M=Fe, Co, Ni or Cu) cores for the oxygen reduction reaction. *Nano Energy* **29**, 261–267 (2016)



Estimation of the Volume Flow Rate at the Anode Side of Hydrogen Fuel Cells

Xing Huang^{1,2}, Ke Song^{1,2}, Zhen Cai^{1,2}, and Feiqiang Li³(✉)

¹ School of Automotive Studies, Tongji University, Shanghai 201804, China

² National Fuel Cell Vehicle and Powertrain System Engineering Research Center, Tongji University, Shanghai 201804, China

³ Beijing SinoHytec Co., Ltd., Zhongguancun, Dongsheng S & T Park, 66 Xixiaokou Road, Haidian District, Beijing, People's Republic of China

lifeiqiang@autoht.com

Abstract. Estimating the volume flow rate of hydrogen is one common problem in the engineering design and application of hydrogen fuel cells. In this paper, models for estimating the volume flow rate of hydrogen are established from the perspectives of the number of electrons transferred by electrochemical reaction and the energy conversion between chemical energy and electric energy, and the sensitivity analysis of the influencing factors is made. The results show that estimation models are reasonable and reliable. In the estimation process, the actual single voltage of the fuel cell needs to be accurately collected and controlled.

Keywords: Hydrogen fuel cells · Volume flow estimation · The number of transferred electrons · Energy conversion · Sensitivity analysis

1 Introduction

The demand for clean and efficient energy promotes the application and development of hydrogen fuel cell technology. At present, hydrogen fuel cells have been practiced and applied in ground transportation [1], Marine ships [2], aerial vehicles [3], heating and energy storage [4] and other scenarios. In the process of engineering design and application, it is common to estimate the volume flow of hydrogen at the anode side according to the environmental conditions and power requirements. At present, there is no unified standard estimation model for the reference of relevant researchers at home and abroad. In this paper, a complete estimation process will be presented and analyzed from the perspectives of the number of electrons transferred by electrochemical reactions and the energy conversion between chemical energy and electric energy.

2 The Theoretical Model of Single Voltage for Fuel Cells

When hydrogen fuel cell is working, electrochemical reaction occurs on both cathode and anode. The reaction equation of the whole process is as follows:



The theoretical output voltage of a single cell of hydrogen fuel cell can be expressed as [5]:

$$E = E^0 - \frac{RT_s}{zF} \ln \frac{1}{P_{H_2} P_{O_2}^{\frac{1}{2}}} + \frac{\Delta s}{zF} (T_s - T^0) \quad (2)$$

where, E^0 is the standard electrode potential, R is the ideal gas constant, Δs is the entropy change of the electrochemical reaction, F is the Faraday constant, T_s , T^0 is the actual and reference temperature inside the reactor, P_{H_2} , P_{O_2} is the pressure of hydrogen and oxygen, z is the number of moles of electrons transferred by the reaction in 1 mol.

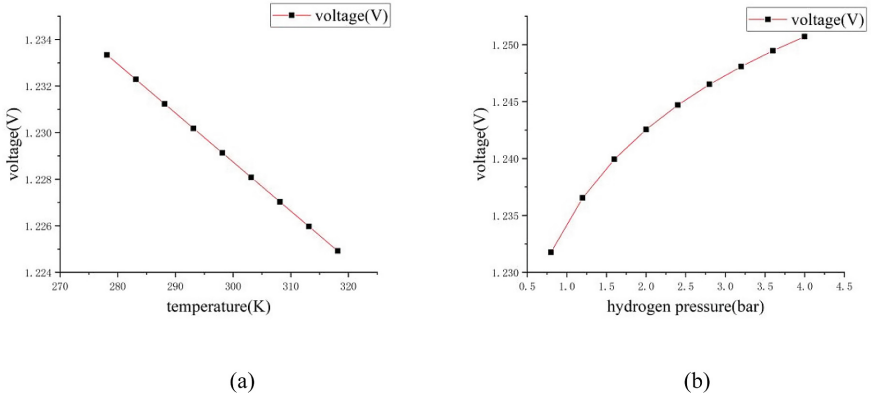


Fig. 1. (a) The relationship between fuel cell single voltage and temperature when hydrogen and oxygen intake pressure is constant; (b) The relationship between fuel cell single voltage and hydrogen intake pressure when temperature and oxygen intake pressure are constant

As shown in Fig. 1, it is noted that when hydrogen intake pressure and temperature change, the voltage of single cell will change accordingly.

3 Methods for Estimation of Volume Flow of Hydrogen

In order to estimate the volume flow rate of hydrogen, we can think from two perspectives: the number of electrons transferred by electrochemical reaction and the energy conversion between chemical energy and electric energy. Here, taking a practical engineering problem as an example. We assume that the inlet pressure of hydrogen P is 0.75 bar, the temperature T is 298.15 K, and the power requirement P_{dem} is 4 kW.

3.1 Perspective 1: The Number of Electrons Transferred in an Electrochemical Reaction

Since 1 mol hydrogen transfers 2 mol electrons during the electrochemical reaction, that is, the output current of the fuel cell I meets:

$$I = zF\dot{m}_{H_2} \quad (3)$$

where, \dot{m}_{H_2} is the molar mass flow rate of hydrogen.

After further processing, the molar mass flow rate of hydrogen can be obtained:

$$\frac{P_{dem}}{U} = zF \dot{m}_{H_2}, \dot{m}_{H_2} = \frac{P_{dem}}{zFU} \quad (4)$$

where, U is the actual voltage of a single battery.

The efficiency of fuel cells η_{fc} can be characterized by the ratio of the actual voltage and the theoretical output voltage E of a single cell [6], namely:

$$\eta_{fc} = \frac{U}{E} \quad (5)$$

The theoretical output voltage of the fuel cell is 1.229 V under standard conditions. According to Fig. 1, the actual theoretical output voltage is also affected by the working environment. The rated operating voltage of the fuel cell is about 0.6 V ~ 0.8 V. Assume that the efficiency of fuel cells is about 0.6.

The efficiency value is properly corrected according to hydrogen pressure and ambient temperature. According to Eq. (4), the actual voltage of a single cell is about $1.229 \times 0.614 \approx 0.755V$.

The volume flow rate \dot{V}_{H_2} and molar mass flow rate \dot{m}_{H_2} of hydrogen meet the following requirements:

$$\dot{V}_{H_2} = \dot{m}_{H_2} V_m \quad (6)$$

where, V_m is the molar volume of the gas.

Under standard conditions, the temperature T^0 is 273.15 K and the pressure P^0 is 1bar. Thus, the standard molar volume $V_m^0 \approx 22.4$ L/mol. According to the ideal gas equation of state, when the temperature and pressure change, the molar volume will also change, namely:

$$V_m^0 = \frac{RT^0}{P^0}, V_m = \frac{RT}{P} \quad (7)$$

$$V_m = V_m^0 \frac{P^0 T}{PT^0} \quad (8)$$

where, R is a constant.

According to Eq. (5), the molar mass flow rate of hydrogen is approximately $\dot{m}_{H_2} = \frac{60 \times 4 \times 1000 \times 22.4}{2 \times 96485 \times 0.755} = 1.6475$ mol/min; according to Eq. (8), the molar volume at this time is about $V_m = 22.4 \times \frac{1}{0.75} \times \frac{298.15}{273.15} \approx 32.6$ L/mol.

Thus, according to Eq. (6), the volume flow rate of hydrogen is about $\dot{V}_{H_2} = 1.6475 \times 32.6 \approx 53.70$ L/min.

In summary, based on the number of electrons transferred in the electrochemical reaction, the volume flow rate of hydrogen at the anode side can be obtained according to Eq. (9):

$$\dot{V}_{H_2} = \frac{P_{dem} V_m^0 \frac{P^0 T}{PT^0}}{zFU} \quad (9)$$

3.2 Perspective 2: The Energy Conversion Between Chemical Energy and Electrical Energy

Fuel cells are able to provide electricity to the outside world because chemical energy from hydrogen and oxygen is converted into energy in an electrochemical reactor. In addition to the ratio between the actual voltage and the theoretical output voltage of a single cell, the efficiency of the fuel cell can also be characterized by the ratio between the electric energy generated by conversion Q_{elec} and the chemical energy contained in the fuel Q_{chem} [7], namely:

$$\eta_{fc} = \frac{Q_{elec}}{Q_{chem}} \quad (10)$$

The low calorific value of hydrogen $LHV_{H_2} = -241.98$ KJ/mol and molar mass flow rate of hydrogen can be expressed as:

$$\dot{m}_{H_2} = \frac{P_{dem}}{\eta LHV_{H_2}} \quad (11)$$

When the efficiency of the fuel cell is about 0.6 and the power demand is 4kW, it can be calculated from Eq. (11) that, $\dot{m}_{H_2} = \frac{60 \times 4}{0.6 \times 241.98} \approx 1.6530$ mol/min, according to Eq. (8), the molar volume at this time is about $V_m = 22.4 \times \frac{1}{0.75} \times \frac{298.15}{273.15} \approx 32.6$ L/mol.

Thus, according to Eq. (6), the volume flow rate of hydrogen is about $\dot{V}_{H_2} = 1.6530 \times 32.6 \approx 53.89$ L/min.

In addition to molar volume V_m , the transformation of molar mass flow to volume flow can also be realized by density ρ .

The mass flow rate \dot{M}_{H_2} and molar mass flow rate \dot{m}_{H_2} of hydrogen meet the following requirements:

$$\dot{M}_{H_2} = \dot{m}_{H_2} M_{H_2} \quad (12)$$

The volume flow rate \dot{V}_{H_2} and mass flow rate \dot{M}_{H_2} of hydrogen meet the following requirements:

$$\dot{M}_{H_2} = \dot{V}_{H_2} \rho \quad (13)$$

According to the ideal equation of state for gas, when the temperature and pressure change, the density of gas will also change, namely:

$$\rho^0 = K \frac{P^0}{T^0}, \rho = K \frac{P}{T} \quad (14)$$

where, K is a constant.

$$\rho = \rho^0 \times (P \times T^0) / (P^0 \times T) \quad (15)$$

Where, ρ , P and T are the actual air density, pressure and temperature, ρ^0 , P^0 and T^0 are the air density, pressure and temperature under the standard state.

Under standard conditions, the temperature T^0 is 273.15K and the pressure P^0 is 1bar. Thus, the standard molar volume $\rho^0 \approx 0.0893\text{g/L}$. Then, according to Eq. (15), the hydrogen density at this time is about $\rho = 0.0893 \times \frac{0.75 \times 273.15}{1 \times 298.15} \approx 0.0614 \text{ g/L}$. According to Eq. (12), the mass flow rate of hydrogen is approximately $\dot{M}_{H_2} = 1.6530 \times 2 = 3.3060 \text{ g/mol}$.

Thus, according to Eq. (13), the volume flow rate of hydrogen is about $\dot{V}_{H_2} = 3.3060/0.0614 \approx 53.84 \text{ L/min}$.

In summary, based on the energy conversion between chemical energy and electric energy, the volume flow rate of hydrogen can be calculated according to Eq. (16):

$$\dot{V}_{H_2} = \frac{P_{dem} V_m^0 \frac{P^0 T}{P T^0}}{\eta_{fc} \times LHV_{H_2}} \quad (16)$$

Table 1. Volume flow of hydrogen obtained by different methods

| Methods | Volume flow of hydrogen (L/min) | Relative deviation (-) |
|---|---------------------------------|------------------------|
| The number of electrons transferred and the current | 53.70 | — |
| Energy conversion and molar volume | 53.89 | 0.35% |
| Energy conversion and molar volume | 53.84 | 0.26% |

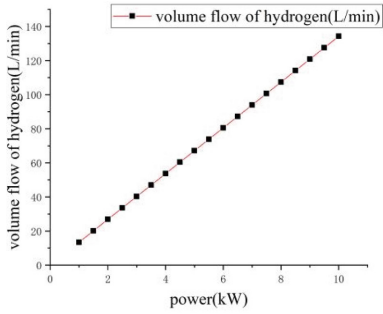
According to Table 1, the results of three hydrogen volume flow rates obtained by different treatment methods are almost consistent, considering the same problem from different perspectives. Therefore, in the process of practical application, any of the methods can be selected for estimation, and other methods can be used to support the estimation results. Similarly, the method can be extended to the estimation of the volume flow of air sucked into the cathode side of the fuel cell.

4 Sensitivity Analysis

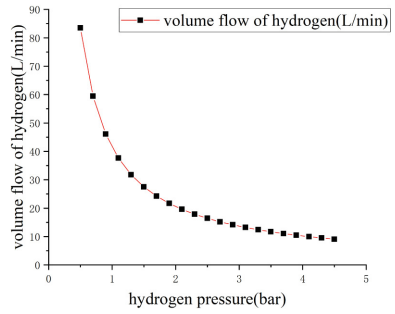
According to Eqs. (3)~(16), in the actual engineering application process, the demand power, the pressure of hydrogen into the reactor, the temperature of hydrogen into the reactor, the actual voltage of a single fuel cell and the efficiency of the fuel cell are the main factors affecting the volume flow rate of hydrogen.

From Eqs. (2), (5) and (9), we can get:

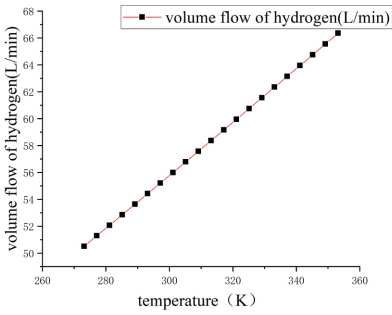
$$\dot{V}_{H_2} = \frac{P_{dem} V_m^0 \frac{P^0 T}{P T^0}}{\eta_{fc} \times zF [E_0 + \frac{RT_s}{zF} \ln P + \frac{1}{2} \frac{RT_s}{zF} \ln P_{O_2} + \frac{\Delta s}{zF} (T_s - T^0)]} \quad (17)$$



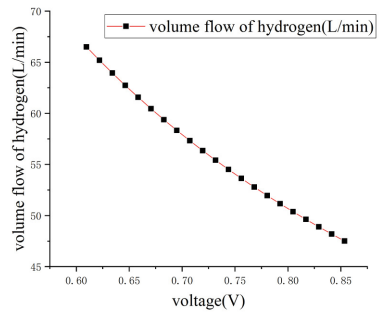
(a)



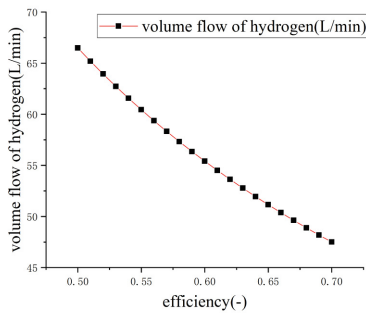
(b)



(c)



(d)



(e)

Fig. 2. The relationship between the volume flow rate of hydrogen consumed and (a) the required power, (b) hydrogen pressure, (c) temperature, (d) the actual voltage of a single fuel cell, and (e) the efficiency

If there is a certain deviation ΔP_{dem} between the actual power and the theoretical power, that is, the actual power is $P_{dem} + \Delta P_{dem}$, then the volume flow rate of hydrogen

actually consumed will also change. The actual consumption will increase:

$$\Delta \dot{V}_{H_2} = \frac{\Delta P_{dem} V_m^0 \frac{P^0 T}{PT^0}}{\eta_{fc} \times zF [E_0 + \frac{RT_s}{zF} \ln P + \frac{1}{2} \frac{RT_s}{zF} \ln P_{O_2} + \frac{\Delta s}{zF} (T_s - T^0)]} \quad (18)$$

Then, the change of hydrogen volume flow consumption caused by the change of power is as follows:

$$\Delta \dot{V}_{H_2} = K_1 \Delta P_{dem} \quad (19)$$

where, K_1 is a constant.

According to Eq. (19) and Fig. 2(a), when other factors do not change, the change in power will lead to a linear change in the volume flow rate of hydrogen expected to be consumed.

If there is a certain deviation ΔP between the actual pressure and the theoretical pressure, that is, the actual pressure is $P + \Delta P$, then the volume flow of hydrogen actually consumed will also change. Usually, $zFE_0 \gg RT \ln P$. As a result, the actual consumption will increase:

$$\begin{aligned} \Delta \dot{V}_{H_2} &= \frac{P_{dem} V_m^0 \frac{P^0 T}{(P+\Delta P)T^0}}{\eta_{fc} \times zF [E_0 + \frac{RT_s}{zF} \ln(P + \Delta P) + \frac{1}{2} \frac{RT_s}{zF} \ln P_{O_2} + \frac{\Delta s}{zF} (T_s - T^0)]} \\ &- \frac{P_{dem} V_m^0 \frac{P^0 T}{PT^0}}{\eta_{fc} \times zF [E_0 + \frac{RT_s}{zF} \ln P + \frac{1}{2} \frac{RT_s}{zF} \ln P_{O_2} + \frac{\Delta s}{zF} (T_s - T^0)]} \\ &\approx - \frac{P_{dem} V_m^0 \frac{P^0 T}{P^2 T^0} \Delta P}{\eta_{fc} \times zF [E_0 + \frac{RT_s}{zF} \ln P + \frac{1}{2} \frac{RT_s}{zF} \ln P_{O_2} + \frac{\Delta s}{zF} (T_s - T^0)]} \end{aligned} \quad (20)$$

Then, the change of hydrogen volume flow consumption caused by the change of hydrogen pressure is as follows:

$$\Delta \dot{V}_{H_2} \approx -K_2 \frac{\Delta P}{P^2} \quad (21)$$

where, K_2 is a constant.

According to Eq. (21) and Fig. 2(b), when other factors do not change, changes in hydrogen pressure will lead to approximately inversely proportional changes in the volume flow rate of hydrogen expected to be consumed. When the hydrogen pressure is not very large, small pressure deviations will have a large effect on the estimated quantity. This means that, when the hydrogen pressure is not very large, the agreement between the estimated result and the actual value will decrease due to the influence of measurement errors and other factors.

If there is a certain deviation ΔT between the actual temperature and the theoretical temperature, that is, the actual temperature is $T + \Delta T$, then the volume flow of hydrogen actually consumed will also change. Usually, $zFE_0 \gg \Delta sT + RT \ln P + \frac{1}{2} RT \ln P_{O_2}$. As a result, the actual consumption will increase:

$$\Delta \dot{V}_{H_2} = \frac{P_{dem} V_m^0 \frac{P^0 (T+\Delta T)}{PT^0}}{\eta_{fc} \times zF [E_0 + \frac{RT_s}{zF} \ln P + \frac{1}{2} \frac{RT_s}{zF} \ln P_{O_2} + \frac{\Delta s}{zF} (T_s - T^0)]}$$

$$\begin{aligned}
& - \frac{P_{dem} V_m^0 \frac{P^0 T}{PT^0}}{\eta_{fc} \times zF [E_0 + \frac{RT_s}{zF} \ln P + \frac{1}{2} \frac{RT_s}{zF} \ln P_{O_2} + \frac{\Delta s}{zF} (T_s - T^0)]} \\
& \approx \frac{P_{dem} V_m^0 \frac{P^0 \Delta T}{PT^0}}{\eta_{fc} \times zF [E_0 + \frac{RT_s}{zF} \ln P + \frac{1}{2} \frac{RT_s}{zF} \ln P_{O_2} + \frac{\Delta s}{zF} (T_s - T^0)]} \quad (22)
\end{aligned}$$

Then, the change of hydrogen volume flow rate consumption caused by temperature change is:

$$\Delta \dot{V}_{H_2} \approx K_3 \Delta T \quad (23)$$

where, K_3 is a constant.

According to Eq. (23) and Fig. 2(c), when other factors do not change, the change of temperature will lead to an approximate linear change in the volume flow rate of hydrogen expected to be consumed.

If there is a certain deviation ΔU between the actual single voltage and the theoretical single voltage, that is $U + \Delta U$, the actual voltage is, then the volume flow of hydrogen actually consumed will also change. The actual consumption will increase:

$$\begin{aligned}
\Delta \dot{V}_{H_2} &= \frac{P_{dem} V_m^0 \frac{P^0 T}{PT^0}}{zF (U + \Delta U)} - \frac{P_{dem} V_m^0 \frac{P^0 T}{PT^0}}{zFU} \\
&\approx \frac{P_{dem} V_m^0 \frac{P^0 T \Delta U}{PT^0}}{zFU^2} \quad (24)
\end{aligned}$$

Then, the change of hydrogen volume flow consumption caused by the change of single voltage is:

$$\Delta \dot{V}_{H_2} \approx -K_4 \frac{\Delta U}{U^2} \quad (25)$$

where, K_4 is a constant.

According to Eq. (5), when other factors do not change, the efficiency of the fuel cell is proportional to the actual voltage of a single cell. Then, it can also be obtained:

$$\Delta \dot{V}_{H_2} \approx -K_5 \frac{\Delta \eta_{fc}}{\eta_{fc}^2} \quad (26)$$

where, K_5 is a constant.

According to Eqs. (25) and (26) and Fig. 2(d) and (e), when other factors do not change, changes in actual single voltage or changes in efficiency will lead to approximately inversely proportional changes in the volume flow rate of expected hydrogen consumption.

When the fuel cell is working normally, its working efficiency is about 0.5 ~ 0.7. If the efficiency changes from 0.5 to 0.52, the volume flow rate of hydrogen will change from 66.5L/min to 64L/min on the assumption that other conditions do not change in this example. Small efficiency deviations will have a large impact on the estimated quantity. In other words, in the process of estimating hydrogen volume flow, it is necessary to focus on ensuring the efficiency of fuel cells. In other words, the actual single voltage of the fuel cell needs to be accurately collected and controlled.

5 Conclusion

In this paper, the problem about the estimation of the volume flow rate of hydrogen that may be faced in engineering design and application is studied, the complete calculation process is given, and the following conclusions are reached:

1. Basically the same estimation results can be obtained from two perspectives: the number of electrons transferred by electrochemical reaction and the energy conversion between chemical energy and electric energy. The required power, hydrogen inlet pressure, hydrogen inlet temperature, fuel cell voltage and fuel cell efficiency are the main factors affecting the results.
2. There is an approximate linear relationship between the required power and the inlet temperature of hydrogen and the volume flow rate of hydrogen consumed.
3. The pressure of hydrogen into the reactor, the voltage of a single fuel cell and the efficiency of the fuel cell are approximately inversely proportional to the volume flow rate of hydrogen consumed. It is important to ensure the accuracy of the fuel cell efficiency values. In other words, enough importance should be given to the data acquisition and control of the actual single voltage of the fuel cell.


Acknowledgement. This work is financially supported by the National Natural Science Foundation of China (Grant No.52072265).

References

1. Khan, U., Yamamoto, T., Sato, H.: Understanding the discontinuance trend of hydrogen fuel cell vehicles in Japan. *Int. J. Hydrogen Energy* **47**(75), 31949–31963, ISSN 0360-3199. <https://doi.org/10.1016/j.ijhydene.2022.07.141>
2. Lee, H., Ryu, B., Duong, P.A., Roh, G., Lee, S., Kang, H.: Thermodynamic analysis and assessment of novel ORC-DEC integrated PEMFC system for liquid hydrogen fueled ship application. *Int. J. Hydrogen Energy* **48**(8), 3135–3153. ISSN 0360-3199. <https://doi.org/10.1016/j.ijhydene.2022.10.135>
3. Nicolay, S., Karpuk, S., Liu, Y., Ali Elham, Conceptual design and optimization of a general aviation aircraft with fuel cells and hydrogen. *Int. J. Hydrogen Energy* **46**(64), 32676–32694. ISSN 0360-3199. <https://doi.org/10.1016/j.ijhydene.2021.07.127>
4. Whiston, M.M., Azevedo, I.M.L., Litster, S., Samaras, C., Whitefoot, K.S., Whitacre, J.F., Paths to market for stationary solid oxide fuel cells: expert elicitation and a cost of electricity model. *Appl. Energy* **304**, 117641 (2021). <https://doi.org/10.1016/j.apenergy.2021.117641>
5. Wang, Y., Li, J., Tao, Q., Bargal, M., Su, C.Q.: Thermal management system modeling and simulation of a full-powered fuel cell vehicle. *J. Energy Res. Technol.* **142**(6), 1–40 (2019)
6. Hayre, R.: Fuel cell fundamentals (2006)
7. Wang, J., Zhou, J., Zhao, W.: Deep reinforcement learning based energy management strategy for fuel cell/battery/supercapacitor powered electric vehicle, *Green Energy Intell. Transp.* **1**(2), 100028, ISSN 2773-1537, <https://doi.org/10.1016/j.geits.2022.100028>



The Energy Consumption Method Based on Synthetic Optimization of Speed and Power Allocation for Fuel Cell-Battery Hybrid Tramway

Guorui Zhang^(✉) 

CRRC Qingdao Sifang Company Ltd, Qingdao 266111, China
guo_rui_zhang@126.com

Abstract. The saving of operating energy consumption of traditional tramway powered by catenary line mainly depends on the optimization of speed curves. Unlike that, the fuel cell-battery hybrid tramway carries multiple power sources with different characteristics to supply power, and the operation energy consumption of fuel cell-battery tramway is related to not only the running speed, but also the power allocation between sources. However, the traditional method for fuel cell hybrid tramway to reduce consumption is using algorithms to optimize the energy management of load power based on the predetermined speed curves. Therefore, this paper develops the synthetic optimization of speed and power allocation to decrease the energy consumption of fuel cell hybrid tramway. Firstly, the tramway's dynamic model is established to analyze the load power. Then, the electricity consumption of battery is converted to the hydrogen consumption based on the equivalent principle. In this way, the energy from battery and fuel cell are transferred as an indicator: the equivalent hydrogen consumption, to evaluate the operating energy of the tramway. Afterwards, the synthetic optimization model is established aiming at the minimizing the consumption within stations. The pseudospectral method is employed to solve this problem. It turns out that the proposed method could obtain the running speed curve and power distribution sequence simultaneously. The speed curve guarantee on time operation and the load power is reasonably allocated.

Keywords: Fuel cell-battery tramway · Synthetic optimization · Pseudospectral method method

1 Introduction

With the trend of global low-carbon transformation, hydrogen energy and fuel cell technology have received extensive attention and been applied into various fields. Hydrogen energy is a secondary energy source with the advantages of being clean, environmentally friendly, large in stock, and easy to obtain [1]. It is regarded as the clean energy with the most development potential in the 21st century. At present, more than 20 countries

around the world have introduced relevant energy policies to vigorously support the development of the hydrogen energy industry. China has also issued the “Medium and Long-Term Plan for the Development of Hydrogen Energy Industry (2021–2025)” for the first time in 2022, in which hydrogen energy is regarded at the national level, as a strategic emerging industry and a key development direction of future industries in China.

Among various ways of utilizing hydrogen energy, fuel cell is one of the most effective way. Firstly, the fuel cell power generation process does not go through the combustion process and is not limited by the Carnot cycle, resulting a high energy conversion efficiency between 45% and 60% [2]. Secondly, the fuel cell power generation is more flexible and has strong building blocks [3]. Therefore, it is easily to combined into power generation system with different power levels for many application scenarios, such as mobile power supply, stationary power generation, cogeneration, etc. [4–6]. In addition, fuel cell power generation does not produce air pollutants such as carbon oxides, nitrogen oxides, and sulfides. Combined with green hydrogen preparation technology, its environmental benefits within the entire life cycle are obvious.

At present, hydrogen energy transportation has become a pioneer in the development of hydrogen energy to drive the hydrogen energy industry in countries around the world, mainly for the automotive field. In the field of rail transit, low-carbon transformation is also urgently needed because there are still a large number of diesel locomotives. And fuel cell technology has become an important technical path for the decarbonization of the railway industry.

In addition to cleanliness and environmental protection, hydrogen energy rail transit vehicles also have the following advantages: 1) Cancellation of external traction power supply system, avoiding pantograph-catenary system failure and reducing the cost of infrastructure [7, 8]; 2) Compared with energy storage locomotives, the energy replenishment speed of hydrogen energy rail transit vehicles is faster (Fig. 1).

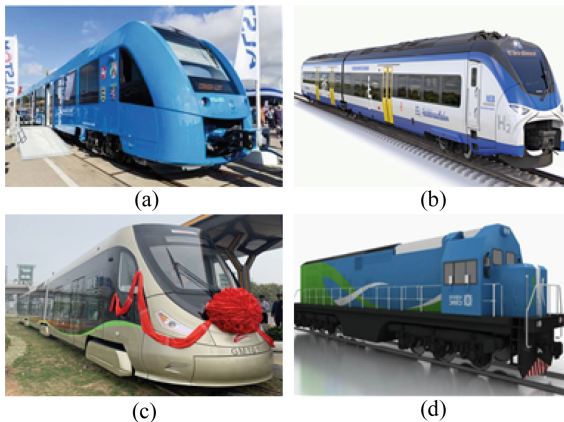


Fig. 1. Successfully developed hydrogen trains (a) iLint from Alstom (b) Mireo Plus H from Siemens (c) Tramway from CRRC Qingdao Sifang (d) Hydrogen locomotive from CRRC Datong

In recent years, countries around the world have been actively developing hydrogen energy rail transit vehicles. Many foreign models have been rolled off the production line, such as the iLint of Alstom in France and the Mireo Plus H of Siemens [9] in Germany, and etc. Some of them are already in commercial trial operation. China's hydrogen energy rail transit vehicles are developing rapidly. Since 2016, hydrogen energy vehicles such as fuel cell shunting locomotives, fuel cell hybrid electric trams, fuel cell engineering trains, and fuel cell city trains have been successfully developed [10]. Among them, the fuel cell hybrid tram developed by CRRC Sifang Co., Ltd. Has been put into commercial operation in Foshan Gaoming in November 2019.

For rail transit vehicles, improving the energy efficiency has been the focus of research. Hydrogen rail vehicles usually use fuel cells as the main power source, and batteries or supercapacitors as auxiliary power systems to provide acceleration power and absorb braking power. Since it is jointly driven by multiple power sources and the power sources have different characteristics, the distribution of load power among the power sources will affect the energy consumption of the whole vehicle. Therefore, the current energy consumption optimization is mainly realized by optimizing the energy management control strategy, and the load power is mainly used as an external input condition that is not optimized. However, by studying the energy consumption optimization of traditional trains, it can be seen that the running speed curve of the train has an impact on its energy consumption level. When the station distance and running time are determined, how to plan the running curve during the period will affect the energy consumption in the interval. This conclusion also applies to hydrogen rail trains. The traditional catenary train only obtains electric energy through the pantograph-catenary system, and the energy source is single. The energy consumption characteristics of the train operation are relatively simple and only related to the load demand, and only the speed curve can be optimized. However, hydrogen energy trains contain multiple power sources. When the speed curve is fixed, the use of different energy allocation algorithms will also affect energy consumption. Therefore, for hydrogen energy trams, it is necessary to carry out joint optimization of speed curve and energy management to further improve the energy efficiency level.

This paper intends to propose an energy consumption method based on synthetic optimization of speed and power allocation for fuel cell hybrid electric tram, in order to minimize the energy consumption of the train interval. The innovation points of this paper are as follows:

- 1) Carry out energy consumption characteristics analysis on fuel cell hybrid electric trams, and use the global equivalent hydrogen consumption as an indicator to measure the energy consumption of the whole vehicle.
- 2) Carry out joint optimization of train running speed and power distribution and realize the overall reduction of energy consumption in train intervals at multiple levels.

The subsequent sections of this article are arranged as follows: Part 2 is the structure and model of the fuel cell hybrid power system, the optimization method theory proposed in the third part, part 4 is the result analysis, and part 5 is the conclusion.

2 Modeling of the Fuel Cell Hybrid Train

2.1 Dynamic Model of the Fuel Cell Hybrid Train

During the operation of the train, it is mainly affected by motor traction/braking force, air resistance, wheel-rail friction resistance, ramp resistance. Normally, the friction resistance and air resistance can be equivalent using the basic resistance formula that can be expressed as a polynomial with respect to velocity [11]. Based on the single-mass model, the force analysis of trains is carried out, and according to Newton's second law, the force balance relationship established is as follows.

$$\begin{cases} (1+\gamma) \cdot M \cdot a = F_t - F_{fb} - F_{gb} \\ F_{fb} = f_b \cdot M \cdot g \\ F_{gb} = M g \sin \beta \\ f_b = A_1 \cdot v^2 + B_1 \cdot v + C_1 \end{cases} \quad (1)$$

where F_t is traction force, F_{fb} is basic resistance, F_{gb} is ramp resistance, M is train's mass, γ is the rotation coefficient, a is acceleration speed, g is gravitational constant, β is slope degree, f_b is unit basic resistance formula in which A_1 , B_1 and C_1 are the coefficients, and v is the velocity.

According to the dynamic model, the wheel traction power can be calculated as follow.

$$P_w = F_t \cdot \frac{v}{3.6} \quad (2)$$

Considering the efficiency loss, the bus power can be calculated as follow.

$$P_{bus} = P_w / \eta_m / \eta_{trans} / \eta_t \quad (3)$$

where η_m , η_{trans} , η_t are respectively motor efficiency, transmission system efficiency and traction converter efficiency.

2.2 Topology of Fuel Cell Hybrid System

The hydrogen fuel cell hybrid power system studied in this paper is composed of fuel cell system and battery system, and its topology is shown in the Fig. 2. The fuel cell is connected to the bus through unidirectional DC/DC, and the battery is directly connected to the bus.

Modeling of Fuel Cell. Since the fuel cell reaction process involves issues in many fields such as water, heat, and electricity, and includes a variety of temporal and spatial scales. Therefore, the modeling methods are also different for different research objects and problems. In this paper, the fuel cell is used as the power supply of the system, and the concern is the external supply voltage and current of the system. Therefore, the model of the fuel cell is established based on the equivalent circuit.

$$V_{FC} = E_{oc} - V_{act} - V_{ohm} \quad (4)$$

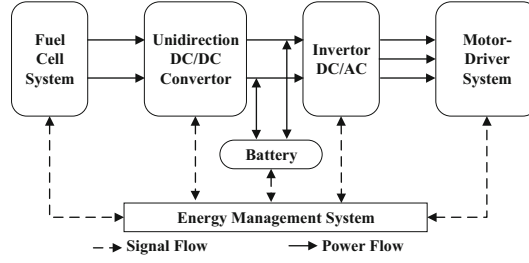


Fig. 2. Topology of fuel cell hybrid system

where V_{FC} , E_{oc} , V_{act} , V_{ohm} are respectively the output voltage, open circuit voltage, activation voltage drop and ohmic voltage drop.

Modeling of Battery Energy System. As a complex electrochemical system, lithium-ion batteries are difficult to accurately model. Currently, there are three main modeling methods: equivalent circuit model, neural network model, and electrochemical model [11]. Among them, the equivalent circuit model focuses on describing the relationship between the input and output of the external voltage and current of the battery. This model has the characteristics of simplicity and easy identification of parameters, which meets the requirements of this paper, so the equivalent circuit method is used to establish its model, as shown below.

$$\begin{cases} V_B = U_{oc} - R_{int}I_B \\ P_B = V_B \cdot I_B \end{cases} \quad (5)$$

where U_{oc} , R_{int} , and I_B are the open circuit voltage, internal resistance, and operating current of the battery energy storage system, respectively.

The SOC of the power battery is an important reference index in energy management. This paper uses the ampere-hour integral method to model it, as shown below.

$$SOC = SOC_0 - \int_0^t I_B dt \quad (6)$$

where SOC_0 is the initial value, I_B is positive when discharging and negative when charging.

Modeling of energy consumption. Since fuel cells and power batteries consume different types of energy during operation, in order to make the two comparable so as to establish a standard for evaluating the energy consumption of train, this paper draws on the equivalent hydrogen consumption theory. It converts the electricity consumed by battery into equivalent hydrogen and added it to the hydrogen consumption of the fuel cell to obtain the overall hydrogen consumption [12], as shown in the following formula.

$$\begin{cases} C_{FC} = a_1 \cdot P_{FC}^2 + a_2 \cdot P_{FC} + a_3 \\ C_B = \begin{cases} k \cdot P_B / \eta_{dis_B} / \eta_{avg_B} & P_B \geq 0 \\ k \cdot P_B \cdot \eta_{chg_B} \cdot \eta_{avg_B} & P_B < 0 \end{cases} \end{cases} \quad (7)$$

where C_{FC} is the fuel cell hydrogen consumption, C_B is the equivalent consumption, P_{FC} is fuel cell output power, a_1, a_2, a_3 and k are constant, η_{dis_B} , η_{chg_B} , η_{avg_B} are discharge efficiency, charge efficiency and average efficiency.

3 Energy Consumption Method Based on Synthetic Optimization of Speed and Power Allocation

3.1 The Description and Objective of Synthetic Optimization

The problem in this paper is minimizing the equivalent hydrogen consumption of fuel cell hybrid urban train under the constraints of train interval operation, such as speed limit and operation schedule. It can be regarded as a typical constrained global optimization problem, and its objective function is as follows, which is a function related to P_{FC} , P_w and SOC :

$$\begin{cases} J = \int_{t=0}^T C_{H2} dt = \int_0^T (C_{FC}(P_{FC}) + C_B(P_B, SOC)) dt \\ (P_{FC} + P_B) \cdot \eta_m \cdot \eta_{trans} \cdot \eta_t = P_w \\ P_{bus} = P_{FC} + P_B \end{cases} \quad (8)$$

where t is operation time, T is the planned operation time, C_{H2} is the instantaneous equivalent hydrogen consumption.

To describe the motion process of the fuel cell hybrid city train, this paper takes the train speed v , position s and lithium battery SOC as the state variables, and takes the train traction force and fuel cell power as the control variables, and the obtained state transition equation is as follows Shown:

$$\begin{cases} \dot{v} = 3.6 \cdot (F_t - F_{tb} - F_{gb}) / (1 + \gamma) \cdot M \\ \dot{s} = v / 3.6 \\ \dot{SOC} = - \frac{U_{oc} - \sqrt{U_{oc}^2 - 4 \cdot R_{int} \cdot (P_{bus} - P_{FC})}}{2 R_{int} \cdot Q_B \cdot 3600} \end{cases} \quad (9)$$

SOC , speed v , mileage s , traction force, and fuel cell power need to meet the limits of their maximum and minimum values. In addition, to achieve train stops on time and SOC maintenance, these constraints need to meet: the first and last value of speed is 0, the first and last value of mileage should be 0 and station distance, and the first and last values of SOC should both equal to the reference value.

3.2 Pseudospectral Method

The problem studied in this paper belongs to the optimal control problem, which can be solved by pseudospectral method. Pseudospectral method uses global interpolation polynomial discretization to approximate the state variables and control variables at a series of discrete orthogonal collocation points. Next, adopts time domain transformation to transfer optimal control problem into large-scale nonlinear programming problems (NLP) in finite dimensions, and then solve it. For the specific theory of this method, please refer to the relevant literature [13].

4 Results and Analysis

In this paper, an actual single section of a tram in China is used as to carry out analysis. The line is 912 m long, and the standard running time is 118 s. The slope information of the section line is shown in the Fig. 3.

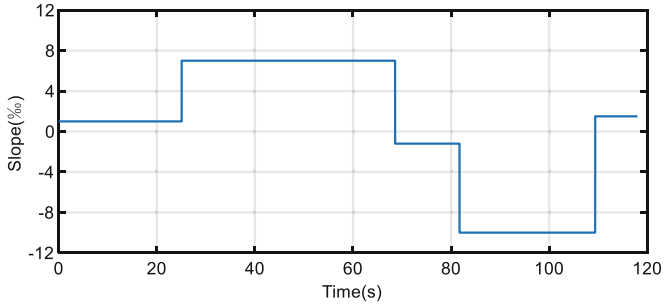


Fig. 3. Slope of the target line

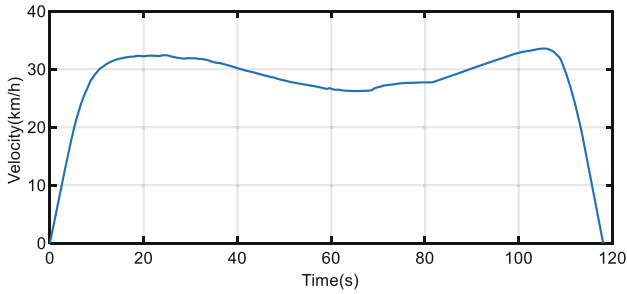


Fig. 4. Operation speed curve of the fuel cell tram

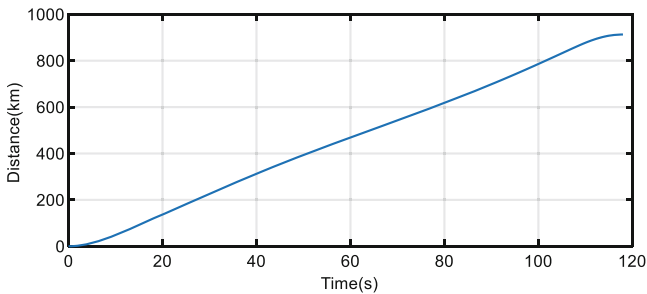


Fig. 5. Distance curve of the fuel cell tram

Under the proposed method, the operating speed curve and distance curve of the fuel cell tram are shown in Fig. 4 and 5 respectively. It can be seen that the speed curve

throughout the operation is relatively stable, with a maximum operating speed of no more than 33 km/h, and the tram can achieve punctual operation. The above results demonstrate that the proposed method can achieve reliable operation of the fuel cell tram.

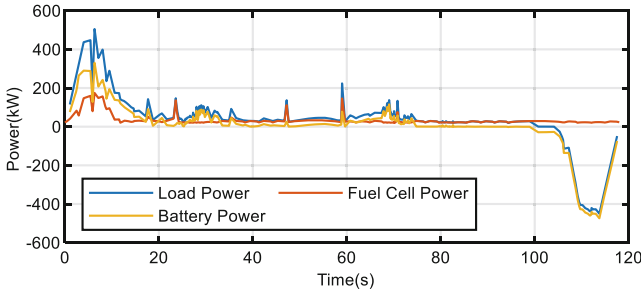


Fig. 6. Power distribution curve of the fuel cell hybrid system of the tram

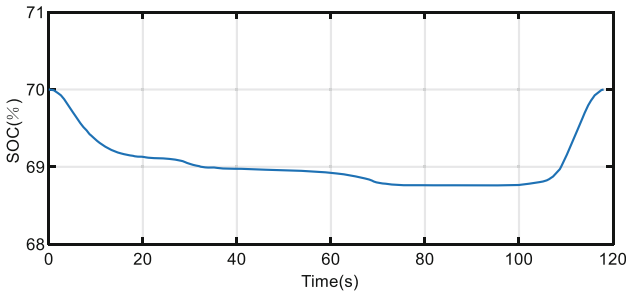


Fig. 7. Battery SOC curve

On this basis, the power distribution curve of the hybrid system of the fuel cell tram is shown in Fig. 6. It can be observed that the power of fuel cells can vary with the load and the operating power is relatively stable. On the other hand, the battery is mainly used to provide transient power for trams by shaving peaks and filling valleys. This kind of power distribution scheme is beneficial for reducing system energy consumption, reducing performance degradation of fuel cells, and extending their service life.

In addition, the battery SOC curve of the tram under the whole operation period is shown in Fig. 7. It turns out under the proposed method, the variation range of the tram battery SOC is narrow, and the initial and final SOC values can be kept equal, which meets the control expectations.

5 Conclusion

In conclusion, the proposed method can realize the collaborative optimization of power distribution and operation curve at the same time. It can make full use of the slope information to reasonably plan the operation curve, arrive on time within the given

inter-station planning operation time. Moreover, the power energy management recover the full braking energy and maintains the SOC, which helps to reduce operating energy consumption. Only energy consumption is considered in the objective function of this paper, but in practice, life is also an important factor to be considered, so in future research, life-related evaluation criteria will be further introduced into the objective to achieve more significant results.

References

1. Ozawa, A., Kudoh, Y., Murata, A., Honda, T., Saita, I., Takagi, H.: Hydrogen in low-carbon energy systems in Japan by 2050: the uncertainties of technology development and implementation. *Int. J. Hydrogen Energy* **43**, 18083–18094 (2018)
2. Sharaf, O.Z., Orhan, M.F.: An overview of fuel cell technology: fundamentals and applications. *Renew. Sustain. Energy Rev* **32**, 810–853 (2014)
3. Yang, Z., Liu, Q., Zhang, L., Dai, J., Razmjoo, N.: Model parameter estimation of the PEMFCs using improved barnacles mating optimization algorithm. *Energy* **212**, 118738 (2020)
4. García-Triviño, P., Llorens-Iborra, F., García-Vázquez, C.A., Gil-Mena, A.J., Fernández-Ramírez, L.M., Jurado, F.: Long-term optimization based on PSO of a grid-connected renewable energy/battery/hydrogen hybrid system. *Int. J. Hydrogen Energy* **39**, 10805–10816 (2014)
5. Njaya Motapon, S., Dessaint, L.-A., Al-Haddad, K.: A comparative study of energy management schemes for a fuel-cell hybrid emergency power system of more-electric aircraft. *IEEE Trans. Ind. Electron.* **61**, 1320–1334 (2014)
6. Hsu, R.C., Chen, S.M., Chen, W.Y., Liu, C.T.: A Reinforcement learning based dynamic power management for fuel cell hybrid electric vehicle. In: *Joint International Conference on Soft Computing & Intelligent Systems* (2016)
7. Zhang, G., Li, Q., Chen, W., Meng, X., Deng, H.: A coupled power-voltage equilibrium strategy based on droop control for fuel cell/battery/supercapacitor hybrid tramway. *Int. J. Hydrogen Energy* **44**, 19370–19383 (2019)
8. Yan, Y., Li, Q., Chen, W., Su, B., Liu, J., Ma, L.: Optimal energy management and control in multimode equivalent energy consumption of fuel cell/supercapacitor of hybrid electric tram. *IEEE Trans. Ind. Electron.* **66**, 6065–6076 (2019)
9. Siwiec, J.: Use of hydrogen fuel cells in rail transport. *Problemy Kolejnictwa—Railway Rep.* **65**, 125–131 (2021)
10. Murray-Smith, D.: A review of developments in electrical battery. Fuel cell and energy recovery systems for railway applications a report for the Scottish association for public transport (2019)
11. Wang, Y., et al.: A comprehensive review of battery modeling and state estimation approaches for advanced battery management systems. *Renew. Sustain. Energy Rev.* **131**, 110015 (2020)
12. Xu, L., Cao, G., Li, J., Yang, F., Lu, L., Ouyang, M.: Equivalent Consumption Minimization Strategies of Series Hybrid City Buses. In: Macia, F. (ed.) *Energy Management*. InTech (2010)
13. Delkhosh, M., Parand, K.: Generalized pseudospectral method: theory and applications. *J Comput Sci.* **34**, 11–32 (2019)



Research on Safety Management Mode of Hydrogen Fuel Cell Vehicle Demonstration Operation Based on Intrinsic Safety Control

Guozhu Liu¹, Yao Lu¹, Liming Wang², Yuzhe Gao³, and Yupeng Yang³(✉)

¹ Hydrogen Power (Beijing) Technology Service Co., Ltd, Beijing 102100, China

² State Power Investment Group Hydrogen Energy Technology Development Co., Ltd, Beijing 102100, China

³ State Key Laboratory of Electromechanical Integrated Manufacturing of High-Performance Electronic Equipment, Xidian University, Xi'an, China
ypyang@xidian.edu.cn

Abstract. To optimize the existing safety management strategies of the hydrogen fuel cell vehicle operations, in this contribution, we analyzed the safety management risks and responsibilities from four aspects, including vehicle technology management, participant organization, environment management and essential safety management. Taking the Beijing 2022 winter (Paralympic) Olympic Games as an example, we proposed four safety management strategies and developed the “441” safety management strategy which is very suitable for the operation safety management of hydrogen fuel cell vehicles. Based on the “441” safety management strategy, we proposed the “PDCA” closed-loop safety management mechanism. The research results could provide positive suggestions for the large-scale operation of hydrogen fuel cell vehicles.

Keywords: Intrinsic safety · Hydrogen fuel cell vehicle · Hydrogen safety · Safety management strategy

1 Introduction

Hydrogen fuel cells directly convert the chemical energy of hydrogen into electricity through electrochemical reactions, obtaining very high energy conversion efficiency. The emissions are only water, which can achieve efficient and environmentally friendly operation of new energy vehicles [1–5]. The safety of fuel cell vehicles is the first concern as the explosion limit of hydrogen is 4%~75%. The explosive level is level 1. Therefore, it is urgent to establish an efficient, closed-loop, and clear safety management strategy for the large-scale operation of hydrogen fuel cell vehicles. At present, various large companies have proposed some advanced safety management strategies, such as Shell’s HSE safety management system [6], safety management strategies based on behavioral safety “2–4” models [7] and “PDCS” safety management strategy [8].

From 4th to 20th February and from 4th to 13th March, 2022, the 2022 Beijing Winter Olympics and Paralympics were successfully held. According to the “Low Carbon Management Report of the Beijing Winter Olympics (Pre Games)”, 816 hydrogen fuel vehicles were used during the events, accounting for 19.9%. According to public data, this is the largest demonstration operation project for hydrogen fuel cell vehicles worldwide and a significant opportunity for the promotion, application, and industrial development of hydrogen fuel cell vehicles. All the fuel cell buses were operated by a specialized hydrogen transportation operation platform company (hereinafter referred to as the “company”). Based on the demonstration operation of hydrogen fuel cell buses at the 2022 Beijing Winter Olympics and Winter Paralympics, this paper developed a safety management system from four dimensions based on the system’s essential safety control concept to provide samples for the safety management of large-scale social operations of hydrogen fuel cell vehicles in the future.

2 Characteristics and Difficulties in Safe Production of Hydrogen Fuel Cell Vehicle Demonstration Operation

2.1 New Technologies and Equipment for Hydrogen Fuel Cell Vehicles

The internal combustion engine vehicles have hundreds of years of history. The safety related technologies, testing, regulations, insurance and other systems for internal combustion engine vehicles have been established. The fuel cell systems and refueling stations for hydrogen fuel cell vehicles are all new technologies. These new technologies and equipment bring more uncertainty to safety management.

2.2 Many Departments Were Involved in Demonstration Operations

During the demonstration operations, many departments were involved, including government management departments, vehicle manufacturers, core equipment suppliers, hydrogen refueling stations, and the Winter (Paralympic) Organizing Committee. Each participant has no experience of large-scale demonstration operation of hydrogen fuel cell vehicles.

2.3 The Demonstration Operation Environment is Subject to Frequent Changes

During the 2022 Winter (Paralympic) Olympics Games, there are many vehicle operation routes and the natural environment is complex, including low temperatures, steep slopes, and sharp turns. There are many rapidly changing units and demands for vehicles. Affected by the COVID-19, the whole process closed-loop management of vehicles and personnel, the safety management of hydrogen fuel cell vehicle operating environment, driver working environment and emergency response are facing new topics and challenges.

2.4 Insufficient Applicability of Safety Management System

The current safety management system of transportation operation companies is mainly applied for traditional internal combustion engines. It is not applicable for the hydrogen fuel cell vehicle operation, resulting in insufficient matching of safety systems. It is necessary to develop a new safety management system for hydrogen fuel cell vehicle operation.

3 Analysis Method for Intrinsic Safety Management Strategy

In order to solve the existing problems of safety production in the demonstration operation of hydrogen fuel cell vehicles, [9–11], an intrinsic safety structural model is developed based on the systemic concept of intrinsic safety control (Fig. 1). This paper analyzes the safety management elements of the demonstration operation of hydrogen fuel cell vehicles from four aspects: vehicles, personnel, environment, and management.

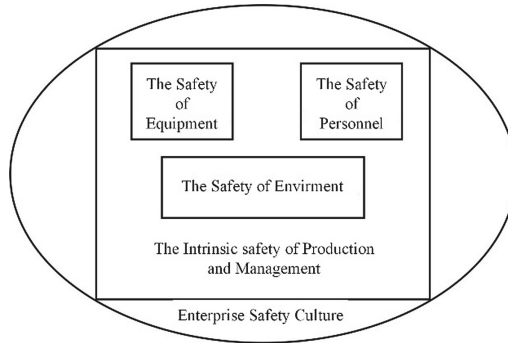


Fig. 1. Intrinsic safety structural model

3.1 Analysis of Safety Risk of Hydrogen Fuel Cell Vehicles

Early safety assessment of new technologies and equipment for hydrogen fuel cell vehicles

Because of the characteristics of hydrogen leakage, volatility, flammability and explosiveness [12], the hydrogen safety protection and daily maintenance of hydrogen fuel cell vehicles are crucial. The safety of hydrogen fuel cells includes five aspects: material safety protection, component protection, hydrogen system safety protection, hydrogen system safety monitoring and collision safety protection. The above five aspects of safety protection are mainly achieved through various safety components.

All components in contact with hydrogen should be made of materials that are resistant to hydrogen brittleness and hydrogen corrosion. Non-metallic materials in contact

with hydrogen gas must meet the flame retardant requirements of V0 level. The sealing between the bipolar plate and the membrane electrode inside the stack must also ensure that the sealing does not fail under conditions such as high temperature, high cold, vibration, impact and aging. It is mainly composed of safety components such as hydrogen refueling port, hydrogen cylinder, pressure reducing valve, temperature sensor, pressure sensor, solenoid valve, etc. These components must undergo reliability verification according to regulations. In daily driving, safety components should be carefully inspected and maintained, and should be regarded as key safety management objects.

Online safety monitoring and remote fault diagnosis of hydrogen fuel cell vehicles

The safety monitoring system of the hydrogen system is crucial for driving safety management. The hydrogen safety monitoring system mainly includes hydrogen system controller, hydrogen leakage sensor, temperature sensor, and pressure sensor. They are used to monitor the safety of hydrogen cylinders and pipelines, hydrogen leakage status and vehicle operation status. In case of any abnormalities, the hydrogen supply system should be actively shut down at any time to ensure the safety of hydrogen fuel cell vehicles. This system is very helpful in vehicle safety check, but it cannot be used for remote data transmission and online fault diagnosis.

3.2 Analysis on Safety Responsibility Attribution of Demonstration Operation Organization Model

Demonstration Operations Participation Department

Taking the Yanqing competition area as an example, during the demonstration operations, the participating departments include government regulatory departments, companies, vehicle suppliers, hydrogen fuel cell suppliers, Winter Olympics Organizing Committee, hydrogen refueling stations, and other units (Fig. 2). It is the first time to conduct large-scale demonstration operations of hydrogen fuel cells for all the participating departments.

The demonstration operation involves a wide range of safety responsibilities

During the demonstration operations, new technologies, equipment, and new operating modes are involved. The existing legal and regulatory system has no clear rules for the division of safety responsibilities, leading to unclear safety production responsibility. For example, the daily operation of hydrogen fuel vehicles involves six safety stakeholders. Moreover, due to the fact that the organizers of Olympic events are governments, relevant government departments have changed from safety supervisors to project organizers, bringing new challenges to safety management.

Particularly, during the vehicle refueling period, there are many overlapping safety management links. There are obvious differences in refueling between fuel cell electrical vehicle refueling and traditional fossil fuel vehicle. It is performed by professional operators at the station, with the driver cooperating with relevant operations. The hydrogen refueling process has more risk points and serious consequences (Table 1).

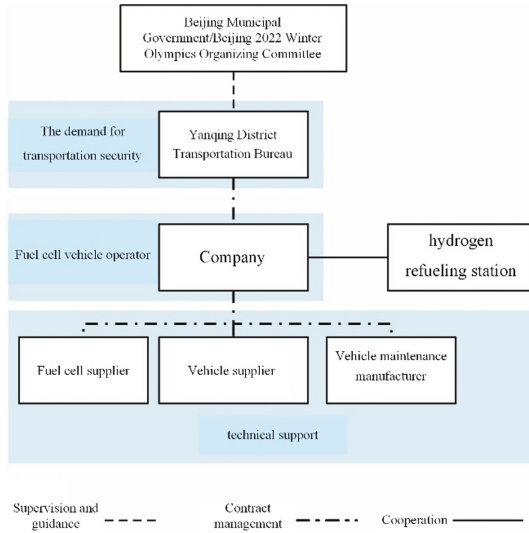


Fig. 2. Participants of demonstration operations in Yanqing competition area

Table 1. Risk points and consequences of hydrogen refueling station operation

| Serial number | Risk points | Consequence |
|---------------|---------------------------------|--------------------|
| 1 | Hydrogen leakage | Burning, explosion |
| 2 | Gas cylinder explosion | Mechanical shock |
| 3 | Hydrogenation hose pulled off | Leakage |
| 4 | Thunderstorm weather | Burning, explosion |
| 5 | Vehicle mode switching | Burning |
| 6 | Electrostatic Discharge | Burning |
| 7 | Electrostatic arc | Burning |
| 8 | Charge accumulation | Burning |
| 9 | Mechanical vibration and impact | Burning |
| 10 | Flame | Burning, explosion |
| 11 | Hot surface | Burning, explosion |
| 12 | High speed jet heating | Burning, explosion |

3.3 Analysis of the Impact of the External Environment on Demonstration Operations of Fuel Cell Vehicles

Meteorological conditions in Yanqing competition area

The Yanqing competition area is located in the Haituoshan area in the northwest of Yanqing District. It mainly undertakes some alpine skiing and national snowmobile

events for the Beijing 2022 Winter Olympics. Based on the 10min dataset from January to March of each year from 2019 to 2020, the average temperature of 11 stations in the Yanqing competition area is calculated. It can be concluded that the average temperature on the racing platform at an altitude of 2194 m is $-11\text{ }^{\circ}\text{C}$, with a minimum temperature below $-25\text{ }^{\circ}\text{C}$ [14]. During the race events, shuttle vehicles need to travel up to a shuttle platform at an altitude of approximately 2000 m.

At present, Li-battery electric vehicles have entered the popularization stage. But Li-battery electric vehicles are difficult to meet the requirements of large commercial vehicles such as long-distance, high-power, fast charging, wide temperature adaptability (especially extreme cold and low temperature), due to the limited energy density of the battery system. Hydrogen fuel cell vehicles can meet these requirements. However, extreme cold weather still poses new challenges to vehicle performance and safety.

During the race, the slope of the vehicle operation route is as high as 16%, with continuous uphill travel of up to 7.5 km [15]. In addition, the requirement for rapid heating poses greater challenges to the performance and thermal management of the vehicles.

When operating at low ambient temperatures, the water generated by fuel cells is prone to freezing, resulting in the shutdown of fuel cells for a short period. Repeated startup may damage the internal structure of the fuel cells, seriously affecting its durability. In working environment of $0\text{ }^{\circ}\text{C}$, the water generated by the electrochemical reaction of fuel cells is prone to freezing, leading to blockage of the catalyst layer and diffusion layer, hindering the electrochemical reaction. Moreover, the volume change caused by water freezing can also damage the internal structure of the fuel cell, leading to decrease in the performance of fuel cells.

At high altitudes, oxygen in the air is relatively scarce and the air system of fuel cells requires greater power, especially in long-term uphill situations where vehicles require greater power. Fuel cell cells must operate at high loads, which has a certain adverse impact on the lifespan of fuel cells.

The Winter Olympics closed-loop management method brings new requirements for safety management

The closed-loop management of the Beijing 2022 Winter (Paralympic) Olympics is a special management method that reduces unnecessary contact and ensures the safety of all Olympic personnel and the Chinese public. During the demonstration operations, all vehicles and drivers need to be managed in a closed-loop manner. According to the requirements of the Winter (Paralympic) Organizing Committee, the closed-loop management period is from January 21, 2022 to March 13, 2022. During the closed-loop management period, drivers are required to reside in designated isolation hotels and not have any contact outside the closed-loop. Over two months of centralized isolation management will have a negative impact on drivers' psychology. The closed-loop management environment of the Winter Olympics also poses challenges to vehicle maintenance.

Defining the attributes of hydrogen brings new safety management issues

The properties of hydrogen are still under hazardous chemical management. The “Catalogue of Hazardous Chemicals (2015 Edition)” released by the former “State Administration of Work Safety” in 2015 is still valid, with a total of 393 pages listing 2828 chemical groups, of which hydrogen has a serial number of 1648 and its hazardous category is flammable gas, category 1, pressurized gas. Although petroleum, gasoline, diesel, etc. are also listed in the “Catalogue of Hazardous Chemicals (2015 Edition)”, their energy attributes have long been a fact, and relevant national departments have special laws, regulations, and normative documents for petroleum and natural gas. This allows them to be used in accordance with energy management requirements, even though they are hazardous chemicals. Figure 3 shows the government departments related to hydrogen safety management.

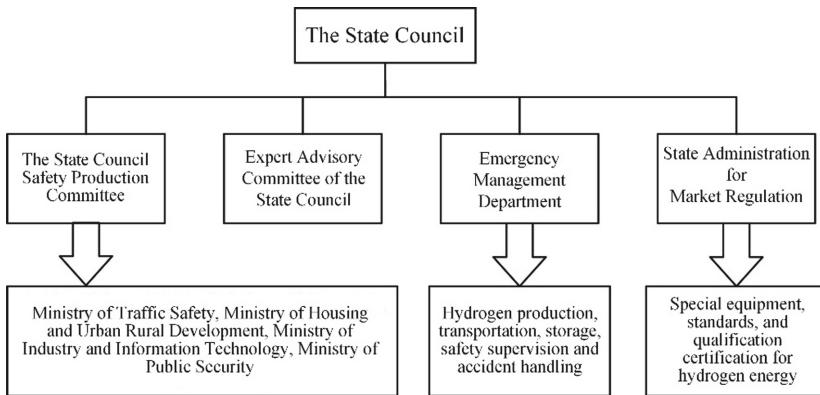


Fig. 3. Government departments for hydrogen safety manage

3.4 Developing of Intrinsic Safety Management Strategy

For the new technologies and equipment of hydrogen fuel cell vehicles, a safety management system applicable to hydrogen fuel cell vehicles should be developed. Safety control should be established for the entire process of vehicle hydrogenation, vehicle hydrogen use, vehicle operation and maintenance to achieve the intrinsic safety of hydrogen fuel cell vehicle operation. At present, the intrinsic safety of equipment and tools is constrained by many factors such as technology and economy, while the intrinsic safety of the working environment is greatly influenced by other factors, such as cost. The intrinsic safety of human beings is greatly influenced by the cultural level and technical level of employees.

4 Strategies for Strengthening Intrinsic Safety Control of Hydrogen Fuel Cell Vehicle Operations

The strengthening strategies are proposed from four aspects: vehicle safety management, implementation of safety responsibilities, standardized process control of operating environment, and essential safety of management.

4.1 Technical Safety Management Strategy for Hydrogen Fuel Cell Vehicles

Strengthen the management of source and intrinsic safety design. While ensuring safety in design, strengthen the daily inspection and maintenance of hydrogen safety systems for hydrogen fuel cell vehicles, and establish standardized safety inspection cards for key safety protection devices.

Strengthen the management of “one car, one gear”. Establish vehicle technical archives, increase fault records of core hydrogen safety related components such as hydrogen fuel cell engines and hydrogen cylinders and provide effective basic support for evaluating the technical status of hydrogen fuel cells.

Improve the remote fault diagnosis function of vehicles. Establish data transmission and remote fault diagnosis functions for hydrogen fuel cells. During the demonstration operations, some faults have been remotely diagnosed [16–18] and relevant operational data has also been remotely transmitted.

4.2 Implementation Strategy for Safety Responsibilities of Demonstration Operation Participants

Clarify the safety responsibilities of all participants. In response to the unclear safety responsibility interface and unclear management requirements caused by the participation of various participants in the large-scale hydrogen fuel cell vehicle demonstration operation for the first time during the demonstration operation period, we have improved the safety agreement and contract terms to clarify the responsibilities of each participant and relevant departments and reduce the risk of accident.

Improve the safety responsibility list. Improve the safety responsibility list of relevant participants and establish standardized operation procedures for key safety management interfaces to reduce human error. For example, we set up a “standardized operation ticket” for hydrogen refueling operations, subdividing vehicle hydrogenation into 28 steps and clarifying the responsibilities of each participant.

Implement the safety responsibilities of all participants. There are multiple participants and some units are both participants and industry regulators. It is difficult to implement safety responsibilities. Various hierarchical management documents are formulated to improve the safety responsibility system.

4.3 Security Management Strategy for the Operational Environment

Strengthen the prevention management. Establish an early warning mechanism and improve emergency rescue plans and strengthen driver safety training and route practice in response to the natural environment of “low temperature and extreme cold, steep slopes and multiple bends” during the race.

Improvement of the driver’s working environment. In response to the situation of long-term closed-loop management, we prepare humanistic care for employees. At the same time, we strengthen real-time safety monitoring during driving and provide safety reminders.

Strengthen the management of hydrogen safety compliance. We collect and organize laws, regulations, rules and regulations related to hydrogen energy, combined with

hazardous chemical management. We conduct research on laws and regulations related to hydrogen management and carry out company business in accordance with the law.

4.4 Intrinsic Safety Management Strategy

With identification of risk, corresponding measures are taken to eliminate or control the risk factors, realizing the scientific management system of “identifying and evaluating risks – reducing and controlling risks – preventing and eliminating accidents”. We use the “PDCA” method for the safety management of the entire operation process of hydrogen fuel cell vehicles to achieve defect free management, leaving “traces” in every link and process. Establish a safety management incentive mechanism. We implement a comprehensive safety reward and punishment system based on job positions and risk tolerance levels, including a safety deposit system, year-end performance deposit system, standardized assessment and reward methods.

5 Research on Intrinsic Safety Management Strategy

Based on the essential safety management analysis, safety management strategies and conclusions on safety management, a logical structure of safety management method is established and a “441” safety management model for hydrogen fuel cell vehicle operation safety management is proposed.

Four module security management analysis. As the foundation layer, it can identify and analyze operational safety management risks from four modules: vehicle, organizational mode, environment, and management, providing a foundation for safety management strategies.

Four dimensional security management strategy layer. As a method layer, based on the conclusions obtained from the four module safety management analysis, hydrogen vehicle technology safety management, safety responsibility, environmental safety and essential safety management strategies are proposed to provide methods for safety management measures.

Strategies. As a strategy layer, based on national laws and regulations, management standards are formulated for the new direction of hydrogen energy, new technologies and equipment of hydrogen fuel cell vehicles. Finally, a new safety management system is established.

6 Conclusions

By analyzing the demonstration operation characteristics of fuel cell vehicles for the 2022 Winter (Paralympic) Olympics in Beijing, the hydrogen safety management and control status and key points of hydrogen fuel cell vehicles are discussed. The safety responsibilities of all parties involved in the demonstration operation, the key safety management cross links and the safety management of hydrogen refueling operations are all studied. The risks of personnel and natural environment, from the internal environment of company management and the external environment of demonstration operation are discussed. Finally, the approach to establish essential safety management for hydrogen fuel cell vehicles has been discussed.

We propose four safety management strategies for hydrogen fuel cell vehicle technology safety management, safety responsibility implementation, environmental safety management and essential safety management.

Based on the closed-loop safety management throughout the entire process, we establish a new safety management system.

Based on the practice, we propose the “441” safety management mode for the operation safety management of hydrogen fuel cell vehicles, forming the “PDCA” closed-loop management mechanism.

References

1. Zongqiang, M.: Hydrogen Safety. Chemical Industry Press, Beijing (2020)
2. Haitao, Y., Gang, W., Zechang, S.: Structural configuration and parameter optimization matching of fuel cell vehicle powertrain. *Automot. Eng.* **28**(8), 729–733 (2006)
3. Zhu Xuancai, X., Ping, D.W., et al.: Design of energy management and control system for fuel cell power generation device. *Proc. CSEE* **11**, 101–106 (2008)
4. Guochao, L.I., Qifei, J., Shaoyun, S.: The application prospects of proton exchange membrane fuel cells in military applications. *J. Ordnance Eng* (4), 487–490 (2007)
5. Feng, W., Wang, S., Ni, W., et al.: The safety of hydrogen energy and hydrogen safety issues in fuel cell vehicles. *J. Solar Energy* **24**(5), 677–682 (2003)
6. Suzhang, C.: Evidence based management—a new trend of scientific management in the West. *Foreign Econ. Manage.* (11), 11–17, 42 (2008)
7. Chen, X., Research on unsafe actions in several major road traffic accidents based on unsafe behavior models. *Technol. Innovation Manage.* (9), 519–523, 37 (2016)
8. Li, H., Hao, J., Li, W.: Research and application of PDCS security management mode. *Chin. J. Saf. Sci.* **32**(2), 22–27 (2022)
9. Wang, Q.: Research on enterprise intrinsic safety model. *Chin. J. Saf. Sci.* **15**(12), 33–36 (2005)
10. Xu, Z., Song, X., Li, M.: Intrinsic safety management thought and empirical research framework. *Chin. J. Saf. Sci.* **16**(12), 79–85 (2006)
11. Li, H., Zhang, X., Gao, H., et al.: Research on the evaluation method of intrinsic safety of smart construction sites. *China Saf. Prod. Sci. Technol.* **18**(1), 139–145 (2022)
12. Shao, Z., Yi, B.: Current status and prospects of hydrogen energy and fuel cell development. *J. Chin. Acad. Sci.* **34**(4), 469–477 (2019)
13. Ling, W., Liu, W., Li, Y., et al.: Research on the development strategy of China’s hydrogen energy infrastructure industry. *Chin. Eng. Sci.* **21**(3), 76–83 (2019)
14. Hu, Y., Fu, J., Tao, Y.: Analysis of the distribution characteristics of meteorological elements in the Yanqing competition area of the Winter Olympics. *Meteorology* **48**(2), 177–189 (2022)
15. Wang, T., Zhao, Y., Wang, Y., et al.: Hydrogen installation for the Winter Olympics. *Technol. Overview* **11**, 66–69 (2021)
16. Dang, H., Ma, R., Zhou, J., et al.: Fault diagnosis of proton exchange membrane fuel cells based on CNN. *Power Electron. Technol.* **54**(12), 52–55 (2020)
17. Chen, W., Liu, J., Li, Q., et al.: Summary and prospect of fault diagnosis methods for proton exchange membrane fuel cells. *Chin. J. Electr. Eng.* **37**(16), 4712–4721 (2017)
18. Zhu, J., Zhao, J.: Research on the digital twin fault diagnosis model for proton exchange membrane fuel cell systems. *Control Theory Citation* **39**(3), 527–534 (2022)



Study on the Effect of Hydrogen Doping Ratio on the Operating Characteristics of Hydrogen-Rich Gas Turbine

Yongyi Li^(✉), Yingqi Liang, and Yi Cai

Department of Power Engineering, North China Electric Power University, Baoding 071003, Hebei, China

liyongyi@ncepu.edu.cn

Abstract. Hydrogen, with its advantages of high calorific value, abundant source and zero pollution, can significantly reduce CO₂ emissions by replacing natural gas in gas turbine power generation, which is conducive to the early achievement of the dual carbon goal. In this study, we adopt a modular modeling approach to develop a predictive model for the characteristics of a gas turbine and its combined cycle system under full operating conditions, and analyze the operating parameters, component operating characteristics and unit energy consumption of the gas turbine unit at full load and partial load when the hydrogen doping ratio ranges from 0 to 100%. The results shown that: compressor power consumption, turbine power, gas turbine power, specific work and power generation efficiency, and combined cycle efficiency all increase with the increase of hydrogen blending ratio, and this trend is more obvious when the hydrogen blending ratio is higher; the effect of hydrogen volume fraction on unit performance at partial load is basically the same as that at full load, but the magnitude of the effect is different; in general, increasing the proportion of hydrogen in fuel can improve the overall unit performance. Overall, the overall performance of the unit can be improved by increasing the proportion of hydrogen in the fuel, but the enhancement effect is slightly weakened as the load decreases.

Keywords: Carbon neutral · Hydrogen blended fuel gas turbine · Gas turbine combined cycle system · Off-design condition · Operating characteristics

1 Introduction

According to the current global energy development trend, the basic framework for promoting global energy green and low-carbon transformation is taking shape, new energy-using technologies and methods are emerging, and the achievements of the energy technology revolution are constantly challenging the dominance of traditional energy sources [1]. As an advanced power equipment, hydrogen-rich gas turbine will definitely have a wide application prospect in the field of power generation because of its low-carbon and low-NO_x emission advantages.

The hydrogen combustion process is characterized by high flame temperature [2] and fast propagation [3], and gas turbine burners using hydrogen doped fuel need to solve the problems of backfire, flame oscillation, and NO_x control. In recent years, some major power equipment manufacturers have obtained more outstanding results and developed significantly in the field of hydrogen-fueled high-power gas turbines. The new premixed burner developed by Mitsubishi-Hitachi can achieve stable combustion of fuel mix with 30% hydrogen blending ratio, and CO_2 emissions can be reduced by 10%, and NO_x emissions are within the specified range. Kahraman et al. [4] analyzed the temperature distribution, combustion efficiency, pressure drop and velocity variation of a gas turbine combustor using pure hydrogen and aviation kerosene as fuels at different heat flows, and hydrogen has some advantages in terms of combustion efficiency, pressure drop and temperature, but it is not favorable for NO_x control at high excess air coefficients. Cui Yaoxin et al. [5] carried out the evaluation of the adaptability to high hydrogen fuel under full temperature, pressure, and flow rate test conditions for an F-class heavy-duty gas turbine combustor and found that safe and stable combustion could be achieved with fuel hydrogen volume fraction within 20% and meet the emission requirements. Cappelletti et al. [6] used a new axial cyclone and co-flow injection system to improve the combustor, and by The control of premixing degree and flow rate can achieve burner control for pure hydrogen fuel. Mustafa et al. [2] numerically solved the conservation equation and reaction equation of turbulent diffusion flame using finite volume method and found that air classification produces a dense and light combustion region which can reduce NO_x generation. The fuel variation will have an important impact on the operation of gas turbine systems, and the study of the system operating characteristics is the key to evaluate the unit performance. Yildiz et al. [7] conducted a study on the performance, fuel cost and emission parameters of a simple cycle and reheat cycle gas turbine fueled by natural gas and hydrogen, and found that the thermal efficiency and the diesel efficiency of the gas turbine when burning hydrogen fuel were higher than those of natural gas fuels. To further improve the performance of the units, Gaeta et al. [8] developed a kinetic model of a micro gas turbine fueled by a mixture of natural gas and hydrogen, and the results showed that the fossil fuel savings ranged from 37.5% to 41.5%. Meziane et al. [9] conducted a numerical study of the performance of a micro gas turbine using a mixture of natural gas and hydrogen and found that at 10% to 90% of hydrogen, and that the use of a higher percentage of hydrogen minimizes the specific fuel consumption of the combustion process.

In this paper, a modular modeling method is used to establish a prognostic model for the variable operating conditions of gas turbine, and the operating characteristics and energy consumption of each component of the gas turbine under full load and partial load are calculated and analyzed at hydrogen blending ratios of 0 to 100%.

2 Gas Turbine Variable Operating Conditions Modeling

In this study, a modular modeling method is used to establish the variable operating conditions model of gas turbine, firstly, the variable operating conditions model of compressor, combustion chamber and turbine is constructed, and the coupling matching relationship between the components is considered, and the matching of the operating

conditions points between the components is realized by the method of parameter transfer, and finally the model of each module is integrated with the load regulation strategy of the unit to form the variable operating conditions calculation model of gas turbine (Fig. 1).

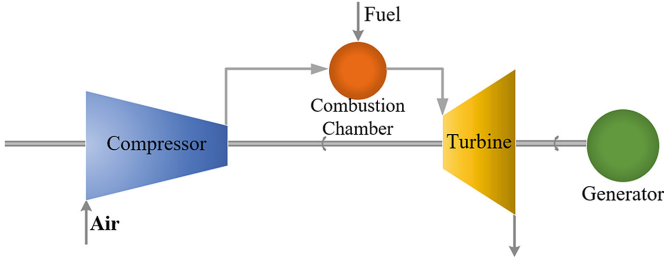


Fig. 1. Schematic diagram of gas turbine structure

2.1 Calculation Model of Multi-stage Axial Flow Compressor with Variable Working Conditions

The compressor variable condition model is built by the step-by-step superposition method, which means that the export parameters of the upper stage are used as the inlet parameters of the next stage in the modeling process and calculated backward step by step.

The modeling process of the compressor is introduced using the first stage of the compressor as an example.

Pressure ratio of the 1st stage:

$$\pi_1 = \frac{p_2^*}{p_1^*} = \left(1 + \frac{\psi_1 u_{sl}^2}{c_p T_{sl}^*} \right)^{\frac{\gamma}{\gamma-1}} \quad (1)$$

Temperature ratio of the 1st stage:

$$\tau_1 = \frac{T_2^*}{T_1^*} = 1 + \frac{\Delta h_1}{c_p \eta_1 T_{sl}^*} = 1 + \frac{\psi_1 u_{sl}^2}{c_p \eta_1 T_{sl}^*} \quad (2)$$

where p_1^* is the inlet stagnation pressure, Pa; p_2^* is the outlet stagnation pressure, Pa; ψ is the level pressure head coefficient; c_p is the specific fixed pressure heat capacity, kJ/(kg K); u_{sl} is the standard sea level circular velocity, m/s; T_{sl}^* is the standard sea level ambient stagnation temperature, K; γ is the air adiabatic index; T_1^* is the level inlet stagnation temperature, K; T_2^* is the level outlet stagnation temperature, K; Δh_1 is the level air enthalpy rise, kJ/kg; η is the level isentropic efficiency.

Using the inlet parameters and the stage pressure ratio, the pressure parameters at the outlet of the first stage compressor can be obtained, and using the inlet parameters and the stage temperature ratio, the temperature of the air at the outlet of the first stage compressor can be obtained. And so on, by calculating step by step backward, we can obtain the

inlet and outlet parameters of each stage, the state parameters of pumping/bleeding of each stage and the characteristic parameters of the whole machine.

Compressor pressure ratio:

$$\pi_C = \prod_{i=1}^z \pi_i \quad (3)$$

Compressor temperature ratio:

$$\tau_C = \prod_{i=1}^z \tau_i \quad (4)$$

Compressor efficiency:

$$\eta_C = \frac{\pi_C^{\frac{\gamma-1}{\gamma}} - 1}{\tau_C - 1} \quad (5)$$

where π_i is Pressure ratio of the i th stage; τ_i is the temperature ratio of the i th stage; Z is the number of compressor stages.

When the inlet adjustable guide vane (IGV) is used to regulate the compressor, assuming that the rotor inlet angle is equal under different working conditions, the flow coefficient and the absolute airflow angle of the blade outlet are related as follows [10]:

$$d\left(\frac{1}{\varphi}\right) = d(\tan \alpha) \quad (6)$$

where φ is the flow coefficient; α is the absolute outlet airflow angle.

Assuming that the relative outlet angle of the moving vane and the stage efficiency are only functions of the inlet angle of the moving vane, the relationship between the pressure coefficient and the flow coefficient can be obtained according to the velocity triangle [11]:

$$\frac{\psi}{\varphi} = \text{constant} \quad (7)$$

2.2 Calculation Model of Multi-stage Axial Flow Compressor with Variable Working Conditions

Gas is a complex mixture, and changes in fuel components, changes in air humidity, and changes in air–fuel ratio can affect the composition of gas, so the calculation of gas properties is very complex. The combustion chamber properties are calculated using the gas properties calculation method proposed in the literature [12]. Once the air parameters and fuel parameters entering the combustion chamber and the efficiency of the combustion chamber are determined, the gas parameters at the exit of the combustion chamber can be obtained using the energy conservation equation and the gas properties calculation method of Ref. [16].

Energy conservation equation for the combustion process in the combustion chamber [13]:

$$(h_{g, t_3} - h_{g, t_0})(1 + \alpha L_0) = (h_{\text{fuel}, t_2} - h_{\text{fuel}, t_0}) + \alpha L_0(h_{\text{air}, t_2} - h_{\text{air}, t_0}) + LHV \eta_{cc} \quad (8)$$

where h is the specific enthalpy of the working mass, kJ/kg; α is the excess air coefficient; LHV is the low level heat of the fuel, kJ/kg; η_{cc} is the combustion chamber efficiency. Subscript: g means the gas; fuel means the fuel; air means the air; t_0 means the reference temperature, K; t_2 means the combustion chamber inlet temperature, K; t_3 means the combustion chamber outlet temperature, K; L_0 is the theoretical air volume, kg/kg.

2.3 Axial Flow Turbine Variable Working Condition Calculation Model

A continuity equation system constructed based on aerodynamic functions is used to establish the calculation model of the variable operating conditions of the axial flow turbine, and a bottom-up step-by-step calculation method [14] is used to calculate from the turbine outlet step by step forward, so as to obtain the characteristic parameters and gas state parameters of the turbine stages, and the calculation process takes into account the influence on the mainstream temperature and pressure when the cooling air converges into the mainstream during the blade cooling process.

The mass equation of each section is established based on the primitive level model using the work mass flow rate, airflow angle, through-flow area and density of each section as follows:

$$\begin{cases} G_{1-1}^{(i)} = c_2^{(i-1)} A_{1-1}^{(i)} \sin \alpha_2^{(i-1)} \rho_{1-1}^{(i)} \\ G_{2-2}^{(i)} = c_1^{(i)} A_{2-2}^{(i)} \sin \alpha_1^{(i)} \rho_{2-2}^{(i)} \\ G_{3-3}^{(i)} = w_1^{(i)} A_{3-3}^{(i)} \sin \beta_1^{(i)} \rho_{3-3}^{(i)} \\ G_{4-4}^{(i)} = w_2^{(i)} A_{4-4}^{(i)} \sin \beta_2^{(i)} \rho_{4-4}^{(i)} \\ G_{5-5}^{(i)} = c_2^{(i)} A_{5-5}^{(i)} \sin \alpha_2^{(i)} \rho_{5-5}^{(i)} \end{cases} \quad (9)$$

where G is the mass flow rate of the work mass, kg/s; α is the absolute airflow angle, ($^\circ$); A is the through-flow area, m^2 ; ρ is the density of the work mass, kg/m^3 ; c is the absolute velocity of airflow, m/s; w is the relative velocity of airflow, m/s; β is the relative airflow angle, ($^\circ$); Subscript: 1 means the static lobe, 2 means the dynamic lobe, 1–1 means the static lobe inlet, 2–2 means the static lobe outlet, 3–3 means the dynamic lobe inlet, 4–4 means the dynamic lobe outlet, 5–5th means the level outlet, i means the i th stage.

Introduction of pneumatic functions:

$$q(\lambda) = \lambda \left(\frac{\gamma+1}{2} \right)^{\frac{1}{\gamma-1}} \left(1 - \frac{\gamma-1}{\gamma+1} \lambda^2 \right)^{\frac{1}{\gamma-1}} \quad (10)$$

where λ is the folded velocity.

As the static and dynamic leaves have cooling air into the mainstream, the introduction of cooling air coefficient θ , the use of Eq. (9) can be obtained for each cross-section

continuity equation system, simplified to obtain:

$$\left\{ \begin{array}{l} \theta_2^{(i-1)} m_{1-1}^{(i)} A_{1-1}^{(i)} \sin \alpha_2^{(i-1)} q(\lambda_{c_2^{(i-1)}}) = \\ m_{2-2}^{(i)} A_{2-2}^{(i)} \sin \alpha_1^{(i)} q(\lambda_{c_1^{(i)}}) \pi \left(\frac{\lambda_{c_1^{(i)}}}{\varphi^{(i)}} \right) / \pi (\lambda_{c_1^{(i)}}) \\ \theta_1^{(i)} m_{2-2}^{(i)} A_{2-2}^{(i)} \sin \alpha_1^{(i)} q(\lambda_{c_1^{(i)}}) \sqrt{\tau(\lambda_{c_1^{(i)}})} / \pi (\lambda_{c_1^{(i)}}) = \\ m_{3-3}^{(i)} A_{3-3}^{(i)} \sin \beta_1^{(i)} q(\lambda_{w_1^{(i)}}) \sqrt{\tau(\lambda_{w_1^{(i)}})} / \pi (\lambda_{w_1^{(i)}}) \\ m_{3-3}^{(i)} A_{3-3}^{(i)} \sin \beta_1^{(i)} q(\lambda_{w_1^{(i)}}) = \\ m_{4-4}^{(i)} A_{4-4}^{(i)} \sin \beta_2^{(i)} q(\lambda_{w_2^{(i)}}) \pi \left(\frac{\lambda_{w_2^{(i)}}}{\psi^{(i)}} \right) / \pi (\lambda_{w_2^{(i)}}) \\ m_{4-4}^{(i)} A_{4-4}^{(i)} \sin \beta_2^{(i)} q(\lambda_{w_2^{(i)}}) \sqrt{\tau(\lambda_{w_2^{(i)}})} / \pi (\lambda_{w_2^{(i)}}) = \\ m_{5-5}^{(i)} A_{5-5}^{(i)} \sin \alpha_2^{(i)} q(\lambda_{c_2^{(i)}}) \sqrt{\tau(\lambda_{c_2^{(i)}})} / \pi (\lambda_{c_2^{(i)}}) \end{array} \right. \quad (11)$$

where $\varphi^{(i)}$ is the i th stage static lobe velocity coefficient; $\psi^{(i)}$ is the i th stage dynamic lobe velocity coefficient.

By introducing the aerodynamic function, the continuity equation can be simplified to a function of the folding velocity between adjacent sections, so that the mathematical relationship between the inlet and outlet of the turbine base element level can be established. After obtaining the folding velocity of the outlet section, the folding velocity values of the intermediate sections and the inlet section can be found forward. Using the folded velocity of each section, the temperature ratio, pressure ratio, isentropic efficiency, power, and flow rate of the turbine base element stage can be obtained.

2.4 Unit Performance Evaluation Index

Gas turbine power generation:

$$W_{GT} = (W_T - W_C) \eta_{mgt} \eta_{GEN} \quad (12)$$

where η_{mgt} is the mechanical efficiency; η_{GEN} is the generator efficiency; W_T is the turbine power, kW; W_C is the compressor power, kW.

Gas turbine power generation efficiency:

$$\eta_{GT} = \frac{W_{GT}}{m_{fuel} LHV} \quad (13)$$

where m_{fuel} is the mass flow rate of fuel, kg/s.

Gas turbine specific power:

$$w_{GT} = \frac{W_{GT}}{m_{air} \eta_{GEN}} \quad (14)$$

where m_{air} is the mass flow rate of air, kg/s.

3 Results and Discussions

3.1 Model Validation

The accuracy of the model was verified by selecting the design data of the unit at 100%, 75%, and 50% load with natural gas as fuel under ISO conditions (ambient temperature of 15 °C, atmospheric pressure of 101.3 kPa, and relative humidity of 60%), and the calculation error of the model was kept within $\pm 1.7\%$ at 50% and above load conditions, which can meet the calculation requirements. A comparison of the data is shown in Table 1.

Table 1. Validation of model accuracy

| Description | Load rate/% | Design condition | Actual value | Error/% |
|------------------------------------|-------------|------------------|--------------|---------|
| Air mass flow/kg·s ⁻¹ | 100 | 675.64 | 673.57 | - 0.31 |
| Fuel mass flow/kg·s ⁻¹ | 100 | 15.50 | 15.38 | - 0.77 |
| Gas turbine exhaust temperature/°C | 100 | 575.50 | 575.47 | - 0.01 |
| Gas turbine power/MW | 100 | 282.52 | 280.05 | - 0.87 |
| Air mass flow/kg·s ⁻¹ | 75 | 553.76 | 555.41 | 0.30 |
| Fuel mass flow/kg·s ⁻¹ | 75 | 12.36 | 12.25 | - 0.89 |
| Gas turbine exhaust temperature/°C | 75 | 575.50 | 575.56 | 0.01 |
| Gas turbine power/MW | 75 | 211.90 | 210.16 | - 0.82 |
| Air mass flow/kg·s ⁻¹ | 50 | 448.38 | 453.19 | 1.07 |
| Fuel mass flow/kg·s ⁻¹ | 50 | 9.44 | 9.28 | - 1.69 |
| Gas turbine exhaust temperature/°C | 50 | 575.50 | 575.77 | 0.05 |
| Gas turbine power/MW | 50 | 141.27 | 140.32 | - 0.67 |

The natural gas components selected for the calculation are shown in Table 2, and the low level heat of natural gas is 34.8161 MJ/m³. In this paper, the operating characteristics of the gas turbine with different hydrogen blending ratios are studied and analyzed at an ambient temperature of 15 °C, an atmospheric pressure of 94.30 kPa and an atmospheric relative humidity of 27%.

3.2 Effect of Hydrogen Blending Ratio on the Full-Load Operating Characteristics of Gas Turbines

The operating characteristics of the gas turbine at the hydrogen doping ratio of 0 ~ 100% are calculated under the environmental parameters mentioned earlier, and the basic assumptions for the performance calculation and analysis of the gas turbine at full load are as follows:

- (1) The initial temperature of the unit's gas at full load operating conditions remains the same as the unit's design value under different hydrogen volume fractions;

Table 2 Natural gas components for calculation

| Composition | Volume fraction/% |
|----------------|-------------------|
| Methane | 91.7291 |
| Ethane | 4.8204 |
| Propane | 1.0798 |
| Isobutane | 0.1115 |
| N-butane | 0.1157 |
| Isopentane | 0.0241 |
| Pentane | 0.0186 |
| Hexane | 0.0419 |
| Nitrogen | 1.3983 |
| Carbon dioxide | 0.6606 |

- (2) The combustion chamber efficiency at full load is consistent with the design value when the volume fraction of hydrogen varies;
- (3) When the volume fraction of hydrogen varies, the IGV is fully opened under full load conditions;

The direct effect of the change of hydrogen volume fraction is the change of fuel calorific value and gas composition. At 100% load the turbine inlet gas temperature remains constant, the increase of hydrogen volume fraction leads to the increase of heat released per unit mass of fuel, the fuel consumption decreases with the same turbine inlet gas initial temperature, the decrease of fuel mass flow rate and the increase of water vapor volume fraction in gas will affect the flow rate of turbine and compressor, changing the operating characteristics and parameter matching relationship between them.

As shown in Fig. 2, as the volume fraction of hydrogen increases, the pressurizer operating point moves up along the isochrones, the pressurizer inlet air flow decreases slightly, and the pressure ratio increases. The advantage of the increase in the volume fraction of hydrogen in the fuel compared to the pure natural gas fueled condition is the increase in the turbine expansion ratio (P_{in}/P_{out}) for a constant exhaust pressure.

As shown in Fig. 3, in the enthalpy entropy diagram of the turbine thermodynamic process, as the volume fraction of hydrogen increases, the turbine inlet state point shifts upward, and at a constant turbine inlet temperature, the increase in the expansion ratio lowers the turbine exhaust temperature, and the effective specific enthalpy drop of the mass in the turbine increases, and the higher the volume fraction of hydrogen, the higher the effective specific enthalpy drop of the turbine with the increase in the volume fraction of hydrogen. The enthalpy drop of gas in the turbine increases and the power of the unit increases, but the operating safety of the compressor is reduced because the operating point of the compressor moves upward and the surge margin of the compressor decreases, so the hydrogen-rich gas turbine should pay more attention to the problem of compressor surge.

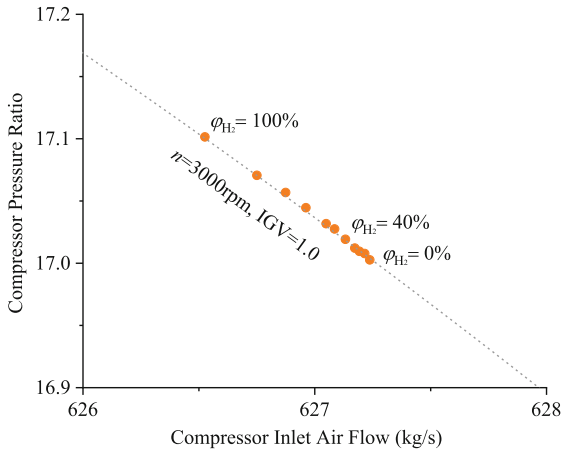


Fig. 2. Variation of compressor operating points with hydrogen volume fraction

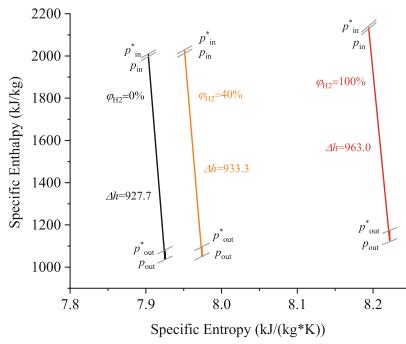


Fig. 3. Enthalpy entropy diagram of turbine thermodynamic process

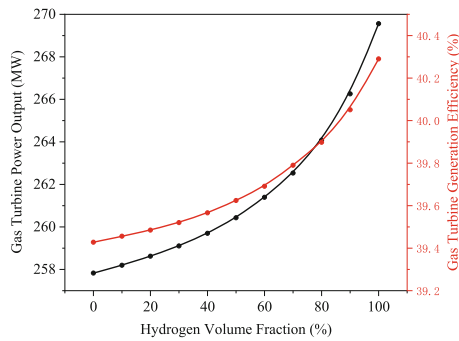


Fig. 4. Variation of gas turbine power output and efficiency with hydrogen volume fraction

Without considering the cost of hydrogen production, as shown in Fig. 4, the power and power generation efficiency of the gas turbine with the blended combustion of

hydrogen and natural gas both increase with the increase of the volume fraction of hydrogen, and both are more sensitive to the change of the volume fraction of hydrogen at high hydrogen volume fraction, and the increasing trend is more obvious.

Due to the higher energy grade of hydrogen, the heat efficiency of the unit decreases when the blending ratio of hydrogen in the fuel increases, and the heat flow diagrams of the unit at 100% load with 0%, 20%, 40% and 100% blending ratio of hydrogen in the fuel for a given environmental parameter are shown in Figs. 5, 6, 7 and 8 respectively. As the hydrogen blending ratio increases, the heat dissipation of fuel input increases significantly, and the heat dissipation of combustion chamber and turbine increases, and the heat dissipation of turbine exhaust decreases due to the increase of specific enthalpy drop of mass in turbine.

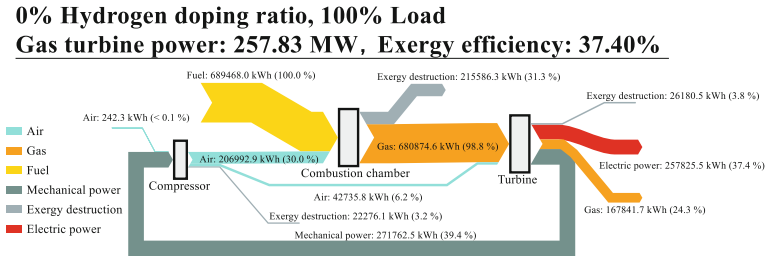


Fig. 5. Exergy flow diagram when hydrogen doping ratio is 0% under full load

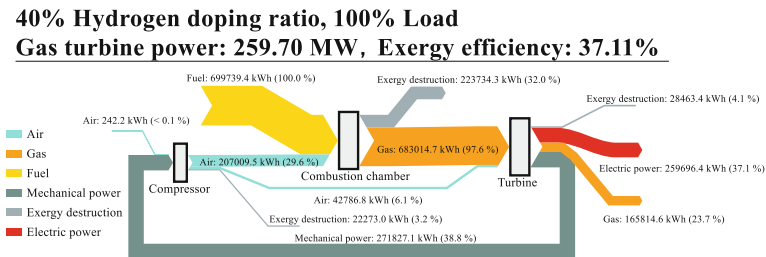


Fig. 6. Exergy flow diagram when hydrogen doping ratio is 20% under full load

3.3 Overall Operating Characteristics of Gas Turbine Under Partial Load

In order to explore the operating performance of the hydrogen-rich gas turbine at partial load, the operating characteristics of the gas turbine at 63% 100% load with hydrogen volume fraction in the range of 0 to 100% were calculated and analyzed under the environmental parameters mentioned in the previous section. In the analysis of the operating performance of the gas turbine unit under variable operating conditions, the exhaust temperature (TET) of the turbine at partial load is kept consistent with the exhaust temperature of the turbine at full load operating conditions of the unit at the corresponding hydrogen volume ratio. The equal TET regulation strategy with IGV control at partial

20% Hydrogen doping ratio, 100% Load
Gas turbine power: 258.62 MW, Exergy efficiency: 37.28%

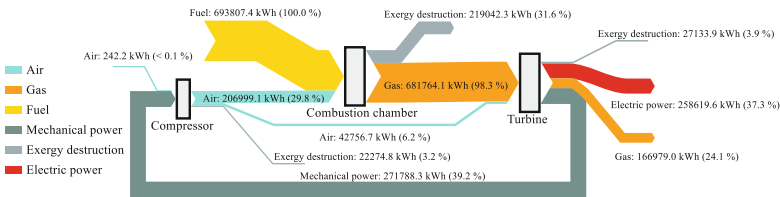


Fig. 7. Exergy flow diagram when hydrogen doping ratio is 40% under full load

100% Hydrogen doping ratio, 100% Load
Gas turbine power: 269.56 MW, Exergy efficiency: 35.75%

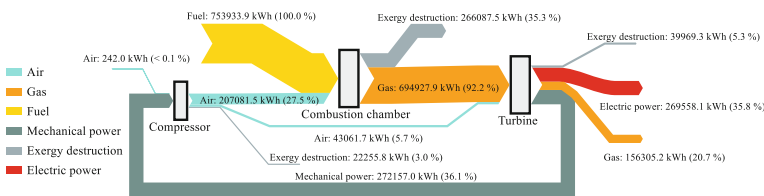


Fig. 8. Exergy flow diagram when hydrogen doping ratio is 100% under full load

load gradually decreases the compressor inlet air flow and turbine inlet air temperature as the unit load decreases.

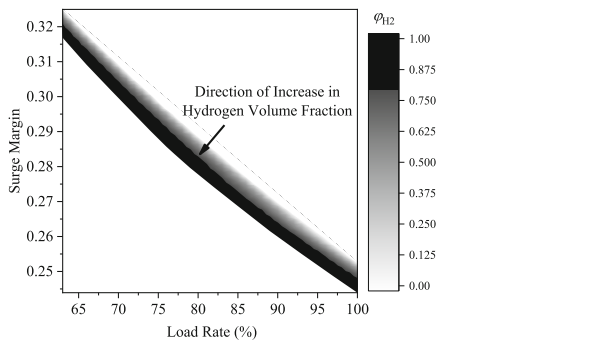


Fig. 9. Variation of compressor surge margin with gas turbine load rate

As shown in Fig. 9, the effect of hydrogen volume fraction on compressor operation is largely gradual as the unit load decreases, the compressor operating point is closer to the snub line, and the safety margin decreases.

The effect pattern of the change of hydrogen volume fraction on the unit performance at partial load is basically the same as that at full load, but the magnitude of the effect changes. As shown in the Fig. 10, in general, increasing the volume fraction of hydrogen in the fuel can improve the power generation efficiency of the unit, but the

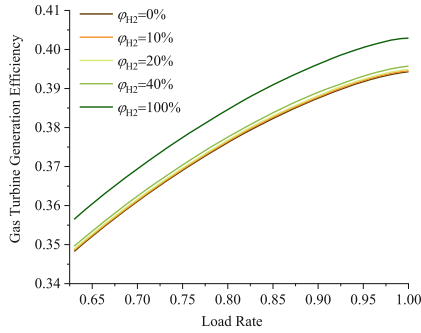


Fig. 10. Variation of compressor surge margin with gas turbine load rate

power generation efficiency of the gas turbine tends to decrease at an accelerated rate with decreasing load. From the perspective of the same load rate, increasing the volume fraction of hydrogen in the fuel can improve the power generation efficiency of the unit, but the effect of improving the power generation efficiency with decreasing load is slightly weakened.

Figures 11, 12, 13 and 14 shown the heat and power flow diagrams of the unit at 70% load with 0%, 20%, 40% and 100% hydrogen blending ratio in fuel under given environment parameters. At 70% load, the effect of the hydrogen blending ratio on the fuel input radiation, the radiation loss of each key component and the turbine exhaust radiation is the same. Comparing with Figs. 5, 6, 7 and 8, it can be seen that as the load of the unit decreases, the fuel input dissipation, the dissipation loss of key components and the turbine exhaust dissipation all tend to decrease.

0% Hydrogen doping ratio, 70% Load

Gas turbine power: 180.53 MW, Exergy efficiency: 34.25%

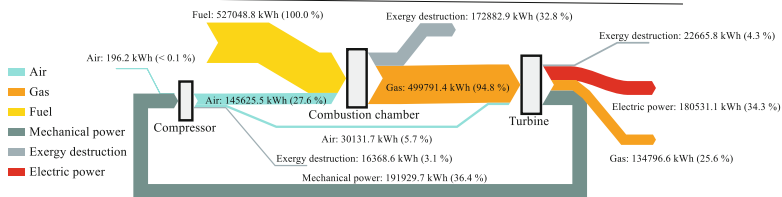


Fig. 11. Exergy flow diagram when hydrogen doping ratio is 0% under 70% load

20% Hydrogen doping ratio, 70% Load
Gas turbine power: 181.02 MW, Exergy efficiency: 34.14%

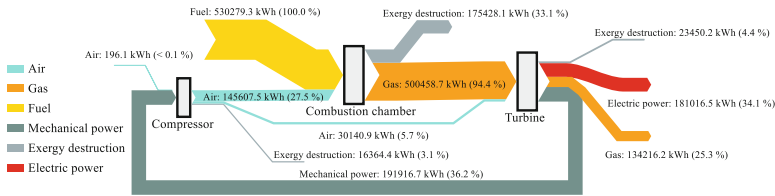


Fig. 12. Exergy flow diagram when hydrogen doping ratio is 20% under 70% load

40% Hydrogen doping ratio, 70% Load
Gas turbine power: 181.83 MW, Exergy efficiency: 34.00%

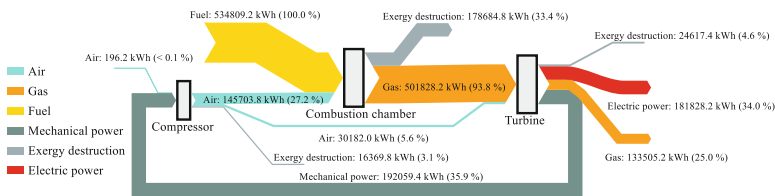


Fig. 13. Exergy flow diagram when hydrogen doping ratio is 40% under 70% load

0% Hydrogen doping ratio, 70% Load
Gas turbine power: 188.70 MW, Exergy efficiency: 32.79%

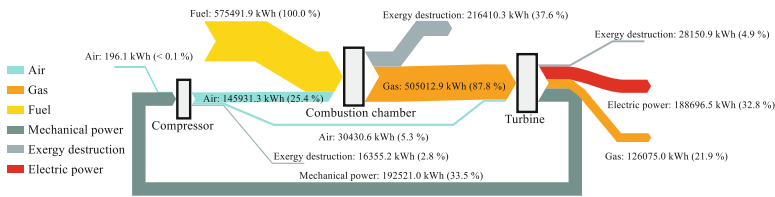


Fig. 14. Exergy flow diagram when hydrogen doping ratio is 100% under 70% load

4 Conclusion

In this study, a variable condition model was built based on an F-class gas turbine. We calculated and analyzed the influence of hydrogen doping ratio on the operating characteristics of key components and the energy consumption characteristics of the unit under full/partial load. Under full load condition, the results show that with the increase of hydrogen doping ratio, the operating point of the compressor moves up along the constant speed line, the surge margin of the compressor decreases, and the operation safety of the compressor decreases. The gas turbine power and power generation efficiency increase with the hydrogen volume fraction rise up, and this trend is more obvious when the hydrogen volume fraction is higher. Under partial load condition, the influence of hydrogen volume fraction on unit performance under partial load is basically the same as that under full load, but the magnitude of the influence changes. As the load

decreases, the influence of hydrogen volume fraction on the compressor pressure ratio gradually increases, the compressor operating point is closer to the surge line, and the safety margin is reduced. Therefore, when increasing the proportion of hydrogen in the fuel, more attention should be paid to the safety of the unit operating under partial load.

References

1. Zhang, S., Ma, B.: development trend of world energy and future development directions of China's energy. *Nat. Resour. Econ. China* **32**(10), 20–27+33 (2019)
2. Ilbas, M., Yılmaz, L., Veziroglu, T.N., et al.: Hydrogen as burner fuel: modelling of hydrogen–hydrocarbon composite fuel combustion and NO_x formation in a small burner. *Int. J. Energy Res.* **29**(11), 973–990 (2010)
3. Funke, H.H.-W., Beckmann, N., Abanteriba, S.: An overview on dry low NO_x micromix combustor development for hydrogen-rich gas turbine applications. *Int. J. Hydrogen Energy* **44**(13), 6978–6990 (2019)
4. Kahraman, N., Tangöz, S., Akansu, S.O.: Numerical analysis of a gas turbine combustor fuelled with hydrogen in comparison with jet-A fuel. *Fuel* **217**, 66–77 (2018)
5. Yaoxin, Cui, Xiaopei, Liu, Mingmin, Chen: Experimental study of natural gas mixed with hydrogen under full pressure of f-class heavy duty gas turbine burner. *Gas Turbine Technol.* **34**(02), 38–42 (2021)
6. Cappelletti, A., Martelli, F.: Investigation of a pure hydrogen fueled gas turbine burner. *Int J Hydrogen Energy* **42**(15), 10513–10523 (2017)
7. Koç, Y., Yağlı, H., Görgülü, A., et al.: Analysing the performance, fuel cost and emission parameters of the 50 MW simple and recuperative gas turbine cycles using natural gas and hydrogen as fuel. *Int J Hydrogen Energy* **45**(41), 22138–22147 (2020)
8. di Gaeta, A., Reale, F., Chiariello, F., et al.: A dynamic model of a 100 kW micro gas turbine fuelled with natural gas and hydrogen blends and its application in a hybrid energy grid. *Energy* **129**, 299–320 (2017)
9. Meziane, S., Bentebbiche, A.: Numerical study of blended fuel natural gas-hydrogen combustion in rich/quench/lean combustor of a micro gas turbine. *Int J Hydrogen Energy* **44**(29), 15610–15621 (2019)
10. Stone, A.: Effects of stage characteristics and matching on axial-flow-compressor performance. *Trans. ASME* **80**, 1273–1293 (1958)
11. Song, T.W., Kim, T.S., Kim, J.H., et al.: Performance prediction of axial flow compressors using stage characteristics and simultaneous calculation of interstage parameters. *Proc. Inst. Mech. Eng. Part A J. Power Energy* **215**(1), 89–98 (2001)
12. Zhang, S.Z.: Polynomial expressions of thermodynamic properties of the products of combustion of fuel with air. *J. Eng. Thermophys.* **1**, 10–16 (1980)
13. Qiusheng, D.: Analysis theory and calculation of thermal performance of gas-steam combined cycle power station. Tsinghua University Press (2010)
14. Xin, J., Zhong, F.: Gas turbine design fundament. Shanghai Jiaotong University Press (2015)



Modeling of a Stand-Alone Microgrid Based on Solar-Hydrogen Energy Systems for the Design of Energy Management Systems

Zhipeng Hou¹ , Fengxiang Chen² , Yafeng Guo¹, Tiande Mo³, Yu Li³, and Fenglai Pei⁴

¹ Department of Control Science and Engineering, Tongji University, Shanghai 201804, China

² School of Automotive Studies, Tongji University, Shanghai 201804, China
fxchen@tongji.edu.cn

³ Smart City Division, Hong Kong Productivity Council, Hong Kong 999077, China

⁴ Shanghai Motor Vehicle Inspection Certification & Tech Innovation Center Co. Ltd., Shanghai 201805, China

Abstract. The high penetration of intermittent renewable energy sources in the distribution generations has necessitated a substantial demand for energy storage systems. A solar-hydrogen microgrid emerges as an enticing solution for establishing a sustainable energy supply. The proposed microgrid consists of five primary components: a photovoltaic (PV) panel, an electrolyzer, a hydrogen storage tank, a fuel cell, and a battery. After specifying the purpose of energy management (EMS), models for each component of the system are established to design the EMS. For the PV panel, a one-diode model is constructed, incorporating the maximum power point tracking (MPPT) algorithm. An empirical relationship is proposed to describe the characteristics of the alkaline electrolyzer. Fuel cells are modeled with mechanistic and empirical equations. A relatively quasi-static model is used to simulate the battery. All components are aggregated into a system model in MATLAB/Simulink environment. Simulations have been conducted to demonstrate that the proposed model is suitable for long-duration simulations and accurately captures the behavior of the system.

Keywords: Solar-hydrogen microgrid · Hydrogen storage system · Battery · Modeling and simulation

1 Introduction

As the share of intermittent renewable energy in distributed generation increases, the significance of energy storage systems is becoming increasingly pronounced. Hydrogen storage has the advantages of high energy density and long storage duration. Although its drawbacks include low energy conversion efficiency and slower response time, working with batteries can be a good solution to this problem. A renewable energy system with energy storage can be regarded as a microgrid system, which can be utilized to meet load requirements [1]. The energy management system (EMS) plays a crucial role in

ensuring a microgrid's economic and reliable operation. There is no universal approach to designing an appropriate energy management strategy, as it depends on the microgrid system and the objectives of EMS. In [2], there are roughly four types of modeling approaches: Component-wise modeling, lumped entity modeling, stochastic modeling and dynamic equivalence modeling.

This paper employs the component-wise modeling approach. The related works are as follow. Ulleberg O introduced and evaluated various models for each component in a solar-hydrogen energy system [3]. Wang C presented a model for hybrid wind/photovoltaic/fuel cell distributed generation systems [4]. Moreover, Valverde L conducted modeling and analysis of the microgrid components, and based on this foundation, designs an energy management strategy [5].

To design an effective EMS, this paper models the primary components of the microgrid system and then aggregates them into a system model. The remaining sections are organized as follows. Section 2 will present the description of the proposed microgrid. The models and simulation results of each component of the system will be presented in Sect. 3. Finally, the conclusion will be offered in Sect. 4.

2 Stand-Alone Microgrid System

The overall configuration of the stand-alone microgrid based on a solar-hydrogen energy system is shown in Fig. 1. It is composed of a photovoltaic (PV) panel, a hydrogen storage system, and a battery. The hydrogen storage system commonly consists of an electrolyzer, a fuel cell, and a hydrogen storage tank. The main characteristics of system components are listed in Table 1. In the microgrid system, the PV serves as the primary energy source to meet the load demands. During periods of sufficient solar radiation, excess power can be stored as hydrogen by the electrolyzer and into the battery. In situations where PV power is inadequate, the fuel cell and battery can serve as backup generators to supplement load demands.

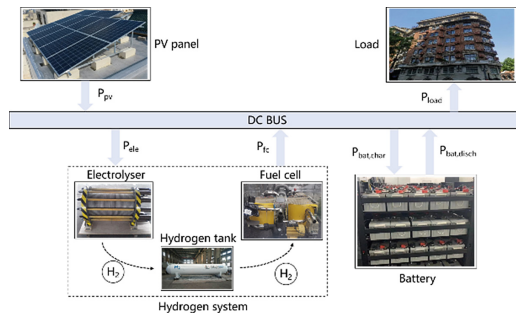


Fig. 1. A stand-alone microgrid based on a solar-hydrogen energy system

Table 1. The main characteristics of system components

| | | | | | |
|-------------------------------------|-------|---|-----|-----------------------------|------|
| Photovoltaic module | | PEM electrolyzer | | | |
| Rated power/kW | 0.15 | H ₂ production nominal rate/Nm ³ /h | 10 | | |
| Peak power voltage/V | 34 | Rated power/kW | 46 | | |
| Peak power current/A | 4.4 | Anode and cathode pressure/bar | 35 | | |
| Open circuit voltage/V | 43.4 | Cell active surface/cm ² | 290 | | |
| Short circuit current/A | 4.8 | Series-connected cells | 60 | | |
| PEM fuel cell | | Hydrogen storage tank | | Lead-acid battery | |
| Rated power/kW | 113 | Maximum operation pressure/bar | 150 | Nominal battery capacity/Ah | 1380 |
| Rated power voltage/V | 236.9 | Volume/m ³ | 15 | Nominal battery voltage/V | 220 |
| Rated power current/A | 477 | Number | 1 | Series-connected cells | 110 |
| Cell active surface/cm ² | 298 | | | | |
| Series-connected cells | 370 | | | | |

3 Modeling and Simulation

3.1 Photovoltaic System

A PV system can convert solar energy into electrical energy by using the photovoltaic effect, and it is typically characterized using the one-diode model [6]. The one-diode model can be applied to model a PV cell, or a module containing multiple cells, or an array containing several modules. The equivalent circuit for the model is depicted in Fig. 2, and is used to represent the characteristics of a PV module.

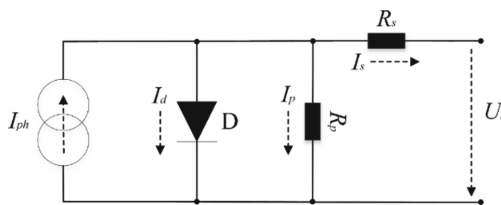


Fig. 2. The equivalent circuit for the one-diode PV module model

The relationship between the operating voltage U_s and the current I_s of the PV module can be expressed as:

$$I_s = I_{ph} - I_d - I_p = I_{ph} - I_{sat} \times \left[\exp\left(\frac{U_s + R_s I_s}{a_s}\right) - 1 \right] - \frac{U_s \times I_s R_s}{R_p} \quad (1)$$

where I_{ph} is the photocurrent, I_{sat} is diode reverse saturation current, R_s and R_p are series resistance and parallel resistance, respectively, a_s is the voltage equivalent of temperature. The parallel resistance R_p can be assumed to be infinitely large compared to the series resistance R_s . The other four parameters depend mainly on the irradiance and the PV module temperature [5] and can be calculated by using data from the PV module manufacturer [7].

According to the given irradiation and temperature conditions, the maximum power point tracking (MPPT) algorithm is responsible for dynamically adjusting the operating voltage or current of the photovoltaic (PV) system to ensure it operates at the maximum power point. Therefore, the output power of the photovoltaic (PV) system is independent of the EMS. [8]. The maximum output power P_{pv} of the PV array with several PV modules is described as follows.

$$P_{pv} = U_{mpp} \cdot N_s \times I_{mpp} \cdot N_p \quad (2)$$

where N_s and N_p are the number of parallel and series PV modules, respectively, U_{mpp} and I_{mpp} represent the operating voltage and operating current corresponding to the maximum power point, respectively. The effects of various irradiances and cell temperatures on the I/V characteristic of the PV module are illustrated in Fig. 3.

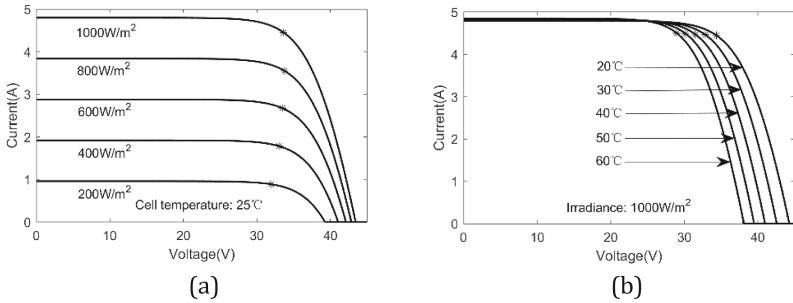


Fig. 3. The I/V characteristic of the PV module. (a) The irradiance effect, (b) the cell temperature effect.

3.2 Hydrogen Storage System

The hydrogen storage system commonly consists of an electrolyzer, a fuel cell, and a hydrogen storage tank. When there is an excess electricity from renewable energy, the system converts it into hydrogen via the electrolyzer. Conversely, the system provides the required power through the fuel cell.

PEM water electrolyzer. an electrolyzer is a device that can convert the electric energy into hydrogen energy through water electrolysis. Proton exchange membrane water electrolyzers (PEMWEs) have demonstrated higher current density capabilities than conventional alkaline water electrolyzers [9]. The empirical current-voltage relationship for an electrolyzer is adopted here.

$$V_{ele} = n_{ele,c} \times (E_{rev} + \frac{r_1 + r_2 T_{ele}}{A_{ele}} I_{ele} + s \ln(\frac{t_1 + t_2 / T_{ele} + t_3 / T_{ele}^2}{A_{ele}} I_{ele} + 1)) \quad (3)$$

where V_{ele} and I_{ele} are the voltage and current of the electrolyzer stack, respectively, $n_{ele,c}$ is the number of cells in series in the electrolyzer stack, E_{rev} is reversible cell voltage, T_{ele} is the stack temperature of the electrolyzer, assumed to be constant values, A_{ele} is the area of the electrolyzer cell, r_1 and r_2 are the empirical parameters of ohmic overvoltage, and t_1 , t_2 , t_3 , and s are the empirical parameters of activation overvoltage. According to the experimental data from the literature [10], the empirical parameters can be obtained by the curve fitting method.

According to Faraday's law, the rate of hydrogen gas generation depends on the operating current of the electrolyzer. The molar flow rate of hydrogen generation $\dot{n}_{H_2}^{gen}$ are as follows.

$$\dot{n}_{H_2}^{gen} = \frac{\eta_{ele,F} \times I_{ele} \times n_{ele,c}}{2F} \quad (4)$$

where, $\eta_{ele,F}$ is the Faraday efficiency. The performance curve of the PEMWE stack at a given operating temperature and pressure conditions is presented in Fig. 4.

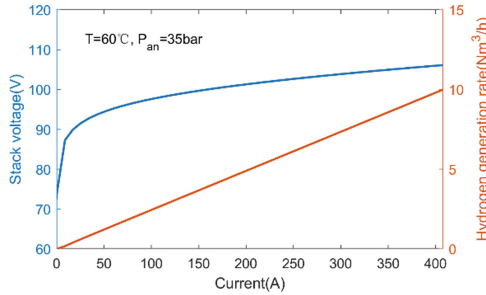


Fig. 4. The performance curve of the PEMWE stack.

PEM fuel cell system. Fuel cell can extract chemical energy from hydrogen into electricity. Proton exchange membrane fuel cells (PEMFCs) are widely acknowledged for their high efficiency, rapid start-up and response times, as well as their compact and lightweight design [11]. The fuel cell stack voltage V_{fc} is modeled as follows.

$$V_{fc} = n_{fc,c} \times (E_{fc} - V_{fc,act} - V_{fc,ohm} - V_{fc,conc}) \quad (5)$$

where $n_{fc,c}$ is the number of cells in the fuel stack, E_{fc} , $V_{fc,act}$, $V_{fc,ohm}$ and $V_{fc,conc}$ are the open-circuit voltage, the activation voltage drop, the ohmic voltage drop, and the

concentrate voltage drop, respectively. Their specific expression are shown below.

$$\left\{ \begin{array}{l} E_{fc} = -\frac{\Delta\hat{g}^0}{2F} + \frac{\Delta\hat{s}^0}{2F}(T_{fc} - T_0) + \frac{RT_{fc}}{2F} \ln(P_{H_2}\sqrt{P_{O_2}}) \\ V_{fc,act} = \frac{RT_{fc}}{2\alpha F} \ln \frac{I_{fc}}{j^0} \times c_{O_2}^0 \\ V_{fc,ohm} = \frac{I_{fc}}{A_{fc}} \frac{t_m}{\sigma_m}, \quad \sigma_m = (0.5139\lambda - 0.326)e^{1268(1/303 - 1/T_{fc})} \\ V_{fc,conc} = \frac{RT_{fc}}{nF} \left(1 + \frac{1}{\alpha}\right) \ln \frac{j_L}{j_L - \frac{I_{fc}}{A_{fc}}}, \quad j_L = 2FD^{eff} \frac{c_{O_2}^0}{\delta_{gdL}} \end{array} \right. \quad (6)$$

where I_{fc} is the fuel cell stack current, T_{fc} , P_{H_2} , P_{O_2} , and c_{O_2} can be calculated according to mass conversation, ideal gas law, mass balance equation, and electrochemical principles [12], The other parameter can be obtained by the manufacturer and curve fitting [13]. The voltage and power of the fuel cell stack at different currents are showed in Fig. 5.

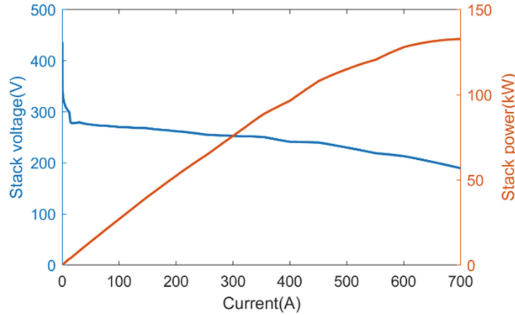


Fig. 5. The voltage and power of the fuel cell stack at different currents

Hydrogen storage tank. High-pressure storage is a commonly used method for storing hydrogen. at high pressures, the ideal gas law fails to accurately describe the gas pressure. The van der waals equation can provides a good description [3], as shown below.

$$P_{H_2}^{tank} = \frac{n_{H_2}^{tank} RT_{H_2}^{tank}}{V_{H_2}^{tank} - n_{H_2}^{tank} b} - a \frac{(n_{H_2}^{tank})^2}{(V_{H_2}^{tank})^2}, \quad (a = \frac{27R^2(T_{cr})^2}{64P_{cr}}, \quad b = \frac{RT_{cr}}{8P_{cr}}) \quad (7)$$

where $P_{H_2}^{tank}$, $V_{H_2}^{tank}$, and $T_{H_2}^{tank}$ are the pressure, volume and temperature of hydrogen in the tank, $n_{H_2}^{tank}$ is the number of moles of hydrogen in the tank, T_{cr} and P_{cr} are the critical temperature and pressure of the hydrogen. The variation of hydrogen in the hydrogen storage tank.

$$\frac{dn_{H_2}^{tank}}{dt} = \dot{n}_{in}^{tank} - \dot{n}_{out}^{tank} \quad (8)$$

where \dot{n}_{in}^{tank} and \dot{n}_{out}^{tank} are the molar flow rates of gas entering and leaving the storage tank, respectively.

3.3 Lead-Acid Battery

Lead-acid battery present a good performance for this kind of application and their low price in comparison to the rest of the battery technologies was a determinant for selecting them for this work [3]. The battery voltage U_{bat} are the sum of the equilibrium voltage U_{equ} and the polarization voltage U_{pol} and the product of the number of battery cells $n_{bat,c}$.

$$U_{bat} = n_{bat,c}(U_{equ} + U_{pol}) = n_{bat,c}\left(U_{equ,0} + U_{equ,1} \frac{SOC}{100} + U_{pol}\right) \quad (9)$$

where SOC is the energy storage state of the battery, $U_{equ,0}$ is the equilibrium cell voltage at $SOC = 0$, $U_{equ,1}$ is the equilibrium cell voltage gradient at $SOC > 0$, U_{pol} is the polarization voltage of the battery, and its expression depends on whether the battery is in a charge or discharge state.

$$\begin{cases} U_{pol,ch} = U_{ch}a_{ch}\left[1 - \exp\left(-\frac{I_{q,norm}}{b_{ch}}\right) + c_{ch}I_{q,norm}\right] & (I_{bat} > 0) \\ U_{pol,disc} = U_{disc}f_{disc}g_{disc} & (I_{bat} < 0) \end{cases} \quad (10)$$

where U_{ch} and U_{disc} are constant, a_{ch} , b_{ch} , and c_{ch} are coefficients that are depend on SOC , f_{disc} and g_{disc} are dimensionless coefficients dependent on $I_{q,norm}$ and SOC , respectively, and $I_{q,norm}$ is expressed as follows.

$$I_{q,norm} = \left| \frac{I_{bat} - I_{gas}}{\frac{Q_{norm}}{10}} \right| = \left| \frac{I_{bat} - \frac{Q_{norm}}{10} g_0 \exp\left(\frac{U_{equ} + U_{pol}}{g_1} - \frac{g_2}{T_{bat}}\right)}{\frac{Q_{norm}}{10}} \right| \quad (11)$$

where Q_{norm} is the nominal battery capacity, g_0 , g_1 , and g_2 are gassing current parameters, T_{bat} is the battery temperature.

The SOC of the battery is as follows:

$$SOC = \frac{Q_{bat}}{Q_{norm}} = \frac{(SOC_{ini}/100)Q_{norm} + \int I_{bat} dt}{Q_{norm}} \quad (12)$$

where SOC_{ini} is the initial SOC of the battery. These above parameters can be obtained from [13]. The I/V profile of the lead-acid battery for SOC in the range 20–100% are shown in Fig. 6.

3.4 Microgrid System Simulation

The above component models are aggregated into a system model, and then simulation are conducted over a period of one day. The profiles of the solar irradiances and ambient temperatures are shown in Fig. 7.

Under the predefined energy management strategy, the power profile of each component are shown in Fig. 8 (a), and the state of charge of energy storage system in Fig. 8 (b).

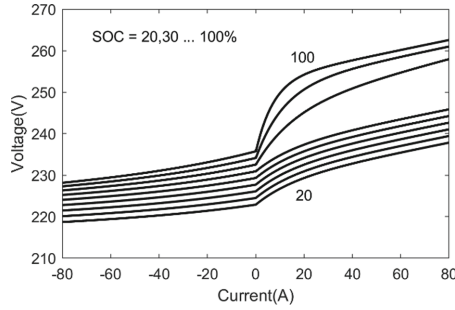


Fig. 6. The I/V profile of a lead-acid battery

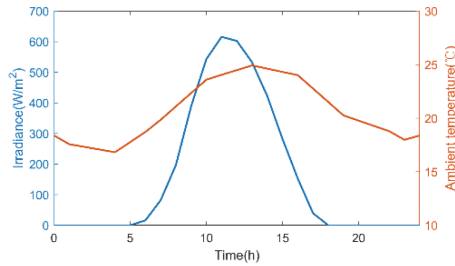


Fig. 7. The solar irradiances and ambient temperatures in one day

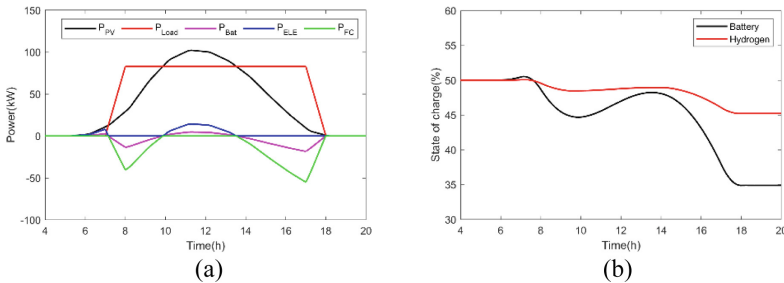


Fig. 8. Microgrid system simulation results. (a) Power profiles, (b) State of charge of energy storage systems

4 Conclusions

This paper aims to model the microgrid system for the design of a long-term energy management strategy. Models for each system component are established, and then are aggregated into a system model. The system model can be regarded as quasi-steady-state, providing a balance between simplicity for long-term simulation processes and accuracy in capturing the characteristics of system components. This component-wise system modeling approach enhances flexibility, facilitating the handling of system expansion

or component replacement. Based on this foundation, future work can focus on further designing suitable long-term energy management strategies to enhance the overall economic competitiveness of the system.

Acknowledgement. This study was supported by the National Natural Science Foundation of China under Grant U21A20166 and Science and Technology Planning Project of Ningbo under Grant 2022Z065 and Key Technology R&D Program of Anhui Province (No.2019b05050004, high power density self-humidification fuel cell system based on a stack of self-owned core technology).

References

1. Lasseter, R.H.: MicroGrids. IEEE Power Engineering Society Winter Meeting **1**, 305–308 (2002)
2. Sachidananda Sen., Vishal Kumar. Microgrid modelling: A comprehensive survey. *Annual Reviews in Control*, 46, 216–250 (2018)
3. Ulleberg, O.: Modeling of advanced alkaline electrolyzers: a system simulation approach. *Int. J. Hydrogen Energy* **28**(1), 21–33 (2003)
4. Wang, C. Modeling and control of hybrid wind/photovoltaic/fuel cell distributed generation systems. Montana State University (2006)
5. Valverde, L., Rosa, F., Del Real, A.J., Arce, A., Bordons, C.: Modeling, simulation and experimental set-up of a renewable hydrogen-based domestic microgrid. *Int. J. Hydrogen Energy* **38**(27), 11672–11684 (2013)
6. Lorenzo, E. Solar electricity: engineering of photovoltaic systems. Earthscan/James & James (1994)
7. Shell Solar - Miller Solar: <https://millersolar.com/MillerSolar/Resources/Shell/ShellSQ150-PC.pdf>
8. Cau, G., Cocco, D., Petrollese, M., Kær, S.K., Milan, C.: Energy management strategy based on short-term generation scheduling for a renewable microgrid using a hydrogen storage system. *Energy Convers. Manage.* **87**, 820–831 (2014)
9. Marshall, A., Børresen, B., Hagen, G., Tsyppkin, M., Tunold, R.: Hydrogen production by advanced proton exchange membrane (PEM) water electrolyzers—Reduced energy consumption by improved electrocatalysis. *Energy* **32**(4), 431–436 (2007)
10. Espinosa-López, M., et al.: Modelling and experimental validation of a 46 kW PEM high pressure water electrolyzer. *Renewable Energy* **119**, 160–173 (2018)
11. Chugh, S., Chaudhari, C., Sonkar, K., Sharma, A., Kapur, G.S., Ramakumar, S.: Experimental and modelling studies of low temperature PEMFC performance. *Int. J. Hydrogen Energy* **45**(15), 8866–8874 (2020)
12. Pukrushpan, J. T. Modeling and control of fuel cell systems and fuel processors. University of Michigan (2003)
13. O’hayre, R., Cha, S. W., Colella, W., & Prinz, F. B. Fuel cell fundamentals. John Wiley & Sons (2016)
14. Ulleberg, O., Glockner, R. Hydrogens: hydrogen energy models (2002)



Coordinated Control Technology for Multi-stack Fuel Cell System

Duankai Li^(✉) and Guorui Zhang^{id}

CRRC Qingdao Sifang Company Ltd., Qingdao 266111, China
Duankay_Lee@163.com

Abstract. At present, the output power of single fuel cell system is limited. Therefore, multiple fuel cell systems are connected in parallel to form a multi-stack system, which can effectively improve the system power level, and is an important means for fuel cells to realize the application of heavy-duty transportation. Considering the power-efficiency characteristics of fuel cell system, how to improve the operation efficiency of the whole multi-stack system has become a hot issue. In this paper, a coordinated control method aiming at the highest instantaneous efficiency for multi-stack system is proposed. Firstly, the objective function is established and then the particle swarm optimization (PSO) algorithm is used for optimization calculation. Within the range of the total power demand, the optimal control sequences are obtained. According to the optimization result, the multi-stack coordinated control is applied to achieve highest instantaneous efficiency. Finally, a ground test verification platform of multi-stack fuel cell system is built to verify the effectiveness of the multi-stack coordinated control strategy.

Keywords: Multi-stack system · Coordinated control · PSO

1 Introduction

Hydrogen fuel cells (FC) are not limited by the Carnot cycle, resulting in extremely high energy conversion efficiency. They also have advantages such as simple module structure and strong building blocks, making them the most promising “green energy” device in the 21st century [1, 2]. Especially Proton Exchange Membrane Fuel Cell (PEMFC) [3–6] not only has the common advantages of fuel cells, such as low pollution and high fuel utilization, but also has the advantages of fast startup, fast response speed, low operating temperature, and long lifespan. Currently, there has been a large amount of basic research and application technology research and development, which has been successfully applied in many fields, such as transportation, communication, power, aerospace, military, etc., Fuel cells have shown broad application prospects in these areas [7–9].

In the field of rail transport, due to its high power demand, multiple sets of electric stacks are often operated in parallel to achieve high power output. For the Multi stack fuel cell system (MFCS), it is necessary to develop control strategies to coordinate the output of each stack. Common control methods include power equalization, daisy chain allocation, and power optimization allocation. Power sharing refers to the equal

distribution of total power, which is suitable for the excellent performance consistency of the stack; daisy chain allocation refers to the operation of the next level fuel cell only after the current level fuel cell reaches its maximum power. This method can improve system efficiency at low power output; power optimization allocation varies according to different optimization objectives. Reference [10] proposed an MFCS power allocation method that considers stack aging, introducing a quantitative indicator of voltage degradation to characterize the aging degree of fuel cells during operation, and thereby determining the output power of fuel cells; In order to optimize MFCS output efficiency and reduce hydrogen consumption, literature [11] proposed a constrained optimization algorithm under KKT conditions. Although these studies have achieved good structures in some aspects, they have not taken into account the economic issues of stack operation with significant aging differences.

This article takes the multi stack fuel cell system of rail vehicles as the research object, introducing the integrated topology and key parameters of the multi stack fuel cell system; based on this, an energy management controller is designed and integrated with a multi reactor coordinated control strategy; Finally, a ground test verification platform for the multi reactor fuel cell system is established to verify the effectiveness of the vehicle's multi reactor coordinated control strategy.

2 A Coordinated Control Method for MFCS Considering System Operation Economy

The integration of multi stack fuel cell systems is an important way to improve system power density and energy density. However, in the long-term operation of multi stack fuel cells, when the performance differences between each stack cannot be avoided, or when a certain stack is replaced by a new stack for some reason, it is necessary to seek a power allocation strategy that can adapt to multi stack systems with significant performance differences and improve system operation economy.

Based on the above considerations, a coordinated control method for a multi stack fuel cell power generation system is proposed, and the control structure of the multi stack fuel cell system is shown in Fig. 1. While ensuring the required power of the system, optimizing algorithms are used to allocate the power of each stack reasonably, ensuring that the multi stack fuel cell system has efficient characteristics at every moment, thereby improving the overall operating economy of rail transport vehicles. Figure 2 shows the control strategy flowchart used.

Under a single MFCS power point, based on the power efficiency curve of a single stack fuel cell, a mathematical model of a multi stack fuel cell system with the highest instantaneous efficiency as the optimization objective is established. The constraints include: meeting the current total demand power of the fuel cell equal to the sum of the output power of each stack; The output power of each single stack must be within the limited range. Particle Swarm Optimization (PSO) algorithm is introduced to optimize the established mathematical model.

In order to adapt to the dynamic response requirements of MFCS, considering the total power range required by the fuel cell, a full range optimization of power is carried out according to the set power interval. the mathematical optimization model of the multi

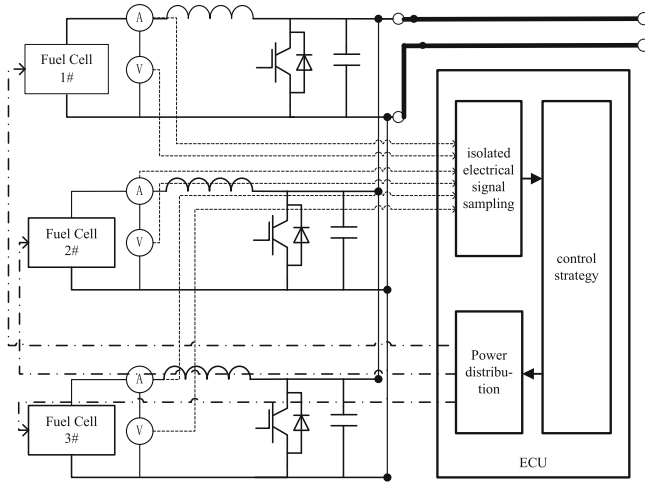


Fig. 1. Schematic diagram of control structure for multi stack fuel cells.

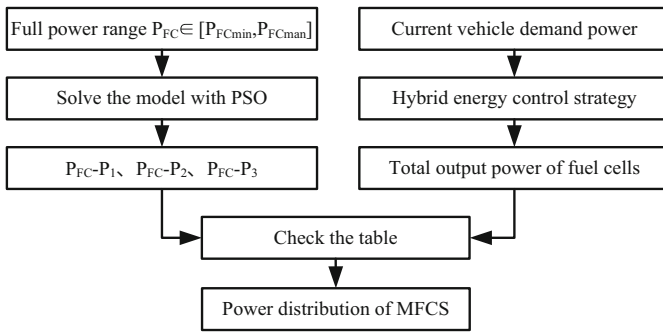


Fig. 2. Efficient coordinated control strategy for quasi online multi stack fuel cells.

stack fuel cell is optimized, and the optimal solution is calculated. based on the optimal solution, the multi stack coordinated control with the highest instantaneous efficiency is carried out.

3 Test Verification

This testing experiment is completed at room temperature. In order to test the effectiveness of this method in practical applications, experimental tests are conducted on the testing platform shown in Fig. 3. The experimental platform consists of three fuel cells (all LLZ-GH-110kW), and the relevant parameters are shown in Table 1.

In order to verify the effectiveness of the proposed power allocation method, one of the stacks is first started to reach the thermal engine state, and then the other stacks are started to simulate the performance differences of the stacks under experimental conditions. The power sharing strategy is used to obtain experimental data; The power

Table 1. Parameters of proton exchange membrane fuel cells.

| Proton exchange membrane fuel cell (LLZ-GH-110 kW) | | | |
|--|--------------|-----------------------------|-------------|
| Type | Water-cooled | Weight | < 800 kg |
| Rated power | 110 kW | Voltage | 420 ~ 720 V |
| Operating temperature | - 25 ~ 60 °C | Relative humidity | ≤ 95% |
| Maximum current | 320 A | Auxiliary power consumption | 28 kW |

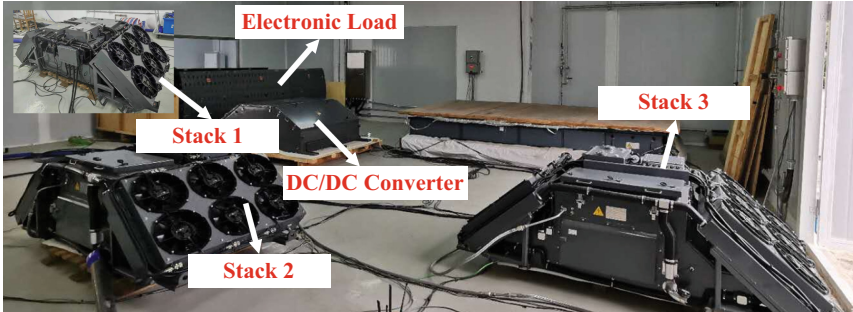


Fig. 3. Experimental testing platform.

efficiency curve of each stack is fitted using MATLAB to obtain the power efficiency curve as shown in the following Fig. 4.

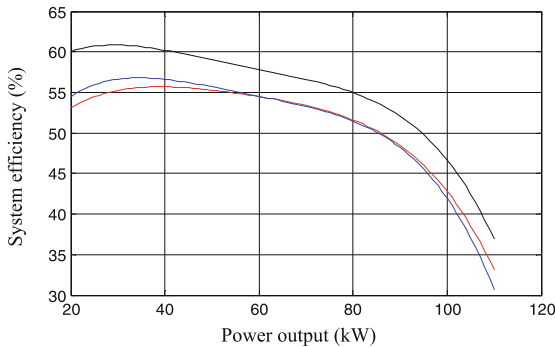


Fig. 4. Stack power efficiency curve.

Taking the obtained power efficiency curve into the PSO algorithm for power allocation optimization, the power allocation of different power points can be obtained as shown in Table 2. It can be found that the power interval for full power range optimization is 10 kW. If the actual demand power value is between two power points with the minimum interval in the allocation table, linear interpolation is used to determine.

Table 2. Power allocation table obtained after optimization based on PSO.

| Total power (kW) | Pf1 (kW) | Pf2 (kW) | Pf3 (kW) | Total power (kW) | Pf1(kW) | Pf2 (kW) | Pf3 (kW) |
|------------------|----------|----------|----------|------------------|---------|----------|----------|
| 60 | 20 | 20 | 20 | 200 | 68.0713 | 67.5622 | 64.3663 |
| 70 | 25.1066 | 20 | 24.8933 | 210 | 70.1203 | 71.1472 | 68.7323 |
| 80 | 29.2426 | 22.7203 | 28.0369 | 220 | 73.0171 | 74.6149 | 72.3678 |
| 90 | 33.3900 | 25.6372 | 30.9727 | 230 | 76.1168 | 77.9470 | 75.9360 |
| 100 | 37.6886 | 28.4707 | 33.8405 | 240 | 79.5230 | 81.1975 | 79.2793 |
| 110 | 42.2785 | 31.1172 | 36.6041 | 250 | 82.9293 | 84.5169 | 82.5537 |
| 120 | 47.3578 | 33.4821 | 39.1600 | 260 | 86.4321 | 87.8707 | 85.6971 |
| 130 | 52.8774 | 35.6211 | 41.5014 | 270 | 90.0847 | 91.0203 | 88.8949 |
| 140 | 58.4743 | 37.5944 | 43.9312 | 280 | 93.5192 | 94.2931 | 92.1876 |
| 150 | 62.9316 | 39.9909 | 47.0774 | 290 | 97.2089 | 97.5211 | 95.2698 |
| 160 | 65.6549 | 42.6664 | 51.6786 | 300 | 100.526 | 100.969 | 98.5046 |
| 170 | 66.7397 | 44.6071 | 58.6531 | 310 | 104.189 | 104.187 | 101.623 |
| 180 | 67.7759 | 48.6276 | 63.5964 | 320 | 107.651 | 107.558 | 104.790 |
| 190 | 66.8659 | 63.5583 | 59.5756 | 330 | 110 | 110 | 110 |

Using the instantaneous efficiency optimal power allocation strategy, the output power of the stack is shown in Fig. 5. The efficiency comparison between this power allocation strategy and the power sharing strategy is shown in Fig. 6. It can be found that at different power points and load changing processes, the efficiency of the instantaneous efficient power allocation strategy is significantly higher than the system efficiency of the traditional power sharing strategy, with a maximum efficiency difference of up to 1%, which verifies the effectiveness of this strategy.

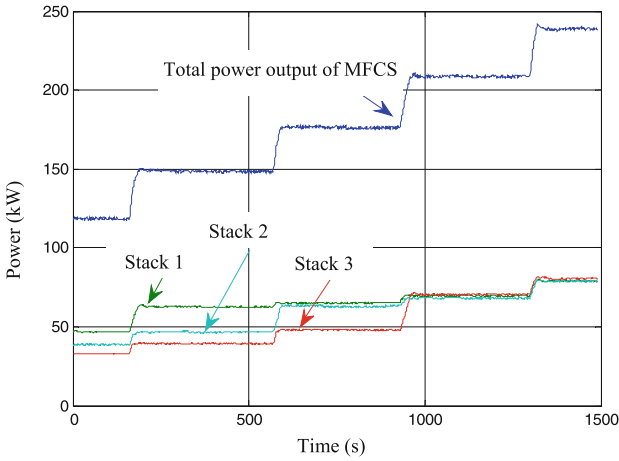


Fig. 5. Power output curve of the stack.

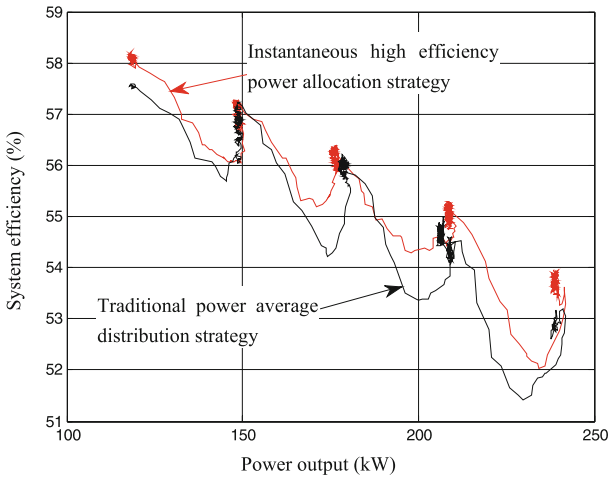


Fig. 6. Comparison of efficiency tests for full power range systems with different control strategies.

4 Conclusion

This article provides a detailed introduction to the application of the multi stack fuel cell system in hydrogen fuel cell rail vehicles, and analyzes and elaborates on the key technologies of the multi stack fuel cell system. Finally, through full physical ground tests, it is verified that the developed fuel cell system meets the requirements of the entire vehicle. Combined with ground tests, it has been fully verified that the efficient coordinated control strategy for multi reactor fuel cells with the highest instantaneous efficiency as the optimization objective can effectively improve the system's operational

economy in the full power range, laying the foundation for the promotion and application of high-power multi reactor hydrogen fuel cell hybrid systems in rail transport in the future.

References

1. Ministry of Science and Technology: Report on Science and Technology Development in the Energy Field over the Past Decade. Science and Technology Literature Press, Beijing (2012)
2. Hu, Y.: A type of rail transit suitable for small and medium-sized cities - a trinity of new energy trams. *Urban Rail Transit*. **18**(8), 4–6 (2015)
3. Lijun, G., Roger, A., Shengyi, L.: Power enhancement of an actively controlled battery/ultracapacitor hybrid. *IEEE Trans. Power Electron.* **20**(1), 236–243 (2005)
4. Yi, B.: The principle, technical status, and prospects of fuel cells. *Battery Industry*, 16–22(2003)
5. Yi, B.: *Fuel Cells—Principles, Technologies*. Chemical Industry Press, Applications (2003)
6. Chen, Q., Weng, Y., Weng, S.: Research on the performance of fuel cell gas turbine hybrid power generation system. *Chin. J. Electr. Eng.* (04), 31–35 (2006)
7. Zhang, H., Ma, Y.: Comparative analysis of contactless power supply schemes for modern trams. *Modern Transp. Technol.* **10**(04), 79–82 (2013)
8. Sun, S., Liu, B., Liu, X.: Research on hybrid power system of modern urban tram. In: *Proceedings of the 11th Session of the 15th China Association for Science and Technology Annual Conference on Comprehensive Transportation and Logistics Development*, pp. 263–266 (2010)
9. Sun, S., Liu, B., Liu, X.: Research on 100% low floor modern tram hybrid power system. *China's New Technologies and Products*, pp. 10–31 (2013)
10. Li, Q., Liu, Q., Li, Y.: Multi stack adaptive power allocation method considering fuel cell aging. *J. Southwest Jiaotong Unive.* 1–9 (2021)
11. Wei, D., Zheng, D., Chu, L.: Optimal performance output control of air-cooled proton exchange membrane fuel cell stack. *CIESC J.* **61**(05), 1293–1300 (2010)



Global Hydrogen Refueling Infrastructures Development Evaluation in 2022

Wei Liu^{1,2}, Yanming Wan^{1,2}, Yan Zhang², and Hanchen Lin²(✉)

¹ CHN Energy Guohua Energy Investment Co., LTD., Beijing 100007, China

² China Hydrogen Alliance Research Institute, Beijing 100007, China

linhanchen@h2cn.org

Abstract. Hydrogen application is developing rapidly based on transportation. According to the study of China Hydrogen Alliance Research Institute, as of end of 2022, there were 829 hydrogen refueling stations (HRS) in total globally. East Asia leads the world in number for 3 consecutive years, while Europe and America's HRS gradually tend to concentrate. China has 358 operation or construction HRS, and realizes various types of HRS put into use. In 2022, the number of HRS in China's fuel cell demonstration city clusters accounts for more than half, and some equipment enterprises achieve products export. Yet, there still are many problems existed in high-pressure and large-displacement HRS equipment technologies, hydrogen pricing mechanisms and quality testing etc. Several necessary measures are proposed to further promote high-quality development of HRS industry in China.

Keywords: Hydrogen refueling station · Fuel cell · Key equipment · Development evaluation

1 Introduction

Hydrogen application is rapidly developing in the world. In the transportation field, the popularization of fuel cell vehicles continues increasing. According to the study of China Hydrogen Alliance Research Institute, as of end of 2022, the number of fuel cell vehicles in main countries has reached 67,315, year-on-year increase 36.3%. Among, China reaches 12,682; South Korea reaches 29,369, which is about to become the first country in the world reaching 30 thousand fuel cell vehicles; the US reaches 14,979; and Japan and Germany reach 8150 and 2135, respectively. The first hydrogen-powered train line in the world opens in Germany, hydrogen-powered plane completes the test flight in the UK, and hydrogen-powered ships are tested in several countries. As main infrastructures, the numbers of hydrogen refueling stations (HRS) continue increasing (Fig. 1).

At present, main organizations in the world such as IEA and CaFCP have launched in-depth analyses of HRS, information on HRS in China has been put online on the Hydrogen Big Data Platform [1], and China's Hydrogen Price Index [2] has been initially established. However, comparing with foreign countries, the development of statistics of

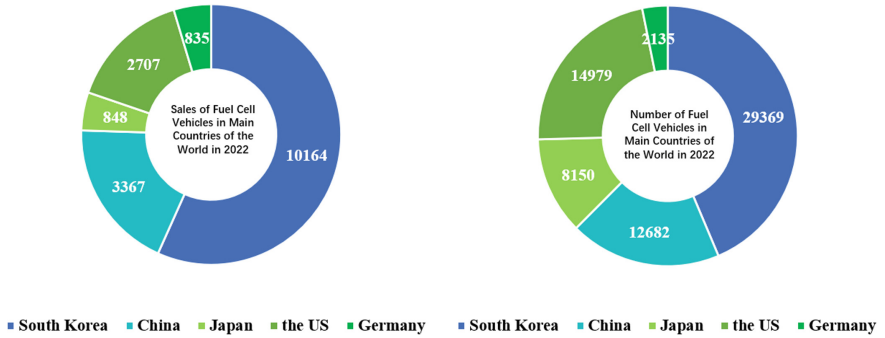


Fig. 1. Sales and number of fuel cell vehicles in main countries of the world

HRS in China are still weak [3]. The paper compares the HRS development situations in the world, summarizes characteristics, analyzes China’s overall situations and provides relevant references, to provide policy recommendations for the high-quality development of HRS.

2 Global Hydrogen Refueling Infrastructures Evaluation

According to the statistics compiled by China Hydrogen Alliance Research Institute, as of end of 2022, there are 829 h in operation worldwide [4]. Among them, East Asia (China/ South Korea/ Japan), Europe and North America reach 577, 176 and 60, respectively (Fig. 2).

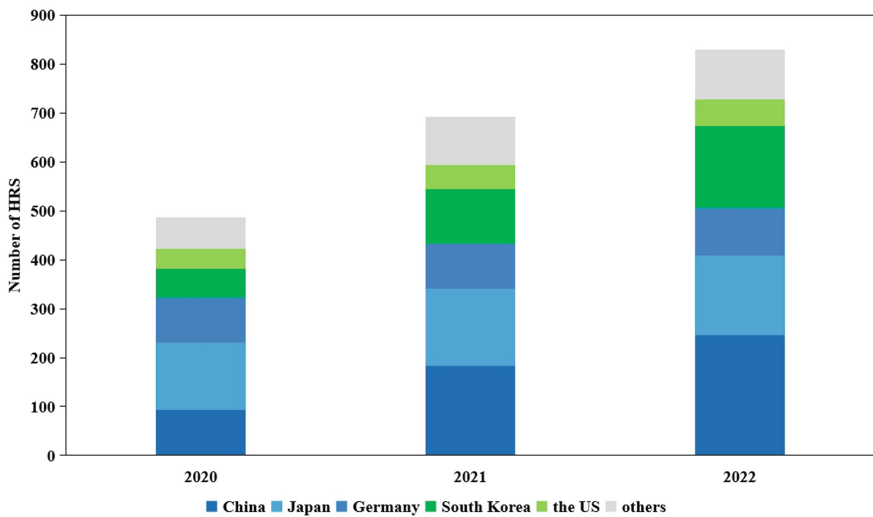


Fig. 2. Number and distribution of hydrogen refueling stations in main countries of the world

2.1 East Asian Countries Take the Top 3 Spots in the World for the Number of HRS in Operation

Operated HRS in East Asia (China/ South Korea/ Japan) once again take the lead in the world, with a total of 577 h, which is more than twice the number of operated HRS in Europe and North America; increases 124. Among them, China has 245 operated HRS, ranking No.1 in the world for 2 consecutive years. South Korea has strong performance, increasing 55 h in 2022 and bringing total number to 168. Japan only increases 7 h, bringing total number of 164 [5]. China's fuel cell vehicles demonstration city cluster and South Korea achieving sales of 10,000 fuel cell vehicle in a single year support the fast development of operated HRS in East Asia.

2.2 European HRS Construction Slows Down, Renewable Hydrogen Supplies Increase

Europe has 176 operated HRS [6], increasing 3 compares with 2021. Number of HRS in Germany increases 4, making total number reach 96, continues taking the lead in Europe. France, Netherland, Switzerland and UK rank No.2 to No.5 in Europe. Compare with 2021, Netherland and Switzerland increase 3 and 4, respectively, reaching 13 and 11; France and UK, however, reduce 1 and 4, respectively, reaching 21 and 9. Scale of most HRS in Europe is below 100kg/d; and 27 operated HRS realize 100% renewable hydrogen supply.

2.3 North America Operated HRS Still Highly Concentrated in California

North America has 60 operated HRS, increasing 6 compares with 2021. Among, operated HRS in the US still highly concentrated in California, with a total of 54 [7], increasing 6 compares with 2021. In 2022, new-increased HRS in the US are still dominated by liquid hydrogen. Canada has 6 operated HRS, same as 2021.

Other countries have 16 operated HRS. Among them, Australia has 16 operated HRS, same as 2021, and Columbia, Cyprus and Israel etc. countries have first operated HRS.

3 China's Hydrogen Refueling Infrastructure Construction Situation

As of end of 2022, China has constructed 358 h, newly constructed 109, and covering a total of 116 prefecture-level cities in 28 provinces /municipalities directly under Central Government /autonomous regions and special zones). Of these, 245 are in operation and 113 are to be operated. Among all the 358 h, 55 are mainly used for internal testing by fuel cell manufacturers and fuel cell stacks/ systems, not open to the public. In 2022, the number of HRS in China remains 3 'the first' in the world in terms of the number of HRS built, HRS in operation and newly built HRS.

3.1 In Terms of Construction Form, Fixed HRS and Skid-Mounted HRS Go Hand in Hand

China's HRS is mainly divided into the fixed type and the skid-mounted type. In 2022, China's fixed HRS accounts for 50.5%. Under promotion of fuel cell vehicle demonstration city clusters, skid-mounted HRS have become favorable choices in some scenarios due to its flexible layout and rapid response. Among all 358 h in China, fixed HRS accounts for 59.8% (Fig. 3).

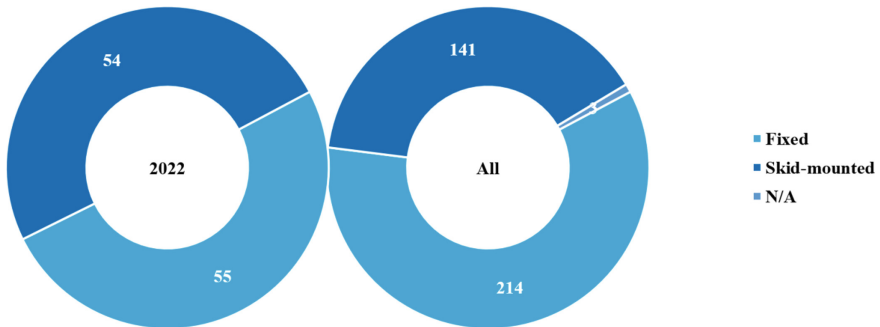


Fig. 3. Classification of China's HRS by construction form

3.2 In Terms of Pressure Level, 35 MPa HRS Dominate the Market

China's HRS pressure level mainly is 35 MPa, accounts for 89.7%. It is consistent with the development status of fuel cell vehicles in China, which are mainly 35 MPa commercial vehicles. In 2022, China new increases 7 h with 70 MPa refueling capability. Wanquan Oil/Hydrogen/Electricity Integrated Energy Station, which is constructed by CHN Energy Guohua Investment Co., Ltd., uses 35 MPa smart and fast dispenser, which is researched and developed independently, and listed into the National Energy Administration the first units (sets) of major technical equipment in the energy sector. Also, the station deployed China's first 70 MPa integrated mobile HRS which meets national standard and has obtained the overall explosion-proof certification, and which is also led, researched and developed independently by Guohua Investment (Fig. 4).

3.3 In Terms of Refueling Capacity, HRS Starts to Move Towards Large Capacity

China's HRS refueling capacity is mainly concentrated in 500–1000 kg/d, accounts for 57.5%. The proportion of small-sized HRS further decreases. Since 2020, some places in China construct large-size HRS to support operation of fuel cell heavy trucks or large quantities of fuel cell vehicles. Beijing Daxing Hydrogen Demonstration Zone HRS trial operation, with hydrogen refueling capacity of 3600 kg/d. Hebei Qian'an 6400 kg/d HRS trial operation, meeting the requirements of 100 fuel cell trucks (Fig. 5).

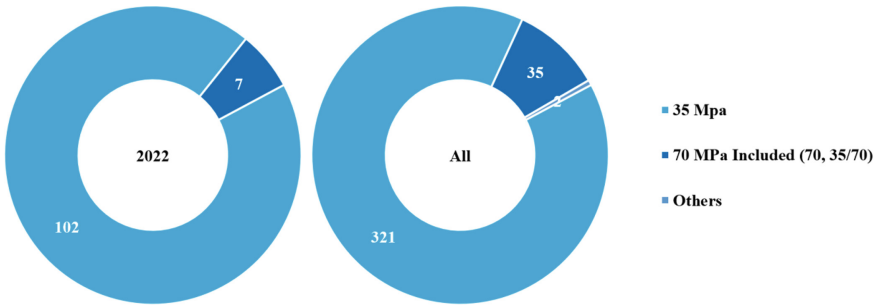


Fig. 4. Classification of China's HRS by pressure level

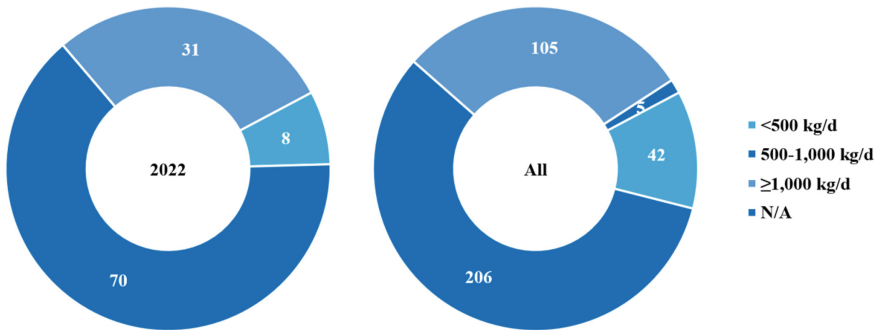


Fig. 5. Classification of China's HRS by Refueling Capacity

4 Development Evaluation of China's Hydrogen Refueling Infrastructures

Year 2022 is the first year that 5 departments of China starting fuel cell demonstration city clusters, and the development of China's hydrogen refueling infrastructures accelerates. Some places actively untied the hydrogen production and refueling integrated stations, not only further reduce the hydrogen arrival price, also explore the applications of clean and low-carbon hydrogen in HRS field. With the fuel cell vehicles gradually increase, China's HRS move towards commercial operation from demonstration, and it is urgent to follow-up on high-end equipment manufacturing, establishment of price mechanism and quality inspection.

4.1 Characteristics of Development

City clusters demonstration advances, bringing rapid development of number of HRS. In 2022, China new increases 3378 vehicles; and from the data of insurance amount, the sales of fuel cell vehicles in China exceeds 5000. Both numbers reach record high. In terms of fuel cell vehicle demonstration city cluster (some cities belong to more than one city cluster, like Zibo, Shandong belongs to 5 city clusters), the insurance amount of Beijing, Shanghai, Guangdong Province, Henan Province and Hebei

Province demonstration city clusters in 2022 reaches 1395, 1284, 450, 1601 and 1,677, respectively. Among all 358 h in China, 183 h are located in demonstration city clusters, account for 51.2%. 55 of 109 h constructed and operated in 2022 are located in demonstration city clusters, account for 50.5%.

Independently researched and developed HRS equipment achieves breakthroughs, some products have been exported. The first 70 MPa integrated mobile HRS which is independently researched and developed by Guohua Investment and met HRS national standard and explosion-proof certification is delivered; the 250 MPa ultra-high pressure hydrogen diaphragm compressor is successfully developed by FENDY JINKAIWEI, with displacement of more than 200 Nm³/h; the high-pressure 2000 Nm³/h large displacement liquid-driven hydrogen filling compressor which cooperated, researched and developed by Sinopec Qingdao Refinery and Qingdao Compress Company passes the test and the installation is completed. Zhejiang Rein realizes application of 90 MPa hydrogen storage bottle group products, with single bottle volume of more than 700 L; and the 2 skid-mounted hydrogen refueling equipment signed by Peric Hydrogen and a Slovakian Energy Company realize delivery.

System of hydrogen production and hydrogen refueling integrated station is loosened, and the way of on-site HRS emerged. In terms of systems, Guangdong Province < Fuel Cell Vehicle HRS Management Interim Measures > solicits opinions, the construction of on-site HRS in non-chemical parks is allowed; Jilin Province launches the construction of the distributed renewable hydrogen production and refueling integrated stations in non-chemical parks; Dalian, Liaoning Province < The Technical Specifications of Hydrogen Production and Refueling Integrated Stations > solicits opinions, which is the first technical specifications of the field in China. In terms of projects, China's first distributed methanol to hydrogen and refueling station puts into operation; first renewable energy + PEM to hydrogen + refueling station trial operation; ammonia to hydrogen and refueling station completes refueling; normal temperature and pressure organic liquid hydrogen storage and refueling integration application project completes; and methane gas to hydrogen and refueling station starts construction.

International oil and gas prices continue rising, China's hydrogen market price remains stable. China Hydrogen Alliance Research proposes 'China Hydrogen Price Index', the production side and the consumption side are evaluated and tracked separately, and which objectively presenting the trend of hydrogen energy cost changes in various regions of China and categories. The production side covers more than 40 cities and 60 samples, while the consumption side covers more than 30 cities and 80 samples. In 2022, the average price of China in production side remains at RMB 35/kg; price of fuel cell vehicle city cluster is quite high, which is about RMB 35–40/kg, and price shows trend of decreasing. The average price of China in consumption side shows trend of decreasing, the average price of China remains at RMB 60/kg; price of fuel cell vehicle city cluster is low, which is averaging RMB 55/kg in H1, and drops to RMB 52/kg since July as the price of HRS begins to follow the target price of demonstration period; price of non-fuel cell vehicle city cluster is high, which remains at around RMB 73/kg.

4.2 Problems and Challenges

Technical capabilities of high-pressure, large displacement HRS equipment need breakthrough. China's vehicle/station ratio has reached 51.8 (since 2014, China's fuel cell vehicle sales has reached 12,682; as of end of 2022, China totally has 245 operated HRS), slightly lower than the global average; single station hydrogen refueling capacity gradually increases, with the largest reaching 6400 kg/d. At present, China's HRS mainly uses 35 MPa dispensers; the compressors mainly use diagrams, while the liquid-driven ones realize batch application, and the displacements of both compressors are between 500 and 1000 Nm³/h; equipment integrated capability has formed. With further increase of vehicle/station ratio and requirement of daily refueling amount, and demonstration and popularization of passenger cars, contradictions between equipment maturity and cost reduction, such as the 70 MPa dispensers and the higher displacement compressors, are intensified; and key technical constraints of liquid HRS further appear. Meanwhile, the hidden problems such as energy consumption of HRS equipment continue to be obvious.

Hydrogen pricing mechanism of fuel cell vehicles needs further standardization. The selling price of hydrogen in HRS mainly depends on hydrogen cost, storage and transportation cost and maintenance cost of HRS. With China's fuel cell vehicles gradually towards marketization from the initial stage of popularization, the HRS gradually towards commercial operation from demonstration. Meanwhile, the demonstration cities will further promote and support application of low-carbon and clean hydrogen. Under the premise of ensuring economy, the operators will gradually face the challenges of increasing the amount of low-carbon and clean hydrogen and reducing the carbon footprint of hydrogen energy. The operation of HRS is affected by number of factors, including operating costs, actual hydrogen supply and demand and operating subsidies, price of hydrogen will beyond the affordability of the market, and will affect the effectiveness of demonstration operations.

Hydrogen quality testing for fuel cell vehicles needs to be further strengthened. At present, hydrogen used in HRS in China is mainly high-purity hydrogen. There are differences between the high-purity hydrogen and the fuel cell hydrogen (hydrogen meet the requirements of GB/T 37244–2018 < Fuel Specification for Proton Exchange Membrane Fuel Cell Vehicles – Hydrogen >), excessive individual impurities may cause poisoning of the fuel cell catalysts and reduce the service lives. The operators of the HRS should provide continuous and stable supply of hydrogen for fuel cells, regularly commission qualified third-party inspection and testing institutions to test the qualities of hydrogen, and publish the test results as required.

5 Recommendations

According to published provincial hydrogen planning, by the end of 14th FYP, China will promote more than 100,000 fuel cell vehicles and build more than 1000 h. Meanwhile, China is actively promoting application of 70 MPa fuel cell vehicles, which will drive the technical level of China's HRS to a new level. To boost the high-quality development of the industry, the current problems faced by China's HRS need to be solved as soon as possible.

Make breakthroughs in key equipment manufacturing technology for HRS. It is suggested to deepen ‘Hydrogen Top Runner Program’, and establish HRS performance test evaluation standard by evaluating performances of HRS, to drive the innovation of core technologies such as dispensers, compressors and station-control, reduce comprehensive cost of hydrogen refueling, and help China’s HRS technologies and equipment move from ‘following’ to ‘running’ and ‘leading’, and accelerate the commercialization of hydrogen energy.

Explore pricing mechanism of hydrogen for fuel cell vehicles. It is suggested to launch the ‘China Hydrogen Cost Assessment’ System to calculate the national and regional costs of hydrogen, clean hydrogen and low-carbon hydrogen, reflecting the comprehensive impact of hydrogen-related equipment manufacturing, energy prices and the carbon market. It is proposed that the system, together with ‘China Hydrogen Price Index’, should be used as basis to accelerate the breakthrough of hydrogen prices for vehicles in fuel cell demonstration city clusters, to avoid the inversion of the price of hydrogen selling at HRS and on arrival, and to maintain normal operation and management of the station.






Strengthen capabilities of quality testing of hydrogen for fuel cell vehicles. It is suggested to set up national hydrogen quality testing platform, to carry out research and test qualities of hydrogen. It is proposed to develop mobile hydrogen testing vehicles based on this platform, forming integrated and mobile fuel hydrogen quality testing systems, completing real-time control of hydrogen quality in the whole process of fuel cell hydrogen, promoting stabilization and scale-up of hydrogen in transportation and power generation, and promoting the improvement of quality management in the hydrogen energy industry.

References

1. Hydrogen Big Data Platform Homepage, <https://www.chinah2data.com>. Last accessed 12 Mar 2023
2. China’s Hydrogen Price Index, https://bi.aliyuncs.com/token3rd/dashboard/view/pc.htm?pageId=8ab29839-81d6-4cd6-8432-1000a50adabf&accessToken=7552c0785d19d7b93f3245ae04790b32&dd_orientation=auto. last accessed 28 Feb 2023
3. Liu, W., Wan, Y., Zhang, Y., Lin, H.: Global and China hydrogen refueling infrastructures development evaluation in 2021. *J. Energy China* (8), 55–61 (2022)
4. China Hydrogen Alliance: China Hydrogen Energy and Fuel Cell Industry Development Report 2021. People’s Daily Press, Beijing (2023)
5. Japan’s Hydrogen Refueling Station, https://www.cev-pc.or.jp/suiso_station/. Last accessed 1 Jan 2023
6. Europe’s Availability Map, <https://h2-map.eu/>. Last accessed 01 Jan 2023
7. California Hydrogen Fuel Cell Partnership, <https://h2fcp.org/stations>. Last accessed 01 Jan 2023



Grid-Connected PV-Hydrogen Systems Providing Secondary Frequency Regulation: Modeling, Controller Design and Verification

Mingjun Zhang¹ , Xiang Cheng¹  , Liandong Sha¹ , Jin Lin¹ , Weijie Qian²,
and Weiliang Liu²

¹ Tsinghua University, Beijing 100084, China
chengx16@tsinghua.org.cn

² State Grid Zhejiang Electric Power Co., Ltd. Jiaxing Power Supply Company, Jiaxing 314500,
China

Abstract. The green hydrogen production system powered by renewable sources is expected to become an important way to decarbonize for the energy, chemical and other industries. The flexibility of the electrolysis system has the potential to alleviate the grid frequency deterioration caused by the integration of large-scale intermittent and fluctuating renewable energy. Considering the power-electronics interface, this paper models the components of the grid-connected PV-Hydrogen system. According to the dynamic behaviors of the joint system, the control method suitable for providing secondary frequency regulation (SFR) is proposed. This paper demonstrates the effectiveness of the proposed controller in a 20 kW photovoltaic (PV) system and a 2 Nm³/h alkaline electrolysis (AEL) system located in Chengdu, China. The simulation and experimental results show that the speed and accuracy of the PV-Hydrogen system with the controller proposed are sufficient to provide SFR.

Keywords: Hydrogen · Photovoltaic system · Electrolysis system · Frequency regulation · Control

1 Introduction

Green hydrogen based on renewable energy is expected to become an important way of decarbonization in chemical and transportation industries. However, when large-scale renewable energy is connected to the power grid, the fluctuation, intermittent and large-scale power electronic devices connected to the power grid, leading to the decrease of inertia of the power system and the deterioration of frequency. Because of the wide range of rapid varying-load ability, electrolysis systems are expected to provide secondary frequency regulation (SFR) by the grid forming mode.

The electrolysis system mainly consists of the stack and the power-electronics interface. The static modeling of the stack mainly focuses on the electrochemical thermodynamic process on the electrodes, while the dynamic modeling of the stack pays more

attention to the electrochemical kinetic process on the electrodes. The nonlinear voltage-current curve [1, 2] of the stack brings challenges to the controller design for a wide range of operation. The electric double-layer effect is formed by the accumulation of charges in the electrodes and the electrolyte [3]. This effect leads to a slow voltage response of the stack, which restricts the dynamic response speed of the stack power. The power-electronics interface of the stack is another important part of the dynamic response of the electrolysis system. The stack is usually connected to the AC or DC grid through a rectifier or DC/DC converter [4]. In order to provide a fast-enough power dynamic response for the electrolysis system to provide SFR, it is necessary to design a power controller through a closed-loop control method.

The model and control strategy of PV-Hydrogen system are proposed in [5], and the maximum power point tracking control of PV-Hydrogen system is carried out by using the incremental conductance method. The effectiveness of the proposed control method is verified by simulation, but only for the vicinity of the maximum power point. In [6], the control model of the PV-Hydrogen system is derived, and the controller was designed. The simulation results show that the electrolysis system can participate in the balance services as a fast response load. However, the ability to provide SFR of the grid-connected PV-Hydrogen system needs to be further verified by experiments.

The cooperation of renewable energy sources (represented by wind farms) and electrolysis systems in SFR has been proven to have complementary effects [7]. The PV system and the electrolysis system can also increase their full load hours by responding to the ramping-down and ramping-up parts of the automatic generation control (AGC) signal respectively to provide SFR. However, [7] only proposes a framework of cooperation and does not discuss the controller design, nor the experimental verification.

The main contributions of this paper are as follows:

1. Considering the power electronic interface, this paper models each part of the grid-connected PV-hydrogen system. According to the system characteristics, the control method for providing SFR is proposed.
2. The system-level simulation and experimental results show that the PV-hydrogen system can quickly and accurately respond to the AGC signal when providing SFR with the proposed controller.

2 PV-Hydrogen System Dynamic Modeling

2.1 PV-Hydrogen system structure

The structure of the grid-connected PV-hydrogen system is shown in Fig. 1. Alkaline electrolytic system is connected to the power grid through three-phase rectifier equipment, photovoltaic module is connected to the grid through DC/DC converter and three-phase rectifier equipment.

2.2 PV System Dynamic Model

Circuit models of the photovoltaic cell have been discussed and studied by many researchers. The Fig. 2 shows the widely recognized single-diode equivalent circuit.

$$I = I_{ph} - I_d - I_{sh}, I_d = I_0 \left(\exp \left(\frac{q(V + IR_s)}{AKT} \right) - 1 \right), I_{sh} = \frac{V + IR_s}{R_{sh}} \quad (1)$$

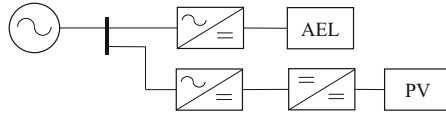


Fig. 1. The grid-connected PV-hydrogen system structure.

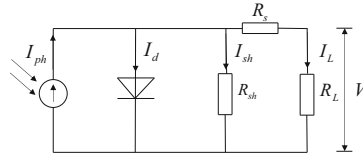


Fig. 2. Electric model of photovoltaic cell.

where, I is the output current of the photovoltaic cell, I_{ph} is the photogenerated current, I_d is the current flowing through the diode, I_{sh} is the current flowing through the internal parallel resistance R_{sh} , V is the output voltage of the photovoltaic cell, K is the Boltzmann constant, R_s is the equivalent series resistance, T is the absolute temperature, A is the ideal factor of the P-N junction, q is the electron charge.

In the practical application, it's difficult to rely on the theoretical model to analyze because the theoretical model will be affected by the manufacturing process and environmental conditions, so some engineering simplification is needed. Reference [8] combined with engineering experience proposed the simplified engineering model of PV cells as Eq. (2).

$$I = I_{scref} \times \frac{S}{S_{ref}} (1 + a\Delta T) \left(1 - C_1 \left(\exp\left(\frac{U}{C_2 U_{ocref} \times (1 - c\Delta T) \ln(e + b\Delta S)} \right) - 1 \right) \right) \quad (2)$$

2.3 Alkaline Electrolysis System Dynamic Model

The voltage of the electrolysis system is mainly composed of three parts, as shown in (3). In the Alkaline electrolysis (AEL) system, the overvoltage due to reactant diffusion can be neglected due to the low current density.

$$U_{cell} = U_{rev} + U_{act} + U_{ohm} \quad (3)$$

The reversible voltage U_{rev} represents the process of converting electrical energy into chemical energy in the product gas. Under the conditions of stable temperature, pressure and electrolyte flow, U_{rev} is fixed. The activation overvoltage U_{act} refers to the voltage lost when the chemical reaction crosses the activation energy barrier. This nonlinear relationship between U_{act} and stack current I_o can be described using a modified Tafel equation:

$$U_{act} = a \ln\left(\frac{I_o}{Sb} + 1\right) \quad (4)$$

The ohmic overvoltage U_{ohm} represents the overvoltage caused by the current passing through the stack and wires.

$$U_{ohm} = I_o R_{ohm} \quad (5)$$

The double-layer effect on the electrode is represented by C_{dl} , which represents the dynamic process of charge accumulation on the contact surface between the electrode and the electrolyte. The stack voltage U_o cannot change immediately, which leads to a slow dynamic response of the stack power. The dynamic model of the electrolysis system is shown in Fig. 3.

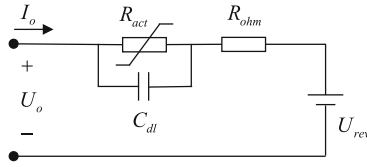


Fig. 3. Equivalent circuit model of AEL system.

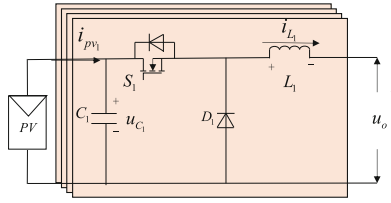


Fig. 4. Circuit diagram of four parallel buck converters.

3 PV-Hydrogen System Controller Design

3.1 PV System Control for Providing SFR

DC/DC Topology for the PV System. Combined with the scale of PV panels laid in the laboratory, multiple parallel Buck converters were used in this paper for voltage conversion. The Fig. 4 shows the circuit diagram of four parallel Buck converters.

In this paper, the transfer function of four parallel Buck converters is presented as the conclusion directly for the space limitation. The small signal model is

$$u_{C_1}^{\vee} = G_{ud}(s) d^{\vee} = \frac{-4I_L L R s - 4D R U_{C_1}}{L C R s^2 + L s + 4R D^2} d^{\vee} \quad (6)$$

Power Controller Design. The original system is a second-order system, and its dynamic performance and steady-state accuracy can be improved by PI. Fig. 5 shows the power control loop of the PV system.

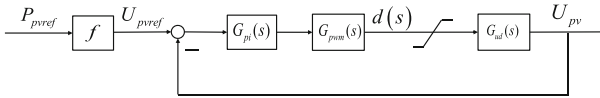


Fig. 5. Power control block diagram of the PV system.

$G_{pi}(s)$ is the transfer function of PI, $G_{pwm}(s)$ is the transfer function of PWM, $G_{ud}(s)$ is the transfer function of input voltage with respect to duty ratio in Eq. (10), f is the mapping of PV power to voltage. In this selection range (U_{load}, U_{mppt}), the mapping curve can be fitted by polynomial fitting. Thus, the output power controller of the PV system can be obtained to respond to the power control signal.

3.2 Electrolysis System Control for Providing SFR

Rectifier Topology for the AEL system. The stack is connected to the AC grid through a power-electronics interface such as a rectifier and a transformer. Double-reverse-star rectifier circuit is often used to provide larger current but lower voltage for the electrolysis system. The topology of the power-electronics interface of the electrolysis system is shown in Fig. 6:

Power controller design. According to the Faraday’s law, the gas production of the electrolysis system is proportional to the charge. Therefore, the electrolysis system is usually equipped with a current closed-loop controller (as shown in Fig. 7a) when it leaves the factory. The electrolysis system needs to be equipped with a new power controller to provide SFR.

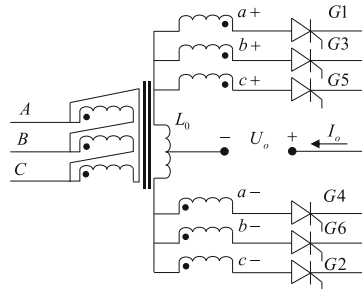


Fig. 6. Double-reverse-star rectifier circuit for the AEL system.

On the basis of the current closed-loop controller, the pre-stage power controller shown in Fig. 7b can be obtained by simply modifying. At different temperatures, based on the nonlinear relationship between absorbed power and load current, the pre-stage controller transfers the power command to the current command, and inputs it into the current closed-loop controller. This kind of power controller is suitable for electrolytic systems with small C_{dl} , such as the AEL system. The dynamic process of voltage and power is much shorter than the AGC signal (2 or 4 s).

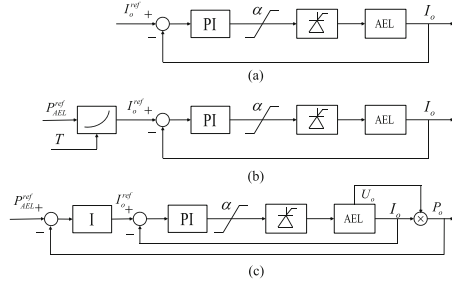


Fig. 7. Different power controllers of the AEL system.

The controller in Fig. 7c directly inputs the error of stack power into the controller. Compared with the existing controller, it is necessary to add a voltage sensor and design a new outer loop controller. This controller is suitable for systems with a relatively large C_{dl} , such as PEM systems. The controller can counteract the slow dynamic response of the stack voltage by adjusting the load current to a higher value during the initial stage of the response.

Based on the dynamic model of the electrolysis system shown in Fig. 3, the transfer function of the electrolysis system from current to power can be obtained by the linearization method:

$$G_{pi}(s) = \frac{[I_o(R_{act} + 2R_{ohm}) + U_{rev}]R_{act}C_{dl}s + 2(R_{act} + R_{ohm})I_o + U_{rev}}{R_{act}C_{dl}s + 1} \quad (7)$$

where I_o represents the current at the linearization point, and the rated current can be selected for design. $G_{pi}(s)$ has a zero and a pole. The frequency difference between zero and pole is:

$$p - z = \frac{1}{[(R_{dl} + 2R_{ohm}) + U_{rev}/I_o]C_{dl}} \quad (8)$$

Since the U_{rev} of the stack is much greater than U_{ohm} and U_{act} , and C_{dl} is generally large (in Table 2), the frequency difference is almost zero. So $G_{pi}(s)$ approximates a proportional element:

$$G_{pi}(s) \approx 2(R_{act} + R_{ohm})I_o + U_{rev} \quad (9)$$

Therefore, the power outer loop can use an I controller to meet the control requirements, as shown in Fig. 7c.

3.3 Power Distribution Between PV and AEL Systems

Providing SFR requires flexible resources to accept the scheduling of the control center and follow the AGC signal to adjust the output or absorbed power. Over a period of time, AGC signals often contain both ramping-up and ramping-down-parts. If the PV system or the electrolysis system provides SFR independently, both need to reserve a

considerable part of the capacity to ensure both up and down capacity, which leads to a considerable part of waste. The cooperation between PV and electrolysis systems to provide SFR can solve this dilemma. As shown in Algorithm 1:

Algorithm 1: Power distribution between PV and electrolysis system to provide SFR

| | | |
|----------|--|--|
| | Initialization: The PV system operates at the MPPT point P_{PV}^{MPPT} and the electrolysis system operates at the rated power P_E^{Rated} Determine the bidding capacity $C_{bid} < \min\{P_{PV}^{MPPT}, P_E^{Rated}\}$ | |
| 1 | Receive the AGC signal $r_t \in [-1, 1]$ | |
| 2 | Calculate $P_{AGC} = r_t C_{bid}$ | |
| 3 | If $P_{AGC} > 0$ then | |
| 4 | The reference power of electrolysis system: $P_E^{ref} = P_E^{Rated} - P_{AGC}$ | |
| 5 | else | |
| 6 | The reference power of PV system: $P_{PV}^{ref} = P_{PV}^{MPPT} - P_{AGC}$: | |
| 7 | end | |
| 8 | Return to 1 and wait for the next AGC signal | |

This control method can run in real-time to drive the PV and electrolysis system to provide SFR. The executions of power reference for PV system and electrolysis system are in Sects. 3.1 and 3.2.

4 Simulation and Experimental Results

4.1 Setup

The lab is located in Chengdu, Sichuan Province, China. The AEL reactor was developed by Xiamen University's Jiageng Laboratory. There are 11 circular batteries with a single electrode area of 2480 cm², rated current is 450 A and rated hydrogen production is 2 Nm³/h. The electrolytic reactor is powered by AC/DC and the rectifier uses six thyristors to form a dual reverse star rectifier topology with balanced reactors, rated at 24 V and 500 A. In the experiment, 34,972 A KEYSIGHT data logger was used to record the results of voltage and current signal measurement at a 1 s interval.

The PV module QC-ZJ-540 M is produced by Qichao New Energy Company in Sichuan, China, whose open circuit voltage, short circuit current, maximum power point voltage and current are 50.04 V, 13.76 A, 41.96 V and 12.87 A. A total of 36 photovoltaic modules are installed on the roof of the laboratory. The number of series and parallel modules can be changed through the Series and Parallel Switching Controller (Fig. 8).



Fig. 8. Experimental equipment.

4.2 PV System Parameters verification

In order to meet the accuracy requirements of engineering application, the parameters of the mathematical model need to be corrected. The output characteristics of PV modules are scanned by electronic load under different working conditions. The calibrated parameters are listed in Table 1 (power control mode).

Table 1. Simulation parameter in different mode.

| Parameter | Values (frequency sweeping mode) | Values (power control mode) |
|----------------------------------|----------------------------------|-----------------------------|
| U_{oc} | 49.60 V | 45.04 V |
| I_{sc} | 13.86 A | 12.38 A |
| U_m | 41.64 V | 37.77 V |
| I_m | 12.97 A | 11.58 A |
| Number of PV modules in parallel | 6 | 6 |
| Number of PV modules in series | 6 | 6 |
| Output voltage | 100 V | 100 |
| Capacitance | 2 mF | 2 mF |
| Inductance | 0.1 mH | 0.1 mH |
| Switching frequency | 30 kHz | 30 kHz |
| Line resistance | 0 | 0.66 Ω |

The Fig. 9 shows the PV output curve obtained from the experiment and the calibrated model. It can be seen that the parameter calibration is successful.

In order to verify whether the theoretical derivation process of the above small signal model of the converter is correct, a simulation model is built for frequency sweep verification. The parameters used in the simulation are shown in Table 1 (frequency sweeping mode).

The Fig. 10 is a comparison between the frequency sweep results in SIMULINK and the bode plots obtained by Eq. (6). It can be seen that the theoretical derivation results in this paper correspond well to the frequency sweep results in amplitude, but there are some differences in phase response caused by the second-order small semaphore ignored, resulting in differences between the theoretical derivation results and the frequency sweep results at high frequency.

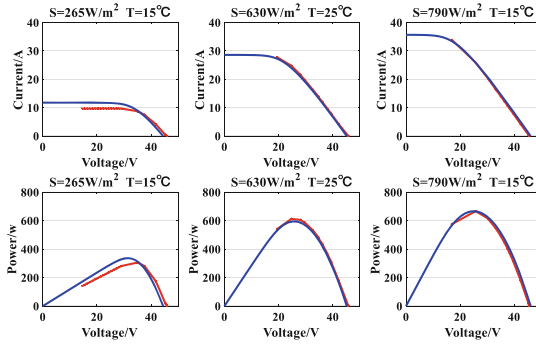


Fig. 9. Output curve obtained from the experiment and the calibrated model (red from experiment, blue from calibrated model).

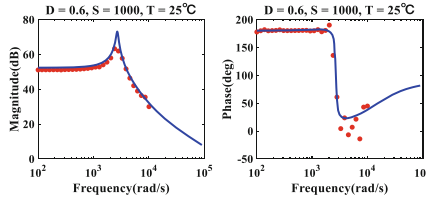


Fig. 10. Bode plots of frequency sweeping and theoretical derivation (red from frequency sweeping, blue from theoretical derivation).

4.3 AEL System Parameters verification

At different temperatures, the UI curve of the stack can be obtained by scanning the voltage and current, as shown in Fig. 11a. The parameters at a temperature of 75 °C are shown in Table 2. The C_{dl} can be measured by calculating the voltage waveform during the current step. The fitted relationship between power and current is shown in Fig. 11b. The power-current curve is closer to a straight line, which is beneficial to the design of the pre-stage power controller. The temperature has little effect on the power-current curve.

According to the dynamic model, the voltage response of the stack is shown in Fig. 12 when the current steps. The transient of U_{cell} is caused by the overvoltage on R_{ohm} , and the slow transition process is caused by the C_{dl} . The transition process lasts about 0.4 s, because of the smaller C_{dl} of the AEL system compared to the PEM system. For the AEL system, a power controller as shown in Fig. 7b can be applied.

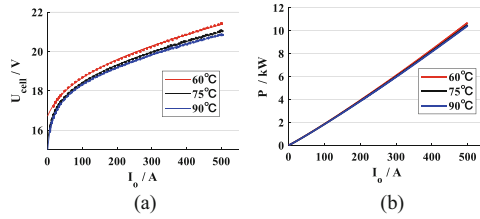


Fig. 11. AEL system parameter fitting.

Table 2. Stack equivalent circuit parameters (75 °C, 1.6 MPa).

| Parameter | Values |
|-----------|----------|
| R_{ohm} | 2.83 mΩ |
| C_{dl} | 57.38 F |
| U_{rev} | 15.39 V |
| a | 0.9241 |
| b | 0.002185 |

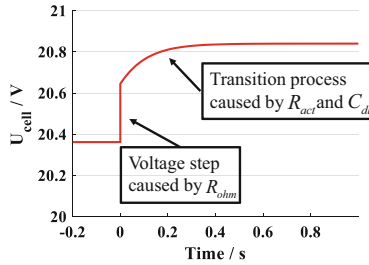


Fig. 12. Voltage response of AEL system with current step (400–500 A).

4.4 Frequency Regulation Results

The Fig. 13 shows the simulation results of the PV power controller. The step power signal can respond within 0.05 s. The PV system power controller designed in this paper can meet the requirements of AGC signal.

Figure 14 shows the results when the AEL system responds to the AGC signal. The bidding capacity C_{bid} is 3 kW. The AGC signal used is from the PJM regulation market in 2019. The duration of each experiment is 15 min (900 s), and the power sampling interval is 1 s.

The experimental results show that using the pre-stage power controller proposed, the AEL system can respond to the AGC signal quickly and accurately enough to support the system frequency stability.

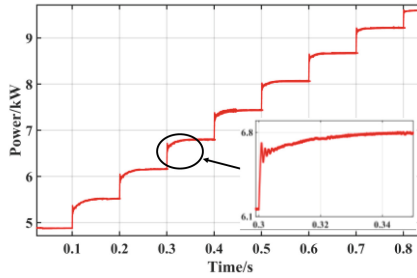


Fig. 13. The simulation results of the PV power controller.

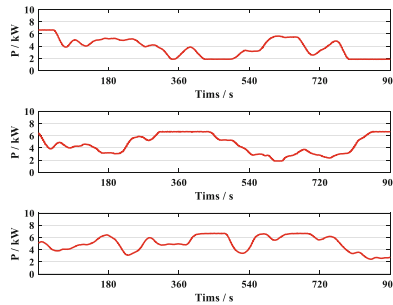


Fig. 14. AEL system follows AEC signal experiment.

5 Conclusion

Using the cooperative distribution method proposed, the PV-Hydrogen system can quickly response to the AGC signal and provide SFR. The simulation results show that the PV power controller designed in this paper can well respond to the power control signal and participate in the auxiliary service of the power system.

The electric double-layer effect of the AEL system is not as significant as that of the PEM system, and the duration of the voltage transient process is shorter when the load current changes. The existing current controller of the AEL system can be simply modified by designing the pre-stage power controller, so that the AEL system can quickly change its absorbed power. AGC signal response tests on a $2 \text{ Nm}^3/\text{h}$ AEL system demonstrate the effectiveness of the proposed controller.

Acknowledgement. This work was financially supported by the State Grid Co., Ltd. Science and Technology Project (5419-202199514A-0-5-ZN).

References

1. Ulleberg, Ø.: Modeling of advanced alkaline electrolyzers: a system simulation approach. *Int J Hydr Energy*. **28**(1), 21–33 (2003)

2. Abdin, Z., Webb, C.J., Mac, E., Gray, A.: Modelling and simulation of an alkaline electrolyser cell. *Energy* vol. **138**, 316–331 (2017)
3. Hernández-Gómez, Á., Ramirez, V., Guilbert, D., Saldivar, B.: Development of an adaptive static-dynamic electrical model based on input electrical energy for PEM water electrolysis. *Int. J. Hydr. Energy* **45**(38), 18817–18830 (2020)
4. Dozein, M.G., De Corato, A.M., Mancarella, P.: Virtual inertia response and frequency control ancillary services from hydrogen electrolyzers. *IEEE Transact. Power Syst.* 1–12 (2022)
5. Han, Z., Yuan, S., Wang, J., Dong, Y., Gao, L., Yang, Y.: Modeling and control of photovoltaic hydrogen production system adapting to power fluctuations. In: 2021 IEEE 5th Conference on Energy Internet and Energy System Integration (EI2), pp. 2835–2840 (2021)
6. Ganeshan, A., Holmes, D.G., Meegahapola, L., McGrath, B.P.: Enhanced control of a hydrogen energy storage system in a microgrid. In: 2017 Australasian Universities Power Engineering Conference (AUPEC), pp. 1–6 (2017)
7. Cheng, X., et al.: A coordinated frequency regulation and bidding method for wind-electrolysis joint systems participating within ancillary services markets. *IEEE Trans. Sustain. Energy.* 1–15 (2022)
8. Su, J., Yu, S., Zhao, W., Wu, M., Shen, Y., He, Y.: Investigation on engineering analytical model of silicon solar cells. *Acta Energiæ Solaris Sinica* **4**, 409–441 (2001)



Ortho- to Para-Hydrogen Spin Conversion Performance of Ho-Fe₂O₃ Catalytic at 77 K

Hong Xu¹, Jiawei Wang², Yisong Han², Mingzhe Xue¹(✉), and Cunman Zhang¹

¹ Clean Energy Automotive Engineering Center, School of Automotive Studies, Tongji University, Shanghai 201804, People's Republic of China
mzxue@tongji.edu.cn

² Hangzhou Oxygen Plant Group Co., Ltd, Hongyuan Building, No. 592, Zhongshan North Road, Gongshu District, Hangzhou 310004, Zhejiang, People's Republic of China

Abstract. In the process of hydrogen liquefaction, the conversion of ortho- to para-H₂ is necessary to ensure the long-time storage of liquid hydrogen. Ortho- to para-H₂ conversion catalysts can accelerate the rate of conversion. In this work, an efficient Ho-F₂O₃ by a simple precipitation method are developed to catalyze the spin conversion from ortho- to para-H₂. Benefiting from the disorder of crystal structure and homogeneity of the nanoparticle distribution after doping with Ho element, Ho-F₂O₃ has excellent catalytic conversion properties. When the hydrogen flow is 100 mL min⁻¹, the content of para-H₂ is 48.67% at 77 K after 1000 min. Our research provides direction for the design of the catalyst.

Keywords: Ortho- to para- H₂ conversion · Catalyst · Ho-F₂O₃ · Crystal structure disorder · Magnetic disorder

1 Introduction

With the global energy and environmental crisis, the demand for sustainable and clean energy is growing in all countries. Hydrogen energy, as a clean secondary energy source with zero emissions, is becoming a focus of attention [1, 2]. Hydrogen energy can reduce greenhouse gas emissions and mitigate the global climate change problem [3]. According to a report by the International Energy Agency, hydrogen energy will become an important part of global energy system in the coming decades, providing a key contribution to the global goal of carbon neutrality [4]. At the same time, as an energy carrier, hydrogen can enable the storage and conversion of renewable energy sources, thus solving the problems of intermittency, instability and territoriality of renewable energy [5]. However, the development of hydrogen energy also faces a number of challenges, including the high-energy storage and transportation of hydrogen. Of the high-pressure gas hydrogen, liquid hydrogen, and pipeline gaseous methods currently used in hydrogen storage and transportation, liquid hydrogen is economical for medium- to long-distance transport [6].

The production of liquid hydrogen is generally achieved through a series of cooling processes such as pre-cooling, turbo-expansion and throttling expansion of hydrogen [7,

8]. This is an energy consuming process with three main components: sensible heat, latent heat and the heat of conversion of ortho- to para-hydrogen (OPH) [9, 10]. The conversion of OPH is an important process in the liquefaction process, which directly affects the thermal stability of the liquid hydrogen. The conversion of OPH is an important process in the liquefaction process, which directly affects the thermal stability of the liquid hydrogen. Ortho-hydrogen (OH) and para-hydrogen (PH) are the spin isomers of the hydrogen molecule. When the nuclei spin in the same or opposite directions, they are referred to as OH or PH respectively [11, 12]. The difference in spin patterns leads to certain differences in energy states and physical properties of OH and PH. At room temperature, the ratio of OH and PH in hydrogen gas is about 3:1 [13]. As the temperature decreases, the high-energy OH is gradually converted into the low-energy PH and heat is released until equilibrium is reached [14]. However, it is important to note that the conversion is slow. If room temperature hydrogen is directly cooled down and liquefied, most of OH will not be converted to PH in time, resulting in a continuous conversion in liquid hydrogen and the release of the heat of conversion. As the heat of conversion is greater than latent heat of vaporization, this leads to the continuous vaporization of liquid hydrogen. It is therefore necessary to use catalyst for the conversion of OPH to accelerate the conversion.

The conversion of OPH is related to the interaction between the hydrogen molecule and the magnetic dipole of the catalyst [15]. Catalysts with paramagnetic active sites have a positive effect on OPH conversion [16, 17]. Commonly used catalysts are transition metal oxides with unpaired electrons such as iron oxide and chromium oxide. Oh's team [18, 19] studied a variety of catalysts and explored the relationship between catalyst material characteristics and catalytic performance. The lanthanide element Ho has high unpaired electrons and importantly its oxides are highly paramagnetic [20], which is advantageous for catalytic conversions. However, as holmium is expensive, doping as a hetero-element in inexpensive iron oxides is a viable way to go.

In this work, a simple co-precipitation method is used to dope holmium elements in iron oxide to assess the catalytic performance of the catalyst by testing the conversion of OPH at 77 K. The reasons for the improved catalytic performance are analyzed by means of multiple material characterization.

2 Experimental Methods

2.1 Material Synthesis

In this work, all chemicals were of analytical grade and unpurified. The samples were prepared by a simple co-precipitation method. 0.02 mol of $\text{Fe}(\text{NO}_3)_3 \cdot 9\text{H}_2\text{O}$ and 0.002 mol of $\text{Ho}(\text{NO}_3)_3 \cdot 5\text{H}_2\text{O}$ were dissolved in 500 ml of water and stirred for 20 min, followed by the dropwise addition of 25–28% NH_4OH until the pH of the solution reached 10. Stirring was continued for 3 h and the resulting precipitate was filtered and washed, then dried at 60 °C to obtain the Ho- Fe_2O_3 catalyst. A sample of pure phase Fe_2O_3 without $\text{Ho}(\text{NO}_3)_3 \cdot 5\text{H}_2\text{O}$ was prepared as described above.

2.2 Materials Characterization

The microscopic morphology of the samples was obtained by scanning electron microscope (SEM, ZEISS Gemini 300) and energy dispersive X-ray spectroscopy (EDS) were observed using OXFORD Xplore. The microstructure of the samples was analyzed by X-ray diffraction (XRD) at a sweep speed of 2° min^{-1} in the range of $20\text{--}80^\circ$ with a Cu-K α radiation (Rigaku Ultimate IV). The surface elemental composition and chemical valence of the samples were obtained by X-ray photoelectron spectroscopy (XPS, Thermo Scientific K-Alpha spectrometer with Al K α X-ray source). The Brunauer-Emmette-Teller (BET) surface area, nitrogen adsorption isotherms and pore characteristics of the samples were tested by a Micromeritics ASAP 2460 analyzer at 77 K. Magnetic measurements were carried out with Quantum Design PPMS-9T dc magnetometers.

2.3 Low Temperature Catalytic Performance Test of the Catalyst

The dried precipitated particles were crushed and sieved to obtain catalyst particles in the size range 40–55 mesh and activated under vacuum at 140°C for 24 h. 0.2 g of catalyst was weighed and filled into a vertical fixed-bed stainless steel reactor (internal diameter: 6 mm, height: 60 mm) with a 3 m long condensing coil. The reactor was placed in liquid nitrogen and the PH content of the converted hydrogen was measured by gas chromatography (with TCD).

3 Results and Discussions

The microstructure of samples is analyzed by XRD. From Fig. 1 that main diffraction peaks of Fe_2O_3 at 35.6° , 39.3° and 54.1° match the standard card of Fe_2O_3 (JCPDS 33–0664). The diffraction peaks of the Fe_2O_3 are not strong due to the lack of high temperature calcination. After doping with Ho, the crystallinity of Ho- Fe_2O_3 decrease dramatically and show an amorphous state. No significant diffraction peaks of holmium oxides appear, indicating that the Ho is uniformly doped in Fe_2O_3 . The doping leads to a more disordered crystal structure and magnetism of the Ho- Fe_2O_3 , which are beneficial for the OPH conversion. At the same time, Ho doping can lead to an increase in paramagnetic defects within Ho- Fe_2O_3 .

As in fixed bed gas-solid catalysis, the catalyst should have a granularity to reduce the effect of bed resistance. Therefore, in our work, a simple co-precipitation method is used to obtain a large particle size sample, which is crushed and sieved to obtain sample particles of suitable particle size. The microscopic morphology of samples is analyzed by SEM. Figure 2a and c show that the samples show irregular shapes. The accumulation of particles allows for the formation of a large number of particle gaps, which facilitates the flow of hydrogen gas. More details are shown in Fig. 2b and d. The catalysts all consisted of nanoparticles. Compared to Fe_2O_3 , the nanoparticles of Ho- Fe_2O_3 are small, well dispersed and with dense interparticle build-up. This facilitates the increase in mechanical strength of Ho- Fe_2O_3 to cope with the prolonged impact of hydrogen gas stream. The energy spectrum of Ho- Fe_2O_3 shows a homogeneous distribution of the doped element Ho in Ho- Fe_2O_3 .

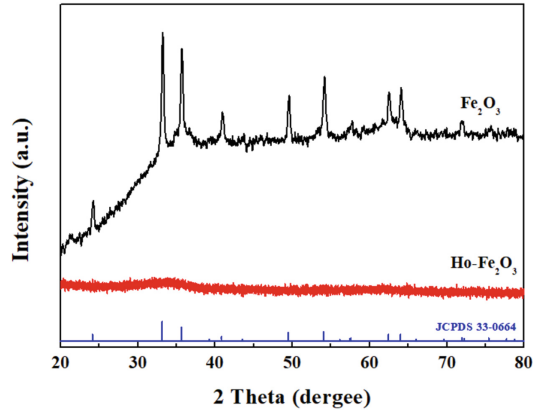


Fig. 1. XRD patterns of Fe_2O_3 and $\text{Ho-Fe}_2\text{O}_3$.

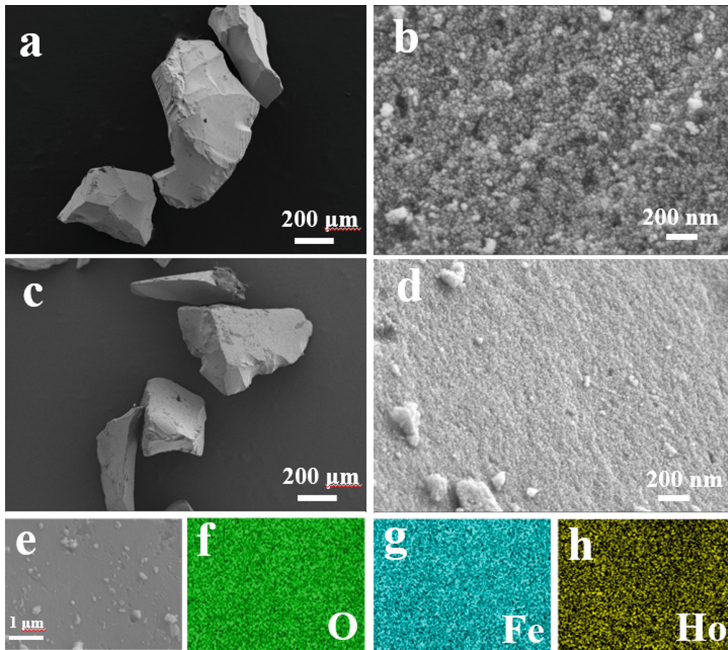


Fig. 2. SEM images of (a–b) Fe_2O_3 and (c–d) $\text{Ho-Fe}_2\text{O}_3$ and EDS mappings of (e–h) $\text{Ho-Fe}_2\text{O}_3$.

In order to further analyze the pore characteristics in Fe_2O_3 and $\text{Ho-Fe}_2\text{O}_3$, nitrogen adsorption and desorption measurements are carried out. Fe_2O_3 and $\text{Ho-Fe}_2\text{O}_3$ are classified as type IV isotherm with a typical mesoporous structure. The saturated adsorption plateau at high relative pressure indicates a homogeneous pore distribution of samples. The pore size distribution curves calculated from adsorption branches visualize the narrow distribution of pore diameters in the range of 2–4 nm. The average pore sizes of

Fe_2O_3 and $\text{Ho-Fe}_2\text{O}_3$ were 3.04 and 2.94 nm respectively. Combined with the SEM, resulted in smaller inter-particle pores due to the relatively small and evenly distributed particles of $\text{Ho-Fe}_2\text{O}_3$. The same conclusion can be obtained in Table 1. It can be visualized that in the pore range of 2.2–1.7 nm, $\text{Ho-Fe}_2\text{O}_3$ still provides 71.54 m^3/g of incremental pore area, which is much higher than the Fe_2O_3 , confirming that $\text{Ho-Fe}_2\text{O}_3$ has more micropores. As the smaller pores have a higher adsorption potential, this facilitates the rapid adsorption of hydrogen molecules. Also, the small pores can reduce the distance between the hydrogen molecules located within the pores and the inner wall of the pores, which facilitates the rapid onset of conversion (Fig. 3).

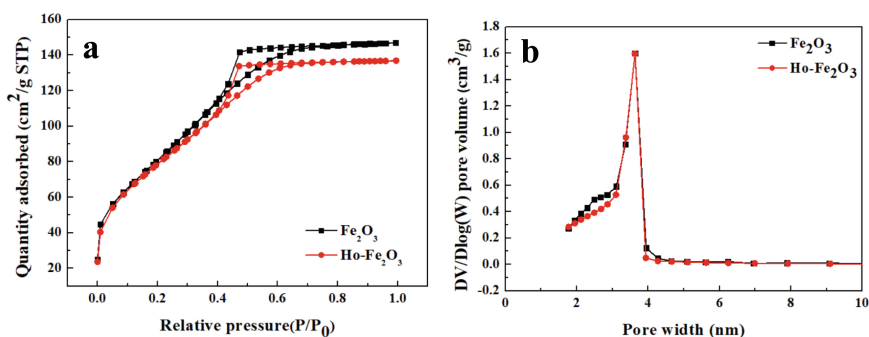


Fig. 3. (a) Nitrogen adsorption-desorption isotherms and (b) pore size distribution graphs of Fe_2O_3 and $\text{Ho-Fe}_2\text{O}_3$.

Table 1. BJH desorption pore distribution

| | Pore diameter range (nm) | Incremental pore area (m^2/g) |
|----------------------------|--------------------------|---|
| Fe_2O_3 | 2.2–1.9 | 36.04 |
| | 1.9–1.8 | 16.73 |
| $\text{Ho-Fe}_2\text{O}_3$ | 2.2–2.0 | 24.74 |
| | 2.0–1.9 | 25.58 |
| | 1.9–1.7 | 21.24 |

The elemental composition and valence states of Fe_2O_3 and $\text{Ho-Fe}_2\text{O}_3$ surfaces are determined by XPS. Figure 4a and b show the high-resolution Fe 2p spectrum of FO and $\text{Ho-Fe}_2\text{O}_3$, the main diffraction peaks of both samples are basically in the same position. After Gaussian fitting, the diffraction peaks consist of Fe^{2+} , Fe^{3+} and shakeup satellites respectively [21, 22]. Compare to Fe_2O_3 , the peak position of the XPS in $\text{Ho-Fe}_2\text{O}_3$ is shifted towards the higher binding energy, indicating that there is an interaction between Ho- and Fe-ion. The binding energies of 162.2 and 160.1 eV in Fig. 4c are characteristic peaks of Ho^{3+} , indicating that Ho is mainly present in the trivalent form in the $\text{Ho-Fe}_2\text{O}_3$ [23]. The Ho^{3+} has four unpaired electrons in its outermost layer and has a high electron magnetic moment, which facilitates catalytic conversion.

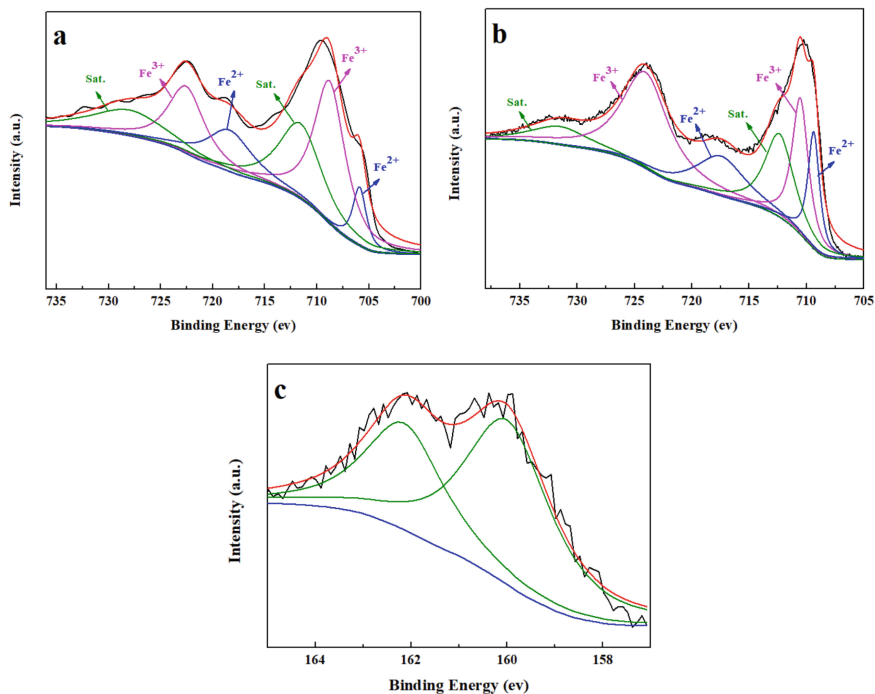


Fig. 4. Fe 2p XPS spectrum of (a) FO and (b) Ho-Fe₂O₃ and (c) Ho 4d spectrum of Ho-Fe₂O₃.

The magnetic properties are analyzed by PPMS. Figure 5 shows that Ho-Fe₂O₃ has negligible remanence and coercivity. The magnetization intensity increases with increasing magnetic field strength, shows a typical paramagnetic property. When the field strength is 30K Oe, the magnetic field strength is 2.65 emu g⁻¹. This indicates that Ho-Fe₂O₃ can provide a large number of paramagnetic active sites for the conversion of OPH.

The Fig. 6 shows the content of PH after catalytic conversion of Fe₂O₃ and Ho-Fe₂O₃ at 77 K for normal hydrogen at a flow rate of 100 mL min⁻¹. Both samples show a decrease in PH content at the beginning of reaction, probably due to the inactivation of active site as the reaction time increased and some of hydrogen molecules adsorbed at the active site could not be desorbed in time. It is obvious that the PH content of Fe₂O₃ is higher than that of Fe₂O₃. After 1000 min, the PH contents of Ho-Fe₂O₃ and Fe₂O₃ are 48.67 and 45.72% respectively. This may be related to the disorder in the crystal structure and the reduction of the nanoparticles caused by the doping of Ho.

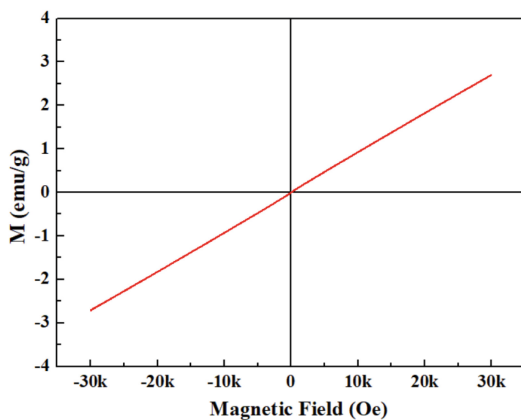


Fig. 5. Hysteresis loops of Ho-Fe₂O₃.

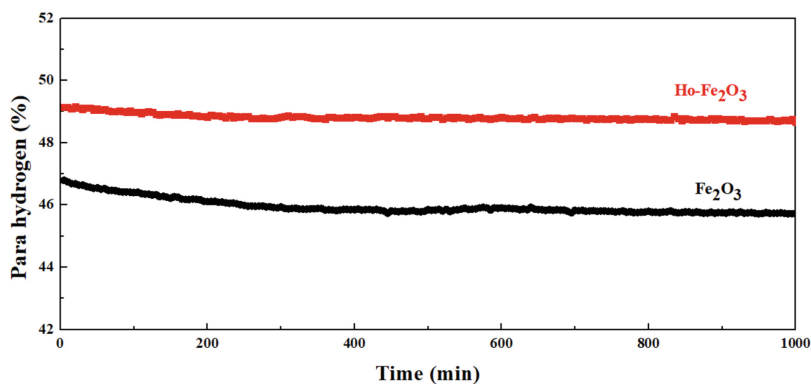


Fig. 6. Content of PH after catalytic conversion at 100 mL min^{-1} of Fe₂O₃ and Ho-Fe₂O₃.

4 Conclusion

The excellent catalytic conversion performance of Ho-Fe₂O₃ is related to the crystal structure and nanoparticle size. On the one hand, the doping Ho leads to a more disordered crystal structure inside the catalyst, paramagnetic defect sites and increased magnetic disorder, which facilitate catalytic conversion. At the same time Ho³⁺ have a high number of unpaired electrons and can provide high forces for conversion. On the other hand, the uniform distribution of small nanoparticles results in a smaller pore size of Ho-Fe₂O₃, which facilitates the adsorption of hydrogen and reduction of the distance between hydrogen and active sites on catalyst surface. The present work uses a simple co-precipitation method with a simple process, no secondary pelletizing and high catalyst particle strength, which provides a reliable experimental basis for the industrial scale production of catalysts.

Acknowledgements. We acknowledge the support provided by National key research and development program of China (grant numbers:2020YFB1506204).

References

1. Pinsky, R., Sabharwall, P., Hartvigsen, J., O'Brien, J.: Comparative review of hydrogen production technologies for nuclear hybrid energy systems. *Prog. Nucl. Energy* **123**, 103317 (2020)
2. Griffiths, S., Sovacool, B.K., Kim, J., Bazilian, M., Uratani, J.M.: Industrial decarbonization via hydrogen: a critical and systematic review of developments, socio-technical systems and policy options. *Energy Res. Soc. Sci.* **80**, 102208 (2021)
3. Dodds, P.E., Staffell, I., Hawkes, A.D., Li, F., Gruenewald, P., McDowall, W.: Hydrogen and fuel cell technologies for heating: a review. *Int. J. Hydrogen Energy* **40**(5), 2065–2083 (2015)
4. Andrews, J., Shabani, B.: The role of hydrogen in a global sustainable energy strategy. *Wiley Interdisciplin. Rev. Energy Environ.* **3**(5), 474–489 (2014)
5. Zhu, Q.L., Qiang, X.: Liquid organic and inorganic chemical hydrides for high-capacity hydrogen storage. *Energy Environ. Sci.* **8**(2), 478–512 (2015)
6. Gerboni, R.: Introduction to hydrogen transportation. *Compendium Hydr. Energy* **2**, 283–299 (2016)
7. Domashenko, A., Golovchenko, A., Gorbatsky, Y.: Production, storage and transportation of liquid hydrogen. experience of infrastructure development and operation. *Int. J. Hydr. Energy* **27**, 753–755 (2002)
8. Zhang, T., Uratani, J., Huang, Y., Xu, L., Griffiths, S., Ding, Y.: Hydrogen liquefaction and storage: Recent progress and perspectives. *Renew. Sustain. Energy Rev.* **176**, 113204 (2023)
9. Teng, J., et al.: Comparative study on thermodynamic performance of hydrogen liquefaction processes with various ortho-para hydrogen conversion methods. *Energy* **271**, 127016 (2023)
10. Zhao, Y., Gong, M., Zhou, Y., Dong, X., Shen, J.: Thermodynamics analysis of hydrogen storage based on compressed gaseous hydrogen, liquid hydrogen and cryo-compressed hydrogen. *Int. J. Hydrogen Energy* **44**(31), 16833–16840 (2019)
11. Furuya, K., Aikawa, Y., Hama, T., Watanabe, N.: H₂ ortho-para spin conversion on inhomogeneous grain surfaces. *Astrophys. J.* **882**, 172 (2019)
12. Ilicsa, E., Paris, S.: Magnetic field acceleration of the ortho-para H₂ conversion on transition oxides. *Phys. Rev. Lett.* **82**(8), 1788–1791 (1999)
13. Romanelli, G., et al.: Visualization of the catalyzed nuclear-spin conversion of molecular hydrogen using energy-selective neutron imaging. *J. Phys. Chemistr. C* **123**(18), 11745–11751 (2019)
14. Ghafri, S., et al.: Hydrogen liquefaction: a review of the fundamental physics, engineering practice and future opportunities. *Energy Environ. Sci.* **15**, 2690–2731 (2022)
15. Zhang, X., Karman, T., Groenenboom, G.C., Avoird, A.V.D.: Para-ortho hydrogen conversion: solving a 90-year old mystery. *Nat. Sci.* **1**(1), 1–8 (2021)
16. Sakurai, M., Okano, T., Tuzi, Y.: Ortho-para conversion of n-H₂ physisorbed on Ag (111) near two-dimensional condensation conditions. *Apple Surf. Sci.* **33**, 245–251 (1988)
17. Polyukhov, D.M., Kudriavkyh, N.A., Gromilov, S.A., Kiryutin, A.S., Poryvaev, A.S., Fedin, M.V.: Efficient MOF-catalyzed ortho-para hydrogen conversion for practical liquefaction and energy storage. *ACS Energy Lett.* **7**(12), 4336–4341 (2022)
18. Das, T., Choi, J.-G., Oh, I.-H.: Synthesis of highly effective α -Fe₂O₃ catalyst for the spin conversion of liquid hydrogen. *Proc. Natl. Acad. Sci. India Sect. A* **90**(3), 399–409 (2019)

19. Kim, J.H., Kang, S.W., Nah, I.W., Oh, I.-H.: Synthesis and characterization of Fe-modified zeolite for spin conversion of hydrogen at cryogenic temperature. *Int. J. Hydr. Energy* **40**(45), 15529–15533 (2015)
20. Lee, H.I., Lee, S.W., Rhee, C.K., Sohn, Y.: Paramagnetic Ho_2O_3 nanowires, nano-square sheets, and nanoplates. *Ceram. Int.* **44**(15), 17919–17924 (2018)
21. Liu, J., Meng, R., Li, J., Jian, P., Wang, L., Jian, R.: Achieving high-performance for catalytic epoxidation of styrene with uniform magnetically separable CoFe_2O_4 nanoparticles. *Appl. Catal. B* **254**, 214–222 (2019)
22. Xu, M., et al.: Catalytic degradation of sulfamethoxazole through peroxymonosulfate activated with expanded graphite loaded CoFe_2O_4 particles. *Chem. Eng. J.* **369**, 403–413 (2019)
23. Fan, Z., Wu, T., Xu, X.: Synthesis of reduced grapheme oxide as a platform for loading $\beta\text{-NaYF}_4\text{:Ho}^{3+}\text{@TiO}_2$ based on an advanced visible light-driven photocatalyst. *Sci. Rep.* **7**, 13833 (2017)



Optimal Scheduling for Integrated Hydrogen Production System Based on Exergy Analysis

Mengshu Zhu, Zhiyao Zhong, Jiakun Fang^(✉), and Xiaomeng Ai

Huazhong University of Science and Technology, Wuhan, China
{ms_zhu, zhongzy9803, jfa, xiaomengai}@hust.edu.cn

Abstract. A stable and consistent hydrogen supply is essential in various engineering scenarios. To address the challenge of meeting the demand for stable and green hydrogen with high proportion and fluctuating renewable energy input, integrated hydrogen production systems (IHPS) have been developed. Exergy balance is employed to assess the quality of energy loss and identify the size, location, and influencing factors of energy quality loss, which differs from the traditional scheduling problem of cost minimization or the black box model of exergy analysis. Firstly, the energy conservation principle along with the exergy concept for second-law assessment are applied to each system component. Secondly, an optimal scheduling model for IHPS is established that considers mass, energy, and exergy balance as well as operational constraints. The Pareto front of a multi-objective optimization problem is then established to obtain an optimal scheduling scheme with comprehensive performance in exergy efficiency and economics. Finally, case studies are conducted to intuitively show the distribution of exergy destruction and validate the applicability of the proposed dispatch method in efficiently bringing up a scheduling scheme with better overall performance.

Keywords: Integrated hydrogen production system · Exergy analysis · Exergy loss · Multi-objective optimization

1 Introduction

In recent years, hydrogen has been increasingly recognized as a clean and versatile energy carrier that can contribute to the transition toward a low-carbon economy. Meeting the demand for stable and green hydrogen is critical for many engineering scenarios, including industrial processes, backup power, and hydrogen refueling stations [1]. Fossil fuels are the main source of hydrogen production, causing large pollution. With the increasing use of fluctuating renewable energy for hydrogen production, ensuring a stable hydrogen supply has become a challenge. To address this challenge, integrated hydrogen production systems (IHPS) have been developed as promising solutions that can provide stable and green hydrogen.

The optimal scheduling of different energy sources in IHPS to improve energy efficiency and reduce operating costs remains an active research area. In [2], a basic framework of an integrated energy system containing multiple energy hubs is proposed, and

a distributed economic dispatching model considering carbon emissions is constructed. A deep deterministic policy gradient-based optimal scheduling method for integrated hydrogen energy systems is proposed to minimize the operating cost [3]. Moreover, The exergy, taking into account the “quantity” and “quality” of energy, has attracted the attention of some scholars. Exergy efficiency is used as an objective function to study integrated energy system planning [4]. The influence of the parameters in the integrated system is investigated on exergy and economic indicators through the parametric study to understand the system performance [5]. In summary, traditional scheduling methods often focus on cost minimization or use black box models for exergy analysis, which may not fully capture the quality of energy loss and its influencing factors [6].

This paper proposes an optimal scheduling model for IHPS based on exergy analysis. The scheduling model considers mass, energy, and exergy balance, along with other operation constraints, to obtain a scheduling scheme with comprehensive performance in exergy efficiency and economics. The rest of the paper is organized as follows: Sect. 2 provides an introduction to IHPS and thermodynamic analysis. Section 3 describes the multi-objective optimization scheduling model of IHPS. Section 4 presents the case studies. Section 5 concludes the paper and outlines potential future work.

2 Problem Description and Thermodynamic Analysis

2.1 Problem Description

The primary reason for integrating multiple hydrogen production technologies is that a single hydrogen production process cannot meet the stable and green hydrogen demand. Hydrogen production from fossil fuels leads to high carbon emissions and is not sustainable. On the other hand, renewable energy sources, such as water, biomass, and photovoltaic (wind power), have emerged as sustainable options for hydrogen production. However, hydrogen production from these sources faces challenges, such as fluctuating energy input and material quality issues. For instance, water electrolysis, a promising method for hydrogen production from renewable sources, requires significant energy storage capacity to maintain stable hydrogen output, resulting in high investment costs. Similarly, biomass-based hydrogen production is limited by the availability of biomass, which cannot meet the hydrogen demand.

Therefore, the IHPS has been developed to address these challenges. Figure 1 shows an IHPS combining water electrolysis (WE), biomass gasification (BG), and natural gas reforming (NGR). Energy and materials in the IHPS are coupled and complementarily utilized to increase exergy efficiency and reduce operating costs. Solar power is used by the WE to produce hydrogen and oxygen, with the oxygen either being stored or fed into BG and NGR. The by-product CH_4 from the BG unit can be supplied to NGR. The heat from the BG's outlet gas is used to heat the oxygen through a heat exchanger (HE).

After heating, the feed water at $75.0\text{ }^\circ\text{C}$ and 101.3 kPa enters the WE, which is directly coupled with renewable energy. The water-splitting reaction in the stack generates H_2 in the cathode and O_2 in the anode. The produced O_2 is compressed to 80.0 bar through compression and cooling and stored in a high-pressure tank. For the BG process, the O_2 supplied from the storage tank is depressurized by a direct expansion. The biomass mixed with O_2 is supplied to a gasifier. The heat of the outlet gas is used to improve the

O₂ temperature. After expansion, the stream enters the pressure swing adsorption (PSA) to yield purified H₂ and off-gas (CO₂, CO, and CH₄), which are then fed into the NGR reactor. Additionally, external input gas is also available.

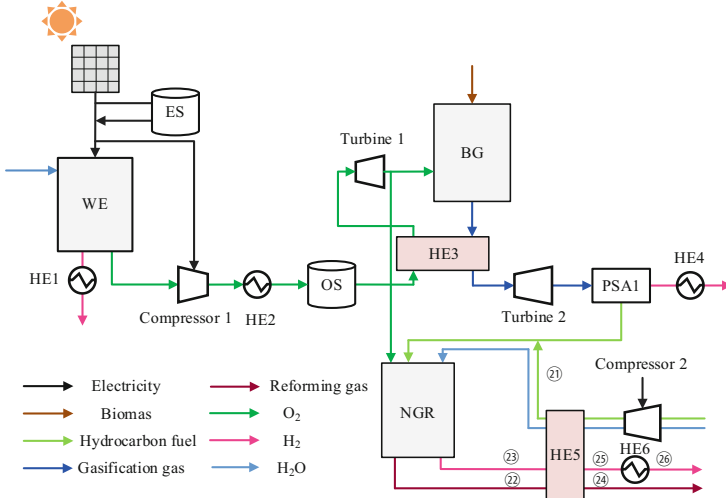


Fig. 1. Flow diagram of the IHPS.

2.2 Modeling and Thermodynamic Analysis

For a general steady-state process, mass and energy balances can be written as:

$$\sum \dot{m}^{in} = \sum \dot{m}^{out} \quad (1)$$

$$\dot{Q} + \sum \dot{m}^{in} h^{in} = \dot{P} + \sum \dot{m}^{out} h^{out} \quad (2)$$

where \dot{Q} is the heat rate, \dot{m}^{in} and \dot{m}^{out} indicate the mass flow rate of inlet and outlet material, \dot{P} is the power, h^{in} and h^{out} are the enthalpy of inlet and outlet material.

Neglecting the potential and kinetic effects, the exergy rate of a fluid stream is shown in (3). The factors $\dot{E}x^{ph}$ and $\dot{E}x^{ch}$ represent the physical and chemical exergy, defined as (4, 5) [7]:

$$\dot{E}x = \dot{E}x^{ph} + \dot{E}x^{ch} \quad (3)$$

$$\dot{E}x^{ph} = \sum_i \dot{m}_i (h_i - h_0 - T_0 (s_i - s_0)) \quad (4)$$

$$\dot{E}x^{ch} = \dot{m} \left[\sum_i x_i e_{0,i} + RT_0 \sum_i x_i \ln x_i \right] \quad (5)$$

where T_0 is the standard conditions temperature, R is the ideal gas constant, x_i denotes the mole fraction of i th specie, and e_0 denotes the standard chemical exergy.

The detailed mass, energy, and exergy balance principles of IHPS components are shown in Table 1. The same type of device is not repeatedly enumerated. $\dot{E}x_D$ is exergy destruction of a component in IHPS.

Table 1. Mass, energy, and exergy balance equations for components in the IHPS.

| Component | Mass balance | Energy balance | Exergy balance |
|--------------|--|---|--|
| WE | – | – | $\dot{m}_t^1 ex^1 + \dot{P}_t^{WE} = \dot{m}_t^2 ex^2 + \dot{m}_t^4 ex^4 + \dot{E}x_D^{WE}$ |
| Intercooler1 | $\dot{m}_t^2 = \dot{m}_t^3$ | $\dot{m}_t^2 h^2 = \dot{m}_t^3 h^3 + H_t^{I1}$ | $\dot{m}_t^2 ex^2 = \dot{m}_t^3 ex^3 + \dot{H}_t^{I1} (1 - \frac{T_0}{T_3}) + \dot{E}x_D^{I1}$ |
| Compressor 1 | $\dot{m}_t^4 = \dot{m}_t^5$ | $\dot{m}_t^4 h^4 + \dot{P}_t^{C1} = \dot{m}_t^5 h^5$ | $\dot{m}_t^4 ex^4 + \dot{P}_t^{C1} = \dot{m}_t^5 ex^5 + \dot{E}x_D^{Comp1}$ |
| Turbine1 | $\dot{m}_t^8 = \dot{m}_t^9$ | $\dot{m}_t^8 h^8 = \dot{m}_t^9 h^9 + \dot{P}_t^{T1}$ | $\dot{m}_t^8 ex^8 = \dot{m}_t^9 ex^9 + \dot{P}_t^{T1} + \dot{E}x_D^{T1}$ |
| BG | – | – | $\dot{m}_t^9 ex^9 + \dot{m}_t^{11} ex^{11} = \dot{m}_t^{12} ex^{15} + \dot{E}x_D^{BG}$ |
| HE 1 | $\dot{m}_t^7 = \dot{m}_t^8$ $\dot{m}_t^{12} = \dot{m}_t^{13}$ | $\dot{m}_t^7 h^7 + \dot{m}_t^{12} h^{12} = \dot{m}_t^8 h^8 + \dot{m}_t^{13} h^{13}$ | $\dot{m}_t^7 ex^7 + \dot{m}_t^{12} ex^{12} = \dot{m}_t^8 ex^8 + \dot{m}_t^{13} ex^{13} + \dot{E}x_D^{HE1}$ |
| PSA | $\dot{m}_t^{14} = \dot{m}_t^{15} + \dot{m}_t^{16}$ | $\dot{m}_t^{14} h^{14} = \dot{m}_t^{15} h^{15} + \dot{m}_t^{20} h^{20}$ | $\dot{m}_t^{14} ex^{14} = \dot{m}_t^{15} ex^{15} + \dot{m}_t^{16} ex^{16} + \dot{E}x_D^{PSA}$ |
| NGR | – | – | $\dot{m}_t^{10} ex^{10} + \dot{m}_t^{18} ex^{21} + \dot{m}_t^{21-H_2O} ex^{21-H_2O} = \dot{m}_t^{22} ex^{22} + \dot{m}_t^{23} ex^{23} + \dot{E}x_D^{FR}$ |

PEM Electrolyzer. Proton exchange membrane (PEM) has a fast dynamic response and is used as a technology for hydrogen production from water electrolysis. More details and discussions about PEM electrolyzer modeling can be found in [8].

$$\dot{P}_t^{PV} - \dot{P}_t^{PV-cur} - \dot{P}_t^{PV-ES} + \dot{P}_t^{ES-WE} - \dot{P}_t^{C1} - \dot{P}_t^{C2} = \dot{P}_t^{WE} \quad (6)$$

$$\dot{P}_t^{WE} = k_1 N^{cell} U_t^{cell} I_t^{cell} \quad (7)$$

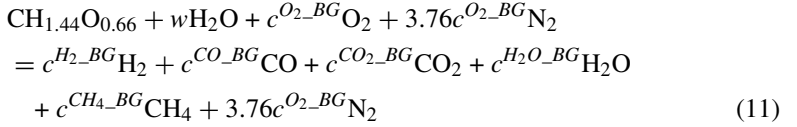
$$U_t^{cell} = E + U_t^{ohm} + U_t^{act} \quad (8)$$

$$I_t^{cell} = A^{cell} i_t^{cell} \quad (9)$$

$$\dot{m}_t^2 = \frac{k_2 N^{cell} I_t^{cell} h^F}{2F}, \dot{m}_t^4 = \frac{k_2 N^{cell} I_t^{cell} h^F}{4F} \quad (10)$$

where \dot{P}^{PV} is the photovoltaic generation, \dot{P}^{PV-cur} is the solar curtailment, \dot{P}_t^{PV-ES} is the power stored to the storage device, \dot{P}_t^{ES-WE} is the energy released from the storage device, \dot{P}_t^{C1} and \dot{P}_t^{C2} denote the power consumed by Compressor 1 and 2, respectively. I^{cell} is WE operating current, N^{cell} is the number of electrolysis cells, U^{cell} is the operating voltage, E is the open circuit voltage, U^{ohm} is the ohmic overvoltage and U^{act} is the activation overvoltage, k_1 and k_2 are unit conversion factor, h^F is Faraday efficiency, F is Faraday constant.

Biomass Gasification Model. The equilibrium model simulates the BG process because it is a reliable way to estimate the composition of syngas [9]. The global gasification reaction using wood as raw material and oxygen as gasifying agent is shown in (11).



where w is the moisture content per mole of wood, c^{O_2-BG} is the oxygen consumption per mole of wood, c^{H_2-BG} , c^{CO-BG} , c^{CO_2-BG} , c^{H_2O-BG} , c^{CH_4-BG} are the output coefficients of H_2 , CO , CO_2 , H_2O , and CH_4 , respectively.

The relationship between biomass feed, oxygen consumption, and gas production can be expressed as (12–14).

$$\dot{m}_t^{12-H_2} = c^{H_2-BG-O_2}\dot{m}_t^{11-O_2} + c^{H_2-BG-Air}\dot{m}_t^{11-Air} \quad (12)$$

$$\dot{m}_t^{9-O_2} = c^{O_2-BG}\dot{m}_t^{11} \quad (13)$$

$$\dot{m}_t^{12-CH_4} = c^{CH_4-BG}\dot{m}_t^{11}, \dot{m}_t^{12-CO_2} = c^{CO_2-BG}\dot{m}_t^{11} \quad (14)$$

Natural Gas Reforming Model. Chemical-looping auto-thermal reforming (CLRa) is applied to smooth out the fluctuations, which can achieve CO_2 capture without additional hydrogen purification. The detailed reactions and processes can be found in [10]. The product compositions are calculated by the reaction equilibrium based on gibbs minimization, mass balance, and heat balance equations. The products can be calculated in (15, 16). The temperature of the inlet gas will affect the coefficient in (17).

$$\dot{m}_t^{23} = c_t^{H_2-NGR-O_2}\dot{m}_t^{18-CH_4-O_2} + c_t^{H_2-NGR-Air}\dot{m}_t^{18-CH_4-Air} \quad (15)$$

$$\begin{aligned} \dot{m}_t^{10} &= c_t^{O_2-NGR}\dot{m}_t^{18-CH_4-O_2}, \dot{m}_t^{22-H_2O} \\ &= c_t^{H_2O-NGR}\dot{m}_t^{21-CH_4} \end{aligned} \quad (16)$$

$$c_t^Y = f(T_t^{NGR}), Y \in \{\text{H}_2, \text{O}_2, \text{H}_2\text{O}, \text{CO}_2\} \quad (17)$$

3 Multi-objective Scheduling Optimization Model for IHPS

3.1 Objective Function

The objective function includes exergy efficiency and economy, where exergy efficiency is considered from the perspective of energy loss.

Exergy loss model of the exergy efficiency objective function. Energy efficiency utilization evaluates the utilization of energy in terms of quantity. However, the behavior of converting high-quality energy (e.g., electrical energy) to low-quality energy (e.g., thermal energy) may occur. Exergy efficiency evaluates how well energy is utilized to achieve high-quality utilization of different energy sources, such as energy cascade use. The exergy loss is regarded as the objective function to cut the wastage of high-quality energy in (18). The exergy loss of the IHPS is determined by adding up the exergy destruction of each component.

$$F^{ExD} = \dot{E}x_D^{WE} + \dot{E}x_D^{BG} + \dot{E}x_D^{NGR} + \dot{E}x_D^{I1} + \dot{E}x_D^{I2} + \dot{E}x_D^{I3} + \dot{E}x_D^{I4} + \dot{E}x_D^{HE1} + \dot{E}x_D^{HE2} + \dot{E}x_D^{Comp1} + \dot{E}x_D^{Comp2} + \dot{E}x_D^{Turb1} + \dot{E}x_D^{Turb2} + \dot{E}x_D^{PSA} \quad (18)$$

Mathematical model of the economic objective function. The main component of the economic objective function is the operating cost. It consists of biomass and gas purchase costs.

$$F^{Eco} = \sum_t \left(\mu_{raw}^{bio} m_t^{11} + \mu_{raw}^{gas} m_t^{19} \right) \quad (19)$$

where μ_{raw}^{bio} and μ_{raw}^{gas} is the price per unit of biomass and natural gas.

3.2 Operation Constraints

Stable Hydrogen Production Constraints. The sum of hydrogen production of each module should meet the stable demand N^{H2} .

$$k_2 * \Delta t * (m_t^3 + m_t^{17} + m_t^{23}) = N^{H2} \quad (20)$$

Operation Constraints of Hydrogen Production Unit.

$$0 \leq P_t^{WE} \leq P^{WE_max}, 0 \leq m_t^{11} \leq m^{11_max}, 0 \leq m_t^{18} \leq m^{18_max} \quad (21)$$

where P^{WE_max} is the maximum output of WE unit, m^{11_max} and m^{18_max} are the maximum input of biomass and gas.

Energy Storage Device Operation Constraints.

$$\begin{aligned} Q_t^{ES} &= Q_{t-1}^{ES} + \eta^{ES} P_t^{PV_ES} - P_t^{ES_WE} / \eta^{ES} \\ 0 &\leq Q_t^{ES} \leq Q^{ES_max}, Q_1^{ES} = Q_T^{ES}, \\ 0 &\leq P_t^{PV_ES} \leq s_t^{ES} P^{ES_max}, 0 \leq P_t^{ES_WE} \leq (1 - s_t^{ES}) P^{ES_max} \end{aligned} \quad (22)$$

where Q^{ES} is the capacity of energy storage, Q^{ES_max} and P^{ES_max} are the upper limit of the capacity and storage/release power of storage, s^{ES} is the 0–1 state variable.

Oxygen and electricity storage constraints are similar and will not be reiterated.

3.3 Multi-objective Processing

For convex optimization problems, when the weight vector λ composed of multiple objective weights is non-negative, the scaling method can obtain the optimal solution on all Pareto front. The original objective (24) can be transferred to (25). Standardizing and normalizing the objective function allows for screening solutions that meet IHPS's multi-objective optimization scheduling requirements from the Pareto front.

$$\min f = (F^{ExD}, F^{Eco}) \quad (23)$$

$$\min \lambda^T f = \lambda^{ExD} F^{ExD} + \lambda^{Eco} F^{Eco} \quad (24)$$

4 Case Studies

Table 2 introduces the input values for the parameters in the study. The proposed problem is implemented to obtain the 24-h scheduling results.

4.1 Multi-objective Optimal Scheduling Results and Comparative Analysis

Multi-objective optimization problems are quantified, and enough Pareto optimal solutions are found by traversing the weight method. The specified weight's traversal step size is 0.01, which is solved by MATLAB R2022b and Gurobi 9.5.2. The Pareto frontier is obtained by interpolation fitting of the Pareto optimal solution in Fig. 2.

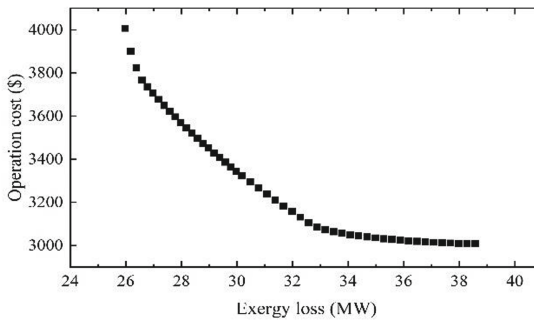
Table 3 presents a comparison of scheduling results obtained using different dominant objective functions. At the maximum operating cost, there is a 12.85 MW difference between the exergy loss and the minimum value, accounting for 32% of the total. The operating cost under the minimum destruction differs from the minimum cost by 839.51 \$, accounting for 21%. Under the cost-dominant scheme, the WE output contributes significantly because the cost of renewable energy is not considered. On the other hand, the NGR output increases significantly in a loss-dominated scheme due to its higher exergy efficiency compared to other technologies. The proposed method effectively balances the economic and efficiency aspects.

4.2 Exergy Analysis of IHPS

Figure 3 illustrates the exergy distribution of IHPS under the multi-objective optimal scheduling results. Although the input biomass exhibits high exergy, the exergy of output hydrogen is the lowest among the three technologies indicating that the exergy efficiency of BG is relatively low. In contrast, NGR has the lowest exergy input and the highest exergy of hydrogen, with the highest exergy efficiency. The analysis reveals that the WE

Table 2. Input data for major parameters for modeling the system.

| Paraments | Value |
|---|-------------------------|
| Stable hydrogen demand, N^{H_2} | 1000 Nm ³ /h |
| Maximum power of WE units, P^{WE_max} | 5 MW |
| Maximum feed rates of BG/NGR units, m^{11_max}/m^{18_max} | 0.36/0.05 kg/s |
| Energy and oxygen storage capacity, Q^{ES_max} | 4 MW |
| Upper limit rate of storage/release oxygen/power, P^{ES_max} | 2 MW |
| Average air temperature surrounding the system, T_0 | 293.15 K |
| Average air pressure surrounding the system, P_0 | 101.3 kPa |
| Temperature/pressure of WE unit | 350 K, 101.3 kPa |
| Temperature/pressure of BG unit | 1100 K, 24 bar |
| Temperature/pressure of NGR unit | 1100 K, 12 bar |
| Faraday constant, F | 96458 C/mol |
| Gas constant, R | 8.314 J/mol·K |
| Number of cells in the stack, N^{cell} | 350 |
| Active service area, A^{cell} | 1200 cm ² |
| Faraday efficiency, h^F | 0.99 |
| Moisture content per mol of wood, w | 10% |

**Fig. 2.** Pareto front for IHPS multi-objective optimal scheduling.

module experiences the highest exergy destruction due to its numerous components and physical transformation processes, including compression and cooling, which can cause partial exergy destruction.

Figure 4 illustrates the various subcomponents and their associated exergy destruction rates under an optimal scheduling scheme. The main destructions exist in WE, BG, and NGR, where chemical reactions occur. Even though the hydrogen production from NGR is the largest in this scenario, the destruction is less than that from WE and BG.

Table 3. Scheduling results dominated by different objective functions.

| Objective function | Minimum operating cost | Minimum exergy loss | Multi-objective optimization |
|--------------------------------------|------------------------|---------------------|------------------------------|
| Operating cost (\$) | 3010.16 | 4007.54 | 3049.59 |
| Exergy loss (MW) | 38.70 | 26.01 | 33.37 |
| Hydrogen from WE (Nm ³) | 8660.52 (36%) | 4016.20 (16%) | 8163.47 (34%) |
| Hydrogen from BG (Nm ³) | 13,198.67 (55%) | 4202.27 (18%) | 6858.48 (29%) |
| Hydrogen from NGR (Nm ³) | 2140.82 (9%) | 1,5781.53 (66%) | 8978.05 (37%) |

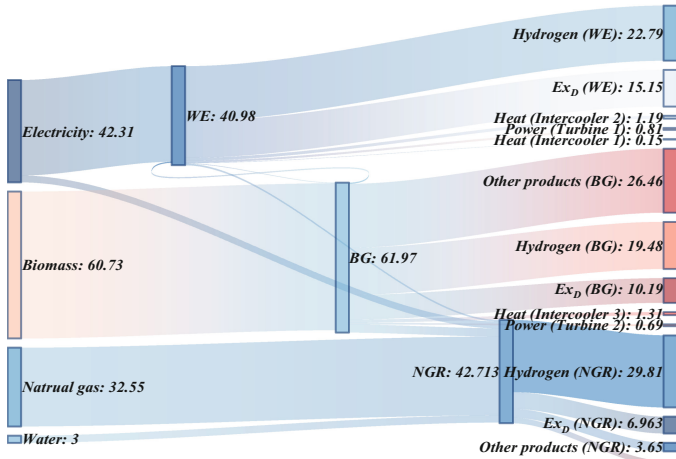


Fig. 3. Sankey diagram of exergy distribution in IHPS (unit: MW).

The exergy destruction from WE is larger than that from BG due to its more considerable input and mass flow rate.

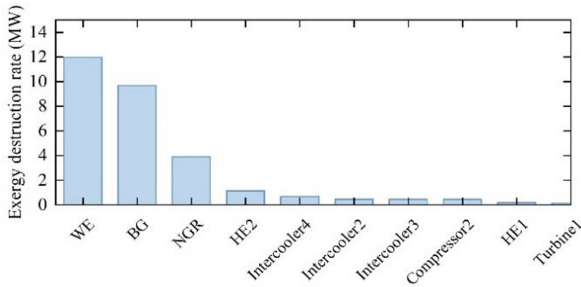


Fig. 4. Main components with respective exergy destruction rates.

5 Conclusion

This paper proposes an optimal scheduling model for IHPS based on exergy analysis. The proposed scheduling model considers mass, energy, and exergy balance, as well as other operational constraints, to develop a scheduling scheme that optimizes both exergy efficiency and economics. Case studies demonstrate the Pareto front and the scheduling results for balancing exergy efficiency and operating costs based on specific needs and goals. Moreover, the exergy distribution and exergy destruction are developed to quantify energy quality and loss in IHPS, which can assist energy managers in identifying areas where energy is being wasted and provide insights on how to improve the overall efficiency of IHPS.

Acknowledgment. The paper is funded by the National Natural Science Foundation of China, Grant ID: 52177088, and the National Natural Science Foundation of China, Grant ID: 52177089.

References

1. Song, P., Sui, Y., Shan, T., et al.: Assessment of hydrogen supply solutions for hydrogen fueling station: a Shanghai case study. *Int. J. Hydrogen Energy* **45**(58), 32884–32898 (2020)
2. Ma, L., Liu, N., Zhang, J., et al.: Real-Time rolling horizon energy management for the energy-hub-coordinated horizon energy management for the energy-hub-coordinated prosumer community from a cooperative perspective. *IEEE Trans. Power Syst.* **34**(2), 1227–1242 (2019)
3. Li, H., Qin, B., Jiang, Y., et al.: Data-driven optimal scheduling for underground space based integrated hydrogen energy system. *IET Renew. Power Gener.* **16**(12), 2521–2531 (2022)
4. Hu, X., Zhang, H., Chen, D., et al.: Multi-objective planning for integrated energy systems considering both exergy efficiency and economy. *Energy* **197**, 117155 (2020)
5. Habibollahzade, A., Gholamian, E., Ahmadi, P.: Multi-criteria optimization of an integrated energy system with thermoelectric generator, parabolic trough solar collector and electrolysis for hydrogen production. *Int. J. Hydrogen Energy* **43**(31), 14140–14157 (2018)
6. Li, J., Wang, D., Jia, H., et al.: Mechanism analysis and unified calculation model of exergy flow distribution in regional integrated energy system. *Appl. Energy* **324**, 119725 (2022)
7. Montazerinejad, H., Fakhimi, E., Ghandehariun, S., et al.: Advanced exergy analysis of a PEM fuel cell with hydrogen energy storage integrated with organic Rankine cycle for electricity generation. *Sustain. Energy Technol. Assess.* **51**, 101885 (2022)

8. Xing, X., Lin, J., Song, Y., Song, J., Mu, S.: Intermodule management within a large-capacity high-temperature power-to-hydrogen plant. *IEEE Trans. Energy Convers.* **35**(3), 1432–1442 (2020)
9. Cao, Y., Dhahad, H.A., Togun, H., et al.: A novel hybrid biomass-solar driven triple combined power cycle integrated with hydrogen production: multi-objective optimization based on power cost and CO₂ emission. *Energy Convers. Manage.* **234**, 113910 (2021)
10. Kang, K., Kim, C., Bae, K., et al.: Oxygen-carrier selection and thermal analysis of the chemical-looping process for hydrogen production. *Int. J. Hydrogen Energy* **35**(22), 12246–12254 (2010)



Fault Diagnosis of PEMFC Stack Based on PSO-DBN

Shaopeng Zhu^{1,5}, Bo Zhang², Liming Wang³, Ping Chen⁴, Huipeng Chen^{1,6}(✉), and Yekai Xu¹

¹ Power Machinery and Vehicular Engineering Institute, College of Energy Engineering, Zhejiang University, Zhejiang, China
hpchen@hdu.edu.cn

² School of Mechanical Engineering, HangZhou DianZi University, Zhejiang, China

³ SPIC Hydrogen Energy Tech Ningbo Research Institute, Zhejiang, China

⁴ State Power Investment Group Hydrogen Technology Development Co., Ltd, Zhejiang, China

⁵ Zhejiang Key Laboratory of Clean Energy and Carbon Neutrality, Zhejiang, China

⁶ Jiaxing Research Institute, Zhejiang University, Zhejiang, China

Abstract. As an important means of fault diagnosis for proton exchange membrane fuel cell (PEMFC), data-driven method can make accurate fault diagnosis by training a large number of fault sample data. Aiming at the problem that the more the dimension of the sample, the longer the learning time, this paper proposes a dimension reduction algorithm based on principal component analysis (PCA), which maps the multi-dimensional original data to the low-dimensional new data, and greatly accelerates the training efficiency under the premise of ensuring the reflection of the fault. At the same time, the fault diagnosis method based on the traditional machine learning model cannot accurately classify the data set of multi-dimensional features generated by the complex system of PEMFC stack, which leads to the low accuracy of fault diagnosis. The particle swarm optimization deep belief network (PSO-DBN) algorithm is designed to realize the PEMFC fault diagnosis method with high diagnostic accuracy. The experimental results show that the accuracy of the fault diagnosis algorithm based on deep learning proposed in this paper can reach 99.7% for the test set, and the efficiency and accuracy of fault diagnosis are better than traditional machine learning fault diagnosis algorithms such as Back propagation (BP) and support vector machine (SVM).

Keywords: Data drive · PSO-DBN · PEMFC · PCA · Deep learning · Fault diagnosis

1 Introduction

In the past decade, researchers have proposed many methods for diagnosing PEMFC faults. These fault diagnosis methods can be divided into two types: model-based methods and non-model-based methods. Polverino Pierpaolo et al. [1] proposed an advanced method based on structural analysis and causal calculation theory for PEMFC system fault detection and isolation based on mechanism model diagnosis algorithm. Esmaili

Qadir et al. [2] proposed an empirical model-based method for PEMFC water management diagnosis. By detecting the gas inlet and outlet pressure drop and the stack voltage, the water management fault of the system can be diagnosed. However, since PEMFC is a multidisciplinary complex nonlinear system, the establishment of PEMFC system simulation model not only requires very accurate modeling of each subsystem, but also fully considers the internal coupling relationship between subsystems. Therefore, the establishment of an accurate simulation model to simulate PEMFC faults under different actual operating conditions requires researchers to have a very deep understanding of the internal operation mechanism of PEMFC system. This reason also greatly limits the development of fault diagnosis methods based on PEMFC model. With the development of machine learning and pattern recognition, more and more researchers have adopted data-driven non-model fault diagnosis methods in the existing research on PEMFC fault diagnosis. Liu Ao et al. [3] proposed an online diagnosis algorithm based on incremental learning of K-means and OS-ELM and constructed a diagnosis system, which makes full use of the characteristics of ELM that does not need gradient-based back propagation, so the training speed is fast and can be well applied to vehicle online diagnosis. Lu Jingjing et al. [4] proposed an improved SVDD algorithm to realize the fault diagnosis of PEMFC. The results show that the improved SVDD algorithm has better fault identification performance than the traditional SVDD algorithm. Since the data-driven method does not need to establish a complex and accurate mathematical model or mechanism model compared with the model-based method, the characteristics representing the PEMFC state are extracted from the test data, that is, the battery voltage, current, temperature, pressure, humidity and other parameters are used as input. Through the pattern recognition method based on artificial intelligence (including machine learning and deep learning), the output can be obtained from these inputs, and the output is the fault type of PEMFC (including normal state).

The data-driven PEMFC fault diagnosis method relies on a large amount of historical data for training, and trains deep learning or machine learning models by learning the characteristics of various fault data in historical data. At present, the basic idea of the data-driven method is shown in Fig. 1. The core of this method is the establishment of historical database and the selection of fault diagnosis algorithm [5].

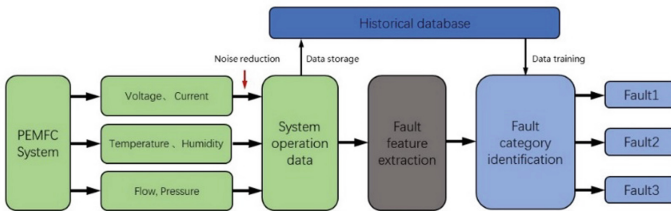


Fig. 1. Diagnostic idea diagram based on data-driven method

Although traditional machine learning algorithms have been applied to most diagnostic cases, they cannot play a good role in signals with poor correlation with training data distribution. In order to improve the accuracy, we must gradually enter the era of

deep learning. In this paper, a fault diagnosis algorithm of deep belief network based on particle swarm optimization in PEMFC stack is proposed. Using the proposed method, a neural network model trained by a large amount of data can be used to construct the nonlinear relationship between the input and output of PEMFC. People do not need to deeply understand the reaction mechanism inside the stack, and do not need to establish a complex PEMFC model. The fault diagnosis of PEMFC stack can be realized based on the black box input and output mode, which gets rid of the limitation of physical parameters in the traditional modeling process.

2 PEMFC System and Operation Data

2.1 PEMFC System

As shown in Fig. 2, this study uses an evaporative cooling (EC) fuel cell system for fault diagnosis. The system consists of two stacks, each of which consists of 300 battery cells. During the operation of this type of PEMFC, hydrogen is used as the cathode source and air is used as the anode source. In the stack, chemical energy is converted into electrical energy to supply power to the load. As the source of the cooling system, liquid water is evaporated into water vapor by injecting the stack, and then condensed into liquid water by the heat exchanger to form a complete cooling system loop [6].

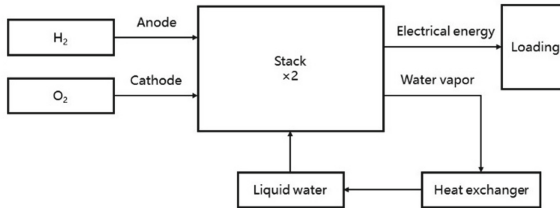


Fig. 2. Model of EC PEMFC system

2.2 System Operation Data

This study is based on multi-dimensional sensor technology, which is used to monitor various physical parameters in the actual operation of the PEMFC system, as shown in Table 1 [7].

In this paper, combined with the fault state data of the existing data set, the most common (more than 50% of PEMFC faults) and the most urgent membrane dry and flooding faults in the stack are selected, and data-driven fault diagnosis is performed under normal conditions [8].

Table 1. PEMFC system monitoring data

| Number | Variable | Unit | Number | Variable | Unit |
|--------|--------------------------------------|------|--------|---|------|
| 1 | Anode outlet pressure from stack 1 | MPa | 11 | Cathode stoichiometry | V |
| 2 | Anode outlet pressure from stack 2 | MPa | 12 | Cathode outlet temperature from stack 2 | °C |
| 3 | Cathode outlet pressure from stack 1 | MPa | 13 | Cathode inlet temperature from stack 2 | °C |
| 4 | Cathode outlet pressure from stack 2 | MPa | 14 | Cathode outlet temperature from stack 1 | °C |
| 5 | Current | A | 15 | Cathode inlet temperature from stack 1 | °C |
| 6 | Anode reactant flow | SLPM | 16 | Primary water inlet pressure from stack 2 | MPa |
| 7 | Anode inlet pressure from stack 1 | MPa | 17 | Primary water inlet pressure from stack 1 | MPa |
| 8 | Anode inlet pressure from stack 2 | MPa | 18 | Primary water inlet flow from stack 2 | SLPM |
| 9 | Cathode air inlet flow | SLPM | 19 | Primary water inlet flow from stack 1 | SLPM |
| 10 | Cathode inlet pressure from stack 1 | MPa | 20 | Water inlet temperature | °C |

2.3 Feature Extraction

2.3.1 Data Normalization

Data normalization is to unify the dimension of each dimension data, and to ensure that when PCA dimension reduction and deep learning weighted summation calculation are performed, the situation that the dimension of large feature participation is extremely large and the dimension of small feature participation is extremely small and negligible is avoided, which effectively ensures the accuracy of the diagnosis algorithm. Assuming that the original data set $D = [x_1, x_2, \dots, x_m]$, where x_i ($i \in [1, m]$) is a variable in Table 1, the deviation is standardized according to Formula 1:

$$x_i^* = \frac{x_i - x_{i_min}}{x_{i_max} - x_{i_min}} \quad (1)$$

where x_{i_max} and x_{i_min} represent the maximum and minimum values of the data in the variable x_i , respectively.

2.3.2 Principle of PCA Algorithm

PCA algorithm is a dimension reduction technique based on linear mapping. It ensures that the main features that can reflect the original fault type are retained as much as possible while reducing the data dimension. In the application, the covariance matrix of the data set is first calculated, and then the eigenvalues and eigenvectors of the covariance matrix are solved, and the vectors corresponding to the largest eigenvalues are selected to form a mapping matrix. The original data is transformed into a new data set by matrix multiplication to achieve the purpose of dimensionality reduction [9]. The ability to reflect the fault is called the variance contribution degree. According to the variance contribution degree, it becomes the first principal component, the second principal component, etc. The sum of the variance contribution degree of each component is called the cumulative contribution degree. If the cumulative contribution degree of the first k principal components reaches a certain value (generally up to 85%), k is taken.

The specific process of PCA algorithm is as follows [10]:

Algorithm 1. PCA algorithm.

| |
|---|
| Input: sample set $D = [x_1, x_2, \dots, x_m]$; |
| low-dimensional space dimension n |
| Process: |
| 1: Centralization $x^{(i)} = x^{(i)} - \frac{1}{m} \sum_{j=1}^m x^{(j)}$; |
| 2: Covariance matrix XX^T ; |
| 3: Eigenvalue decomposition of matrix XX^T ; |
| 4: The feature vector composed of the largest n eigenvalues is taken out and normalized to form the feature vector matrix W ; |
| 5: Obtain new sample $z^{(i)} = W^T x^{(i)}$; |
| 6: Return sample set $D' = [z_1, z_2, \dots, z_m]$ |
| Output: sample set D' after dimension reduction |

2.4 Fault Diagnosis

2.4.1 Deep Belief Network (DBN)

The deep belief network is a feedforward neural network stacked by multiple restricted Boltzmann machines (RBM), and its top layer is usually a back propagation layer (BP). The RBM layer is used to pre-train the data and determine the initialization parameters of the DBN network. The BP layer is used to reverse the network structure parameters, and the error back propagation method is used. Because it is stacked by multi-layer neural networks, DBN is a kind of deep learning. The bottom layer represents the original data signal, and the high layer represents the attributes or features of the data. A typical DBN structure model is shown in Fig. 3. Each RBM has a two-layer network consisting of a visual layer v and a hidden layer h . The layers are connected by weights, and the neurons in each layer are not connected to each other.

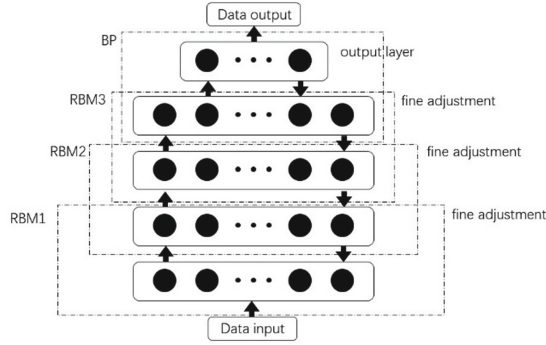


Fig. 3. DBN structure diagram

RBM is a probability distribution model based on energy, which is composed of input layer and output layer (feature extraction layer). As shown in Fig. 4, the energy of input layer and output layer.

$$E(v, h; \theta) = - \sum_{i=1}^m a_i v_i - \sum_{j=1}^n b_j h_j - \sum_{i=1}^m \sum_{j=1}^n v_i h_j \omega_{ij} \quad (2)$$

Here, $\theta = \{\omega, a, b\}$ is the parameter of the network; ω is the connection weight of input layer and hidden layer; a and b are the bias of the input layer node and the bias of the output layer node; $v = \{v_1, v_2, \dots, v_m\}$ is the input variable, $h = \{h_1, h_2, \dots, h_n\}$ is the output variable, and the energy function is used to characterize the probability distribution of the input data.

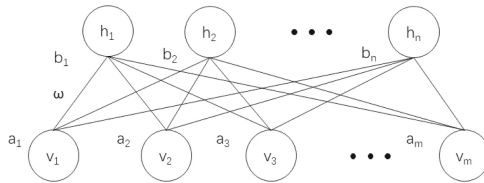


Fig. 4. RBM structure diagram

When RBM is stacked into a DBN network, the output layer of the previous RBM is introduced as the input layer of the next RBM, and the output characteristics of the previous RBM are output, extracted layer by layer, and the final data characteristics are obtained in the last layer. BP realizes the function of multi-classification. The training process of the DBN network is divided into two stages: the first stage is the forward unsupervised pre-training, and the RBM is greedy initialized layer by layer to obtain the initial value of the model parameters; the second stage is the reverse supervised fine-tuning learning process, which uses the known labels to fine-tune the model parameters from top to bottom to further optimize the network parameters [11].

2.4.2 PSO Trains DBN Network Structure

Particle swarm optimization algorithm is a population-based optimization algorithm. In PSO algorithm, the solution of each optimization problem is a particle in the search space. All particles have a fitness value determined by an optimized function, and each particle also has a speed v that determines the direction and distance of their flight. PSO initializes a group of particles, and then searches the optimal solution in the solution space according to the current optimal particle in the particle swarm. In each iteration, the particle updates itself by tracking two ‘extreme values’. One is the optimal solution found by the particle itself, called individual extreme value (p_{best}); another extreme value is the optimal solution found by the whole group, which is called global extremum (g_{best}). PSO algorithm needs less parameters to be adjusted, and it is simple and easy to implement. It is suitable for optimization in dynamic and multi-objective optimization environment. Compared with traditional algorithms, it has faster calculation speed and better global search ability [12].

For the four hidden layers of DBN in Fig. 3, there are m_1, m_2, m_3 and m_4 neurons in each layer, and the learning rate $\eta \in [0,1)$. When encoding the particle swarm, each particle in the PSO is set as a four-dimensional vector $X(m_1, m_2, m_3, m_4, \eta)$. The number of particles is N , and N is generally 10–20. In this paper, N is 10, and the maximum iteration number M of PSO is set to 400. The algorithm optimization process is shown in Fig. 5.

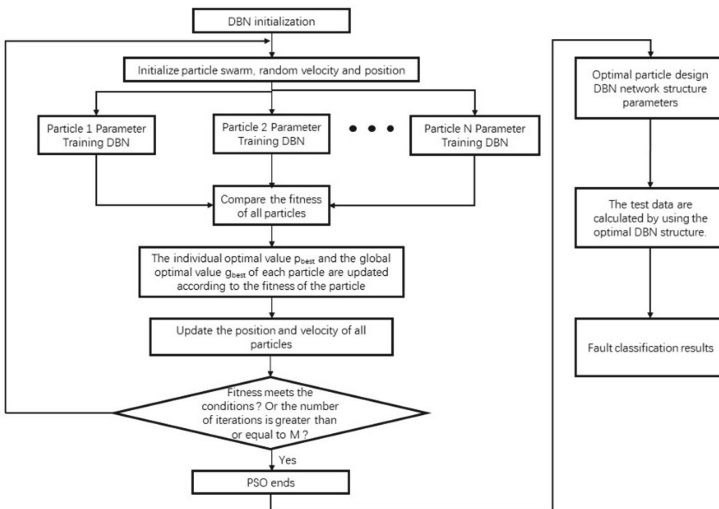


Fig. 5. PSO optimizes DBN process

Algorithm 2. PSO-DBN algorithm.

Input: data set D ' after dimensionality reduction;

Process:

1: Initialize the particle swarm

The initialized particle position $X_k^i = 0$, velocity $V_k^i = 0$;

2: Fitness value calculation

The fitness value (misclassification rate) of each particle is calculated, and the optimal particle X_{igbest}^k and the optimal particle X_{ipbest}^k in search history are found;

3: Update the velocity and position of particles

Using formula (3), formula (4), update the velocity and position of all particles;

$$X_i^{k+1} = X_i^k + V_i^{k+1} \quad (3)$$

$$V_i^{k+1} = \omega V_i^k + c_1 r_1 (X_{ipbest}^k - X_i^k) + c_2 r_2 (X_{igbest}^k - X_i^k) \quad (4)$$

In the formula: ω represents the inertia weight, the value is between $[0,1]$, generally take $\omega = 0.9$; c_1 and c_2 are acceleration parameters. Generally, c_1 and c_2 are equal and the value range is $[0, 4]$. Shi and Eberhart have been tested many times. It is suggested that $c_1 = c_2 = 2$ is the best to balance the effect of random factors[13]. r_1 and r_2 are two random values in the range of $[0, 1]$

4: If the misclassification rate of the training samples meets the set conditions or the number of iterations is equal to M, the PSO optimization ends, otherwise go to step 2, $k = k + 1$, and repeat steps 3 and 4 until the discriminant conditions are met

5: Using the trained DBN network to train the test data;

Output: Diagnostic results

3 Example Analysis

The training data includes three operating states of normal, flooded and membrane dry. The data are collected by 20 sensors distributed at the entrance and exit of the stack. The sensor variables are shown in Table 1, including 2000 groups of normal state data (Label 1), 2000 groups of membrane dry state data (Label 2), 2000 groups of flooded state data (Label 3), a total of 6000 groups of operating state data. The data set is divided as shown in Table 2.

3.1 PCA Dimensionality Reduction

PCA spatial feature extraction is performed on 20-dimensional data, and the feature vectors after feature extraction are selected according to the cumulative variance contribution. As shown in Fig. 6, the cumulative variance contribution rate of the first three feature vectors has reached 91%, which meets the requirements of characterizing the original data (more than 85%). Therefore, it shows that the first three feature vectors already contain enough information, so the original data set of the dimension 6000×20 is reduced to a new spatial feature data set of 6000×3 .

Table 2. Dataset partitioning

| Operating status (label) | Training set | Testing set | Total |
|--------------------------|--------------|-------------|-------|
| Normal (table 1) | 1400 | 600 | 2000 |
| Membrane dry (table 2) | 1400 | 600 | 2000 |
| Flooding (table 3) | 1400 | 600 | 2000 |
| Total | 4200 | 1800 | 6000 |

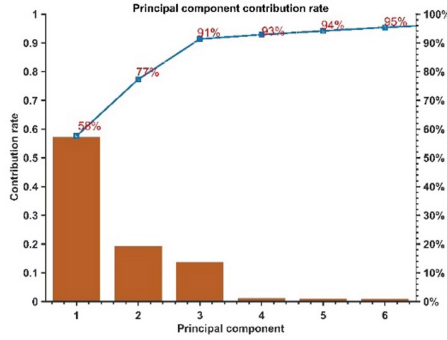


Fig. 6. Cumulative contribution rate of characteristics

3.2 Fault Diagnosis

3.2.1 Training Model Building

The PSO-DBN parameters are shown in Table 3 under the computer configuration of 64-bit R7-6800H, main frequency 3.2 GHz and RAM 16 GB.

Table 3. PSO-DBN algorithm parameters

| Parameter description | Parameter value |
|--------------------------------|-----------------|
| PSO acceleration factor | $c_1 = c_2 = 2$ |
| PSO particle swarm number N | 10 |
| PSO training iteration times M | 400 |
| PSO inertia weight | 0.5 |

3.2.2 Results Comparison

In the actual diagnosis, various fault diagnosis algorithms are used to train the diagnosis model in advance with the training set. By calling the model, the diagnosis efficiency can be greatly improved, which lays a good foundation for on-board online fault diagnosis.

The relevant experimental results are shown in Fig. 7:

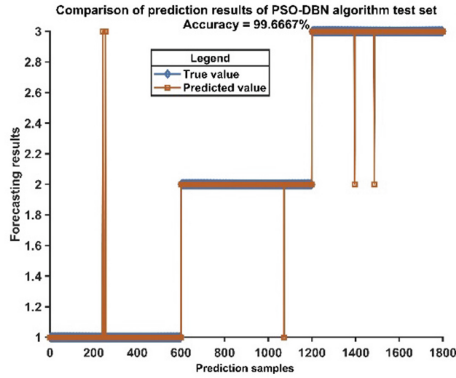


Fig. 7. Fault diagnosis accuracy results

Table 4. Comparative analysis of test set data algorithm

| Algorithm | Testing set accuracy/% | Running time/s |
|-----------|------------------------|----------------|
| PSO-DBN | 99.7 | 0.91 |
| BP | 93.1 | 0.25 |
| SVM | 93.9 | 0.34 |
| DBN | 96.8 | 0.41 |

From Table 4, it can be seen that in the test process, the traditional DBN algorithm is significantly better than the BP neural network algorithm and the SVM support vector machine algorithm in the test accuracy, but the test time is slightly longer than the SVM and BP algorithm, the difference is not more than 0.2 s. However, the DBN algorithm optimized by PSO has an accuracy rate of 99.7%. Although it is the longest test time in the above four algorithms, it does not exceed 1 s, which fully meets the efficiency requirements of online fault diagnosis and has a good engineering application prospect. In short, the DBN algorithm has a better classification effect than the traditional shallow network, and the DBN algorithm optimized by PSO has greatly improved the accuracy.

4 Conclusion

Aiming at the problem that the more the dimension of the sample, the longer the learning time, this paper proposes a dimension reduction algorithm based on principal component analysis (PCA), which maps the multi-dimensional original data to the low-dimensional new data, and greatly accelerates the training efficiency under the premise of ensuring the reflection of the fault. Aiming at the problem that the fault diagnosis method based

on traditional machine learning model cannot accurately classify the multi-dimensional feature data set generated by the complex system of PEMFC stack, which leads to low fault diagnosis accuracy, a PSO-DVN algorithm is proposed. The PSO-DBN method can adaptively select the optimal number and learning rate of each hidden layer neuron, without spending a lot of time to repeatedly adjust the network layer structure, saving a lot of time and energy. The experimental results show that the PSO-DBN method can effectively extract fault features by mining the fault information of the PEMFC stack, and has a high accuracy rate for the test set, and the efficiency is similar to other shallow networks. It has achieved good fault classification results and has good application prospects.

Acknowledgments. This work is supported by the National key research and development program, Fuel cell stack with High performance membrane electrode and ultrathin titanium electrode plate under Grant 2022YFB2502401.

References

1. Pierpaolo, P., et al.: Model-based diagnosis through structural analysis and causal computation for automotive polymer electrolyte membrane fuel cell systems. *J. Power Sour.* **357**, 26–40 (2017)
2. Qadir, E., et al.: Model based water management diagnosis in polymer electrolyte membrane fuel cell. *Int. J. Hydrogen Energy* **45**(31), 15618–15629 (2020)
3. Liu, A.: Research and Design on Safety Monitoring System and Fault Diagnosis of Hydrogen Fuel Cell. Taiyuan University of Technology, MA thesis (2021)
4. Lu, J.: Research on Fault Diagnosis and Application of Proton Exchange Membrane Fuel Cell based on Support Vector Data Description. University of Electronic Science and Technology of China, MA thesis (2022)
5. Ma, R., et al.: A review of fault mechanism analysis and diagnostic methods of proton exchange membrane fuel cell system. *Proceedings of the CSEE.* <https://doi.org/10.13334/j.0258-8013.pcsee.222031>
6. Mao, L., Jackson, L., Dunnett, S.: Fault diagnosis of practical polymer electrolyte membrane (PEM) fuel cell system with data-driven approaches. *Fuel Cells* **17**(2), 247–258 (2017)
7. Tiejiang, Y., Zelin, G., Tong, F.: PEMFC fault diagnosis based on spatiotemporal features of running data and Stacking ensemble learning
8. Zhou, S., et al.: Machine learning as an online diagnostic tool for proton exchange membrane fuel cells. *Curr. Opin. Electrochemistr.* **31**, 100867 (2022)
9. Jingcheng, C., Jidong, Z., Peicai, W.: Research on feature extraction technology of massive data based on PCA dimensionality reduction. *Commun. World* **27**(07), 83–84 (2020)
10. Beibei, L.: Research on single cell dimensionality reduction algorithm based on manifold learning. Harbin University of Technology, MA thesis (2020)
11. Xiao, C., Jurong, C.: Single-phase grounding fault line selection method for distribution network based on PSO-DBN. *Electric. Technol.* (2021)
12. Yibing, L., Lei, W., Li, J.: Rolling bearing fault diagnosis based on PSO improved deep belief network. *Vibr. Shock* **39**(5), 8 (2020)
13. Shi, Y.H., Eberhart, R.C.: Parameter selection in particle swarm optimization[M]. Springer, Berlin Heidelberg (1998)



Impact of Operational Parameters on Shutdown Characteristic of Industrial AWE Cell

Danji Huang, Ang Lu, Xiaomeng Ai, Zhiyao Zhong, Kewei Hu, and Jiakun Fang (✉)

State Key Laboratory of Advanced Electromagnetic Engineering and Technology, School of Electrical and Electronic Engineering, Huazhong University of Science and Technology, Wuhan 430074, China
jfa@hust.edu.cn

Abstract. The increasing share of renewable energy sources (RES) is placing higher demands on the dynamic response performance of energy storage equipment in power systems, including water electrolysis equipment. Alkaline Water Electrolysis (AWE), the most mature method of water electrolysis, is prone to reverse current during shutdown, resulting in prolonged shutdown and electrode degradation. This study investigates the influence of temperature, current density, and catalyst surface area on AWE shutdown characteristics. The results show that AWE exhibits an immediate surge of reverse current with a high amplitude following shutdown, followed by a gradual voltage drop over hundreds of seconds, accompanied by a reverse current at the milliamper level. The study also finds that operating conditions, such as increasing current density and temperature, affect the shutdown characteristics of AWE. Additionally, increasing the specific surface area of electrodes aggravates the impact of reverse impulse current. These insights can be used to optimize the design and operation of industrial AWE and provide a reference for the development of device control strategies.

Keywords: AWE · Reverse current · Shutdown process · Primary battery effect

1 Introduction

As the global push for Net-Zero intensifies, the integration of RES into the power system has been increasing [1, 2]. The water electrolysis technology has emerged as a promising solution to combine RES with hard-to-electrify areas, leading to the rise of the renewable hydrogen peak [3, 4]. Among various water electrolysis technologies, AWE is the most mature and cost-effective solution [5–7].

However, large-scale integration of AWE into the power system faces various challenges, and the flexibility issue due to the shutdown process is a crucial factor that needs to be addressed [8, 9]. During shutdown, the voltage can take tens of minutes to completely drop, and a large reverse current appears, which can degrade the catalyst and affect the performance of the power sources [10, 11]. To mitigate the impact of sudden shutdown, the current density is usually reduced gradually in steps during electrolyzer factory operations.

The flexibility of accessing AWE to the power system is greatly influenced by the characteristics of its shutdown process, making it a topic of interest in both academic and industrial research. There are two methods for studying the shutdown process of industrial electrolyzers. The first method uses the electric double layer (EDL) effect to explain the slow voltage drop process after shutdown [12, 13]. The model reflecting the EDL effect explains the time of the voltage drop through the modeling of the equivalent circuit [14]. The second method describes the shutdown process from the primary battery effect [8]. During water electrolysis, the cathode electrode is reduced while the anode electrode is oxidized. When power is turned off, a primary reaction occurs between the two electrodes connected through the KOH solution, leading to re-oxidation of the cathode electrode and re-reduction of the anode electrode [11]. This process is known as the primary battery effect, which not only predicts the voltage drop trend during the shutdown process but also explains the occurrence of reverse current.

Despite significant research on turn-off characteristics, current studies have limitations. Models based on the electric double layer effect can only explain the voltage variation trend during turn-off, but the equivalent capacitance lacks physical meaning, and the models cannot account for the reverse current. On the other hand, while models based on the galvanic effect accurately explain the reverse current and voltage variation during turn-off, research on industrial AWE electrolyzers lacks specificity and quantitative experimental results. To address these limitations, this paper explores the influence of different industrial operating conditions on the shutdown characteristics of the AWE electrolyzer using the galvanic cell effect, providing a better understanding of its turn-off behavior.

This paper aims to overcome the limitations of current research by experimentally investigating the shutdown characteristics of AWE electrolyzers cell under different industrial operating conditions. Using the primary battery effect as a starting point, the study will examine the voltage and reverse current behaviors of the electrolyzer during the shutdown process, varying temperature, electrolyte concentration, and operating current density. The results of this research will offer valuable insights into the operation and optimization of industrial AWE. The paper is structured as follows: Chapter 2 presents the problem statement, Chapter 3 describes the experimental methodology, Chapter 4 presents the experimental results, and Chapter 5 provides a conclusion.

2 Problem Statement

The industrial AWE electrolyzer has a bipolar plate structure where each plate acts as the anode and cathode of adjacent cells, except for the end plates, as shown in Fig. 1. Nickel-based materials are typically used for anode and cathode catalysts. During operation, the anode electrode oxidizes to generate Ni^{2+} and Ni^{3+} ions, while the cathode undergoes a reduction reaction to generate simple nickel. When the power is turned off, a primary battery reaction occurs due to the different potentials of the metal element and high-valence state oxide of the metal in the potassium hydroxide solution.

The primary battery effect affects the electrolyzer shutdown in two ways. Firstly, reverse current has a significant impact, with an instantaneous current effect occurring when power is cut off, generating a huge reverse current that can last between milliseconds to seconds. Impurities may also precipitate on the anode surface due to the

reverse current, affecting electrolytic performance. Secondly, the residual voltage after shutdown also affects the process, with a voltage drop that may take several minutes to occur until the primary battery effect on the cathode and anode materials subsides.

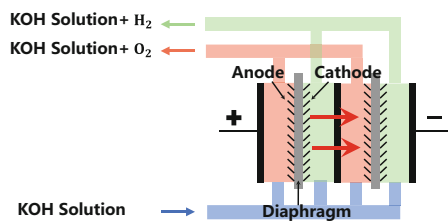


Fig. 1. Bipolar construction of industrial AWE

3 Experimental Methods

3.1 Experimental System

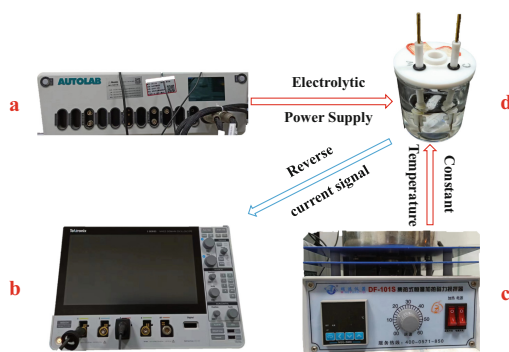


Fig. 2. Experimental apparatus. **a** power system; **b** measurement system; **c** temperature control system; **d** reaction system.

The experimental setup includes four systems: the power system, reaction system, temperature control system, and measurement system, as shown in Fig. 2. The power system uses a programmable AutoLab electrochemical workstation to supply electrolysis power and measure electrical signals up to a frequency of 1 kHz. The reaction system consists of a two-electrode electrolysis water system with commercial Raney nickel as the electrode catalyst. The temperature control system features an adjustable oil bath device that maintains a temperature range of 20–100 °C and includes an electromagnetic stirring function to simulate actual flow conditions. The measurement system utilizes a Tektronix 3-series oscilloscope to capture and store data at a maximum frequency of 10 MHz.

3.2 Experimental Procedure

The experiment involves a duration of 40 s using an adjustable current source in the AutoLab programming. The electrode voltage decay within 330 s after shutdown is recorded. Data measurement and saving are done at a frequency of 1 kHz during the first 30 s after shutdown and 1 Hz during the 30–330 s period. The experiment includes four different parameters with their respective values outlined in Table 1. The designed programming flow is shown in Fig. 3. Additionally, a measurement module is used to record the instantaneous reverse current process at a frequency of 10 MHz after shutdown.



Fig. 3. AutoLab program flow

Table 1. Experimental parameters.

| Parameters | Electrode material | Temperature (°C) | Current density (A/cm ²) |
|------------|--------------------|------------------|--------------------------------------|
| Values | Ni-Mesh Ni-Foam | Range (40,20,80) | Range (0.2,0.1,0.6) |

4 Experimental results

4.1 The Shutdown Characteristic of AWE Cell

Figure 4a presents the approximate changes in voltage and current of the AWE cell during the shutdown process. The power is turned off at $t = 40$ s. It can be observed that at $t = 42$ s, the current had decreased to near zero and the voltage had dropped to about 1.56 V. Between 42 and 100 s, the voltage slowly dropped to 1.20 V, and the current of the electrolytic cell oscillated around -1 mA, as shown in Fig. 4b. The slow voltage decrease accompanied by reverse current is caused by the primary battery effect after the shutdown. During normal operation of the device, the nickel mesh of the anode is oxidized to high-valence nickel ions, and the nickel mesh of the cathode is reduced to metallic nickel. When the power is turned off, the anode and cathode are connected by the electrolyte, and the primary battery reaction occurs between metallic nickel and high-valence nickel oxide, resulting in the appearance of reverse current.

The primary battery effect reaches maximum reaction speed at the moment the power is turned off. Subsequently, due to the continuous consumption of the electrode

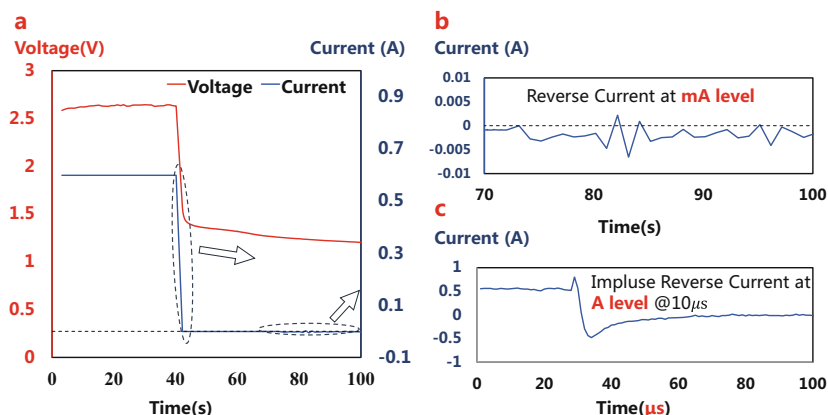


Fig. 4. **a** Shutdown voltage and current of AWE cell; **b** reverse current of AWE cell from 70 to 100 s; **c** impulse reverse current at A level of AWE cell

materials, the reaction rate gradually decreases. To study the instantaneous reaction, the current within 100 ms after the power-off is measured using an oscilloscope (sampling frequency 1 MHz), and the results are shown in Fig. 4c. It can be seen from the figure that within a few microseconds after the power-off, the reverse current reaches its peak amplitude, which can reach a level of negative 0.1 amps. After a few tens of microseconds of reaction, the value of the reverse current gradually decreases to the milliamp level. The phenomenon of impulse reverse current that occurs within the scale of tens of microseconds after the power is turned off will have a huge impact on the performance of the electrode materials. Many studies ignore the phenomenon of impulse current after the reaction, mainly because of the difference in time scale that is not paid attention to. During the turn-off process, when using the sampling frequency of Figure (a) (1–1000 Hz), it can be found that there is a milliamp-level reverse current after turn-off, but the data of impulse reverse current cannot be collected. In order to observe the reverse current phenomenon, the sampling frequency must be increased to the MHz level. This paper experimentally observes the situation of impulse reverse current under different operating conditions.

4.2 Influence of Operating Current Density

Figure 5a shows the current variations during the shutdown process under different operating current densities. It can be observed that the peak value of reverse impulse current at 0.6 A/m^2 operating current density can reach 0.424 A, which is about 1.55 times that at 0.4 A/m^2 and 2.15 times that at 0.3 A/m^2 . Therefore, the peak value of reverse current increases with the increase of operating current density. Previous research suggests that the operating current density does not affect the magnitude of the reverse current. This is due to the low sampling rate of the measurement system. As shown in Fig. 5a, after 150 ms, the reverse current values of different curves tend to be equal. When the sampling resolution of the detection system is lower than 1 MHz, it is difficult to capture the impulse current during the shutdown process. In fact, although

the operating current density has little effect on the value of reverse current in minutes, it has a significant impact on the peak value of impulse current during shutdown. Figure 5b shows the integral value of current during 50 ms (from 100 to 150 ms) after the peak value of reverse current is reached. The integral of reverse current is roughly proportional to the operating current of AWE.

The time integral of the impulse reverse current is a key factor affecting electrode materials. The peak value of the impulse reverse current is three orders of magnitude larger than the steady-state reverse current amplitude. During this stage, a large amount of charge is rapidly released, causing a significant impact on the electrode materials of both the anode and cathode. Therefore, the size of the time integral of the impulse reverse current should be focused on. The time integral of the impulse reverse current is related to the degree of oxidation-reduction of the electrode materials during operation. In this experiment, new nickel mesh was selected as the catalyst material, and the change in material mass during the same operating time was proportional to the magnitude of the operating current. Therefore, in the shutdown process, the time integral of the impulse reverse current is proportional to the magnitude of the operating current. For industrial water electrolysis equipment, when the equipment operates continuously for a long time, the electrode materials will be fully oxidized or reduced, resulting in a significant time integral of the impulse reverse current. To mitigate the impact of reverse current, it is necessary to extend the shutdown time of the equipment.

Note that the duration of the impulse reverse current is not always in the microsecond range, but closely related to the electrode area and the hydrogen Production capacity of the hydrogen production equipment. In industrial-grade equipment, large impulse reverse current with amplitudes ranging from hundreds of milliseconds to seconds may occur. This poses a great challenge for power electronics equipment. Therefore, during the shutdown process of the electrolytic cell, in order to prevent the impact of reverse current, direct shutdown from high current density should not be employed. Instead, a step-by-step reduction of current density should be used to protect the equipment.

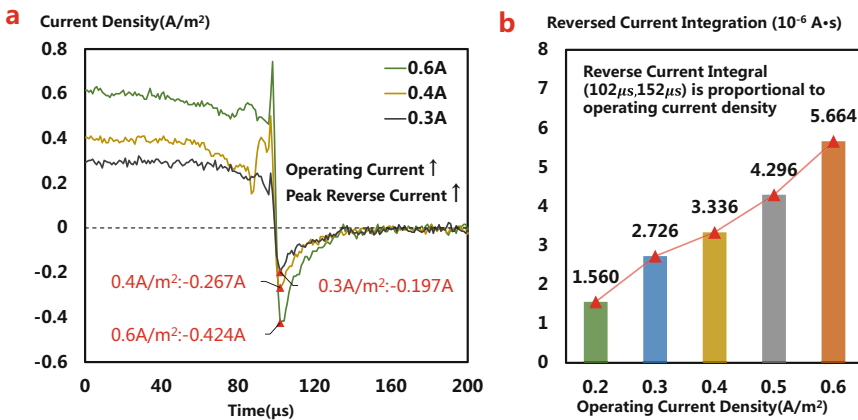


Fig. 5. a Shutdown current under different operating current density; b Reverse current integration from 102 to 152 μs

4.3 The Influence of Electrode Material

When selecting electrode materials for industrial AWE cells, it's important to consider not only their electrolytic performance, but also their impact on the electrolytic equipment during the shutdown process, particularly the peak value of the reverse current. Figure 6 illustrates the shutdown characteristics of electrolytic cell electrodes with different materials. The reverse current discharge time of the foam nickel electrode and the nickel mesh electrode is identical, and their reverse current curves converge after 5 μ s. However, the peak reverse current of the foam nickel electrode is 0.4824 A, which is approximately 30% higher than that of the nickel mesh electrode under the same experimental conditions. The reason for the higher peak reverse current in the foam nickel electrode compared to the nickel mesh electrode can be attributed to the difference in their surface area. Specifically, the foam nickel electrode has a larger specific surface area compared to the nickel mesh electrode. This results in a larger contact area between the foam catalyst and the electrolyte under the same electrode area. Therefore, the oxidation degree inside the foam nickel electrode is deeper during electrolysis, which makes the primary battery effect between the electrodes more pronounced, leading to a higher peak value of reverse current.

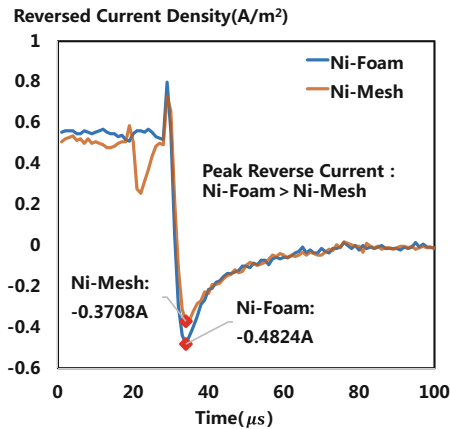


Fig. 6. Reversed current density under different electrode materials.

4.4 The Influence of Temperature

Figure 7 illustrates the shutdown characteristics of an electrolytic cell at different temperatures. In Fig. 7a, it is apparent that the turn-off reverse current behavior of the cell remains consistent at different temperatures. This is because the amount of charge accumulated in the electrode plate is constant when the electrolytic time and current are held constant, resulting in identical discharge times and reverse current characteristics. On the other hand, Fig. 7b demonstrates that both the electrolytic voltage and shutdown voltage of the cell decrease as the temperature rises, given the same electrolytic current.

As shown in Fig. 7a, the voltage of the electrolytic cell is influenced by the cell's conductivity when the current behavior of the cell is constant. The higher the temperature, the better the cell's conductivity, resulting in lower voltage during the electrolysis and shutdown processes.

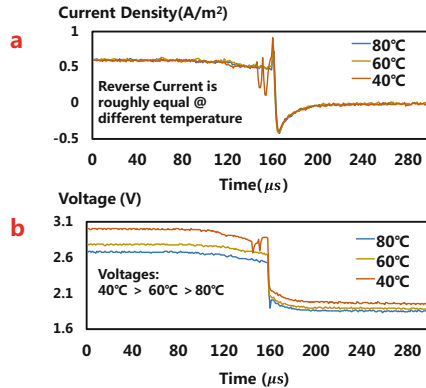


Fig. 7. Current and voltage in shutdown period at different temperatures, **a** current; **b** voltage.

In addition, a higher shutdown voltage indicates a greater corresponding reverse power when the reverse current is the same. Therefore, thermal management is critical during the shutdown process of industrial electrolytic cells.

5 Conclusion

This paper has investigated the shutdown characteristics of Awe cells under different temperatures, current densities, and electrode materials. The results provide insights into the shutdown process of industrial electrolyzers, making the following contributions:

- (1) The shutdown process of the electrolyzer is influenced by the primary battery effect, resulting in a impulse reverse current immediately after the power is turned off. Within a period of several hundred seconds after shutdown, the voltage gradually drops and the current reverses.
- (2) The operating conditions have a significant impact on the shutdown characteristics of the equipment. Increasing the current density leads to an increase in the peak value of the impulse reverse current, while increasing the reaction temperature results in a higher voltage drop rate, both of which weaken the shutdown characteristics of AWE equipment. Therefore, a stepwise reduction in the reaction current density and a lowering of the reaction temperature are recommended when shutting down the electrolyzer.
- (3) Increasing the specific surface area of the electrode can improve the efficiency and steady-state performance of the equipment, but it also increases the value of the reverse surge current during the turn-off process, which affects the shutdown capability of the device.

These findings can help optimize the design and operation of industrial AWE and provide guidance for developing control strategies for AWE systems.

References

1. Yang, X., Nielsen, C.P., Song, S., McElroy, M.B.: Breaking the hard-to-abate bottleneck in China's path to carbon neutrality with clean hydrogen. *Nat. Energy* **7**(10), 955–965 (2022)
2. Fankhauser, S., et al.: The meaning of net zero and how to get it right. *Nat. Clim. Chang.* **12**(1), 15–21 (2021)
3. Kojima, H., Nagasawa, K., Todoroki, N., Ito, Y., Matsui, T., Nakajima, R.: Influence of renewable energy power fluctuations on water electrolysis for green hydrogen production. *Int. J. Hydrogen Energy* **48**(12), 4572–4593 (2023)
4. Brauns, J., Turek, T.: Alkaline water electrolysis powered by renewable energy: a review. *Processes* **8**(2) (2020)
5. Ehlers, J.C., Feidenhans', A.A., Therkildsen, K.T., Larrazábal, G.O.: Affordable green hydrogen from alkaline water electrolysis: key research needs from an industrial perspective. *ACS Energy Lett.* **8**(3), 1502–1509 (2023)
6. Sebbahi, S., Nabil, N., Alaoui-Belghiti, A., Laasri, S., Rachidi, S., Hajjaji, A.: Assessment of the three most developed water electrolysis technologies: alkaline water electrolysis, proton exchange membrane and solid-oxide electrolysis. *Mater. Today Proceed.* **66**, 140–145 (2022)
7. Hu, K. et al.: Comparative study of alkaline water electrolysis, proton exchange membrane water electrolysis and solid oxide electrolysis through multiphysics modeling. *Appl. Energy* **312** (2022)
8. Abdel Haleem, A. et al.: Effects of operation and shutdown parameters and electrode materials on the reverse current phenomenon in alkaline water analyzers. *J. Power Sour.* **535** (2022)
9. Amireh, S.F., et al.: Impact of power supply fluctuation and part load operation on the efficiency of alkaline water electrolysis. *J. Pow. Sour.* **560** (2023)
10. Uchino, Y., et al.: Dependence of the reverse current on the surface of electrode placed on a bipolar plate in an alkaline water electrolyzer. *Electrochemistry* **86**(3), 138–144 (2018)
11. Uchino, Y., et al.: Relationship between the redox reactions on a bipolar plate and reverse current after alkaline water electrolysis. *Electrocatalysis* **9**(1), 67–74 (2017)
12. Du, H., Lin, X., Xu, Z., Chu, D.: Electric double-layer transistors: a review of recent progress. *J. Mater. Sci.* **50**(17), 5641–5673 (2015)
13. Wu, J.: Understanding the electric double-layer structure, capacitance, and charging dynamics. *Chem. Rev.* **122**(12), 10821–10859 (2022)
14. Shin, S.J., et al.: On the importance of the electric double layer structure in aqueous electrocatalysis. *Nat. Commun.* **13**(1), 174 (2022)



Performance Analysis Based on Energetic and Exergetic Ecological Index of a High-Temperature Proton Exchange Membrane Fuel Cell

Zhaoda Zhong^(✉), Samuel Simon Araya, and Vincenzo Liso

AAU Energy, Aalborg University, Pontoppidanstraede 111, 9220 Aalborg, Denmark
zhzh@energy.aau.dk

Abstract. The recent escalation in exergetic ecological evaluations in high-temperature proton exchange membrane fuel cells (HT-PEMFCs) stems from their ability to quantify emissions and ecological impacts. This study thus employs an isothermal, zero-dimensional model to investigate the exergy, energy, and exergetic ecological implications for an HT-PEMFC. Firstly, mathematical modeling for the exergetic ecological index and ecological function for the HT-PEMFC was derived. Among them, exergetic ecological index has yet to be applied to the research of this field before. The proposed HT-PEMFC model's accuracy is subsequently validated by utilizing two statistics methods, affirming its precision. Lastly, the study utilizes the exergetic ecological index's optimization criteria to explore ideal operational regions. Results illustrate that this index efficiently analyzes and optimizes the ecological impact of the HT-PEMFC.

Keywords: HT-PEMFC · Ecological analysis · Exergetic ecological index · Energy · Exergy analysis

1 Introduction

As a widely accepted energy conversion technology, the proton exchange membrane fuel cells (PEMFC) have emerged that are efficient and environmentally friendly. The widespread application of PEMFC in automotive and household devices can be attributed to their inherent benefits of reduced pollution, enhanced power density, and reduced noise levels [1]. There are two types of PEMFC according to the operating temperature: high-temperature PEMFC (120–200 °C), and low-temperature PEMFC (60–80 °C) [2, 3]. The advantages of HT-PEMFC include enhanced tolerance to impurities, simplified water management, and easier heat dissipation [4].

Currently, the majority of HT-PEMFC research focuses on aspects such as lifetime, corrosion, durability, and degradation [4]. However, only a limited number of researchers, particularly in ecological performance analysis utilizing exergy analysis, have incorporated the principles of the laws of thermodynamics to evaluate the HT-PEMFC characteristics. For instance, Bayat et al. [5] conducted a study to investigate the HT-PEMFC

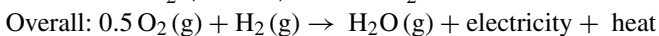
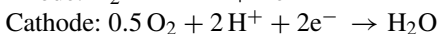
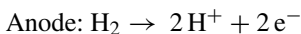
characteristics by utilizing a simulation model and employing ecological, exergy, and energy assessment. The investigation specifically examined the ecological coefficient of performance (ECOP) and ecological function as ecological performance indicators. Furthermore, the findings indicated that higher leak current density resulted in a decrease in all ecological indicators. Conversely, increasing the doping level enhanced the significance of ecological indicators. Li et al. [6] also performed a study using a simulation model, focusing specifically on the ECOP. The findings revealed a positive correlation between the higher doping level and operating temperature with the improved ECOP. Li et al. [7] presented a simulation model for HT-PEMFC and examined the correlation between some indicators related to energy and exergy. The aim was to compare these indicators and their relationship. The findings demonstrated that the exergetic performance coefficient considered both the exergetic loss rate and the power density to enhance the HT-PEMFC efficiency and maximize power output. Guo et al. [8] proposed a simulation model and aimed to probe the impact of various influencing factors on ECOP. The findings revealed that higher doping level and operating temperature have greatly contributed to enhancing the ECOP. On the other hand, the influence of operating pressure and relative humidity is relatively minor. Although previous studies have explored the ecological performance of HT-PEMFC, they primarily focused on the relationship between output power and entropy production, neglecting the connection with the exergy source.

Thus, to fill the research gap, an evaluation criterion called the exergetic ecological index from the heat engine field is introduced to investigate the relationship between the ecological performance and the exergy source. A steady-state HT-PEMFC model is formulated using MATLAB 2021b. The simulation results are compared to experimental data using two statistical techniques: the Root-mean-square error (*RMSE*) and the R-Squared (R^2). Two ecological indexes, namely exergetic ecological index and ecological function, are compared to deduce the optimal operating current density for ecological performance. The study not only optimizes the operating current density but also explores the relationship among exergy source, exergy product, and exergy destruction from the second thermodynamic perspective to enhance the ecological performance of the HT-PEMFC.

2 Method

2.1 Electrochemical Modeling of the HT-PEMFC

The HT-PEMFC involves some chemical reactions taking place internally.



Several reasonable and generally accepted assumptions are used to formulate the proposed model for purpose of simplifying the process:

- The operating state of the HT-PEMFC is steady-state;
- Air and hydrogen serve as the primary reactants;
- The supply of air and hydrogen corresponds to the produced electrical current;
- Reactant flow is assumed to be steady, laminar and incompressible;

- All reactants are treated as ideal gases;
- The electrical energy consumption associated with reactant compression is disregarded in this analysis.

The establishment of the electrochemical model is based on references [3, 9–12] and the parameters used in modeling are shown in Table 1. The energy analysis was referred to as Refs. [13, 14], and the exergy analysis was referred to as Refs. [15–17], Table 2 illustrates the related thermodynamic parameters.

Table 1 Physical parameters used in this model

| Parameters | Value | Units |
|-----------------------------|--|-------------------|
| Faraday constant | 96,485 | C/mol |
| Number of electrons | 2 | / |
| Universal gas constant | 8.314 | J/(mol·K) |
| Operating temperature | 453 | K |
| Membrane thickness | 0.01 | cm |
| Limiting current density | 2 | A/cm ² |
| Charge transfer coefficient | 0.5 | / |
| Doping level | 5.6 | / |
| Relative humidity | 3.8 | % |
| Anode gas | 100% H ₂ | / |
| Cathode gas | 21% O ₂ /79% N ₂ | / |
| Anode pressure | 1 | atm |
| Cathode pressure | 1 | atm |
| Temperature of environment | 298.15 | K |

Table 2 Thermodynamic parameters of substances

| Chemical species | Δg^0 (J mol ⁻¹) | Δh^0 (J mol ⁻¹) | Δs^0 (J mol ⁻¹) | $\varepsilon_{\text{chem},k}^0$ (J mol ⁻¹) |
|----------------------|-------------------------------------|-------------------------------------|-------------------------------------|--|
| H ₂ O (l) | 237,200 | 285,800 | 70 | 9500 |
| H ₂ O (g) | / | / | / | / |
| O ₂ (g) | 0 | 0 | 205 | 3970 |
| H ₂ (g) | 0 | 0 | 131 | 236,090 |

2.2 Ecological Analysis

Ecological function [5]

$$\dot{E} = P - T_0 \dot{S} \quad (1)$$

where P stands for the output power, and \dot{S} refers to the entropy production rate, and T_0 is the environmental temperature.

Exergetic ecological index [18]

$$\xi = \varphi - DP \quad (2)$$

where φ is the exergy efficiency and DP stands for the depletion ratio.

2.3 Validation

To verify the precision of the proposed model used in this study, a comparison is made [19] for the net output voltage curve at various current densities, as illustrated in Fig. 1a. The net output voltage is calculated and compared under the conditions of 453 K and an atmospheric pressure of 1 atm. In the experiment, air and hydrogen are used as reactants, with a doping level of 5.6% and a relative humidity of 3.8%.

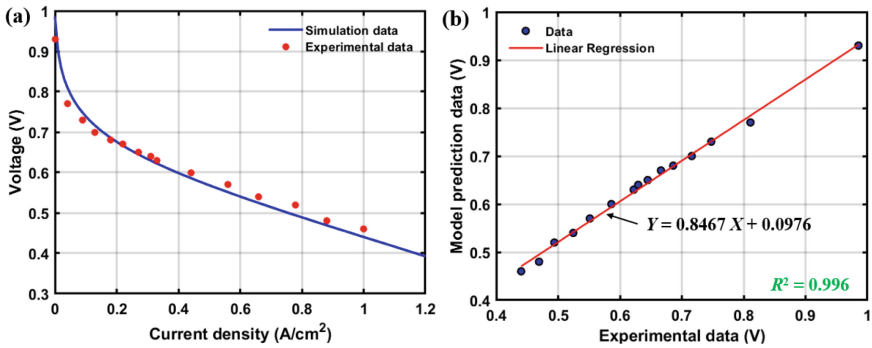


Fig. 1 (a) Validation of the HT-PEMFC and (b) correlation distribution of R^2 at 453 K

The performance evaluation of the proposed model was conducted by assessing the $RMSE$ and R^2 values between the experimental and modeled data [20, 21]. For operating temperatures at 453 K, the $RMSE$ value was found to be 0.022. Additionally, the R^2 value calculated at 453 K was determined to be 0.996. Furthermore, Fig. 1b illustrates the R^2 correlation coefficient between the experimental and modeled datasets. The analysis reveals a strong correlation between the two datasets, confirming the high level of validation across a wide range of current densities of the HT-PEMFC.

3 Results and Discussions

Figure 2 exhibits the fluctuations of normalized ecological function (e), power output (p), fuel exergy rate (exf), and exergy destruction rate (exd) with the change of normalized current density. Notably, both normalized power output (p) and normalized ecological function (e) exhibit distinct maximum points. The normalized ecological function (e) peaks at a normalized current density of 0.18, whereas the normalized power density

attains its highest value at a normalized current density of 0.68. Importantly, the optimal points for normalized ecological function (e) and normalized power output (p) do not coincide. There are multiple instances where the normalized ecological function (e) becomes negative, indicating that the lost power surpasses the useful exergy, and a significant portion of the rate of fuel exergy is depleted. Interestingly, at the maximum power density, the normalized ecological function (e) does not achieve its maximum value. Instead, the normalized ecological function (e) becomes negative when the normalized current density exceeds 0.38, signifying that the valuable power is outweighed by the lost power.

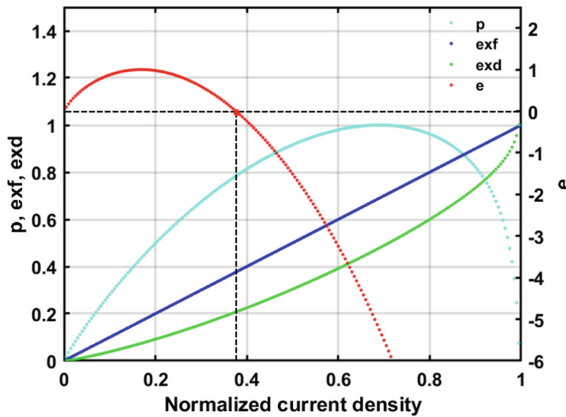


Fig. 2 The curve of the normalized current density on normalized output power, ecological function, fuel exergy, and exergy destruction of HT-PEMFC

Figure 3 illustrates the fluctuations of the exergetic ecological index (ξ), exergy efficiency (φ), depletion ratio (DP), and energy efficiency (η) with the change of normalized current density. All parameters, except for DP, exhibit a decreasing trend as the normalized current density increases. Specifically, as the DP rises, the exergy efficiency decreases. Moreover, when the rate of exergy destruction surpasses the power density, the exergetic ecological index assumes negative values, particularly when the normalized current density exceeds 0.3. It can be seen from Eq. (2) that the ranges of ξ from -1 to 1 . Based on the obtained findings, at a normalized current density of 0.02, the exergetic ecological index is 0.531, suggesting a conversion of over 53% of the fuel exergy into power output. In addition, when the normalized current density reaches 0.98, the index of -0.784 signifies that the exergy destruction (exd) rate surpasses the output power (p), causing the depletion of more than 78% of the fuel exergy.

Figure 4 depicts the fluctuations in normalized power density, ecological function, and energy efficiency. Notably, the ecological function (e) reaches a value of -5.2 at the maximum normalized power density, indicating a significant imbalance between lost power and useful power. At this particular point, the energy efficiency (η) is only 28%.

Figure 5 presents the fluctuations in the exergetic ecological index (ξ), depletion ratio (DP), and exergy efficiency (φ) with the change of the normalized power density.

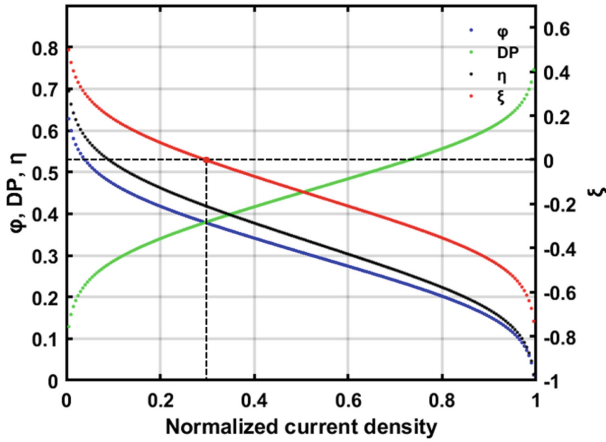


Fig. 3 The outcome of the normalized current density on exergetic ecological index, depletion ratio, exergy efficiency, and energy efficiency of HT-PEMFC

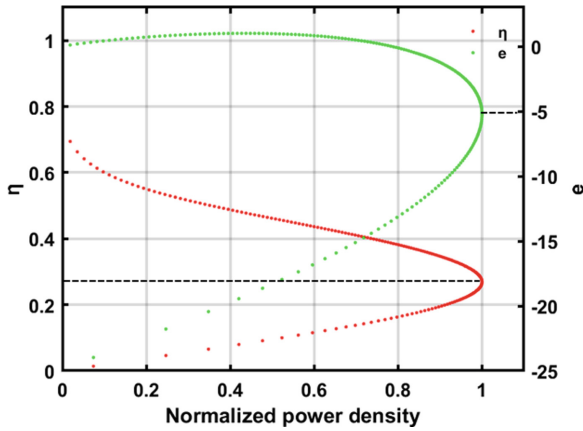


Fig. 4 The influence of the normalized power density on ecological function and energy efficiency of HT-PEMFC

The exergetic ecological index (ξ) reaches -0.273 at maximum normalized power density based on obtained results, indicating that the exd surpasses the p, resulting in the destruction of over 27% of the fuel exergy. At this particular point, the HT-PEMFC exhibits an exergy efficiency φ of merely 24%, accompanied by a depletion ratio of 51%. These findings suggest that the optimized current density range for the considered HT-PEMFC should be selected as $i_{\xi} \leq i \leq i_e$, where i_{ξ} denotes the normalized current density associated with the maximum exergetic ecological index, and i_e stands for the normalized current density associated with the maximum ecological function.

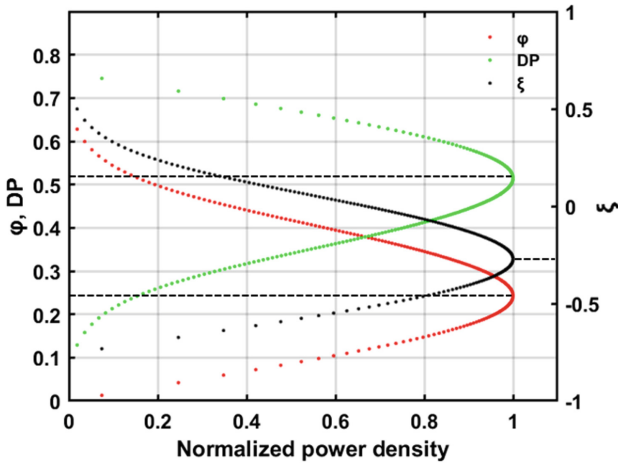


Fig. 5 The consequence of the normalized power density on the exergetic ecological index, DP, and exergy efficiency

4 Conclusions

To investigate the relationship among the exergy source, exergy product, and exergy destruction of the HT-PEMFC, this study proposes an isothermal, zero-dimensional model of the single HT-PEMFC. The specific conclusions from the paper are as follows:

- (1) The optimal points for normalized ecological function (e) and power output (p) do not coincide. The ecological function is negative, while the normalized current density exceeds 0.38.
- (2) The exergetic ecological index (ξ) ranges from -1 to 1 . Its value is negative, while the normalized current density exceeds 0.3.
- (3) The normalized ecological function (e) reaches -5.2 while the maximum normalized power density is reached, meaning that the loss power is much greater than the useful power.
- (4) Upon reaching the peak of the normalized power density, the corresponding value of ξ descends to -0.273 , indicating an exergy destruction rate surpassing the power output and the depletion over 27% of the fuel exergy.

References

1. Haider, R., Wen, Y., Ma, Z.-F., Wilkinson, D.P., Zhang, L., Yuan, X., Song, S., Zhang, J.: High temperature proton exchange membrane fuel cells: progress in advanced materials and key technologies. *Chem. Soc. Rev.* **50**, 1138–1187 (2021)
2. Saedan, M., Afshari, E., Ziaei-Rad, M.: Modeling and optimization of turbulent flow through PEM fuel cell cooling channels filled with metal foam—a comparison of water and air cooling systems. *Energy Convers. Manage.* **258**, 115486 (2022)

3. Wu, W., Zhai, C., Sui, Y., Zhang, H.: A novel distributed energy system using high-temperature proton exchange membrane fuel cell integrated with hybrid-energy heat pump. *Energy Convers. Manage.* **235**, 113990 (2021)
4. Araya, S.S., Zhou, F., Liso, V., Sahlin, S.L., Vang, J.R., Thomas, S., et al.: A comprehensive review of PBI-based high temperature PEM fuel cells. *Int. J. Hydr. Energy* **41**(46), 21310–21344 (2016)
5. Bayat, M., Özalp, M.: Effects of leak current density and doping level on energetic, exergetic and ecological performance of a high-temperature PEM fuel cell. *Int. J. Hydr. Energy* (2023)
6. Li, D., Li, S., Ma, Z., Xu, B., Lu, Z., Li, Y., et al.: Ecological performance optimization of a high temperature proton exchange membrane fuel cell. *Mathematics* **9**(12), 1332 (2021)
7. Li, D., Li, Y., Ma, Z., Zheng, M., Lu, Z.: Exergetic performance coefficient analysis and optimization of a high-temperature proton exchange membrane fuel cell. *Membranes* **12**(1), 70 (2022)
8. Guo, Y., Guo, X., Zhang, H., Hou, S.: Energetic, exergetic and ecological analyses of a high-temperature proton exchange membrane fuel cell based on a phosphoric-acid-doped polybenzimidazole membrane. *Sustain. Energy Technol. Assess.* **38**, 100671 (2020)
9. Guo, X., Zhang, H., Yuan, J., Wang, J., Zhao, J., Wang, F., et al.: Energetic and exergetic analyses of a combined system consisting of a high-temperature polymer electrolyte membrane fuel cell and a thermoelectric generator with Thomson effect. *Int. J. Hydr. Energy* **44**(31), 16918–16932 (2019)
10. Nalbant, Y., Colpan, C.O., Devrim, Y.: Development of a one-dimensional and semi-empirical model for a high temperature proton exchange membrane fuel cell. *Int. J. Hydr. Energy* **43**(11), 5939–5950 (2018)
11. Guo, X., Zhang, H., Zhao, J., Wang, F., Wang, J., Miao, H., et al.: Performance evaluation of an integrated high-temperature proton exchange membrane fuel cell and absorption cycle system for power and heating/cooling cogeneration. *Energy Convers. Manage.* **181**, 292–301 (2019)
12. Olapade, P.O., Meyers, J.P., Borup, R.L., Mukundan, R.: Parametric study of the morphological proprieties of HT-PEMFC components for effective membrane hydration. *J. Electrochem. Soc.* **158**(6), B639 (2011)
13. Zhang, X., Cai, L., Liao, T., Zhou, Y., Zhao, Y., Chen, J.: Exploiting the waste heat from an alkaline fuel cell via electrochemical cycles. *Energy* **142**, 983–990 (2018)
14. Wu, Z., Zhu, P., Yao, J., Tan, P., Xu, H., Chen, B., et al.: Thermo-economic modeling and analysis of an NG-fueled SOFC-WGS-TSA-PEMFC hybrid energy conversion system for stationary electricity power generation. *Energy* **192**, 116613 (2020)
15. Ye, L., Jiao, K., Du, Q., Yin, Y.: Exergy analysis of high-temperature proton exchange membrane fuel cell systems. *Int. J. Green Energy* **12**(9), 917–929 (2015)
16. Li, L., Liu, Z., Deng, C., Ren, J., Ji, F., Sun, Y., et al.: Conventional and advanced exergy analyses of a vehicular proton exchange membrane fuel cell power system. *Energy* **222**, 119939 (2021)
17. Szargut, J.: *Exergy Method: Technical and Ecological Applications*. WIT Press (2005)
18. Açıkkalp, E., Ahmadi, M.H.: Exergetic ecological index as a new exergetic indicator and an application for the heat engines. *Therm. Sci. Eng. Progr.* **8**, 204–210 (2018)
19. Ubong, E., Shi, Z., Wang, X.: Three-dimensional modeling and experimental study of a high temperature PBI-based PEM fuel cell. *J. Electrochem. Soc.* **156**(10), B1276 (2009)
20. Barnston, A.: Correspondence among the correlation [root mean square error] and Heidke Verification measures. In: *Refinement of the Heidke Score* (1992)
21. Han, I.-S., Chung, C.-B.: Performance prediction and analysis of a PEM fuel cell operating on pure oxygen using data-driven models: a comparison of artificial neural network and support vector machine. *Int. J. Hydr. Energy* **41**(24), 10202–10211 (2016)



Dynamically Fed Anion-Conducting Matrix-Based Water Electrolyzer

Dmitry G. Kondratyev¹, Konstantin G. Bolshakov², Alexander S. Stikhin³, Vladimir I. Matrenin², and Mikhail A. Aboimov⁴(✉)

¹ The Scientific and Production Association “Centrotech”—RME Centrotech, Novouralsk, Russia

² RME Centrotech LLC, Novouralsk, Russia

³ RME Centrotech, Novouralsk, Russia

⁴ TVEL JSC, Novouralsk, Russia

AAIStepanova@tvel.ru

Dedication to the development of low-carbon energy and decarbonization of the global economy as a whole is in the focus of the efforts of the global community. Achieving carbon neutrality in various energy and industrial sectors (metallurgical and chemical industries, oil refinery, motor transport, freight traffic, etc.) is inextricably interwoven with the use of the “green” hydrogen, which is considered a universal energy agent. Unavoidably, the wide spread of the “green” hydrogen is unimaginable without the enhancement of the conventional and development of the new electrolysis systems of its production.

State Atomic Energy Corporation Rosatom (ROSATOM) is one of the technological leaders of the world economy, which supports the global environmental agenda for the transition to low-carbon technologies and implements a strategic program for the development of hydrogen energy in Russia. The development of production and increasing the practical use of low-carbon hydrogen in the energy sector and industry is impossible without improving existing technologies of hydrogen production and developing of new ones. ROSATOM’s largest enterprises are currently developing efficient and competitive solutions, including new advanced electrolysis systems.

Within the framework of these overarching efforts, Scientific and Production Association “Centrotech” LLC (an entity of the State Corporation “Rosatom”, enters the Fuel Company “TVEL” JSC) has developed the technology for hydrogen production through electrolysis of water, featuring the use of an anion-conducting inorganic matrix in the electrochemical cell (Fig. 1), as well as an electrolyzer systems of a filter press design that utilize the aforesaid technology. The said R&D work was sponsored by Concern “Rosenergoatom” (the Electrical Energy Department of “Rosatom”, the biggest energy generating company in Russia, the second biggest one in the world by the nuclear generating capacities). Since there is currently no acronym for systems of this type in the literature, the developed electrolysis method is referred to hereinafter in this paper as ACM-EL, an abbreviation standing for “Anion-Conducting Matrix Electrolysis”.

The long haul experience gained by Centrotech in the area of alkaline matrix electrochemical current generators was applied to electrolysis technology. Electrochemical reactions in generators are reverse to those occurring in electrolysis cells.

As a matter of priority, the developers sought to integrate into their authentic technology the strong features of already existing means of water electrolysis, such as that of the mature flow-through Alkaline Electrolysis (hereinafter referred to as “A-EL”) and the emerging Anion-Exchange Membrane Electrolysis (hereinafter referred to as “AEM-EL”), while mitigating a number of relative weaknesses of these technologies as well as compensating for some disadvantages of the rapidly commercializing Proton-Exchange Membrane Electrolysis (hereinafter referred to as “PEM-EL”).

It should be noted that in the scientific literature (e.g., in [1]), an anion-exchange membrane refers to a non-porous organic polymer, such as polysulfone, polyphenylene oxide, and others that are intrinsically anion-conductive due to cationic functional groups that are present therein, such as the ammonia group (NH_4^+). The matrix developed by Centrotech does not feature sufficient intrinsic anionic conductivity, unlike the materials of well-known brands such as Fumasep[®], Aemion[™], SUSTAINION[®], and initially this is a porous material. Nevertheless, the introduction of potassium cations into the matrix during its soaking provides the same effect of anionic conduction. Therefore, we refer to this matrix as an anion-conducting matrix (ACM-EL) rather than an anion-exchange membrane (AEM-EL).

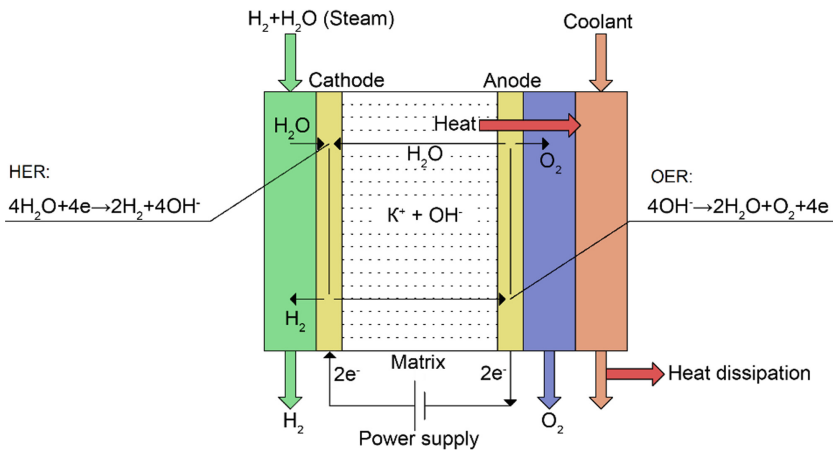


Fig. 1. Concept of ACM-EL cell operation

The matrix, used for separating electrodes and lying at the core of the invention, represents an inorganic fibrous material treated in a special way and soaked with a water solution of potassium hydroxide (KOH) in the process of manufacturing of an array of electrolysis cells. The matrix is further edged with a non-porous dielectric material. The matrix is characterized by a low electrical resistivity that is below $0.05 \Omega/\text{cm}^2$. It has properties that are crucial for the efficient and long-term operation of the electrolysis unit, while the combination of these properties can be viewed as unique, namely:

- proper alignment of the matrix backbone with the porous structure of the other components of the electrochemical cell;
- prevention of mixing of working gases with the changes of the cell moisture load;

- corrosion resistance in the environment of the working media, i.e. potassium hydroxide solution, hydrogen and oxygen at temperatures up to 100 °C;
- there are no processes resulting in electrolyte contamination with substances that poison the electrode catalysts;
- the matrix backbone features swelling when soaked with electrolyte;
- the mechanical strength of the matrix fiber web is adequate for performing of assembly operations;
- thermal stability of the edge of the matrix (no shrinkage was manifested at temperatures up to 100 °C under the load of up to 30 MPa);
- crack resistance of the edge of the matrix in contact with working media during the entire period of operation of an electrolyzer battery.

It is well known that at the state-of-the-art level of technology development, in order to ensure a sufficiently high conductivity of AEM-EL, it is not yet possible to avoid using an alkali solution in the process of operation of electrolyzers, even if it is at a low concentration (0.1–1 M) [2, 3]. In this aspect, the matrix developed by Centrotech surpasses the current level of development of AEM-EL in terms of consumer value, since the anionic conductivity in it is increased initially during production and soaking of matrix pores with a KOH solution, rather than in the course of operation of an installation at consumers' sites. Since the degradation of anionic conductivity of Centrotech's matrix with the lapse of time due to the attack of cationic groups by hydroxyl ions is significantly lower, the operational life is longer and mechanical strength of the matrix is higher than these properties of the state-of-the-art anion-exchange membrane materials that are commercially available.

Owing to the absence of an alkali flow during the operation of the electrolyzer units developed by Centrotech, another important distinctive feature was implemented, namely, a dynamic method of supplying water to the battery by organizing the circulation of a steam-hydrogen mixture through the evaporator and the electrolysis battery. This dynamic water feeding technique results in decreased specific energy consumption of an electrolyzer system as well as in substantially less stringent requirements to the purity of the feed water.

Centrotech developed also a mathematical model for simulating the stationary mode of operation of the electrolyzer with steam dynamic supply in the form of a steam-hydrogen mixture in various operating modes. This model serves as the "digital twin" of the physical installation, thus enabling to establish the required characteristics of its nodes and instrumental gauges.

The unique anion-conducting matrix and dynamic water supply were combined to eliminate or mitigate a number of disadvantages of alkaline flow-through (A-EL) technology [4, 5]:

- the operating range of current density increases due to the reduced ohmic resistance, which means that the specific area factor, materials consumption and carbon footprint in the manufacture processes of the electrolyzers are reduced;
- hydrogen pressure is 1.5 MPa with potential of further increase;
- since there is no gas leakage through matrix, operation becomes safer, and load-following capability also increases with a hydrogen generation performance range of up to 115% of the rated nameplate capacity, which is especially important when an

electrolysis unit is integrated with intermitted renewable energy sources to be used as part of an energy storage system;

- Centrotech has achieved specific energy consumption of the battery of electrolysis cells as low as 4.0–4.1 kWh/nm³.

In relation to PEM-EL, the electrolyzer system, developed by Centrotech, also features a number of advantages [6]:

- since the water is supplied in the form of steam, the requirements for water purity are much less stringent: purification by pre-coagulation and then by reverse osmosis is sufficient, no double distillation is required;
- the content of platinum group metals in the catalyst on the cathode side (hydrogen evolution reaction, or HER) is substantially lower, while nickel is predominantly used on the anode side (oxygen evolution reaction, or OER);
- as noted, a lower power consumption was achieved on both the battery and turn-key system levels;
- the matrix is fluorine-free, and, therefore, its production is much more environmentally friendly.

Notably, the ACM-EL technology, developed by Centrotech, as well as the AEM-EL technology [7], based on non-porous membranes with inherent anionic conductivity can, eventually, lead to the complete exclusion of platinum group metals from the composition of catalysts on both the cathode (HER) and anode (OER) sides.

The ongoing R&D efforts of Centrotech and its partners are aimed at further enhancement of the ACM-EL technology advantages while bringing it progressively closer to AEM-EL going forward. In particular, in partnership with a number of scientific organizations, Centrotech's team is working on promising anion-exchange materials and conducting research towards further reducing the specific content of platinum group metals in catalysts, with the objective of the complete exclusion.

Comparison of Centrotech's technology and electrolyzer system parameters with the typical ranges thereof for A-EL, PEM-EL and AEM-EL is provided in Table 1 [1, 8].

Figures 2 and 3 show the electrolysis battery assembly and the electrolyzer unit developed and designed by Centrotech.

As evidenced by the averaged current-voltage characteristic measured by Centrotech for a number of electrolysis cells (Fig. 4), the performance of the electrochemical cell is quite efficient.

Although the current-voltage characteristic could be extended further into the range of higher current densities above 1.0 A/cm² what has been tested through multiple experiments.

Currently, Centrotech is developing a line of electrolyzer units with a nameplate capacity exceeding 50 nm³/h based on the presented technology and destined for large-scale production of hydrogen, both in monoblock and container layouts. Prototypes with different capacities have already been developed and go through testing.

The level of automation and safety of our installations makes remote control of the entire production process possible. Monitoring and diagnostic systems track plant operating parameters and hydrogen quality (oxygen and moisture content) *in situ* and

Table 1. . .

| Technical parameters | Electrolyzer system developed by Centrotech (ACM-EL) | Typical range of technology parameters | | |
|--|---|--|---|---|
| | | A-EL ^a | PEM-EL ^a | AEM-EL today (2050 perspective) ^a |
| Range of nominal (rated) capacity of a single module (battery) in terms of hydrogen, nm ³ /h H ₂ | 5–50 (<i>100 going forward</i>) | 0.5–1000 | 0.5–200 | 0.25 (400) |
| Specific power consumption at rated performance of (i) battery; (ii) plant (without purification and drying), kWh/nm ³ H ₂ | (i) 4.0–4.2 (ii) 5.0 | (i) ≥ 4.5 (ii) ≥ 5.2* | (i) ≥ 4.5 (ii) ≥ 5.5* | (i) 4.6–5.9 (< 3.8) (ii) 5.1–6.2 (< 4.0) |
| Cell pressure (due to electrochemical reaction), bar | 15 | up to ~ 10 | 15–30 | < 35 (>70) |
| Battery life, hours | > 60,000 (<i>predicted</i>) | > 60,000* | > 60,000* | ~ 5000 (100,000) |
| Performance range in terms of hydrogen, % from the rated capacity | 5–115 | 50–100* | 5–115* | 5–100 (5–200%) |
| Water treatment requirements | <i>Reverse osmosis with pre-coagulation is sufficient</i> | Distillation, addition of concentrated KOH | Distillation | Distillation, addition of 0.1–1 M alkali solution (w/o alkali solution) |
| Hydrogen purity, % | 99.9 (<i>without purification system</i>) | 99.8* (<i>without purification system</i>) | Up to 99.99* (<i>after purification system</i>) | 99.9–99.999% (<i>continued</i>) |

Table 1. (continued)

| Technical parameters | Electrolyzer system developed by Centrotech (ACM-EL) | Typical range of technology parameters | | |
|---|--|--|-------|------------|
| Electric efficiency of the unit at the rated performance, % | > 80 | ~ 80* | ~ 70* | > 70 |
| Operating temperature (ECB), °C | 85 ± 5 | 70–90 | 50–80 | 40–60 (80) |

^a Parameters marked with an asterisk “*” were taken from other sources, including characteristics of particular models of electrolyzers



Fig. 2. Electrolysis battery with the nameplate capacity of 25 nm³/h

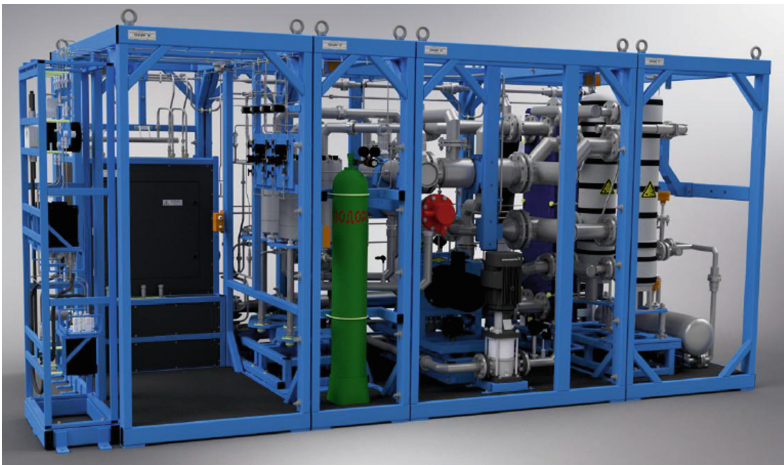


Fig. 3. Model of electrolyzer unit with the nameplate capacity of 50 nm³/h

prevent deviations from customer requirements. The electrolyzer and auxiliary units operate, start and stop automatically.

Notably, an important advantage of the developed ACM-EL technology over large-scale alkaline flow technology is a wide range of performance up to 115% from the nameplate capacity and a high dynamics of its change. These advantages make it possible to combine electrolyzer units, developed by Centrotech, with wind and PV renewable energy sources to serve as component of energy storage systems based on hydrogen cycle.

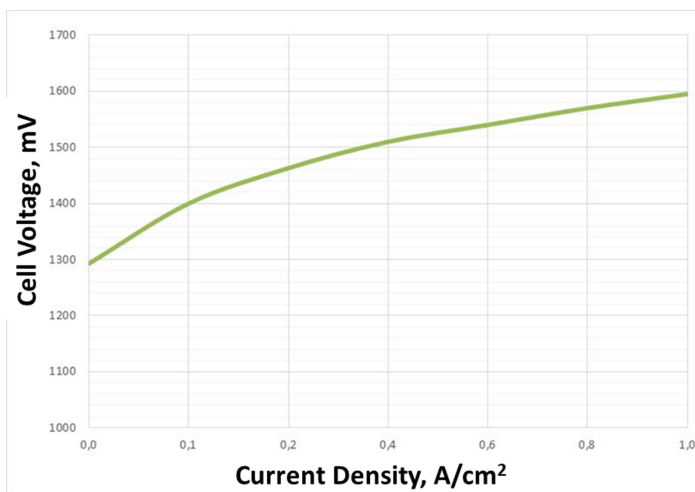


Fig. 4. Averaged current-voltage characteristic of alkaline matrix-based electrolyzer stack, tested by Centrotech

Capitalizing on its experience in the area electrochemical current generators on the basis of hydrogen fuel cells, Centrotech targets the development of turn-key energy storage systems on the hydrogen power-to-gas-to-power, as well as uninterruptible power supply (UPS) systems, intended for use at facilities where resilient power supply is crucial.

A higher level of safety is combined with the fact that working with alkali during operation is not required. This combination makes the invention of Centrotech also optimal for operation at the sites of nuclear power plants, both for generating hydrogen to cool the coils of electric generator machines, and its industrial-scale production.

Currently, Centrotech is engaged in improving the manufacturing technologies and enhancing the design of the electrolytic cell in order to reduce its cost and increase the reliability of components and assemblies. Research work is advancing to develop new non-precious catalysts and polymer membranes.

Findings

Compared to other electrolysis techniques, including AEM-EL technology at its current level of development as well as the PEM-EL, the anion-conducting matrix-based electrolyzers developed by Centrotech feature improved performance characteristics, namely: low power consumption, less stringent requirements for feed water, effective operation in dynamic mode, long battery life and high corrosion resistance.

References

1. Santoro, C., Lavacchi, A., Mustarelli, P., Di Noto, V., Elbaz, L., Dekel, D.R., Jaouen, F.: What is next in anion-exchange membrane water electrolyzers? Bottlenecks, benefits, and future? *HemSusChem* (2022)
2. Naiying, D., Roy, C., Peach, R., Turnbull, M., Thiele, S., Bock, C.: Anion-exchange membrane water electrolyzers. *Chem. Rev.* **122**(13), 11830–11895 (2022)
3. Vincent, I., Kruger, A., Bessarabov, D.G.: Development of efficient membrane electrode assembly for low cost hydrogen production by anion exchange membrane electrolysis. *Int. J. Hydr. Energy* **42**(16), 10752–10761, 20 Apr 2017. DST HySA Infrastructure, Centre of Competence, Faculty of Engineering, North-West University, Potchefstroom, 2520, South Africa
4. HyunAhn, S., Lee, B.-S., et al.: Development of a Membrane Electrode Assembly for Alkaline Water Electrolysis by Direct Electrodeposition of Nickel on Carbon Papers. *Fuel Cell Research Center, Korea Institute of Science and Technology (KIST), Seoul*, pp. 136–791. School of Integrative Engineering, Chung-Ang University, Seoul, pp. 156–756
5. Liu, Z., Sajjad, S.D., Hongzhou Yang, Y.G., Kaczur, J.J., Masel, R.I.: The effect of membrane on an alkaline water electrolyzer. *Int. J. Hydr. Energy* **42**(50), 29661–29665
6. Shiva Kumar, S., Himabindu, V.: Hydrogen production by PEM water electrolysis—a review. *Mater. Sci. Energy Technol.* **2**(3), 442–454
7. Faida, A.Y., Xieb, L., Barnett, A.O., et al.: Effect of anion exchange ionomer content on electrode performance in AEM water electrolysis. *Int. J. Hydr. Energy* **45**(53), 28272–28284 (2020). Department of Materials Science and Engineering, Norwegian University of Science and Technology, Norway; Department of Applied Chemistry and Chemical Engineering, University of Toronto, Canada; SINTEF Industry, New Energy Solutions, Norway; Department of Energy and Process Engineering, Norwegian University of Science and Technology, Norway
8. Green Hydrogen Cost Reduction: Scaling Up Electrolysers to Meet the 1.5 °C Climate Goal. IRENA (2020)
9. The 8th All-Russian Conference with International Participation: Fuel Cells and Power Plants Based on Them. Chernogolovka, Moscow Region 19–23 Sept 2021. Kondratyev, D.G., Stikhin, A.S., Matrenin, V.I.: Dynamically Fed Anion-Conducting Matrix Based Hydrogen Generators. RME Centrotech, Novouralsk, Ekaterinburg Region



Thermal Insulation Simulation of Small Proton Exchange Membrane Fuel Cell

Zhifei Fang, Jiayu Zhou, and Huichao Deng^(✉)

Beihang University, Beijing 100191, China
denghuichao@buaa.edu.cn

Abstract. The 10 W air-cooled proton exchange membrane fuel cell (PEMFC) is a cost-effective and readily available power source with a wide range of applications in daily and industrial production. However, due to cost and process limitations, low-cost and low-power air-cooled PEMFCs can only be stored in environments above 0 °C, unlike PEMFCs for vehicles which can be stored and operated in temperatures as low as – 30 °C. Overcoming the limitation of low-temperature storage and starting at 0 °C would significantly expand the application of air-cooled PEMFCs. Therefore, this study aims to propose a solution by introducing auxiliary heating to preserve and operate the stack in environments as low as – 10 °C, making it applicable to most of the national application scenarios. To achieve this, a thermal model was developed to analyze the performance of a 10 W fuel cell stack operating at – 10 °C. The results indicate that an insulation box can effectively minimize heat loss from the stack, and the use of two ceramic heating plates with a power output of 0.11 W can maintain the stack's minimum temperature above 0 °C.

Keywords: Proton exchange membrane fuel cell · Insulation box · Heat transfer simulation

1 Introduction

Proton Exchange Membrane Fuel Cells (PEMFCs), which utilize hydrogen as fuel and only emit water as a byproduct, are widely regarded as an ideal alternative to fossil fuels. However, in environments below 0 °C, the presence of water can lead to freezing, resulting in blockages within the flow channels and hindering the fuel cell's continuous operation. Additionally, the expansion of ice can cause damage to the membrane electrode assembly (MEA), consequently reducing the lifespan of the fuel cell. In China, specifically in regions north of the Qinling-Huaihe Line where winter temperatures regularly fall below 0 °C, approximately 41.6% of the population resides [1]. Consequently, the ability of PEMFCs to operate effectively at low temperatures is of paramount importance for their practical application in these northern regions.

To enhance the storage and operational capabilities of PEMFCs in low-temperature conditions, several common strategies are employed. Firstly, thorough purging is conducted to remove free water and weakly bound water from the fuel cell stack after

shutdown. Secondly, auxiliary heating is utilized by heating the reactant gases or the fuel cell stack itself to initiate the stack operation. Thirdly, self-starting without auxiliary devices is achieved by allowing the stack to operate at lower voltages during startup. Although this approach reduces the stack efficiency and generates more heat, the heat produced during the reactions is utilized to warm up the fuel cell, facilitating self-starting. Fourthly, hydrogen pumping-assisted startup involves the application of reverse direct current between both ends of the fuel cell stack to accelerate hydrogen ion transport, resulting in heat release at the cathode. Lastly, hydrogen-oxygen catalytic low-temperature startup involves mixing hydrogen and oxygen reaction gases within the flow channels to promote reactions outside the explosive limits, utilizing the inherent catalyst of the fuel cell to heat the stack [2–4].

Although the methods mentioned above have been successfully applied in the automotive field, there are still cost and process issues associated with small-scale, low-power, air-cooled stacks. Even when the stack is purged and stored in a low-temperature environment, there is a risk of damaging the MEAs and sealing components. Therefore, it is necessary to place the stack in a thermal insulation box during storage and preheat it before startup. Li et al. [5] conducted a simulation analysis of insulation measures; however, their model simplified the three-dimensional stack model into a two-dimensional model and reduced the bipolar plate structure to a rectangular thin plate, which sacrificed a certain degree of accuracy. To overcome this limitation, this study establishes a three-dimensional heat transfer model for a 10 W stack and sets the ambient temperature to $-10\text{ }^{\circ}\text{C}$. By comparing the natural cooling time with the cooling time inside the box, numerical calculations are performed to determine the required auxiliary heating power to maintain the stack at $0\text{ }^{\circ}\text{C}$. The focus of this study is on the thermal balance calculation of the stack and does not involve chemical reaction aspects. Through this thermal balance calculation, the heat demand for low-temperature storage can be accurately assessed, and targeted auxiliary heating measures can be implemented to ensure the safety of the stack.

2 Modeling Methods

This paper employed the following modeling methods to investigate the thermal balance of a 10 W fuel cell stack.

First, a transient thermal analysis was performed to calculate the heat dissipation process of the stack without any insulation measures. In this analysis, the ambient temperature was set to $-10\text{ }^{\circ}\text{C}$, and the initial temperature of the stack was $80\text{ }^{\circ}\text{C}$.

Next, a thermal analysis was conducted with the introduction of a thermal insulation box, calculating the heat dissipation process of the stack inside the insulation box. The distance between the inner wall of the insulation box and the stack was set to 0.5 cm, and the thickness of the insulation box was 2 cm. In this analysis, the initial temperature of the insulation box was set to $-10\text{ }^{\circ}\text{C}$.

Finally, heating ceramic plates were embedded in the upper and lower end plates of the stack to maintain the minimum temperature of the stack at around $0\text{ }^{\circ}\text{C}$. Once thermal equilibrium was reached, the temperatures of the stack and other components would stabilize, and the heat generated by the heating ceramic plates would be entirely dissipated to the surroundings through convection. To achieve this goal, a three-dimensional

steady-state computational fluid-solid heat transfer method was employed. The solid and fluid surfaces were coupled through boundary conditions to ensure that the heat flux at the same surface in different regions was equal. The volume heat source power of the heating ceramic plates was set in the software, while monitoring the minimum temperature of the stack and other components simultaneously. If the minimum temperature of the stack was below 0 °C, the heat power of the heating ceramic plates needed to be increased until convergence was achieved and the minimum temperature of the stack met the requirements. Once the temperatures of the components no longer changed with further iterations and the minimum temperature of the stack was maintained around 0 °C, the obtained heating power was considered as the required heat power.

Figure 1 illustrates the finite element model of the 10 W fuel cell stack, which consists of end plates, bipolar plates, and MEAs. The thermodynamic parameters of each component, as well as the parameters of the polyurethane foam board and heating ceramics, are detailed in Table 1.

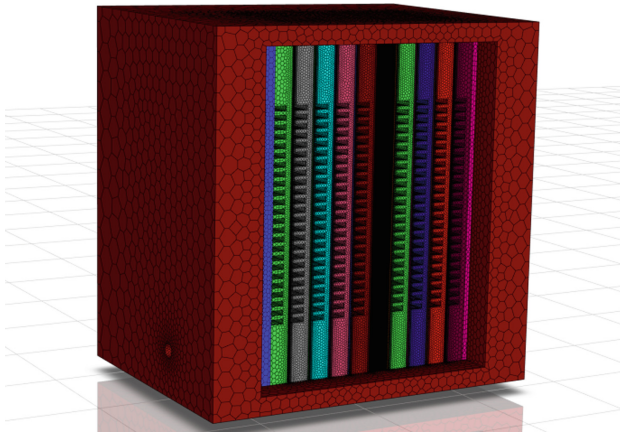


Fig. 1. Finite Element Model of the Fuel Cell Stack.

3 Results and Discussion

In the low-temperature storage of proton exchange membrane fuel cells, water content plays a crucial role. By completely purging the free water and weakly bound water inside the fuel cell, the membrane electrode assembly can maintain a good state [6, 7]. Studies have shown that during the low-temperature startup process, the generated water does not freeze inside the catalyst layer; only when water reaches the surface of the catalyst layer does it freeze [8]. Therefore, the focus of this study is on the temperatures of the membrane electrode assembly and bipolar plates.

Under the assumption of an initial temperature of 80 °C for the fuel cell stack, it should be noted that the end plates, being directly exposed to the environment, have the lowest temperatures during the heat dissipation process. However, the concern for the

Table 1. Thermodynamic Parameters of the Components of the Fuel Cell and the Thermal Insulation Materials

| Component | Thermal Conductivity ($\text{W m}^{-1} \text{K}^{-1}$) | Thermal Resistance ($\text{J kg}^{-1} \text{K}^{-1}$) | Density (g/cm^3) | Thickness (cm) |
|-------------------------|--|---|-----------------------------|----------------------------------|
| End plate | 0.035 | 794.2 | 2.4 | Left/right 0.8 Top/bottom 0.3 |
| Bipolar plate | 95 | 710 | 1.78 | 0.3 |
| MEA | 0.36 | 500 | 1 | 0.045 |
| Polyurethane foam Board | 0.024 | 2000 | 0.035 | 2 |
| Heating ceramic | 30 | 840 | 4.0 | 0.2 |

safety temperature of the fuel cell stack lies in ensuring that the minimum temperature of the bipolar plates and membrane electrode assembly does not drop below $0\text{ }^{\circ}\text{C}$. Therefore, any subsequent mention of the minimum temperature refers to the minimum temperature of the bipolar plates and membrane electrode assembly.

3.1 Simulation Analysis Without Insulation Measures

Figure 2 illustrates the temperature variation of different components of the fuel cell stack over time in an environment with a temperature of $-10\text{ }^{\circ}\text{C}$, without any insulation measures. It can be observed that initially, there is a significant temperature difference between the fuel cell stack and the environment, resulting in substantial heat loss and a rapid decrease in temperature. As the minimum temperature reaches $0\text{ }^{\circ}\text{C}$, the temperature difference within the fuel cell stack is $0.35\text{ }^{\circ}\text{C}$. It takes approximately 5397 s, or about 1.5 h, for the minimum temperature of the fuel cell stack to reach $0\text{ }^{\circ}\text{C}$.

3.2 Simulation Analysis with Thermal Insulation

In order to reduce the heat dissipation of the fuel cell stack, a thermal insulation box was implemented. The thermal insulation box consists of a 2 cm-thick rigid polyurethane foam board and is covered with an aluminum film to minimize thermal radiation. Although thermal radiation was neglected in the simulation calculations, using this material helps minimize the deviation from real-world conditions. Figure 3 illustrates the temperature-time curves of the fuel cell stack and the interior of the thermal insulation box with the thermal insulation measures in place. As the lowest temperature of the fuel cell stack drops to $0\text{ }^{\circ}\text{C}$, the internal temperature difference is only $0.24\text{ }^{\circ}\text{C}$, indicating a relatively uniform temperature distribution within the thermal insulation box. The duration for this process is 9600 s, equivalent to 160 min, approximately 1.78 times longer than without thermal insulation measures.

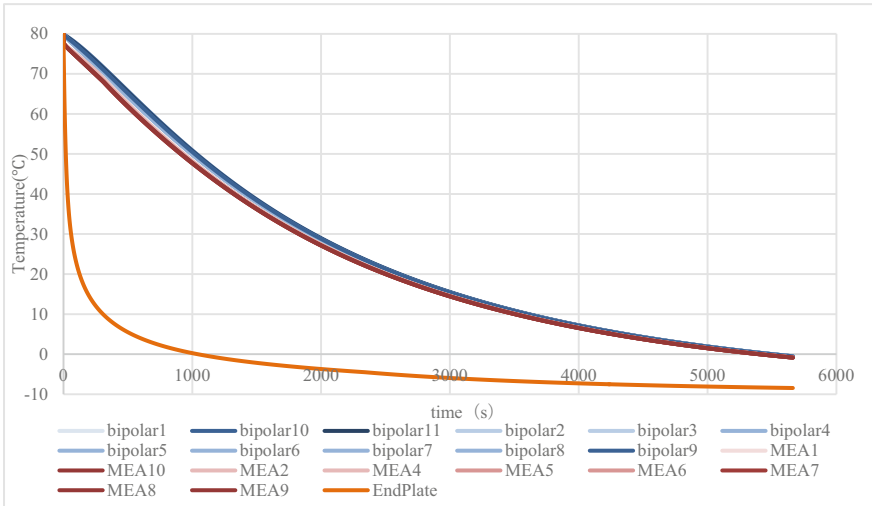


Fig. 2. Temperature-time curves of the fuel cell stack components at $- 10\text{ }^{\circ}\text{C}$.

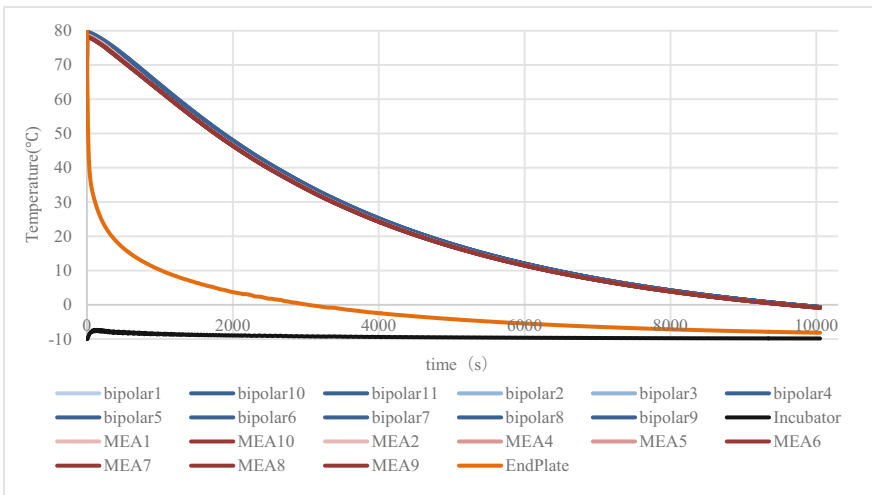


Fig. 3. Temperature-time curves of the fuel cell stack components and thermal insulation box at $- 10\text{ }^{\circ}\text{C}$.

3.3 Calculation of Required Heating Power for Thermal Balance

With the ambient temperature maintained at $- 10\text{ }^{\circ}\text{C}$, the electric stack is heated by embedding heating ceramics in the upper and lower end plates. To ensure that the lowest temperature inside the stack does not fall below $0\text{ }^{\circ}\text{C}$, a heating ceramics unit volume power of 136000 W/m^3 is applied.

The temperature distribution in the stack under the thermal balance condition is shown in Fig. 4. The length and width of a single heated ceramic are both 2 cm, and the

thickness is 0.2 cm. Therefore, the power of a single heated ceramic is approximately 0.11 W.

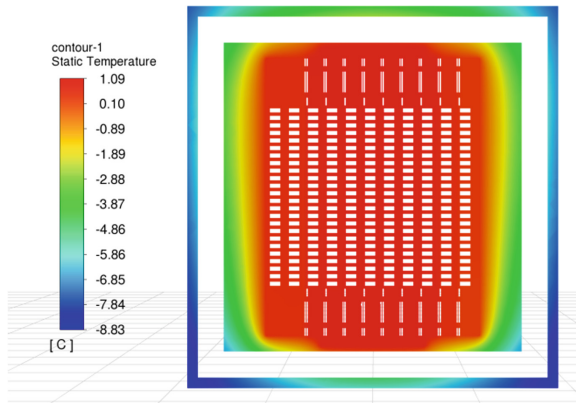


Fig. 4. Section temperature distribution of electric stack and thermal insulation box when unit volume power of heated ceramic is $136,000 \text{ W/m}^3$.

4 Conclusion

Based on the results of the simulation analysis, the following conclusions can be drawn:

- (1) Without insulation measures, the temperature of the MEAs in the fuel cell stack decreased from an initial value of $80\text{--}0 \text{ }^\circ\text{C}$ in approximately 1.5 h, with an internal temperature difference of about $0.35 \text{ }^\circ\text{C}$.
- (2) By using a 2 cm thick polyurethane rigid foam board for insulation, the heat loss of the fuel cell stack can be significantly reduced. Inside the insulated box, the temperature of the stack decreases from 80 to $0 \text{ }^\circ\text{C}$ in approximately 2.7 h, which is 1.78 times longer than without insulation measures. Furthermore, the internal temperature difference is reduced to approximately $0.24 \text{ }^\circ\text{C}$. This indicates that the insulated box helps achieve a more uniform temperature distribution within the stack.

By using a 2 cm thick polyurethane rigid foam board for insulation, the heat loss of the fuel cell stack was significantly reduced. Inside the insulated box, the temperature of the stack decreased from 80 to $0 \text{ }^\circ\text{C}$ in approximately 2.7 h, which was 1.78 times longer than without insulation measures. Additionally, the internal temperature difference was reduced to approximately $0.24 \text{ }^\circ\text{C}$, indicating a more uniform temperature distribution within the stack.

- (3) To prevent the internal temperature of the stack from dropping below $0 \text{ }^\circ\text{C}$, the integration of two pieces of heating ceramics, each measuring $2 \text{ cm} \times 2 \text{ cm} \times 0.2 \text{ cm}$, in the upper and lower end plates of the stack was determined. Through calculations, it is determined that a power of approximately 0.11 W is required to maintain the desired minimum temperature.

In conclusion, by employing measures such as an insulated box and heating ceramics, the fuel cell stack can be protected effectively in low-temperature environments, ensuring that the minimum temperature of the stack remains above 0 °C. This is of great significance for the application of those low-cost proton exchange membrane fuel cells in cold regions.

References

1. National Bureau of Statistics Homepage. <http://www.stats.gov.cn/sj/pcsj/rkpc/d7c/202111/P020211126523667366751.pdf>. Last accessed 05 Jan 2023
2. Yi, B., Yu, H., Hou, Z.: Hydrogen Fuel Cell. Chemical Industry Press, Beijing (2021)
3. Luo, Y., Jiao, K.: Cold start of proton exchange membrane fuel cell. *Progr. Energy Combust. Sci.* **64**, 29–61 (2018)
4. Amamou, A., Kelouani, S., Boulon, L., Agbossou, K.: A comprehensive review of solutions and strategies for cold start of automotive proton exchange membrane fuel cells. *IEEE Access* **4**, 4989–5002 (2017)
5. LI, Y.: Simulation study on thermal insulation of proton exchange membrane fuel cell stack for automotive applications. *Power Supply Technol.* **40**(3), 580–582 (2016)
6. Hao, L.: Study on the Effect of Water Content in Proton Exchange Membrane Fuel Cell MEA on Its Performance. Dalian Institute of Chemical Physics, Chinese Academy of Sciences (2010)
7. Sinha, P., Halleck, P., Wang, C.: Quantification of liquid water saturation in a PEM fuel cell diffusion medium using x-ray microtomography. *Electrochem. Solid-State Lett.* **9**(7), A344–A348 (2006)
8. Tajiri, K., Tabuchi, Y., Wang, C.: Isothermal cold start of polymer electrolyte fuel cells. *J. Electrochem. Soc.* **154**(2), B147 (2007)



Investigation of the Effect of Operating Conditions on the Polarization Process of Proton Exchange Membrane Fuel Cells Based on the Distribution of Relaxation Times Using Orthogonal Test Method

Tiancai Ma^{1,2}, Ziheng Gu¹, Chang Du¹, Jinxuan Qi¹, and Juexiao Chen¹(✉)

¹ School of Automotive Studies, Tongji University, Shanghai 201804, China
chenjuexiao@tongji.edu.cn

² Institute of Carbon Neutrality, Tongji University, Shanghai 200092, People's Republic of China

Abstract. Proton exchange membrane fuel cell (PEMFC) performance is significantly influenced by different operating conditions. In this study, the effects of temperature, cathode back pressure, cathode relative humidity (RH), and air stoichiometry on the mass and charge transfer processes within the electrochemical reaction are investigated using orthogonal test methodology. Polarization curves and electrochemical impedance spectra (EIS) are analyzed, and the distribution of relaxation times (DRT) method is employed to separate and quantify different polarization processes. A 3rd-order RC equivalent circuit model is constructed, and the DRT-based method identifies three peaks within the frequency spectrum to represent the cathodic mass transfer process, cathodic catalytic layer oxygen reduction reaction (ORR) process and anodic process, respectively. The influence weight of each operating factor is investigated using the range analysis method. The experimental results demonstrate that air stoichiometry has the dominant influence on mass transfer resistance throughout the entire current density range, with the most significant effect found at low and high current densities. The impact of temperature on activation resistance dominates at low and medium current densities, especially at low current densities. In contrast, for high current densities ($> 1 \text{ A cm}^{-2}$), the influence of air stoichiometry on charge transfer processes outweighs that of temperature.

Keywords: PEMFC · Distribution of relaxation times · Orthogonal test method · Mass transfer · Charge transfer

1 Introduction

With the depletion of fossil energy and the increase in environmental pollution, there is an urgent need to find an alternative clean energy source. In recent years, hydrogen energy has garnered significant attention as a potential clean energy source [1]. PEMFC

is a viable solution due to its high efficiency and environmental friendliness. PEMFCs are typically employed as backup power sources and portable power sources, utilizing hydrogen and oxygen as fuel, producing only water as a reaction product, thus being environmentally friendly and non-polluting [2]. However, PEMFCs are multi-scale systems with coupled multi-physical fields, heat, and mass transfer, resulting in some ambiguity regarding the decay mechanism within them. The performance of PEMFC is sensitive to operating conditions such as temperature, pressure, flow rate, and relative humidity. Improper operating conditions can cause water flooding or membrane dehydration inside the cell, even potentially leading to irreversible damage through membrane cracking or perforation [3]. Frequent start-stop [4, 5], variable load [6–8], idling [9, 10], and overload [11–13] can also affect the lifetime of PEMFCs.

Numerous studies have investigated the effect of operating conditions on fuel cell performance [15–20]. Ozen et al. investigated the effects of reaction gas relative humidity and temperature on PEM fuel cell performance [19]. Wang et al. studied the effects of hydrogen relative humidity, air relative humidity, operating temperature, and air stoichiometry ratio on PEMFC performance using orthogonal tests, finding that air stoichiometry ratio had the most significant impact on performance, followed by air relative humidity and operating temperature, while the effect of hydrogen relative humidity was negligible [20]. Electrochemical impedance spectroscopy is commonly used as an in-situ characterization tool to decouple electrochemical processes within a PEMFC. Researchers often use the equivalent circuit approach to analyze impedance spectra, but this method requires a priori knowledge and may have multiple equivalent circuit models for a single result, making its interpretation controversial. Recently, the distribution of relaxation times method has been applied to the field of PEMFCs, providing improved impedance spectrum resolution and further decoupling of electrochemical processes within the cell [21–23]. Zhu et al. proposed an integrated regularized DRT method based on eigenfrequency resolution and hyperparameters, avoiding peak overlap and further enhancing DRT accuracy [24].

In this paper, orthogonal tests are employed to investigate the effects of temperature, cathode back pressure, cathode relative humidity, and air stoichiometry on mass and charge transfer processes in electrochemical reactions. A 3rd-order RC equivalent circuit model based on the DRT method is developed to separate and quantify the different polarization processes. The influence weight of each factor is determined through range analysis. Section 2 describes the selection of impact factors and experimental arrangements. Experimental results are demonstrated and analyzed in Sect. 3. Finally, the conclusion is summarized in Sect. 4.

2 Experiment

2.1 Experimental Equipment

In this study, a commercial membrane electrode assembly (MEA) with a 25 cm² active surface area was utilized. The platinum loadings of the anode and cathode were 0.1 and 0.4 mg cm⁻², respectively. The membrane thickness was 15 μm, and the inlet channels featured a serpentine design. The Hephas HS-660 fuel cell test bench provided the necessary temperature, pressure, and flow for the experiment, while the humidity

was controlled by adjusting the temperature of the humidifying bottle. Electrochemical impedance spectroscopy measurements were conducted using electrochemical workstations with the assistance of an electronic load. Figure 1 presents a schematic diagram of the test system.

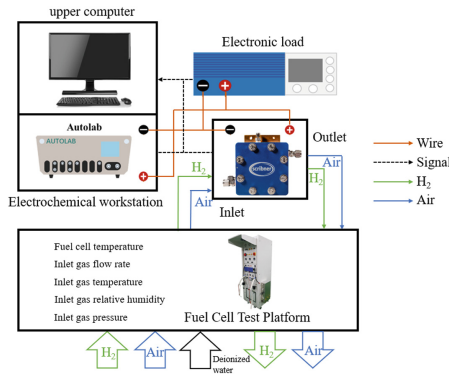


Fig. 1. Schematic diagram of the test system.

2.2 Orthogonal Experimental Design

The orthogonal experimental method is an efficient, rapid, and economical experimental design method used to study multiple factors and levels, significantly reducing the number of experiments, experimental time, and costs [25]. Among these, selecting orthogonal factors is particularly important. Operating temperature influences the reaction rate and water content of PEMFCs, with high temperatures causing membrane dryness and low temperatures leading to flooding. Consequently, temperature is one of the key factors affecting PEMFC performance. The stoichiometric ratio impacts the reactant concentration and water content. Since the anode uses pure hydrogen and the cathode is air, only the effect of the air stoichiometric ratio is considered, as the oxygen reduction reaction rate is much slower than the hydrogen oxidation rate. Additionally, the effects of cathode relative humidity and back pressure are considered. In this study, temperature, air stoichiometry, cathode back pressure, and cathode relative humidity are selected as orthogonal factors.

The levels (from level 1 to level 3) of operating temperature were 60, 70, and 80 °C. The levels of air inlet pressure were 70, 80, and 90 kPa. The air stoichiometric ratio had three levels: 1.8, 2.1, and 2.5. Cathode relative humidity levels were 50, 70, and 90%. Additionally, the hydrogen stoichiometric ratio remained at 2 in all experiments without humidification, and the back pressure was maintained at ambient pressure. Table 1 displays the orthogonal table with four factors and three levels.

2.3 The Performance Characterization and Testing Means of PEMFC

Several electrochemical methods are commonly employed to characterize PEMFC performance, decoupling multiple internal electrochemical processes.

Table 1. The orthogonal table with four factors and three levels.

| Experimental numbers | Factors | | | |
|----------------------|----------------------------------|-------------------------------|------------------------------|-------------------|
| | Operating temperature (Factor A) | Air inlet pressure (Factor B) | Air stoichiometry (Factor C) | Air RH (Factor D) |
| Case 1 | 60 | 70 | 1.8 | 50 |
| Case 2 | 60 | 80 | 2.1 | 70 |
| Case 3 | 60 | 90 | 2.5 | 90 |
| Case 4 | 70 | 70 | 2.1 | 90 |
| Case 5 | 70 | 80 | 2.5 | 50 |
| Case 6 | 70 | 90 | 1.8 | 70 |
| Case 7 | 80 | 70 | 2.5 | 70 |
| Case 8 | 80 | 80 | 1.8 | 90 |
| Case 9 | 80 | 90 | 2.1 | 50 |

2.3.1 Electrochemical Impedance Spectroscopy

For the EIS measurements, the anode hydrogen stoichiometry was maintained at 2 and without humidification, while the other operating conditions are shown in Table 2. The measured spectrum ranged from 0.1 Hz to 10 kHz, measuring 10 points per decade. The applied sinusoidal perturbation was 5% of the DC. The system was run steadily for 5 min before each measurement to ensure accurate results.

2.3.2 Polarization Curves

The polarization curve is among the most common and intuitive methods employed to characterize PEMFC performance. By measuring the voltage values at different current densities, the three polarization processes in PEMFCs can be observed. Activation polarization dominates at low current densities, ohmic polarization at medium current densities, and concentration differential polarization at high current densities. The voltage values were measured at 0.1, 0.2, 0.4, 0.5, 0.6, 0.8, 1.0, 1.2 and 1.3 A cm⁻², respectively, and each measurement point was held for 5 min. The specific operating conditions are shown in Table 2.

2.4 Distribution of Relaxation Times

The relaxation time distribution is an impedance deconvolution method with high resolution [26]. It comprises a series of RC series circuits representing different polarization processes. This method imposes high requirements for measuring impedance data. The relationship between the impedance $Z(\omega)$ and the distribution function of relaxation time $g(\tau)$ is shown in Eq. (1) [27]:

$$Z(\omega) = R_0 + Z_{pol}(\omega) = R_0 + R_{pol} \int_{-\infty}^{\infty} \frac{\gamma \ln(\tau)}{1 + j\omega\tau} d\ln\tau \quad (1)$$

where R_0 is the value corresponding to the intersection of the high frequency of the impedance spectrum with the real axis, $Z_{\text{pol}}(\omega)$ is the polarization impedance, R_{pol} is the polarization resistance, and τ is the time constant of the corresponding RC equivalent circuit. The impedance data requires a Kramers-Kronig (K-K) test, which the fitting error is less than 1%, to ensure the linearity, time invariance, and causality of the data [28, 29].

2.5 Range Analysis

In this paper, the results of the orthogonal tests were analyzed by range analysis. The range analysis is an intuitive analysis method, also called the R method, which calculates the R-value (factor range value) to determine the strengths and weaknesses of the factors, and of course, the optimal level of a factor to obtain the final combination. The calculation process of range analysis is shown in Eqs. (2), (3), and (4) [30].

$$\delta_{Xm} = \bar{I}_{Xm} - Y \quad (2)$$

$$R_{0X} = \max(\delta_{X1}, \delta_{X2}, \delta_{X3}); R_{1X} = \min(\delta_{X1}, \delta_{X2}, \delta_{X3}) \quad (3)$$

$$T_X = R_{0X} - R_{1X} \quad (4)$$

where \bar{I}_{Xm} represents the average of all experimental values of the impact factor X at the m level and Y is the average of all experimental results. δ_{Xm} reflects the difference between the average value of the experimental results which contain the factor X in level m and the average value of all the test results. T_X stands for the influence degree of factor X [31].

3 Results and Discussion

3.1 Polarization Curve

The nine polarization curves under the orthogonal test are shown in Fig. 2. The current interval can be divided into three: 0–0.4 A cm⁻² for a small current density range, 0.4–1.0 A cm⁻² for a medium current density range, and 1.0–1.3 A cm⁻² for a large current density range. In the medium and high current density regions, the cell voltage varies greatly under different operating conditions. The highest voltage is for the case 3 condition, with a temperature of 60 °C and cathode back pressure, stoichiometry, and relative humidity of 90 kPa, 2.5, and 90%, respectively. The voltage value at 1.2 A cm⁻² current density is 0.56 V. The worst cases are case 8 and case 9, with corresponding voltage values of only 0.46 V. Therefore, different operating conditions significantly impact PEMFC performance. The voltage is only a combined external representation of the electrochemical processes inside the cell, so the following section will further decouple the different electrochemical processes.

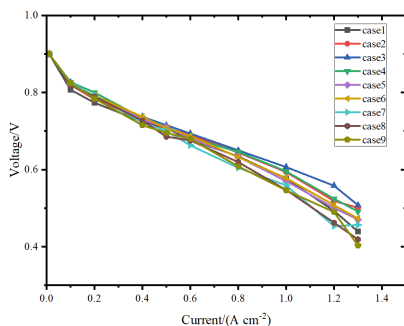


Fig. 2. 9 polarization curves of the orthogonal experiments.

3.2 Electrochemical Impedance Spectroscopy and Distribution of Relaxation Times

Electrochemical impedance spectroscopy is a widely employed in-situ characterization method. Due to space constraints, only case 5 was chosen for analysis in this study. As depicted in Fig. 3a, an increase in current density leads to a decrease and subsequent increase in both the low-frequency mass transfer region and the medium-high frequency charge transfer region. This phenomenon can be attributed to the marginally enhanced mass transfer performance of the catalytic layer, and the increased electrochemical reaction kinetics of the cathode as the current density gradually rises from the small current region, causing water production to increase. However, in the large current density region, the produced water cannot be discharged promptly, limiting gas transport and further reducing reaction kinetics.

In EIS, overlapping arcs, low resolution, and a lack of intuitiveness are common issues. In contrast, the distribution of relaxation times method enables different polarization processes to be represented as peaks, as illustrated in Fig. 3b. In the small current density region, the P2 peak is dominant, while in the large current density region, the P1 peak prevails. According to previous research [32], the P1 peak primarily represents the mass transfer process, and the P2 peak mainly signifies the cathodic oxygen reduction process. The P3 peak has not been extensively studied due to its relatively small contribution to the peak and its general association with the anodic process. The results obtained from the figure align with previous studies. The area of each peak can be approximated to represent the resistance value of the corresponding RC circuit. A 3rd-order RC equivalent circuit, as shown in Fig. 3d, can be employed for fitting. The resistance values of each electrochemical process at different current densities are obtained, as shown in Fig. 3c. The activation resistance R_{act} initially decreases rapidly and then changes slowly, while the mass transfer resistance R_{diff} fluctuates slightly at first before increasing linearly. The ohmic resistance R_{ohmic} and anode resistance exhibit minimal variation and account for a relatively small percentage.

3.3 Range Analysis

Using the aforementioned method, the mass transfer resistance and charge transfer resistance values were calculated for each group under the orthogonal test, as shown in Fig. 4.

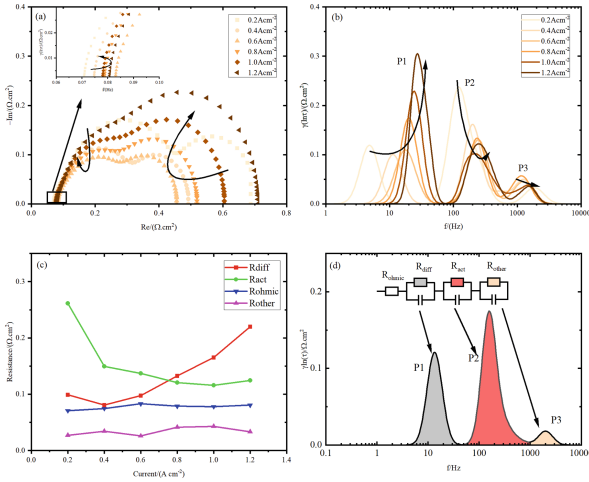


Fig. 3. Variation of current density from 0.2 to 1.2 A cm⁻²; (a) impedance spectroscopy; (b) According to DRT results; (c) each polarization loss; (d) A 3rd-order RC-element model developed via DRT.

The figure reveals that the corresponding R_{diff} in case3, case5, case7, and case9 conditions is smaller compared to the other groups. For R_{act}, the impedance in case 5, case 7, and case 9 is smaller. The trend of impedance with current density is also evident in the figure. The mass transfer impedance does not change significantly at small current densities, while the cathodic activation impedance decreases sharply from 0.2 to 0.4 A cm⁻². Subsequently, the mass transfer impedance increases gradually with increasing current density, and the charge transfer impedance increases slightly.

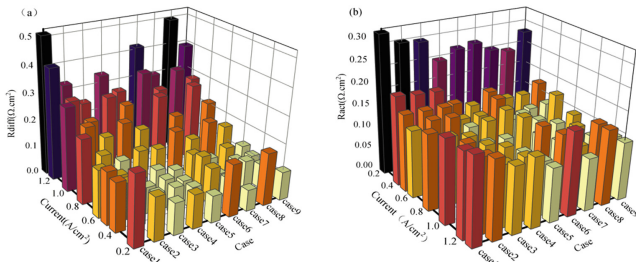


Fig. 4. Impedance values of orthogonal tests at different current densities; (a) Mass transfer impedance R_{diff}; (b) Charge transfer impedance R_{act}.

The impedance values for different operating conditions at the same current density also vary significantly. To examine the degree of influence of each operating condition on the impedance, the obtained impedance values were analyzed using the range analysis method. Due to space limitations, only the analysis results at 0.5 A cm⁻² are provided. The maximum R_{diff} and R_{act} of 0.1922 Ω cm² and 0.1782 Ω cm², respectively, are observed for case 1 operation. The minimum R_{diff} and R_{act} of 0.0682 Ω cm² and

0.1091 $\Omega \text{ cm}^2$, respectively, are observed for Case7 operation. The reduction in R_{diff} and R_{act} is 64.5 and 36.9%, respectively.

Tables 2 and 3 present the results of the calculation of the degree of influence of the four factors on the impedance values, respectively. As indicated in Table 2, the sequence TC (0.0673) > TA (0.0509) > TD (0.0228) > TB (0.0157) suggests that, at a current density of 0.5 A cm^{-2} , the effect of air stoichiometry on R_{diff} is the most significant, followed by operating temperature, while the cathode back pressure has the least impact on R_{diff} . Table 3 shows that the sequence TA (0.0558) > TC (0.0168) > TB (0.0149) > TD (0.0047) implies that temperature has the greatest effect on R_{act} at a current density of 0.5 A cm^{-2} , followed by air stoichiometry, while cathode relative humidity has the least influence on R_{act} .

Table 2. Calculation results of R_{diff} under 500 mA cm^{-2}

| Factors | Levels | | | Influence degree T |
|---------|----------------------|------------------------|------------------------|--------------------|
| | 1 | 2 | 3 | |
| A | $\delta A1 = 0.0266$ | $\delta A2 = - 0.0023$ | $\delta A3 = - 0.0243$ | 0.0509 |
| B | $\delta B1 = 0.0070$ | $\delta B2 = - 0.0088$ | $\delta B3 = 0.0018$ | 0.0157 |
| C | $\delta C1 = 0.0345$ | $\delta C2 = - 0.0017$ | $\delta C3 = - 0.0328$ | 0.0673 |
| D | $\delta D1 = 0.0096$ | $\delta D2 = 0.0036$ | $\delta D3 = - 0.0132$ | 0.0228 |

Table 3. Calculation results of R_{act} under 500 mA cm^{-2}

| Factors | Levels | | | Influence degree T |
|---------|----------------------|------------------------|------------------------|--------------------|
| | 1 | 2 | 3 | |
| A | $\delta A1 = 0.0266$ | $\delta A2 = - 0.0023$ | $\delta A3 = - 0.0243$ | 0.0509 |
| B | $\delta B1 = 0.0070$ | $\delta B2 = - 0.0088$ | $\delta B3 = 0.0018$ | 0.0157 |
| C | $\delta C1 = 0.0345$ | $\delta C2 = - 0.0017$ | $\delta C3 = - 0.0328$ | 0.0673 |
| D | $\delta D1 = 0.0096$ | $\delta D2 = 0.0036$ | $\delta D3 = - 0.0132$ | 0.0228 |

By applying the above method to analyze different current densities, the degree of influence of the four factors, along with the variation curve with current density, is depicted in Fig. 5. As shown in Fig. 5a, the effect of air stoichiometry ratio on R_{diff} is dominant across the entire current density range, with the most pronounced effect observed at small and large current densities and a decrease in the middle range of 0.4–0.6 A cm^{-2} . This can be attributed to the small electrochemical reaction kinetics, slow reaction rate, low reaction gas consumption, and small reaction gas diffusion coefficient at low current densities. Conversely, at high current densities, the reaction consumes gas more rapidly, generates more water, and obstructs gas transport channels, necessitating a larger stoichiometric ratio of reaction gas to expel the excess water. Cell temperature at

low and medium current densities ($< 0.6 \text{ A cm}^{-2}$) has a substantial impact on R_{diff} . This is because lowering the temperature at low current densities can significantly improve water management within the cell, adequately humidify the membrane and catalytic layer, and enhance gas transport. The effects of cathode back pressure and relative humidity on gas on R_{diff} are not significant.

Figure 5b demonstrates that temperature's effect on R_{act} is dominant at low and medium current densities, particularly at small current densities. This is due to the small electrochemical reaction kinetics and low catalytic activity at low current densities while increasing the temperature can enhance the reaction rate, reduce activation loss, and improve catalyst efficiency. At high current densities ($> 1 \text{ A cm}^{-2}$), the influence of air stoichiometry ratio is more significant than temperature and becomes the dominant factor. The effects of cathode back pressure and relative humidity on R_{act} remain small.

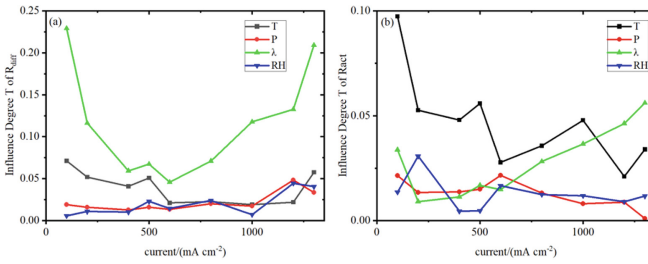


Fig. 5. Impact degree of different impact factors at different current densities; (a) Mass transfer impedance R_{diff} ; (b) Charge transfer impedance R_{act} .

3.4 The Optimal Combination of Influence Factors

In this study, the optimal combination refers to a collection of factors including operating temperature, air inlet pressure, air stoichiometry, and air relative humidity (RH), which jointly determine the value of resistance. Taking 500 mA cm^{-2} current density as an example, it is observed that $\delta A1 > \delta A2 > \delta A3$, $\delta B1 > \delta B3 > \delta B2$, $\delta C1 > \delta C2 > \delta C3$, and $\delta D1 > \delta D2 > \delta D3$ (Table 2) for R_{diff} , while $\delta A1 > \delta A2 > \delta A3$, $\delta B3 > \delta B2 > \delta B1$, $\delta C1 > \delta C2 > \delta C3$, and $\delta D2 > \delta D1 > \delta D3$ (Table 3) for R_{act} . Since the objective is to select the operating condition with the lowest impedance, the smallest set should be chosen. Consequently, the optimal parameter combination for R_{diff} is: operating temperature at $80 \text{ }^\circ\text{C}$ (third level of factor A), air inlet pressure at 80 kPa (second level of factor B), air stoichiometry at 2.5 (third level of factor C), and air RH at 90% (third level of factor D). For R_{act} , the optimal parameters are identical. The optimal combination of the four factors for R_{diff} at low and medium current densities ($< 600 \text{ mA cm}^{-2}$) is: operating temperature at $80 \text{ }^\circ\text{C}$ (third level of factor A), air inlet pressure at 90 kPa (third level of factor B), air stoichiometry at 2.5 (third level of factor C), and air RH at 90% (third level of factor D). At high current densities ($> 800 \text{ mA cm}^{-2}$), the optimal combination is: operating temperature at $70 \text{ }^\circ\text{C}$ (second level of factor A), air inlet pressure at 90 kPa (third level of factor B), air stoichiometry at 2.5 (third level of factor C), and air RH at 90% (third level of factor D).

The optimal combination of the four factors for R_{act} at low and medium current densities ($< 800 \text{ mA cm}^{-2}$) is: operating temperature at $80 \text{ }^\circ\text{C}$ (third level of factor A), air inlet pressure at 80 kPa (second level of factor B), air stoichiometry at 2.5 (third level of factor C), and air RH at 90% (third level of factor D). At high current densities ($> 1000 \text{ mA cm}^{-2}$), the optimal combination is: operating temperature at $80 \text{ }^\circ\text{C}$ (third level of factor A), air inlet pressure at 80 kPa (third level of factor B), air stoichiometry at 2.5 (third level of factor C), and air RH at 50% (first level of factor D).

4 Conclusions

This study investigates the effects of temperature, cathode back pressure, cathode relative humidity, and air stoichiometry on the mass and charge transfer processes in electrochemical reactions using orthogonal tests. The DRT-based method separates and quantifies different polarization processes and establishes a 3rd-order RC equivalent circuit model. The influence weight of each factor is examined via polar difference analysis. The following conclusions are drawn:

- (1) The DRT-based method for resolving the electrochemical impedance spectrum can distinguish the spectrum into three peaks, representing the cathodic mass transfer process, cathodic catalytic layer oxygen reduction process, and anodic process, respectively, from low to high frequencies.
- (2) The effect of the air stoichiometry ratio on R_{diff} is dominant across the entire current density range, particularly at small and large current densities. The effect of temperature on R_{act} is predominant at low and medium current densities, especially at small current densities. However, at high current densities ($> 1 \text{ A cm}^{-2}$), the weight of the air stoichiometry's effect surpasses that of temperature.
- (3) The optimal combination of the four factors for R_{diff} at current densities below 600 mA cm^{-2} is: operating temperature at $80 \text{ }^\circ\text{C}$, air inlet pressure at 90 kPa , air stoichiometry at 2.5 , and air RH at 90% . At current densities above 800 mA cm^{-2} , the optimal combination is: operating temperature at $70 \text{ }^\circ\text{C}$, air inlet pressure at 90 kPa , air stoichiometry at 2.5 , and air RH at 90% .
- (4) The optimal combination of the four factors for R_{act} at current densities below 800 mA cm^{-2} is: operating temperature at $80 \text{ }^\circ\text{C}$, air inlet pressure at 80 kPa , air stoichiometry at 2.5 , and air RH at 90% . At current densities above 1000 mA cm^{-2} , the optimal combination is: operating temperature at $80 \text{ }^\circ\text{C}$, air inlet pressure at 80 kPa , air stoichiometry at 2.5 , and air RH at 50% .

References

1. Wang, Y., Pang, Y., Xu, H.: PEM Fuel cell and electrolysis cell technologies and hydrogen infrastructure development—a review. *Energy Environ. Sci.* **15**(6), 2288–2328 (2022)
2. Dutta, S.: A review on production, storage of hydrogen and its utilization as an energy resource. *J. Ind. Eng. Chem.* **20**, 1148 (2014)
3. Lin, R., Cui, X., Shan, J., Técher, L., Xiong, F., Zhang, Q.: Investigating the effect of start-up and shut-down cycles on the performance of the proton exchange membrane fuel cell by segmented cell technology. *Int. J. Hydr. Energy* **40**(43)

4. Ettingshausen, F., Kleemann, J., Marcu, A., Toth, G., Fuess, H., Roth, C.: Dissolution and migration of platinum in PEMFCs investigated for start/stop cycling and high potential degradation. *Fuel Cell* **11**, 238 (2011)
5. Durst, J., Lamibrac, A., Charlot, F., Dillet, J., Castanheira, L.F., Maranzana, G., Dubau, L., Maillard, F., Chatenet, M., Lottin, O.: Degradation heterogeneities induced by the repetitive start/stop events in proton exchange membrane fuel cell: inlet vs. outlet and channel vs. land. *Appl. Catal B Environ.* **138–139**, 416
6. Venkatesan, S.V., Dutta, M., Kjeang, E.: Mesoscopic degradation effects of voltage cycled cathode catalyst layers in polymer electrolyte fuel cells. *Electrochem. Commun.. Commun.* **72**, 15 (2016)
7. Wong, K.H., Kjeang, E.: Mitigation of chemical membrane degradation in fuel cells: understanding the effect of cell voltage and iron ion redox cycle. *Chemsuschem* **8**, 1072 (2015)
8. Aindow, T.T., O'Neill, J.: Use of mechanical tests to predict the durability of polymer fuel cell membranes under humidity cycling. *J. Power. Sources* **196**, 3851 (2011)
9. Han, M., Shul, Y.-G., Lee, H., Shin, D., Bae, B.: Accelerated testing of polymer electrolyte membranes under open-circuit voltage conditions for durable proton exchange membrane fuel cells. *Int. J. Hydr. Energy* **42**, 30787 (2017)
10. Ze, L., Xu, S., Sida, G.: High-potential control for durability improvement of the vehicle fuel cell system based on oxygen partial pressure regulation under low-load conditions. *Int. J. Hydr. Energy* **47(76)** (2022)
11. Andres, J., Daniel, H., Vincent, H., Mathias, G., Sebastien, R.: Prognostic methods for proton exchange membrane fuel cell under automotive load cycling: a review. *IET Electr. Syst. Transp.* **10(4)** (2020)
12. Zhang, B., Wang, X., Gong, D., Xu, S.: Experimental analysis of the performance of the air supply system in a 120 kW polymer electrolyte membrane fuel cell system. *Int. J. Hydr. Energy* **47(50)** (2022)
13. Shan, J., Lin, R., Xia, S., Liu, D., Zhang, Q.: Local resolved investigation of PEMFC performance degradation mechanism during dynamic driving cycle. *Int. J. Hydr. Energy* **41**, 4239 (2016)
14. Stefanos, T., Kavadias Kosmas, A., Marnellos George, E., George, X.: A review study on proton exchange membrane fuel cell electrochemical performance focusing on anode and cathode catalyst layer modelling at macroscopic level. *Renew. Sustain. Energy Rev.* **151** (2021)
15. Chen, H., Liu, B., Liu, R., Weng, Q., Zhang, T., Pei, P.: Optimal interval of air stoichiometry under different operating parameters and electrical load conditions of proton exchange membrane fuel cell. *Energy Convers. Manage.* **205(C)** (2020)
16. Zhang, Q., Lin, R., Técher, L., Cui, X.: Experimental study of variable operating parameters effects on overall PEMFC performance and spatial performance distribution. *Energy* **115** (2016)
17. Jin, L., Wang, X.-J., Zhu, J.-W., Wang, C.-F., Zhou, T.-T., Zhang, X.-W.: Sensitivity analysis of proton exchange membrane fuel cell performance to operating parameters and its applicability assessment under different conditions. *Energy Convers. Manage.* **228** (2021)
18. Hu, D., Wang, Y., Li, J., Yang, Q., Wang, J.: Investigation of optimal operating temperature for the PEMFC and its tracking control for energy saving in vehicle applications. *Energy Convers. Manage.* **249** (2021)
19. Dilek, N.O., Bora, T., Kemal, A.: Effects of operation temperature and reactant gas humidity levels on performance of PEM fuel cells. *Renew. Sustain. Energy Rev.* **59** (2016)
20. Wang, B., Lin, R., Liu, D., Xu, J., Feng, B.: Investigation of the effect of humidity at both electrode on the performance of PEMFC using orthogonal test method. *Int. J. Hydr. Energy* **44(26)** (2019)

21. Marcel, H., Weber, A., Ivers-Tiffée, W.: Advanced impedance study of polymer electrolyte membrane single cells by means of distribution of relaxation times. *J. Power Sour.* **402** (2018)
22. Yuan, H., Dai, H., Ming, P., Wang, X., Wei, X.: Quantitative analysis of internal polarization dynamics for polymer electrolyte membrane fuel cell by distribution of relaxation times of impedance. *Appl. Energy* **303** (2021)
23. Zhu, D., Yang, Y., Ma, T.: Evaluation the resistance growth of aged vehicular proton exchange membrane fuel cell stack by distribution of relaxation times. *Sustainability* **14**(9) (2022)
24. Zhu, D., Ma, T., Yang, Y.: Optimization and application of the distribution of relaxation times based on characteristic frequency resolution and hyperparameters. *J. Power Sources* **545** (2022)
25. Costa, S., Barroso, M., Castanera, A., Dias, M.: Design of experiments, a powerful tool for method development in forensic toxicology: application to the optimization of urinary morphine 3-glucuronide acid hydrolysis. *Anal. Bioanal. Chem.* **396**, 2533 (2010)
26. Wan, T.H., Saccoccio, M., Chen, C., Ciucci, F.: Influence of the discretization methods on the distribution of relaxation times deconvolution: implementing radial basis functions with DRTtools. *Electrochim. Acta.* **184**, 483–499 (2015)
27. Ciucci, F.: Modeling electrochemical impedance spectroscopy. *Curr. Opin. Electrochem.* **13**, 132–139 (2019)
28. Schönleber, M., Klotz, D., Ivers-Tiffée, E.: A method for improving the robustness of linear Kramers-Kronig validity tests. *Electrochimica Acta* **131** (2014)
29. Boukamp, B.A.: *J. Electrochem. Soc.* **142**, 1885 (1995)
30. Peng, J., Dong, F., Xu, Q., Xu, Y., Qi, Y., Han, X., et al.: Orthogonal test design for optimization of supercritical fluid extraction of daphnoretin, 7-methoxy-daphnoretin and 1,5-diphenyl-1-pentanone from *Stellera chamaejasme* L. and subsequent isolation by high-speed counter-current chromatography. *J. Chromatogr. A* **1135**, 151e7 (2006)
31. Xia, S., Lin, R., Cui, X., Shan, J.: The application of orthogonal test method in the parameters optimization of PEMFC under steady working condition. *Int. J. Hydr. Energy* **41**, 11380e90 (2016)
32. Hu, Z., Xu, L., Li, J., Gan, Q., Xu, X., Song, Z., Shao, Y., Ouyang, M.: A novel diagnostic methodology for fuel cell stack health: performance, consistency and uniformity. *Energy Convers. Manage.* **185**, 611–621 (2019)



Development of 130 kW Self-Humidifying Proton Exchange Membrane Fuel Cell System

Tiancai Ma^{1,2}, Jixuan Qi¹, Ziheng Gu¹, Chang Du¹, and Weikang Lin³(✉)

¹ School of Automotive Studies, Tongji University, Shanghai 201804, China

² Institute of Carbon Neutrality, Tongji University, Shanghai 200092, China

³ Shanghai Champspower Technology Co., Ltd., Shanghai 201800, China

linwk@champspower.com

Abstract. Replacing external humidifiers with self-humidification technology can simplify the structure of fuel cell systems and improve their cost-effectiveness. This paper analyzes a feasible method for achieving self-humidification at the system level, suggesting that membrane drying can be prevented by increasing the hydrogen circulation pump revolutions, reducing the air stoichiometric ratio, and controlling the stack temperature. A theoretical design for each subsystem of the 130 kW PEMFC-based self-humidifying fuel cell system was also proposed. The system was built and tested under steady-state conditions, achieving an efficiency of 86.7% under the rated power. Additionally, the stack's high-frequency resistance, voltage, and cathode/anode pressure drop were measured to analyze the water content status inside. The results indicate that the high-frequency resistance of the stack was $57.17 \text{ m}\Omega\cdot\text{cm}^2$, and the single-cell voltage difference was 0.03 V, which means no membrane drying failure occurred under the rated power. The construction of the 130 kW self-humidifying fuel cell system described in this paper provides guidance for designing and integrating self-humidification systems based on PEMFC.

Keywords: Fuel cell · Self-humidification · System design

1 Introduction

The adoption of hydrogen and other renewable energies is widely recognized as a prospective solution for mitigating the increasing global energy consumption and environmental pollution caused by the abuses of fossil fuel energy. One aspect of this approach is the utilization of fuel cell electric vehicles (FCEVs), which are highly efficient, environmentally sustainable, and produce zero emissions, making that an optimal option for utilizing hydrogen energy in the transportation field [1, 2].

The Proton Exchange Membrane Fuel Cell (PEMFC), is an electrochemical device that generates electrical energy through the reaction of hydrogen and oxygen. Due to its low operating temperature and quick start-up, it becomes a focal point in new energy vehicles and has been extensively studied in recent years [3]. Since the proton conductivity of the PEMFC relies heavily on the level of hydration of the Nafion membrane

the incoming gas of the system is commonly humidified to preserve conductive membrane hydration and ensure high stack performance [4, 5]. The methods for humidifying PEMFC can be classified as external and internal humidification [6]. Automotive fuel cell systems commonly employ hydrogen circulation to humidify the hydrogen in the anode, combined with an external membrane humidifier to humidify the air in the cathode. The membrane humidifier divides the dry and wet channels using a porous polymer membrane, introducing the dry and wet air into respective channels. The water between the two channels is transferred from the wet side to the dry side via diffusion, thus achieving the humidification of dry air [7, 8].

Despite the benefits of membrane humidifier in increasing air humidity, there are several issues.

The size of the membrane humidifier is huge, which complicates and increases the cost of system layouts for vehicle applications. It also increases the airflow resistance, which subsequently increases the power consumption of the compressor. Furthermore, water management in the fuel cell system utilizing membrane humidifier is challenging during some operations, any malfunction of the membrane humidifier may lead to membrane drying or flooding. Thus, internal humidification is more suitable for automotive fuel cell systems [9].

In recent years, a significant amount of research has been conducted on internal humidification strategies for fuel cells. These strategies mainly focus on two approaches: changing the composition of the membrane to promote water storage and changing the physical structure of the bipolar plate channels to facilitate humidification.

Vengatesan et al. [10] added SiO_2 to both the catalyst layer and the membrane to achieve self-humidification and high proton conductivity. The results showed that the addition of a small amount of SiO_2 to the cathode catalyst layer significantly improved the cell's performance at high temperatures. Cha et al. [11] found that short-side-chain membranes exhibit better reliability and higher water retention capacity than long-side-chain ones. Tsai et al. [12] utilized silica aerogel (SA) as a carrier for Pt. The high surface area and porosity of SA resulted in Pt-SA/Nafion self-humidifying films showing exceptional performance in terms of both proton conductivity and water retention. Qi and Martins Belchor et al. [13, 14] designed a new channel with two gas inlets and two gas outlets, where the inlet of one channel is adjacent to the outlet of the other flow channel. Thus, the dry gas entering the channel can be humidified by the wet gas. Wang et al. [15] surrounded the active electrode region with an inactive 'water transfer zone' so that the output water in the cathode can be transferred through the membrane to the anode to wet hydrogen.

In addition to the above methods, self-humidification could be attained by regulating the operational parameters of the fuel cell system. Previous studies have demonstrated that fuel cell performance and internal water content state rely on operating temperature, stoichiometric ratio, ambient humidity, and current density [16]. Appropriate operating parameters for the stack could prevent membrane drying. This approach does not necessitate changing the fuel cell structure, which is more suitable for the actual system.

Most of the current research on self-humidification in PEMFCs has focused on single cell or short stack tested in laboratory setting, without considering the practical situations for high-power fuel cell systems, which are characterized by large reaction areas and

thin proton exchange membranes [17–19]. These factors can significantly influence the water transport process in the fuel cell.

In this paper, the development of a 130 kW self-humidifying PEMFC-based system for a high-power truck is described in detail. Calculations are provided for matching the fuel cell stack, hydrogen subsystem, air subsystem, and thermal management subsystem. A steady-state conditions test was carried out, during which high-frequency resistance, pressure drop, and single-cell voltage were measured and compared with those of an 80 kW fuel cell system with external humidification. Based on experimental results, an analysis of the internal water status and the power consumption of the balance of plant (BOP) was conducted, which demonstrated that the 130 kW self-humidifying system had high system efficiency.

2 PEMFC-Based Self-Humidifying System Design

The following content elaborates on the design principles of the system that caters to a high-power truck necessitating an output rating of 130 kW. The system comprises a fuel cell stack module, a hydrogen supply subsystem, an air supply subsystem, and a thermal management subsystem.

2.1 Fuel Cell Stack Selection

To meet the design requirements, the output power of the stack needs to exceed 130 kW, taking into account the power consumption of the BOP. The hydrogen conversion efficiency of the fuel cell stack must be at least 50%, and the minimum voltage is determined by Eq. (1). Accordingly, the operational voltage V_{\min} of the stack is computed as 0.627 V.

$$V_{\min} \gg \eta \cdot E_{LHV} \quad (1)$$

η is the hydrogen conversion efficiency, E_{LHV} is the equilibrium potential of hydrogen at a low calorific value.

To achieve optimal performance and prolong service life, the stack should be operated near the rated point. The matching results of subsystems reveal that the power consumption of the BOP at the rated point is approximately 25 kW. Furthermore, accounting for the losses of the DC/DC converter, the rated output power of the stack should be more than 155 kW. To ensure a certain overload capacity, a stack with a maximum power of 175 kW and a maximum operating current of 660 A is selected, and the rated operating point is 157 kW with a current of 561 A. At that point, the hydrogen-electric conversion efficiency is roughly 53.3%.

2.2 Air Supply Subsystem Design

The air supply subsystem provides oxygen for the cathode reaction. To achieve this, a centrifugal air compressor is employed. The compressor increases the air pressure to the required conditions for the stack inlet. Given that the stack's appropriate operating temperature is generally below 80 °C, while the air compressor can heat the compressed

air to a temperature above 100 °C. If the high-temperature air enters the stack without any cooling treatment, it will result in a reduction in stack performance. Therefore, an intercooler is equipped to cool the air for the stack. The coupling control of air pressure and flow rate is achieved by adjusting the revolution of the air compressor and the opening of the back pressure valve (BPV) which is fixed at the stack outlet. The air supply subsystem designed in this paper utilizes an open-loop control strategy to reduce control complexity. The structure of the air supply subsystem is shown in Fig. 1.

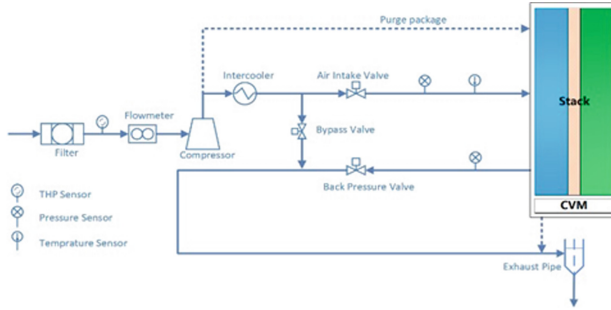


Fig. 1. Schematic of air supply subsystem

The required airflow for the stack can be calculated using Eqs. (2) and (3), based on the requirements listed above.

$$Q_m = \frac{M_{Air}}{0.21 \times 4F} \times I \times N \times \lambda \quad (2)$$

$$Q_v = \frac{60 \times RT}{0.21 \times P \times 4F} \times I \times N \times \lambda \quad (3)$$

Q_m is air mass flow rate, g/s, Q_v is volume flow rate, L/min, M_{Air} is the molar mass flow of air, g/mol, I is the current of stack, N is the number of single cells, λ is the stoichiometric ratio of air, R is the molar gas constant J/mol K, T is the temperature of air K, P is the standard atmospheric pressure Pa, F is Faraday's constant, 96,485 C/mol.

To ensure a low concentration of hydrogen leakage, it is necessary to use an air purge for the stack package. If this is the case, the air compressor will provide an air purge flow rate, which should be calculated based on the maximum allowable hydrogen leakage concentration. Equation (4) shows the relationship between the airflow resistance H and the fluid medium, pipe size, material, and air density at different flow rates. K is a constant and is described by the above parameters.

$$H \propto K \cdot Q_v^2 \quad (4)$$

Based on the above principles, the flow and pressure design parameters of the air supply subsystem at the rated condition can be obtained as shown in Table 1.

The centrifugal air compressor exhibits operating limits in terms of airflow and pressure ratios, specifically limited by wheezing and blockage. Hence, it is crucial to align design requirements with the air compressor's MAP (Meaningful Application Parameters) diagram.

Table 1. Design requirement parameters of air supply subsystem

| Current A | Stoichiometric ratio | Airflow L/min | Air pressure kPa a | Stack inlet temperature °C |
|-----------|----------------------|---------------|--------------------|----------------------------|
| 561 | 1.8 | 6914 | 241.5 | 68.5 |

2.3 Hydrogen Supply Subsystem Design

The hydrogen supply subsystem delivers the required hydrogen for the anodic reaction. High-pressure hydrogen is released from the hydrogen tank and is subsequently depressurized by a pressure-reducing valve, following which the medium-pressure hydrogen is passed through a proportional valve for secondary depressurization to meet the specified requirements of the stack inlet. The hydrogen subsystem functions as a closed-loop system whereby hydrogen gas, discharged from the stack outlet, undergoes gas-water separation, followed by the elimination of water and nitrogen via a drain valve and a nitrogen discharge valve, respectively. The purified hydrogen gas is then circulated by the hydrogen circulation pump. The flow of the circulating hydrogen can be adjusted by changing the revolutions of the circulating pump. The pressure within the hydrogen subsystem is regulated using incremental PID closed-loop feedback control. Figure 2 depicts the hydrogen subsystem structural design.

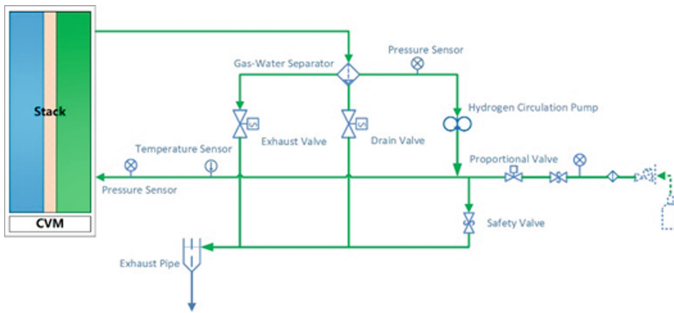


Fig. 2. Schematic of hydrogen supply subsystem

The calculation of the hydrogen flow is similar to the air, as in Eqs. (5) and (6)

$$Q_m = \frac{M_{H_2}}{2F} \times I \times N \tag{5}$$

$$Q_v = \frac{60 \times RT}{P \times 2F} \times I \times N \tag{6}$$

M_{H_2} is the molar mass flow of hydrogen g/mol.

Table 2 presents the necessary operating conditions for the stack. To ensure the proper selection of the proportional valve, its volumetric flow coefficient (K_v) must meet the demand under the rated operating conditions specified in Table 2. The K_v can

be calibrated using Eqs. (7) and (8), with consideration of the front-end pressure and primary flow rate [20].

$$K_v = \frac{Q_v}{514} \cdot \sqrt{\frac{T \cdot \rho_N}{P_2 \cdot \Delta P}} \left(P_2 > \frac{P_1}{2} \right) \quad (7)$$

$$K_v = \frac{Q_v}{257 \cdot P_1} \cdot \sqrt{T \cdot \rho_N} \left(P_2 < \frac{P_1}{2} \right) \quad (8)$$

K_v is the volumetric flow coefficient m^3/h , Q_v is the standard flow rate m^3/h , P_1 is the inlet pressure of proportional valve *bar*, P_2 is the outlet pressure of proportional valve *bar*, ρ_N is the standard density of hydrogen kg/m^3 , T is the medium temperature K.

A proportional valve with a K_v of 0.195 is chosen for the system, according to the stack outlet pressure and primary flow rate to metering ratio stated in Table 2. The hydrogen circulation pump can enhance hydrogen utilization and improve water management on the anode side of the stack. Although the operating gas may contain several components, the design process assumes that only hydrogen is used for circulation.

Table 2. Design requirement parameters of hydrogen supply subsystem

| Current A | Hydrogen Stoichiometric ratio | H ₂ inlet pressure kPa.a | H ₂ outlet pressure kPa.a |
|-----------|-------------------------------|-------------------------------------|--------------------------------------|
| 561 | 1.5 | 256.5 | 240 |

In this paper, a vortex-structured gas-water separator is selected to make the gas mixture flow in a specific direction and accumulate liquid water at the bottom. The drain valve is opened and closed based on the internal liquid level sensor feedback to drain the accumulated liquid water.

2.4 Thermal Management Subsystem Design

The thermal management subsystem comprises the main cooling system and the auxiliary cooling system. The main cooling system maintains a stable temperature by circulating coolant. To control the stack temperature, a thermostat, a pump, and a radiator are utilized. The auxiliary cooling system cools equipment such as the air compressor and DC/DC converter that generate heat, by a separate circulation loop. A schematic representation of the thermal management subsystem structure is shown in Fig. 3.

The total heat dissipation in the main cooling system comprises the heat generated by the stack and the heat exchange of the intercooler. Equation (9) can be used to calculate the heat produced by the stack.

$$H_{s,stack} = \frac{(E_{LHV} - E_{cell}) \times I \times N}{1000} \quad (9)$$

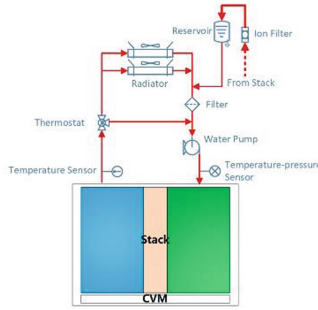


Fig. 3. Schematic of Thermal management subsystem

H_{stack} is the heat production of the stack kW, E_{cell} is the average cell voltage of the stack V.

The required heat exchange for the intercooler can be calculated using Eq. (10), which considers the air flow rate and the temperature difference between the inter-cooler’s inlet and outlet on the air side.

$$H_{ic} = Q_{mair} \cdot C_{air} \cdot (T_{inn} - T_{iout}) \tag{10}$$

H_{ic} is the heat exchange of the intercooler kW, Q_{mair} is the air mass flow rate kg/s, C_{air} is the specific heat capacity of air kJ/kg K. T_{inn} is the inlet air temperature of the intercooler K, T_{iout} is the outlet air temperature of the intercooler K.

Assuming that the stack inlet and outlet temperatures are equivalent to those of the intercooler, Eqs. (11) and (12) can be used to calculate the coolant flow rate.

$$H_c = H_{stack} + H_{ic} \tag{11}$$

$$Q_{vcl} = \frac{60000 \times H_{ic}}{C_{cl} \times (T_{stkout} - T_{stkin}) \times \rho_{cl}} \tag{12}$$

H_c is the total heat production kW, Q_{vcl} is the required coolant volume flow rate L/min, T_{stkout} is the stack coolant outlet temperature K, T_{stkin} is the stack coolant inlet temperature K, C_{cl} is the specific heat capacity of the coolant kJ/kg K, ρ_{cl} is the coolant density, kg/m³.

Design requirement of the thermal management subsystem is shown in Table 3.

Table 3. Design requirements of the thermal management subsystem

| | |
|---|------------------------------|
| Coolant | 40% Ethylene glycol solution |
| Heat power of the stack kW | 137 |
| Heat transfer power of the intercooler kW | 6.2 |
| Total flow rate L/min | 280 |

Under rated operating conditions, the pressure drop in the stack's water chamber and the thermal management subsystem is approximately 200 kPa in total. The chosen pump must satisfy the design requirements. The thermal management system utilizes a cooperative PID control algorithm, which simultaneously regulates the thermostat opening and fan revolutions to ensure temperature stability.

3 System Integration

The 130 kW self-humidifying system integration is accomplished based on the matching design mentioned above. The photograph of the assembled system is presented in Fig. 4. The fuel cell system is connected to LabVIEW via CAN protocol.

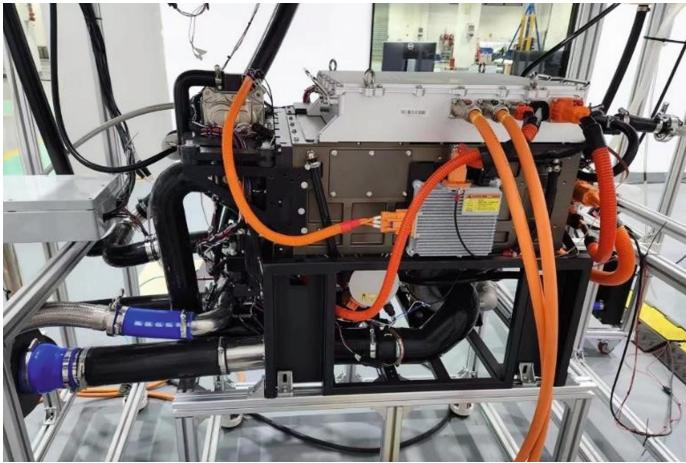


Fig. 4. Photograph of the completed system

3.1 Experimental Activities

The system was loaded according to the prescribed method and operated steadily for 3 min at various power points to conduct the steady-state experiment, while the fuel cell system's required power was simulated through electronic loads. The chosen power points and operating conditions for the system are displayed in Table 4.

The results of the experiment are depicted in Fig. 5a, and the actual polarization curve of the stack is presented in Fig. 5b. Since the external humidifier was not used in this system, the potential occurrence of membrane drying failure was closely monitored. The main elements evaluated were the high-frequency resistance, the pressure drop of the hydrogen and air, and the single-cell voltage. The steady-state data of the 80 kW fuel cell system (hereafter referred to as the 80 kW system) with an external membrane humidifier were compared to those of the 130 kW system. The stack selected for the 80 kW system is identical to the 130 kW system except for the number of cells.

Table 4. Operating conditions for the steady-state test

| System power demand kW | Stack current A | Air stoichiometric ratio | Hydrogen circulation pump revolution rpm |
|------------------------|-----------------|--------------------------|--|
| 30.6 | 99 | 2.4 | 3000 |
| 39.4 | 132 | 2 | 3000 |
| 47.6 | 165 | 2 | 3000 |
| 55.9 | 198 | 2 | 3500 |
| 63.8 | 231 | 1.9 | 3500 |
| 71.0 | 264 | 1.9 | 4000 |
| 77.8 | 297 | 1.9 | 4500 |
| 85.2 | 330 | 1.9 | 4500 |
| 92.9 | 363 | 1.9 | 4800 |
| 99.7 | 396 | 1.8 | 5000 |
| 106.0 | 429 | 1.8 | 5000 |
| 113.7 | 462 | 1.8 | 5200 |
| 120.1 | 495 | 1.8 | 5500 |
| 126.0 | 528 | 1.8 | 5700 |
| 132.0 | 561 | 1.8 | 5700 |

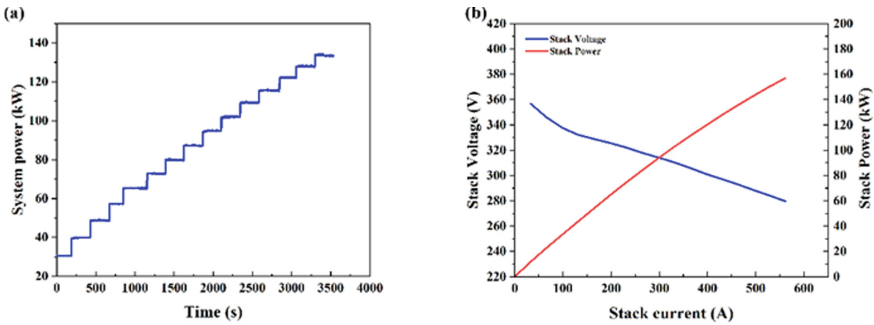


Fig. 5. Steady-state experiment (a) and performance of the fuel cell stack (b).

3.2 Results and Discussion

Water content status. Currently, there are no standardized definitions or diagnostic criteria for detecting membrane drying in PEMFC fault diagnosis [21]. However, membrane drying is typically characterized by low water content in the membrane, unchanged hydrogen, and air pressure drops, and reduced output voltage [22]. High-frequency resistance is also a diagnostic indicator for membrane drying, as it can show a decrease in proton conductivity and membrane water content [23]. In general, a higher high-frequency resistance value suggests lower membrane water content.

The steady-state test data of the 130 kW system, including the voltage, pressure drop, and high-frequency resistance at 1000 Hz frequency, were recorded and compared to those of the 80 kW system. The experimental data were converted into single-cell values for analysis.

Figure 6 displays the stack single-cell voltage data and maximum single-cell voltage difference for both 130 and 80 kW systems under steady-state conditions. As shown, the maximum single-cell voltage difference remained below 0.03 V, indicating high voltage consistency for the self-humidifying system, which is comparable to the externally-humidified system. Additionally, the 130 kW self-humidifying system exhibits higher stack voltage than the 80 kW externally-humidified system, likely due to the latter's larger air metering ratio and higher operating temperature resulting in suboptimal internal water content despite using external humidifier. These findings are consistent with the response curves presented in Fig. 7(a). Notably, at rated operating conditions, the self-humidifying system demonstrates a high-frequency resistance value of $57.17 \text{ m}\Omega\cdot\text{cm}^2$, while the externally-humidified system is $63.8 \text{ m}\Omega\cdot\text{cm}^2$. The lower resistance value of the self-humidifying system reflects optimal membrane water status and proton conductivity, indicating the superior performance of the 130 kW system.

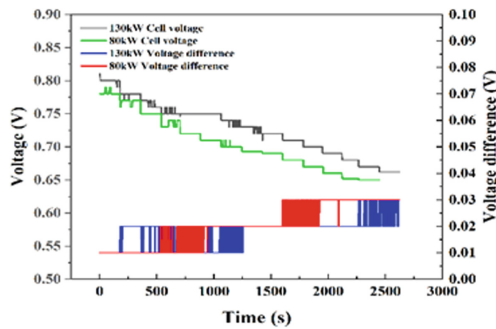


Fig. 6. Data of single-cell voltage

Figure 7b illustrates the pressure drop of the cathode and anode. The pressure drop remains relatively stable at each operating point during steady-state conditions, and there is no noticeable voltage drop. These observations suggest that the membrane water status in the stack is sufficient at this time, and there is no occurrence of membrane drying failure.

System output efficiency. The output efficiency of the fuel cell system is a critical evaluation criterion and can be determined through Eq. (13):

$$\eta_{\text{sys}} = \frac{P_{\text{stack}} - P_{\text{BOP}}}{P_{\text{stack}}} \quad (13)$$

η_{sys} is the system output efficiency %, P_{stack} is the power output of the stack kW, P_{BOP} is the parasitic power consumption brought by the BOP kW.

The total power consumption of the BOP is 20.65 kW, which includes 18.3 kW for the air compressor, 1.5 kW for the water pump, and 0.9 kW for the hydrogen circulation

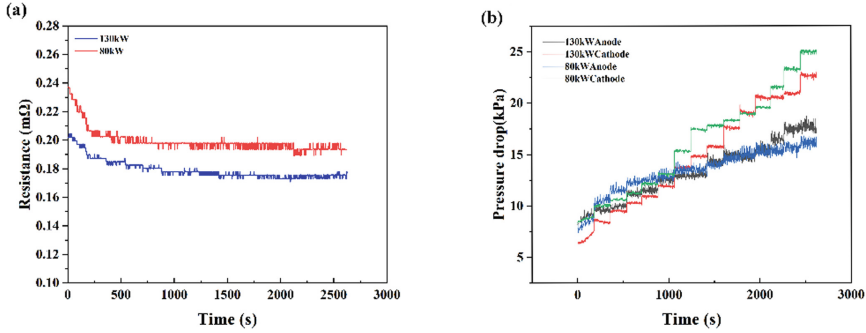


Fig. 7. Data of high frequency resistance (a) and pressure drop (b)

pump, with the remainder going to the low-voltage devices for 0.48 kW. The system efficiency at the rated power is 86.7%.

The power consumption of the air compressor is relatively low may due to the elimination of the external membrane humidifier, which reduces the overall flow resistance of the air supply subsystem and the required pressure ratio of the compressor. Additionally, the air stoichiometric ratio of the system is only 1.8 at the rated operating condition, which further decreases power consumption.

4 Conclusions

The application of fuel cell technology in high-power transportation scenes is a crucial way to reduce carbon emissions as part of global energy conservation. The utilization of self-humidification technology can simplify the fuel cell system structure and improve hydrogen efficiency. The main contributions of this paper are as follows.

- The detailed calculation method used to match the parameters of each subsystem of the 130 kW self-humidifying PEMFC-based system was analyzed, and the development of the system prototype was also completed.
- Steady-state experiments were conducted on the system using appropriate operating conditions. Measurements of single-cell voltage, high-frequency resistance, and pressure drop were taken and compared with the 80 kW system with an external membrane humidifier. Results showed that the self-humidifying PEMFC-based system had a high-frequency resistance of $57.17 \text{ m}\Omega \text{ cm}^2$ under rated operating conditions, the maximum single-cell voltage difference is less than 0.03 V, which shows no membrane dry failure occurred.
- The system efficiency was measured at rated power to be 86.7%, indicating that removing the external membrane humidifier and reducing the air stoichiometric ratio properly can reduce the power consumption of the air compressor, thereby improving system efficiency.

In future research, the performance of 130 kW self-humidifying PEMFC-based system under extreme operating conditions such as low temperature and plateau scenarios will be examined, these investigations will help advance the development of hydrogen energy applications in the transportation field.

References

1. Jiao, K.: Designing the next generation of proton-exchange membrane fuel cells. *Nature* **595**, 361–369 (2021)
2. Kurtz, J.M.: Fuel cell electric vehicle durability and fuel cell performance. Natl. Renew. Energy Lab (NREL) Technical Rep. (2019)
3. Rahnavard, A.: The effect of sulfonated poly (ether ether ketone) as the electrode ionomer for self-humidifying nanocomposite proton exchange membrane fuel cells. *Energy* **82**, 746–757 (2015)
4. Kadyk, T.: Nonlinear frequency response analysis of dehydration phenomena in polymer electrolyte membrane fuel cells. *Int. J. Hydrogen Energy* **37**(9), 7689–7701 (2012)
5. Sahraoui, M.: Three-dimensional modeling of water transport in PEMFC. *Int. J. Hydrogen Energy* **38**(20), 8524–8531 (2013)
6. Park, C.H.: Nanocrack-regulated self-humidifying membranes. *Nature* **532**, 480–483 (2016)
7. Baharlou Houreh, N.: Experimental study on performance of membrane humidifiers with different configurations and operating conditions for PEM fuel cells. *Int. J. Hydr. Energy* **45**(7), 4841–4859 (2020)
8. Hwang, J.J.: Experimental study on performance of a planar membrane humidifier for a proton exchange membrane fuel cell stack. *Power Sources* **215**, 69–76 (2012)
9. Chang, Y.: Humidification strategy for polymer electrolyte membrane fuel cells—a review. *Appl. Energy* **230**, 643–662 (2018)
10. Vengatesan, S.: Operation of a proton exchange membrane fuel cell under non-humidified conditions using a membrane electrode assemblies with composite membrane and electrode. *Power Sources* **167**, 325–329 (2017)
11. Cha, D.: Comparative performance evaluation of self-humidifying PEMFCs with short-side-chain and long-side-chain membranes under various operating conditions. *Energy* **150**, 320–328 (2018)
12. Tsai, C.-H.: Microwave-assisted synthesis of silica aerogel supported pt nanoparticles for self-humidifying proton exchange membrane fuel cell. *Int. J. Hydrogen Energy* **37**, 7669–7676 (2012)
13. Qi, Z.: PEM fuel cell stacks operated under dry-reactant conditions. *Power Sources* **109**, 469–476 (2002)
14. Martins, B.P.: Parallel serpentine-baffle flow field design for water management in a proton exchange membrane fuel cell. *Int. J. Hydrogen Energy* **37**, 11904–11911 (2012)
15. Wang, E.D.: A novel self-humidifying membrane electrode assembly with water transfer region for proton exchange membrane fuel cells. *Power Sources* **175**, 183–188 (2008)
16. Riascos, L.A.M.: Relative humidity control in polymer electrolyte membrane fuel cells without extra humidification. *Power Sources* **184**, 204–211 (2008)
17. Zhang, L.: Model predictive control for electrochemical impedance spectroscopy measurement of fuel cells based on neural network optimization. *IEEE Trans. Transp. Electrification* **5**(2), 524–534 (2019)
18. Kurz, T.: An impedance-based predictive control strategy for the state-of-health of PEM fuel cell stacks. *J. Power. Sources* **180**(2), 742–747 (2008)
19. Wang, H.: Online electrochemical impedance spectroscopy detection integrated with stepup converter for fuel cell electric vehicle. *Int. J. Hydrogen Energy* **44**(2), 1110–1121 (2019)
20. Ma, T.: Development of 10 kW proton exchange membrane fuel cell combined heat and power system for domestic building services. SAE Technical Paper 2022-01-7036 (2022)
21. Wang, X.: Review on water management methods for proton exchange membrane fuel cells. *Int. J. Hydrogen Energy* **46**(22), 12206–12229 (2021)

22. Pei, P.: A review on water fault diagnosis of PEMFC associated with the pressure drop. *Appl. Energy* **173**, 366–385 (2016)
23. Cadet, C.: Diagnostic tools for PEMFCs: from conception to implementation. *Int. J. Hydr. Energy* **39**(20), 10613–10626 (2014)



A Neural Network Based PEMFC Dynamic Model for Hardware-in-the-Loop Application

Naiyuan Yao¹, Tiancai Ma¹(✉), Ruitao Li¹, Kun Yuan², Weikang Lin²,
and Yonghao Liang¹

¹ Tongji University, NO.1239 Siping Road, Shanghai, China
07024@tongji.edu.cn

² Shanghai Champspower Technology Limited Company, NO.518 Hengyong Road, Shanghai,
China

Abstract. As the pace of decarbonization continues to accelerate around the world, hydrogen energy as one of the energy solutions of the future has achieved considerable development. Automobiles based on PEMFC are one of the main products for the promotion of hydrogen energy at this stage. The complex operating conditions of fuel cell vehicles put higher requirements on the fuel cell system's dynamic response performance, and the system's dynamic response performance is closely related to the system's dynamic control strategy. The hardware-in-the-loop testbench is an important role in the toolchain of the fuel cell system's controller development. The fuel cell system model in the real-time controller and signal transceiver board can be used to simulate the characteristics of the system. Facing fuel cell system dynamic control strategy development needs, the hardware-in-the-loop testbench requires a high-precision dynamic model. The data-driven neural network model has long been widely used in the field of non-linear modeling. The input of the regression neural network structure considers both historical output and current input parameters, which is consistent with the actual situation of fuel cells. In this paper, experiments are carried out based on an 80kW fuel cell system, and the test sequences are designed within the allowable range of load change rules. Then the test result of the whole test sequence is divided into a training dataset and a verification dataset. The fuel cell model based on the regression neural network was trained by using the training dataset, and the influence of network hyperparameters on the loss function was analyzed. Finally, the model simulation accuracy is verified in the hardware-in-the-loop application scenario.

Keywords: PEMFC · Automotive · Hardware-in-the-loop · Dynamic model · Recurrent neural network

1 Introduction

Hydrogen energy, as a secondary energy source that has the advantages of being environment-friendly, abundant sources, high energy density, and high conversion efficiency, has received extensive attention and in-depth research [1, 2]. Vehicles based on

PEMFC have the advantages of zero-emission, low noise, and high efficiency, and are considered to be one of the strong competitors for the next generation of transportation power source solutions [3]. However, the vehicular fuel cell system inevitably faces complex and changeable working conditions such as acceleration, deceleration, idling, start-up and shut-down [4]. Under different external working conditions, it is necessary for the system to quickly adjust its output power to meet the needs of the vehicle, which puts forward higher requirements on the transient response performance of the fuel cell system. The transient response performance is related not only to the fuel cell stack but also to the auxiliary systems. The auxiliary systems of PEMFC provide sufficient fuel and oxidant for the stack during the operation of the system, control the output current of the stack, and takes away the heat generated by the stack due to the electrochemical reaction. Under the same configuration, an excellent system dynamic control strategy can significantly improve the transient response performance of the system and prolong the system's lifespan at the same time [5, 6].

The development of the system control strategy is often based on the fuel cell controller hardware-in-the-loop testbench [7]. Hardware-in-the-loop testing is a key step in the development of controllers. During the process of hardware-in-the-loop testing, the model of the controlled object will run in the real-time processor, and the model is connected to the system controller under test through the board card, and the actual system or components are not required to participate in the test [8, 9]. To ensure the validity of the HIL test and the reliability of the results, the simulation accuracy of the simulation model is vital. To meet the development requirements of the system dynamic control strategy, a high-precision fuel cell system dynamic model is required [5].

As a multivariable, strongly nonlinear, time-varying complex system [10], the existing fuel cell system dynamic models are mainly divided into three categories: mechanism model, empirical model and numerical model. The mechanism model is a mathematical model established based on the internal mechanism of the modeling object or the transfer mechanism of the material flow. All parameters in the model have clear physical meanings. Pasricha [11] established a fuel cell dynamic model based on the electrochemical mechanism formula, and the accuracy of the model was cross-validated by the experimental data of a 500 W stack. Gong [12] established a real-time dynamic fuel cell model, which coupled the three physical fields of electrochemistry, fluid, and heat, fully considering the heat and mass transfer phenomenon of the fuel cell, which could simulate the fuel cell behavior at room temperature and cold start. Hasegawa [13] established a one-dimensional lumped parameter mechanism model of the system under the Simulink platform for the second-generation Toyota MIRAI, which can reproduce the transient response of the system under acceleration and deceleration conditions. Andreas [14] explored the physical and electrochemical characteristics of the gas diffusion layer and the catalyst layer using a three-dimensional model, and simplified the three-dimensional model to run it on the HIL test bench to ensure the real-time performance of the test process.

Since all the parameters in the formula of the mechanism model have luciferous physical meanings, many unmeasurable physical quantities will affect the accuracy of the model. At the same time, the formula of the mechanism model is complicated, and multiple equations need to be solved simultaneously. Many researchers use the method

of parameter identification to establish the fuel cell empirical model, which greatly simplifies the modeling process and obtains higher model accuracy at the same time. Xi [15] established a PEMFC mathematical model based on a semi-empirical method to study the influence of key parameters such as membrane water content, air pressure, reaction temperature, and electric double layer phenomenon on output characteristics. Zhao [16] analyzed the relationship among current density, cooling water flow rate, number of cells, temperature, and cooling water outlet temperature in a stack composed of 5–30 cells, to meet the simulation needs of the heat demand of the CCHP system. Saleh [17] used a zero-dimensional simplified empirical model to model a 1kW class fuel cell stack, including the main electrical and thermodynamic variables and parameters that affect the operation of the stack, and the model can be extrapolated to a higher power with a similar configuration. Atlam [18] established the RC equivalent circuit model of the PEMFC and added the fuel cell operating parameters as influencing factors to the electrical components of the equivalent circuit model. Then he studied the fuel cell current-voltage characteristics and power generation efficiency under load and no-load conditions.

Most of the mechanism fuel cell system models and empirical models have a high prediction accuracy under steady-state conditions, but the establishment of complex equations and adjustment of parameters need to be done in the process of modeling the mechanism models and empirical models. The model for HIL testing and system dynamic control strategy development also needs to accurately describe the input-output relationship of the system under various steady-state and dynamic conditions, and have low complexity at the same time. In recent years, the vigorous development of artificial intelligence and deep learning has made data-driven fuel cell models more and more widely used. Gomathi [19] used the data set obtained by the empirical model to train the three networks on the simulation data and analyzed the prediction results of the dynamic network model in static and dynamic prediction scenarios, among which the performance of the NARX network was the best under all indicators. Francisco [20] used NARX to establish a black-box dynamic model of PEMFC and obtained a good predictive ability of fuel cell stack dynamic performance. Based on the modeling method of artificial neural network (ANN) and support vector machine (SVM), Han [21] established a fuel cell system model for underwater application scenarios. The results show that the ANN model is accurate in polarization curve prediction higher than that of the SVM model. Li [22] combined LSTM and ANN networks into a new type of neural network LBF, in which the LSTM part is responsible for dynamic prediction, and the ANN network is responsible for steady-state prediction. Experiments have proved that it can provide good prediction performance in both steady-state and dynamic working conditions.

It can be found that from the input type of the neural network model, the existing fuel cell models based on neural networks are mainly divided into two categories. One is BPNN which only considers the current input, and this type of model have good prediction performance under static working conditions such as the prediction of polarization curve, etc., but the prediction error of the model is relatively large under dynamic working conditions. The other type is the regression neural network and its variants that consider the historical fuel cell voltage information, and this type of model often fits well under dynamic and steady-state conditions. However, in the citation mentioned above, most

of the regression neural network models are running in the open-loop mode. In other words, the historical voltage sequence input of the model is the actual voltage sequence rather than the simulated voltage sequence, and the regression neural network model is only performing a single-step forecast. In the HIL application scenario, because there is no measured data, the model has to run in closed-loop mode, that is, the historical voltage sequence of the model input is the historical output of the model itself.

To obtain a fuel cell system dynamic model which is usable in the hardware-in-the-loop test application scenario, the following work was carried out in this paper. In the second part, the test sequences are designed considering the allowable range of load change rules, and the system dynamic condition experiments are carried out on a vehicular fuel cell system to obtain a test dataset. In the third part, based on nonlinear autoregressive with exogenous input (NARX) neuron network in closed-loop mode while mean square error (MSE) and mean absolute error (MAE) are selected as the predictive performance indexes of the model, the influence of training options and hyperparameters on model performance is discussed. In the fourth part, the simulation accuracy of the trained neural network model is verified by using the verification data set from the test data set.

2 Experimental Setup

As mentioned above, the experiment in this paper is based on a vehicular PEMFC system with a rated power of 80 kW, and its schematic diagram and actual photo are shown in Fig. 1. The PEMFC system includes a fuel cell stack, a hydrogen supply subsystem, an oxygen supply subsystem, and a cooling subsystem. The stack is the core component of the system which is made by AT&M. It can convert chemical energy from the reaction of hydrogen and oxygen into electrical energy. The hydrogen supply subsystem and the oxygen supply subsystem respectively provide a certain amount of hydrogen and oxygen to the stack for reaction, and at the same time keep the cathode and anode of the stack within a certain humidity range, and the cooling subsystem takes away the waste heat generated during the reaction. The control of the system is in charge of the fuel cell controller (FCU) attached to the system which runs in the automatic mode. When the output power of the system changes, the controller is responsible for scheduling the operation status of each subsystem in the system to ensure the operation of the stack is under conditions recommended by the manufacturer. The system is equipped with a fuel cell stack which has 238 cells, with a single active area of 330 cm^2 and a rated operating current density of 2 A/cm^2 .

When the system is running in the automatic mode, under the control of the FCU, it will run at a limited number of operating points with constant output current to generate constant output power. The minimum operating current density is 0.2 A/cm^2 and the maximum is 2 A/cm^2 , and the operating point is set every 0.2 A/cm^2 . As the vehicle's power demand varies, the fuel cell system switches between these operating points to match the vehicle's power demand. The operating conditions and voltage response of the fuel cell system are shown in Fig. 2a, b.

As the figure shows that, the test conditions are divided into two sections. The first section will be used as the training data set of the neural network model. The training

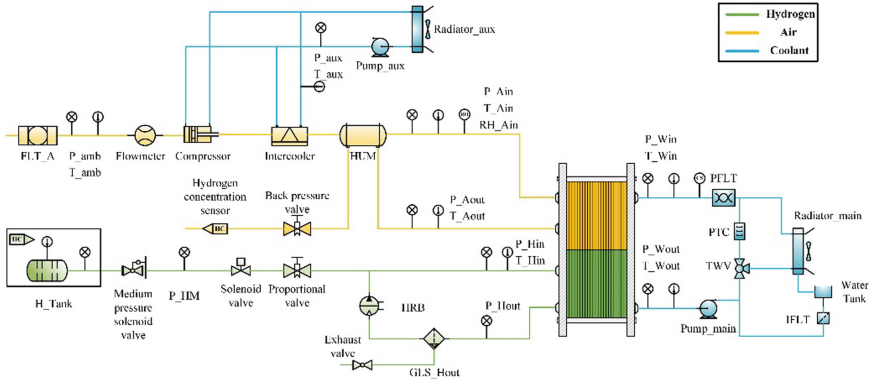


Fig. 1. Fuel cell system schematic

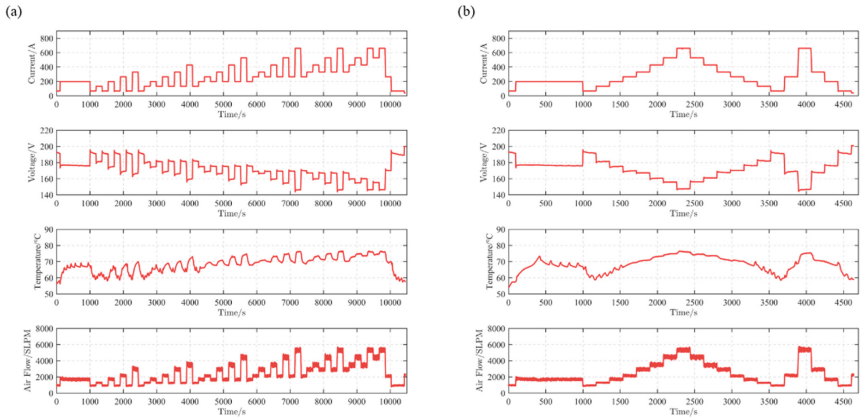


Fig. 2. PEMFC system operation dataset for training (a) and verification (b) purpose

conditions include all possible situations of load changes during operation within the system’s allowable load change rules as follows:

$$\Delta I \leq 50\% \times I_{Rated} \tag{1}$$

where ΔI is the change in operating current, I_{Rated} is the rated operating current density. The second dataset will be used as the verification dataset of the neural network model. The working conditions of the system during the experiment are shown in Table 1. During the test, the CAN recorder was used to record the data on the CAN bus at a frequency of 10 Hz. The collected data include stack voltage, stack current, stack temperature, stack anode gas pressure, stack anode gas temperature, stack cathode gas pressure, stack cathode gas temperature, and stack cathode gas flow. The entries and specifications of the sensors and data acquisition equipment used to collect data are listed in Table 2.

Table 1. The working conditions of the system during the experiment

| Name | Min. value | Max. value |
|----------------------------|------------|------------|
| Output Current (A) | 0 | 661.11 |
| Output Voltage (V) | 143.75 | 237.98 |
| Stack's Temperature (°C) | 56.11 | 76.59 |
| Pressure of Hydrogen (kPa) | 128.26 | 251.38 |
| Pressure of Air (kPa) | 101.24 | 197.21 |
| Temperature of Air (°C) | 51.98 | 72.38 |
| Flow Rate of Air (SLPM) | 0 | 5698 |

Table 2. Specifications of the sensors and data acquisition equipment

| Name | Model | Description |
|--|------------------|---|
| DC/DC converter | FRF140-27D1803BW | Controlling the fuel cell stack's output current, measure the output current and voltage of the stack |
| Temperature and pressure integrated sensor (Gas) | 30CP42-06 | Measure the temperature and pressure of gas in the anode and cathode |
| Temperature and pressure integrated sensor (Coolant) | 31CP02-05-ENV | Measure the temperature of coolant in the stack |
| Air flowmeter | MFM281006270 | Measure the flow rate of air in the cathode |
| Data recorder | INQ-1000 | Acquisition of all the data in can bus at a sampling rate of 10 Hz |

3 Neural Network Based PEMFC Dynamic Model Architecture

3.1 Model Implementation

The NARX network is a shallow recurrent neural network that can be used for modeling nonlinear dynamic systems. The input of the neural network consists of two parts, one is the historical sequence of external conditions, and the other is the historical sequence of the output of the modeling object. Its hidden layer is usually a fully connected layer. The structure of NARX is shown in Fig. 3a, where $u(n)$ represents the historical sequence of external conditions, in this paper, it represents the operating parameters of the system. While $y(n)$ represents the historical sequence of the output of the modeling object itself, in this paper, it represents the stack output voltage. Z^{-1} represents a time-delayed operation, the order of the model defined here is the number of input delays.

As shown in Fig. 3b, c, the NARX model has two operating modes. When the output of the real system is available, the historical sequence of the system output in the model

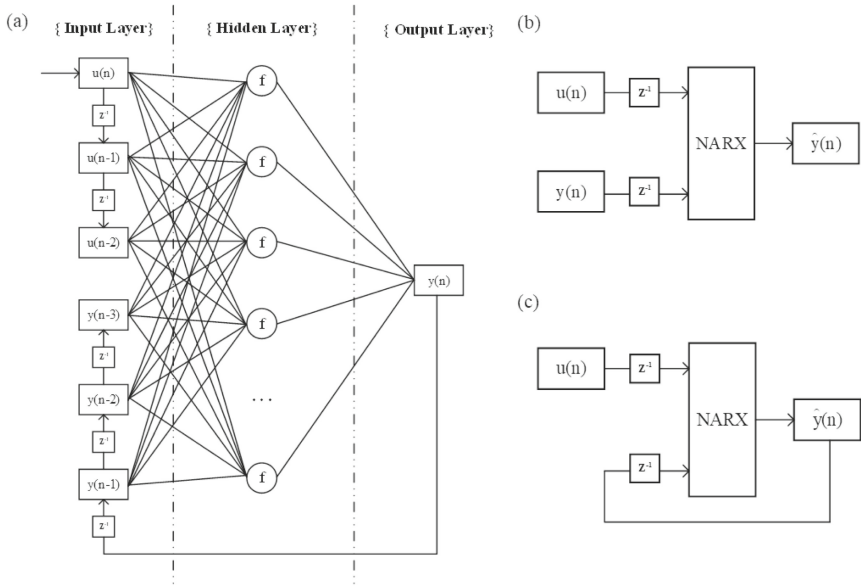


Fig. 3. (a) Overall structure of NARX, (b) open-loop mode of NARX, (c) closed-loop mode of NARX

input comes from the output of the real system. This operating mode is called the open-loop mode. If the output of the real system is not available, and the historical sequence of system output in the input of the model comes from the prediction of the neural network. This operating mode is called the closed-loop mode. The NARX model running in the open-loop mode has been widely used in the field of real-time control of the system, and it can realize the short-term behavior prediction of the dynamic system with algorithms such as Kalman filtering. In this paper, during the training process of the neural network model, the real output is available, and the serial-parallel architecture is used to complete the training of the network. In the process of model verification and use, since the model is oriented to the HIL application scenario, the real output is no longer available, the closed-loop mode of NARX is selected.

3.2 Network Training Options and Hyperparameters Optimization

To better evaluate the performance of the model and make a horizontal comparison between the performance of trained models, this paper uses MSE and MAE as performance indicators. The formulas are as follows:

$$MSE = \frac{1}{n} \sum_{i=1}^n (y_i - \hat{y}_i)^2 \tag{2}$$

$$MAE = \frac{1}{n} \sum_{i=1}^n |\hat{y}_i - y_i| \tag{3}$$

where y_i is the actual value, \hat{y}_i is the model predicted value and n is the number of sampling point in the data set. The smaller the value of MSE and MAE, the better the prediction performance of the neural network model. Since the initial value of the network training is random, to ensure the credibility of the conclusion of the paper, all the training examples in this paper will be repeated at least 5 times, and the performance of the model under the verification data set will be calculated, after removing the outliers, the average value will be taken as final results.

First of all, all the neural network models in this paper are trained on Matlab R2023a, which runs on a personal computer with Windows 11 22H2 operating system. In the Matlab neural network toolbox, the most widely used neural network training algorithms are Levenberg-Marquardt backpropagation (L-M), bayesian regularization backpropagation (Bayesian) and scaled conjugate gradient backpropagation (SCG). Among them, the L-M backpropagation algorithm is a combination of the Gauss-Newton algorithm and the steepest descent method, which can train any network as long as its weight, net input and transfer function have derivative functions. Bayesian regularization algorithm is a machine learning algorithm based on the bayesian probability framework. Bayesian regularization minimizes a linear combination of squared errors and weights. It also modifies the linear combination so that at the end of training the resulting network has good generalization qualities. Scaled conjugate gradient backpropagation updates weights and bias values according to the scaled conjugate gradient method, which uses less RAM during training. To determine the algorithm used in training, firstly, the other options are set as the default state (training epochs 200, model order 2, hidden layer size 8), only change the training algorithm, and train the network with the training data set and compare the neural network model's performance with the validation dataset.

As shown in Fig. 4a, it can be seen intuitively that the model trained by the scaled conjugate gradient backpropagation algorithm has the smallest MSE in the verification data set, which means the model's prediction performance is the best. Therefore, this paper will mainly use the SCG algorithm for training. The maximum training epochs of the neural network can also be the learning time of the neural network. Within a certain range of training epochs, increasing the number of training epochs can improve the generalization ability of the neural network. However, over-fitting often occurs during the training of neural networks, that is, as the training epoch increases, the model performance in the training dataset gradually decreases, but the model performance in the verification dataset which is not contained in the training dataset gradually increases. As shown in Fig. 4b, as the number of training increases, the performance of the model on the training dataset is gradually increased. The performance of the model on the verification dataset does not increase monotonically with the number of training, but decreases after exceeding a certain epoch of training. After the training epoch is greater than 200, the performance of the model on the verification dataset drops significantly, and its performance index is not in the same order of magnitude as its performance index on the training dataset. Therefore, it can be considered that after the number of training times is greater than 200, overfitting occurs. Thus, this paper sets the number of training sessions at 200.

After the training algorithm and training are determined, the number of neurons in the hidden layer and the order of the model will be determined next. The determination

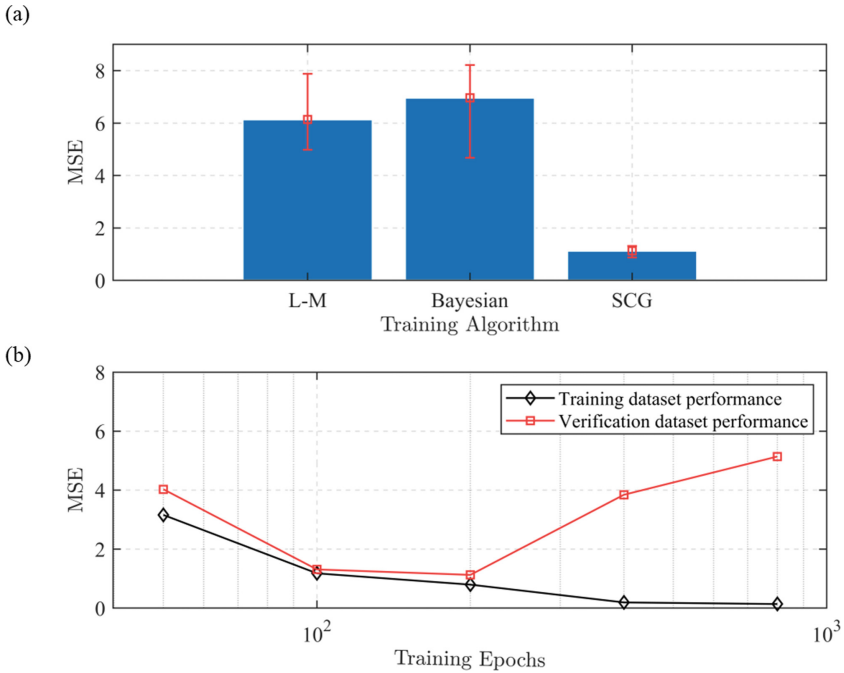


Fig. 4. Training algorithm comparison (a) and training epochs optimization (b)

of the number of neurons has always been a relatively complicated problem, which is often obtained through multiple adjustments based on the experience of the designer. If the number of neurons is too small, it cannot fit the high-complexity model object with a large degree of nonlinearity. Too many neurons in the hidden layer will also prolong the training time of the network, and the accuracy of the trained model will also decrease due to overfitting. For comprehensive consideration, the following empirical formula was proposed:

$$n_{hidden} = \sqrt{n + m} + a \quad (4)$$

where n and m are the numbers of neurons in the input layer and the number of neurons in the output layer, respectively. a is a constant number whose value range is 0 to 10. n_{hidden} is the number of neurons in the hidden layer. To determine the optimal number of neurons in the hidden layer, the order of the model was set as 2 at first. Then the number of neurons in the hidden layer was set from 4 to 10. After training, the performance of the model on the verification dataset was calculated.

Results are shown in Fig. 5a, When the number of neurons in the hidden layer is 7, the model is optimal. As mentioned above, the order of the model is the number of delayed samples in the input layer. The higher the order of the model, the more historical information it retains, but the complexity of the model increases proportionally, and it will take up more time and computing resources in the training and application stages. The order of the model is set from 1 to 7 for training. Results are shown in Fig. 5b, when the model's order is 3, the model is optimal.

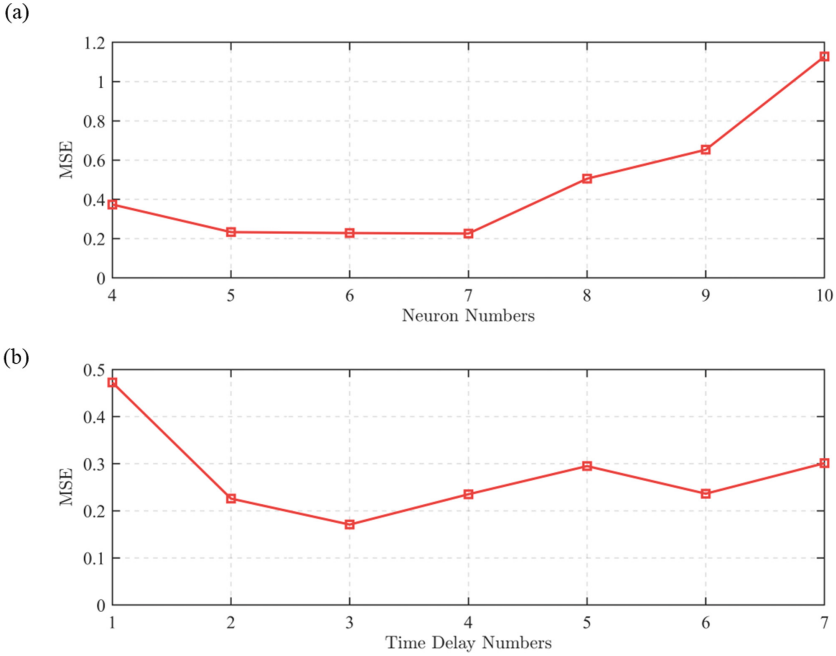


Fig. 5. Numbers of neurons in the hidden layer optimization (a) and time delay numbers optimization (b)

4 Model Verification and Analysis

After determining the training options and network hyperparameters mentioned above, the network was trained multiple times based on this configuration, and used the verification dataset to calculate the prediction performance of the trained model. The voltage forecast curve and the error of the close-loop NARX-based fuel cell system dynamic model are shown in Fig. 6a, b, respectively. It can be seen from the figure that the predicted voltage value of the model is in good agreement with the real voltage value, the maximum absolute error is less than 3V, and the maximum relative error is less than 1.43%. The MSE and MAE of the model under the validation dataset are 0.1809 and 0.3388, respectively. Its voltage prediction performance fully meets the hardware-in-the-loop platform’s requirements of model accuracy and can support the development of fuel cell system dynamic control strategies.

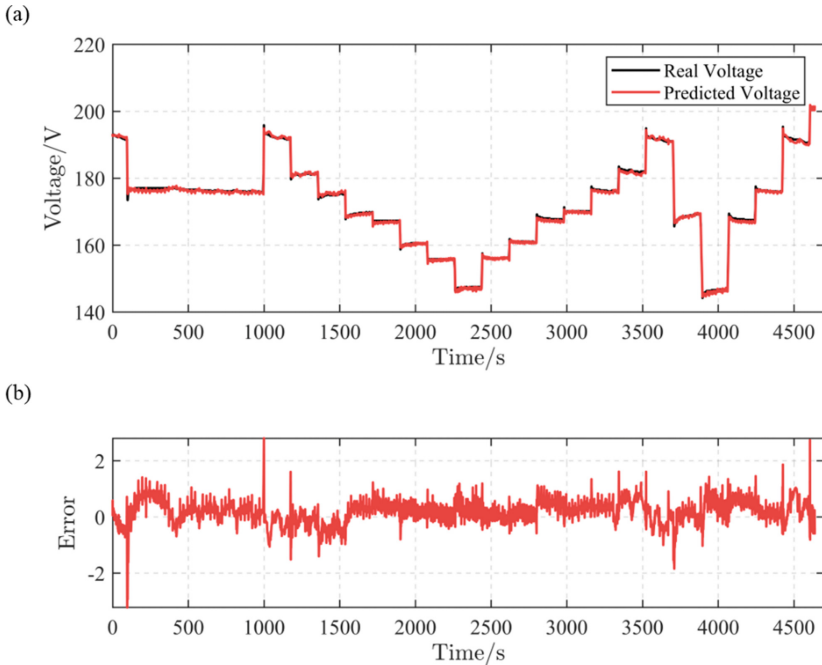


Fig. 6. Prediction results of Closed-Loop NARX-based fuel cell system dynamic model (a) and its error (b)

5 Conclusion

Based on the NARX neural network running in closed-loop mode, this paper constructs a dynamic model of a fuel cell system oriented to the requirements of hardware-in-the-loop applications. Firstly, the training and verification sequences of the dynamic model of the fuel cell system are designed, in which the training sequence included all possible situations of variable load, and is tested on a vehicular PEMFC system with a rated power of 80 kW to obtain the training dataset and verification dataset. Then, the influence of the training algorithm and the training epoch is discussed. Based on the above results, the influence of the number of neurons in the hidden layer and the order of the model on the prediction performance of the model is further explored. After determining the optimal training options and several hyperparameters of the model, the training dataset was used to train the model, and the prediction performance of the model was verified on the verification dataset. The MSE and MAE of the model under the validation dataset are 0.1809 and 0.3388, respectively. Its voltage prediction performance fully meets the hardware-in-the-loop platform's requirements of model accuracy. In future work, testing under different environmental conditions can be done to further improve the generality of the model.

References

1. Li, X., Raorane, C.J., Xia, C., Wu, Y., Tran, T.K.N., Khademi, T.: Latest approaches on green hydrogen as a potential source of renewable energy towards sustainable energy: spotlighting of recent innovations, challenges, and future insights. *Fuel* **334**, 126684 (2023). <https://doi.org/10.1016/j.fuel.2022.126684>
2. Falcone, P.M., Hiete, M., Sapio, A.: Hydrogen economy and sustainable development goals: Review and policy insights. *Curr. Opin. Green Sustain. Chem.* **31**, 100506 (2021). <https://doi.org/10.1016/j.cogsc.2021.100506>
3. Mohideen, M.M., Subramanian, B., Sun, J., Ge, J., Guo, H., Radhamani, A.V., et al.: Techno-economic analysis of different shades of renewable and non-renewable energy-based hydrogen for fuel cell electric vehicles. *Renew. Sustain. Energy Rev.* **174**, 113153 (2023). <https://doi.org/10.1016/j.rser.2023.113153>
4. Lin, R., Li, B., Hou, Y.P., Ma, J.M.: Investigation of dynamic driving cycle effect on performance degradation and micro-structure change of PEM fuel cell. *Int. J. Hydrogen Energy* **34**, 2369–2376 (2009). <https://doi.org/10.1016/j.ijhydene.2008.10.054>
5. Derbeli, M., Charaabi, A., Barambones, O., Napole, C.: High-performance tracking for proton exchange membrane fuel cell system PEMFC using model predictive control. *Mathematics* **9**, 1158 (2021). <https://doi.org/10.3390/math9111158>
6. Yang, B., Li, J., Li, Y., Guo, Z., Zeng, K., Shu, H., et al.: A critical survey of proton exchange membrane fuel cell system control: Summaries, advances, and perspectives. *Int. J. Hydrogen Energy* **47**, 9986–10020 (2022). <https://doi.org/10.1016/j.ijhydene.2022.01.065>
7. Moore, R.M., Hauer, K.H., Randolph, G., Virji, M.: Fuel cell hardware-in-loop. *J. Power. Sources* **162**, 302–308 (2006). <https://doi.org/10.1016/j.jpowsour.2006.06.066>
8. Mihalič, F., Truntič, M., Hren, A.: Hardware-in-the-loop simulations: a historical overview of engineering challenges. *Electronics* **11**, 2462 (2022). <https://doi.org/10.3390/electronics11152462>
9. Brayonov, N., Stoyanova, A.: Review of hardware-in-the-loop a hundred years progress in the pseudo-real testing
10. Larminie, J., Dicks, A.: *Fuel Cell Systems Explained*, 2nd edn., Vol. 28 (2013). <https://doi.org/10.1002/9781118878330>
11. Pasricha, S., Shaw, S.R.: A Dynamic PEM Fuel Cell Model. *IEEE Trans. Energy Convers.* **21**, 484–490 (2006). <https://doi.org/10.1109/TEC.2005.860402>
12. Gong, Z., Wang, B., Wu, K., Miao, T., Yang, K., Zhai, S., et al.: A 1 + 1-D multiphase proton exchange membrane fuel cell model for real-time simulation. *IEEE Trans. Transp. Electrific.* **8**, 2928–2944 (2022). <https://doi.org/10.1109/TTE.2021.3115794>
13. Hasegawa, S., Kimata, M., Ikogi, Y., Kageyama, M., Kawase, M., Kim, S.: Modeling of fuel cell stack for high-speed computation and implementation to integrated system model. *ECS Trans.* **104**, 3–26 (2021). <https://doi.org/10.1149/10408.0003ecst>
14. Vath, A., Lemš, Z., Mäncher, H., Söhn, M., Nicoloso, N., Hartkopf, T.: Dynamic modelling and hardware-in-the-loop testing of PEMFC. *J. Power. Sources* **157**, 816–827 (2006). <https://doi.org/10.1016/j.jpowsour.2006.02.102>
15. Xi, C., Qian, W., Peipei, P., Junhui, C., Yajie, Y.: Output characteristics simulation analysis of PEMFC. In: 2020 IEEE 3rd International Conference on Automation, Electronics and Electrical Engineering (AUTEEE), pp. 253–258. IEEE, Shenyang, China (2020). <https://doi.org/10.1109/AUTEEE50969.2020.9315571>
16. Zhao, J., Li, S., Tu, Z.: Development of practical empirically and statistically-based equations for predicting the temperature characteristics of PEMFC applied in the CCHP system. *Int. J. Hydrogen Energy* (2023). <https://doi.org/10.1016/j.ijhydene.2022.12.180>

17. Saleh, I.M.M., Ali, R., Zhang, H.: Simplified mathematical model of proton exchange membrane fuel cell based on horizon fuel cell stack. *J. Mod. Power Syst. Clean Energy* **4**, 668–679 (2016). <https://doi.org/10.1007/s40565-016-0196-5>
18. Atlam, Ö., DüNDAR, G.: A practical equivalent electrical circuit model for proton exchange membrane fuel cell (PEMFC) systems. *Int. J. Hydrogen Energy* **46**, 13230–13239 (2021). <https://doi.org/10.1016/j.ijhydene.2021.01.108>
19. Gomathi, K., Karthik, M., Usha, S.: An intelligent parametric modeling and identification of a 5 kW Ballard PEM fuel cell system based on dynamic recurrent networks with delayed context units. *Int. J. Hydrogen Energy* **46**, 15912–15927 (2021). <https://doi.org/10.1016/j.ijhydene.2021.02.065>
20. da Costa, L.F., Watanabe, E.H., Rolim, L.G.B.: A control-oriented model of a PEM fuel cell stack based on NARX and NOE neural networks. *IEEE Trans. Ind. Electron.* **62**, 5155–5163 (2015). <https://doi.org/10.1109/TIE.2015.2412519>
21. Han, I.-S., Chung, C.-B.: Performance prediction and analysis of a PEM fuel cell operating on pure oxygen using data-driven models: a comparison of artificial neural network and support vector machine. *Int. J. Hydrogen Energy* **41**, 10202–10211 (2016). <https://doi.org/10.1016/j.ijhydene.2016.04.247>
22. Li, W., Wang, X., Wang, L., Jia, L., Song, R., Fu, Z., et al.: An LSTM and ANN fusion dynamic model of a PEM Fuel Cell. *IEEE Trans. Ind. Inform.* 1–9 (2022). <https://doi.org/10.1109/TII.2022.3196621>
23. Ma, T., Liang, Y., Cong, M., Yao, N., Wang, K.: Remaining Useful Life Prediction Based on LSTM with Peephole for PEMFC, pp. 2022–01–7037 (2022). <https://doi.org/10.4271/2022-01-7037>



Hydrogen Energy Application in Rail Transit Under the “Double Carbon” Strategy: The State of the Art and Prospects

Liang Jianying^(✉)

National Innovation Center of High Speed Train, Qingdao 610000, China
sf_liangjianying@163.com

Abstract. Under the background of the goal of “carbon peaking and carbon neutrality”, the demand for green rail transit is urgent, and there is huge market space for hydrogen energy to replace traditional energy in rail transit. In the stage where hydrogen energy rail transit applications are advancing towards multiple scenarios and commercial operations, cost and lifetime issues still limit the widespread use of fuel cells. Therefore, this paper analyzes the key technologies of hydrogen fuel cells in rail transit applications, focusing on the research status and problems of prognostics and health management (PHM) of proton exchange membrane fuel cell (PEMFC) for rail transit and energy management strategies (EMS) of fuel cell hybrid systems for rail transit. Finally, based on the future development of hydrogen rail transit, the development of fuel cell technology was analyzed and prospected.

Keywords: Hydrogen energy · Rail transit · Multi-stack fuel cells · Prognostics and health monitoring · Energy management strategy

1 Introduction

With the continuously rapid development of China’s economy and society, China’s total energy consumption has jumped to the top in the world, and issues such as energy security, carbon emissions, and environmental pollution are becoming increasingly prominent. As a major energy consumer in China, the transportation sector has a total carbon emissions of approximately 1.1 billion tons in 2021, accounting for 10% of the total social emissions [1]. Therefore, it is urgent to accelerate the construction of a low-carbon transportation system to achieve the strategic goal of carbon neutrality.

The power system of hydrogen energy fuel cells has been applied to rail vehicles, breaking away from the power supply system of the catenary along the line, significantly reducing construction investment, and having advantages such as high efficiency, pollution-free, and low noise [2]. With the application of the world’s first commercially operated hydrogen energy tram demonstration line with a maximum speed of 70 km/h developed by CRRC Qingdao Sifang Locomotive and Rolling Stock Co., Ltd. in Gaoming, Foshan, China,, fuel cell trams have been commercialized, and their operating life

and safety have been recognized by the market [3]. In other applications, the Coradia iLint, a hydrogen fuel cell suburban commuter train developed by Alstom in France with a maximum speed of 140 km/h, was put into commercial operation in Germany, proving that it has a good application prospect in the field of suburban transportation to replace internal combustion engines [4]. In 2022, the world's first hydrogen energy urban train jointly developed by CRRC CHANGCHUN RAILWAY VEHICLES CO., LTD and Chengdu Rail Transit Group officially rolled off the line in Chengdu, Sichuan, with a maximum speed of 160 km/h [5]. In 2023, Beijing Infrastructure Investment Co., LTD released the first urban hydrogen energy articulated light rail car independently developed in China with a speed of 200 km/h. In January 2021, the hydrogen energy hybrid shunting locomotive developed by CRRC DATONG CO.,LTD. rolled off the production line, using a hybrid system of "hydrogen fuel cell + lithium titanate battery" with a vehicle power of 700 kW. Since then, the hydrogen energy hybrid shunting locomotive developed by CRRC Qishuyan Institute CO., LTD. has rolled off the production line, equipped with a 400 kW hydrogen fuel cell system a whole vehicle power of 1400 kW, and a design speed of 100 km/h. In freight locomotive research field, Canadian Pacific Railway company began a transformation study of hydrogen fuel cell freight locomotives in 2020. According to the "2021 Railway Statistical Bulletin" [6], China maintained 21,000 locomotives, including 74,000 diesel locomotives, 2800 DC electric locomotives and 10,200 AC electric locomotives. Considering the future low-carbon transformation projects of transportation in border countries and other overseas markets along the "One Road, One Belt", there is huge space for hydrogen rail transit alternative markets.

Different from the system for automobile, the special features of fuel cells used in rail transit are: (1) The bus voltage level of the power supply system is higher, generally 750, 1200, 1500 and 1800 V [7]; (2) The load fluctuation greater, with a second-level fluctuation range of several megawatts or even tens of megawatts [8]; (3) The demand power larger, with a larger power of the fuel cell system of usually hundreds of kilowatts or even several megawatts [9]. Therefore, the main problems and countermeasures faced by the application of fuel cell systems in the field of rail transit are as follows:

- (1) The single-stack fuel cell system (SFCS) has low and limited output power, which is difficult to meet the needs of rail transit. To solve this problem, rail transit fuel cell has to require the use of a multi-stack system to meet the power requirements of rail vehicles [10].
- (2) Due to the characteristics of the dynamic performance, lifetime and efficiency, the fuel cell system needs to be combined with the energy storage power supply to form a hybrid system in rail transit [11]. The hydrogen fuel cell system provides the energy required for the operation of rail vehicles. Meanwhile, the energy storage responds to train power fluctuations, and absorbs train regenerative braking energy, thereby reducing the degradation rate of fuel cell stacks.

However, cost and lifetime issues still limit the widespread use of fuel cells [12]. Therefore, in order to further improve the adaptability of hydrogen energy in rail transit applications, this paper provides an overview of the key technologies for improving system service life, reducing fuel cell system operation and maintenance costs, with a focus on the prognostics and health monitoring (PHM) key technologies for proton exchange membrane fuel cells, as well as the research status and problems faced by

Energy management strategies (EMS) for hybrid power systems used in rail transit. Finally, the development and application of hydrogen energy in the rail transit field is analyzed and prospected, in order to provide a certain reference for future hydrogen rail transit technology and engineering.

2 Prognostic and Health Monitoring of PEMFC for Rail Transit

The prognostic and health monitoring of PEMFC for rail transit is the key technology to ensure the safe and stable operation of hydrogen fuel cell trains, and the main process includes three stages: monitoring, analysis, and decision-making [13], as shown in Fig. 1 [14]. In the monitoring stage, the health status of PEMFC is judged by acquiring and processing useful sensor data and combining diagnostic and prognostics methods. Finally, in the decision-making phase, the corresponding maintenance measures are taken to improve the reliability and durability of the system.

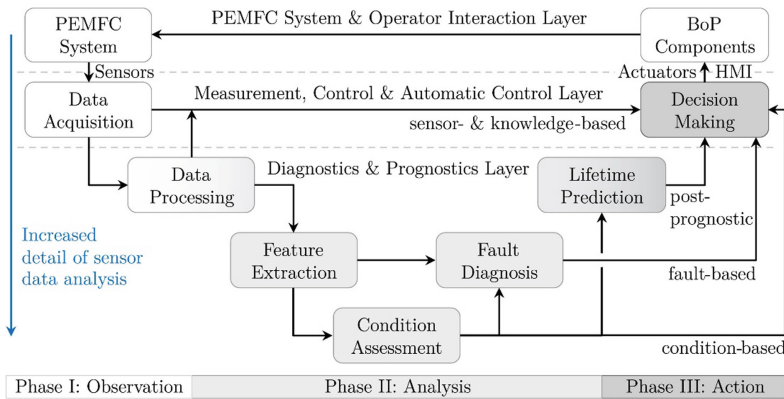


Fig. 1. Prognostic and health monitoring scheme.

The fuel cell systems for rail transit vehicles need to operate in a multi-stack mode to meet the high-power needs of the rail vehicles. The electrical architectures, reaction gas architectures and cooling system architectures of multi-stack fuel cell system (MFCS) are more complex than single-stack fuel cell system (SFCS), which adds a lot of difficulties to the implementation of PHM. To this end, this section first reviews the structure of MFCS, and then review the PHM method for health management of hydrogen fuel cell from the perspectives of fault diagnosis, prognostics, and post-prognosis of decision-making.

2.1 Multi-stack Fuel Cell Architecture

Electrical architecture. The electrical structure of MFCS can be divided into two types: electrical structure without converters and electrical architectures with converters [15]. In order to adapt to rail transit applications and improve the reliability, MFCS are often

configured based on the electrical architectures with converters, as shown in Fig. 2 [15], and can be subdivided into series, parallel, cascade and hybrid structures.

In a series configuration of Fig. 2a, the fuel cell is connected in series to the DC bus through a DC/DC converter. Compared with the series connection without converters, it can achieve more flexible power switching and voltage control. But when one of the fuel cells does not work, the overall performance of the system will be affected, and the reliability will be lower. To meet the reliability requirements of rail transit, parallel configuration such as Fig. 2b are often used. By connecting each fuel cell unit to the DC bus using a DC/DC converter, the fuel cell system can be started and stopped independently [16]. In the case of redundant output power, the fault tolerance of the system is improved. However, due to the low voltage and high current characteristics of fuel cell, DC/DC converters in parallel structure need a high voltage ratio, while the switching device needs to withstand a large current. To reduce the voltage ratio of DC/DC converter and the cost of fuel cell system, the cascade structure of Fig. 2c can be used, where the series connected stack are connected to the DC voltage bus through a power converter. Through the series structure, the overall input voltage is increased, thereby the switching pressure of the power converter is reduced [17]. Figure 2d shows a hybrid structure that optimizes system efficiency and reduces power conversion devices by mixing series and parallel structures with the benefits of both series and parallel structures[18].

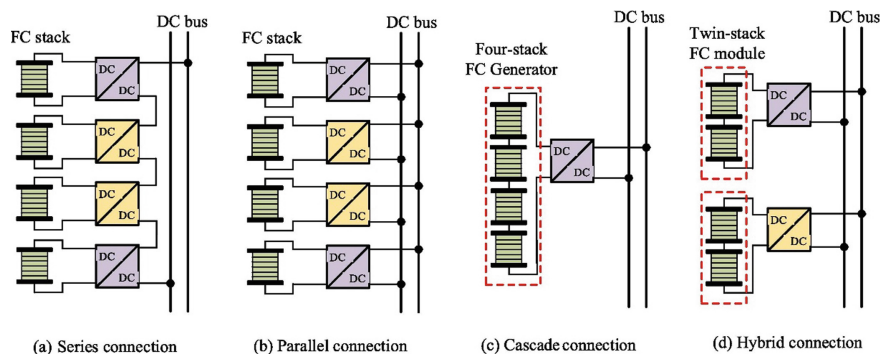


Fig. 2. The electrical architectures with converters

In the electrical architectures with converters, the reliability of Fig. 2a, c is relatively low. Figure 2b, d are more suitable for rail applications. On the one hand, rail transit must output high power with a higher bus voltage, and requires the system to have high reliability, so the parallel structure has a wide range of applications. On the other hand, the higher boost ratio and large current stress have high requirements for DC/DC converter technology, considering the cost and system efficiency, the hybrid structure of Fig. 2d is the best choice for rail transit.

Gas supply architecture. The gas supply architecture consists of air supply system and hydrogen supply system, providing stable reactants for each stack, respectively, and its

structure is shown in Fig. 3, including series, parallel and improved series configuration [14].

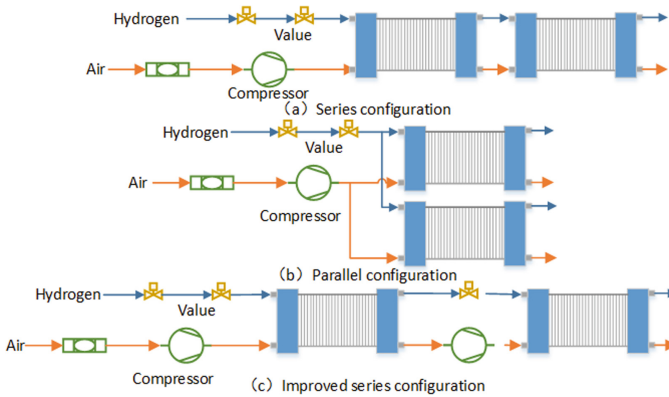


Fig. 3. Gas supply architecture of MFCS

The series gas supply configuration enables the supply of reactants to both stacks by installing a set of air compressor units and hydrogen control devices on the first stack at the far left, as shown in Fig. 3a. To overcome the pressure difference of the reaction gas after passing through the stack, a stronger pressure needs to be applied upstream [19]. Therefore, under the series gas supply configuration, the power consumption of the air compressor will increase. Although the structure of this method is simple, the way the stack is connected in series will reduce the fault tolerance of the system. Figure 3b shows a parallel gas supply structure that supplies reaction gas to a parallel stack through the same gas supply device. In this structure, the inlet pressure between the stacks is the same. Figure 3c shows the improved gas supply configuration, which provides reactants for each stack through two independent gas supply methods, improving the fault-tolerant energy of the system and reducing the power consumption of the air compressor. However, the two sets of gas supply structure both increase the cost of the system.

In the gas supply architectures, the structure reliability of Fig. 3a is low, the structural system of Fig. 3c is costly, in contrast, the parallel structure of Fig. 3b is more suitable for rail transit applications. With the same fluid structure, when the currents are equal, the output voltage of the two stacks is equal, which can ensure the equilibrium between the MFCS.

Cooling system architectures. The cooling system is usually composed of cooling fans, heat exchanger, water pump, etc., as shown in Fig. 4, which can be divided into a series structure and a parallel structure [20].

The series structure is shown in Fig. 4a, where the coolant flows sequentially through each stack cooling channel while the temperature of the coolant gradually increases. To maintain the operating temperature of each stack, the temperature of the system needs to be controlled to rise the coolant temperature to a specific level. The parallel structure is shown in Fig. 4b, with coolant flowing through the cooling channels of each stack

simultaneously. Under this structure, the amount of heat dissipation depends on the operating conditions of the stack, and the flow control system that controls the coolant inlet of the stack is the key to system control. Due to the simple control and favorable fault detection, the parallel structure has been widely used.

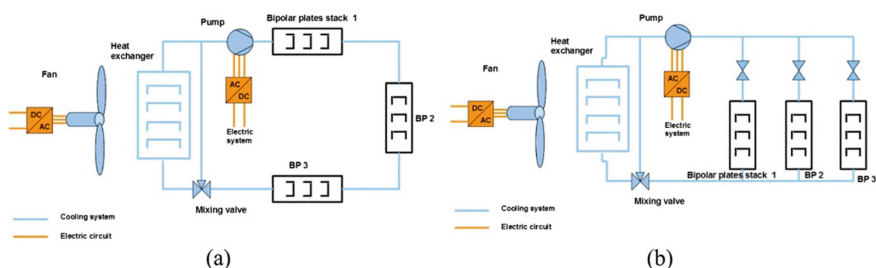


Fig. 4. Cooling system architectures of MFCS

The parallel structure of Fig. 4b is conducive to reduce the system voltage drop and improve the system efficiency. At the same time, it is convenient for independent control [21] to improve heat dissipation capacity, and ensure the balance between multiple reactors, which is widely used in the field of rail transit.

2.2 Prognostic and Health Monitoring

Because of the complexity of the MFCS structure, several parameters are highly correlated with each other, there is a high likelihood of failure, and control is much more challenging. Therefore, how to accurately and timely detect faults and predict life of MFCS is critical to improve the overall performance of the system [22].

Fault Diagnostic. Fuel cell systems often fail in practice, such as flooding and membrane dry failures, and these minor faults can cause a decrease in the output power or even system stop [23]. Severe faults can cause permanent damage to the stacks and even a hydrogen explosion. Therefore, reliable fault diagnosis technology is essential to ensure the safe and smooth operation of fuel cells [24].

Unlike SFCS, MFCS are more complex in terms of auxiliary system and stack structure. The most obvious difference between MFCS and SFCS is the interaction between the stacks. In the event of fuel starvation, current and voltage redistribution occurs within the stacks [25], and due to the electrical connection relationship between the stacks in the MFCS, the distribution of current and voltage will be limited by adjacent cells, which will affect the distribution process of current and voltage inside the fuel cell. At the same time, the interaction of operating temperature between the reactors will also increase the difficulty of fault diagnosis of centralized thermal management structures.

Aiming at the fault diagnosis research of MFCS, Lee et al. [26] proposed a hierarchical logic method to detect the faults. Considering the faults of various parts of the subsystem separately, such as whether there are reversible or irreversible faults in the stacks, where reversible faults include drying, flooding, insufficient reactants, etc. Auxiliary system faults need to be analyzed from the perspective of sensors, actuators, pipes,

or core components. Hu et al. [27] proposed a multi-point monitoring method to monitor fuel starvation faults in MFCS by observing specific voltages along the straight channel direction. Liu et al. [28] divided the faults of the fuel cell system for trams into four levels, of which the first-level alarm will reduce the output power of the fuel cell module and will not cause the system to stop, and the tram is still operating under traction. When a Level 1 alarm is not immediately detected and isolated, the system will enter a Level 2 (or Level 3) alarm. If the system is in a Level 2 (or Level 3) state, the digital output of the fuel cell module switches to a fault state. A discrete hidden Markov model based on K-means clustering was proposed to identify six types of faults that often occur in tram fuel cell systems with a fault identification rate of 94.17%. Zhang et al. [29] proposed the use of deep confidence network and information fusion method to identify the secondary fault of the PEMFC of tram. The back propagation neural network was applied to extract high-dimensional abstract features from the original data and reconstruct them into feature maps. Then, the deep convolutional neural network was used to classify the feature map with a fault identification rate of 98.48%.

Prognostic. Under steady conditions, the lifetime of fuel cell can reach more than 5000 h, while the life under dynamic conditions will be greatly shortened [30]. For rail transit applications, PEMFC mainly operates under dynamic cycle conditions. Under the working conditions of start-stop, idling, loading, and un-loading, fuel cells are prone to the faults such as fuel starvation and local hot spots, which accelerate the decay of PEMFC [31]. At the same time, the inconsistency of fuel cell performance at different positions of the stack will also affect the life of PEMFC, which is especially obvious in high-power MFCS. Prognostics research on PEMFC can better understand the degradation law of fuel cells, provide data support for the whole life cycle service management system, and make timely maintenance decisions on this basis, which can effectively extend the service life of PEMFC.

In the dynamic operation state, the uncertain change of load current will affect the evaluation of the health state of fuel cell, which brings great challenges to prognostics. Bressel et al. [32] analyzed the linear degradation law of the ultimate current and ohmic resistance of fuel cell, and predicted the life of the fuel cell under dynamic conditions based on the polarization curve equation and a kalman filter algorithm. Based on the linear parameter change model, Li et al. [33] extracted the virtual steady-state voltage from the profile of conventional dynamic working conditions to reflect the health state of the fuel cell, and proposed an integrated echo state network (ESN) method to predict the life of fuel cell. Hua et al. [13] calculated the relative power loss rate under different contour tasks based on the measured voltage and current data, combined with the initial polarization curve equation, and then proposed an ESN method with dual input structure to predict the life of fuel cells under dynamic working conditions.

In the study of MFCS, Chrétien et al. [34] predicted the lifetime of MFCS by assuming that the degradation rate of each stack is consistent. However, the degradation rate of each stack of MFCS in actual operation is often inconsistent. Lopse et al. [35] proposed a modeling methodology based on recurrent neural networks to perform prediction tasks for each stack in MFCS, but this method failed to take into account the interaction between each stack. Based on the particle filter algorithm, Liu et al. [36] proposed a collaborative life prediction method considering the current information between each

stack to predict the life of MFCS in combined heat and power applications. Compared with the life prediction task alone, the proposed method had higher prediction accuracy in MFCS application scenarios.

Post-prognostics of decision-making. The ultimate objective of PHM is not only to predict lifetime and identify failures, but more importantly, to take the necessary actions to extend the whole life cycle of fuel cells through the lifetime and fault information [37].

Yue et al. [37] discussed and prospected the research on post-prognostics of decision-making for fuel cell from four aspects: aging tolerance control, MFCS control, energy management and maintenance scheduling. Bressel et al. [38] introduced the time-varying parameters into the control model to consider the aging of fuel cells to realize the required PEMFC power adjustment in the case of performance degradation. Kong et al. [39] developed a control strategy based on interconnection and damping distribution-passivity to control the hybrid system composed of fuel cells and supercapacitors, estimated the degradation of fuel cells by filtering algorithms. The proposed method can ensure the normal operation of the system while avoiding overload. Li et al. [40] proposed a power adaptive allocation method considering the aging of fuel cells to ensure that the overall degradation performance of each stack gradually tends to be consistent during operation. Compared with the average power distribution method and chain power distribution method, the proposed strategy reduces the hydrogen consumption of MFCS by 13.59 and 8.04%, respectively. Based on the life prediction information of PEMFC, Jian et al. [41] proposed the load redivision criterion of decision probability to determine the optimal load division between the two stacks, and the simulation results showed that the system life result using the prognostic decision strategy was 2234 h, which was much higher than the 1029 h after no decision. Zuo et al. [42] took fuel battery life and hydrogen consumption as the goals in EMS, combined with the life prediction information of MFCS, to formulate a prognosis decision-making strategy.

3 Energy Management Strategy for Rail Transit Hydrogen Hybrid System

The EMS for hybrid system of hydrogen fuel cell train is one of the key contents of hybrid system research, and the core is to meet the power demand of rail vehicle operation by controlling the optimization of power and energy distribution between power sources, while reducing the energy consumption of the system, which has a significant impact on the power and economy of hybrid system. Existing hydrogen fuel cell train energy management strategies can be divided into two categories, namely rule-based and optimization-based strategies.

3.1 Rule-Based Control Strategy

Rule-based energy management method, according to the real-time power demand of the vehicle and the current state information of the hybrid system, set the threshold value and deterministic rules to adjust the power distribution and operating state switching of

the system. The disadvantage is that it is too dependent on engineering experience, and the effect is often affected by the accuracy of the model to ensure optimal performance. Rule-based energy management strategies can be divided into two kinds: deterministic rule and fuzzy logic rule.

Deterministic rule strategies. Deterministic rule strategies include power following, state machine control, switch control, etc. The power following strategy is to adjust the output power of the fuel cell and control the charging and discharging strategy of the battery based on the control of the state of the battery, so as to balance the SOC of the battery; The state machine control strategy determines the output power of each power supply according to the power demand of the load and the SOC of the battery.

Garcia et al. [45] proposed an energy management strategy based on operating mode for fuel cell/supercapacitor/power battery trams. Li et al. [46] divided the operating modes of the hybrid system according to the finite state machine theory, and then optimized the fuel cell operating point in each mode through the equivalent minimum consumption theory. Yan et al. [47] divided the running state of the train into four modes: traction, idle, braking and stopping, and solved the system power allocation with a goal of minimizing the equivalent hydrogen consumption in each state.

Fuzzy logic rule strategies. The fuzzy logic rule strategy is a nonlinear strategy in which the judgment condition is not a simple switch value, but a state like human thinking. The practice is to obfuscate the operation experience, form fuzzy rule statements, and then use fuzzy logical reasoning to process real-time input state observations, and finally output the judgment of logical reasoning. The strategies of fuzzy logic rules include traditional fuzzy logic control strategy, adaptive fuzzy control strategy and predictive fuzzy control strategy.

Considering the nonlinear and multivariate characteristics of the fuel cell hybrid system, Xiao et al. [48] aimed to save the energy consumption of high-power fuel cell locomotives and improve the durability of locomotives, and integrated fuzzy logic rules, adaptive compensation strategies and equivalent hydrogen consumption strategies, which surpassed the use of a single algorithm. Hong et al. [49] designed a fuzzy controller for a hybrid system composed of fuel cell, lithium battery and super capacitor, using the total demand power, the SOC of lithium battery and super capacitor as the input variable, and the expected output power of the hydrogen fuel cell as the output signal, and verified the control effect under different working conditions.

In general, rule-based energy management strategies rely on both the accuracy of rules and the accuracy of models, as well as engineering experience, and cannot guarantee optimal control. However, due to its small computational amount and high real-time performance, it has been widely used in the early stage of research.

3.2 Optimization-Based Strategy

The optimization-based strategy takes fuel economy, power, etc. as a cost function, and minimizes the cost function to obtain the optimal torque, gear ratio and power distribution. At present, optimization-based methods can be divided into instantaneous optimization strategy and global optimization strategy.

Real-time optimization strategy. Real-time optimization strategy includes the instantaneous equivalent hydrogen consumption minimization method based on convex optimization, quadratic programming and swarm intelligence algorithm, etc.

Torreglosa et al. [50] applied the equivalent minimal hydrogen consumption method to trams, which could reduce hydrogen consumption by about 14% compared to the finite state machine method. Han et al. [51] proposed a method to determine the optimal equivalent factor under a given working condition by dynamic programming method, and explored the change of equivalent factor under different working conditions. Aiming at the problem that the SOC equilibrium coefficient of the equivalent hydrogen consumption method is difficult to determine when the working conditions are unknown, Zhang et al. [52] proposed an equivalent hydrogen consumption energy management method based on the operation mode and dynamic mixing degree, which adjusted the equilibrium coefficient by dividing the vehicle operation mode and analyzing the relationship between the equilibrium coefficient and hydrogen consumption in each mode, and verified that the proposed method can effectively reduce hydrogen consumption and improve economy by comparing with the traditional equivalent hydrogen consumption method.

In addition, for multi-objective optimization problems, convex optimization, quadratic programming, and swarm intelligence algorithms can also be used to optimally solve them. Wang et al. [53] conducted research on the energy management problem of fuel cell locomotives based on the sequential quadratic programming algorithm, and the results showed that the global energy consumption level of the locomotive was reduced. Farouk et al. [54] comprehensively considered multiple optimization indicators such as hydrogen consumption and vehicle acceleration performance, and used genetic algorithms to solve multi-objective energy management problems.

Global optimization strategy. The global optimization strategy mainly includes dynamic programming and minimum principles, both of which are optimal control methods. The dynamic programming algorithm is based on Bellman's optimal principle, which can optimize the objective function in a limited time domain and meet certain initial and terminal state constraints, so in the energy management problem, the two main goals of energy efficiency improvement and SOC maintenance can be well balanced. The principle of minimum value constructs the Hamiltonian function by introducing the Lagrange multiplier, transforming the optimal control problem with constraints into an unconstrained problem, and then obtaining the optimal control law of the control variable by finding the extreme value of the Hamiltonian function.

Chen et al. [55] introduced the SOC penalty function and the fuel cell load change penalty function to form the objective function, and solved them by using the dynamic programming algorithm. For multi-source hybrid systems, multi-dimensional dynamic programming methods are required to solve energy management problems. Jiang et al. [56] used two-dimensional dynamic programming to study the power distribution problem of hybrid system containing fuel cells, super capacitor and battery, and proposed a joint optimization scheme for energy management and system parameter matching. Simmons et al. [57] showed that the initial value of the costate variable was closely related to the working condition by analyzing the situation of different working conditions. Although the principle of minimum has the same results as dynamic programming in theory, its control effect is often inferior to dynamic programming by more than 1%

due to various simplification and omitted factors. Wu et al. [58–60] constructed a mixed integer linear programming model to optimize the hydrogen consumption, the volume and cost of hydrogen storage devices, and verified the effectiveness of the model based on the actual line.

4 Conclusion and Prospect

This paper reviewed the latest research progress of PHM of PEMFC hybrid systems for rail transit. Firstly, the application characteristics and the existing methods of PHM technology were introduced from the perspectives of fault diagnosis, prognostics, and post-prognostics. Then, the research status of EMS of hybrid system of fuel cell in rail transit is analyzed from the perspectives of rule-based and optimization-based. In the stage of falling hydrogen prices and the development of fuel cell technology, the current speed of hydrogen energy trains has reached 200 km/h, and related research is being carried out towards a speed of 250 km/h. In the future, the speed less than 250 km/h's hydrogen passenger trains, freight locomotives and operation and maintenance vehicles will be widely used. In order to meet the challenges of hydrogen energy in high-speed rail transit applications, future fuel cell technology needs to strengthen research on:

- (1) **Multi-fault diagnosis under various conditions.** Currently, most existing fault diagnosis methods were fully designed and validated under laboratory conditions. In high-power application scenarios, some fault mechanisms of MFCS could be inconsistent with SFCS, such as flooding faults. For high-power system, the flooding faults can present inconsistencies in the impedance spectrum of monolithic cells, multiple cells, and even multiple stacks [43]. For MFCS, the probability of concurrent faults is higher due to the interaction between stacks, and the fault characteristics may affect each other, which greatly increases the complexity of fault diagnosis. Therefore, in practical engineering applications, it is necessary to develop more multi-fault real-time diagnosis strategies for MFCS.
- (2) **Convenient and efficient dynamic health indicators (HI).** The health state of PEMFC stack is particularly critical for the judgment of prognostic decision, but under dynamic working conditions, the monotonous downward trend of static HI is less obvious due to the uncertain changes in load current [44]. Although some dynamic HI have been proposed, more HI with low computational complexity should be developed, which can be applied online and adapted to all working states.
- (3) **Different prognostic methods for MFCS.** Currently, there are few durability experiments and data analysis for MFCS, and the degradation phenomenon and mechanism of MFCS and SFCS may differ. The problem of synergistic life of MFCS requires more experimental studies and proposes more complex aging models to predict the life of MFCS.
- (4) **More post-prognostic strategies.** Currently, prognostic decisions for MFCS mainly focus on adjusting the EMS of MFCS through prognostic outcomes, thus extending the overall lifespan of the system, but the overall studies are few. In the future, further attention should be paid to proposing prognostic decision methods such as aging fault-tolerant control, MFCS control, energy management and preventive maintenance.

- (5) **New energy management strategies based on optimization in actual rail transit.** At present, although many energy management strategies of fuel cell hybrid systems for rail transit are proposed, in practice, rule-based energy management strategies are still the main application, and some emerging strategies are still mainly based on theoretical research. Therefore, emerging strategies need to continue to develop from research to implementation.
- (6) **The layout and control of air supply system in high-speed application scenarios.** Studies have shown that when the train is moving at high speed, it will bring the following problems: (i) The pressure fluctuation between the train body and the atmospheric boundary especially when entering, passing through and exiting a tunnel at high speed [61]; (ii) Long distance driving may face high and low altitude or high and low temperature switching cycles [62]; (iii) Pressure fluctuations caused by trains passing in the same direction and in the opposite direction [63]. These have a great impact on the internal pressure and oxygen molecular distribution in the fuel cell stack, endangering the life and performance of the stack [64]. Therefore, it is necessary to analyze the pressure change of the train at high speed based on aerodynamics and finite element analysis, and further explore the position of the fuel cell system intake and exhaust ports and the structure scheme of the air supply system in the high-speed application scenario, as well as the control method for the multi-temporal and spatial scale of hydrogen/oxygen/water/heat system.
- (7) **High energy density hydrogen storage technology.** At present, the hydrogen storage technology commonly used in hydrogen energy rail transit vehicles are 35 MPa high-pressure hydrogen storage tanks [65]. With the increase of hydrogen energy rail transit vehicle speed and mileage, traditional hydrogen storage technology will inevitably increase the hydrogen storage tank volume and weight, which brings difficulties to the vehicle design. Hence, it is necessary to promote the development and utilization of high energy density hydrogen storage technology, including 70 MPa compression hydrogen storage, solid metal hydride hydrogen storage, low-temperature liquid hydrogen storage, high-pressure low-temperature liquid phase hydrogen storage and high-pressure low-temperature gas phase hydrogen storage and etc. [66], in order to better adapt to the current railway high-speed and heavy-load development trend.
- (8) **High-power fuel cell thermal management technology.** In the high-power application scenario in rail transit field, a large amount of heat needs to be brought out through the cooling system. In addition, at low ambient temperatures and cold-starts, the system needs to be heated by a heating facility to maintain a suitable reaction temperature [67]. Therefore, thermal management is a key technology that affects the performance of fuel cells, and it is also a difficult point in the development of high-power fuel cell technology. Phase change heat dissipation technology is a current research hotspot [68], which takes away the heat generated by the fuel cell system and accelerates the heat loss of the system by spraying water. However, there are still few studies on phase change heat dissipation technology for high-power fuel cells. Therefore, it is also necessary to carry out such related studies to ensure and improve the overall performance of the system.

References

1. Wei, L., Wan, Y., Xiong, Y., et al.: Outlook of low carbon and clean hydrogen in China under the goal of “carbon peak and neutrality.” *Energy Storage Sci. Technol.* **11**(2), 635–642 (2022)
2. Chen, W., Bu, Q., Liu, Z., et al.: Power system design for a fuel cell hybrid power tram. *J. Southwest Jiaotong Univ.* **29**(3), 430–436 (2016)
3. Fan, Y., Long, Y., Jiang, D., et al.: Overview of development status and key technologies of new energy hybrid electric locomotive. *Electr. Locomotives Mass Transit Veh.* **46**(1), 1–11 (2023)
4. Yang, Y., Chen, Z.: Study on the adaptability of hydrogen fuel cell tram. *Electr. Locomotives Mass Transit Veh.* **43**(2), 1–3 (2020)
5. Kang, J., Li, H., Ma, Y., et al.: Review on energy management strategy of hydrogen fuel cell trains. *Railway Rolling Stock* **61**(02), 1–9 (2023)
6. National Railway Administration: *Railway Statistics Bulletin 2021*. State Railway Administration, Beijing (2023)
7. Li, J., Liu, J., Tang, L.: Study on the application of hydrogen energy in the field of rail transit. *Rail Transp. Equip. Technol.* **1**, 25–27+32 (2023)
8. Han, Y., Li, Q., Wang, T., et al.: Multisource coordination energy management strategy based on SOC consensus for a PEMFC-battery-supercapacitor hybrid tramway. *IEEE Trans. Veh. Technol.* **67**(1), 296–305 (2018)
9. Danushka, M., Stuart, H., Clive, R., et al.: Analysis of a fuel cell hybrid commuter railway vehicle. *J. Power Sour.* **195**(23), 7829–7837 (2010)
10. Chen, W., Zhu, Y., Li, Q., et al.: Review and prospect of structures, control and detection schemes of multi-stack fuel cell power generation system used in rail traffic. *Proc. CSEE* **38**(23), 6967–6980 (2018)
11. Sun, Y., Anwar, M., Hassan, N.M.S., et al.: A review of hydrogen technologies and engineering solutions for railway vehicle design and operations. *Railway Eng. Sci.* **29**, 212–232 (2021)
12. Choi, R.C., Lim, M., Dong, Y.K., et al.: Life prediction of membrane electrode assembly through load and potential cycling accelerated degradation testing in polymer electrolyte membrane fuel cells. *Int. J. Ener. Res.* **47**(39), 17379–17392 (2022)
13. Hua, Z., Zheng, Z., Pahon, E., et al.: Remaining useful life prediction of PEMFC systems under dynamic operating conditions. *Energy Convers. Manage.* **231**, 113825–113840 (2021)
14. Steffe, D., Julian, L., Philipp, F., et al.: Prescriptive lifetime management for PEM fuel cell systems in transportation applications, Part I: State of the art and conceptual design. *Energy Convers. Manage.* **277**, 116598–116612 (2023)
15. Candusso, D., Bernardinis, A.D., Pera, M.C., et al.: Fuel cell operation under degraded working modes and study of diode by-pass circuit dedicated to multi-stack association. *Energy Convert. Manage.* **49**(4), 880–895 (2008)
16. Marx, N., Boulon, L., Gustin, F., et al.: A review of multi-stack and modular fuel cell systems: interests, application areas and on-going research activities. *Int. J. Hydr. Energy* **39**(23), 12101–12111 (2014)
17. Candusso, D., Bernardinis, A.D., Péra, M.C., et al.: Fuel cell operation under degraded working modes and study of diode by-pass circuit dedicated to multi-stack association. *Energy Convers. Manage.* **49**(4), 880–895 (2008)
18. Cardozo, J., Marx, N., Boulon, L., et al.: Comparison of multi-stack fuel cell system architectures for residential power generation applications including electrical vehicle charging. In: *IEEE Vehicle Power and Propulsion Conference (VPPC)*, pp. 1–6. Montreal, Canada (2015)
19. Katz, M.: Reactant distribution for multi-stack fuel cell power plants. *European Patent 1991*:1
20. Su, Z., Lei, F., Gang, Z., et al.: A review on proton exchange membrane multi-stack fuel cell systems: architecture, performance, and power management. *Appl. Ener.* **310**, 11855–11880 (2022)

21. Shen, W., Fan, L., Pan, Z., et al.: Comparison of different topologies of thermal management subsystems in multi-stack fuel cell systems. *Energies* **15**(14), 5030–5046 (2022)
22. Sutharssan, T., Montalvao, D., Chen, Y.K., et al.: A review on prognostics and health monitoring of proton exchange membrane fuel cell. *Renew. Sustain. Energy Rev.* **75**, 440–450 (2017)
23. Endoh, E., Terazono, S., Widjaja, H., et al.: Degradation study of MEA for PEMFC under low humidity condition. *Electrochem. Solid-State Lett.* **7**(7), A209–A211 (2004)
24. Ma, R., Dang, H., Zhang, Y., et al.: A review of fault mechanism analysis and diagnostic methods of proton exchange membrane fuel cell system. In: *Proceedings of the CSEE*, pp. 1–21 (2022)
25. Heidary, H., Kermani, M.J., Dabir, B.: Influences of bipolar plate channel blockages on PEM fuel cell performances. *Energy Convers. Manage.* **124**, 51–60 (2016)
26. Lee, W., Oh, H., Kim, M., et al.: Hierarchical fault diagnostic method for a polymer electrolyte fuel cell system. *Int. J. Hydr. Energy* **45**(47), 25733–25746 (2020)
27. Hu, Z., Xu, L., Li, J., et al.: A cell interaction phenomenon in a multi-cell stack under one cell suffering fuel starvation. *Energy Convers. Manage.* **174**, 465–474 (2018)
28. Liu, J., Li, Q., Chen, W., et al.: A discrete hidden Markov model fault diagnosis strategy based on K-means clustering dedicated to PEM fuel cell systems of tramways. *Int. J. Hydr. Energy* **43**(27), 12428–12441 (2018)
29. Zhang, X., Guo, X.: Fault diagnosis of proton exchange membrane fuel cell system of tram based on information fusion and deep learning. *Int. J. Hydr. Energy* **46**(60), 30828–30840 (2021)
30. Lin, R., Li, B., Hou, Y.P., et al.: Investigation of dynamic driving cycle effect on performance degradation and micro-structure change of PEM fuel cell. *Int. J. Hydr. Energy* **34**(5), 2369–2376 (2009)
31. Schmittinger, W., Vahidi, A.: A review of the main parameters influencing long-term performance and durability of PEM fuel cells. *J. Power. Sources* **180**(1), 1–14 (2008)
32. Bressel, M., Hilairret, M., Hissel, D., et al.: Extended Kalman filter for prognostic of proton exchange membrane fuel cell. *Appl. Energy* **164**, 220–227 (2016)
33. Li, Z., Zheng, Z., Outbib, R., et al.: Adaptive prognostic of fuel cells by implementing ensemble echo state networks in time-varying model space. *IEEE Trans. Industr. Electron.* **67**(1), 379–389 (2020)
34. Chrétien, S., Herr, N., Nicod, J.M., et al.: A post-prognostics decision approach to optimize the commitment of fuel cell systems in stationary applications. In: *2015 IEEE Conference on Prognostics and Health Management (PHM)*, pp. 1–7. Austin, USA (2015)
35. Lopes, F., Kelouwani, S., Boulon, L., et al.: Neural network modeling strategy applied to a multi-stack PEM fuel cell system. In: *2016 IEEE Transportation Electrification Conference and Expo (ITEC)*, pp. 1–7. Dearborn, USA (2016)
36. Liu, J., Zio, E.: Prognostics of a multistack PEMFC system with multiagent modeling. *Energy Sci. Eng.* **7**(1), 1–12 (2019)
37. Yue, M., Jemei, S., Zerhouni, N., et al.: Proton exchange membrane fuel cell system prognostics and decision-making: current status and perspectives. *Renew. Energy* **179**, 2277–2294 (2021)
38. Bressel, M., Hilairret, M., Hissel, D., et al.: Model-based aging tolerant control with power loss prediction of Proton exchange membrane fuel cell. *Int. J. Hydr. Energy* **45**(19), 11242–11254 (2020)
39. Kong, S., Bressel, M., Hilairret, M., et al.: Advanced passivity-based, aging-tolerant control for a fuel cell/super-capacitor hybrid system. *Control Eng. Pract.* **105**, 10436 (2020)
40. Li, Q., Liu, Q., Li, Y., et al.: Multi-stack adaptive power allocation method considering fuel cell aging. *J. Southwest Jiaotong Univ.* **57**(04), 713–721 (2022)

41. Jian, Z., Cadet, C., Li, Z., et al.: Post-prognostics decision making for a two-stacks fuel cell system based on a load-dependent deterioration model. In: 5th European Conference of the Prognostics and Health Management Society, pp. 1–9. Turin, Italy (2021)
42. Zuo, J., Cadet, C., Li, Z., et al.: Post-prognostics decision making strategy to manage the economic lifetime of a two-stack PEMFC system. In: 2021 Annual Reliability and Maintainability Symposium (RAMS), pp. 1–7. Orlando, USA (2021)
43. Ma, R., Chai, X., Geng, R., et al.: Recent progress and challenges of multi-stack fuel cell systems: fault detection and reconfiguration, energy management strategies, and applications. *Energy Convers. Manage.* **285**, 117015–117046 (2023)
44. Hua, Z., Zheng, Z., Paphon, E., et al.: A review on lifetime prediction of proton exchange membrane fuel cells system. *J. Power Sour.* **529**, 1–17 (2022)
45. Garcia, P., Fernandez, L.M., Torreglosa, J.P., et al.: Operation mode control of a hybrid power system based on fuel cell/battery/ultracapacitor for an electric tramway. *Comput. Electr. Eng.* **39**(7), 1993–2004 (2013)
46. Li, Q., Su, B., Pu, Y., et al.: A state machine control based on equivalent consumption minimization for fuel cell/supercapacitor hybrid tramway. *IEEE Trans. Transp. Electr.* **5**(2), 552–564 (2019)
47. Yan, Y., Li, O., Chen, W., et al.: Optimal energy management and control in multimode equivalent energy consumption of fuel cell/supercapacitor of hybrid electric tram. *IEEE Trans. Ind. Electron.* **66**(8), 6065–6076 (2019)
48. Xiao, Y., Liao, H., Zhou, Y., et al.: An adaptive fuzzy logic control strategy for high power hybrid locomotive. In: 2018 13th World Congress on Intelligent Control and Automation (WCICA), pp. 1172–1177. Changsha, China (2018)
49. Hong, Z., Li, Q., Chen, W., et al.: Energy management strategy of fuel cell hybrid power system for locomotive based on PMP. *Proc. CSEE* **39**(13), 3867–3879 (2019)
50. Torreglosa, J.P., Jurado, F., García, P., et al.: Hybrid fuel cell and battery tramway control based on an equivalent consumption minimization strategy. *Control. Eng. Pract.* **19**(10), 1182–1194 (2011)
51. Han, J., Park, Y., Kum, D.: Optimal adaptation of equivalent factor of equivalent consumption minimization strategy for fuel cell hybrid electric vehicles under active state inequality constraints. *J. Power Sour.* **267**, 491–502 (2014)
52. Zhang, G., Li, Q., Han, Y., et al.: Study on equivalent consumption minimization strategy based on operation mode and DDOH for fuel cell hybrid Tramway. *Proc. Chin. Soc. Electr. Eng.* **38**(23), 6905–6914 (2018)
53. Wang, X., Li, Q., Wang, T., et al.: Optimized energy management strategy based on SQP algorithm for PEMFC hybrid locomotive. In: 2019 IEEE Transportation Electrification Conference and Expo, pp. 1–5. Pacific, Asia (2019)
54. Farouk, O., Jürgen, R., Angelika, H.: Power management optimization of an experimental fuel cell/battery/supercapacitor hybrid system. *Energies* **8**(7), 6302–6327 (2015)
55. Chen, W., Hu, B., Li, Q., et al.: Energy management method for hybrid electric tram based on dynamic programming algorithm. *J. Southwest Jiaotong Univ.* **55**(5), 903–911 (2020)
56. Jiang, H., Xu, L., Li, J., et al.: Energy management and component sizing for a fuel cell/battery/supercapacitor hybrid powertrain based on two-dimensional optimization algorithms. *Energy* **177**, 386–396 (2019)
57. Simmons, K., Guezennec, Y., Onori, S.: Modeling and energy management control design for a fuel cell hybrid passenger bus. *J. Power Sour.* **246**, 736–746 (2014)
58. Wu, C., Lu, S., Xue, F., et al.: Optimal sizing of onboard energy storage devices for electrified railway systems. *IEEE Trans. Transp. Electrif.* **6**(3), 1301–1311 (2020)
59. Wu, C., Lu, S., Xue, F., et al.: A two-step method for energy-efficient train operation, timetabling, and onboard energy storage device management. *IEEE Trans. Transp. Electrif.* **7**(3), 1822–1833 (2021)

60. Wu, C., Xue, B., Lu, S., et al.: Adaptive eco-driving strategy and feasibility analysis for electric trains with onboard energy storage devices. *IEEE Trans. Transp. Electrification*. **7**(3), 1834–1848 (2021)
61. Ji, P., Wang, T., Wu, F.: Calculation grid and turbulence model for numerical simulating pressure fluctuations in high-speed train tunnel. *J. Central South Univ.* **26**, 2870–2877 (2019)
62. Wan, Y., Zhou, X., Mei, Y.: Characteristics of pressure wave inside and outside high-speed train passing through high-elevation and large gradient tunnels. *China Railway Sci.* **44**(01), 167–176 (2023)
63. Li, R., Cuan, Y.: Investigation of air pressure pulse when two high-speed trains passing by each other in tunnel. *J. Mechan. Eng.* **48**(20), 130–137 (2012)
64. Renau, J., Lozano, A., Barroso, J., et al.: Use of fuel cell stacks to achieve high altitudes in light unmanned aerial vehicles. *Int. J. Hydr. Energy* **40**(42), 14573–14583 (2015)
65. Peng, F., Chen, W., Liu, Z., et al.: System integration of China's first proton exchange membrane fuel cell locomotive. *Int. J. Hydr. Energy* **39**(25), 13886–13893 (2014)
66. Ding, L., Tang, T., Wang, Y., et al.: Current status and prospects of hydrogen storage and transportation technology. *Nat. Gas Chem. Ind.* **47**(2), 35–40 (2022)
67. Xue, L., Liu, B., Jia, H.: Design of 350 kW fuel cell thermal control system for locomotive. *Mechan. Electr. Eng. Technol.* **50**(7), 253–255+279 (2021)
68. Liu, B., Zhao, F., Li, X.: Review on thermal management technology of PEMFC. *Battery Bimonthly* **48**(3), 202–205 (2018)



Optimization of the Hollow Shaft in an Air Compressor Rotor for Hydrogen Fuel Cell

Shang Sang^(✉), Wei Ni, Ming Cheng, and Zhixue He

CRRC Yongji Electric Co. LTD, Xi'an 710000, China
sangdavinc@163.com

Abstract. Hollow shaft with light weight and small moment of inertia is suitable for the motor rotor due to the demand for high speed and energy conservation. In this paper, the influence of hollow aperture on strength and critical speed was calculated by simulation method. It is concluded that for a three-section type rotor, when the ratio of the inner and outer diameters of the hollow shaft is 0.18–0.55 while the interference between sheath and shaft is 0.06–0.08 mm, difference of the sheath stress, the shaft stress, the pressure between sheath and shaft, the maximum deformation and the critical speed between the hollow shaft rotor and the solid shaft rotor is within 5%. The change rate of rotor strength and critical speed caused by the increase of hollow diameter is much lower than the change rate of rotor mass. Optimal design of the hollow aperture, hole length and interference between sheath and shaft was performed considered the minimum mass, the minimum interference, the restrict of strength and rotor dynamics based on response surface method. The rotor dynamics of the gas foil bearing-rotor system under real conditions was calculated. It was verified by prototype test that the selected hollow shaft structure meets the requirements.

Keywords: Hollow shaft · Air compressor · Finite element simulation · Stiffness and strength · Optimization · Rotor dynamics

1 Introduction

The centrifugal air compressor for hydrogen fuel cell generally adopts the direct drive mode of permanent magnet synchronous motor (PMSM), and the mainstream rotor speed is about 100000 r/min, which requires high rotor strength and rotor dynamics [1–4]. Using hollow shaft can reduce the weight while reduce the moment of inertia, which is very suitable for air compressor high-speed rotor [5]. At present, the hollow aperture of shaft is generally selected by “mechanics of materials” [6] or “mechanical design handbook” [7]. There are many simplifications and assumptions. The simulation method can more accurately obtain the variation of rotor strength and critical speed with the hollow aperture, and then select appropriate structure by optimal method [8, 9]. In actual operation, the stiffness and damping of gas foil bearing vary greatly with the speed. Rotor dynamics analysis of gas foil bearing-rotor system under real conditions is very important to ensure the reliability of the design structure [10].



In this paper, finite element simulation was used to calculate the influence of hollow aperture of shaft on the strength and critical speed. The change rate of rotor strength, critical speed and rotor mass caused by the increase of hollow diameter was compared with the solid shaft rotor. Optimization design was performed for a three-section type rotor considering both the minimum mass, the minimum interference and the restrict of strength and rotor dynamics. Rotor dynamics analysis under real conditions for the design was carried on. A prototype test was performed to verify the selected structure.

2 The Influence of Hollow Aperture on Rotor Strength and Critical Speed

2.1 Calculation of Simple Hollow Shafts

The bending and torsional section modulus of the hollow shaft and the solid shaft are as shown in Table 1. When the ratio of the inner and outer diameters of the hollow shaft is 0.5 and 0.6, the bending normal stress and torsional shear stress of the hollow shaft are only 6.67% and 14.89% larger than those of the solid shaft under the same force, while the weight can be reduced by more than 20% [11].

Table 1. Bending and torsion section modulus of shaft

| Cross-sectional shape | Bending section modulus | Torsional section modulus |
|---|---------------------------------|---------------------------------|
|  | $\frac{\pi d^3}{32}$ | $\frac{\pi d^3}{16}$ |
|  | $\frac{\pi d^3}{32}(1 - \nu^4)$ | $\frac{\pi d^3}{16}(1 - \nu^4)$ |

Note: $\nu = d_1/d$, ν is the ratio of hollow shaft inner diameter and outer diameter

The maximum stress of a shaft shown in Fig. 1 with an outer diameter of 20 mm and a length of 100 mm is calculated by simulation. When the ratio of the inner and outer diameters of the hollow shaft is 0.6, the maximum stress increases by 14.92% and the mass decreases by 36% compared with the solid shaft. It is consistent with the calculation results of analytical algorithm. Since actual structure is always under complex stress condition, finite element simulation can be obtained as an effective method [12].

2.2 The Influence of Hollow Aperture on Rotor Strength

The structure analyzed is a three-section type rotor with cylindrical permanent magnet in it, as shown in Fig. 2. The shaft and the sheath are interference fitted, and the outer diameter of the shaft at the mounting position is 33 mm. The material of sheath and

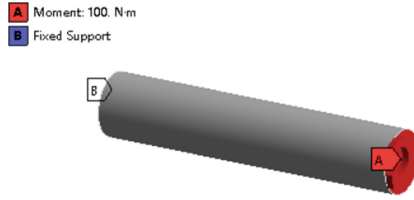
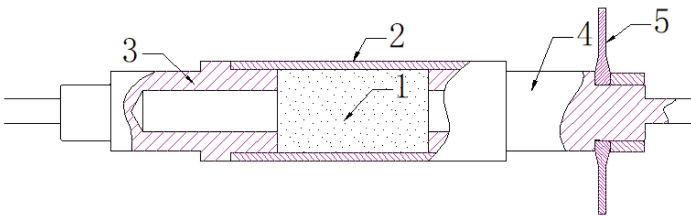


Fig. 1. Loading and constraint conditions

shaft is GH4169 with yield strength of 1100 MPa. The influence of hollow aperture on rotor strength mainly focuses on the mounting position of shaft and sheath, because this position has interference pressure in addition to centrifugal force. Using ANSYS to calculate the sheath stress, the shaft stress, the pressure between sheath and shaft and the maximum radial deformation under different interference and hollow aperture.



1.permanent magnet, 2.sheath, 3.left shaft, 4.right shaft, 5.thrust plate

Fig. 2. The three-section type rotor structure

The interference is set to 0.06 mm, 0.07 mm, 0.08 mm, and the rotating speed is set to 95000 r/min. The performance index of solid shaft is listed in Table 2.

Table 2. Performance index of solid shaft.

| Interference mm | Sheath stress Mpa | Shaft stress Mpa | Pressure Mpa | Deformation mm |
|-----------------|-------------------|------------------|--------------|----------------|
| 0.06 | 733.06 | 60.92 | 66.48 | 0.0592 |
| 0.07 | 846.49 | 76.41 | 83.60 | 0.0682 |
| 0.08 | 959.95 | 92.85 | 100.71 | 0.0773 |

Considering the process requirements, the analyzed hollow aperture is from 6 mm to 20 mm, which means the ratio of hole diameter and shaft diameter is 0.18–0.61. The changes of performance index under different hollow apertures are obtained as shown in Fig. 3.

Figure 3 shows that the interference has more effect on the four performance index than hollow aperture. When the interference is 0.07 mm or 0.08 mm, the sheath stress,

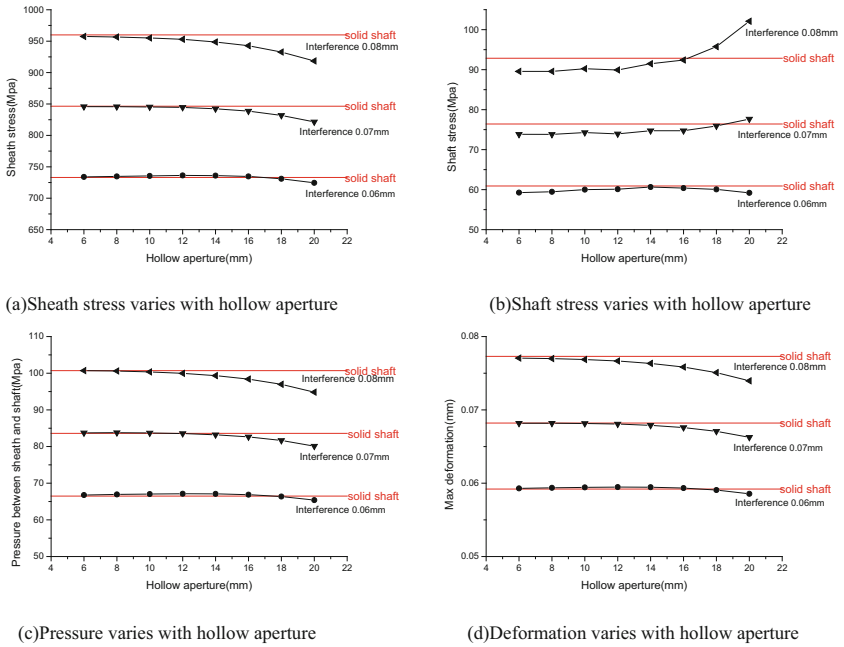


Fig. 3. Changes of performance index under different hollow apertures

the pressure between shaft and sheath and the maximum deformation tend to decrease with the increase of the aperture. The shaft stress tends to increase with the increase of the aperture, but the maximum shaft stress is 148.55Mpa, which is far less than the yield stress limit. When the interference is 0.06 mm, all the performance index shows first increase and then decrease. When the ratio of the inner and outer diameters of the hollow shaft is 0.18–0.55 under three kinds of interference, difference of all the performance index between the hollow shaft design and the solid shaft design is within 5%.

It can also be seen that when the ratio of the inner and outer diameter of hollow shaft is 0.55–0.61 while the interference is 0.06 mm, all the performance index is less than that of the solid shaft. When the ratio is 0.36–0.55 while the interference is 0.07 mm, all the performance index is smaller than that of the solid shaft. When the ratio is 0.18–0.48 while the interference is 0.08 mm, all the performance index are smaller than the solid shaft. It shows that there is a variation range of the ratio of the inner and outer diameter of hollow shaft that the rotor strength is higher than solid shaft, and the range is different under different interference.

2.3 The Influence of Hollow Aperture on Rotor Critical Speed

There are impellers at both ends of the air compressor rotor, which will influence the moment of inertia and stiffness of the rotor. Calculation results is more accurate with actual structure [13]. The structure is shown in Fig. 4.

The direct stiffness coefficients k_{xx} , k_{yy} of bearings are set to $1E6$ N/m while the direct damping coefficients C_{11} and C_{22} are set to 100 N-s/m. Other coefficients are

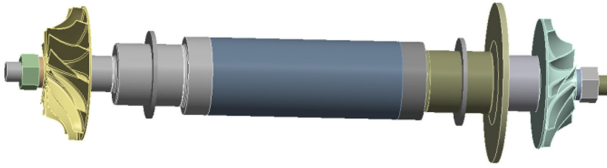


Fig. 4. The rotor structure with impellers

set to 0 and the rotor dynamics analysis is carried out. The first bending critical speed of solid shaft is 165790rpm. The change of the first bending critical speed with variable hollow aperture is shown in Fig. 5, and the difference of the first bending critical speed, the rotor mass between the hollow shaft and the solid shaft is shown in Fig. 6.

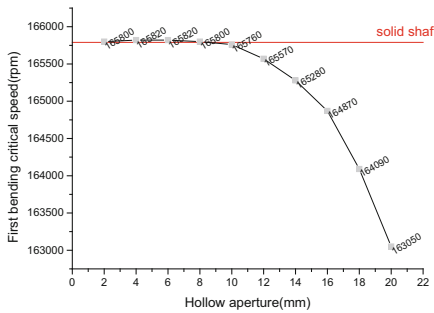


Fig. 5. The change of the first bending critical speed

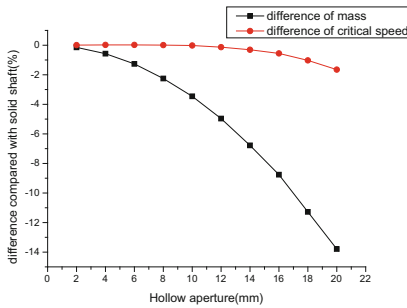


Fig. 6. The difference compared with solid shaft

It can be seen that when the hollow aperture is smaller than 8 mm, which means the ratio of hole diameter and shaft diameter is under 0.24, the critical speed is higher than that of the solid shaft. With the increase of the aperture, the change rate of the first bending critical speed of the rotor is less than the decline rate of the rotor mass. When the hollow aperture is 20 mm, which means the ratio of inner and outer diameter of hollow shaft is 0.61, the first bending critical speed of the rotor is only 1.65% lower while the mass is about 14% lower than that of the solid shaft.

3 Optimization of Hollow Shaft Rotor

The hollow shaft rotor is optimized by setting the hollow aperture, hole length and interference between sheath and shaft as optimization parameters. Parameters variation settings are as Table 3. The stress of each component, the maximum radial deformation of the rotor, and the first bending critical speed of the rotor is calculated.

Table 3. Parameters variation setting.

| Optimization parameters | Parameters variation mm |
|---------------------------------------|-------------------------|
| Hollow aperture | [6, 20] |
| Hole length | [50, 60] |
| Interference between sheath and shaft | [0.05,0.08] |

The response surface construction is to use the experimental design method to arrange the experimental design table, and construct the fitting model to simulate the relationship between the variables and the objective [14].The experimental design method in this paper adopts the optimal space-filling design method. After parameter setting, the experimental design table is updated as Fig. 7.

| P13 - hole aperture (mm) | P14 - hole length (mm) | P18 - Frictional - To Surface Offset (mm) | P7 - Equivalent Stress Maximum (MPa) | P8 - Directional Deformation Maximum (mm) | P9 - Frictional - Surface Body To Surface Body Offset (m) | P10 - Normal Stress Maximum (MPa) | P11 - Normal Stress Minum (MPa) | P12 - First bending modal Frequency (Hz) |
|--------------------------|------------------------|---|--------------------------------------|---|---|-----------------------------------|---------------------------------|--|
| 17.667 | 57.667 | 0.055 | 681.63 | 0.082047 | 5.3E-05 | 34.438 | -58.06 | 2501.5 |
| 11.133 | 58.333 | 0.053 | 660.36 | 0.080464 | 5.3E-05 | 37.683 | -54.806 | 2520.9 |
| 7.4 | 56.333 | 0.073 | 294.78 | 0.053114 | 7.3E-05 | 5.2275 | -87.34 | 2523.3 |
| 16.733 | 51 | 0.071 | 294.78 | 0.053114 | 7.1E-05 | 8.4731 | -84.087 | 2509.6 |
| 6.4667 | 51.667 | 0.067 | 813.01 | 0.09185 | 6.7E-05 | 14.964 | -77.58 | 2523.5 |
| 19.533 | 53.667 | 0.061 | 736.81 | 0.086165 | 6.1E-05 | 24.701 | -67.82 | 2492.4 |
| 14.867 | 53 | 0.051 | 641.34 | 0.079029 | 5.1E-05 | 40.929 | -51.553 | 2515.9 |
| 18.6 | 55.667 | 0.075 | 294.78 | 0.053114 | 7.5E-05 | 1.982 | -90.593 | 2498.3 |
| 13.933 | 54.333 | 0.063 | 768.45 | 0.088525 | 6.3E-05 | 21.455 | -71.073 | 2518 |
| 13 | 57 | 0.079 | 294.78 | 0.053114 | 7.9E-05 | 1.0288 | -97.1 | 2518.9 |
| 9.2667 | 59.667 | 0.065 | 791.33 | 0.090233 | 6.5E-05 | 18.21 | -74.327 | 2521.9 |
| 8.3333 | 55 | 0.057 | 702.51 | 0.083594 | 5.7E-05 | 31.192 | -61.313 | 2523.3 |
| 12.067 | 50.333 | 0.059 | 726.09 | 0.085354 | 5.9E-05 | 27.946 | -64.566 | 2521.2 |
| 15.8 | 59 | 0.069 | 294.78 | 0.053114 | 6.9E-05 | 11.719 | -80.833 | 2508.1 |
| 10.2 | 52.333 | 0.077 | 294.78 | 0.053114 | 7.7E-05 | 1.0662 | -93.847 | 2522.7 |

Fig. 7. The experimental design table

The response surface is generated by genetic algorithm [15], The relationship between hollow aperture, hole length and the first bending modal frequency is shown in Fig. 8. Refinement points were used to optimize the response surface.

Multi-objective genetic algorithm (MOGA) is selected. The optimization objectives and constraints are set as Table 4.

ANSYS provides a sort function of decision support management, and uses fuzzy evaluation to sort design variables. A set of candidate points satisfying the constraint conditions is generated by iterative solution. As there is certain error in response surface prediction, the prediction and accurate calculation for the candidate points shown in Table 5. The generated response surface has good prediction effect.

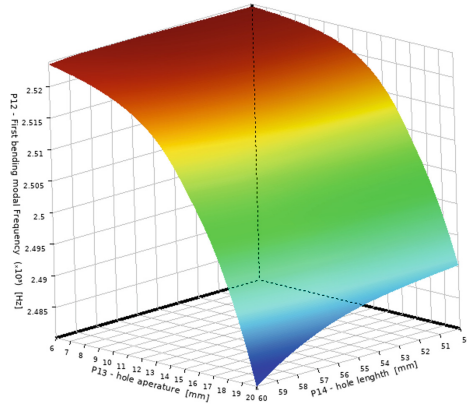


Fig. 8. The response surface of parameters

Table 4. Optimization objectives and constraints.

| Output parameters | Objectives and constraints |
|--|----------------------------|
| Max [σ_{sleeve} , σ_{shaft}] | < 1100Mpa |
| $\sigma_{\text{mag-pull}}$ | < 35Mpa |
| The first bending modal frequency | > 2500Hz |
| Rotor mass | Minimize |
| Interference between sheath and shaft | Minimize |

Table 5. Candidate points

| Parameters | Prediction | | | Accurate calculation | | |
|---|------------|--------|--------|----------------------|--------|--------|
| | Point1 | Point2 | Point3 | Point1 | Point2 | Point3 |
| Hollow aperture(mm) | 17.608 | 17.82 | 17.795 | 17.608 | 17.82 | 17.795 |
| Hole length(mm) | 59.04 | 57.565 | 58.138 | 59.04 | 57.565 | 58.138 |
| Interference between sheath and shaft(mm) | 0.055 | 0.055 | 0.055 | 0.055 | 0.055 | 0.055 |
| Max [σ_{sleeve} , σ_{shaft}](MPa) | 679.87 | 679.7 | 679.7 | 684.22 | 684.12 | 684.11 |
| $\sigma_{\text{mag-pull}}$ (MPa) | 34.08 | 34.05 | 34.05 | 34.03 | 34.01 | 34.01 |
| The first bending modal frequency(Hz) | 2500.3 | 2500.7 | 2500.4 | 2498.3 | 2500.8 | 2499.7 |
| Rotor mass(kg) | 1.8153 | 1.8156 | 1.814 | 1.8153 | 1.8156 | 1.814 |

4 Calculation of Gas Foil Bearing-Rotor System and Test Verification

4.1 Dynamic Characteristic Curve of the Bearing

In the gas foil bearing-rotor system, the rigid rotor is supported by the gas film pressure and the foil structure [16–18]. The dynamic stiffness coefficient and damping coefficient structure are calculated by the Reynolds equation. The dynamic characteristic curve of the bearing direct and cross stiffness/damping coefficient is shown in Figs. 9 and 10.

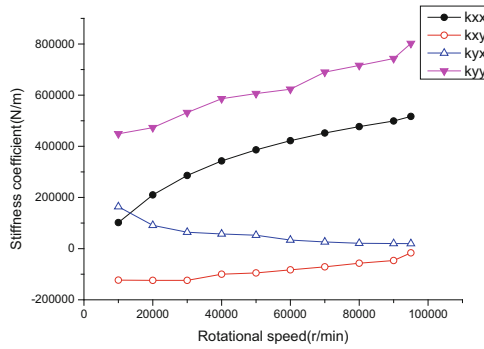


Fig. 9. The variation of stiffness coefficient

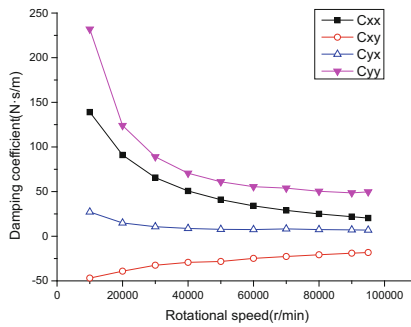


Fig. 10. The variation of damping coefficient

Gas foil bearings have greater direct stiffness and direct damping in the vertical direction than in the horizontal direction, which is due to the greater rotor eccentricity caused by static load in the vertical direction. When the rotational speed is above 10000 r/min, the direct stiffness of the bearing increases with the increase of the rotational speed, and the direct damping of the bearing decreases with the increase of the rotational speed. The cross stiffness and damping dynamic coefficient of the bearing show similar variation rules.

4.2 Critical Speed of the Optimized Rotor

Considering the process requirements, This paper choose 18 mm as the hollow aperture, 57 mm as the hole length and 0.05 mm as the interference. The critical speed of optimized rotor is calculated with dynamic bearing coefficient. The first bending vibration mode of the rotor is shown in Fig. 11, and the corresponding critical speed is 164520 r/min, which is 50% higher than the rated speed of the rotor(95000 r/min), indicating that the selected hollow shaft rotor supported by gas foil bearing meets the use requirement.

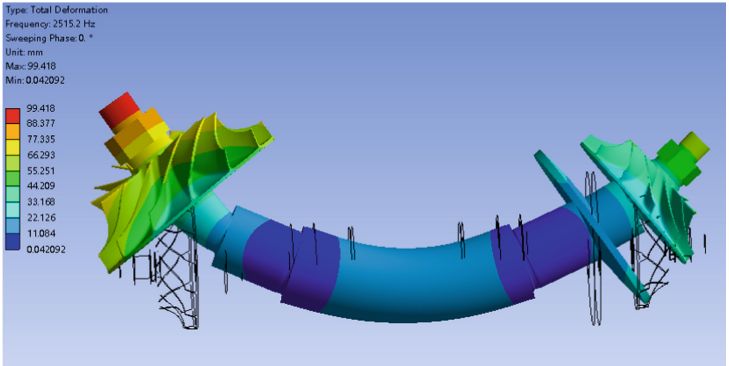


Fig. 11. The first bending vibration mode

4.3 Prototype Test

The manufacturing and installation of the air compressor are completed. The physical photos of the air compressor are shown in Figs. 12 and 13. The air compressor runs normally under rated condition, which means the selected rotor structure meets the requirement.

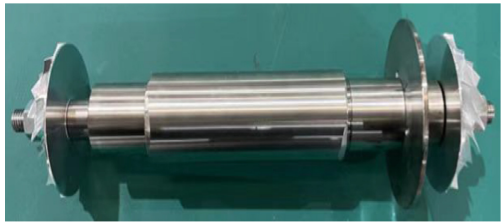


Fig. 12. The rotor shafting

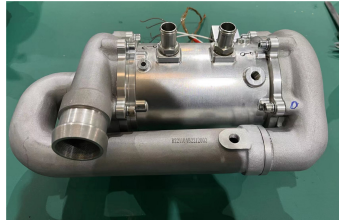


Fig. 13. The air compressor

5 Conclusions

In this paper, the influence of hollow aperture on strength and critical speed was calculated by simulation method. Optimal design of the hollow shaft rotor was performed. Calculation of gas foil bearing-rotor system under real bearing parameters and test verification were carried out. The conclusions are as follows:

- 1) When the ratio of the inner and outer diameters of the hollow shaft is 0.18–0.55 while the interference between sheath and shaft is 0.06–0.08 mm, difference of the sheath stress, the shaft stress, the pressure between sheath and shaft, the maximum radial deformation and the critical speed between the hollow shaft rotor and the solid shaft rotor is less than 5%. The change rate of rotor strength and critical speed caused by the increase of hollow diameter is much lower than the change rate of rotor mass.
- 2) The response surface optimization and multi-objective genetic algorithm method was applied to achieve the lightest and easy processing design of rotor by taking hollow aperture, hole length and interference between sheath and shaft as optimization parameters. Three candidate points were get by response surface prediction and verified by accurate calculation.
- 3) Dynamic characteristic curve of the gas foil bearing were calculated. The critical speed of optimized rotor considering the process requirements is calculated with dynamic bearing coefficient. It is more than 50% higher than the rated speed which means resonance will not occur. It was verified by prototype test that the selected hollow shaft structure meets the requirements.

References

1. Jiahao, F., Peipei, Z., et al.: Research status of key components of hydrogen fuel cell. *Automobile Parts* **12**, 102–105 (2020)
2. Tuo, Z., Shuzhan, B., et al.: Current analysis of air compressor special for vehicle fuel cell. *Compressor Technol.* **01**, 45–50 (2021)
3. Penglong, B., Daobiao, Z., et al.: Development status and trend of air compressor in fuel cells vehicle. *Chinese J. Power Sour.* **140**(8), 1731–1734 (2016)
4. Jianning, D., Yunkai, H., et al.: Review on high speed permanent magnet machines including design and analysis technologies. *Proc. CSEE* **34**(27), 4640–4653 (2014)
5. Gerada, D., Mebarki, A., et al.: High-speed electrical machines: technologies, trends, and developments. *IEEE Trans. Industr. Electron.* **61**(6), 2946–2959 (2014)

6. Hongwen, L.: *Mechanics of Materials*, 6th edn. Higher Education Press, Beijing (2017)
7. Daxian, C.: *Mechanical Design Handbook*, 6th edn. Chemical Industry Press, Beijing (2016)
8. Xiao, W., Hongliang, Y.: Discussion on structural design of high speed permanent motor rotor applied to passenger car. *Automobile Parts* **11**, 45–48 (2022)
9. Ruibin, Z., Rui, W.: Optimal design of reduced diameter hollow shaft based on response surface method. *Manufact. Autom.* **44**(12), 57–60 (2022)
10. Wanli, X., Jian, W., et al.: Review of research status and development of foil air bearings. *J. Mech. Eng.* **58**(21), 92–113 (2022)
11. Cheng, Y., Xingxing, L., et al.: Research status on forming technology for hollow shaft. *Forging and Stamp. Technol.* **43**(1), 1–8 (2016)
12. Guoliang, H.: *Research on the application of hollow shaft rotor in high power high speed permanent magnet synchronous motor*. Shenyang University of Technology (2017)
13. Jin, X.: *Research on the structural modeling and dynamic characteristics of typical rotor system for high speed electric machine*. Hunan University (2017)
14. Lee, T., Hong, D., Jung, T.: High-speed, high-power motor design for a four-legged robot actuator optimized using the weighted sum and response surface methods. *CES Trans. Electri. Mach. Syst.* **5**(3), 224–323 (2021)
15. Millo, F., Arya, P., Mallamo, F.: Optimization of automotive diesel engine calibration using genetic algorithm techniques. *Energy* **158**(SEP.1), 807–819 (2018)
16. Hong, D.K., Woo, B.C., Lee, J.Y. et al.: Ultra high speed motor supported by air foil bearings for air blower cooling fuel cells. *IEEE Trans. Magnet.* **48**(2), 871–874 (2012)
17. Zhang, H., Yu, W., Hua, W.: Design and key technology of oil-free centrifugal air compressor for hydrogen fuel cell. *CES Trans. Electri. Mach. Syst.* **6**(1), 11–19 (2022). <https://doi.org/10.30941/CESTEMS.2022.00003>
18. Beer, P., Tessaro, J. et al.: High speed motor design for gas compressor applications. In: *35th Turbomachinery Symposium*. College Station, Texas, Texas A&M University, pp. 103–112. (2006)
19. Yuanlong, C.: *Exploration on the performance of a controllable stiffness gas bearing with shape memory alloy springs and its rotor dynamic response*. Hunan University (2020)



Numerical Simulation of a Two-Stage Centrifugal Air Compressor Cooling Structure for Hydrogen Fuel Cells

Cheng Yang^(✉), Wei Ni, Cong Pang, and Zhixue He

CRRCC Yongji Electric Co. LTD, Xi'an 710000, China
1271187590@qq.com

Abstract. A two-stage centrifugal Air compressor cooling system for a hydrogen fuel cell with a rated power of 17.5 kw and a rotating speed of 95,000 rpm was numerically simulated. Firstly, the accuracy of CFD method to calculate air friction loss is verified by empirical formula, and then the advantages and disadvantages of three different cooling cases are analyzed. The results show that the rotor air friction loss increases with the increase of axial cooling air flow, rotating speed and Surface roughness. The air friction loss is negligible when the rotating speed is below 35000r/min. The average temperature of the stator coil is reduced by 20.9% compared with that of the fully enclosed motor due to internal air cooling. In addition, because of the high temperature distribution of the thrust disc, it is necessary to increase the cooling of the thrust disc if the design conditions permit.

Keywords: Two-stage centrifugal air compressor · High speed permanent magnet motor · Friction loss · Cooling design

1 Introduction

The centrifugal air compressor has the advantages of small size, high efficiency and long service life. Therefore, it is widely used in the air supply system of fuel cells [1, 2]. Centrifugal air compressors usually use high-speed motors to drive the impeller to compress the air. As one of the main components of centrifugal air compressor, high-speed permanent magnet synchronous motor (HSPMSM) has the advantages of high speed and energy density. And the gas foil bearing does not need oil lubrication, which is more conducive to the stable operation of the fuel cell gas supply system [3]. In the design of HSPMSM, material, electromagnetic, mechanical and thermal characteristics are considered as key technologies [4, 5]. For the thermal analysis of HSPMSM, the motor power density is too high so that the overtemperature is studied. The key problem is not to minimize the loss as much as possible, but to allocate the loss reasonably to avoid local overtemperature [5]. Heat network model [6], finite element method (FEM) [7] and computational fluid dynamics method (CFD) [8] are widely used to obtain the temperature distribution of the motor. In Reference [9], the aerodynamic performance of oil-free centrifugal air compressor for hydrogen fuel cell was tested and calculated

by CFD. It was found that the experimental and numerical results were in good agreement. Reference [10] used CFD method to analyze the temperature distribution of a 36 kr/min, 75 kW high power permanent magnet synchronous motor, and verified the accuracy through experiments. Reference [11] optimized the cooling structure of the shaft by numerical simulation. It is found that after optimization, the stator temperature is significantly reduced to 33 °C, and the rotor temperature is reduced by 19 °C.

A HSPMSM for centrifugal air compressor is studied in this paper. CFD method was used to analyze different cooling cases. The aim of this paper is to compare the temperature distribution of each component in the motor, and to provide help for the design of HSPMSM.

2 Design of Air Compressor Cooling Structure

As shown in Fig. 1, the two-stage centrifugal air compressor used in the study is mainly composed of volute, bend, permanent magnet synchronous motor and so on. As the driving part of air compressor, HSPMSM has the advantages of small size and high efficiency [12]. Usually, the impeller is installed on both sides of the shaft, and the volute is connected to the motor end cover, and the motor volute is connected by bend. It is worth noting that a branch pipe is installed on the bend to flow part of the air into the drive motor, which has a positive effect on the cooling inside the motor. In order to meet the CFD calculation conditions, Fig. 2 simplifies the two-stage centrifugal air compressor model shown in Fig. 1. It can be seen that the air flows from the first volute through the first impeller, and flows into the second stage turbine through the bend. The air is compressed again inside the secondary volute. In order to cool the HSPMSM, the branch airflow in the bend realizes the forced air cooling of the motor. In addition, a spiral water channel is installed on the motor frame to cool the motor.

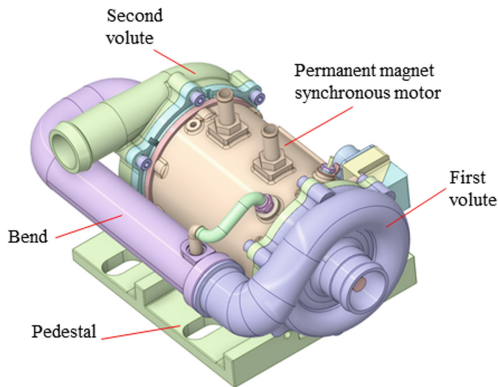


Fig. 1. Two-stage centrifugal air compressor model

3 Control Equations and Assumptions

The governing equations for steady-state analysis are as follows:

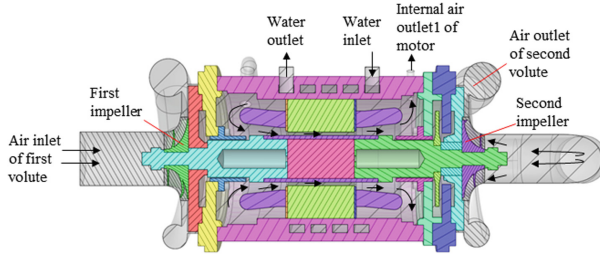


Fig. 2. Section of a simplified two-stage centrifugal air compressor

Continuity equation:

$$\frac{\partial}{\partial x_i} u_i = 0 \quad (1)$$

Momentum equation:

$$\frac{\partial}{\partial x_i} (\rho u_i u_j) = -\frac{\partial p}{\partial x_j} + \frac{\partial}{\partial x_i} \left((\mu + \mu_t) \frac{\partial u_j}{\partial x_i} \right) \quad (2)$$

where ρ is fluid density, p is pressure, μ and μ_t are the fluid dynamic viscosity and turbulent dynamic viscosity respectively.

Energy equation:

$$\frac{\partial}{\partial x_i} (\rho C_p u_i T) = \frac{\partial}{\partial x_i} \left((\lambda + \lambda_t) \frac{\partial T}{\partial x_i} \right) \quad (3)$$

where C_p is heat capacity, T is temperature, λ and λ_t are the thermal conductivity and turbulent thermal conductivity respectively.

In the calculation, it is assumed that the fluid flow conforms to the continuous medium hypothesis. All solid surfaces are non-slip boundary conditions. The air velocity does not exceed the speed of sound and it is assumed to be an incompressible fluid flow, but when calculating the flow inside the volute, the air is regarded as an ideal gas. The flow state is steady and there is no viscous dissipation. The effects of radiation heat transfer and gravity are not considered.

4 Numerical Calculation of Air Compressor Temperature Rise

4.1 Numerical Solution of Air Friction Loss

When the high-speed motor is rotating, the air friction loss generated on the rotor surface is related to the velocity distribution and vortex diffusion of the fluid. The air friction loss of the rotor can be calculated by the existing empirical formula for the specific rotor air gap structure. When the cooling fluid flows through the rotor air gap structure, the friction loss of the cylindrical rotor surface is calculated as follows [13].

$$P = k C_f \rho \pi \omega^3 r^4 l \quad (4)$$

where ρ is fluid density. ω , r and l are the angular velocity, radius and axial length of the rotor respectively. k is roughness coefficient, $k = 1$ for smooth surface and $k = 2.5$ for axial slotted surface [14]. C_f is the air friction coefficient, defined as follows [13, 15]:

$$C_f = \frac{0.0152}{Re_\delta^{0.24}} \left[1 + \left(\frac{8}{7} \right)^2 \left(\frac{4Re_a}{Re_\delta} \right)^2 \right]^{0.38} \quad (5)$$

where $Re_\delta = \rho\omega r\delta/\mu$, δ is the radial length of air gap, ρ and μ are the density and dynamic viscosity of air. $Re_a = \rho v_m 2\delta/\mu$, v_m is the average axial velocity, which is calculated by dividing the volume flow of the cooling fluid by the cross section of the air gap.

The air friction loss can also be obtained by numerical calculation. Figure 3 shows the fluid domain model and grid at the rotor air gap in Fig. 2. The outer surface radius of the rotor is $r = 19.5\text{mm}$, and the axial length is $l = 59\text{mm}$. The number of stator slots is 24, and the height and width of the slots are both 2mm. The number of grid units is 244,307.

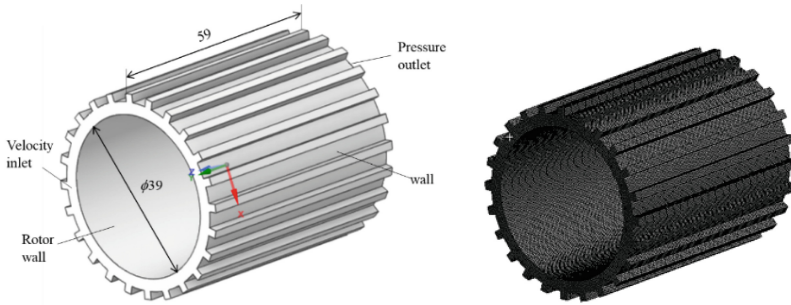


Fig. 3. Rotor air gap structure and grid

The front surface of the fluid domain shown in Fig. 3 is the velocity inlet boundary. The rear surface is the pressure outlet boundary. The inner surface of the fluid domain is a rotating surface. The outer surface of the fluid domain is an adiabatic wall. The stator cooling of high-speed motors generally adopts liquid cooling such as water cooling, oil cooling and mixed liquid cooling, but air cooling is usually used for internal cooling of motors. According to the empirical formulas (4) and (5), it can be found that the air flow rate also affects the air friction loss inside the rotor. Figure 4 shows the effect of axial cooling air flow on the air friction loss of the rotor. It can be found from the figure that the air friction loss of the rotor increases with the increase of mass flow rate. The maximum error between the analytical solution and the simulation value of air friction loss is 13.6%. With the increase of air flow, the volume average temperature of the rotor air gap fluid domain gradually decreases, which is due to the larger air flow rate taking away more heat. The axial cooling flow also increases the friction loss, so the axial air flow inside the rotor should not be too large, and it is very important to select a reasonable axial cooling air flow rate.

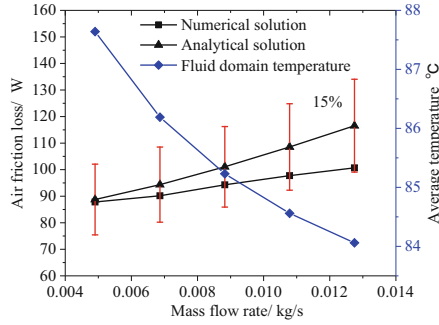


Fig. 4. Effect of axial cooling air flow on the air friction loss of the rotor

The influence of rotating speed on air friction loss cannot be ignored. When the axial cooling air inlet is 10m / s, the physical model shown in Fig. 3 changes the rotation speed to study the influence of rotation speed on air friction loss. The variation of rotor air friction loss with rotation speed is shown in Fig. 5. From the diagram, it can be found that the air friction loss increases with the increase of the rotational speed. The maximum error between the analytical solution and the simulation value is 13.9%, which shows that this simulation method can accurately calculate the air friction loss. In addition, when the rotor speed is 35000 r/min, the air friction loss is about 7.5W. At this time, the average temperature rise of the fluid domain is 0.64 K. Therefore, it can be considered that when the speed is lower than 35000 r/min, the influence of wind wear on temperature rise can be ignored. When the rotational speed is 95000 r/min, the air friction loss is 88.76 W, and the average temperature rise in the fluid domain is 7.64K. It can be seen that the larger air friction loss heats the fluid domain.

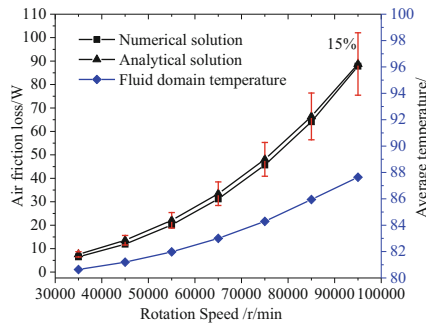


Fig. 5. The variation of rotor air friction loss with rotation speed

In addition to the influence of axial flow and rotation speed on air friction loss, wall roughness also has a certain influence on air friction loss. In the numerical calculation, the equivalent sand roughness height K_s and the roughness constant C_s are usually used to describe the wall roughness [16]. In our calculation model, the rotor surface roughness $Ra = 0.8\mu\text{m}$, assuming that the rotor surface is a uniformly polished surface,

$K_s = 10Ra$, $C_s = 0.5$. Figure 6 shows the influence of rotor surface roughness on air friction loss when the axial cooling air inlet is 10m/s and the rotor rotation speed is 95000 r/min. Therefore, when processing the rotor, the surface roughness should be as small as possible to achieve the purpose of reducing air friction loss.

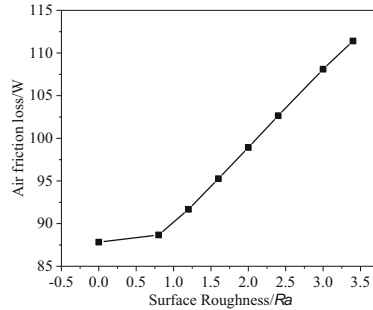


Fig. 6. Effect of surface roughness on air friction loss

4.2 Numerical Calculation of Internal Flow in Volute

In order to facilitate the use of conjugate heat transfer method to calculate the temperature rise of the air compressor, the fluid flow inside the volute and the motor is calculated separately. Firstly, the temperature and flow of air flowing into the motor through the bend branch are calculated, and then the temperature rise simulation analysis of the HSPMSM is carried out.

The purpose of the internal flow calculation of the volute is to obtain the air flow and temperature at the branch inlet. The fluid domain inside the volute is divided into grids, and the grid independence is verified by using 8.87 million, 1.106 million and 14.55 million grid numbers respectively. It is found that the branch outlet flow and temperature are basically unchanged, and the corresponding maximum average relative error is less than 2%. Therefore, the number of 11.6 million grids is enough to meet the calculation requirements. The rotation of the impeller is simulated by MRF [17], and the rotation speed is 95000 r/min. The air temperature cloud inside the volute is shown in Fig. 7. The results show that the air with an inlet temperature of 25 °C is heated after being compressed by the impeller. The flow rate into the branch of the motor is 13.88g/s, accounting for 6.25% of the total flow rate, and the temperature is 80.8 °C. The temperature cloud diagram can be found that the aerodynamic heating phenomenon occurs when the air is compressed through the impeller and volute. This phenomenon makes the volute wall and air heated, and the wall temperature is higher than the fluid temperature.

4.3 Numerical Calculation of Different Cooling Cases of Motor

The temperature rise directly affects the service life of the motor, and the temperature rise of 10K will reduce the insulation life by almost 50% [18]. Therefore, in order to

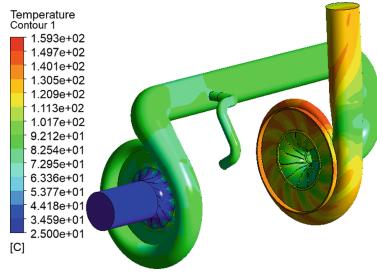


Fig. 7. The air temperature cloud inside the volute

reduce the temperature rise of the motor, the cooling design of the three cases is given in Fig. 8. The structure of Case1 and Case2 includes water cooling and air cooling. The difference is that the inlet position of cooling water is different. The water cooling structure adopts spiral channel. Case3 is a structure without air cooling. This design is to verify the highest temperature rise inside the motor without air cooling.

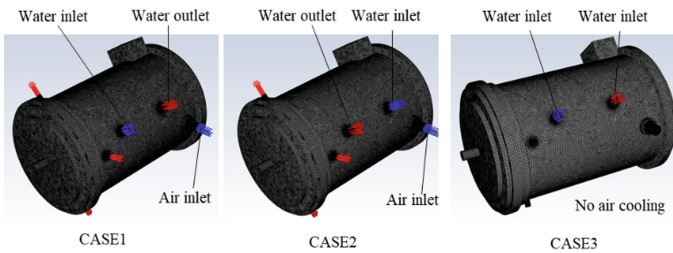


Fig. 8. The cooling design of the three cases

In order to verify the grid independence, the model of Case1 is divided into 13.24 million, 16.24 million and 25.11 million grids for temperature rise calculation. The maximum average relative errors of the volume average temperature of the coil, sheath and stator core calculated under the three grids are 3.2%, 0.4% and 0.5% respectively, so the influence of the number of grids on the calculation can be ignored. In the subsequent calculation of the whole machine, the number of grids is controlled at about 16 million. The $K \omega$ -SST turbulence model, which is insensitive to the boundary layer grid, is selected for calculation, and the boundary layer grid is determined according to Y plus less than 30.

The inlet boundary of cooling water is flow inlet. The inlet flow rate is 16L/min and the temperature is 60 °C. Table 1 gives the physical parameters of the solid material, in which the thermal conductivity of the stator core lamination is anisotropic. The motor frame, external end cover and bearing outer cover are all cast aluminum materials. The material of shaft, sheath and thrust plate is GH4169. The motor loss is shown in Table 2, where the stray loss is added in half on the core and coil.

The temperature cloud diagram of the section $x = 0m$ is shown in Fig. 9. From case1, it can be found that the highest temperature inside the motor is distributed on the

Table 1. The physical parameters of the solid material

| | Density / kg/m ³ | λ_i W/(m·K) | λ_j W/(m·K) | λ_k W/(m·K) | C_p J/(kg·K) |
|---------------------|-----------------------------|---------------------|---------------------|---------------------|----------------|
| Insulating material | 290 | 0.15 | | | 860 |
| Copper | 8930 | 398 | | | 386 |
| Stator core | 7800 | 40 | 40 | 1.2 | 460 |
| GH4169 | 8240 | 14 | | | 481 |
| Permanent magnet | 7500 | 7.6 | | | 460 |
| Aluminum | 2719 | 202.4 | | | 871 |

Table 2. The motor loss

| Stator copper loss (W) | Magnetic steel loss (W) | Iron loss (W) | Stray loss (W) | Sheath loss (W) | Total loss (W) |
|------------------------|-------------------------|---------------|----------------|-----------------|----------------|
| 170 | 22.8 | 444 | 90 | 171.7 | 898.5 |

sheath and permanent magnet. The high temperature of the thrust disc is caused by air friction, but the overall maximum temperature does not exceed 200 °C. The temperature limit of each component material can meet the design requirements. The temperature distribution trend shown in case2 is consistent with case1, which shows that the change of the inlet and outlet of the water channel has little effect on the temperature rise of the motor components. Case3 shows the temperature distribution cloud diagram without air cooling. It can be seen that the heating of the permanent magnet inside the closed motor becomes the main heat source, and the heat cannot be effectively distributed outside the environment. Therefore, the temperature of the permanent magnet and the sheath is very high, and the axial air flow can effectively cool the heat generated by the motor rotor.

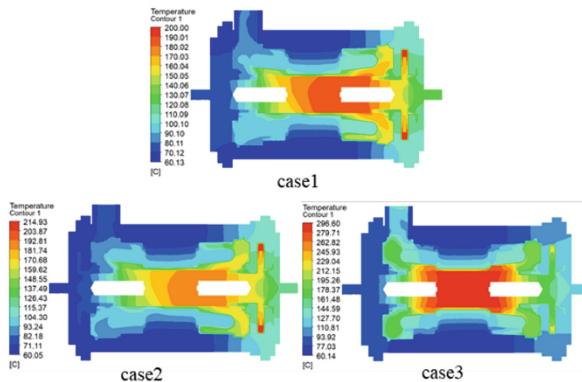


Fig. 9. The temperature distribution cloud of three cases, section $x = 0m$

In order to more clearly observe the temperature distribution of high-speed rotating parts such as shaft, sheath and thrust plate. Figure 10 shows the curve of the average temperature distribution along the axial direction of the motor rotor surface. It can be found that the axial temperature under the three cases is high in the middle and low on both sides. From the temperature rise at the thrust disc, it can be found that case1 is better than case2, and case3 has the worst cooling effect. The high temperature rise at the thrust plate is due to the large diameter design of the thrust plate, and the larger disc generates large friction loss at high rotation speed.

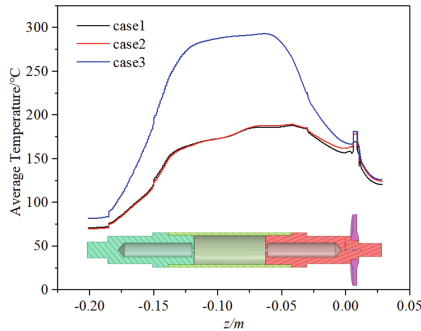


Fig. 10. The average temperature of the rotor surface is distributed along the axial direction in three cases.

5 Conclusion

It is effective to use computational fluid dynamics (CFD) method to calculate air friction damage. The air friction loss increases with the increase of axial cooling air flow rate, rotor rotation speed and wall roughness. However, when the speed is lower than 35000 r/min, the air friction loss can be ignored. The average temperature of the stator coil is reduced by 20.9% compared with that of the fully enclosed motor due to internal air cooling. In addition, because of the high temperature distribution of the thrust disc, it is necessary to increase the cooling of the thrust disc if the design conditions permit.

References

1. Gerada, D., Mebarki, A., Brown, N.L., Gerada, C.: High-speed electrical machines: technologies, trends, and developments. *IEEE Trans. Industr. Electron.* **61**(6), 2946–2959 (2013)
2. Zhang, F., Du, G., Wang, T., Liu, G.: Review on development and design of high speed machines. *Trans. China Electrotech. Soc.* (2016)
3. Wenguang, L.I., Feng, G.: Design and experimental study of centrifugal compressor in fuel cell vehicle. *Mechanika* **27**(1), 52–61 (2021)
4. Tenconi, A., Vaschetto, S., Vigliani, A.: Electrical machines for high-speed applications: design considerations and tradeoffs. *IEEE Trans. Industr. Electron.* **61**(6), 3022–3029 (2013)

5. Shen, J., Qin, X., Wang, Y.: High-speed permanent magnet electrical machines—applications, key issues and challenges. *CES Trans. Electri. Mach. Syst.* **2**(1), 23–33 (2018)
6. Gerada, D., Mebarki, A., Brown, N.L., Bradley, K.J., Gerada, C.: Design aspects of high-speed high-power-density laminated-rotor induction machines. *IEEE Trans. Industr. Electron.* **58**(9), 4039–4047 (2010)
7. Kolondzovski, Z., Sallinen, P., Arkkio, A.: Thermal analysis of a high-speed PM machine using numerical and thermal-network method. In: *The XIX International Conference on Electrical Machines-ICEM 2010*, pp. 1–6. September, IEEE (2010)
8. Sim, K., Lee, Y.B., Jang, S.M., Kim, T.H.: Thermal analysis of high-speed permanent magnet motor with cooling flows supported on gas foil bearings: part I-coupled thermal and loss modeling. *J. Mech. Sci. Technol.* **29**, 5469–5476 (2015)
9. Zhang, H., Yu, W., Hua, W.: Design and key technology of oil-free centrifugal air compressor for hydrogen fuel cell. *CES Trans. Electri. Mach. Syst.* **6**(1), 11–19 (2022)
10. Dong, J., et al.: Electromagnetic and thermal analysis of open-circuit air cooled high-speed permanent magnet machines with gramme ring windings. *IEEE Trans. Magn.* **50**(11), 1–4 (2014)
11. Wu, Z.P., Li, B.Z., Yang, J.G., Feng, R.J.: Steady-state thermal analysis and temperature control of high-speed permanent magnet synchronous motorized spindle. *Appl. Mech. Mater.* **44–47**, 1943–1947 (2010)
12. Hu, D., Liu, J., Yi, F., Yang, Q., Zhou, J.: Enhancing heat dissipation to improve efficiency of two-stage electric air compressor for fuel cell vehicle. *Energy Convers. Manage.* **251**, 115007 (2022)
13. Saari, J.: Thermal analysis of high-speed induction machines. Helsinki University of Technology (1998)
14. Huang, Z., Fang, J., Liu, X., Han, B.: Loss calculation and thermal analysis of rotors supported by active magnetic bearings for high-speed permanent-magnet electrical machines. *IEEE Trans. Industr. Electron.* **63**(4), 2027–2035 (2015)
15. Yamada, Y.: Torque resistance of a flow between rotating co-axial cylinders having axial flow. *Bulletin of JSME* **5**(20), 634–642 (1962)
16. Kadivar, M., Tormey, D., McGranaghan, G.: A review on turbulent flow over rough surfaces: fundamentals and theories. *Int. J. Thermofluids* **10**, 100077 (2021)
17. Boscaglia, L., Boglietti, A., Nategh, S., Bonsanto, F., Scema, C.: Numerically based reduced-order thermal modeling of traction motors. *IEEE Trans. Ind. Appl.* **57**(4), 4118–4129 (2021)
18. Jokinen, T., Hrabovcova, V., Pyrhonen, J.: In: *Design of Rotating Electrical Machines*. Wiley (2013)



PEMFC Seal Design and Optimization by Taking into Account of Gasket Shape Profile and Stack-Up Assembly Tolerance

Zhicheng Cao¹, Wenfeng Zhu¹(✉), Zhiguo Cheng², Zhen Yang¹, and Yue Fang¹

¹ School of Mechanical Engineering, Tongji University, 201804 Shanghai, People's Republic of China

zhuwenfeng@tongji.edu.cn

² Legend New Energy Technology Co., Ltd, 201805 Shanghai, People's Republic of China

Abstract. Stable seals are essential for the safe operation of the PEMFC. However, manufacturing errors of PEMFC components and assembly errors during assembly process often result in great variability in PEMFC sealing performance. This study investigates the relationship between stack-up assembly tolerances and profile tolerances of sealing gasket surface on PEMFC leakage rates during assembly process. A tolerance analysis was first carried out to determine the relationship between stack-up assembly tolerances and section alignment errors, and the relationship between gasket surface profile tolerances and gasket section errors. Finite element and Roth models were then used to investigate the relationship between manufacturing errors and leakage rates. The results show that assembly errors have a significant effect on the leakage rate and there is a linear increasing relationship between height error and leakage rate; on the other hand, an increase in the width error leads to a linear decrease in the leakage rate. The method clearly shows the relationship between the manufacturing tolerances of seals and bipolar plates and the leakage rate of the PEMFC, providing an important theoretical basis for the design of tolerances of seals and bipolar plates.

Keywords: Sealing · Stack assembly · Profile of sealing gasket surface · Tolerance analysis · Proton exchange membrane fuel cell

1 Introduction

Ultra-thin metal bipolar plates (BPPs), multi-layer polymer membrane electrode assemblies (MEAs) and precision sealing gaskets are the core components of a hydrogen fuel cell [1–3]. A high-power Proton Exchange Membrane Hydrogen Fuel Cell (PEMFC) is composed of 400–500 individual cells to meet the high-power demands of vehicles as showed in Fig. 1. Sealing gaskets are compressed by ultra-thin metal BPPs and MEA frames to form a rigid-flexible heterogeneous complex contact sealing interface. Precision and stable sealing is a significant prerequisite for the safe operation of a PEMFC and an important aspect in assessing the quality of the assembly as well [1, 4].

During the stamping and welding of bipolar plates, as well as during the rubber molding process, dimensional and positional errors are unavoidable [5]. Different degrees of misalignment will occur between the polar plates due to the superposition of dimensional and shape errors; the actual surface profile of the sealing gaskets may also deviate slightly from the ideal elements [5–10]. Barzegari et al. [11] evaluated key parameters in the stamping process and controlled the maximum error uniformity of the channel depth to within 2.9% with an improved stamping process. Tran et al. [12] proposed a new die design based on a multi-stage stamping process, which significantly improved the formability of ultra-thin BPP and achieved a more uniform thickness distribution and less rebound. Qiu et al. [13] investigated the relationship between shape error and GDL contact stress distribution and gave an acceptable range of shape error.

Under the coupling effect of these manufacturing errors, the heterogeneous contact interface cannot produce adequate interfacial elastic contact stress and contact area that may cause the PEMFC stack to have a higher rate of leakage than the ideal design, so that the design of high reliability seals for hydrogen fuel cells must consider the coupling effects of shape tolerances of metal polar plates and gaskets, and assembly tolerances of the PEMFC stacks. However, the geometry of the seal section has been optimized in conventional seal designs based on ideal assembly [4] and do not accurately account for the influence of cross-sectional shape tolerances and assembly tolerances on sealing performance.

The aim of this research is to analyze the effect of stack-up assembly tolerances and gasket surface profile tolerances on interface leakage rates and provide an important theoretical basis for the optimization of the tolerance design of seals and bipolar plates. Firstly, the tolerance zones for the assembly of bipolar plates under stack-up lamination and the tolerance zones for the surface profile of sealing gaskets is analyzed. Secondly, the effect of the coupling of different misalignment and profile deviations of sealing gasket surface on the leakage rate was investigated using finite element and Roth models. Finally, reasonable tolerance design recommendations are given based on a comprehensive consideration of the negative impact of increased accuracy on manufacturing costs.

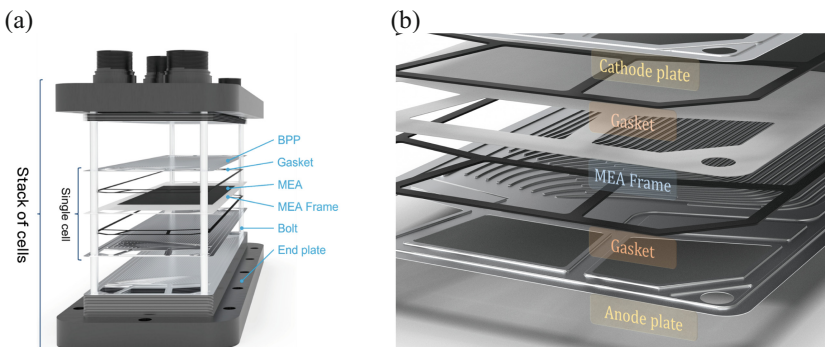


Fig. 1. Composition and structure of a PEMFC: (a) PEMFC stack and (b) single cell.

2 Methodology

The schematic plot of the methodology is shown in Fig. 2, which is composed of the following three steps:

- (1) Analyzing the principle of coupling assembly tolerances of the stack and shape profile tolerance of sealing section, obtain tolerance design ranges for the cross-sectional dimensions of metal bipolar plates and sealing gaskets.
- (2) A numerical simulation model for the sealing contact of dissimilar materials of metal bipolar plates and non-metallic sealing gaskets is then developed to calculate the contact stress and the contact area at the seal interface for a variety of assembly tolerances and profiles of the surface. The interface leakage rate is also calculated based on the Roth model.
- (3) The design of the hydrogen fuel cell sealing parameters, taking into account the cross-sectional profile and assembly tolerances, was obtained by considering the cost of tolerance design and the assembly process for the evaluation of the leakage rate.

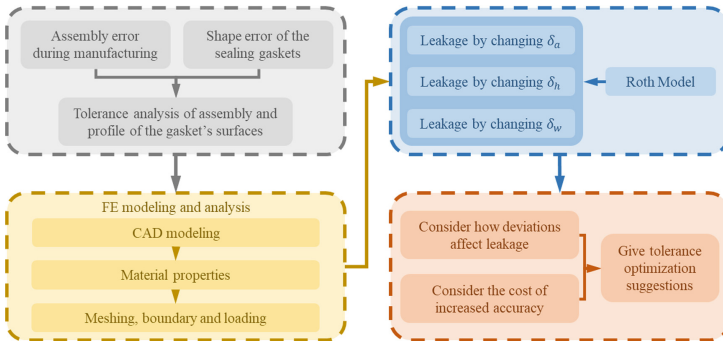


Fig. 2. Schematic diagram of the methodology

3 Tolerance Analysis and Numerical Simulation

3.1 Analysis of Assembly Tolerance Zones and Sealing Gasket Surface Profile Tolerance Zones

The tolerances of the bipolar plate assembly holes are shown in Fig. 3(a) according to a particular type of bipolar plate. The dimensional tolerances of the assembled shaft are $\phi 12_{-0.014}^0$, and the assembly tolerance zone is calculated using the following formula:

$$\begin{aligned} D_{ft} &= D_{LVh} - D_{LVb} = (D_{Lh} + t) - D_{Lb} \\ &= (12 + 0.036 + 0.15) - (12 - 0.014) = 0.2 \end{aligned} \quad (1)$$

where: D_{LVh} is the least material virtual size of assembly hole, D_{LVb} is the least material virtual size of assembly shaft, D_{Lh} is the least material size of assembly hole, D_{Lb} is the least material size of assembly shaft.

Variation of the gasket alignment error δ_t on the bipolar plate cross section from 0 mm to 0.2 mm according to the assembly tolerance zone, as shown in Fig. 3(b).

The sealing gasket has a semi-circular cross-section. The semi-circular sealing surface in contact with MEA frame, and the profile tolerance of semi-circular surface is 0.05mm, as shown in Fig. 3(b). Assumption of a continuous curve in the cross-sectional profile of the gasket, height deviation of the sealing gasket δ_h varies within ± 0.025 mm, and width deviation of the sealing gasket δ_w varies within ± 0.05 mm.

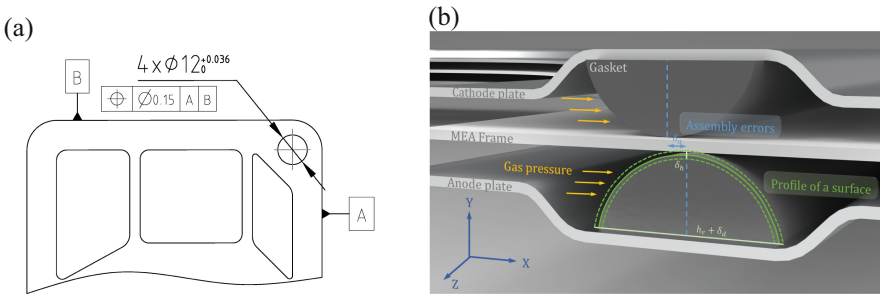


Fig. 3. Tolerance analysis diagram: (a) bipolar plate assembly hole tolerance and (b) misalignment and profile errors of sealing gasket surface.

3.2 Material Properties

The sealing gaskets used for the calculations are made of silicone rubber. Silicone rubber is a super-elastic material that is virtually incompressible. A 5-parameter Mooney-Rivlin model was used to better describe the mechanical properties of silicone rubber under compression. The strain energy density function for the 5-parameter Mooney-Rivlin model is shown below:

$$W = c_{10}(\bar{I}_1 - 3) + c_{01}(\bar{I}_2 - 3) + c_{11}(\bar{I}_1 - 3)(\bar{I}_2 - 3) + c_{20}(\bar{I}_1 - 3)^2 + c_{02}(\bar{I}_2 - 3)^2 + \frac{1}{D_1}(J - 1)^2 \tag{2}$$

where: W is strain energy density; $c_{01}, c_{10}, c_{11}, c_{02}, c_{20}$ is Mooney-Rivlin model coefficients; \bar{I}_1 and \bar{I}_2 are the first and second bias strain invariants, J is elastic volume ratio, $\bar{I}_1 = \lambda_1^2 + \lambda_2^2 + \lambda_3^2$, $\bar{I}_2 = \lambda_1^2\lambda_2^2 + \lambda_2^2\lambda_3^2 + \lambda_1^2\lambda_3^2$.

The parameters of the rubber Mooney-Rivlin model and the specific coefficients for the MEA frame material are shown in Table 1.

3.3 Assembly Model and Boundary Conditions for Sealing Analysis

Compression of PEMFC seals is typically a non-linear process involving material non-linearity, geometric non-linearity and contact non-linearity. In this thesis, the commercial

Table 1. Material of the components in the model

| | | | | | | |
|-----------|-----------------------|-------|-------|-----------------|-------|----|
| Gaskets | C10 | C01 | C20 | C11 | C02 | D1 |
| | -2.687 | 3.774 | 0.303 | -1.385 | 2.553 | 0 |
| MEA frame | Elastic modules (MPa) | | | Poisson's ratio | | |
| | 1200 | | | 0.3 | | |
| BPPs | Elastic modules (MPa) | | | Poisson's ratio | | |
| | 2.1×10^5 | | | 0.3 | | |

finite element software ANSYS is used for the non-linear calculations. The ideal geometric model and its specific parameters are given in Fig. 4(a) and Table 2. Implicit format is used in implicit format, and the element type is Plane183. As shown in Fig. 4(a), there are four contact surfaces in the sealing structure of the PEMFC. These are labelled I1, I2, I3 and I4. Conta172 and Targe169 elements are used on all contact surfaces. In addition, to minimize penetration at the contact interface, the normal Lagrange contact algorithm was used with a coefficient of friction of 0.1.

The boundaries are applied as shown in Fig. 4(b). A symmetrical boundary is placed on the left side of the MEA frame. The load step is applied in a two-step process. In the first step, a displacement load is applied along the y-axis on both sides of the bipolar plate to precisely control the compression rate of the seal, and the compression rate of the gaskets increase linearly from 0% to 20%. In the second step, the gas pressure load is linearly applied to the same side of the sealing gaskets from 0MPa to 0.16MPa. This type of load application is equivalent to the actual assembly procedure of compression followed by a pressure test.

Figure 4(c) shows the finite element simulation results of the ideal seal geometry for the 0.2 mm assembly error after the above steps.

4 Results and Discussions

4.1 Roth Model

Leakage occurs in two main ways, firstly by permeation due to the presence of pores between the molecules of the material through which the gas passes, and secondly between the contact surfaces. Roth. A suggests that leakage between contact surfaces is due to the presence of micron-scale leakage channels between two contacting surfaces, through which gases leak from the higher-pressure side to the lower pressure side [14]. As a result, Roth proposes a model to assess the leakage rate at the interface, establishing a relationship between the leakage rate and other variables, as shown in Eq. 3.

$$Q = C \Delta_p \approx 4 \sqrt{\frac{T}{M}} A^2 \frac{L}{w} e^{-\frac{3P}{K}} \Delta_p \quad (3)$$

where, C is leakage coefficient at seal interface; Δ_p is differential pressure of hydrogen on both sides of the gasket; P is contact stress on the contact surface; L is the length of contact surface; w is the width of contact surface; T is absolute temperature of the gas;

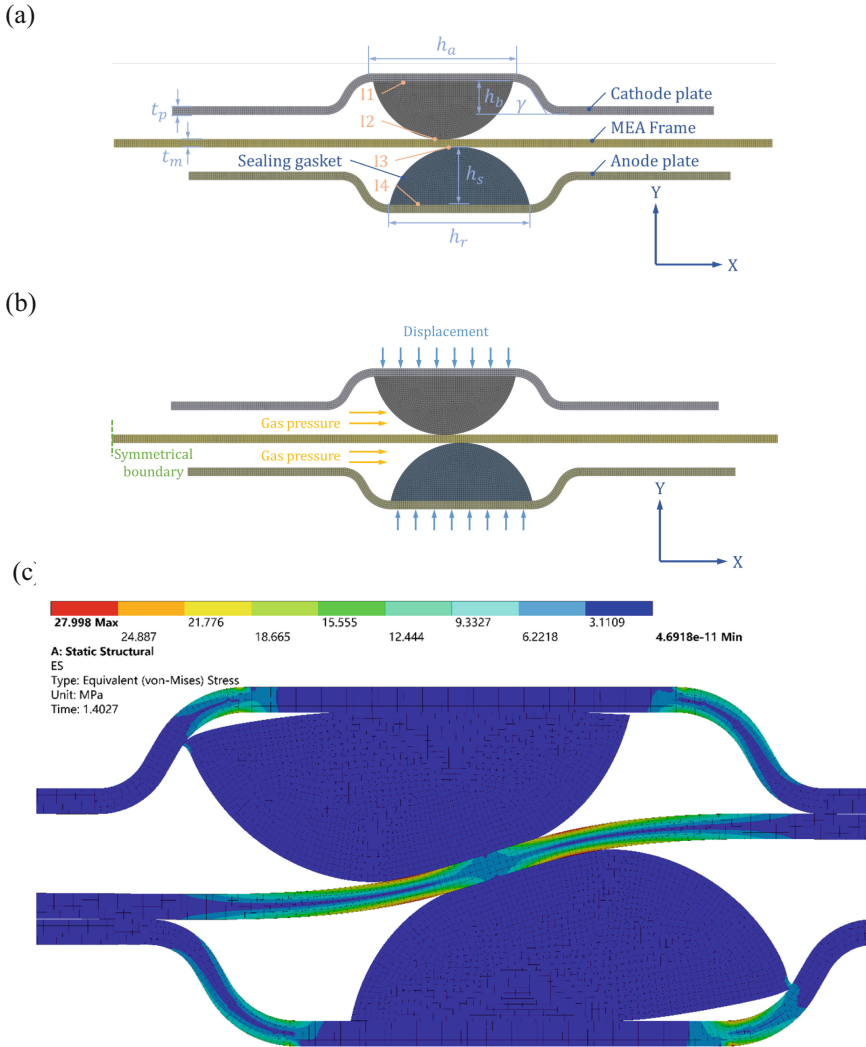


Fig. 4. Geometric model, finite element boundary conditions and calculation results: (a) Two-dimensional model of the sealing structure, (b) Finite element model boundary conditions and (c) Finite element calculation results.

M is relative molecular mass of a gas; A is roughness of contact surfaces; R is sealing coefficient. The relationship between the sealing factor R and the contact stress P is shown in Eq. 4.

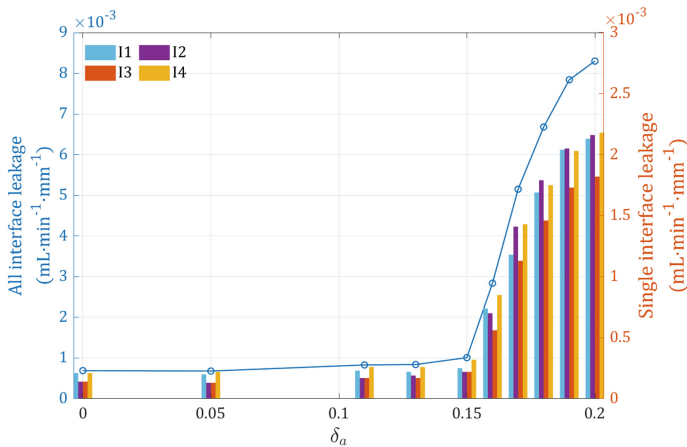
$$\frac{P}{R} = -\ln\left(\frac{h}{h_0}\right) \quad (4)$$

Table 2. The simulation parameters of geometry model

| h_a (mm) | h_b (mm) | h_r (mm) | h_s (mm) |
|------------|------------|-----------------------|------------|
| 2.0 | 0.4 | 1.7 | 0.7 |
| t_p (mm) | t_m (mm) | γ ($^\circ$) | – |
| 0.1 | 0.1 | 60 | – |

4.2 Influence of Assembly Errors on Leakage Rate and Tolerance Optimization

This study evaluates the effect on leakage rates of various assembly errors. According to the tolerance analysis in Sect. 3, the range of alignment errors at specified assembly tolerance is between 0 mm and 0.2 mm. In order to quantitatively analyze the effect of alignment errors on the leakage rate, several δ_a between 0 mm and 0.2 mm were selected for $\delta_h = \delta_w = 0$, as shown in Fig. 5, and found that as the misalignment increased, the leakage rate of individual sealing surfaces increased, as did the total leakage rate of the entire sealing section. The total leakage rate of the seal section increases slowly with increasing misalignment when the misalignment is less than 0.15 mm. In this case, the contact stress at the two semicircular sealing interfaces I_2 and I_3 is slightly higher than at I_1 and I_4 , so the leakage rate is also slightly lower. When the alignment error exceeds 0.15 mm, the total leakage rate of the seal section tends to increase rapidly with the alignment error. This is due to the fact that when the alignment error exceeds 0.15 mm, the sealing gasket slips more, this coupled with the gas pressure causes the cathode plate seal gasket to slip more than the anode seal, resulting in a progressively larger single interface leakage rate for I_1 and I_2 than for I_3 and I_4 . When the seal gasket is perfectly aligned, the total leakage rate is reduced by 31% compared to an alignment error of 0.15 mm. When the alignment error increases to 0.2 mm, the leakage rate increases by nearly an order of magnitude compared to the fully aligned case.

**Fig. 5.** The effect of assembly errors on the leakage rate

So, based on the relationship between the total leakage rate of the seal section and the alignment error, the assembly tolerance zone should be kept within 0.15 mm for safe operation of the PEMFC, taking into account the negative impact of increased accuracy on manufacturing costs.

4.3 Influence of Profile of Gaskets Surface on Leakage Rate

In order to analyze the effect of profile error of sealing gasket on the leakage rate, the effect of sealing gasket width error and height error on the leakage rate was observed at an assembly error of 0.2 mm. Figure 6(a) shows the effect of height error on the leakage rate. The leakage rate increases linearly with height error when the width is kept at 1.7 mm. With the sealing gasket height of 0.725 mm, the leakage rate increases by approximately 15% compared to 0.675 mm. This may be due to the fact that increasing the height of the sealing gasket results in a lower compression rate for the same displacement, resulting in lower contact stresses. The increased height also results in a greater curvature of the semi-circular surface profile of the rubber gasket. If the coefficient of friction remains constant, greater surface curvature may allow the gasket to slip further, resulting in greater leakage.

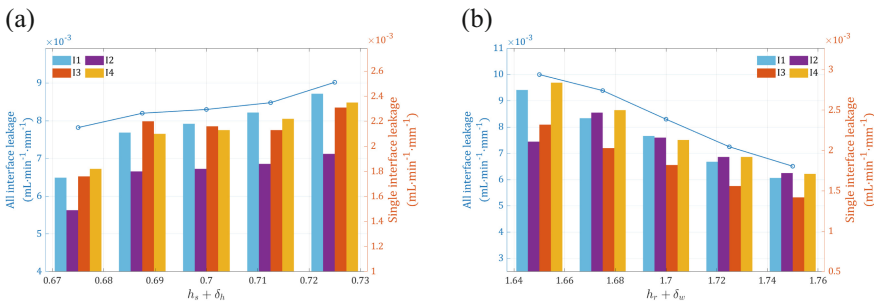


Fig. 6. The effect of profile errors of sealing gasket on the leakage rate: (a) width errors on the leakage rate and (b) height errors on the leakage.

Figure 6(b) shows the effect of sealing gasket width on the leakage rate. If the height of the seal is kept at 0.7 mm, the leakage rate decreases linearly with increasing width. Compared to the ideal profile, the total section leakage rate increases by 20% and decreases by 21% for section widths of 1.65 mm and 1.75 mm respectively. This may be because increasing the width of the gasket increases the contact area at the seal interface and, according to Roth model, a larger contact area results in a lower leakage rate. Also, for a given height, the greater width results in a greater curvature of the semicircular surface profile of the rubber gasket, resulting in a lower leakage rate.

5 Summary and Conclusion

In this study, to investigate the effect of PEMFC stack-up assembly errors and gasket shape errors on leakage rates, tolerance analysis is first performed to determine the assembly tolerance zone of the bipolar plate and the face profile tolerance zone of the

sealing gasket. Finite element models are then built to obtain the contact stress and contact area of the gasket under different errors, based on the size of the tolerance zone, and the Roth model is used to establish the relationship between the leakage rate and the face profile and assembly error. Results of the study show that:

- (1) When the alignment tolerance of the bipolar plate is between 0 and 0.15 mm, the leakage rate continues to increase slowly with the alignment error, and when the alignment error of the bipolar plate exceeds 0.15 mm, the increase in the alignment error causes the leakage rate to increase significantly.
- (2) Within the profile tolerance of the rubber gasket surface, the leakage rate rises linearly with increasing height error, and the leakage rate decreases linearly with increasing width error. The effect of the profile of the rubber gasket surface on the total leakage rate of the section is less than the effect of an alignment error of more than 0.15 mm on the leakage rate.
- (3) Based on the relationship between the alignment error and the profile of the rubber gasket surface on the section leakage rate, the tolerance optimization recommendation given is that the assembly tolerance band should be kept within 0.15 mm.

Therefore, manufacturing and assembly errors that occur during the manufacturing process are important factors that affect the leakage rate of the PEMFC. The numerical simulation of the seal contact and seal compression process reveals the quantitative relationship between profile error of sealing gasket surface and bipolar plate assembly error and PEMFC leakage rate, providing an important theoretical basis for the tolerance design of seals and bipolar plates.

Acknowledgements. This study was supported by cooperative project of Tongji University—Legend New Energy Technology Co., Ltd Collaborative Research Project (LZDD230121-M). The authors also appreciate the help of Dr. Zhiguo Cheng to improve the paper.

References

1. Qiu, D., Peng, L., Yi, P., et al.: Review on proton exchange membrane fuel cell stack assembly: quality evaluation, assembly method, contact behavior and process design. *Renew. Sustain. Energy Rev.* **152** (2021)
2. Pourrahmani, H., Siavashi, M., Yavarinasab, A. et al.: A review on the long-term performance of proton exchange membrane fuel cells: from degradation modeling to the effects of bipolar plates, sealings, and contaminants. *Energies* **15** (2022)
3. Sharaf, O.Z., Orhan, M.F.: An overview of fuel cell technology: fundamentals and applications. *Renew. Sustain. Energy Rev.* **32**, 810–853 (2014)
4. Liang, P., Qiu, D., Peng, L., et al.: Structure failure of the sealing in the assembly process for proton exchange membrane fuel cells. *Int. J. Hydrogen Energy* **42**, 10217–10227 (2017)
5. Peng, L., Yi, P., Lai, X.: Design and manufacturing of stainless-steel bipolar plates for proton exchange membrane fuel cells. *Int. J. Hydrogen Energy* **39**(36), 21127–21153 (2014)
6. Liu, Q., Lan, F., Zeng, C., et al.: A review of proton exchange membrane fuel cell's bipolar plate design and fabrication process. *J. Power Sour.* **538**, 231543 (2022)

7. Kolahdooz, R., Asghari, S., Rashid-Nadimi, S., et al.: Integration of finite element analysis and design of experiment for the investigation of critical factors in rubber pad forming of metallic bipolar plates for PEM fuel cells. *Int. J. Hydrogen Energy* **42**(1), 575–589 (2017)
8. Jin, C.K., Jeong, M.G., Kang, C.G.: Fabrication of titanium bipolar plates by rubber forming and performance of single cell using TiN-coated titanium bipolar plates. *Int. J. Hydrogen Energy* **39**(36), 21480–21488 (2014)
9. Nawi, I.N., Fadhali, M., Hussain, M.S., et al.: Nd: YAG laser welding of stainless steel 304 for photonics device packaging. *Proc. Eng.* **8**, 374–379 (2011)
10. Ventrella, V.A., Berretta, J.R., De Rossi, W.: Pulsed Nd: YAG laser seam welding of AISI 316L stainless steel thin foils. *J. Mater. Process. Technol.* **210**(14), 1838–1843 (2010)
11. Barzegari, M.M., Khatir, F.A.: Study of thickness distribution and dimensional accuracy of stamped metallic bipolar plates. *Int. J. Hydrogen Energy* **44**(59), 31360–31371 (2019)
12. Tran, M.T., Lee, D.H., Lee, H.W., et al.: Formability improvement in multi-stage stamping of ultra-thin metallic bipolar plate for proton exchange membrane fuel cell. *Int. J. Hydrogen Energy* **47**(94), 40008–40025 (2022)
13. Qiu, D., Yi, P., Peng, L., et al.: Study on shape error effect of metallic bipolar plate on the GDL contact pressure distribution in proton exchange membrane fuel cell. *Int. J. Hydrogen Energy* **38**, 6762–6772 (2013)
14. Roth, A.: In: *Vacuum Sealing Techniques*. Springer Science & Business Media, (1994)



Research on the Scale Coefficient in the Interface Leakage Rate Multi-scale Model and the Performance Study of the Gasket-BPP Sealing Interface in PEMFCs

Zhen Yang¹ , Wenfeng Zhu^{1,1}  , Zhiguo Cheng², and Zhicheng Cao¹ 

¹ School of Mechanical Engineering, Tongji University, Shanghai 201804, People's Republic of China

zhuwenfeng@tongji.edu.cn

² Legend New Energy Technology (Shanghai) Co., Ltd, Shanghai 201805, People's Republic of China

Abstract. The existing of rough asperities on the surfaces of rubber Gaskets and metal BPPs at microscopic scales is the basic reason why the gas leaks from the sealing interface. Characterizing the non-smooth asperities of the sealing interface is crucial to realize the calculation and analysis of the leakage rate. But the microscopic features are strongly related to the observation scale, so the multi-scale interface leakage prediction model is established to exclude the negative influence on modeling micro-scale rough surfaces of a single observation scale. In this paper, the scale coefficient in the multi-scale model is studied to improve the accuracy of the interface leakage rate multis-scale model by analyzing the linear relationship between the interface leakage rate and the volume of the leakage channel. Continuously based on the multi-scale model which maintains the studied scale coefficient, the interface leakage rates of different Gasket-BPP sealing structures are investigated. And the reliability and accuracy of the multi-scale model are verified by comparing to the traditional interface leakage model.

Keywords: Gasket-BPP sealing · Interface leakage · Multiscale · Scale coefficient

1 Introduction

As a substitute for traditional fossil fuels, hydrogen energy has the advantages of renewable, zero pollution, and sustainable development [1]. Proton exchange membrane fuel cells (PEMFCs) are an important device for converting hydrogen into electrical energy. PEMFC is mainly composed of bipolar plates (BPP), membrane electrode assembly (MEA), seal gaskets, and other auxiliary components, which is shown in Fig. 1.

It is necessary to ensure that the internal reaction space is pure, clean, and kept at a certain pressure when the PEMFC is working. However, since the surface of any object in nature will inevitably show non-smooth characteristics if being enlarged, the interface

leaking from the gap between the rubber gasket and the metal BPP sealing interface at the micro-scale is unavoidable. Researching the leaking mechanism of the sealing interface at the micro-scale can essentially ascertain the cause of seal failure, predict and control the leakage rate, and effectively improve the safety and reliability of PEMFCs.

In a PEMFC, the value of the leakage rate of the Gasket-BPP sealing interface is extremely small [2], so it is difficult to be measured by experiments. And it is important to establish an accurate mathematical model to evaluate the interface leakage rate of the Gasket-BPP interface. In this paper, the failure and the leaking behavior of the Gasket-BPP sealing interface are studied, and the multi-scale prediction model of interface leakage rate is improved by solving the scale coefficient. Based on the multi-scale model the quantitative calculation of the interface leakage rate is realized, and the leakage rates of different PEMFC sealing structures are calculated and compared.

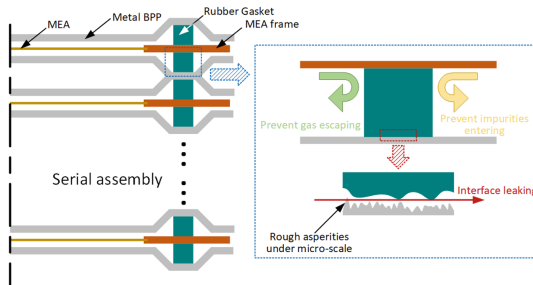


Fig. 1. The sealing structure of a PEMFC and the interface leaking

1.1 Macroscopic Study on the Performance of Sealing Interface

Macro-mechanical research is an intuitive approach to analyzing the sealing performance of PEMFCs [3, 4]. Researchers have established several mathematical models between macroscopic mechanical characteristics such as contact pressure, contact length, internal stress of gaskets and interface sealing performance by a large number of experimental data and engineering practices [5–7]. Kim et al. [4] established a fuel cell stack model that can contain different numbers of cells to analyze the relationship between the number of cells and the sealing contact pressure. In addition, researchers have analyzed the stress distribution characteristics of a single gasket and solved the stress concentration problem to improve the average sealing capability by optimizing the structure of gaskets. For example, Qiang et al. [8] studied the characteristics of the contact pressure and internal stress of gaskets in PEMFC stacks under different packaging loads and analyzed the interface leakage rate and cross-sectional leakage rate of a sealing structure by studying mechanical parameters. Dong et al. [9] studied the differences in sealing forces of fuel cells, which are in different positions of a PEMFC stack.

Based on the macroscopic mechanical behavior research of gaskets in PEMFCs, it can be easily realized to design and optimize the sealing structure of PEMFCs. But this qualitative method cannot fundamentally explain the reasons for sealing failure and

leaking of Gasket-BPP interfaces, and cannot realize the detection of leaking points and the prediction of PEMFC reliability.

1.2 Leaking Study of Gasket-BPP Interface by Single-Scale Methods

The macroscopic mechanical characteristics of the gaskets are affected by their own material properties and contact behavior at the microscopic scale. A surface in nature is going to show non-smooth characteristics if it is enlarged to a microscopic scale.

Based on the G-W model, Peng researched the contact behavior of the Gasket-BPP interface at the microscopic scale and analyzed and predicted the interface leakage rate [10]. Ren Xiao optimized the Reynolds equation of gas flow under the influence of a rough surface and established a correction method for the gas flow factor under the anisotropic surface [11].

The numerical simulation method is also applied in the research on the calculation of the leakage rate of the Gasket-BPP sealing interface in PEMFCs. For example, Huang researched and improved the accuracy of the correction factor in the leakage prediction model by analyzing the gas leaking between two Gaussian random rough surfaces at a single scale [12]. Based on the Roth theory, Lu simplified the Gaussian rough surface into a flat surface with triangular convex peaks and established the 3D model of the interface leaking channel [13].

1.3 Multi-scale Modeling of Gasket-BPP Interface Leakage Rate

The microscopic asperities of the Gasket-BPP sealing interface are able to affect the microscopic contact behavior of the two rough surfaces, which determines the size of the interface leakage channel and the interface leakage rate. Therefore, it is important to character the microscopic asperities accurately of the Gasket-BPP sealing interface for calculating the interface leakage rate. In traditional research, the parameters of the microscopic non-smooth features are closely related to the equipment resolution and sampling accuracy at the observation scale, and it is difficult to establish the rough surface accurately at a single scale.

In order to exclude the above problem, the multi-scale model of the interface leakage rate has been studied. Persson believes that the rough surface topography has self-affine and self-similar characteristics and establishes a full-contact analysis model [14]. SHI et al. used the wavelet method to filter the microscopic roughness of the metal surface and analyzed contact behavior at a series of micro-scales [15]. Our group described the sealing rough interface based on fractal theory and the leakage multi-scale model was established [16].

Multi-scale models have the capability to exclude the negative influence of the observation scale on the leakage rate prediction results. In current multi-scale research, it could analyze the influence of scales on sealing performances. But there is seldom research that converges the interface leakage rates to the actual result, so it is hard to compare the theoretical analysis results with the experimental data. In response to the above problem, the scale coefficient in the multi-scale model will be discussed in this paper (as shown in Fig. 2) to improve the prediction accuracy. And the precision of the multi-scale model with the studied coefficient has been verified.

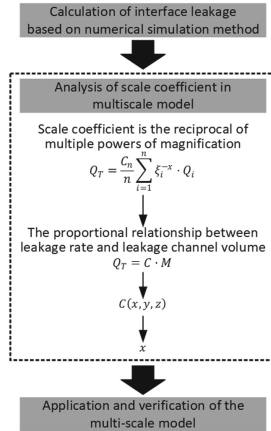


Fig. 2. The approach to study the scale coefficient in the multi-scale model

2 Methods and Processes

2.1 Calculation of Gasket-BPP Interface Leakage Rate by Numerical Simulation

In the previous research [16], a method for calculating the leakage rate of the PEMFC sealing interface through numerical simulation has been established. And it is used in this paper to calculate the interface leakage rate of Gasket-BPP sealing.

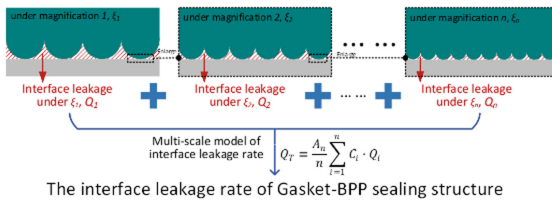


Fig. 3. The principle of the interface leakage multi-scale model

2.2 Research on the Scale Coefficient in the Multi-scale Model

Obviously, the multi-scale leakage rate of the PEMFC interface should be the weighted sum of the interface leakage rates at each scale, which is shown in Fig. 3, specifically expressed as follows:

$$Q_T = \frac{A_n}{n} \sum_{i=1}^n C_i \cdot Q_i \tag{1}$$

where the Q_T is the prediction result of the interface leakage rate by multi-scale model, the A_n is the correction factor to exclude the deviation of the calculation result, the n

is the number of scales in the multi-scale model, Q_i is the interface leakage rate at a single scale, and the C_i is the scale coefficient. And in the previous research, the C_i is calculated by the magnification ξ :

$$C_i = \xi_i^{-x} \tag{2}$$

It can be seen that the power, x , of the magnification is the key coefficient of the scale coefficient. In order to find out the value of x , the proportional relationship between the interface leakage rate Q and the interface leaking volume M is used, which can be shown as:

$$Q_T = C \cdot M \tag{3}$$

where C is a constant number with dimension, the M is the total interface leakage channel volume, it can be written as:

$$M = \sum_{j=1}^n C_j \cdot M_j^y \tag{4}$$

where the M_j is the interface leakage channel volume at a single scale, and the C_j is the average coefficient of M .

It can be seen that the total M of the multi-scale model is related to two factors. The first one is the power of the M_j , as the y shown above, like some traditional theories, which is able to improve the accuracy of the model. For example, in the Roth model, the total interface leakage channel volume is proportional to the 4th power of the channel height after the compression and in the parallel plate gap flow theory, the volume is related to the 3rd power of the plate gap height. The second factor is the magnification, which is like the function Q . And the Eq. (3) can be written as:

$$\sum_{i=1}^n \xi_i^{-x} \cdot Q_i = C \cdot \sum_{j=1}^n \xi_i^{-z} \cdot M_j^y \tag{5}$$

And there is a function $C(x, y, z)$ can be established:

$$C(x, y, z) = C = \sum_{i=1}^n \xi_i^{-x} \cdot Q_i / \sum_{j=1}^n \xi_i^{-z} \cdot M_j^y$$

Based on the discussion above, the function $C(x, y, z)$ should be horizontal in a coordinate system because the C is a constant. That means the values of x , y , and z should make the function $C(x, y, z)$ as a horizontal line whatever the values of the Q_i and the M_m , which is the basis to study the value of x and the scale coefficient C_i in the multi-scale model of the interface leakage rate.

The values of z and y are discussed first, because the both factors are in the denominator at the same time with a close relationship. From the Fig. 4a)-b), it can be seen the curves of M under different z values remain parallel when the y remains unchanged, which means that the value of z will not affect the trend of the calculation results on the right side of the Eq. (5). To the $C(x, y, z)$ calculated by the ratio, the value of z will not

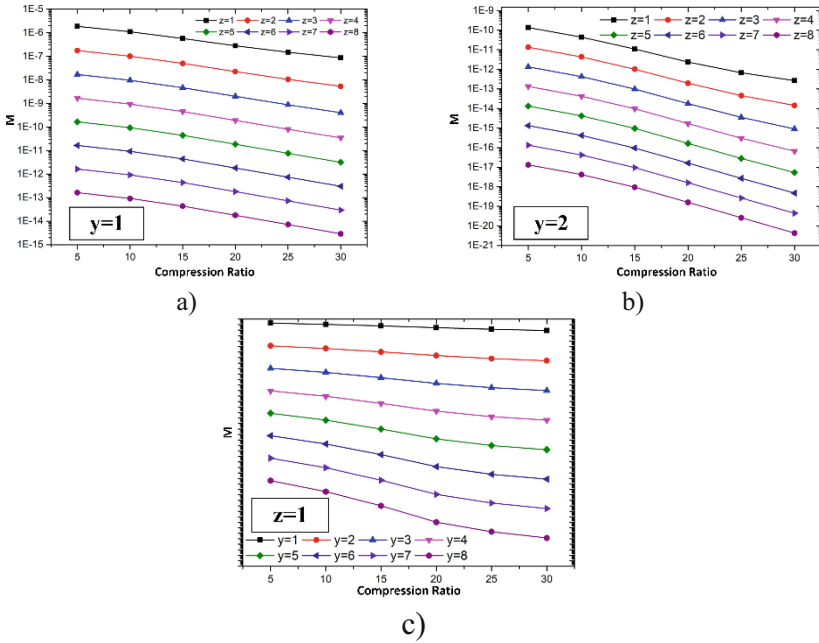


Fig. 4. The influence of the values of y and z on the interface leakage volume M : a) $y = 1$, b) $y = 2$, and c) $z = 1$

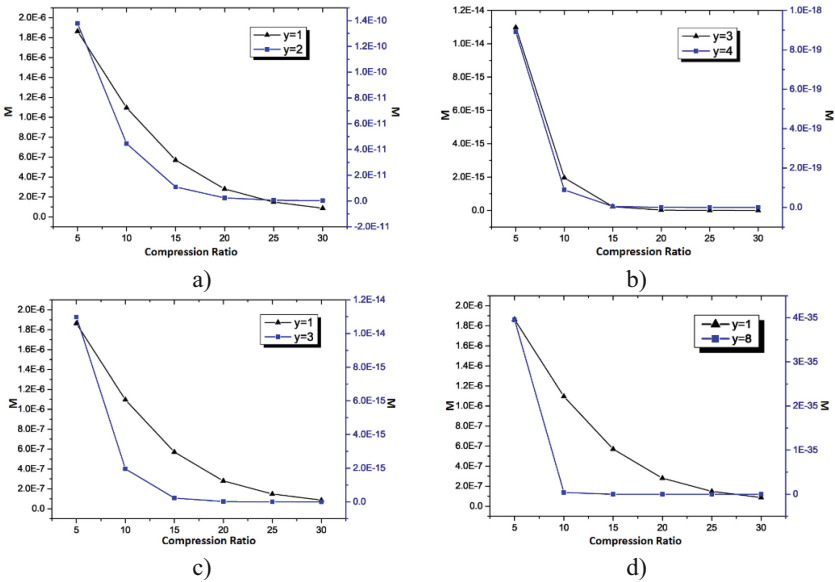


Fig. 5. The influence of y on the curves of M when $z = 1$

determine the function is horizontal or not. But as shown in Fig. 4c), the value of y has an obvious influence on the horizontal feature of $C(x, y, z)$, and affecting the value of x and the scale coefficient C_i in the multi-scale model. It is necessary to further study the y to increase the reliability of the scale coefficient.

Based on the proportional relationship between the Q and M , it could be realized that determining the value of y . In Fig. 5a), it can be seen that when the value of y changes from 1 to 2, the trend of the M curve in $C(x, y, z)$ changes, which proves that the $C(x, y, z)$ could not be horizontal constantly if $y = 2$. On the contrary, it can be seen from Fig. 5b) that the trends of two M curves are similar, which means when $y > 3$, the trend of the M will no longer change sharply. To further verify the selection of the value, there are the comparisons between different curves of the M based on the non-linear feature of the M which is generated by the non-linear characteristics of the geometry, the materials, and the contacting. In Fig. 5c), it can be seen the curve keeps the non-linear well if $y = 3$, and that is becoming to be non-smooth if the value of y is hugely large as shown in Fig. 5d). And it is hardly to reflect the non-linear feature of the interface leakage volume M .

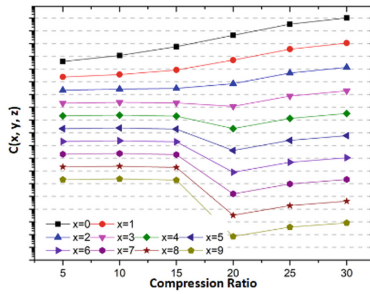


Fig. 6. The curves of M under different values of z

After selecting the values of z and y , it can determine the x by analyzing the horizontal feature of the function $C(x, y, z)$. Figure 6 shows the M curves with different values of x . It can be considered that the constant C will be more stable if the curve of $C(x, y, z)$ is more horizontal in the coordinate system, and the scale coefficient C_i can be more accurate for calculating the interface leakage rate of Gasket-BPP sealing by the multi-scale model.

Based on the above analysis, by establishing the function $C(x, y, z)$ it can obtain the interface leakage rate multi-scale model with the studied scale coefficient:

$$Q_T = \frac{A_n}{n} \sum_{i=1}^n \xi_i^{-4} \cdot Q_i$$

2.3 The Prediction of the Gasket-BPP Sealing Interface Leakage Rate Based on the Multi-scale Model

The sealing structures of the Gasket-BPP in PEMFCs are multifarious, and two sealing structures with different kinds of cross-sections, as shown in Fig. 7, are studied and compared in this paper.

It can be seen that in Fig. 8, the maximum contact pressures are close but the distributions are significantly different. On the semicircle Gasket, the top value of the contact pressure appears in the center point, and that decreases along both sides. In contrast, the long-D Gasket maintains a more uniform distribution of contact pressure in the contact area. This uniformity can improve the sealing efficiency if the contact length does not change anymore. And it can also make the interface leakage calculation realized conventionally for designing and optimizing the sealing structure of the Gasket-BPP in PEMFCs.

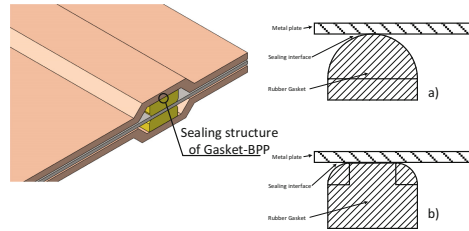


Fig. 7. Gasket-BPP sealing structures with different cross-sections: a) semicircle cross-section and b) long-D cross-section

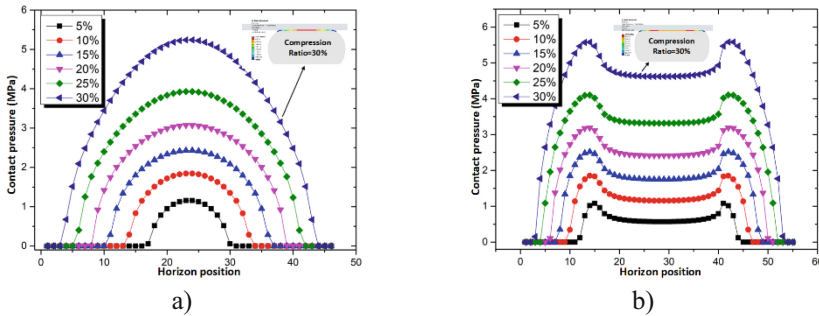


Fig. 8. The contact pressure of the Gaskets with different cross-sections: a) the semicircle Gasket and b) the long-D Gasket

Figure 9 shows the contact lengths of the Gaskets. The contact length is going to increase with the increase of the Gasket compression ratio. But there will be a fluctuation if the compression is larger than 20%, which means the influence of the Gasket compression ratio on the sealing contact behavior is not linear and unstable.

The interface leakage rates of the Gasket-BPP sealing can be calculated by the above results, as shown in Fig. 10.

It can be seen in Fig. 10, the interface leakage rate of the Gasket-BPP is going to decrease constantly with the Gasket compression increasing, which is inconsistent with the conclusions of the previous research. While the interface leakage rate results calculated by the multi-scale model maintain a stable and slower slope and decreases more gently if the compression ratio is larger than 20%. That means the interface leakage

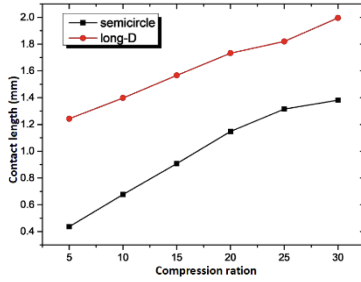


Fig. 9. The contact length of the Gasket under different compression ratio

of the Gasket-BPP exists under any constrains and it could not be controlled if just increasing the compression ratio.

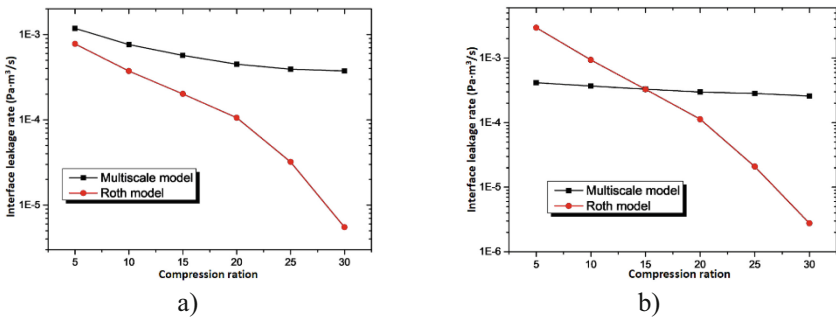


Fig. 10. The interface leakage rates under different compression ratios: a) the semicircle Gasket and b) the long-D Gasket

Besides that, the curves obtained by the Roth model are similar whatever the sealing structure of the Gasket-BPP interface is, which means the model has no capacity to perceive differences in the sealing structures. The most likely reason for this phenomenon is the traditional model takes the average contact pressure as the input instead of the real distribution of that, which is non-uniform on the contact surface. In contrast, the influence of the sealing structure on the interface leakage rate of the Gasket-BPP is reflected in the multi-scale model better, and this is more consistent with the actual experiences.

3 Conclusions

Based on the numerical simulation method of PEMFC rubber seal-metal bipolar plate interface leakage rate, this paper studies the scale coefficient in the multi-scale model of interface leakage rate and calculates and analyzes the interface leakage rate of Gasket-BPP seal under different cross-sectional shapes. By comparison, the validity and accuracy of the multi-scale model of the PEMFC interface leakage rate are verified.

1. Based on the proportional relationship between the interface leakage rate and the interface leaking channel volume the function $C(x,y,z)$ had been established to settle the scale coefficient in the interface leakage rate multi-scale model by analyzing the power of the magnification.
2. By comparing with the traditional interface leakage rate prediction model, the reliability and accuracy of the multi-scale model are verified. It can be found that the Gasket compression ratio is limited to reduce the interface leakage of the Gasket-BPP in the multi-scale model. And the multi-scale model has a higher sensitivity to the sealing structure on calculating the interface leakage rate.
3. The Gasket with a long-D cross-section obtains a longer contact length, more even distribution of the contact pressure, and the lower interface leakage.

Acknowledgements. This research is supported by the cooperative project of Tongji university-Legend New Energy Technology (Shanghai) Co., Ltd (NO. LZDD230121-M).

References

1. Leng, Y. et al.: Stainless steel bipolar plates for proton exchange membrane fuel cells: materials, flow channel design and forming processes. *J. Power Sour.* **451**, 227783 (2020)
2. Xu, Z. et al.: Fabrication of micro channels for titanium PEMFC bipolar plates by multistage forming process. *Int. J. Hydrogen Energy* **46.19**, 11092–11103 (2021)
3. Kim, H.-K. et al.: Evaluation of O-ring stresses subjected to vertical and one side lateral pressure by theoretical approximation comparing with photoelastic experimental results. *Eng. Failure Anal.* **16.6**, 1876–1882 (2009)
4. Kulkarni, N. et al.: The effect of non-uniform compression on the performance of polymer electrolyte fuel cells. *J. Power Sour.* **521**, 230973 (2022)
5. Pacheco, C., et al.: Design, simulation and experimental characterization of a high-power density fuel cell. *Int. J. Hydrogen Energy* **46(51)**, 26197–26204 (2021)
6. Wang, Z. et al.: Elastic leak for a better seal. *J. Appl. Mechan.* **82.8** (2015)
7. Husar, A., Serra, M., Kunusch, C.: Description of gasket failure in a 7 cell PEMFC stack. *J. Power. Sour.* **169(1)**, 85–91 (2007)
8. Xu, Q. et al.: Effects of gas permeation on the sealing performance of PEMFC stacks. *Int. J. Hydrogen Energy* **46.73**, 36424–36435 (2021)
9. Guan, D. et al.: Quantitative modeling and bio-inspired optimization the clamping load on the bipolar plate in PEMFC. *Energy* **263**, 125951 (2023)
10. Liang, P. et al.: Structure failure of the sealing in the assembly process for proton exchange membrane fuel cells. *Int. J. Hydrogen Energy* **42.15**, 10217–10227 (2017)
11. Ren, X., Wu, C., Zhou, P.: Gas sealing performance study of rough surface. *Jixie Gongcheng Xuebao (Chinese J. Mech. Eng.)* **46.16**, 176–181 (2010)
12. Huang, X. et al.: A mechanism leakage model of metal-bipolar-plate PEMFC seal structures with stress relaxation effects. *Int. J. Hydrogen Energy* **47.4**, 2594–2607 (2022)
13. Lyu, X.K., Yang, W.J., Xu, J.L.: The influence of characteristic of rough surface on gas sealing performance in seal structure. *J. Mech. Eng* **51**, 23 (2015)
14. Persson, B.N.J.: Theory of rubber friction and contact mechanics. *The J. Chem. Phys.* **115.8**, 3840–3861 (2001)
15. Jiancheng, S.H.I., et al.: On the multi-scale contact behavior of metal rough surface based on deterministic model. *J. Mech. Eng.* **53(3)**, 111–120 (2017)
16. Yang, Z. et al.: Multi-scale dimensionless prediction model of PEMFC sealing interface leakage rate based on fractal geometry. *Int. J. Hydrogen Energy* **48(13)**, 5276–5287 (2023)

Author Index

A

Aboimov, Mikhail A. 234
Ai, Xiaomeng 195, 217
Araya, Samuel Simon 226

B

Bao, Wei 91
Bolshakov, Konstantin G. 234

C

Cai, Yi 136
Cai, Zhen 108
Cao, Zhicheng 325, 335
Chen, Fengxiang 150
Chen, Huipeng 59, 206
Chen, Juexiao 250
Chen, Ping 59, 206
Chen, Rui 76
Chen, Xiaolu 91
Cheng, Ming 304
Cheng, Xiang 174
Cheng, Zhiguo 325, 335

D

Dai, Jianfeng 69
Deng, Huichao 243
Dong, Yan 52
Du, Chang 250, 262
Duan, Wei 69

F

Fang, Jiakun 195, 217
Fang, Yue 325
Fang, Zhifei 243

G

Gao, Dingyun 99
Gao, Yuan 7
Gao, Yuzhe 126
Gu, Ziheng 250, 262

Guo, Xiumei 20
Guo, Yafeng 150

H

Han, Yisong 186
He, Zhixue 304, 315
Hou, Yongping 7
Hou, Zhipeng 150
Hu, Kewei 217
Huang, Danji 217
Huang, Xing 108
Huo, Miaomiao 91
Huo, Yanda 69

J

Jiang, Jintao 69
Jiang, Lijun 20
Jiaying, Liang 288

K

Kondratyev, Dmitry G. 234

L

Li, Congxin 59
Li, Duankai 159
Li, Feiqiang 108
Li, Ruitao 28, 275
Li, Shihao 1
Li, Yongyi 136
Li, Yu 150
Li, Zhinian 20
Liang, Bowen 7
Liang, Yingqi 136
Liang, Yonghao 275
Lin, Hanchen 166
Lin, Jin 44, 174
Lin, Ling 91
Lin, Weikang 262, 275
Liso, Vincenzo 226
Liu, Bin 52

Liu, Guozhu 126
 Liu, Wei 166
 Liu, Weiliang 174
 Liu, Xiaomin 91
 Liu, Ye 1
 Lu, Ang 217
 Lu, Yao 126
 Luo, Wenhua 59
 Lv, Hong 99

M

Ma, Hongcan 52
 Ma, Tiancai 28, 250, 262, 275
 Matrenin, Vladimir I. 234
 Mo, Tiande 150

N

Ni, Wei 304, 315
 Ni, Zhonghua 1

P

Pan, Dongting 59
 Pang, Cong 315
 Pei, Fenglai 150
 Peng, Yuanting 76

Q

Qi, Jinxuan 250
 Qi, Jixuan 262
 Qi, Ruomei 44
 Qian, Weijie 174

S

Sang, Shang 304
 Sha, Liandong 44, 174
 Shi, Hongqiang 20
 Song, Ke 108
 Stikhin, Alexander S. 234
 Sun, Yongwen 99

W

Wan, Yanming 166
 Wang, Haolin 28

Wang, Jiawei 186
 Wang, Juan 91
 Wang, Liming 126, 206
 Wang, Shumao 20
 Wang, Zhen 76
 Wei, Huanxia 7
 Wei, Wei 1
 Wu, Zhen 69

X

Xu, Hong 186
 Xu, Yekai 206
 Xu, Zengshi 76
 Xu, Zishun 28
 Xue, Mingzhe 186

Y

Yan, Yan 1
 Yang, Cheng 315
 Yang, Yanmei 91
 Yang, Yupeng 126
 Yang, Zhen 325, 335
 Yao, Naiyuan 28, 275
 Yao, Riwu 69
 Yuan, Baolong 20
 Yuan, Kun 275
 Yuanfang, Wu 20

Z

Zhang, Bo 206
 Zhang, Cunman 99, 186
 Zhang, Guorui 117, 159
 Zhang, Mingjun 174
 Zhang, Tong 7
 Zhang, Yan 166
 Zhao, Hao 69
 Zhong, Zhaoda 226
 Zhong, Zhiyao 195, 217
 Zhou, Jiaxu 243
 Zhu, Mengshu 195
 Zhu, Shaopeng 59, 206
 Zhu, Wenfeng 325, 335